Topics in Applied Physics
Volume 105

Topics in Applied Physics

Topics in Applied Physics is a well-established series of review books, each of which presents a comprehensive survey of a selected topic within the broad area of applied physics. Edited and written by leading research scientists in the field concerned, each volume contains review contributions covering the various aspects of the topic. Together these provide an overview of the state of the art in the respective field, extending from an introduction to the subject right up to the frontiers of contemporary research.
Topics in Applied Physics is addressed to all scientists at universities and in industry who wish to obtain an overview and to keep abreast of advances in applied physics. The series also provides easy but comprehensive access to the fields for newcomers starting research.
Contributions are specially commissioned. The Managing Editors are open to any suggestions for topics coming from the community of applied physicists no matter what the field and encourage prospective editors to approach them with ideas.

Managing Editor

Dr. Claus E. Ascheron

Springer-Verlag GmbH
Tiergartenstr. 17
69121 Heidelberg
Germany
Email: claus.ascheron@springer.com

Assistant Editor

Dr. Werner Skolaut

Springer-Verlag GmbH
Tiergartenstr. 17
69121 Heidelberg
Germany
Email: werner.skolaut@springer.com

Karin M. Rabe Charles H. Ahn
Jean-Marc Triscone (Eds.)

Physics of Ferroelectrics

A Modern Perspective

With 129 Figures and 24 Tables

Springer

Professor Karin M. Rabe

Department of Physics and Astronomy
Rutgers University
136 Frelinghuysen Road, Piscataway
NJ 08854-8019, USA
rabe@physics.rutgers.edu

Professor Charles H. Ahn

Departements of Applied Physics and Physics
Yale University
P. O. Box 208284, New Haven
CT 06520-8284, USA
charles.ahn@yale.edu

Professor Jean-Marc Triscone

Condensed Matter Physics Department
University of Geneva
24 Quai Ernest Ansermet
CH-1211 Geneva 4, Switzerland
jean-marc.triscone@physics.unige.ch

Library of Congress Control Number: 2006938273

Physics and Astronomy Classification Scheme (PACS):
77.80.-e,77.84.-s,68.35.-p,81.15.-z,85.50.-n

ISSN print edition: 0303-4216
ISSN electronic edition: 1437-0859
ISBN 978-3-540-34590-9 Springer Berlin Heidelberg New York

Typesetting: DA-TEX · Gerd Blumenstein · www.da-tex.de
Production: LE-TEX Jelonek, Schmidt & Vöckler GbR, Leipzig
Cover design: WMXDesign GmbH, Heidelberg

Printed on acid-free paper 57/3180/YL 5 4 3 2 1 0

Preface

During the past two decades, revolutionary breakthroughs have occurred in the understanding of ferroelectric materials, both from the perspective of theory and of experiment. First principles approaches, including the Berry phase formulation of ferroelectricity, now allow accurate, quantitative predictions of material properties, and single crystalline thin films are now available for fundamental studies of these materials. In addition, the need for high dielectric constant insulators and nonvolatile memories in semiconductor applications has motivated a renaissance in the investigation of these materials.

In this book, we present the modern physics of ferroelectricity in oxides through a set of chapters on topics that collectively represent some of the key advances and innovations over the last thirty years. After the introductory chapter, the next four contributions by *Resta* and *Vanderbilt*, *Chandra* and *Littlewood*, *Rabe* and *Ghosez*, and *Spaldin* together cover the main recent theoretical developments in the field. In contrast, the following three contributions by *Posadas* et al., *Lichtensteiger* et al. and *Paruch* et al. comprise a highly selective presentation of experimental developments, giving illustrations of what can be achieved using the high quality epitaxial oxide films that can be obtained using the advanced deposition techniques described in the contribution by *Posadas* et al. We have chosen to focus on this particular area, as it is not possible in one book to cover the entire large body of recently obtained results on new materials using new experimental techniques. At the end of this book, the interested reader will find handy tables containing key material properties and useful substrates and growth methods.

We would like to emphasize that this book should not be regarded as covering the same breadth of subject matter as the classic book by *Lines* and *Glass* (*Principles and Applications of Ferroelectrics and Related Materials*) which so definitively codified the knowledge of the first "Golden Age" of research in ferroelectric oxides, but rather as a complement that brings the reader from that sound foundation up to the present. Completely new topics include the modern theory of polarization (*Resta* and *Vanderbilt*), first principles studies of ferroelectrics (*Rabe* and *Ghosez*), and the novel physics of nanoscale ferroelectric structures and probes, including ultrathin ferroelectric films and short-period superlattices (*Posadas* et al., *Lichtensteiger* et al., *Paruch* et al. and Appendix B). New perspectives transform the presentation of the phenomenological Landau-Devonshire theory in the contribution

of *Chandra* and *Littlewood* and in Appendix A, and the discussion of the relationship between ferroelectricity and ferromagnetism by *Spaldin*. Indeed, in this latter contribution, we will see that reexamination of the physics of magnetic ferroelectrics in the current context has led to a lively renaissance for research in the design, synthesis, characterization and theory of so-called "multiferroic" materials.

June, 2007

Rutgers University, Piscataway NJ, USA — *Karin M. Rabe*
Yale University, New Haven CT, USA — *Charles H. Ahn*
University of Geneva, Geneva, Switzerland — *Jean-Marc Triscone*

Contents

Modern Physics of Ferroelectrics: Essential Background

Karin M. Rabe[1], Matthew Dawber[2], Céline Lichtensteiger[2], Charles H. Ahn[3], and Jean-Marc Triscone[2]

[1] Department of Physics and Astronomy, Rutgers University, 136 Frelinghuysen Road, Piscataway, NJ 08854-8019, USA
rabe@physics.rutgers.edu
[2] Condensed Matter Physics Department, University of Geneva, 24 quai Ernest Ansermet, CH-1211 Geneva 4, Switzerland
jean-marc.triscone@physics.unige.ch
[3] Departments of Applied Physics and Physics, Yale University, New Haven CT 06520-8120, USA
charles.ahn@yale.edu

Abstract. Principles of ferroelectricity and information about ferroelectric materials and their applications are reviewed. The characterization of ferroelectric behavior through measurement of electrical hysteresis is discussed in detail. The main families of ferroelectric oxides, including perovskite compounds and solid solutions, lithium niobate, layered oxides, magnetic ferroelectric oxides, and electronic ferroelectrics are presented and their crystal structures and polarizations given. The effects of pressure and epitaxial strain on perovskites are described. Recent advances in the understanding of ferroelectricity in thin films, superlattices and nanostructures are mentioned. Finally, an overview of applications of feroelectric materials, both established applications and those under development, is included.

1 Introduction

A ferroelectric is an insulating system with two or more discrete stable or metastable states of different nonzero electric polarization in zero applied electric field, referred to as "spontaneous" polarization. For a system to be considered ferroelectric, it must be possible to switch between these states with an applied electric field, which changes the relative energy of the states through the coupling of the field to the polarization $-\boldsymbol{E}\cdot\boldsymbol{P}$.

The concept of electric polarization is thus key to an understanding of ferroelectricity. For a finite system, electric polarization is straightforwardly defined as the dipole moment, obtained from the charge density, divided by the system volume (though it should be noted that for ultrasmall systems, the boundaries of the system are not sharp). For an infinite crystal, the definition of polarization as a bulk property long proved considerably more difficult to formulate. The resolution, suggested by Resta, King-Smith and Vanderbilt and now generally referred to as the "modern theory of polarization," is to identify the polarization as an integrated current through a transformation

K. Rabe, C. H. Ahn, J.-M. Triscone (Eds.): Physics of Ferroelectrics: A Modern Perspective, Topics Appl. Physics **105**, 1–30 (2007)

from one variant to another, the result being expressed as a Berry phase. This focus on the induced current has the additional advantage of making a direct connection to the electrical and optical means of measuring polarization. Another novel aspect of this formalism is that polarization is not a vector property, but rather a lattice $\boldsymbol{P}_0 + 2e\boldsymbol{R}/\Omega$, where $\boldsymbol{R}$ is a vector of the crystal Bravais lattice and Ω is the volume of the unit cell. An intuitive structure-based picture is provided by a reformulation of the Berry-phase expression in terms of the centers of crystalline Wannier functions. These ideas and their application to ferroelectrics are more fully explained in the contribution by *Resta* and *Vanderbilt*.

In this overview, we present an introduction to ferroelectric materials with the information needed as background for reading the subsequent chapters of this book. We only include the most essential points, with special attention to those not available elsewhere; for more comprehensive background we refer the reader to the classic book by *Lines* and *Glass* [1], which is still very useful despite its copyright date of 1977, and to the invaluable compilations of data from the literature in the series of volumes of *Landolt Börnstein* [2,3]. We start by discussing the characterization of ferroelectric behavior through measurement of polarization switching hysteresis loops. This is followed by a discussion of the relation between ferroelectricity and crystal structure (more generally, atomic arrangement), and then a description of the crystal structures, electric polarizations and phase diagrams of the most commonly studied ferroelectric oxides; this information will be a handy reference as these materials are discussed in the various chapters of this book. Finally, we give up-to-date perspectives on two areas in which there has been rapid developments in recent years: (1) finite-size effects in ferroelectric thin films, superlattices and nanostructures, and (2) technological applications of ferroelectric oxides.

2 Switching and Hysteresis Loops

As mentioned above, a defining property of ferroelectricity is the switching between different metastable states by the application and removal of an electric field. The mechanism of switching is understood to take place on scales longer than the unit-cell scale, and generally to require the growth and shrinking of domains through the motion of domain walls, as will be discussed in more detail in the contribution by *Lichtensteiger*, *Dawber* and *Triscone*, and the contribution by *Paruch*, *Giamarchi* and *Triscone*. While the "small distortion" crystallographic criterion discussed in the next section should generally allow switching, the observation of an electric hysteresis loop (Fig. 1) is considered necessary to establish ferroelectricity.

In its canonical form, the ferroelectric P–E hysteresis loop is symmetric and the remnant polarization and coercive fields are easily defined and extracted. There are, however, a number of potential pitfalls in the accurate

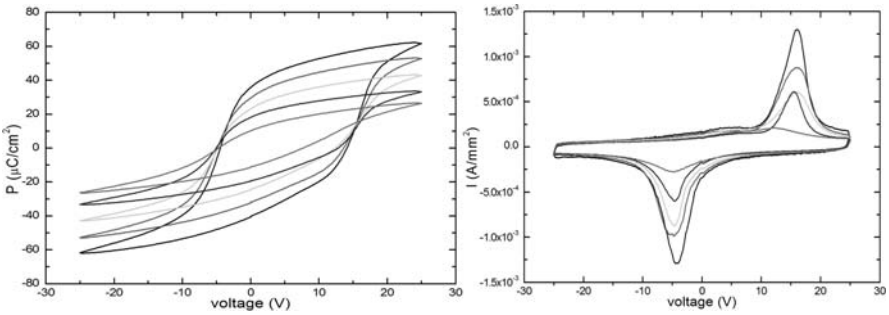

Fig. 1. (**a**) Hysteresis loops for a number of $PbTiO_3/SrTiO_3$ superlattice samples with different polarizations. (**b**) The corresponding current–voltage loops (obtained during voltage sweeps in which the voltage is cycled, in contrast to leakage current I–V curves that measure current when the voltage is held constant for a period of time) from which the polarization–voltage hysteresis loops are obtained, showing clear switching peaks at the coercive voltage of the sample

performance of this measurement. The starting point for any measurement of this kind is to realize that the electrical properties of a ferroelectric film can only be measured when it is fabricated as a device (most typically a capacitor). Thus, any measurement actually involves a whole system, with electrodes, wires and interfaces, and sometimes it is these other components of the system that dominate the electrical response, rather than the intrinsic properties of the material of interest. In this section we briefly cover the key ways in which ferroelectric hysteresis measurements are made, with special attention to the potential errors that can be made and the methods that can be used to avoid them.

The Sawyer–Tower circuit [4], the original method for measuring ferroelectric hysteresis, is simple in concept. It is essentially just a capacitance bridge, relying on the fact that two capacitors in series should have the same charge. One of these capacitors is comprised of the ferroelectric, and the other is a standard capacitor with a well-defined capacitance. The potential across the standard capacitor is plotted on the y-axis, and the ac voltage applied to the ferroelectric sample is plotted on the x-axis in the X–Y mode of an oscilloscope. The standard capacitor should be chosen to have a large capacitance so that the potential across it is small enough not to affect the potential across the ferroelectric sample. In the ideal case where the current flowing during this measurement is purely displacive, this measurement will give accurate values of the ferroelectric polarization. A simple implementation of this circuit, along with a description of a simple classroom experiment to observe ferroelectric hysteresis in KNO_3, is described in [5].

Unfortunately, especially when they are grown as thin films, ferroelectrics are seldom perfectly resistive, and a host of factors, such as grain boundaries, defects, conduction processes such as Schottky injection or Fowler–Nordheim

tunneling, can allow significant leakage currents to exist. These can make it difficult to tell the difference between a sample that is simply a linear dielectric and one that is truly ferroelectric. An ideal linear dielectric measured in a Sawyer–Tower circuit gives a straight line, as the charge on the capacitor follows the applied voltage. An ideal resistor gives an ellipse in the case of an applied sine wave, or a football shape when a triangular wave is applied. Unfortunately, one sometimes measures near the RC time constant of the sample, and the result is a tilted ellipse or football, which is not very different from the measurement observed for an undersaturated hysteresis loop. Crucially, the zero-field intercept of the polarization axis is NOT a ferroelectric polarization; it just means the sample is leaky. The problem can be even more subtle in the case where the sample is a leaky nonlinear dielectric, which can give the appearance of saturation of the polarization, when in fact it is simply a reduction of the dielectric constant material at high fields. It is also common to have samples that, while ferroelectric, are also quite leaky, leading to rounding of the top of the loop and an overestimate of the value of the remnant polarization. It is important to note also that the leakage current in ferroelectric thin films is usually not linear, and thus a sample may be quite insulating at low applied fields (and have a low dielectric loss), but be highly conducting when higher fields are applied in the switching experiment. Further discussion of these and other artifacts can be found in [6].

There are a number of methods that can be used to avoid these problems. Measurements can be made at several different frequencies, as artifacts are usually highly frequency dependent. If a sample only appears to be ferroelectric in a narrow range of measurement frequency it is probably not ferroelectric. Secondly, it is useful to look at the switching current, as done by current commercial ferroelectric testers, for example the Aixacct TF Analyzer or the Radiant Precision Pro, though it is equally possible to do this with home-built setups. If the sample is ferroelectric, switching peaks are visible in the I–V curve measured during the switching process (Fig. 1). It should be noted, though, that the standard hysteresis measurement provided by these testers will still display the tilted football shape if the sample is a leaky dielectric.

A number of options are available to distinguish ferroelectric switching from artifacts. For example, applying a series of voltage pulses and measuring the current transients that result from them allows for separation of the different components of the electrical response of a ferroelectric device. The PUND (positive up negative down) measurement is especially useful for this purpose. In this measurement a train of five pulses is sent. First, an initial pulse (Pulse 0) to polarize the sample in a definite polarization state is sent. Pulse 1 then switches the polarization to the other direction. Pulse 2 is then applied in the same direction as Pulse 1 and so should not switch the sample. Pulse 3 and Pulse 4 are like Pulses 1 and 2 but in the opposite direction. In the example shown in Fig. 2, the switching phase can be seen as the voltage is increased. Following this the voltage is held constant, and if the leakage is

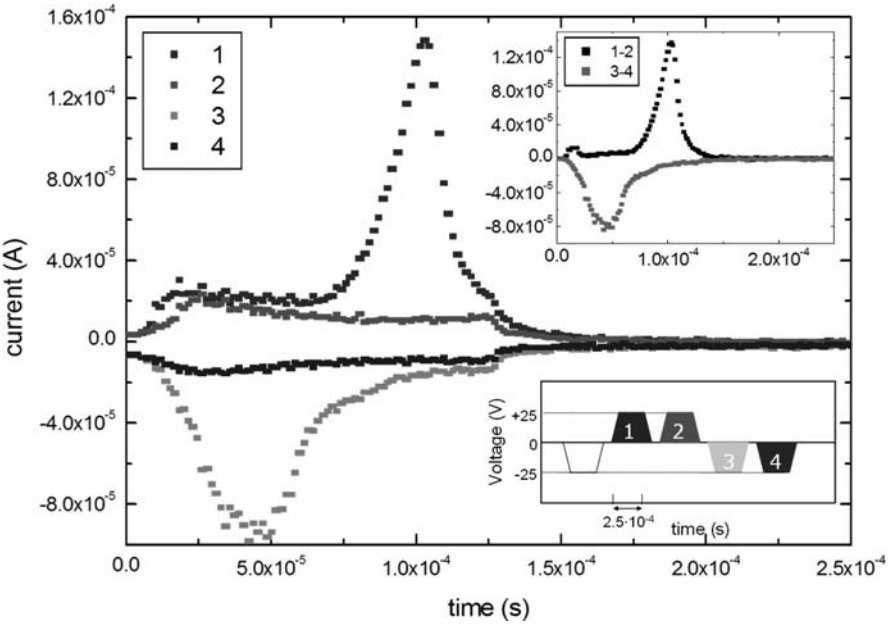

Fig. 2. Result of a PUND measurement on a ferroelectric sample. The *lower inset* shows the pulse train applied to the sample. In this case the delay time between pulses was 1 s. The *upper inset* shows the difference between the current for the 1st and 2nd pulse, and also the 3rd and 4th pulse. This corresponds to the charge that is switched when the polarization state of the sample is reversed. This measurement was performed on a $PbTiO_3/SrTiO_3$ superlattice

low, as is the case in this sample, no current is seen. A leaky sample would show a constant current in this phase of the measurement. For Pulse 2, which is applied after a certain delay time, switching will not be seen in the case that the polarization is stable. In this case the current measured is due to the charging arising from the linear component of the dielectric response. Sometimes a switching peak may be observed when Pulse 2 is applied, which shows that while there does appear to be a ferroelectric polarization, it is not stable against backswitching, either to the opposite polarization, or to a polydomain state, with lower or no net polarization. In this case it is interesting to vary the delay between pulses, which allows one to determine the relaxation time of the polarization. A recent example of this approach can be seen in [7].

To determine the switched ferroelectric polarization that is stable for the chosen delay time, one subtracts the 2nd curve from the 1st and takes the integral of this switching current to find the switched polarization. For most devices the value of most interest is that of the polarization that can be switched and remain switched for a long period of time.

Comparison of numbers obtained from these kinds of experiments with results obtained from theoretical first-principles calculations is interesting, but requires some care. For example, if a calculation does not take into account domain formation or other extrinsic factors that might affect the stability of a net polarization on a device, should one compare the polarization obtained from it to the stable polarization one measures in the PUND experiment, or rather to the maximum polarization that can be switched by using a very short delay time between pulses? One may think that it is the latter, but it is also possible that in this case the charge that remains on the device is not because of ferroelectricity, but rather because insufficient time was given for the charge put onto the capacitor due to the linear charging effect to discharge. Measurements done over a large parameter space (e.g., frequency, field, delay time between pulses, temperature, etc.) allow meaningful comparisons to be made.

3 Crystallographic Signature of Ferroelectricity

In all known ferroelectric crystals, the spontaneous polarization is produced by the atomic arrangement of ions in the crystal structure, depending on their positions, as in conventional ferroelectrics, or on charge ordering of multiple valences, as in electronic ferroelectrics. A nonzero spontaneous polarization can be present only in a crystal with a polar space group. However, for ferroelectricity it must also be possible to switch between different variants with an applied electric field, which implies that many polar crystals, a good example being wurtzite-structure insulators, are not considered ferroelectric. One condition that ensures the presence of discrete states of different polarization and enhances the possibility of switching between them with an accessible electric field is that the crystal structure can be obtained as a "small" symmetry-breaking distortion of a higher-symmetry reference state. This involves a polar displacement of the atoms in the unit cell, which may be coupled to nonpolar atomic displacement patterns and to the corresponding strain; the latter coupling can be quite strong in some ferroelectric oxides, producing piezoelectric behavior and rich pressure–temperature and epitaxial strain phase diagrams, as discussed for perovskite oxides below. The magnitude of the spontaneous polarization can be estimated using Born effective charges Z^*e and displacements u from the reference structure as $\frac{1}{\Omega}\sum Z^*eu$, where Ω is the volume of the unit cell; this linearized approximation in many cases gives a value close to the full Berry-phase or Wannier-function result. In our overview of ferroelectric oxides below, we will include the high-symmetry nonpolar and low-symmetry polar structures, with information about the polarization of the latter, both measured and computed, as available.

In most ferroelectrics, there is a phase transition from the ferroelectric state, with multiple symmetry-related variants, to a nonpolar paraelectric phase, with a single variant, with increasing temperature. In most of these

cases the high-symmetry reference structure is the same as the crystallographic structure observed in the paraelectric phase. Measured ferroelectric transition temperatures range from very low (1 K) to very high (over 1000 K); for the latter systems there is the possibility that the material melts before the transition temperature is reached. The symmetry-breaking relation between the high-symmetry paraelectric structure and the ferroelectric structure is consistent with a second-order transition, and can be described with a Landau theory where polarization is the primary order parameter (discussed in detail in Chap. 4). This analysis naturally leads to the prediction that the dielectric susceptibility diverges at the transition. From there, the link is made, through the Lyddane–Sachs–Teller relation, to the vanishing frequency of a polar phonon, which is the central idea of the soft-mode theory of ferroelectrics [8, 9]. Indeed, observation of the temperature dependence of polar phonons was a key ingredient in the great progress made in understanding the physics of ferroelectricity in the 1960s and 1970s. Phonon spectroscopy continues to play a central role in the characterization of ferroelectric transitions, both via neutron scattering and optical spectroscopy [10, 11]. The soft-mode theory is illuminating, despite the fact that in many perovskite ferroelectrics, the transition is weakly first order (that is, there is a discontinuity in polarization and structural parameters, and a latent heat, at the transition), which may be the result of polarization–strain coupling.

Landau theory analysis, with polarization as the primary order parameter, suggests a comparison to magnetic phase transitions. Indeed, Landau analysis allows also the consideration of a broader range of "improper" ferroelectrics where polarization is a secondary order parameter coupled to a primary nonpolar lattice distortion or to a magnetic order parameter; these have proved to be especially important in the study of magnetic ferroelectrics.

The principle that ferroelectric structure represents a small distortion of a high-symmetry reference phase is a powerful one. It has been developed into a structural criterion for the identification of ferroelectricity in the crystallographic database by *Abrahams* [12], who has also proposed an empirical relation between the magnitude of the displacements and the ferroelectric transition temperature. This approach has been further developed and applied in, for example, [13, 14]. This principle also provides a systematic approach for first-principles studies, described in the contribution by *Rabe* and *Ghosez*, where the phonons of the high-symmetry reference structure are computed and the unstable modes used as guides to identify energy-lowering distortions [15].

Most of the information about crystal structure of ferroelectrics has been experimentally obtained from X-ray and neutron-diffraction structural determinations. These yield the average crystallographic structure. Studies of diffuse scattering [16] and local probes, such as pair-density correlation function (PDF) analysis [17] and extended X-ray absorption fine-structure spectroscopy (EXAFS) [18] reveal that local distortions and fluctuations are also very important features of the crystal structure. As will be discussed in the

contribution by *Rabe* and *Ghosez*, first-principles predictions of the crystal structure and polarization can be a valuable complement to experimental structural determinations to obtain atomic-scale information about atomic arrangements and electronic states in these complex oxides.

4 Materials

In this section, we provide an overview of the main families of ferroelectric oxides. While ferroelectricity was discovered in hydrogen-bonded materials, Rochelle salt and subsequently KDP, the discovery in 1949 of ferroelectricity in the much simpler, nonhydrogen-containing, perovskite oxide $BaTiO_3$ dramatically changed the physical understanding of this phenomenon. $BaTiO_3$ is the prototypical example of the now very large and extensively studied perovskite oxide family, which includes not only perovskite compounds, but also ordered and disordered solid solutions. The relative simplicity of the perovskite structure led to a deeper understanding of the origin of ferroelectricity and quantitative phenomenological and first-principles modeling, which will be described in the following section. Additional families of important ferroelectric materials are closely related to the perovskites, being intergrowths of perovskite layers with other oxides. Finally, we will refer to some additional ferroelectric oxide structural families that are not related to the perovskites.

4.1 Perovskite Oxides

The most studied family of ferroelectric oxides is that known as the *perovskite* oxides (from the mineral perovskite $CaTiO_3$). This is a very large family of composition ABO_3, where A and B each represent a cation element or mixture of two or more such elements or vacancies. The physical properties of the entire family are extremely diverse: depending on the composition and cationic ordering, they can be metallic or insulating and exhibit many different types of structural and magnetic order. The perovskite oxides that are ferroelectrics in bulk crystalline form are a subfamily; other related compounds might have a tendency to a ferroelectric instability that is, however, not manifest in the bulk crystal due to the dominance of other, nonferroelectric, competing types of order.

The ideal perovskite structure, which can be taken as the high-symmetry reference structure and is the structure of the high-temperature paraelectric phase for most ferroelectric perovskite oxides, has space group $Pm\bar{3}m$, with a simple cubic lattice and a basis of 5 atoms. The following description of the perovskite structure is taken from [19]. As shown in Fig. 3, if the A atom is taken at the corner of the cube, the B atom is at the center and there is an oxygen at the center of each face; alternatively, if the B atom is taken at the corner, the A atom is at the center and O atoms are located at the midpoint of each edge.

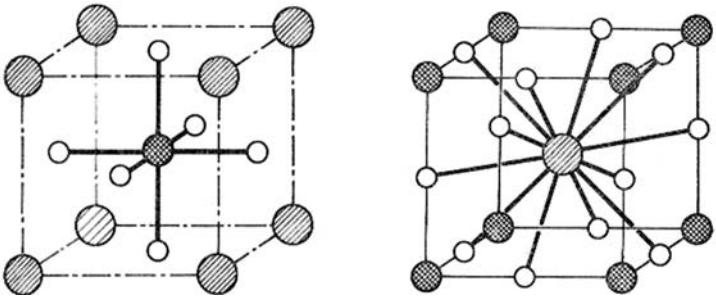

Fig. 3. Two different views of the unit cell of the ABO_3 ideal cubic perovskite structure. The B atom (*grilled pattern*) is at the center of an octahedron composed of oxygen atoms (*white pattern*). The A atom (*dashed pattern*) has 12 oxygen first neighbors. From [20]

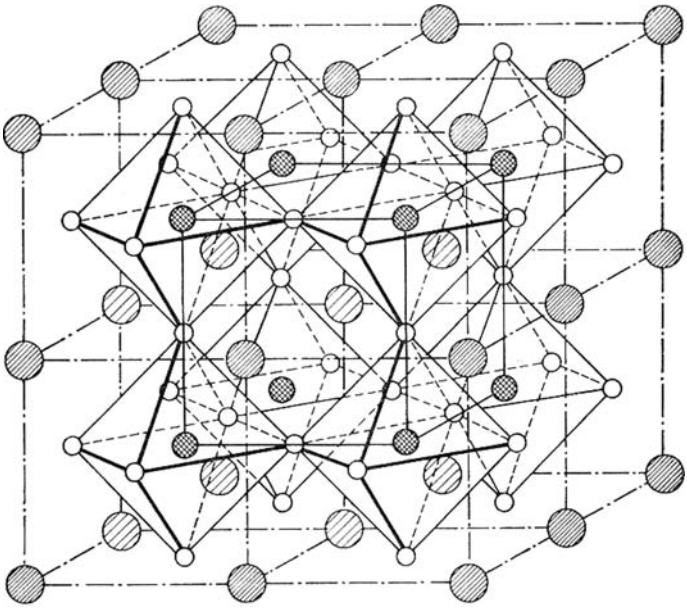

Fig. 4. Another view of the ABO_3 ideal cubic perovskite structure. From [20]

As is shown more clearly in Fig. 4, in the perovskite structure, the B atom is at the center of 6 oxygen first neighbors, arranged at the corners of a regular octahedron. The octahedra are linked at their corners into a 3-dimensional simple-cubic network, enclosing large holes that are occupied by A atoms. Each A atom is surrounded by 12 equidistant O atoms. The oxygens have a lower-symmetry coordination environment: each O atom is adjacent to 2 B atoms and 4 A atoms. The structure can also be characterized by the

straight, infinite interpenetrating B–O chains that run in parallel along all three Cartesian directions.

The prevalence of distortions for compounds crystallizing in the perovskite structure is related to the structural frustration of the cubic perovskite structure regarded as an ionic solid. An empirical criterion for the stability of the perfect perovskite-type structure was put forward by Goldschmidt (1926), based on the rules he had previously derived for ionic binary compounds. His model is based on the concept of ionic radius and the following rules: (i) a cation will be surrounded by as many anions as can touch it, but no more; (ii) all the anions must touch the cations and the anion–cation distance is obtained as the sum of their ionic radii. The perovskite structure is fully determined by the size of the oxygen octahedra containing the B atoms, while the A atoms must fit the holes between the octahedra. Following the rules of Goldschmidt, this condition provides an ideal relation between ionic radii:

$$r_{\mathrm{A}} + r_{\mathrm{O}} = \sqrt{2}(r_{\mathrm{B}} + r_{\mathrm{O}}). \tag{1}$$

In the ideal cubic perovskite structure, this will in general not be satisfied. The deviation can be measured through a tolerance factor t defined as follows:

$$t = \frac{r_{\mathrm{A}} + r_{\mathrm{O}}}{\sqrt{2}(r_{\mathrm{B}} + r_{\mathrm{O}})}. \tag{2}$$

Goldschmidt has shown that the perovskite structure is formed when the condition expressed by (1) is satisfied ($t \approx 1$). When $t > 1$, the structure is imposed by the A–O distance and the B atom is too small for the oxygen octahedron so that the structure will develop a small polar distortion, as in $BaTiO_3$. Conversely, when $t < 1$, the A atom is small in comparison to the hole between the oxygen octahedra: the A atom cannot effectively bond with all 12 neighboring O atoms. If t is only slightly less than one, rotations and tilting of the oxygen octahedra will be favored (as in $SrTiO_3$ and $CaTiO_3$); for smaller t the compound will favor a strongly distorted structure with only 6 neighbors for the A atom as in $LiNbO_3$, to be discussed below. If the value of t is very different from unity, then the perovskite-type structures will be unfavorable relative to another of the known ABO_3 structure types, which will not be considered here.

The first perovskite oxide compound identified as being ferroelectric was $BaTiO_3$. The formal valences are +2 for Ba and +4 for Ti, exactly balancing the negative total valence of the oxygens. At high temperature, it has a paraelectric cubic perovskite structure ($Pm\bar{3}m$). At 393 K, it transforms from a cubic phase to a ferroelectric tetragonal phase ($P4mm$), as shown in Fig. 5. This phase remains stable until 278 K, where there is a second transformation to a ferroelectric phase of orthorhombic symmetry ($Amm2$). The last transition occurs at 183 K. The low-temperature ferroelectric phase is rhombohedral ($R3m$). Each transition is accompanied by small atomic displacements, dominated by displacement of the Ti ion relative to the oxygen octahedron network, and a macroscopic strain. In the successive ferroelec-

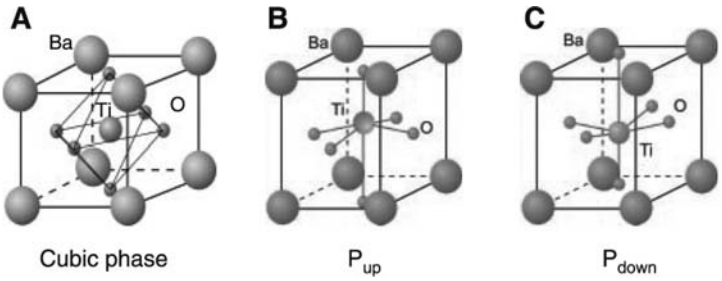

Fig. 5. Crystal structure of the perovskite ferroelectric $BaTiO_3$. (**A**) High-temperature, paraelectric, cubic phase. (**B** and **C**) Room-temperature, ferroelectric, tetragonal phases, showing up and down polarization variants. The atomic displacements are scaled to be clearly visible. From [23]

tric phases, the polar axis is aligned respectively along the <100>, <110> and <111> directions corresponding to the direction of the atomic displacements with respect to their position in the cubic reference structure (a recent structural determination of the ferroelectric phases is reported in detail in [21]). The measured polarizations in the R, O and T phases are $33\,\mu C/cm^2$, $36\,\mu C/cm^2$ and $27\,\mu C/cm^2$, respectively [2, 3]. There is reason to think that the measured polarization in the R phase may be smaller than the true intrinsic polarization, as the first-principles value is $43\,\mu C/cm^2$, which is also more consistent with a geometric $1:\sqrt{2}:\sqrt{3}$ relation [22]. The space group of each of these phases is a subgroup of that of the cubic structure $Pm\bar{3}m$. However, there is no group–subgroup relation for the T−O and O−R transitions, so that from Landau theory they are expected to be first order. $KNbO_3$ is isostructural with $BaTiO_3$, exhibiting the same sequence of phases, though the valences of the cations are +1 (K) and +5 (Nb) rather than +2/+4. The transition temperatures are 701 K (C−T), 488 K (T−O) and 210–265 K (O−R) with spontaneous polarization in the tetragonal phase measured to be about $35\,\mu C/cm^2$ [2, 3].

The structures of a number of other +2/+4 perovskites are closely related. $PbTiO_3$ has a paraelectric–ferroelectric transition at 760 K to a tetragonal $P4mm$ ground state, with a polarization of about $75\,\mu C/cm^2$ measured at room temperature [2,3,24]. The difference in ground state relative to $BaTiO_3$ can be attributed to a difference in the strain–polarization coupling (see the contribution of *Rabe* and *Ghosez* on first-principles calculations). Another difference is that displacement of the Pb ion, in addition to that of Ti, is substantial and contributes signficantly to the spontaneous polarization. Other substitutions of alkaline-earth cations for Ba^{2+} yield structural behavior in general agreement with the tolerance ratio arguments. $SrTiO_3$ exhibits a tendency to a polar instability, with a polar phonon that strongly decreases in frequency as the temperature is decreased. However, at low temperature, the phonon stabilizes and the transition does not in fact occur, leading to the

term "incipient ferroelectric". This stabilization is presumed to be the effect of quantum fluctuations, which is consistent with the observation of a ferroelectric transition in samples with ^{18}O [25]. In addition, there is a structural phase transition at 120 K in which the oxygen octahedra rotate around a cartesian axis (taken as the z-axis) to lower the symmetry to tetragonal $I4/mcm$, called an antiferrodistortive transition [26]. $KTaO_3$ similarly is an incipient ferroelectric, bearing an analogous relation to $KNbO_3$; however, it does not undergo an antiferrodistortive transition and remains cubic down to low temperatures [27]. Ca^{2+} being an even smaller cation than Sr, the tendency to rotational transitions is even greater, and $CaTiO_3$ has a complex 20-atom nonpolar orthorhombic $Pbnm$ structure, common to a number of other perovskites, including $GdFeO_3$ and $DyScO_3$.

Ferroelectricity in the perovskite oxide ferroelectrics can exhibit high sensitivity to changes in strain state, typically produced by external stress. Ferroelectrics such as $Pb(Zr,Ti)O_3$, because of their favorable piezoelectric properties, have a significant technological role in actuators and transducers, the more so as polycrystalline ferroelectric material can be poled by an applied electric field. More recently, colossal piezoelectric response has been observed in single-crystal perovskite solid solutions [28]. It has long been accepted that application of pressure initially reduces the paraelectric–ferroelectric transition temperature, presumably by favoring the more symmetric paraelectric structure [29]. The phase diagrams up to high pressures have recently been the subject of much interest. For $PbTiO_3$, there is theoretical and experimental evidence for a rich phase diagram at sufficiently high pressures [30, 31]. For $BaTiO_3$, the experimentally determined pressure–temperature phase diagram [32] is shown in Fig. 6a. The same R–O–T–C sequence is observed with increasing pressure as with increasing temperature. The phase diagram for epitaxial strain in $BaTiO_3$ thin films is shown in Fig. 6b. The epitaxial strain constraint changes the phase sequence [33]; the orthorhombic phase disappears altogether, and the rhombohedral phase (which appears only at temperatures below those included in Fig. 6b) has a monoclinic distortion imposed by matching to the square surface of the substrate [34]. For $SrTiO_3$, epitaxial strain transforms the bulk paraelectric phase into a ferroelectric [35, 36].

The perovskite oxides readily form solid solutions, many of which show complete miscibility from one endpoint compound to the other. The isoelectronic substitutions, for example Ba/Sr and Ti/Zr, are particularly relevant to the study of ferroelectricity, as the formal valence counting yields insulating behavior across the phase diagram, while the change in the cation can lead to shifts in transition temperatures as well as the appearance or disappearances of particular phases. As a very simple example, the subsitution of Sr for Ba in $BaTiO_3$ lowers the transition temperatures in the phase sequence, with the transitions being suppressed altogether as the $SrTiO_3$ endpoint is approached [37], as shown in Fig. 7a. The details of the diagram in this region are nontrivial and have been the subject of experimental and theoretical investigation (see the contribution of *Rabe* and *Ghosez*).

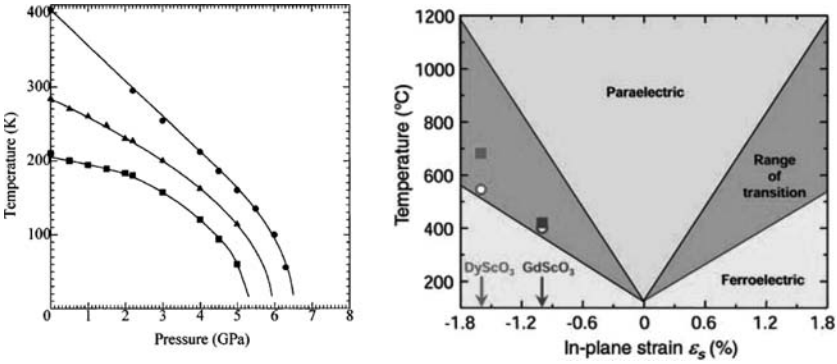

Fig. 6. (**a**) Critical temperature vs. pressure phase diagram of $BaTiO_3$, deduced from X-ray and neutron–diffraction studies. From [32]. (**b**) Expected T_c of (001) $BaTiO_3$ under biaxial inplane strain σ, based on thermodynamic analysis. The green region represents the range (*error bars*) in the predicted T_c resulting from the spread in reported property coefficients for $BaTiO_3$ that enter into the thermodynamic analysis. The data points show the observed σ and T_c values of coherent $BaTiO_3$ films grown by molecular beam epitaxy (MBE) on $GdScO_3$ (*blue circle*) and $DyScO_3$ (*red circle*) substrates and by pulsed laser deposition (PLD) on $GdScO_3$ (*blue square*) and $DyScO_3$ (*red square*) substrates. From [34]

The most extensively studied and technologically important solid solution is $PbZr_{1-x}Ti_xO_3$ (PZT). The standard phase diagram is reproduced in Fig. 7b. The endpoint compound $PbZrO_3$ is an antiferroelectric with 40 atoms per unit cell. However, the antiferroelectric structure is destabilized by even small amounts of Ti substitution to yield two rhombohedral ferroelectric phases. The vertical phase boundary at about 50%, called the morphotropic phase boundary (MPB), is associated with the favorable piezoelectric properties of this system. At the MPB, an applied electric field can easily induce a transition between the rhombohedral and tetragonal phases, with a large associated strain response that is relatively insensitive to temperature. Recently, careful re-examination of the phase diagram showed the presence of a previously unknown monoclinic phase in a very narrow composition range in the vicinity of the MPB [38] (see also the recent review in [40]). Structurally, this phase acts as a bridge between the tetragonal and the rhombohedral phase, as confirmed by first-principles investigation [41]; this behavior appears to be common to other lead-based perovskites as well [42].

For heterovalent substitutions on the A or B site (or both), the substitution must be in a fixed ratio in order to produce an insulating state. For mixtures of +3 and +5, the balance is 1/2 to 1/2, for example $Pb(Sc_{1/2}Ta_{1/2})O_3$ (PST) and $Pb(Sc_{1/2}Nb_{1/2})O_3$ (PSN). For mixtures of +2 and +5, the balance is 1/3 to 2/3, for example $PbMg_{1/3}Nb_{2/3}O_3$ (PMN) and $PbZn_{1/3}Nb_{2/3}O_3$ (PZN). The more pronounced difference between substituents, relative to the isovalent solid solutions, produces new phenomena, such as short-range and

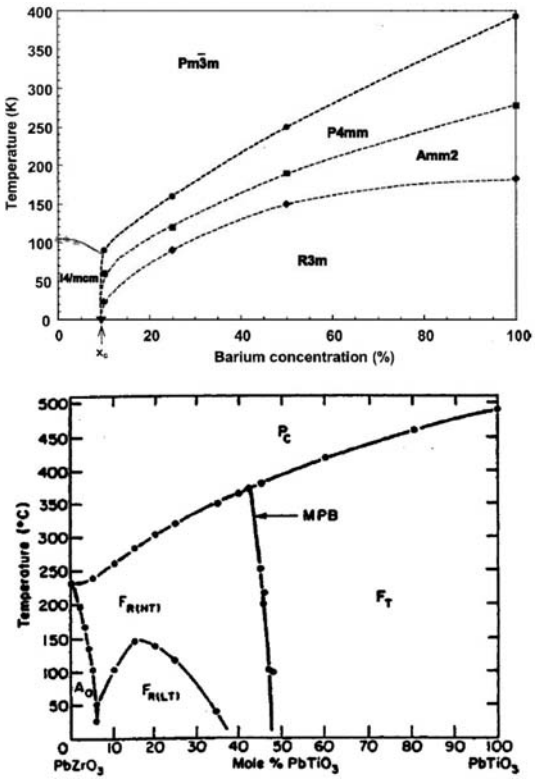

Fig. 7. (**a**) Critical temperature vs. concentration phase diagram of $Sr_{1-x}Ba_xTiO_3$, deduced from X-ray and neutron-diffraction studies. From [37]. (**b**) PZT phase diagram. From [38], after *Jaffe* et al. [39]

long-range ordering of the cation arrangement, and relaxor behavior rather than true ferroelectricity. For a recent review of relaxor phenomenology and first-principles investigations, see [43].

4.2 $LiNbO_3$

$LiNbO_3$ and related materials are ferroelectric oxides with a trigonal paraelectric structure. While this structure can, in principle, be obtained through a distortion of the cubic perovskite structure, the necessary distortion is quite large, so that these compounds do not revert to the cubic perovskite phase at high temperatures, and the cubic perovskite structure is not an appropriate high-symmetry reference structure. Thus, it is often not considered a perovskite [1], though it is crystallographically the same as $R3c$ $BiFeO_3$ (see Fig. 2b in the contribution of *Rabe* and *Ghosez*), differing only in the values of the structural parameters.

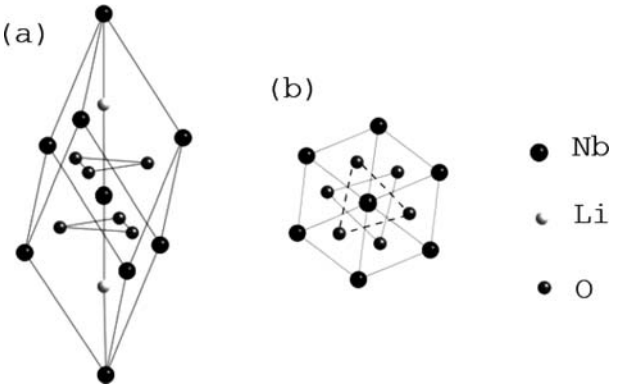

Fig. 8. Primitive unit cell of the R$\bar{3}$c trigonal structure of $LiNbO_3$. Views (**a**) perpendicular and (**b**) parallel to the three-fold axis. From [19]

The paraelectric phase has a rhombohedral unit cell of $R\bar{3}c$ symmetry with two formula units per unit cell. The positions of the 10 atoms in the rhombohedral primitive unit cell are shown in Fig. 8. The threefold axis is formed by a chain of equidistant A and B atoms. Each B atom is located at the center of an octahedron formed by 6 oxygen atoms. As for the perovskites, the $R\bar{3}c$ structure is composed of oxygen octahedra containing the B atom and surrounded by the A atoms. However, relative to the perovskite structure, the oxygen octahedra have been rotated around [111], so that the A atoms only have 6 oxygen first neighbors, rather than twelve as in the cubic perovskite structure.

The low-temperature $R3c$ ferroelectric phase is obtained from the paraelectric $R\bar{3}c$ phase by displacements of the cations along the [111] direction, breaking the mirror-plane symmetry and resulting in a nonzero spontaneous polarization. For $LiNbO_3$, the paraelectric–ferroelectric transition occurs at 1483 K, with a spontaneous polarization of 71 $\mu C/cm^2$ at room temperature. The structurally analogous system $LiTaO_3$ has a lower critical temperature of 838 K, with a spontaneous polarization of 50 $\mu C/cm^2$ [2, 3].

4.3 Layered Oxide Ferroelectrics

The Aurivillius phases are layered bismuth oxides $Bi_{2m}A_{n-m}B_nO_{3(n+m)}$, formed by the regular stacking of Bi_2O_2 slabs and perovskite-like blocks $A_{p-1}B_pO_{3p+1}$, as described in [45]. Various A and B cations are allowed, so that this family has numerous representatives. Examples include Bi_2WO_6 ($n = 1$), $SrBi_2Ta_2O_9$ ($n = 2$) and $Bi_4Ti_3O_{12}$ ($n = 3$) (see Fig. 9). Additional members can be generated by allowing the stacking of perovskite-like blocks of different sizes. $SrBi_2Ta_2O_9$ (SBT), because of its very low fatigue [46], has been intensively studied both experimentally and theoretically [47]. The room-temperature structure is orthorhombic $A21am$, with

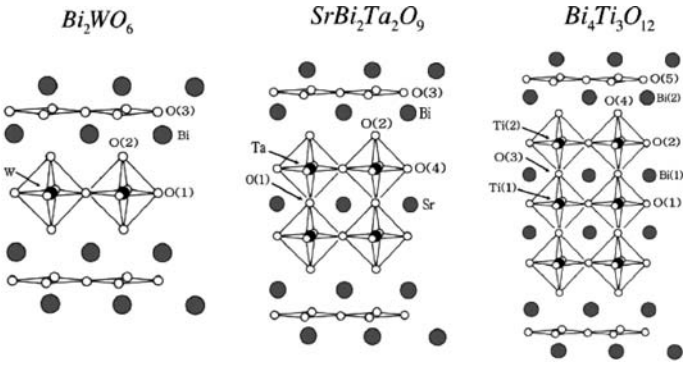

Fig. 9. Tetragonal structures of Aurivillius compounds Bi_2WO_6, $SrBi_2Ta_2O_9$ and $Bi_4Ti_3O_{12}$. Only atoms between $1/2c$ and $3/4c$ are shown. From [44]

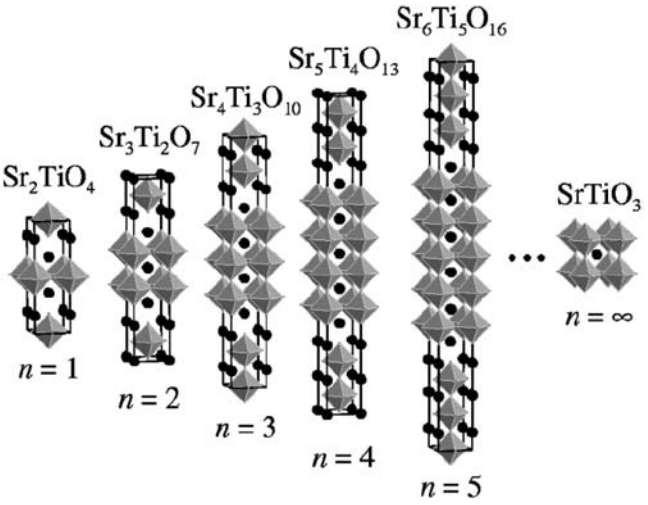

Fig. 10. Schematic of the crystal structure of a unit cell of the $n = 1, 2, 3, 4, 5$ and ∞ members of the $Sr_{n+1}Ti_nO_{3n+1}$ Ruddlesden–Popper homologous series. *Circles* represent Sr atoms, while Ti atoms are at the center of the octahedra with oxygen atoms at each apex. From [48]

28 atoms in the primitive unit cell. The polar axis is a, with a polarization of about $5\,\mu C/cm^2$ [44]. This relatively small value is not generic to Aurivillius ferroelectrics; the polarization of $Bi_4Ti_3O_{12}$, for example, is reported as $50\,\mu C/cm^2$ along the a-axis [44].

The Ruddlesden–Popper (RP) family of transition-metal oxides represents another mode of stacking perovskite blocks, in this case with rocksalt-structure layers. The members of the family are indexed by n, where n specifies the thickness of the perovskite layer $A_{n+1}B_nO_{3n+1}$, terminated on both

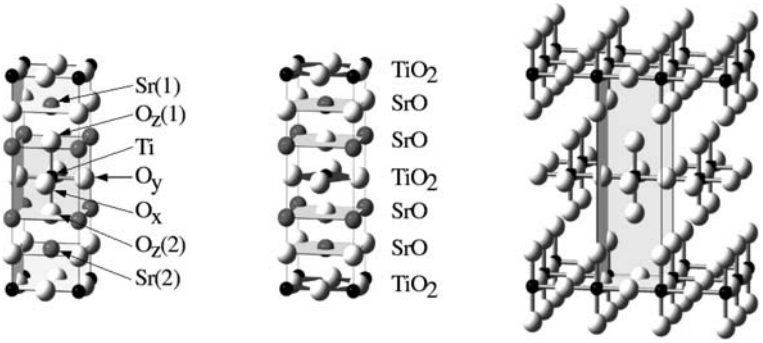

Fig. 11. The structure of Sr_2TiO_4 (space group $I4/mmm$) can be viewed as (**a**) a stacking of SrO-terminated $SrTiO_3$ perovskite [001] slabs, (**b**) a stacking of TiO_2 and of SrO planes along [001], and (**c**) a series of Ti–O chains, infinitely long in the plane along [001] and [010], and of finite extent along [001] (the Sr atoms have been removed for clarity.) From [49]

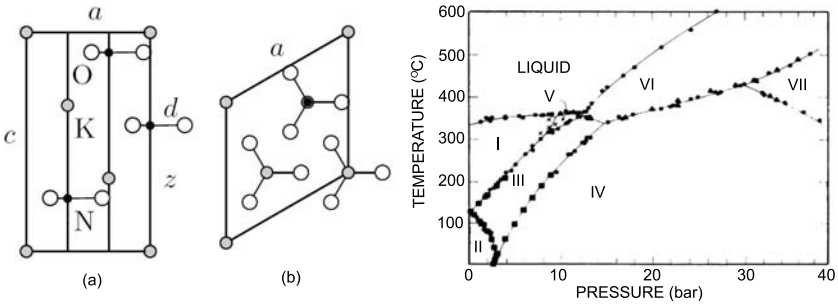

Fig. 12. (**a**) The crystal structure of KNO_3. From [51]. (**b**) The pressure–temperature phase diagram of bulk KNO_3. From [52]

sides by AO. These are stacked with a lateral shift of $1/2(a_0,a_0,0)$, giving a rocksalt-like relationship between the two adjacent AO layers. The series $Sr_{n+1}Ti_nO_{3m+1}$ is shown in Fig. 10; the structure of the $n = 1$ RP phase is analyzed in detail in Fig. 11. The Sr−Ti series does not contain any ferroelectrics; the possibility of ferroelectricity for other compositions has been the subject of experimental and theoretical speculation[1] [49, 50].

4.4 Other Ferroelectric Oxide Families

The existence of numerous additional families of ferroelectric oxides has long been well known. The types include tungsten bronzes, boracites, Mn_3TeO_6, $Pb_5Ge_3O_{11}$, $Gd_2(MoO_4)_3$, $R_3Sb_5O_{12}$, $LiNaGe_4O_9$, $BaAl_2O_4$, and $Li_2Ge_7O_{15}$ [1].

[1] private communication with D. G. Schlom

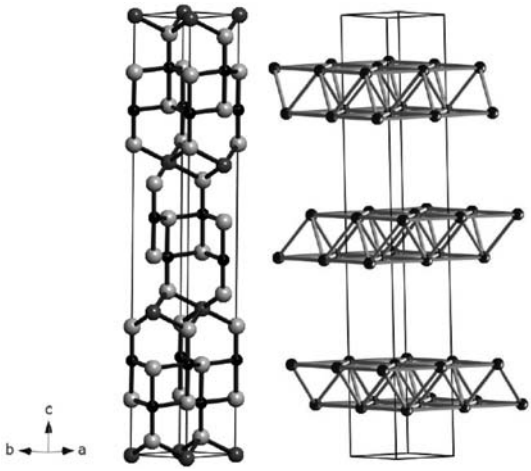

Fig. 13. Crystal structure of $LuFe_2O_4$ showing the layered arrangement of Lu (*large dark-gray spheres*), Fe (*small black spheres*) and oxygen (*large white spheres*) along the *c*-axis (*left*). The Fe double layers are shown with a triangular interconnectivity (*right*). From [57]

With the rapid development of experimental techniques and theoretical frameworks for studying and understanding the physics of ferroelectric oxides, renewed investigation of these families may bring to light examples of materials with novel mechanisms for ferroelectricity, as well as previously unknown members of these families with desirable physical properties. As just one example, KNO_3, with a crystal structure based on stacking of triangular NO_3 units with K ions (shown in Fig. 12a), has recently been the subject of both theoretical [51] and experimental [53] investigation, building on earlier results including [54] and [52]. This structural complexity, with the ferroelectric distortion coupling to rotation of the triangular units, is closely related to the rich pressure–temperature phase diagram shown in Fig. 12b.

4.5 Magnetic Ferroelectric Oxides

The ferroelectric hexagonal manganites, exemplified by $YMnO_3$, have recently been of interest due to their magnetic properties [55], and their structure and properties are therefore discussed at length in the contribution by *Spaldin*. Briefly, the high-temperature paraelectric phase is quite distinct from the perovskite structure. This appears to be an example of an improper ferroelectric, where the primary order parameter for the transition appears to be the rotation of the oxygen polyhedra, which breaks symmetry, leading to the development of a nonzero polarization along c [56]. The magnetism is produced by the Mn cations, which are relatively passive in the ferroelectric transition.

4.6 Electronic Ferroelectrics

Attention has only recently begun to be paid to the possibility of electronic ferroelectrics, which in principle would exhibit a symmetry-breaking instability of the electronic ground state that occurs even if the ions are held fixed. There has been theoretical work on the Falicov–Kimball model [58–60], which is relevant to mixed-valent transition-metal and rare-earth compounds, such as SmB_6. Another mechanism for electronic ferroelectricity is based on charge-ordering phenomena (including charge-density waves) in complex oxides, for example in the perovskite-structure manganites. While multiple valence is most prevalent in transition metals, a few other elements can undergo a form of charge ordering called charge disproportionation. For example, in $BaBiO_3$ it has been suggested that $2\ Bi^{4+} \rightarrow Bi^{3+} + Bi^{5+}$, which leads to a cell-doubling transition as discussed further in the contribution by *Rabe* and *Ghosez*. In this as in most other cases, the charge-ordered states are still of relatively high symmetry. but there have been reports of systems with spontaneous polarization ($LuFe_2O_4$ and YFe_2O_4) [61–65], accompanied by large dielectric response above a phase-transition temperature. The ferroelectric and magnetic properties of $LuFe_2O_4$ in particular, shown in Fig. 13, have recently stimulated considerable research [57, 66]. Intriguing dielectric behavior related to charge ordering has also been reported for Fe_2BO_4 [67, 68]. The large dielectric constant of $La_{1.5}Sr_{0.5}NiO_4$ has been attributed to charge-density waves (CDWs) [69]; the connection between electronic ferroelectric and CDW systems is discussed further in the contribution by *Chandra* and *Littlewood*.

4.7 Nonbulk Ferroelectrics

Within the last decade, thinking about ferroelectricity in systems with one or more reduced dimensions has undergone a marked evolution. Up until the late 1990s, it was widely accepted that ferroelectricity in perovskite oxides would disappear below a critical size of about 10 nm. Since then, through combined experimental and theoretical investigation, a new view has emerged to the effect that this suppression is an extrinsic effect, produced by electrical and mechanical boundary conditions rather than by intrinsic size effects related to the collective nature of the ferroelectric instability.

A key result in initiating this change of view was the experimental finding that PZT films can maintain switchable polarization normal to the film down to thicknesses of a few nm [70], a result supported by the theoretical prediction that $PbTiO_3$ will maintain a switchable spontaneous polarization normal to the film down to thicknesses below three unit cells as long as the depolarization field is fully compensated [71]. This led to a focus on the role of the depolarization field in producing apparent size effects, with an analysis by *Dawber* et al. [72] showing that the expected thickness dependence of the measured coercive field is due to fixed voltage drops in realistic electrodes,

along with numerous studies on the effect of incomplete compensation of the field [73]. In addition to suppressing ferroelectricity, incomplete compensation may alternatively drive the formation of complex domain structures [74, 75].

With the possibility of ferroelectricity in ultrasmall systems, new questions arise. In a finite system (a nanoparticle or a dot), formally there is no ferroelectric–paraelectric phase transition and the criterion for a stable switchable polarization may have to be formulated dynamically. Another issue is that finite systems, such as films or particles, may be embedded in asymmetric environments (e.g., different top and bottom electrodes for films). Even if there are multiple metastable states, these could differ in the degree of stability. In both cases, the criterion for ferroelectricity should be based on the stability of two or more variants with different polarizations and the switchability from one to another by an applied electric field.

The brief overview above highlights just a few of the important results in recent fundamental and applied research in the physics of nonbulk ferroelectrics. More discussion can be found in the next section (on applications), in the contribution by *Rabe* and Ghosez (on first-principles theoretical studies) and in the contribution by *Lichtensteiger*, *Dawber*, and *Triscone* (on finite-size effects).

5 Applications of Ferroelectric Materials

Much interest in ferroelectric materials arises because they possess properties that are of use in a number of applications. In some cases ferroelectrics are already among the leading materials for a particular application; in others the possibilities that are presented by novel materials and geometries are starting to be realized. Here we present a brief overview of both established applications and those that may still come.

5.1 Pyroelectric and Piezoelectric Devices

Many applications for ferroelectric materials do not make use of the ferroelectricity itself but of the related properties of pyroelectricity and piezoelectricity. By symmetry these properties are required for ferroelectricity to exist (they are necessary but not sufficient, i.e., all ferroelectrics are pyroelectric and piezoelectric, but not all piezoelectrics are pyroelectric and not all pyroelectrics are ferroelectric). Pyroelectrics are useful in a variety of imaging and detection applications. Piezoelectrics find a host of uses in electromechanicial devices. In particular in MEMS, the large piezoelectric coefficients of ferroelectric solid solutions such as PZT allow for novel miniature electromechanical devices. More details on these applications can be found in the review by *Muralt* [76].

5.2 Ferroelectric Memory Technology

The desirability of nonvolatile memory technology in computing applications, in particular in mobile devices, has long been evident, as demonstrated by the current success of FLASH-based technology, in digital cameras, mobile phones, MP3 players and a host of other portable devices. FLASH is not, however, the long-term nonvolatile memory of choice, because of limitations regarding endurance, scalability and voltage requirements.

Ferroelectrics have been considered for almost twenty years [77] to be a leading candidate for the next generation of nonvolatile memories. Commercially available devices do exist, but seem to be more common in niche applications, or as part of an integrated memory device involving several different memory technologies, rather than as a standalone high-capacity nonvolatile memory. Other competing technologies also exist, most notably MRAMs and phase-change memory.

One of the issues that has hindered widespread implementation of ferroelectrics as memory elements is that, to determine the polarization state of a ferroelectric, it is usually necessary to attempt to switch the polarization; the data stored is then erased and must be rewritten, i.e., the read-out operation is destructive. As ferroelectrics can suffer from fatigue with repetitive cycling, this destructive read-out places a limitation on the reliability, though over the years fatigue resistance has been improved by the use of oxide electrodes. There is still also considerable interest in nondestructive read-out devices, including ferroelectric field-effect transistors, or through the use of materials or composite structures where ferroelectric and ferromagnetic orderings are coupled and the electrical polarization direction can be measured from the magnetization. More information on multiferroics can be found in the contribution by *Spaldin* in this volume and in a recent review [78].

More detailed reviews on ferroelectrics for memory applications can be found elsewhere [6, 79].

5.3 Potential Future Applications

Here, we take a look at a number of interesting possible applications of ferroelectrics that are in the earlier stages of development. This section is intended to be inspiring rather than comprehensive.

5.3.1 Ferroelectric Nanostructures

In recent years ferroelectrics have been fabricated in a number of novel geometries, which in turn have suggested some new applications.

Ferroelectric materials appear to retain their properties on reduction of size remarkably well, with ferroelectric nanoparticles remaining ferroelectric to sizes at least as small as 20 nm [80, 81]. The critical thickness in ferroelectric thin films is on the order of a few unit cells (being highly dependent on

boundary conditions) [71, 73, 82, 83] (see the contribution by *Lichtensteiger*, *Dawber* and *Triscone*). High-density arrays of ferroelectric nanocapacitors are thus feasible as the basis for extremely high capacity memory devices. Focused-ion-beam (FIB) milling [84] and e-beam direct writing [85] can be used effectively to make capacitors with nanoscale dimensions. A key problem that remains, is, however, to produce these high-density arrays in a time- and cost-effective manner, while maintaining good registry and material properties, which has led to interest in the idea of self-patterning of ferroelectric nanocapacitors [86].

Ferroelectric nanoshell tubes (polycrystalline ceramic tubes with walls of nanoscale thickness) have been fabricated by a number of groups [87, 88] and show significant potential for applications, ranging from high aspect ratio memories to microfluidic delivery systems. The tubes are made by growth in a porous matrix, which gives them a high degree of regularity and good registry. Another approach for fabricating ferroelectrics with novel nanoscale geometries that is yielding interesting results is the FIB technique used by the group in Belfast [89–91] to cut single crystals into thin films, rings, and a variety of other interesting shapes.

5.3.2 Field-Effect Devices

Earlier we mentioned briefly the idea of using ferroelectric field-effect transistors in which the gate dielectric on a conventional FET is replaced by a ferroelectric material. The conductivity of the semiconductor channel is modified by the screening charge of the ferroelectric. This is an active area of research, reviewed in more detail elsewhere [6]; the key obstacle to be overcome is the poor retention times typical of these devices. The ferroelectric field effect can also be used to modify the properties of more exotic systems, particularly superconducting or magnetic oxides [92].

5.3.3 Ferroelectric Device Fabrication Using Atomic Force Microscopy

Ferroelectricity can be controlled on the nanoscale using an atomic force microscope (AFM) tip as a mobile top electrode (see the contribution by *Paruch*, *Giamarchi* and *Triscone*). With this approach, one can envisage using an AFM tip to write extremely dense arrays of ferroelectric domains for use as a memory device [93]. Another idea is to make a surface acoustic wave device (commonly used as a frequency filter in mobile phones) with reduced feature size by using the AFM tip to write a nanoscale ferroelectric domain structure in place of the conventional interdigital electrodes, thereby achieving a much higher operating frequency [94]. Combining the nanoscale control of ferroelectric domain structure achievable with the AFM with the modulation of electrical conductivity allowed by the ferroelectric field effect allows one to locally define in the same material regions of differing electronic

properties [95]. Using this approach on highly correlated electronic materials, such as high-temperature superconductors, one could potentially design one-dimensional superconducting wires, superconducting rings and junctions, superconducting quantum interference devices (SQUIDs) or arrays of pinning centers.

5.3.4 Ferroelectric Cooling Devices

The idea of using the thermoelectric effect associated with aferroelectric phase transition for cooling has some history [96, 97], but has recently received revived attention through the demonstration that with moderate voltages applied to thin films [98], significant cooling can conceivably be achieved. This approach is of interest in computing applications where the problem of heat production is a key challenge.

In this section we have only just scratched the surface of what can conceivably be achieved with ferroelectrics. Several other proposals already exist and an interesting overview of some other novel device ideas has recently been written by *Scott* [99]; beyond this, new ideas are sure to continually emerge as we push the boundaries of material design in ferroelectric systems.

6 Note from the Editors

At the beginning of this chapter, we described our strategy in selecting topics for inclusion in this book, highlighting key advances since the classic work of *Lines* and *Glass* [1]. Here, we would add the note that with the nearly exponential growth of the scientific literature, it is impossible to do justice to all relevant work in a single volume, even with this selective focus. In many cases we have been able to include only brief references to original papers, which the reader is encouraged to consult for full information and understanding. Indeed, there will inevitably be cases where mention of relevant papers was inadvertently omitted. We apologize to the authors of these papers, and to those of papers published during work on the book that were not included, and urge the reader interested in particular subjects to extend their study of the literature beyond the starting points provided.

References

[1] M. E. Lines, A. M. Glass: *Principles and Applications of Ferroelectrics and Related Materials* (Clarendon, Oxford 1977) 2, 14, 17, 23

[2] T. Mitsui, S. Nomura, M. Adachi, J. Harada, T. Ikeda, E. Nakamura, E. Sawaguchi, T.Shigenari, Y. Shiozagi, J. Tatsuzaki, K. Toyoda, T. Yamada, K. Gesi, Y. Marita, M. Marutake, T. Shiosaki, K. Wakino: *Oxides, Landolt–Börnstein: Numerical Data and Functional Relationships in Science and Technology, Group III*, vol. 16, Part A (Springer, Berlin 1981) 2, 11, 15

[3] E. Nakamura, M. Adachi, Y. Akishige, K. Deguchi, J. Harada, T. Ikeda, M. Okuyama, E. Sawaguchi, Y. Shiozaki, K. Toyoda, T. Yamada, K. Gesi, T. Hikita, Y. Makita, T. Shigenari, I. Tatsuzaki, T. Yahi: *Oxides, Landolt–Börnstein: Numerical Data and Functional Relationships in Science and Technology, Group III*, vol. 28 (Springer, Berlin 1981) 2, 11, 15
[4] C. B. Sawyer, C. H. Tower: Rochelle salt as a dielectric, Phys. Rev. **35**, 269 (1930) 3
[5] M. Dawber, I. Farnan, J. F. Scott: A classroom experiment to demonstrate ferroelectric hysteresis, Am. J. Phys. **71**, 819 (2003) 3
[6] M. Dawber, K. M. Rabe, J. F. Scott: Physics of thin film ferroelectric oxides, Rev. Mod. Phys. **77**, 1083 (2005) 4, 21, 22
[7] D. J. Kim, et al.: Polarization relaxation induced by a depolarization field in ultrathin ferroelectric $BaTiO_3$ capacitors, Phys. Rev. Lett. **95**, 237602 (2005) 5
[8] W. Cochran: Crystal stability and the theory of ferroelectricity, Adv. Phys. **9**, 387 (1960) 7
[9] P. W. Anderson: in G. Skanavi (Ed.): *Fizika Dielectrikov* (Akad. Nauk, Moscow 1960) 7
[10] A. A. Sirenko, C. Bernhard, A. Golnik, A. M. Clark, J. H. Hao, X. X. Xi: Soft-mode hardening in $SrTiO_3$ thin films, Nature **404**, 373 (2000) 7
[11] P. M. Gehring, S. Wakimoto, Z. G. Ye, G. Shirane: Soft mode dynamics above and below the Burns temperature in the relaxor $Pb(Mg_{1/3}Nb_{2/3})O_3$, Phys. Rev. Lett. **87**, 277601 (2001) 7
[12] S. C. Abrahams: Structurally based predictions of ferroelectricity in seven inorganic materials with space group *Pba*2 and two experimental confirmations, Acta Crystallogr. B **45**, 228 (1989) 7
[13] E. Kroumova, M. I. Aroyo, J. M. Perez-Mato: Prediction of new displacive ferroelectrics through systematic pseudosymmetry search: Results for materials with *Pba*2 and *Pmc*2(1) symmetry, Acta Crystallogr. B **58**, 921 (2002) 7
[14] C. Capialls, M. I. Aroyo, J. M. Perez-Mato: Search for new *Pna*2(1) ferroelectrics, Ferroelectrics **301**, 203 (2004) 7
[15] K. M. Rabe: *Lattice Instabilities of Complex Perovskite Oxides from First Principles*, Computer Simulation Studies in Condensed Matter Physics XVI, Springer Proceedings in Physics (Springer, New York 2003) 7
[16] R. Comes, M. Lambert, A. Guinier: The chain structure of $BaTiO_3$ and $KNbO_3$, Solid State Commun. **6**, 715 (1968) 7
[17] T. Egami, S. Teslic, W. Dmowski, D. Viehland, S. Vakhrushev: Local atomic structure of relaxor ferroelectric solids determined by pulsed neutron and X-ray scattering, Ferroelectrics **199**, 103 (1997) 7
[18] N. Sicron, B. Ravel, Y. Yacoby, E. A. Stern, F. Dogan, J. J. Rehr: Nature of the ferroelectric phase transition in $PbTiO_3$, Phys. Rev. B **50**, 13168 (1994) 7
[19] P. Ghosez: *Microscopic properties of ferroelectric oxides from first principles: Selected topics* (Troisieme Cycle de la Physique en Suisse Romande, Lausanne 2002) 145 pages URL: `http://www.phythema.ulg.ac.be/Books/Cours_Ferro.Ghosez.pdf` 8, 15
[20] L. Eyraud (Ed.): *Dielectriques Solides Anisoptropes et Ferroelectricite* (Gauthier-Villars, Paris 1967) 9
[21] G. H. Kwei, A. C. Lawson, S. J. L. Billinge, S. W. Cheong: Structures of the ferroelectric phases of barium titanate, J. Phys. Chem. **97**, 2368 (1993) 11

[22] W. Zhong, D. Vanderbilt, K. M. Rabe: Phase transitions in $BaTiO_3$ from first principles, Phys. Rev. Lett. **73**, 1861 (1994) 11
[23] C. H. Ahn, K. M. Rabe, J.-M. Triscone: Ferroelectricity at the nanoscale: Local polarization in oxide thin films and heterostructures, Science **303**, 488 (2004) 11
[24] A. W. Hewat: Soft modes and the structure, spontaneous polarization and Curie constants of perovskite ferroelectrics: Tetragonal potassium niobate, J. Phys. C: Solid State Phys. **6**, 1074 (1973) 11
[25] M. Itoh, R. Wang, Y. Inaguma, T. Yamaguchi, Y. J. Shan, T. Nakamura: Ferroelectricity induced by oxygen isotope exchange in strontium titanate perovskite, Phys. Rev. Lett. **82**, 3540 (1999) 12
[26] P. A. Fleury, J. F. Scott, J. M. Worlock: Soft phonon modes and the 110 K phase transition in $SrTiO_3$, Phys. Rev. Lett. **21**, 16 (1968) 12
[27] G. A. Samara, B. Morosin: Anharmonic effects in $KTaO_3$: Ferroelectric mode, thermal expansion and compressibility, Phys. Rev. B **8**, 1256 (1973) 12
[28] S. E. Park, T. R. Shrout: Ultrahigh strain and piezoelectric behavior in relaxor based ferroelectric single crystals, J. Appl. Phys. **82**, 1804 (1997) 12
[29] G. A. Samara: Pressure and temperature dependence of the dielectric properties and phase transitions of the ferroelectric perovskites: $PbTiO_3$ and $BaTiO_3$ pressure studies, Ferroelectrics **2**, 277 (1971) 12
[30] Z. Wu, R. E. Cohen: Pressure-induced anomalous phase transitions and colossal enhancement of piezoelectricity in $PbTiO_3$, Phys. Rev. Lett. **95**, 196804 (2005) 12
[31] I. A. Kornev, L. Bellaiche, P. Bouvier, P. E. Janolin, B. Dkhil, J. Kreisel: Ferroelectricity of perovskites under pressure, Phys. Rev. Lett. **95**, 196804 (2005) 12
[32] T. Ishidate, S. Abe, H. Takahashi, N. Moêri: Phase diagram of $BaTiO_3$, Phys. Rev. Lett. **78**, 2397 (1997) 12, 13
[33] D. A. Tenne, X. X. Xi, Y. L. Li, L. Q. Chen, A. Soukiassian, M. H. Zhu, A. R. James, J. Lettieri, D. G. Schlom, W. Tian, X. Q. Pan: Absence of low-temperature phase transitions in epitaxial $BaTiO_3$ thin films, Phys. Rev. B **69**, 174101 (2004) 12
[34] J. H. Haeni, P. Irvin, W. Chang, R. Uecker, P. Relche, Y. L. Li, S. Choudhury, W. Tian, M. E. Hawley, B. Craigo, A. K. Tagantsev, X. Q. Pan, S. K. Streiffer, L. Q. Chen, S. W. Kirchoefer, J. Levy, D. G. Schlom: Room-temperature ferroelectricity in strained $SrTiO_3$, Nature **430**, 758 (2004) 12, 13
[35] A. Antons, J. B. Neaton, K. M. Rabe, D. Vanderbilt: Tunability of the dielectric response of epitaxially strained $SrTiO_3$ from first principles, Phys. Rev. B **71**, 024102 (2005) 12
[36] K. J. Choi, M. Biegalski, Y. L. Li, A. Sharan, J. Schubert, R. Uecker, P. Reiche, Y. B. Chen, X. Q. Pan, V. Gopalan, L.-Q. Chen, D. G. Schlom, C. B. Eom: Enhancement of ferroelectricity in strained $BaTiO_3$ thin films, Science **306**, 1005 (2004) 12
[37] C. Menoret, J. M. Kiat, B. Dkhil, M. Dunlop, H. Dammak, O. Hernandez: Structural evolution and polar order in $Sr_{1-x}Ba_xTiO_3$, Phys. Rev. B **65**, 224104 (2002) 12, 14
[38] B. Noheda, D. E. Cox, G. Shirane, J. A. Gonzalo, L. E. Cross, S. E. Park: A monoclinic ferroelectric phase in the $Pb(Zr_{1-x}Ti_x)O_3$ solid solution, Appl. Phys. Lett. **74**, 2059 (1999) 13, 14

[39] B. Jaffe, W. R. Cook, H. Jaffe: *Piezoelectric Ceramics* (Academic Press, London 1971) p. 136 14
[40] B. Noheda, D. E. Cox: Bridging phases at the morphotropic boundaries of lead oxide solid solutions, Phase Transitions **79**, 5 (2006) 13
[41] L. Bellaiche, A. Garcia, D. Vanderbilt: Finite-temperature properties of $Pb(Zr_{1-x}Ti_x)O_3$ alloys from first principles, Phys. Rev. Lett. **84**, 5427 (2000) 13
[42] D. E. Cox, B. Noheda, G. Shirane, Y. Uesu, K. Fujishiro, Y. Yamada: Universal phase diagram for high-piezoelectric perovskite systems, Appl. Phys. Lett. **79**, 400 (2001) 13
[43] B. P. Burton, E. Cockayne, S. Tinte, U. V. Waghmare: First-principles-based simulations of relaxor ferroelectrics, Phase Transitions **79**, 91 (2006) 14
[44] R. Machado, M. G. Stachiotti, R. L. Migoni, A. H. Tera: First-principles determination of ferroelectric instabilities in Aurivillius compounds, Phys. Rev. B **70**, 214112 (2004) 16
[45] J. M. Perez-Mato, M. Aroyo, A. Garcia, P. Blaha, K. Schwarz, J. Schweifer, K. Parlinski: Competing structural instabilities in the ferroelectric Aurivillius compounds, Phys. Rev. B **70**, 214111 (2004) 15
[46] C. Araujo, J. D. Cuchiaro, L. D. McMillan, M. C. Scott, J. F. Scott: Fatigue-free ferroelectric capacitors with platinum electrodes, Nature **374**, 627 (1995) 15
[47] M. G. Stachiotti, C. O. Rodriguez, C. Ambrosch-Draxl, N. E. Christensen: Electronic structure and ferroelectricity in $SrBi_2Ta_2O_9$, Phys. Rev. B **61**, 14434 (2000) 15
[48] J. H. Haeni, C. D. Theis, D. G. Schlom, W. Tian, X. Q. Pan, H. Chang, I. Takeuchi, X. D. Xiang: Epitaxial growth of the first five members of the $Sr_{n+1}Ti_nO_{3n+1}$ Ruddlesden–Popper homologous series, Appl. Phys. Lett. **78**, 3292 (2001) 16
[49] C. J. Fennie, K. M. Rabe: Structural and dielectric properties of Sr_2TiO_4 from first principles, Phys. Rev. B **68**, 184111 (2003) 17
[50] C. J. Fennie, K. M. Rabe: First-principles investigation of ferroelectricity in epitaxially strained Pb_2TiO_4, Phys. Rev. B **71**, 100102 (2005) 17
[51] O. Dieguez, D. Vanderbilt: First-principles calculations for insulators at constant polarization, Phys. Rev. Lett **96**, 056401 (2006) 17, 18
[52] J. F. Scott, M. Zhang, R. B. Godfrey, C. Araujo, L. McMillan: Raman spectroscopy of submicron KNO_3 films, Phys. Rev. B **35**, 4044 (1987) 17, 18
[53] J. F. Scott: Phase transitions in very thin ($< 100\,\mathrm{nm}$) films of ceramic $Ba_{1-x}Sr_xTiO_3$ (BST) and single-crystal $BaTiO_3$ (2005) URL: `http//www.mri.psu.edu/conferences/ferro2005/Ferro05AbstractBook.pdf` 18
[54] H. M. Lu, J. R. Hardy: First principles study of phase transitions in KNO_3, Phys. Rev. B **44**, 7387 (1991) 18
[55] B. B. van Aken, T. T. Palstra, A. Filippetti, N. A. Spaldin: The origin of ferroelectricity in magnetoelectric $YMnO_3$, Nature Mater. **3**, 164 (2004) 18
[56] C. J. Fennie, K. M. Rabe: Ferroelectric transition in $YMnO_3$ from first principles, Phys. Rev. B **72**, 100103 (2005) 18
[57] M. A. Subramanian, T. He, J. Z. Chen, N. S. Rogado, T. G. Calvarese, A. W. Sleight: Giant room-temperature magnetodielectric response in the electronic ferroelectric $LuFe_2O_4$, Adv. Mater. **18**, 1737 (2006) 18, 19

[58] C. D. Batista: Electronic ferroelectricity in the Falicov–Kimball model, Phys. Rev. Lett. **89**, 166403 (2002) 19
[59] P. Farkasovsky: Falicov–Kimball model and the problem of electronic ferroelectricity, Phys. Rev. B **65**, 081102 (2002) 19
[60] T. Portengen, T. Ostreich, L. J. Sham: Theory of electronic ferroelectricity, Phys. Rev. B **54**, 17452 (1996) 19
[61] N. Ikeda, S. Nohdo, Y. Yamada, E. Takahashi, K. Kohn: Charge ordering of $LuFe_2O_4$ observed by an anomalous X-ray dispersion, J. Korean Phys. Soc. **32**, S165 (1998) 19
[62] N. Ikeda, M. Tanaka, H. Kito, S. Sasaki, Y. Yamada: Synchrotron observation of the charge ordering and spontaneous polarization in $LuFe_2O_4$, Ferroelectrics **222**, 485 (1999) 19
[63] N. Ikeda, K. Kohn, N. Myouga, E. Takahashi, H. Kitoh, S. Takeawa: Charge frustration and dielectric dispersion in $LuFe_2O_4$, J. Phys. Soc. Jpn. **69**, 1526 (2000) 19
[64] N. Ikeda, R. Mori, S. Mori, K. Kohn: Dielectric and structure properties of charge competing system YFe_2O_4, Ferroelectrics **272**, 2301 (2002) 19
[65] N. Ikeda, R. Mori, K. Kohn, M. Mizumaki, T. Akao: Structure transition and charge competition on YFe_2O_4, Ferroelectrics **286**, 897 (2003) 19
[66] N. Ikeda, H. Ohsumi, K. Ohwada, K. Ishii, T. Inami, K. Kakurai, Y. Murakami, K. Yoshii, S. Mori, Y. Horibe, H. Kito: Ferroelectricity from iron valence ordering in the charge-frustrated system $LuFe_2O_4$, Nature **436**, 1136 (2005) 19
[67] J. P. Attfield, A. M. T. Bell, L. M. Rodriguez-Martinez, J. M. Greneche, R. J. Cernik, J. F. Clarke, D. A. Perkins: Electrostatically driven charge-ordering in Fe_2OBO_3, Nature **396**, 655 (1998) 19
[68] N. Suda, K. Kohn, S. Nakamura: Dielectric and magnetic properties of a mixed valence oxide Fe_2BO_4, Ferroelectrics **286**, 877 (2003) 19
[69] J. Rivas, B. Rivas-Murias, A. Fondado, J. Mira, M. A. Senaris-Rodriguez: Dielectric response of the charge-ordered two-dimensional nickelate $La_{1.5}Sr_{0.5}NiO_4$, Appl. Phys. Lett. **85**, 6224 (2004) 19
[70] T. Tybell, C. H. Ahn, J.-M. Triscone: Ferroelectricity in thin perovskite films, Appl. Phys. Lett. **75**, 856 (1999) 19
[71] P. Ghosez, K. M. Rabe: A microscopic model of ferroelectricity in stress-free $PbTiO_3$ ultrathin films, Appl. Phys. Lett. **76**, 2767 (2000) 19, 22
[72] M. Dawber, P. Chandra, P. B. Littlewood, J. F. Scott: Depolarization corrections to the coercive field in thin-film ferroelectrics, J. Phys. Condens. Matter **15**, 393 (2003) 19
[73] J. Junquera, P. Ghosez: Critical thickness for ferroelectricity in perovskite ultrathin films, Nature **422**, 506 (2003) 20, 22
[74] V. Nagarajan, J. Junquera, J. Q. He, C. L. Jia, R. Waser, K. Lee, Y. K. Kim, S. Baik, T. Zhao, R. Ramesh, P. Ghosez, K. M. Rabe: Scaling of structure and electrical properties in ultrathin epitaxial ferroelectric heterostructures, J. Appl. Phys. **100**, 51609 (2006) 20
[75] I. Kornev, H. Fu, L. Bellaiche: Ultrathin films of ferroelectric solid solutions under a residual depolarizing field, Phys. Rev. Lett. **93**, 196104 (2004) 20
[76] P. Muralt: Ferroelectric thin films for micro-sensors and actuators: A review, J. Micromech. Microeng. **10**, 136 (2000) 20
[77] J. F. Scott, C. A. P. De Araujo: Ferroelectric memories, Science **246**, 1400 (1989) 21

[78] W. Eerenstein, N. D. Mathur, J. F. Scott: Multiferroic and magnetoelectric materials, Nature **442**, 759 (2006) 21
[79] J. F. Scott: *Ferroelectric Memories* (Springer, Berlin 2000) 21
[80] A. Roelofs, T. Schneller, K. Szot, R. Waser: Towards the limit of ferroelectric nanosized grains, Nanotechnology **14**, 250 (2003) 21
[81] A. Rudiger, T. Schneller, A. Roelofs, S. Tiedke, T. Schmitz, R. Waser: Nanosize ferroelectric oxide-tracking down the superparaelectric limit, Appl. Phys. A **80**, 1247 (2005) 21
[82] C. Lichtensteiger, J.-M. Triscone, J. Junquera, P. Ghosez: Ferroelectricity and tetragonality in ultrathin $PbTiO_3$ films, Phys. Rev. Lett. **94**, 047603 (2005) 22
[83] D. D. Fong, G. B. Stephenson, S. K. Streiffer, J. A. Eastman, O. Auciello, P. H. Fuoss, C. Thompson: Ferroelectricity in ultrathin perovskite films, Science **304**, 1650 (2004) 22
[84] S. Tideke, T. Schmitz, K. Prime, A. Roelofs, T. Schneller, U. Kall, R. Waser, C. S. Ganpule, V. Nagarajan, A. Stanishevsky, R. Ramesh: Direct hysteresis measurements of single nanosized ferroelectric capacitors contacted with an atomic force microscope, Appl. Phys. Lett **79**, 3678 (2001) 22
[85] M. Alexe, C. Harnagea, U. Gosele: Patterning and switching of nanosize ferroelectric memory cells, Appl. Phys. Lett. **75**, 1793 (1999) 22
[86] M. Alexe, D. Hesse: Self-assembled nanoscale ferroelectrics, J. Mater. Sci. **41**, 1 (2006) 22
[87] Y. Luo, I. Szafraniak, N. D. Zakharov, V. Nagarajan, M. Steinhart, R. B. Wehrspohn, J. H. Wendorff, R. Ramesh, M. Alexe: Nanoshell tubes of ferroelectric lead zirconate titanate and barium titanate, Appl. Phys. Lett. **83**, 440 (2003) 22
[88] F. D. Morrison, L. Ramsay, J. F. Scott: High aspect ratio piezoelectric strontium-bismuth-tantalate nanotubes, J. Phys. Condens. Matter **15**, L527 (2003) 22
[89] M. M. Saad, P. Baxter, R. M. Bowman, J. M. Gregg, F. D. Morrison, J. F. Scott: Intrinsic dielectric response in ferroelectric nano-capacitors, J. Phys. Condens. Matter **16**, L451 (2004) 22
[90] M. M. Saad, P. Baxter, A. Schilling, T. Adams, X. Zhu, R. M. Bowman, J. M. Gregg, P. Zubko, F. D. Morrison, J. F. Scott: Exploring the fundamental effects of miniaturization on ferroelectrics by focused ion beam processing of single crystal material, J. Physique IV **128**, 63 (2005) 22
[91] A. Schilling, T. B. Adams, R. M. Bowman, J. M. Gregg, G. Catalan, J. F. Scott: Scaling of domain periodicity with thickness measured in $BaTiO_3$ single crystal lamellae and comparison with other ferroics, Phys. Rev. B **74**, 024115 (2006) 22
[92] C. H. Ahn, J.-M. Triscone, J. Mannhart: Electric field effect in correlated oxide systems, Nature **424**, 1015 (2003) 22
[93] P. Paruch, T. Tybell, J.-M. Triscone: Nanoscale control of ferroelectric polarization and domain size in epitaxial $Pb(Zr_{0.2}Ti_{0.8})O_3$ thin films, Appl. Phys. Lett. **79**, 530 (2001) 22
[94] A. K. S. Kumar, P. Paruch, J. M. Triscone, W. Daniau, S. Ballandras, L. Pellegrino, D. Marre, T. Tybell: High-frequency surface acoustic wave device based on thin-film piezoelectric interdigital transducers, Appl. Phys. Lett. **85**, 1757 (2004) 22

[95] K. S. Takahashi, M. Gabay, D. Jaccard, K. Shibuya, T. Ohnishi, M. Lippmaa, J.-M. Triscone: Local switching of two-dimensional superconductivity using the ferroelectric field effect, Nature **441**, 195 (2006) 23
[96] B. A. Strukov: Electrocaloric effect in single-crystal triglycine sulfate, Sov. Phys. Crystallogr. **11**, 757 (1967) 23
[97] B. A. Tuttle, D. A. Payne: The effects of microstructure on the electrocaloric properties of Pb(Zr,Sn,Ti)O_3 ceramics, Ferroelec. **37**, 603 (1981) 23
[98] A. S. Mischenko, Q. Zhang, J. F. Scott, R. W. Whatmore, N. D. Mathur: Giant electrocaloric effect in thin-film $PbZr_{0.95}Ti_{0.05}O_3$, Science **311**, 1270 (2006) 23
[99] J. F. Scott: Applications of modern ferroelectrics, Science **315**, 954 (2007) 23

Index

Theory of Polarization: A Modern Approach

Raffaele Resta[1,2] and David Vanderbilt[3]

[1] INFM–DEMOCRITOS National Simulation Center,
Via Beirut 4, I-34014, Trieste, Italy
resta@democritos.it
[2] Dipartimento di Fisica Teorica, Università di Trieste,
Strada Costiera 11, I-34014, Trieste, Italy
[3] Department of Physics and Astronomy, Rutgers University,
136 Frelinghuysen Road, Piscataway, NJ 08854-8019, USA
dhv@physics.rutgers.edu

Abstract. In this Chapter we review the physical basis of the modern theory of polarization, emphasizing how the polarization can be defined in terms of the accumulated adiabatic flow of current occurring as a crystal is modified or deformed. We explain how the polarization is closely related to a Berry phase of the Bloch wavefunctions as the wavevector is carried across the Brillouin zone, or equivalently, to the centers of charge of Wannier functions constructed from the Bloch wavefunctions. A resulting feature of this formulation is that the polarization is formally defined only modulo a "quantum of polarization" – in other words, that the polarization may be regarded as a multi-valued quantity. We discuss the consequences of this theory for the physical understanding of ferroelectric materials, including polarization reversal, piezoelectric effects, and the appearance of polarization charges at surfaces and interfaces. In so doing, we give a few examples of realistic calculations of polarization-related quantities in perovskite ferroelectrics, illustrating how the present approach provides a robust and powerful foundation for modern computational studies of dielectric and ferroelectric materials.

1 Why is a Modern Approach Needed?

The macroscopic polarization is the most essential concept in any phenomenological description of dielectric media [1]. It is an intensive vector quantity that intuitively carries the meaning of electric dipole moment per unit volume. The presence of a spontaneous (and switchable) macroscopic polarization is the defining property of a ferroelectric (FE) material, as the name itself indicates ("*ferro*electric" modeled after *ferro*magnetic), and the macroscopic polarization is thus central to the whole physics of FEs.

Despite its primary role in all phenomenological theories and its overwhelming importance, the macroscopic polarization has long evaded microscopic understanding, not only at the first-principles level, but even at the level of sound microscopic models. What really happens inside a FE and, more generally, inside a polarized dielectric? The standard picture is almost invariably based on the venerable Clausius–Mossotti (CM) model [2, 3], in which the presence of identifiable polarizable units is assumed. We shall show that

K. Rabe, C. H. Ahn, J.-M. Triscone (Eds.): Physics of Ferroelectrics: A Modern Perspective,
Topics Appl. Physics **105**, 31–68 (2007)

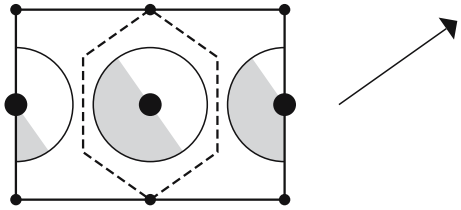

Fig. 1. A polarized ionic crystal having the NaCl structure, as represented within an extreme Clausius–Mossotti model. We qualitatively sketch the electronic polarization charge (*shaded areas indicate negative regions*) in the $(1\bar{1}0)$ plane linearly induced by a constant field $\boldsymbol{\mathcal{E}}$ in the [111] direction as indicated by the arrow. The anions (*large circles*) are assumed to be polarizable, while the cations (*small circles*) are not. The boundary of a Wigner–Seitz cell, centered at the anion, is also shown (*dashed line*)

such an extreme model is neither a realistic nor a useful one, particularly for FE materials.

Experimentalists have long taken the pragmatic approach of measuring polarization *differences* as a way of accessing and extracting values of the "polarization itself". In the early 1990s it was realized that, even at the theoretical level, polarization differences are conceptually more fundamental than the "absolute" polarization. This change of paradigm led to the development of a new theoretical understanding, involving formal quantities such as Berry phases and Wannier functions, that has come to be known as the "modern theory of polarization". The purpose of the present chapter is to provide a pedagogical introduction to this theory, to give a brief introduction to its computational implementation, and to discuss its implications for the physical understanding of FE materials.

1.1 Fallacy of the Clausius–Mossotti Picture

Within the CM model the charge distribution of a polarized condensed system is regarded as the superposition of localized contributions, each providing an electric dipole. In a crystalline system the CM macroscopic polarization $\boldsymbol{P}_{\mathrm{CM}}$ is *defined* as the sum of the dipole moments in a given cell divided by the cell volume. We shall contrast this view with a more realistic microscopic picture of the phenomenon of macroscopic polarization.

An extreme CM view of a simple ionic crystal having the NaCl structure is sketched in Fig. 1. The essential point behind the CM view is that the distribution of the induced charge is resolved into contributions that can be ascribed to identifiable "polarization centers". In the sketch of Fig. 1 these are the anions, while in the most general case they may be atoms, molecules, or even bonds. This partitioning of the polarization charge is obvious in Fig. 1, where the individual localized contributions are drawn as nonoverlapping.

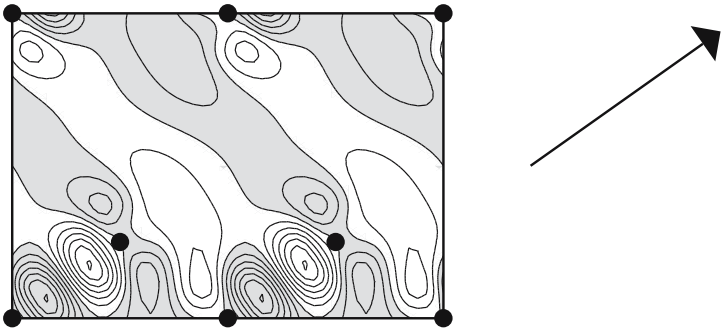

Fig. 2. Induced (pseudo)charge density $\rho^{(\mathrm{ind})}(\boldsymbol{r})$ in the $(1\bar{1}0)$ plane linearly induced by a constant field $\boldsymbol{\mathcal{E}}$ in the [111] direction, indicated by the arrow, in crystalline silicon. The field has unit magnitude (in a.u.) and the contours are separated by 30 charge units per cell. Shaded areas indicate regions of negative charge; circles indicate atomic positions

But what about real materials? This is precisely the case in point: the electronic polarization charge in a crystal has a periodic continuous distribution, which cannot be unambiguously partitioned into localized contributions.

In typical FE oxides the bonding has a mixed ionic/covalent character [4], with a sizeable fraction of the electronic charge being shared among ions in a delocalized manner. This fact makes any CM picture totally inadequate. In order to emphasize this feature, we take as a paradigmatic example the extreme covalent case, namely, crystalline silicon. In this material, the valence-electron distribution essentially forms a continuous tetrahedral network, and cannot be unambiguously decomposed into either atomic or bond contributions. We show in Fig. 2 the analog of Fig. 1 for this material, with the electronic distribution polarized by an applied field along the [111] direction. The calculation is performed in a first-principle framework using a pseudopotential implementation of density-functional theory [5, 6]; the quantity actually shown is the induced polarization *pseudo*charge of the valence electrons.

Clearly, the induced charge is delocalized throughout the cell and any partition into localized polarization centers, as needed for establishing a CM picture, is largely arbitrary. Looking more closely at the continuous polarization charge of Fig. 2, one notices that in the regions of the bonds parallel to the field the induced charge indeed shows a dipolar shape. It is then tempting to identify the CM polarization centers with these bond dipoles, but we shall show that such an identification would be incorrect. The clamped-ion (also called static high-frequency) dielectric tensor [7, 8] can be defined as

$$\varepsilon_\infty = 1 + 4\pi\chi = 1 + 4\pi \frac{\partial \boldsymbol{P}}{\partial \boldsymbol{\mathcal{E}}} \,, \tag{1}$$

where $\boldsymbol{P}$ is the macroscopic polarization and $\boldsymbol{\mathcal{E}}$ is the (screened) electric field. One would like to replace $\boldsymbol{P}$ with $\boldsymbol{P}_{\mathrm{CM}}$, i.e., the induced bond dipole per

cell. However, in order to actually evaluate $\boldsymbol{P}_{\rm CM}$, one must choose a recipe for truncating the integration to a local region, which is largely arbitrary. Even more importantly, no matter which reasonable recipe one adopts, the magnitude of $\boldsymbol{P}_{\rm CM}$ is far too small (by at least an order of magnitude) to reproduce the actual value $\varepsilon_\infty \simeq 12$ in silicon. The magnitude of the local dipoles seen in Fig. 2 may therefore account for only a small fraction of the actual $\boldsymbol{P}$ value for this material. In fact, as we shall explain below, it is generally *impossible* to obtain the value of $\boldsymbol{P}$ from the induced charge density alone.

1.2 Fallacy of Defining Polarization via the Charge Distribution

Given that $\boldsymbol{P}$ carries the meaning of electric dipole moment per unit volume, it is tempting to try to define it as the dipole of the macroscopic sample divided by its volume, i.e.,

$$\boldsymbol{P}_{\rm samp} = \frac{1}{V_{\rm samp}} \int_{\rm samp} {\rm d}\boldsymbol{r}\ \boldsymbol{r}\rho(\boldsymbol{r})\,. \tag{2}$$

We focus, once more, on the case of crystalline silicon polarized by an external field along the [111] direction. In order to apply (2), we need to assume a macroscopic but *finite* crystal. But the integral then has contributions from both the surface and the bulk regions, which cannot be easily disentangled. In particular, suppose that a cubic sample of dimensions $L\times L\times L$ has its surface preparation changed in such a way that a new surface charge density $\Delta\sigma$ appears on the right face and $-\Delta\sigma$ on the left; this will result in a change of dipole moment scaling as L^3, and thus, a change in the value of $\boldsymbol{P}_{\rm samp}$, despite the fact that the conditions in the interior have not changed. Thus, (2) is not a useful *bulk* definition of polarization; and even if it were, there would be no connection between it and the induced periodic charge density in the sample interior that is illustrated in Fig. 2.

A second tempting approach to a definition of the bulk polarization is via

$$\boldsymbol{P}_{\rm cell} = \frac{1}{V_{\rm cell}} \int_{\rm cell} {\rm d}\boldsymbol{r}\ \boldsymbol{r}\rho(\boldsymbol{r})\,, \tag{3}$$

where the integration is carried out over one unit cell deep in the interior of the sample. However, this approach is also flawed, because the result of (3) depends on the shape and location of the unit cell. (Indeed, the average of $\boldsymbol{P}_{\rm cell}$ over all possible translational shifts is easily shown to vanish.) It is only within an extreme CM model – where the periodic charge can be decomposed with no ambiguity by choosing, as in Fig. 1, the cell boundary to lie in an interstitial region of vanishing charge density – that $\boldsymbol{P}_{\rm cell}$ is well defined. However, in many materials a CM model is completely inappropriate, as discussed above.

As a third approach, one might imagine defining $\boldsymbol{P}$ as the cell average of a microscopic polarization $\boldsymbol{P}_{\text{micro}}$ defined via

$$\nabla \cdot \boldsymbol{P}_{\text{micro}}(\boldsymbol{r}) = -\rho(\boldsymbol{r})\,. \tag{4}$$

However, the above equation does *not* uniquely define $\boldsymbol{P}_{\text{micro}}(\boldsymbol{r})$, since any divergence-free vector field, and in particular any constant vector, can be added to $\boldsymbol{P}_{\text{micro}}(\boldsymbol{r})$ without affecting the left-hand side of (4).

The conclusion to be drawn from the above discussion is that a knowledge of the periodic electronic charge distribution in a polarized crystalline solid cannot, even in principle, be used to construct a meaningful definition of bulk polarization. This has been understood, and similar statements have appeared in the literature, since at least 1974 [9]. However, this important message has not received the wide appreciation it deserves, nor has it reached the most popular textbooks [7, 8].

These conclusions may appear counterintuitive and disturbing, since one reasonably expects that the macroscopic polarization in the bulk region of a solid should be determined by what "happens" in the bulk. But this is precisely the basis of a third, and finally rewarding, approach to the problem, in which one focuses on the *change* in $\boldsymbol{P}_{\text{samp}}$ that occurs during some process such as the turning on of an external electric field. The change in internal polarization $\Delta\boldsymbol{P}$ that we seek will then be given by the change $\Delta\boldsymbol{P}_{\text{samp}}$ of (2), *provided* that any charge that is pumped to the surface is not allowed to be conducted away. (Thus, the sides of the sample must be insulating, there must be no grounded electrodes, etc.) Actually, it is preferable simply to focus on the charge *flow* in the interior of the sample during this process, and write

$$\Delta\boldsymbol{P} = \int \mathrm{d}t\, \frac{1}{V_{\text{cell}}} \int_{\text{cell}} \mathrm{d}\boldsymbol{r}\; \boldsymbol{j}(\boldsymbol{r},t)\,. \tag{5}$$

This equation is the basis of the modern theory of polarization that will be summarized in the remainder of this chapter. Again, it should be emphasized that the definition (5) has nothing to do with the periodic static charge distribution inside the bulk unit cell of the polarized solid.

So far, we have avoided any experimental consideration. How is $\boldsymbol{P}$ measured? Certainly no one relies on measuring cell dipoles, although induced charge distributions of the kind shown in Fig. 2 are accessible to X-ray crystallography. A FE material sustains, by definition, a spontaneous macroscopic polarization, i.e., a nonvanishing value of $\boldsymbol{P}$ in the absence of any perturbation. But once again, while the microscopic charge distribution inside the unit cell of a FE crystal is experimentally accessible, actual measurements of the spontaneous polarization are based on completely different ideas, more closely related to (5). As we will see below in Sect. 2, this approach defines the observable $\boldsymbol{P}$ in a way that very naturally parallels experiments, both for spontaneous and induced polarization. We also see that the theory vindicates

the concept that macroscopic polarization is an intensive quantity, insensitive to surface effects, whose value is indeed determined by what "happens" in the bulk of the solid and not at its surface.

2 Polarization as an Adiabatic Flow of Current

2.1 How is Induced Polarization Measured?

Most measurements of bulk macroscopic polarization $\boldsymbol{P}$ of materials do not access its absolute value, but only its derivatives, which are expressed as Cartesian tensors. For example, the permittivity

$$\chi_{\alpha\beta} = \frac{\mathrm{d}P_\alpha}{\mathrm{d}\mathcal{E}_\beta} \tag{6}$$

appearing in (1) is defined as the derivative of polarization with respect to field. Here, as throughout this chapter, Greek subscripts indicate Cartesian coordinates. Similarly, the pyroelectric coefficient

$$\Pi_\alpha = \frac{\mathrm{d}P_\alpha}{\mathrm{d}T}\,, \tag{7}$$

the piezoelectric tensor

$$\gamma_{\alpha\beta\delta} = \frac{\partial P_\alpha}{\partial \epsilon_{\beta\delta}} \tag{8}$$

of Sect. 4.3, and the dimensionless Born (or "dynamical" or "infrared") charge

$$Z^*_{s,\alpha\beta} = \frac{\Omega}{e}\frac{\partial P_\alpha}{\partial u_{s,\beta}} \tag{9}$$

of Sect. 4.2, are defined in terms of derivatives with respect to temperature T, strain $\epsilon_{\beta\delta}$, and displacement $\boldsymbol{u}_s$ of sublattice s, respectively. Here, $e > 0$ is the charge quantum, and from now on we use Ω to denote the primitive-cell volume V_{cell}. (In the above formulas, derivatives are to be taken at fixed electric field and fixed strain when these variables are not explicitly involved.)

We start by illustrating one such case, namely, piezoelectricity, in Fig. 3. The situation depicted in (a) is the one where (2) applies. Supposing that $\boldsymbol{P}$ is zero in the unstrained state (e.g., by symmetry), then the piezoelectric constant is simply proportional to the value of $\boldsymbol{P}$ in the final state. The disturbing feature is that piezoelectricity appears as a surface effect, and indeed the debate whether piezoelectricity is a bulk or a surface effect lasted in the literature until rather recently [10–16]. The modern theory parallels the situation depicted in (b) and provides further evidence that piezoelectricity is a bulk effect, if any was needed. While the crystal is strained, a transient

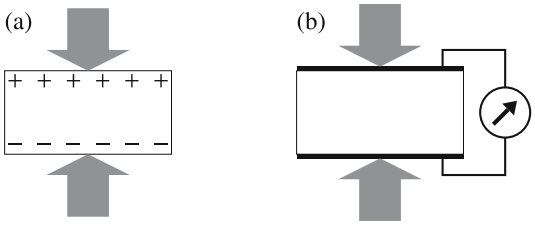

Fig. 3. Two possible realizations of the piezoelectric effect in a crystal strained along a piezoelectric axis. In (**a**) the crystal is not shorted, and induced charges pile up at its surfaces. Macroscopic polarization may be defined via (2), but the surface charges are an essential contribution to the integral. In (**b**) the crystal is inserted into a shorted capacitor; the surface charges are then removed by the electrodes, and the induced polarization is measured by the current flowing through the shorting wire

electrical current flows through the sample, and this is precisely the quantity being measured; the polarization of the final state is *not* obtained from a measurement performed on the final state only. In fact, the essential feature of (b) is its *time dependence*, although slow enough to ensure adiabaticity. The fundamental equation

$$\frac{\mathrm{d}\boldsymbol{P}(t)}{\mathrm{d}t} = \boldsymbol{j}(t)\,, \tag{10}$$

where $\boldsymbol{j}$ is the macroscopic (i.e., cell-averaged) current density, implies

$$\Delta\boldsymbol{P} = \boldsymbol{P}(\Delta t) - \boldsymbol{P}(0) = \int_0^{\Delta t} \mathrm{d}t\; \boldsymbol{j}(t)\,. \tag{11}$$

Notice that, in the adiabatic limit, $\boldsymbol{j}$ goes to zero and Δt goes to infinity, while the integral in (11) stays finite. We also emphasize that currents are much easier to measure than dipoles or charges, and therefore (b), much more than (a), is representative of actual piezoelectric measurements.

At this point we return to the case of permittivity, i.e., polarization induced by an electric field, previously discussed in Sect. 1.1. It is expedient to examine Figs. 1 and 2 in a time-dependent way by imagining that the perturbing $\boldsymbol{\mathcal{E}}$ field is adiabatically switched on. There is then a transient macroscopic current flowing through the crystal cell, whose time-integrated value provides the induced macroscopic polarization, according to (11). This is true for both the CM case of Fig. 1 and the non-CM case of Fig. 2. The important difference is that in the former case the current displaces charge within each individual anion but vanishes on the cell boundary, while in the latter case the current flows throughout the interior of the crystal.

Using the examples of piezoelectricity and of permittivity, we have shown that the induced macroscopic polarization in condensed matter can be defined

and understood in terms of adiabatic flows of currents within the material. From this viewpoint, it becomes very clear how the value of $\boldsymbol{P}$ is determined by what happens in the bulk of the solid, and why it is insensitive to surface effects.

2.2 How is Ferroelectric Polarization Measured?

FE materials are insulating solids characterized by a switchable macroscopic polarization $\boldsymbol{P}$. At equilibrium, a FE material displays a broken-symmetry, noncentrosymmetric structure, so that a generic vector property is not required to vanish by symmetry. The most important vector property is indeed $\boldsymbol{P}$, and its equilibrium value is known as the *spontaneous polarization*.

However, the value of $\boldsymbol{P}$ is never measured directly as an equilibrium property; instead, all practical measurements exploit the switchability of $\boldsymbol{P}$. In most crystalline FEs, the different structures are symmetry-equivalent; that is, the allowed values of $\boldsymbol{P}$ are equal in modulus and point along equivalent (enantiomorphous) symmetry directions. In a typical experiment, application of a sufficiently strong electric field switches the polarization from $\boldsymbol{P}$ to $-\boldsymbol{P}$, so that one speaks of polarization *reversal*.

The quantity directly measured in a polarization-reversal experiment is the difference in polarization between the two enantiomorphous structures; making use of symmetry, one can then equate this difference to twice the spontaneous polarization. This pragmatic working definition of spontaneous polarization has, as a practical matter, been adopted by the experimental community since the early days of the field. However, it was generally considered that this was done only as an expedient, because direct access to the "polarization itself" was difficult to obtain experimentally. Instead, with the development of modern electronic-structure methods and the application of these methods to FE materials, it became evident that the previous "textbook definitions" [7, 8] of $\boldsymbol{P}$ were also unworkable from the *theoretical* point of view. It was found that such attempts to define $\boldsymbol{P}$ as a single-valued equilibrium property of the crystal in a given broken-symmetry state, in the spirit of (3), were doomed to failure because they could not be implemented in an unambiguous way.

In response to this impasse, a new theoretical viewpoint emerged in the early 1990s and was instrumental in the development of a successful microscopic theory [17–19]. As we shall see, this modern theory of polarization actually elevates the old pragmatic viewpoint to the status of a postulate. Rather than focusing on $\boldsymbol{P}$ as an equilibrium property of the crystal in a given state, one focuses on *differences* in polarization between two different states [17]. From the theoretical viewpoint, this represents a genuine change of paradigm, albeit one that is actually harmonious with the old experimental pragmatism.

We illustrate a polarization-reversal experiment by considering the case of the perovskite oxide $PbTiO_3$, whose equilibrium structure at zero temper-

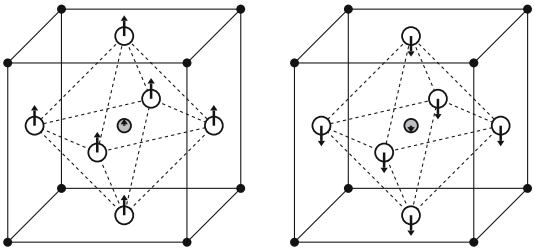

Fig. 4. Tetragonal structure of $PbTiO_3$: solid, shaded, and empty circles represent Pb, Ti, and O atoms, respectively. The arrows indicate the actual magnitude of the atomic displacements, where the origin has been kept at the Pb site (the Ti displacements are barely visible). Two enantiomorphous structures, with polarization along [001], are shown here. Application of a large enough electric field (coercive field) switches between the two and reverses the polarization

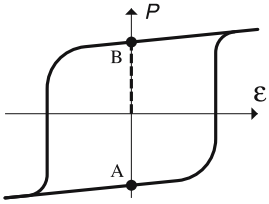

Fig. 5. A typical hysteresis loop; the magnitude of the spontaneous polarization is also shown (*vertical dashed segment*). Notice that spontaneous polarization is a zero-field property

ature is tetragonal. There are six enantiomorphous broken-symmetry structures; two of them, having opposite nuclear displacements and opposite values of $\boldsymbol{P}$, are shown in Fig. 4.

A typical measurement of the spontaneous polarization, performed through polarization reversal, is schematically shown in Fig. 5. The hysteresis cycle is in fact the primary experimental output. The transition between the two enantiomorphous FE structures A and B of Fig. 4 is driven by an applied electric field; the experimental setup typically measures the integrated macroscopic current flowing through the sample, as in (11). One half of the difference $\boldsymbol{P}_{\mathrm{B}} - \boldsymbol{P}_{\mathrm{A}}$ defines the magnitude $\boldsymbol{P}_{\mathrm{s}}$ of the spontaneous polarization in the vertical direction. From Fig. 5, it is clear that $\boldsymbol{P}_{\mathrm{s}}$ can also be defined as the polarization difference $\Delta\boldsymbol{P}$ between the broken-symmetry B structure and the centrosymmetric structure (where the displacements are set to zero). Notice that, while a field is needed to induce the switching in the actual experiment, ideally one could evaluate $\Delta\boldsymbol{P}$ along the vertical axis in Fig. 5, where the macroscopic field is identically zero. We stress that the experiment measures neither $\boldsymbol{P}_{\mathrm{A}}$ nor $\boldsymbol{P}_{\mathrm{B}}$, but only their *difference*. It is only an additional symmetry argument that allows one to infer the value of each of them from the actual experimental data.

2.3 Basic Prescriptions for a Theory of Polarization

For both induced and spontaneous polarization, we have emphasized the role of adiabatic currents in order to arrive at a microscopic theory of $\boldsymbol{P}$, which by construction must be an intensive bulk property, insensitive to the boundaries. The root of this theory is in (11), whose form we simplify by introducing a parameter λ having the meaning of a dimensionless adiabatic time: λ varies continuously from zero (corresponding to the initial system) to 1 (corresponding to the final system). Then we can write (11) as

$$\Delta \boldsymbol{P} = \int_0^1 \mathrm{d}\lambda \, \frac{\mathrm{d}\boldsymbol{P}}{\mathrm{d}\lambda} \,. \tag{12}$$

In general, "initial" and "final" refer to the state of the system before and after the application of some slow sublattice displacements, strains, electric fields, etc. The key feature exploited here is that $\mathrm{d}\boldsymbol{P}/\,\mathrm{d}\lambda$ is a well-defined bulk vector property. We notice, however, that an important condition for (12) to hold is that the system remain insulating for all intermediate values of λ, since the transient current is otherwise *not* uniquely defined. Note that for access to the response properties of (6)–(9), no integration is needed; the physical quantity of interest coincides by definition with $\mathrm{d}\boldsymbol{P}/\,\mathrm{d}\lambda$ evaluated at an appropriate λ.

In order to focus the discussion onto the spontaneous polarization of a FE, we now let λ scale the sublattice displacements (the lengths of the arrows in Fig. 4) leading from a centrosymmetric reference structure ($\lambda = 0$) to the spontaneously polarized structure ($\lambda = 1$). Then the spontaneous polarization may be written [17]

$$\boldsymbol{P}_{\mathrm{eff}} = \int_0^1 \mathrm{d}\lambda \, \frac{\mathrm{d}\boldsymbol{P}}{\mathrm{d}\lambda} \qquad (\lambda = 0 : \text{centrosymmetric reference}) \,. \tag{13}$$

For later reference, note that this is the "effective" and not the "formal" definition of polarization as given later in (20) and discussed in the later parts of Sect. 3.

The current-carrying particles are electrons and nuclei; while the quantum nature of the former is essential, the latter can be safely dealt with as classical point charges, whose current contributions to (11) and to (12) are trivial. We focus then mostly on the electronic term in the currents and in $\boldsymbol{P}$, although it has to be kept in mind that the overall charge neutrality of the condensed system is essential. Furthermore, from now on we limit ourselves to a zero-temperature framework, thus ruling out the phenomenon of pyroelectricity.

We refer, once more, to Fig. 2, where the quantum nature of the electrons is fully accounted for. As explained above, in order to obtain $\boldsymbol{P}$ via (11), one needs the adiabatic electronic current that flows through the crystal while the perturbation is switched on. Within a quantum-mechanical description of the electronic system, currents are closely related to the *phase* of the wavefunction

(for instance, if the wavefunction is real, the current vanishes everywhere). But only the *modulus* of the wavefunction has been used in drawing the charge distribution of Fig. 2; any phase information has been obliterated, so that the value of $\boldsymbol{P}$ cannot be retrieved. Interestingly, this argument is in agreement with the general concept, strongly emphasized above, that the periodic polarization charge inside the material has nothing to do with the value of macroscopic polarization.

Next, it is expedient to discuss a little more thoroughly the role of the electric field $\boldsymbol{\mathcal{E}}$. A direct treatment of a finite electric field is subtle, because the periodicity of the crystal Hamiltonian, on which the Bloch theorem depends, is absent unless $\boldsymbol{\mathcal{E}}$ vanishes (see Sect. 5.1). However, while $\boldsymbol{\mathcal{E}}$ is by definition the source inducing $\boldsymbol{P}$ in the case of permittivity in (6), a source *other* than the electric field is involved in the cases of pyroelectricity (7), piezoelectricity (8), dynamical effective charges (9), and spontaneous polarization (13). While it is sometimes appropriate to take these latter derivatives under electrical boundary conditions other than those of a vanishing field, we shall restrict ourselves here to the most convenient and fundamental definitions in which the field $\boldsymbol{\mathcal{E}}$ is set to zero. For example, piezoelectricity, when measured as in Fig. 3b, is clearly a zero-field property, since the sample is shorted at all times. Spontaneous polarization, when measured as in Fig. 5, is obviously a zero-field property as well. Born effective charges, which will be addressed below, are also defined as zero-field tensors. Then, as an example of two different choices of boundary conditions to address the same phenomenon, we may consider again the case of piezoelectricity, Fig. 3. While in Fig. 3b the field is zero, in Fig. 3a a nonvanishing ("depolarizing") field is clearly present inside the material. The two piezoelectric tensors, phenomenologically defined in these two different ways, are not equal but are related in a simple way (in fact, they are proportional via the dielectric tensor).

Thus, it is possible to access many of the interesting physical properties, including piezoelectricity, lattice dynamics, and ferroelectricity, with calculations performed at zero field. We will restrict ourselves to this case for most of this chapter. As for the permittivity, it is theoretically accessible by means of either the linear-response theory (see [20] for a thorough review), or via an extension of the Berry-phase theory to finite electric field that will be described briefly in Sect. 5.1.

3 Formal Description of the Berry-Phase Theory

In this section, we shall give an introduction to the modern theory of polarization that was developed in the 1990s. Following important preliminary developments of *Resta* [17], the principal development of the theory was introduced by *King-Smith* and *Vanderbilt* [18] and soon afterwards reviewed by *Resta* [19]. This theory is sometimes known as the "Berry-phase theory of

polarization" because the polarization is expressed in the form of a certain quantum phase known as a Berry phase [21, 22].

In order to deal with macroscopic systems, both crystalline and disordered, it is almost mandatory in condensed-matter theory to assume periodic (Born–von Kármán) boundary conditions [7, 8]. This amounts to considering the system in a finite box that is periodically repeated, in a ring-like fashion, in all three Cartesian directions. Eventually, the limit of an infinitely large box is taken. For practical purposes, the thermodynamic limit is approached when the box size is much larger than a typical atomic dimension. Among other features, a system of this kind has no surface and all of its properties are by construction "bulk" ones. When the system under consideration is a many-electron system, the periodic boundary conditions amount to requiring that the wavefunction and the Hamiltonian be periodic over the box. As indicated previously, our discussion will be restricted to the case of vanishing electric field unless otherwise stated.

We give below only a brief sketch of the derivation of the central formulas of the theory; interested readers are referred to [18, 19, 23] for details.

3.1 Formulation in Continuous k-Space

If we adopt for the many-electron system a mean-field treatment, such as the Kohn–Sham one [5], the self-consistent one-body potential is periodic over the Born–von Kármán box, provided the electric field $\boldsymbol{\mathcal{E}}$ vanishes, for any value of the parameter λ. Furthermore, if we consider a *crystalline* system, the self-consistent potential also has the lattice periodicity. The eigenfunctions are of the Bloch form $\psi_{n\boldsymbol{k}}(\boldsymbol{r}) = \mathrm{e}^{\mathrm{i}\boldsymbol{k}\cdot\boldsymbol{r}}\, u_{n\boldsymbol{k}}(\boldsymbol{r})$, where u is lattice-periodical, and obey the Schrödinger equation $H|\psi_{n\boldsymbol{k}}\rangle = E_{n\boldsymbol{k}}\,|\psi_{n\boldsymbol{k}}\rangle$, where $H = p^2/2m + V$. Equivalently, the eigenvalue problem can be written as $H_{\boldsymbol{k}}|u_{n\boldsymbol{k}}\rangle = E_{n\boldsymbol{k}}\,|u_{n\boldsymbol{k}}\rangle$, where

$$H_{\boldsymbol{k}} = \frac{(\boldsymbol{p} + \hbar\boldsymbol{k})^2}{2m} + V\,. \tag{14}$$

All of these quantities depend implicitly on a parameter λ that changes slowly in time, such that the wavefunction acquires, from elementary adiabatic perturbation theory, a first-order correction

$$|\delta\psi_{n\boldsymbol{k}}\rangle = -\mathrm{i}\hbar\,\dot{\lambda} \sum_{m\neq n} \frac{\langle\psi_{m\boldsymbol{k}}|\partial_\lambda\psi_{n\boldsymbol{k}}\rangle}{E_{n\boldsymbol{k}} - E_{m\boldsymbol{k}}}\,|\psi_{m\boldsymbol{k}}\rangle\,, \tag{15}$$

where $\dot{\lambda} = \mathrm{d}\lambda/\,\mathrm{d}t$ and ∂_λ is the derivative with respect to the parameter λ. The corresponding first-order current arising from the entire band n is then[1]

$$\boldsymbol{j}_n = \frac{\mathrm{d}\boldsymbol{P}_n}{\mathrm{d}t} = \frac{\mathrm{i}\hbar e\dot{\lambda}}{(2\pi)^3 m} \sum_{m\neq n} \int \mathrm{d}\boldsymbol{k}\, \frac{\langle\psi_{n\boldsymbol{k}}|\boldsymbol{p}|\psi_{m\boldsymbol{k}}\rangle\langle\psi_{m\boldsymbol{k}}|\partial_\lambda\psi_{n\boldsymbol{k}}\rangle}{E_{n\boldsymbol{k}} - E_{m\boldsymbol{k}}} \;+\; \text{c.c.}\,, \quad (16)$$

where "c.c." denotes the complex conjugate. Time t can be eliminated by removing $\dot{\lambda}$ from the right-hand side and replacing $\mathrm{d}\boldsymbol{P}/\,\mathrm{d}t \;\rightarrow\; \mathrm{d}\boldsymbol{P}/\,\mathrm{d}\lambda$ on the left-hand side above. Then, making use of ordinary perturbation theory applied to the dependence of $H_{\boldsymbol{k}}$ in (14) upon $\boldsymbol{k}$, one obtains, after some manipulation,

$$\frac{\mathrm{d}\boldsymbol{P}_n}{\mathrm{d}\lambda} = \frac{\mathrm{i}e}{(2\pi)^3} \int \mathrm{d}\boldsymbol{k}\, \langle\nabla_{\boldsymbol{k}} u_{n\boldsymbol{k}}|\partial_\lambda u_{n\boldsymbol{k}}\rangle \;+\; \text{c.c.}\,. \quad (17)$$

It is noteworthy that the sum over "unoccupied" states m has disappeared from this formula, corresponding to our intuition that the polarization is a ground-state property. Summing now over the occupied states, and inserting in (12), we get the spontaneous polarization of a FE. The result, after an integration with respect to λ, is that the effective polarization (13) takes the form

$$\boldsymbol{P}_{\text{eff}} = \Delta\boldsymbol{P}_{\text{ion}} + \left[\,\boldsymbol{P}_{\text{el}}(1) - \boldsymbol{P}_{\text{el}}(0)\,\right], \quad (18)$$

where the nuclear contribution $\Delta\boldsymbol{P}_{\text{ion}}$ has been restored, and

$$\boldsymbol{P}_{\text{el}}(\lambda) = \frac{e}{(2\pi)^3}\, \Im \sum_n \int \mathrm{d}\boldsymbol{k}\, \langle u_{n\boldsymbol{k}}|\nabla_{\boldsymbol{k}}|u_{n\boldsymbol{k}}\rangle\,. \quad (19)$$

Here, the sum is over the occupied states, and $|u_{n\boldsymbol{k}}\rangle$ are understood to be implicit functions of λ. In the case that the adiabatic path takes a FE crystal from its centrosymmetric reference state to its equilibrium polarized state, $\boldsymbol{P}_{\text{eff}}$ of (18) is just exactly the spontaneous polarization.

Equation (19) is the central result of the modern theory of polarization. Those familiar with Berry-phase theory [21, 22] will recognize $\boldsymbol{A}(\boldsymbol{k}) = \mathrm{i}\langle u_{n\boldsymbol{k}}|\nabla_{\boldsymbol{k}}|u_{n\boldsymbol{k}}\rangle$ as a "Berry connection" or "gauge potential"; its integral over a closed manifold (here the Brillouin zone) is known as a "Berry phase". It is remarkable that the result (19) is independent of the path traversed through parameter space (and of the rate of traversal, as long as it is adiabatically slow), so that the result depends only on the endpoints. Implicit in the analysis is that the system must remain insulating everywhere along the path, as otherwise the adiabatic condition fails.

[1] In this and subsequent formulas, we assume that n is really a composite index for band and spin. Alternatively, factors of two may be inserted into the equations to account for spin degeneracy.

To obtain the total polarization, the ionic contribution must be added to (19). The total polarization is then $\boldsymbol{P} = \boldsymbol{P}_{\rm el} + \boldsymbol{P}_{\rm ion}$ or

$$\boldsymbol{P} = \frac{e}{(2\pi)^3}\,\Im \sum_n \int \mathrm{d}\boldsymbol{k}\,\langle u_{n\boldsymbol{k}}|\nabla_{\boldsymbol{k}}|u_{n\boldsymbol{k}}\rangle + \frac{e}{\Omega}\sum_s Z_s^{\rm ion}\,\boldsymbol{r}_s\,, \tag{20}$$

where the first term is (19) and the second is $\boldsymbol{P}_{\rm ion}$, the contribution arising from positive point charges $eZ_s^{\rm ion}$ located at atomic positions $\boldsymbol{r}_s$. In principle, the band index n should run over all bands, including those made from core states, and $Z^{\rm ion}$ should be the bare nuclear charge. However, in the frozen-core approximation that underlies pseudopotential theory, we let n run over valence bands only, and $Z^{\rm ion}$ is the net positive charge of the nucleus plus core. We adopt the latter interpretation here.

We refer to the polarization of (20) as the "formal polarization" to distinguish it from the "effective polarization" of (13) or (18). The two definitions coincide only if the formal polarization vanishes for the centrosymmetric reference structure used to define $\boldsymbol{P}_{\rm eff}$, which, as we shall see in Sect. 3.4, need not be the case.

3.2 Formulation in Discrete *k*-Space

In practical numerical calculations, equations such as (16), (17), and (19) are summed over a discrete mesh of $\boldsymbol{k}$-points spanning the Brillouin zone. Since the $\nabla_{\boldsymbol{k}}$ operator is a derivative in $\boldsymbol{k}$-space, its finite-difference representation will involve couplings between neighboring points in $\boldsymbol{k}$-space.

For pedagogic purposes, we illustrate this by starting from the one-dimensional version of (19), namely, $P_n = (e/2\pi)\,\varphi_n$, where

$$\varphi_n = \Im \int \mathrm{d}k\,\langle u_{nk}|\partial_k|u_{nk}\rangle\,, \tag{21}$$

and note that this can be discretized as

$$\varphi_n = \Im \ln \prod_{j=0}^{M-1} \langle u_{n,k_j}|u_{n,k_{j+1}}\rangle\,, \tag{22}$$

where $k_j = 2\pi j/Ma$ is the jth k-point in the Brillouin zone. This follows by inserting the expansion $u_{n,k+dk} = u_{nk} + \mathrm{d}k\,(\partial_k u_{nk}) + \mathcal{O}(\mathrm{d}k^2)$ into (21) and keeping the leading term.

In (22), it is understood that the wavefunctions at the boundary points of the Brillouin zone are related by $\psi_{n,0} = \psi_{n,2\pi/a}$, so that

$$u_{n,k_0}(x) = \mathrm{e}^{2\pi \mathrm{i} x/a}\,u_{n,k_M}(x) \tag{23}$$

and there are only M independent states u_{n,k_0} to $u_{n,k_{M-1}}$. Thus, it is natural to regard the Brillouin zone as a *closed space* (in 1D, a loop) as illustrated in Fig. 6.

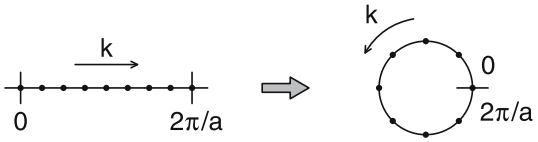

Fig. 6. Illustration showing how the Brillouin zone in one dimension (*left*) can be mapped onto a circle (*right*), in view of the fact that wavevectors $k = 0$ and $k = 2\pi/a$ label the same states

Equation (22) makes it easy to see why this quantity is called a Berry "phase". We are instructed to compute the global product of wavefunctions

$$\ldots \langle u_{k_1} | u_{k_2} \rangle \langle u_{k_2} | u_{k_3} \rangle \langle u_{k_3} | u_{k_4} \rangle \ldots \tag{24}$$

across the Brillouin zone, which in general is a complex number; then the operation "$\Im \ln$" takes the phase of this number. Note that this global phase is actually insensitive to a change of the phase of any one wavefunction u_k, since each u_k appears once in a bra and once in a ket. We can thus view the "Berry phase" φ_n, giving the contribution to the polarization arising from band n, as a global phase property of the manifold of occupied one-electron states.

In three dimensions (3D), the Brillouin zone can be regarded as a closed 3-torus obtained by identifying boundary points $\psi_{n\boldsymbol{k}} = \psi_{n,\boldsymbol{k}+\boldsymbol{G}_j}$, where $\boldsymbol{G}_j$ is a primitive reciprocal lattice vector. The Berry phase for band n in direction j is $\varphi_{n,j} = (\Omega/e)\, \boldsymbol{G}_j \cdot \boldsymbol{P}_n$, where $\boldsymbol{P}_n$ is the contribution to (19) from band n, so that

$$\varphi_{n,j} = \Omega_{\mathrm{BZ}}^{-1} \, \Im \int_{\mathrm{BZ}} \mathrm{d}^3 k \, \langle u_{n\mathbf{k}} | \boldsymbol{G}_j \cdot \nabla_{\boldsymbol{k}} | u_{n\mathbf{k}} \rangle \, . \tag{25}$$

We then have

$$\boldsymbol{P}_n = \frac{1}{2\pi} \frac{e}{\Omega} \sum_j \varphi_{n,j} \, \boldsymbol{R}_j \, , \tag{26}$$

where $\boldsymbol{R}_j$ is the real-space primitive translation corresponding to $\boldsymbol{G}_j$. To compute the $\varphi_{n,j}$ for a given direction j, the sampling of the Brillouin zone is arranged as in Fig. 7, where $k_\parallel$ is the direction along $\boldsymbol{G}_j$ and $\boldsymbol{k}_\perp$ refers to the 2D space of wavevectors spanning the other two primitive reciprocal lattice vectors. For a given $\boldsymbol{k}_\perp$, the Berry phase $\varphi_{n,j}(\boldsymbol{k}_\perp)$ is computed along the string of M k-points extending along $k_\parallel$ as in (22), and finally a conventional average over the $\boldsymbol{k}_\perp$ is taken:

$$\varphi_{n,j} = \frac{1}{N_{\boldsymbol{k}_\perp}} \sum_{\boldsymbol{k}_\perp} \varphi_n(\boldsymbol{k}_\perp) \, . \tag{27}$$

Note that a subtlety arises in regard to the "choice of branch" when taking this average, as discussed in the next subsection. Moreover, in 3D crystals,

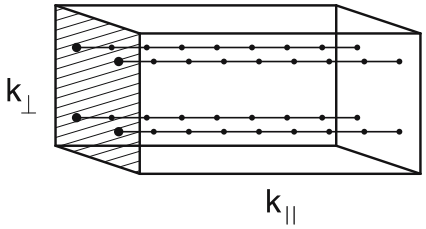

Fig. 7. Arrangement of Brillouin zone for computation of component of $\boldsymbol{P}$ along $k_{\parallel}$ direction

it may happen that some groups of bands must be treated using a many-band generalization of (22) due to degeneracy at high-symmetry points in the Brillouin zone; see [18, 19] for details.

The computation of $\boldsymbol{P}$ according to (26) is now a standard option in several popular electronic-structure codes (ABINIT[2], CRYSTAL[3], PWSCF[4], SIESTA[5], and VASP[6]).

3.3 The Quantum of Polarization

It is clear that (22), being a phase, is only well-defined mod 2π. We can see this more explicitly in (21); let

$$|\widetilde{u}_{nk}\rangle = \mathrm{e}^{-\mathrm{i}\beta(k)}\,|u_{nk}\rangle \tag{28}$$

be a new set of Bloch eigenstates differing only in the choice of phase as a function of k. Here $\beta(k)$ is real and obeys $\beta(2\pi/a) - \beta(0) = 2\pi m$, where m is an integer, in order that $\widetilde{\psi}_{n,0} = \widetilde{\psi}_{n,2\pi/a}$. Then inserting into (22) we find that

$$\widetilde{\varphi}_n = \varphi_n + \int_0^{2\pi/a} \mathrm{d}k \left(\frac{d\beta}{dk}\right) \mathrm{d}k = \varphi_n + 2\pi m\,. \tag{29}$$

Thus, φ_n is really only well-defined "mod 2π".

In view of this uncertainty, care must be taken in the 3D case when averaging $\varphi_n(\boldsymbol{k}_\perp)$ over the 2D Brillouin zone of $\boldsymbol{k}_\perp$ space: the choice of branch cut must be made in such a way that $\varphi_n(\boldsymbol{k}_\perp)$ remains continuous in $\boldsymbol{k}_\perp$. In practice, a conventional mesh sampling is used in the $\boldsymbol{k}_\perp$ space, and the average is computed as in (27). Consider, for example, Fig. 7, where $N_{\boldsymbol{k}_\perp} = 4$. If the branch cut is chosen independently for each $\boldsymbol{k}_\perp$ so as to map $\varphi_n(\boldsymbol{k}_\perp)$ to the interval $[-\pi, \pi]$, and if the four values were found to be 0.75π, 0.85π, 0.95π, and -0.95π, then the last value must be remapped to become 1.05π

[2] http://www.abinit.org/
[3] http://www.crystal.unito.it/
[4] http://www.pwscf.org
[5] http://www.uam.es/departamentos/ciencias/fismateriac/siesta
[6] http://cms.mpi.univie.ac.at/vasp/

before the average is taken in (27). That is, the correct average is 0.90π, or equivalently -1.10π, but *not* 0.40π as would be obtained by taking the average blindly.

In other words, care must be taken to make a *consistent* choice of phases on the right-hand side of (27). However, it is still permissible to shift all of the $N_{\boldsymbol{k}_\perp}$ phases by a common amount $2\pi m_j$. Thus, each $\varphi_{n,j}$ in (26) is only well-defined mod 2π, leading to the conclusion that $\boldsymbol{P}_n$ is only well-defined mod $e\boldsymbol{R}/\Omega$, where $\boldsymbol{R} = \sum_j m_j \boldsymbol{R}_j$ is a lattice vector. The same conclusion results from generalizing the argument of (28) and (29) to 3D, showing that a phase twist of the form $|\widetilde{u}_{n\boldsymbol{k}}\rangle = \exp[-\mathrm{i}\beta(\boldsymbol{k})]\,|u_{n\boldsymbol{k}}\rangle$ results in

$$\widetilde{\boldsymbol{P}}_n = \boldsymbol{P}_n + \frac{e\boldsymbol{R}}{\Omega}\,, \tag{30}$$

where $\boldsymbol{R}$ is a lattice vector.

These arguments are for a single band, but the same obviously applies to the sum over all occupied bands. *We thus arrive at a central result of the modern theory of polarization*: the formal polarization, defined via (20) or calculated through (26), is *only well-defined mod* $e\boldsymbol{R}/\Omega$, where $\boldsymbol{R}$ is any lattice vector and Ω is the primitive-cell volume.

At first sight the presence of this uncertainty modulo the quantum $e\boldsymbol{R}/\Omega$ may be surprising, but in retrospect it should have been expected. Indeed, the ionic contribution given by the second term of (20) is subject to precisely the same uncertainty, arising from the arbitrariness of the nuclear location $\boldsymbol{r}_s$ modulo a lattice vector $\boldsymbol{R}$. The choice of one particular value of $\boldsymbol{P}$ from among the lattice of values related to each other by addition of $e\boldsymbol{R}/\Omega$ will be referred to as the "choice of branch".

Summarizing our results so far, we find that the *formal polarization* $\boldsymbol{P}$, defined by (20), is only well-defined mod $e\boldsymbol{R}/\Omega$, where $\boldsymbol{R}$ is any lattice vector. Moreover, we have found that the change in polarization $\Delta\boldsymbol{P}$ along an adiabatic path, as defined by (12), is connected with this formal polarization by the relation

$$\Delta\boldsymbol{P} \;:=\; \left(\boldsymbol{P}_{\lambda=1} - \boldsymbol{P}_{\lambda=0}\right) \mod \frac{e\boldsymbol{R}}{\Omega}\,. \tag{31}$$

This central formula, embodying the main content of the modern theory of polarization, requires careful explanation. For a given adiabatic path, the change in polarization appearing on the left-hand side of (31), and defined by (12), is given by a single-valued vector quantity that is perfectly well defined and has no "modulus" uncertainty. On the right-hand side, $\boldsymbol{P}_{\lambda=0}$ and $\boldsymbol{P}_{\lambda=1}$ are, respectively, the formal polarization of (20) evaluated at the start and end of the path. The symbol ":=" has been introduced to indicate that the value on the left-hand side is equal to one of the values on the right-hand side. Thus, the precise meaning of (31) is that the actual integrated adiabatic current flow $\Delta\boldsymbol{P}$ is equal to $(\boldsymbol{P}_{\lambda=1} - \boldsymbol{P}_{\lambda=0}) + e\boldsymbol{R}/\Omega$ for some lattice vector $\boldsymbol{R}$.

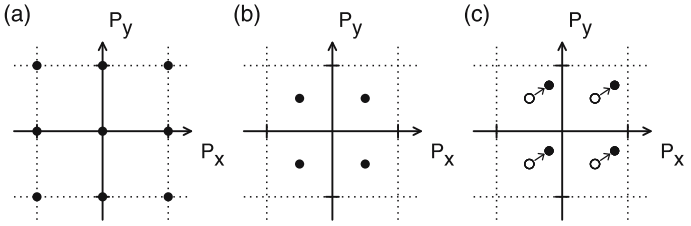

Fig. 8. Polarization as a lattice-valued quantity, illustrated for a 2D square-lattice system. Here, (**a**) and (**b**) illustrate the two possible states of polarization consistent with full square-lattice symmetry, while (**c**) illustrates a possible change in polarization induced by some symmetry-lowering change of the Hamiltonian. In (**c**), the *arrows* show the "effective polarization" as defined in (13)

It follows that (31) cannot be used to determine $\Delta \boldsymbol{P}$ completely; it only determines $\Delta \boldsymbol{P}$ within the same uncertainty mod $e\boldsymbol{R}/\Omega$ that applies to $\boldsymbol{P}_\lambda$. Fortunately, the typical magnitude of $\boldsymbol{P}_{\rm eff}$, and of polarization differences in general, is small compared to this "quantum". For cubic perovskites, $a \simeq 4$ Å, so that the effective quantum for spin-paired systems is $2e/a^2 \simeq 2.0\,\mathrm{C/m^2}$. In comparison, the spontaneous polarization of perovskite ferroelectrics is typically in the range of about 0.3 to $0.6\,\mathrm{C/m^2}$, significantly less than this quantum. Thus, this uncertainty mod $e\boldsymbol{R}/\Omega$ is rarely a serious concern in practice. If there is doubt about the correct choice of branch for a given path, this doubt can usually be resolved promptly by computing the polarization at several intermediate points along the path; as long as $\Delta \boldsymbol{P}$ is small for each step along the path, the correct interpretation of the evolution of the polarization will be clear.

3.4 Formal Polarization as a Multivalued Vector Quantity

A useful way to think about the presence of this "modulus" is to regard the formal polarization as a *multivalued vector quantity*, rather than a conventional single-valued one. That is, the question "What is $\boldsymbol{P}$?" is answered not by giving a single vector, but a lattice of vector values related by translations $e\boldsymbol{R}/\Omega$. Here, we explain how this viewpoint contributes to an understanding of the role of symmetry and provides an alternative perspective on the central result (31) of the previous subsection.

Let us begin with symmetry considerations, where we find some surprising results. Consider, for example, $KNbO_3$ in its ideal cubic structure. Because of the cubic symmetry, one might expect that $\boldsymbol{P}$ as calculated from (20) would vanish; or more precisely, given the uncertainty expressed by (30), that it would take on a lattice of values $(m_1, m_2, m_3)e/a^2$ that includes the zero vector (m_j are integers). This expected situation is sketched (in simplified 2D form) in Fig. 8a.

Table 1. Atomic positions $\boldsymbol{\tau}$ and nominal ionic charges Z for $KNbO_3$ in its centrosymmetric cubic structure with lattice constant a

Atom	τ_x	τ_y	τ_z	Z^{ion}
K	0	0	0	+1
Nb	$a/2$	$a/2$	$a/2$	+5
O_1	0	$a/2$	$a/2$	−2
O_2	$a/2$	0	$a/2$	−2
O_3	$a/2$	$a/2$	0	−2

However, when the result is actually calculated from (20) using first-principles electronic-structure methods, *this is not what one finds.* Instead, one finds that

$$\boldsymbol{P} = \left(m_1 + \frac{1}{2}, m_2 + \frac{1}{2}, m_3 + \frac{1}{2}\right) \frac{e}{a^2} \qquad (\text{integer } m_j)\,, \tag{32}$$

which is indeed a multivalued object, but corresponding to the situation sketched in Fig. 8b, not Fig. 8a!

While this result emerges above from a fully quantum-mechanical calculation, it is not essentially a quantum-mechanical result. Indeed, it could have been anticipated based on purely classical arguments as applied to an ideal ionic model of the $KNbO_3$ crystal. In such a picture, the formal polarization is written as

$$\boldsymbol{P} = \frac{e}{\Omega} \sum_s Z_s^{\text{ion}} \boldsymbol{\tau}_s\,, \tag{33}$$

where $\boldsymbol{\tau}_s$ is the location, and Z_s^{ion} is the nominal (integer) ionic charge, of ion s. Evaluating (33) using the values given in Table 1 yields $\boldsymbol{P} = (\frac{1}{2}, \frac{1}{2}, \frac{1}{2})e/a^2$. However, each vector $\boldsymbol{\tau}_s$ is arbitrary modulo a lattice vector. For example, it is equally valid to replace $\boldsymbol{\tau}_{\text{K}} = (0,0,0)$ by $\boldsymbol{\tau}_{\text{K}} = (a,a,a)$, yielding $\boldsymbol{P} = (\frac{3}{2}, \frac{3}{2}, \frac{3}{2})e/a^2$, which is again consistent with (32). Similarly, since each Z_s^{ion} is an integer,[7] the shift of any $\boldsymbol{\tau}_s$ by a lattice vector $\Delta\boldsymbol{R}$ simply generates a shift to one of the other vectors on the right-hand side of (32). This heuristic ionic model then leads to the same conclusion expressed in (32), i.e., that Fig. 8b and not Fig. 8a is appropriate for the case of cubic $KNbO_3$.

This may appear to be a startling result. We are saying that the polarization as defined by (20) does not necessarily vanish for a centrosymmetric structure (or more precisely, that the lattice of values corresponding to $\boldsymbol{P}$ does not contain the zero vector). Is this in conflict with the usual observation that

[7] For precisely this reason, it is necessary to use an ionic model with formal integer ionic charges for arguments of this kind. This requirement can be justified using arguments based on a Wannier representation.

a vector-valued physical quantity must vanish in a centrosymmetric crystal? No, because this theorem applies only to a normal (that is, single-valued) vector quantity. Instead, *the formal polarization is a multivalued vector quantity.* The constraint of centrosymmetry requires that the polarization must get mapped onto itself by the inversion operation. This would be impossible for a nonzero single-valued vector, but it *is* possible for a lattice of vector values, as illustrated in Fig. 8b. Indeed, the lattice of values shown in Fig. 8b is invariant with respect to all the operations of the cubic symmetry group, as are those of Fig. 8a. Actually, for a simple cubic structure with full cubic symmetry, these are the *only two possibilities* consistent with symmetry. It is not possible to know, from symmetry alone, which of these representations of the formal polarization is correct. A heuristic argument of the kind leading to (32) can be used to guess the correct result, but it should be confirmed by actual calculation. The heuristic arguments suggest, and first-principles calculations confirm, that the formal polarizations of $BaTiO_3$ and $KNbO_3$ are not equal, even though they have identical symmetry; they correspond to Fig. 8a and Fig. 8b, respectively!

How should we understand the spontaneous polarization $\boldsymbol{P}_{\rm s}$ of ferroelectrically distorted $KNbO_3$ in the present context? Recall that $\boldsymbol{P}_{\rm s}$ is defined as the effective polarization $\boldsymbol{P}_{\rm eff}$ of (13) for the case of an adiabatic path carrying $KNbO_3$ from its unstable cubic to its relaxed FE structure. Suppose that one were to find that this adiabatic evolution carried the polarization along the path indicated by the arrows in Fig. 8c. In this case, the effective polarization $\boldsymbol{P}_{\rm eff}$ of (13) is definitely known to correspond to the vector sketched repeatedly in Fig. 8c. However, when one evaluates $\Delta\boldsymbol{P}$ from (31), using only a knowledge of the endpoints of the path, the knowledge of the correct branch is lost. For example, one could not be certain that the actual $\Delta\boldsymbol{P}$ associated with this path is the one shown in Fig. 8c, rather than one pointing from an open circle in one cell to a closed one in a neighboring cell (and differing by the "modulus" $e\boldsymbol{R}/\Omega$). This is, of course, just the same uncertainty attached to (31) and discussed in detail in the previous subsection, now expressed from a more graphical point of view.

3.5 Mapping onto Wannier Centers

Another way of thinking about the meaning of the Berry-phase polarization, and of the indeterminacy of the polarization modulo the quantum $e\boldsymbol{R}/\Omega$, is in terms of Wannier functions. The Wannier functions are localized functions $w_{n\boldsymbol{R}}(\boldsymbol{r})$, labeled by band n and unit cell $\boldsymbol{R}$, that span the same Hilbert subspace as do the Bloch states $\psi_{n\boldsymbol{k}}$. In fact, they are connected by a Fourier-transform-like expression

$$|w_{n\boldsymbol{R}}\rangle = \frac{\Omega}{(2\pi)^3}\int \mathrm{d}\boldsymbol{k}\ \mathrm{e}^{\mathrm{i}\boldsymbol{k}\cdot\boldsymbol{R}}\,|\psi_{n\boldsymbol{k}}\rangle\,, \tag{34}$$

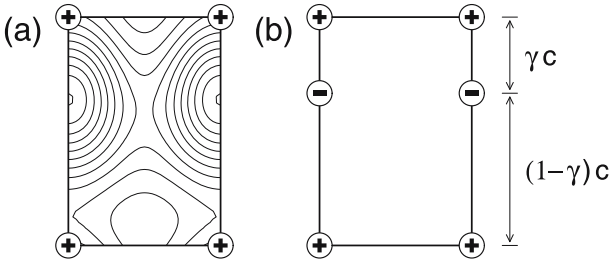

Fig. 9. Illustrative tetragonal crystal (cell dimensions $a \times a \times c$) having one monovalent ion at the cell corner (origin) and one occupied valence band. (**a**) The distributed quantum-mechanical charge distribution associated with the electron band, represented as a contour plot. (**b**) The distributed electron distribution has been replaced by a unit point charge $-e$ located at the Wannier center $\boldsymbol{r}_n$, as given by the Berry-phase theory

where the Bloch states are normalized to unity over the crystal cell. Once we have the Wannier functions, we can locate the "Wannier centers" $\boldsymbol{r}_{n\boldsymbol{R}} = \langle w_{n\boldsymbol{R}} | \boldsymbol{r} | w_{n\boldsymbol{R}} \rangle$. It turns out that the location of the Wannier center is simply

$$\boldsymbol{r}_{n\boldsymbol{R}} = \frac{\Omega}{e} \boldsymbol{P}_n + \boldsymbol{R} \,. \tag{35}$$

That is, specifying the contribution of band n to the Berry-phase polarization is really just equivalent to specifying the location of the Wannier center in the unit cell. Because the latter is indeterminate mod $\boldsymbol{R}$, the former is indeterminate mod $e\boldsymbol{R}/\Omega$.

Thus, the Berry-phase theory can be regarded as providing a mapping of the distributed quantum-mechanical electronic charge density onto a lattice of negative point charges of charge $-e$, as illustrated in Fig. 9. While the CM picture obviously *cannot* be applied to the situation of Fig. 9a, because the charge density vanishes nowhere in the unit cell, it *can* be applied to the situation of Fig. 9b without problem. The only question is whether the negative charge located at $z = (1 - \gamma)c$ in this figure should be regarded as "living" in the same unit cell as the positive nucleus at the origin or the one at $z = c$; this uncertainty corresponds precisely to the "quantum of polarization" $e\boldsymbol{R}/\Omega$ for the case $\boldsymbol{R} = c\hat{z}$.

It therefore appears that, by adopting the Wannier-center mapping, the CM viewpoint has been rescued. We are in fact decomposing the charge (nuclear and electronic) into localized contributions whose dipoles determine $\boldsymbol{P}$. However, one has to bear in mind that the *phase* of the Bloch orbitals is essential to actually perform the Wannier transformation. Knowledge of their *modulus* is not enough, while we stress once more that the modulus uniquely determines the periodic polarization charge, such as the one shown in Fig. 9a.

Before leaving this discussion, it is amusing to consider the behavior of the Wannier centers $\boldsymbol{r}_n$ under a *cyclic* adiabatic evolution of the Hamiltonian.

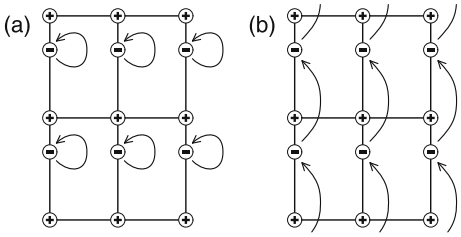

Fig. 10. Possible evolution of positions of Wannier centers (−), relative to the lattice of ions (+), as the Hamiltonian evolves adiabatically around a closed loop. Wannier functions must return to themselves, but can do so either (**a**) without, or (**b**) with, a coherent shift by a lattice vector

That is, we want to integrate the net adiabatic current flow as the system is taken around a *closed loop* in some multidimensional parameter space. (For example, one atomic sublattice might be displaced by 0.1 Å first along $+\hat{x}$, then $+\hat{y}$, then $-\hat{x}$, and then $-\hat{y}$.) Referring to (12) and (13), we have for this case

$$\Delta \boldsymbol{P}_{\rm cyc} = \oint_0^1 \mathrm{d}\lambda \, \frac{\mathrm{d}\boldsymbol{P}}{\mathrm{d}\lambda} \qquad \text{(cyclic evolution: } H_{\lambda=0} = H_{\lambda=1}\text{)}\,. \tag{36}$$

From (31), it follows that $\Delta \boldsymbol{P}_{\rm cyc}$ is either exactly zero or else exactly $e\boldsymbol{R}/\Omega$ for some non-zero lattice vector $\boldsymbol{R}$. The latter case corresponds to the "quantized charge transport" (or "quantum pumping") first discussed by *Thouless* [24].

Now suppose we follow the locations of the Wannier centers $\boldsymbol{r}_n$ during this adiabatic evolution. Since the initial and final points are the same, the Wannier centers must return to their initial locations at the end of the cyclic evolution. However, they can do so in two ways, as illustrated in Figs. 10a,b. If each Wannier center returns to itself, then $\Delta \boldsymbol{P}_{\rm cyc}$ is truly zero. However, as illustrated in Fig. 10b, this need not be the case; it is only necessary that each Wannier center return to one of its periodic images. If it does not return to itself, a quantized charge transport occurs.[8]

4 Implications for Ferroelectrics

Most of the fundamental and technological interest in FE materials arises from their polarization and related properties, including the dielectric and piezoelectric responses. The rigorous formulation of the polarization has allowed detailed quantitative investigation of these properties from first prin-

[8] We emphasize that this discussion is highly theoretical. While such a situation could occur in principle, it is not known to occur in practice in any real ferroelectric material.

ciples. In this section, we give an overview of the analysis of three key quantities – the spontaneous polarization, the Born effective charges, and the piezeoelectric response – and discuss case studies for specific perovskite oxides, primarily the tetragonal phase of the FE perovskite oxide $KNbO_3$.

4.1 Spontaneous Polarization

The experimental P_s values for the most common single-crystal FE perovskites in their different crystalline phases have been known for several decades. However, despite the fact that P_s is the very property characterizing FE materials, there was no theoretical access to it until 1993. As discussed above, the common-wisdom microscopic definition of what P_s was basically incorrect. The modern theory of polarization provides the correct definition of P_s, as well as the theoretical framework allowing one to compute it from the occupied Bloch eigenstates of the self-consistent crystalline Hamiltonian. As soon as *King-Smith* and *Vanderbilt* developed the theory [18] – as outlined in Sect. 3 – *Resta* et al. [25] implemented and applied it to compute the spontaneous polarization of a prototypical perovskite oxide from first principles.

The case study was $KNbO_3$ in its tetragonal phase, in a frozen-nuclei geometry taken from crystallographic data. The reciprocal cell is tetragonal: the integral in (19) was computed according to Sect. 3.2 (see Fig. 7), using the occupied Kohn–Sham orbitals [5]. The electronic phase so evaluated depends on the choice of the origin in the crystalline cell, but translational invariance is restored when the nuclear contribution is accounted for.

The computed phase turns out to be approximately $\pi/3$. This is large enough that it is advisable to check whether the correct choice of branch has been made for the multivalued function "$\Im\ln$" in (22), in order to eliminate the 2π ambiguity discussed in Sect. 3.3. This is done by repeating the calculation for smaller amplitudes of the FE distortion and making sure that the phase is a continuous function of the amplitude, as discussed earlier at the end of Sect. 3.3.

The first-principles calculation of [25] for tetragonal $KNbO_3$ yielded a value $P_s = 0.35\,\mathrm{C/m^2}$, to be compared to a best experimental value of $0.37\,\mathrm{C/m^2}$. A similar level of agreement was later found for other perovskites and using computational packages with different technical ingredients.

One aspect of the calculation deserves some comment. As stated above, we have adopted a frozen-nuclei approach, which in principle is appropriate for describing the polarization of the zero-temperature structure only. In the calculation for $KNbO_3$ discussed above, as well as in other calculations in the literature, one addresses instead the spontaneous polarization of a finite-temperature crystalline phase. In fact, the tetragonal phase of $KNbO_3$ only exists between 225 and 418 °C, while the equilibrium structure at zero temperature is rhombohedral and *not* tetrahedral. Crystallographic data provide

the time-averaged crystalline structure, while polarization-reversal experiments provide the time-averaged spontaneous polarization. The question is then whether the time-averaged polarization is equal, to a good approximation, to the polarization of the time-averaged structure, as the latter is in fact the quantity that is actually computed. The answer to this question is essentially "yes", supported by the finding that the macroscopic polarization is roughly linear, at the ±10–20 % level, in the amplitude of the structural distortion. This essential linearity could *not* have been guessed from model arguments, and in fact has only been discovered from the ab-initio calculations [25, 26].

4.2 Anomalous Dynamical Charges

The Born effective-charge tensors measure the coupling of a macroscopic field $\boldsymbol{\mathcal{E}}$ with relative sublattice displacements (zone-center phonons) in the crystal; they also go under the name of dynamical charges or infrared charges. Within an extreme rigid-ion model the Born charge coincides with the static charge of the model ion ("nominal" value), while in a real material the Born charges account for electronic polarization as well. Before the advent of the modern theory of polarization in the 1990s, the relevance of dynamical charges to the phenomenon of ferroelectricity had largely been overlooked.

There are two equivalent definitions of the Born tensor Z^*_s. 1. $Z^*_{s,\alpha\beta}$, as defined in (9), measures the change in polarization $\boldsymbol{P}$ in the α direction linearly induced by a sublattice displacement $\boldsymbol{u}_s$ in the β direction in zero macroscopic electric field. (Other kinds of effective charge can be defined using other electrical boundary conditions [27], but this choice of $\boldsymbol{\mathcal{E}} = 0$ is the "Born charge" one.) 2. Alternatively, $Z^*_{s,\alpha\beta}$ measures the force $\mathbf{F}$ linearly induced in the α direction on the sth nucleus by a uniform macroscopic electric field $\boldsymbol{\mathcal{E}}$ in the β direction (at zero displacement):

$$F_{s,\alpha} = -e \sum_{\beta} Z^*_{s,\beta\alpha}\, \mathcal{E}_\beta \,. \tag{37}$$

Notice that, in low-symmetry situations, Z^*_s is not symmetric in its Cartesian indices. Since any rigid translation of the whole solid does not induce macroscopic polarization, the Born effective-charge tensors obey

$$\sum_{s} Z^*_{s,\alpha\beta} = 0 \,, \tag{38}$$

a result that is generally known as the "acoustic sum rule" [28].

The Berry-phase theory of polarization naturally leads to an evaluation of the derivative in (9) as a finite difference, and this is the way most Z^*_s calculations are performed for FE perovskites. However, expressions (9) or (37) based on linear response approaches [20] can be used

whenever an electronic-structure code implementing such an approach (e.g., `http://www.abinit.org/`, `http://www.pwscf.org`) is available.

The Born effective-charge tensors are a staple quantity in the theory of lattice dynamics for polar crystals [29], and their experimental values have long been known to a very good accuracy for simple materials such as binary ionic crystals and simple semiconductors. As for FE materials, some experimentally derived values for $BaTiO_3$ were proposed long ago [30]. However, the subject remained basically neglected until 1993, when [25] appeared. This ab-initio calculation demonstrated that in FE perovskites the Born charges are strongly "anomalous", and that this anomaly has much to do with the phenomenon of ferroelectricity. Since then, ab-initio investigations of the Z_s^* have become a standard tool for the study of FE oxides, and have provided invaluable insight into ferroelectric phenomena [4, 27, 31].

For most FE ABO_3 perovskites the nominal static charges are either 1 or 2 for the A cation, either 5 or 4 for the B cation, and -2 for oxygen. On the contrary, modern calculations have demonstrated that in these materials the Born charges typically assume much larger values. We discuss this feature using as a paradigmatic example the case of $KNbO_3$, which was the first to be investigated in 1993 [25]. The paraelectric prototype structure is cubic, and the cations sit at cubic sites, thus warranting isotropic Z_s^* tensors. The oxygens sit instead at noncubic sites so that $Z_{\rm O}^*$ has two independent components: one (called O1) for displacements pointing towards the Nb ion, and the other (called O2) for displacements in the orthogonal plane. The results of [25] are that Z_s^* takes values of 0.8 for K, 9.1 for Nb, -6.6 for O1, and -1.7 for O2. Both the Nb and O1 values are thus strongly anomalous, being much larger (in modulus) than the corresponding nominal values.

Such a finding appears counterintuitive, since one would expect that the extreme ionic picture provides an upper bound on the ionic charges. In partly covalent oxides one would naively guess values smaller, and *not* larger, than the nominal ones, for all ions. Instead, anomalous values for the transition element and for O1 ions have been later confirmed by all subsequent calculations, using quite different technical ingredients and/or for other perovskite oxides [27, 32, 33]. The physical origin of the giant dynamical charges is precisely the borderline ionic–covalent character of ABO_3 oxides, specifically owing to the hybridization of $2p$ oxygen orbitals with the $4d$ or $5d$ orbitals of the B cation. A thorough discussion of this issue can be found in [4, 31].

4.3 Piezoelectric Properties

Piezoelectricity has been an intriguing problem for many years. Even the *formal* proof that piezoelectricity is a well-defined bulk property – independent of surface termination – is relatively recent (1972), and is due to R. M. Martin. This proof was challenged, and the debate lasted for two decades [10–16]. The piezoelectric tensor γ measures the coupling of a macroscopic field $\boldsymbol{\mathcal{E}}$

with macroscopic strain. The root of the problems with understanding piezoelectricity is in the fact that – within periodic Born–von Kármán boundary conditions – strain is *not* a perturbing term in the Hamiltonian; instead, it amounts to a change of boundary conditions.

As in the case of the Born effective charges, there are two equivalent definitions of γ, which is a third-rank Cartesian tensor. 1. $\gamma_{\delta\alpha\beta}$ measures the polarization linearly induced in the δ direction by macroscopic strain $\epsilon_{\alpha\beta}$ at zero field:

$$\gamma_{\delta\alpha\beta} = \frac{\partial P_\delta}{\partial \epsilon_{\alpha\beta}} \,. \tag{39}$$

2. Alternatively, $\gamma_{\delta\alpha\beta}$ measures the stress $\sigma_{\alpha\beta}$ linearly induced by a macroscopic field in the δ direction at zero strain:

$$\sigma_{\alpha\beta} = \sum_\delta \gamma_{\delta\alpha\beta} \, E_\delta \,. \tag{40}$$

The first ab-initio calculation of piezoelectric constants appeared in 1989 [34]; therein, the III–V semiconductors were chosen as case studies. This work exploited (40), linear-response theory [20], and the Nielsen–Martin stress theorem [35–37]. Nowadays, most calculations of the piezoelectric effect in FE materials are based on the finite-difference approximation to (39), in conjunction with a Berry-phase calculation. The first such calculation, for $PbTiO_3$, was performed in 1998 [38, 39]; other calculations for other materials, including some ordered models of FE alloys, were performed soon afterwards [40, 41].

Macroscopic strain typically induces *internal strain* as well. That is, when the cell parameters are varied, the internal coordinates relax to new equilibrium positions, in general not mandated by symmetry. This effect is characterized by a set of material-dependent constants known as internal-strain parameters. In principle, there is no need to deal with internal strain separately; (39) is in fact exact, *provided that* the internal coordinates are continually relaxed to their equilibrium values as the strain is applied. However, it is often more convenient to exploit linearity and to compute the piezoelectric tensor γ as the sum of two separate terms. The first term is the "clamped-nuclei" one, evaluated by applying a homogeneous macroscopic strain without including internal strain (i.e., without allowing any internal coordinates to relax). The second term accounts only for the change in polarization induced by the internal strain, and can easily be evaluated – knowing the internal-strain parameters and the Born charges – as the change in polarization associated with induced displacements associated with polar zone-center phonons.

Whenever the crystal has a nonvanishing spontaneous polarization, the definition of the piezoelectric response becomes more subtle. The simplest and most natural definition, usually called the "proper" piezoelectric response [42], is based on the current density flowing through the bulk of a

sample in adiabatic response to a slow strain deformation, as in Fig. 3b. The proper response corresponds in most circumstances to the actual experimental setup, and, furthermore, is the one having the most direct link to the modern theory. In order to evaluate a proper piezoelectric coefficient as a finite difference, it is enough to adopt a Berry-phase formulation in scaled coordinates as in (26) and evaluate derivatives of the $\varphi_{n,j}$ [19, 42]. It is worth emphasizing that the arbitrary quantum of polarization, Sect. 3.3, does *not* give rise to any ambiguity in the proper piezoelectric response, since its strain derivative is zero [42].

5 Further Theoretical Developments

In this section, we briefly introduce a few advanced topics associated with the theory of polarization, providing references to the literature for those readers who desire a fuller treatment.

5.1 Polarization in an Applied Electric Field

Up to this point, our treatment has been limited to the case of insulators in a vanishing macroscopic electric field. Clearly there are many situations, in which it is very desirable to treat the application of an electric field directly, especially for FEs and for other types of dielectric materials. However, the usual theory of electron states in crystals is based on Bloch's theorem, which requires that the crystal potential be periodic. This rules out the presence of a macroscopic electric field $\boldsymbol{\mathcal{E}}$, since this would imply a change by $e\boldsymbol{\mathcal{E}} \cdot \boldsymbol{R}$ of the electron potential under a translation by a lattice vector $\boldsymbol{R}$.

Indeed, the difficulties in treating the case of a finite electric field are quite severe. Even a small field changes the qualitative nature of the energy eigenstates drastically, and a theory based on such energy eigenstates is no longer useful. Even more seriously, because the potential is unbounded from below, there is no well-defined ground state of the electron system! The "state" that one has in mind is one in which all "valence" states are occupied and all "conduction" states are empty. However, for an insulator of gap E_{g} in a field $\boldsymbol{\mathcal{E}}$, it is always possible to lower the energy of the system by transferring electrons from the valence band in one region to the conduction band in a region a distance $\gg L_{\mathrm{t}} = E_{\mathrm{g}}/\mathcal{E}$ down-field. This "Zener tunneling" is analogous to the autoionization that also occurs, in principle, for an atom or molecule in a finite electric field.

Nevertheless, we expect that if we start with an insulating crystal in its ground state and adiabatically apply a modest electric field, there should be a reasonably well-defined "state" that we can solve for. Indeed, perturbative treatments of the application of an electric field have long been known, and are a standard feature of modern electronic structure theory (for a review,

see [20]). In 1994, *Nunes* and *Vanderbilt* [43] proposed a Wannier-function-based solution to the finite-field problem that, while successful in principle, was not very useful in practice. Transforming back to Bloch functions, *Nunes* and *Gonze* showed in 2001 [44] how the known perturbative treatments could be obtained (and, in some cases, extended) by deriving them from a variational principle based on minimizing an energy functional F of the form

$$F = E_{\rm KS}(\{\psi_{n\boldsymbol{k}}\}) - \boldsymbol{\mathcal{E}} \cdot \boldsymbol{P}(\{\psi_{n\boldsymbol{k}}\})\,. \tag{41}$$

Here, $E_{\rm KS}(\{\psi_{n\boldsymbol{k}}\})$ is the usual Kohn–Sham energy per unit volume expressed as a function of all occupied Bloch functions, and similarly $\boldsymbol{P}(\{\psi_{n\boldsymbol{k}}\})$ is the usual zero-field Berry-phase expression for the electronic polarization. This equation is to be minimized with respect to all $\{\psi_{n\boldsymbol{k}}\}$ in the presence of a given field $\boldsymbol{\mathcal{E}}$; thus, the Bloch functions at minimum become functions of $\boldsymbol{\mathcal{E}}$, so that the first term in (41) also acquires an implicit $\boldsymbol{\mathcal{E}}$ dependence.

Subsequently, *Souza* et al. [45] and *Umari* and *Pasquarello* [46] demonstrated that (41) was suitable for use as an energy functional for a variational approach to the *finite*-field problem as well. The justification for such a procedure is not obvious, in view of the fact that the occupied wavefunction solutions $\{\psi_{n\boldsymbol{k}}\}$ *are not eigenstates* of the Hamiltonian. Instead, they can be regarded as providing a representation of the one-particle density matrix, which can be shown to remain periodic in the presence of a field [45, 47], or by treating the system from a time-dependent framework [47] in which the field is slowly turned on from zero.

Because the "state" of interest is, in principle, only a long-lived resonance in the presence of a field, there should be some sense in which the above theory fails to produce a perfectly well-defined solution. This is so, and it comes about in an unfamiliar way: the variational solution breaks down if the k-point sampling is taken to be too fine. Indeed, if $\Delta k \ll 1/L_{\rm t}$, where $L_{\rm t} = E_{\rm g}/\mathcal{E}$ is the Zener tunneling length mentioned above, the variational procedure fails [45, 46]. The theory is thus limited to modest fields (more precisely, to $\boldsymbol{\mathcal{E}} \ll E_{\rm g}/a$, where a is a lattice constant).

In any case, it is interesting to discover that the problem of computing $\boldsymbol{P}$ in an electric field provides, in a sense, the solution to the problem of computing *any* property of an insulator in a finite field: it is precisely the introduction of the Berry-phase polarization into (41) that solves the problem.

5.2 Interface Theorem and the Definition of Bound Charge

It is well known from elementary electrostatics that the bound charge density in the presence of a spatially varying polarization field is

$$\rho_{\rm b}(\boldsymbol{r}) = -\nabla \cdot \boldsymbol{P}(\boldsymbol{r})\,, \tag{42}$$

where $\rho_{\rm b}(\boldsymbol{r})$ and $\boldsymbol{P}(\boldsymbol{r})$ are macroscopic fields (i.e., coarse grained over a length scale much larger than a lattice constant). As long as the polarization changes

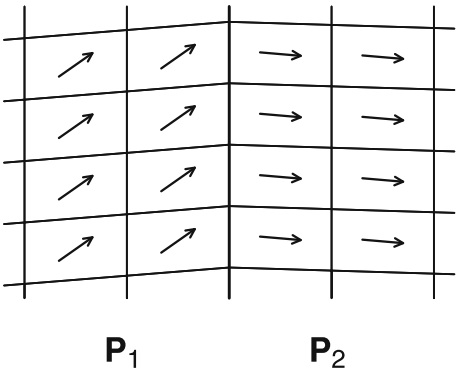

Fig. 11. Sketch of epitaxial interface between two different FE crystals, or between FE domains of a single crystal. The difference in the interface-normal components of $\boldsymbol{P}_1$ and $\boldsymbol{P}_2$ leads to an interface bound charge given by (43)

gradually over space, as in response to a gradual strain field or composition gradient, there is no difficulty in associating $\boldsymbol{P}(\boldsymbol{r})$ with the Berry-phase polarization of Sect. 3.3 computed for a crystal whose global structure matches the local structure at $\boldsymbol{r}$. There is no difficulty with respect to the "choice of branch" (see Sect. 3.3) since the gradual variation of $\boldsymbol{P}$ allows the choice of branch to be followed from one region to another, and the bound charge of (42) is clearly independent of branch.

The case of an interface between two FE materials, or of a FE domain wall in a single FE material, is more interesting. Consider an epitaxial interface between two FE materials, as shown in Fig. 11. One naively expects a relation of the form $\sigma_{\rm b} = \hat{\boldsymbol{n}} \cdot (\boldsymbol{P}_1 - \boldsymbol{P}_2)$, where $\sigma_{\rm b}$ is the macroscopic bound surface charge at the interface and $\hat{\boldsymbol{n}}$ is a unit vector normal to the interface. However, in general the two materials may be quite dissimilar, so that a choice of branch needs to be made for the Berry-phase expressions for $\boldsymbol{P}_1$ and $\boldsymbol{P}_2$ separately, leading to an uncertainty in the definition of the bound interface charge $\sigma_{\rm b}$.

Indeed, a careful analysis of situations of this type is given in [23], where it is shown that the interface bound charge is given by

$$\sigma_{\rm b} = \hat{\boldsymbol{n}} \cdot (\boldsymbol{P}_1 - \boldsymbol{P}_2) \mod \frac{e}{A_{\rm int}} \tag{43}$$

under the following conditions: 1. the epitaxial match is perfect and dislocation free, with a common 1×1 interface unit cell area $A_{\rm int}$; and 2. material 1, material 2, and the interface are all insulating, with a common gap. The interface need not be as abrupt as illustrated in Fig. 11; some relaxations may occur in the first few neighboring cells to the interface. It is only necessary to identify $\boldsymbol{P}_1$ and $\boldsymbol{P}_2$ with the Berry-phase polarizations of the crystalline structures far enough from the interface for these relaxations to have healed, and to interpret $\sigma_{\rm b}$ as the macroscopic excess interface charge density integrated over this interface region.

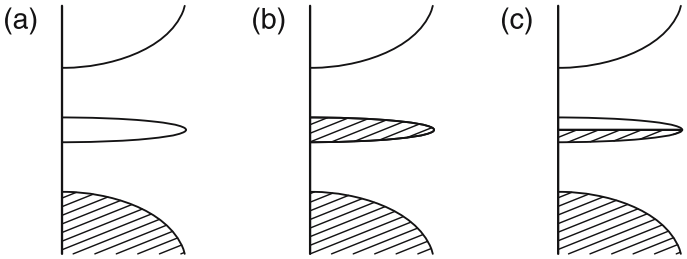

Fig. 12. Sketch of density of states that could be associated with the epitaxial interface of Fig. 11. Valence bands of materials 1 and 2 are hashed; conduction bands are unfilled; and a band of interface states may either be (**a**) entirely empty; (**b**) entirely filled; or (**c**) partially filled (i.e., metallic)

The appearance of the caveat "mod $e/A_{\rm int}$" in (43) is remarkable, and confirms that, at least in principle, there can be an uncertainty in the definition of the interface bound charge. This can be understood in two ways. First, the uncertainty of $\boldsymbol{P}_1$ and $\boldsymbol{P}_2$ mod $e\boldsymbol{R}/\Omega$ leads to the uncertainty $(e\boldsymbol{R}/\Omega)\cdot\hat{\boldsymbol{n}} = e/A_{\rm int}$, as can be confirmed from simple geometry. Second, on more physical grounds, we can expect such an uncertainty because of the flexibility of the condition (2) stating that material 1, material 2, and the interface must all be insulating with a common gap. Consider a situation like that illustrated in Fig. 12, where there are m (counting spin) discrete interface bands lying near the middle of a gap that is common to both materials 1 and 2. Panels (a) and (b) both show situations that satisfy the conditions (1) and (2) of (43), but the interface charge clearly differs by precisely $em/A_{\rm int}$ between these two situation. Panel (c) shows a situation that does not satisfy the stated conditions, as the interface is metallic. In this case, the charge counting may be done either with reference to the situation of Panel (a), in which case one either says that a large free-electron charge density is present on top of the bound charge defined by situation (a), or else that a large free-hole charge density is present on top of the bound charge defined by situation (b).

Similar considerations lead to a "surface theorem" [23] relating the macroscopic bound surface charge at a FE/vacuum interface to the surface-normal component of the polarization of the underlying medium, mod $e/A_{\rm surf}$.

In practice, the change in polarization $(\boldsymbol{P}_1 - \boldsymbol{P}_2)$ between two FE materials is usually much smaller than the quantum, in which case there is a "natural" choice of branch for the definition of the interface bound charge $\sigma_{\rm int}$ in (43). However, for materials with large polarizations, such as certain Pb- and Bi-based perovskites (see, e.g., [48]), the ambiguity in the definition of interface bound charge may need to be considered with care.

5.3 Many-Body and Noncrystalline Generalizations

The treatment given so far is based on the 1993 paper by *King-Smith* and *Vanderbilt* [18] and assumes an independent-particle scheme, where polarization is evaluated as a Berry phase of one-electron orbitals, typically the Kohn–Sham ones [5], which in a crystalline material assume the Bloch form. Shortly after the appearance of [18], *Ortiz* and *Martin* [49] provided the many-body generalization of the theory, where polarization is expressed as a Berry phase of the many-body wavefunction.

A subsequent development, by *Resta* [50], provides a unified treatment of macroscopic polarization, dealing on the same footing with either independent-electron or correlated systems, and with either crystalline or disordered systems. This approach is based on a novel viewpoint, which goes under the (apparently oxymoronic) name of "single-point Berry phase". On practical grounds, such a single-point Berry phase is universally adopted in order to evaluate macroscopic polarization within first-principle simulations of disordered systems.[9]

Here, we give a flavor of the approach, while we refer to the literature for more complete accounts [50–52]. Let us consider, for the sake of simplicity, a system of N one-dimensional spinless electrons. The many-body ground wavefunction is then $\Psi(x_1, x_2, \ldots x_j, \ldots x_N)$, and all the electrons are confined to a segment of length L. Eventually, we will be interested in the thermodynamic limit, defined as the limit $N \to \infty$ and $L \to \infty$, while the density N/L is kept constant. The wavefunction Ψ is Born–von Kàrmàn periodic, with period L, over each electronic variable x_j separately. Equivalently, one can imagine the electrons to be confined in a circular rail of length L: the coordinates x_j are then proportional to the angles $2\pi x_j/L$, defined mod 2π.

The key quantity is the ground-state expectation value

$$z_N = \langle \Psi | U | \Psi \rangle = \int_0^L \mathrm{d}x_1 \ldots \int_0^L \mathrm{d}x_N |\Psi(x_1, \ldots x_N)|^2 U(x_1, \ldots x_N)\,, \qquad (44)$$

where the unitary operator U, called a "twist operator", is defined as

$$U(x_1, \ldots x_N) = \exp\left(\mathrm{i} \frac{2\pi}{L} \sum_{j=1}^{N} x_j \right)\,, \qquad (45)$$

and clearly is periodic with period L. The expectation value z_N is a dimensionless complex number, whose modulus is no larger than one. The electronic contribution to the macroscopic polarization of the system can be expressed in the very compact form [50, 52]:

$$P_{\mathrm{el}} = -\frac{e}{2\pi} \lim_{N\to\infty} \Im \ln z_N\,, \qquad (46)$$

[9] http://www.cpmd.org/

Notice that, for a one-dimensional system, the polarization has the dimensions of a charge (dipole per unit length). The essential ingredient in (46) is $\Im \ln z_N$, i.e., the *phase* of the complex number z_N. This phase can be regarded as a very peculiar kind of Berry phase.

So far, we have assumed neither independent electrons nor crystalline order; (46) is in fact a very general definition of macroscopic polarization. In the special case of a crystalline system of independent electrons, the many-body wavefunction Ψ is a Slater determinant of single-particle orbitals. For any finite N, (44) and (46) can then be shown to be equivalent to a discretized Berry phase of the occupied bands, of the same kind as those addressed in Sect. 3.2.

5.4 Polarization in Kohn–Sham Density-Functional Theory

Suppose we are given the ground-state interacting electron density $n(\boldsymbol{r})$ of an insulating crystal. From this, the Kohn–Sham theory [5] gives a unique prescription for determining a noninteracting system, with an effective Kohn–Sham potential, having the same ground-state electron density. The following question then arises: If one computes the Berry-phase polarization from this noninteracting Kohn–Sham system, does one arrive, in principle, at the correct many-body polarization?

As shown by *Gonze* et al. [53, 54], the answer to this question is that, in general, one *does not* obtain the correct polarization.

There are three ways to approach this issue. First, one may restrict one's considerations to a strictly infinite crystalline system with a given cell shape and with a uniform macroscopic electric field $\boldsymbol{\mathcal{E}}$ [53, 54]. One can then demonstrate a generalized Hohenberg–Kohn theorem stating that a given periodic density $n(\boldsymbol{r})$ and macroscopic polarization $\boldsymbol{P}$ together uniquely determine a periodic external potential $V_{\rm per}(\boldsymbol{r})$ and electric field $\boldsymbol{\mathcal{E}}$. Moreover, the corresponding Kohn–Sham construction involves finding an effective periodic potential $V_{\rm per}^{\rm KS}(\boldsymbol{r})$ and effective electric field $\boldsymbol{\mathcal{E}}^{\rm KS}$ that yield, for a *noninteracting* system, the same $n(\boldsymbol{r})$ and $\boldsymbol{P}$. In this theory of *Gonze* et al. [53, 54], the polarization is correct by construction, but at the expense of introducing a correction $\boldsymbol{\mathcal{E}}^{\rm KS} - \boldsymbol{\mathcal{E}}$ that they referred to as an "exchange-correlation electric field". The reader is directed to [53, 54] for details.

A second approach is to consider conventional Kohn–Sham theory in the context of finite macroscopic sample geometries, surrounded by vacuum, and having particular surfaces, interfaces, or FE domain configurations. An analysis of this type [55] again leads to the conclusion that the local polarization obtained from exact Kohn–Sham theory is not, in general, the correct one. In general, one finds that the *longitudinal* part of the polarization field $\boldsymbol{P}(\boldsymbol{r})$ must be correct (since the corresponding charge density $-\nabla \cdot \boldsymbol{P}$ must be correct), but the *transverse* part of the polarization field need *not* be correct.

A third approach is suggested by (44). The wavefunction $\Psi_{\rm KS}$ of the noninteracting Kohn–Sham system is a Slater determinant and is necessarily

different from Ψ, despite sharing the same single-particle density. Since the twist operator U is a genuine many-body operator, its expectation value over $\Psi_{\rm KS}$ is in general different from the one over Ψ. The polarization (46), is different as well.

5.5 Localization, Polarization, and Fluctuations

An insulator is distinguished from a metal by its vanishing dc conductivity at low temperature. In contrast to what happens in metals, the electronic charge in insulators (and quite generally nonmetals) cannot flow freely under an applied dc field; instead it undergoes static polarization. As first pointed out in 1964 by *Kohn*, this fact stems from a basic qualitative difference in the organization of the electrons in their *ground state* [56]. The modern theory of polarization has provided much insight into such different organization.

An insulator sustains a nontrivial, material-dependent, macroscopic polarization, which is nonvanishing whenever the Hamiltonian is noncentrosymmetric. Instead, the polarization of a metallic sample is determined by the Faraday-cage effect and therefore is *not* a well-defined property of the bulk material. At the independent-electron level, the polarization of a crystalline insulator can be expressed in terms of Wannier functions, as discussed in Sect. 3.5. The key feature is that, in insulators, a set of well-localized orbitals (the Wannier functions) spans the same Hilbert space as do the Bloch orbitals of the occupied bands. This is indeed a qualitative difference in the organization of the electrons between insulators and metals. In the latter, in fact, it is impossible to span the Hilbert space of the occupied Bloch orbitals using well-localized orbitals. This statement can be made more precise by addressing the spherical second moments of the charge distributions of the localized orbitals [57]. Such second moments can be made finite in insulators, while they necessarily diverge in metals, as discussed below. It therefore emerges that the key qualitative feature differentiating the ground state of an insulator from that of a metal is electron localization. This applies well beyond the independent-electron level; in fact, as emphasized already by Kohn in 1964, the ground wavefunction of *any* insulator is localized. The modern theory of polarization leads to a simple and elegant measure of such localization [52].

It is expedient to refer, as in Sect. 5.3, to a system of N one-dimensional spinless electrons. From (46) it is clear that macroscopic polarization is a well-defined quantity whenever the modulus of z_N is nonvanishing in the large N limit. In the latter case, the second moment of the electron distribution can be defined, following *Resta* and *Sorella* [58], as

$$\langle x^2 \rangle_{\rm c} = - \lim_{N\to\infty} \frac{1}{N} \left(\frac{L}{2\pi} \right)^2 \ln |z_N|^2 \,, \tag{47}$$

where the subscript "c" stands for "cumulant". The same concept generalizes to a Cartesian tensor $\langle r_\alpha r_\beta \rangle_{\rm c}$ in three dimensions. This localization tensor,

having the dimension of a squared length, is an intensive property and applies on the same footing to ordered/disordered and correlated/uncorrelated many-electron systems; it is finite in any insulator and divergent in any metal. In the special case of an insulating crystalline system of independent electrons, the meaning of $\langle r_\alpha r_\beta \rangle_c$ becomes more perspicuous. In fact, the trace of this tensor is a lower bound to the average spherical second moment of the charge distributions of the Wannier functions of the occupied bands [57]; in the metallic case, the lower bound is formally divergent.

Two important questions were left unanswered by Resta and Sorella. Given that in any insulator the localization tensor $\langle r_\alpha r_\beta \rangle_c$ is, at least in principle, a well-defined ground-state observable, the first question is whether this can be measured, and by which kind of experiments. The second question is whether $\langle r_\alpha r_\beta \rangle_c$ can be related in some way to dc conductivity, given that the vanishing of the latter characterizes – in addition to macroscopic polarization – the insulating state of matter. Both questions received a positive answer owing to the work of *Souza* et al. [51]. They began by showing that $\langle r_\alpha r_\beta \rangle_c$ measures the mean-square fluctuation of the polarization; then, by exploiting a fluctuation-dissipation theorem, they explicitly linked $\langle r_\alpha r_\beta \rangle_c$ to the conductivity of the system.

6 Summary

In this chapter we have reviewed the physical basis of the modern theory of polarization. From a physical viewpoint, we have emphasized that the polarization may be defined in terms of the accumulated adiabatic flow of current occurring as a crystal is modified or deformed, and have discussed the consequences of this picture for the theory of polarization reversal and piezoelectric effects in FE materials. From a mathematical viewpoint, we have explained how the polarization is closely related to a Berry phase of the Bloch wavefunctions as the wavevector traverses the Brillouin zone, and to the centers of charge of the Wannier functions that may be constructed from the Bloch wavefunctions. An essential feature of the theory is the fact that the polarization is formally defined only modulo a "quantum of polarization," or equivalently, that it must be regarded as a multivalued quantity. We have also attempted to clarify how piezoelectric effects and surface and interface charges are to be understood in terms of the modern theory.

The capability of computing polarization is now available in almost all commonly used software packages for bulk electronic-structure calculations. While initially formulated in vanishing electric field, the case of finite field can be treated by letting the external electric field couple to the polarization while retaining the Bloch form of the wavefunctions. These methods allow for the computation of numerous quantities of interest, including spontaneous polarization, Born effective charges, linear piezoelectric coefficients, nonlinear dielectric and piezoelectric responses, and the like. Indeed, taken together, they provide a robust and powerful foundation for modern computational studies of the polarization-related properties of FE materials.

References

[1] L. D. Landau, E. M. Lifshitz: *Electrodynamics of Continuous Media* (Pergamon, Oxford 1984) 31

[2] O. F. Mossotti: Azioni e deformazioni nei dielettrici, Memorie di Matematica e di Fisica della Società Italiana delle Scienze Residente in Modena **24**, 49 (1850) 31

[3] R. Clausius: *Die Mechanische Behandlung der Electrica* (Vieweg, Berlin 1879) 31

[4] M. Posternak, R. Resta, A. Baldereschi: Role of covalent bonding in the polarization of perovskite oxides: The case of $KNbO_3$, Phys. Rev. B **50**, 8911 (1994) 33, 55

[5] S. Lundqvist, N. H. March (Eds.): *Theory of the Inhomogeneous Electron Gas* (Plenum, New York 1983) 33, 42, 53, 61, 62

[6] W. E. Pickett: Pseudopotential methods in condensed matter applications, Comput. Phys. Rep. **9**, 115 (1989) 33

[7] C. Kittel: *Introduction to Solid State Physics*, 7th ed. (Wiley, New York 1996) 33, 35, 38, 42

[8] N. W. Ashcroft, N. D. Mermin: *Solid State Physics* (Saunders, Philadelphia 1976) 33, 35, 38, 42

[9] R. M. Martin: Comment on calculations of electric polarization in crystals, Phys. Rev. B **9**, 1998 (1974) 35

[10] R. M. Martin: Piezoelectricity, Phys. Rev. B **5**, 1607 (1972) 36, 55

[11] R. M. Martin: Comment on piezoelectricity under hydrostatic pressure, Phys. Rev. B **6**, 4874 (1972) 36, 55

[12] W. F. Woo, W. Landauer: Comment on "piezoelectricity under hydrostatic pressure", Phys. Rev. B **6**, 4876 (1972) 36, 55

[13] R. Landauer: Pyroelectricity and piezoelectricity are not true volume effects, Solid State Commun. **40**, 971 (1981) 36, 55

[14] C. Kallin, B. J. Halperin: Surface-induced charge disturbances and piezoelectricity in insulating crystals, Phys. Rev. B **29**, 2175 (1984) 36, 55

[15] R. Landauer: Introduction to ferroelectric surfaces, Ferroelectrics **73**, 41 (1987) 36, 55

[16] A. K. Tagantsev: Electric polarization in crystals and its response to thermal and elastic perturbations, Phase Transitions **35**, 119 (1991) 36, 55

[17] R. Resta: Theory of the electric polarization in crystals, Ferroelectrics **136**, 51 (1992) 38, 40, 41

[18] R. D. King-Smith, D. Vanderbilt: Theory of polarization of crystalline solids, Phys. Rev. B **47**, 1651 (1993) 38, 41, 42, 46, 53, 61

[19] R. Resta: Macroscopic polarization in crystalline dielectrics: The geometric phase approach, Rev. Mod. Phys. **66**, 899 (1994) 38, 41, 42, 46, 57

[20] S. Baroni, S. de Gironcoli, A. Dal Corso, P. Giannozzi: Phonons and related crystal properties from density-functional perturbation theory, Rev. Mod. Phys. **73**, 515 (2001) 41, 54, 56, 58

[21] A. Shapere, F. Wilczek (Eds.): *Geometric Phases in Physics* (World Scientific, Singapore 1989) 42, 43

[22] R. Resta: Manifestations of Berry's phase in molecules and condensed matter, J. Phys. Condens. Matter **12**, R107 (2000) 42, 43

[23] D. Vanderbilt, R. D. King-Smith: Electric polarization as a bulk quantity and its relation to surface charge, Phys. Rev. B **48**, 4442 (1993) 42, 59, 60
[24] D. J. Thouless: Quantization of particle transport, Phys. Rev. B **27**, 6083 (1983) 52
[25] R. Resta, M. Posternak, A. Baldereschi: Towards a quantum theory of polarization in ferroelectrics: The case of $KNbO_3$, Phys. Rev. Lett. **70**, 1010 (1993) 53, 54, 55
[26] S. Dall'Olio, R. Dovesi, R. Resta: Spontaneous polarization as a Berry phase of the Hartree-Fock wave function: The case of $KNbO_3$, Phys. Rev. B **56**, 10105 (1997) 54
[27] P. Ghosez, J.-P. Michenaud, X. Gonze: Dynamical atomic charges: The case of ABO_3 compounds, Phys. Rev. B **58**, 6224 (1998) 54, 55
[28] R. Pick, M. H. Cohen, R. M. Martin: Microscopic theory of force constants in the adiabatic approximation, Phys. Rev. B **1**, 910 (1970) 54
[29] M. Born, K. Huang: *Dynamical Theory of Crystal Lattices* (Oxford University Press, Oxford 1954) 55
[30] J. D. Axe: Apparent ionic charges and vibrational eigenmodes of $BaTiO_3$ and other perovskites, Phys. Rev. **157**, 429 (1967) 55
[31] R. Resta: Dynamical charges in oxides: Recent advances, J. Phys. Chem. Solids **61**, 153 (1999) 55
[32] W. Zhong, R. D. King-Smith, D. Vanderbilt: Giant LO-TO splittings in perovskite ferroelectrics, Phys. Rev. Lett. **72**, 3618 (1994) 55
[33] P. Ghosez, X. Gonze, P. Lambin, J.-P. Michenaud: Born effective charges of barium titanate: Band-by-band decomposition and sensitivity to structural features, Phys. Rev. B **51**, 6765 (1995) 55
[34] S. de Gironcoli, S. Baroni, R. Resta: Piezoelectric properties of III-V semiconductors from first-principles linear-response theory, Phys. Rev. Lett. **62**, 2853 (1989) 56
[35] O. H. Nielsen, R. M. Martin: First-principles calculation of stress, Phys. Rev. Lett. **50**, 697 (1983) 56
[36] O. H. Nielsen, R. M. Martin: Quantum-mechanical theory of stress and force, Phys. Rev. B **32**, 3780 (1985) 56
[37] O. H. Nielsen, R. M. Martin: Stresses in semiconductors: Ab initio calculations on Si, Ge, and GaAs, Phys. Rev. B **32**, 3792 (1985) 56
[38] G. Sághi-Szabó, R. E. Cohen, H. Krakauer: First-principles study of piezoelectricity in $PbTiO_3$, Phys. Rev. Lett. **80**, 4321 (1998) 56
[39] H. Fu, R. E. Cohen: Polarization rotation mechanism for ultrahigh electromechanical response in single-crystal piezoelectrics, Nature **403**, 281 (2000) 56
[40] G. Sághi-Szabó, R. E. Cohen, H. Krakauer: First-principles study of piezoelectricity in tetragonal $PbTiO_3$ and $PbZr_{1/2}Ti_{1/2}O_3$, Phys. Rev. B **59**, 12771 (1999) 56
[41] L. Bellaiche, D. Vanderbilt: Intrinsic piezoelectric response in perovskite alloys: PMN-PT versus PZT, Phys. Rev. Lett. **83**, 1347 (1999) 56
[42] D. Vanderbilt: Berry-phase theory of proper piezoelectric response, J. Phys. Chem. Solids **61**, 147 (2000) 56, 57
[43] R. W. Nunes, D. Vanderbilt: Real-space approach to calculation of electric polarization and dielectric constants, Phys. Rev. Lett. **73**, 712 (1994) 58
[44] R. W. Nunes, X. Gonze: Berry-phase treatment of the homogeneous electric field perturbation in insulators, Phys. Rev. B **63**, 155107 (2001) 58

[45] I. Souza, J. Ìñiguez, D. Vanderbilt: First-principles approach to insulators in finite electric fields, Phys. Rev. Lett. **89**, 117602 (2002) 58
[46] P. Umari, A. Pasquarello: Ab initio molecular dynamics in a finite homogeneous electric field, Phys. Rev. Lett. **89**, 157602 (2002) 58
[47] I. Souza, J. Ìñiguez, D. Vanderbilt: Dynamics of Berry-phase polarization in time-dependent electric fields, Phys. Rev. B **69**, 085106 (2004) 58
[48] J. Íñiguez, L. Bellaiche, D. Vanderbilt: First-principles study of $(BiScO_3)_{1-x}$–$(PbTiO_3)_x$ piezoelectric alloys, Phys. Rev. B **67**, 224107 (2003) 60
[49] G. Ortiz, R. M. Martin: Macroscopic polarization as a geometric quantum phase: Many-body formulation, Phys. Rev. B **49**, 14 202 (1994) 61
[50] R. Resta: Quantum-mechanical position operator in extended systems, Phys. Rev. Lett. **80**, 1800 (1998) 61
[51] I. Souza, T. Wilkens, R. M. Martin: Polarization and localization in insulators: Generating function approach, Phys. Rev. B **62**, 1666 (2000) 61, 64
[52] R. Resta: Why are insulators insulating and metals conducting?, J. Phys. Condens. Matter **14**, R625 (2002) 61, 63
[53] X. Gonze, P. Ghosez, R. W. Godby: Density-polarization functional theory of the response of a periodic insulating solid to an electric field, Phys. Rev. Lett. **74**, 4035 (1995) 62
[54] X. Gonze, P. Ghosez, R. W. Godby: Density-functional theory of polar insulators, Phys. Rev. Lett. **78**, 294 (1997) 62
[55] D. Vanderbilt: Nonlocality of Kohn-Sham exchange-correlation fields in dielectrics, Phys. Rev. Lett. **79**, 3966 (1997) 62
[56] W. Kohn: Theory of the insulating state, Phys. Rev. **133**, A171 (1964) 63
[57] N. Marzari, D. Vanderbilt: Maximally localized generalized Wannier functions for composite energy bands, Phys. Rev. B **56**, 12847 (1997) 63, 64
[58] R. Resta, S. Sorella: Electron localization in the insulating state, Phys. Rev. Lett. **82**, 370 (1999) 63

Index

A Landau Primer for Ferroelectrics

Premi Chandra[1] and Peter B. Littlewood[2]

[1] Center for Materials Theory, Department of Physics, Rutgers University, Piscataway, NJ 08854-8019, USA
pchandra@physics.rutgers.edu
[2] Physics Department, University of Cambridge, Cambridge, CB2 1RX, England
pbl21@cam.ac.uk

Abstract. This contribution begins with a discussion of the homogeneous Landau theory for bulk ferroelectrics with spatially uniform polarizations, reviewing first- and second-order transitions and the dielectric response. Next, we allow the polarization to vary with position within a bulk sample, and discuss Landau–Ginzburg theory and correlation functions. Surface boundary conditions, corresponding to the situation for thin films, are then added and the resulting polarization profile is discussed. Here, screening effects, depolarization fields and strain will be important. The enigmatic extrapolation length is described with remarks about its underlying physical meaning. Then we switch to a treatment of inhomogeneous systems in the bulk, where strain effects and domain formation become very important. We end with a number of open questions for further exploration. Generally, we emphasize the underlying philosophy and methodology of this phenomenology.

1 Introduction

Based solely on symmetry considerations, Landau theory can provide a reliable description of a system's equilibrium behavior near a phase transition. This phenemenological approach relates measurable quantities to one another using a minimum set of input parameters that can be determined either by comparison to experiment or from first-principles approaches. Landau theory (LT) can therefore serve as a conceptual bridge between microscopic models and observed macroscopic phenomena. Because it assumes spatial averaging of all local fluctuations, LT is particularly well suited to systems with long-range interactions such as superconductors and ferroelectrics. In this chapter we hope to give the curious reader a self-contained contemporary presentation of the application of Landau theory to ferrolectrics, including references to more extensive treatments for those who wish more detail [1–6]. We begin by developing LT for homogeneous bulk ferroelectrics, and then consider the finite-size (thin-film) case [7] within the related Landau–Ginzburg (LG) approach. Next, we discuss the treatment of inhomonogeneity within this framework. We end with a number of open questions for future pursuits.

Let us begin by stating in general terms what Landau theory is and then subsequently what it is not. In a nutshell, Landau theory is a symmetry-based analysis of equilibrium behavior near a phase transition. In his classic 1937

K. Rabe, C. H. Ahn, J.-M. Triscone (Eds.): Physics of Ferroelectrics: A Modern Perspective, Topics Appl. Physics **105**, 69–116 (2007)

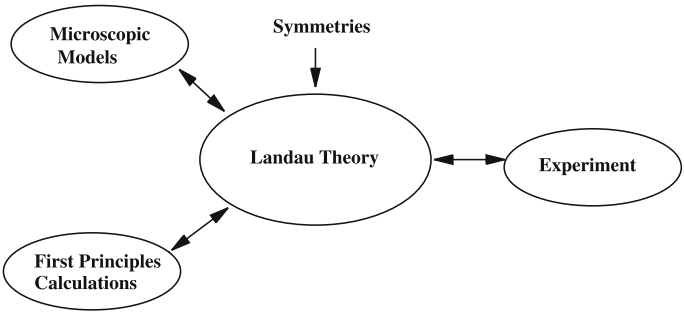

Fig. 1. Schematic of relationship of Landau theory and first-principles calculations, microscopic models and experiment in the vicinity of a phase transition

papers, *Landau* [8–10] notes that a system cannot change smoothly between two phases of different symmetry; the continuous path that a system can take between liquid and gaseous states around a first-order critical point is only possible because there is no symmetry change involved. Furthermore, because the thermodynamic states of two phases that are symmetrically distinct must be the same at their shared transition line, the symmetry of one phase must be higher than that of the other. Landau then characterizes the transition in terms of an order parameter, a physical entity that is zero in the high-symmetry (disordered) phase, and changes continuously to a finite value once the symmetry is lowered; for the case of the paraelectric–ferroelectric transition [11–16], this order parameter is the polarization P. The free energy, $\mathcal{F}$, in the vicinity of the transition is then expanded as a power series of the order parameter ($\mathcal{F}(P)$) where only symmetry-compatible terms are retained. The state of the system is then found by minimizing this free energy $\mathcal{F}(P)$ with respect to P to obtain P_0, and specific thermodynamic functions are subsequently computed by differentiating $\mathcal{F}$ accordingly. As an aside, we note that if the order parameter is multicomponent, then the Landau free energy is constructed from all scalar terms consistent with the system's symmetries that are powers and scalar products of the order-parameter components. Here, for simplicity, we'll consider a scalar order parameter (P) unless otherwise specified.

The appeal of the Landau approach is that it is a straightforward phenemenology for linking measurable thermodynamic quantities in the vicinity of a phase transition. However, it is only as good as its input parameters, the coefficients of the series-expansion terms in $\mathcal{F}(P)$, which can be determined from experiment or from first-principles calculations. We emphasize that Landau theory is strictly a macroscopic approach and thus it cannot describe any microscopic physics (e.g., atomic displacements, etc.) associated with the phase transition. In its simplest rendition, the order parameter (e.g., P) is considered to be completely uniform.

Table 1. Phenomenologies and relevant ferroelectric systems (close to T_c)

Phenomenology	**Ferroelectric (near T_c)**
Landau–Devonshire theory (uniform polarization)	Poled bulk system
Landau–Ginzburg theory (polarization with spatial gradient)	Bulk system
Landau–Ginzburg theory with boundary conditions	Film

A central ansatz of the Landau approach is that the free energy can be represented as a series expansion of the order parameter in the vicinity of the transition. At first glance, it may be surprising that singular behavior associated with a transition can emerge from such a regular expansion. This occurs because the value of the order parameter that minimizes the free energy (e.g., P_0) is itself a singular function of the expansion coefficients that are temperature dependent. However, more generally we expect that this power-law form of $\mathcal{F}$ may not be valid very close to the transition. Furthermore, Landau theory is based on the premise that local fluctuations in the order parameter are small, whereas we expect that this will not be the case in the immediate vicinity of the transition.

So when does Landau theory break down? *Levanyuk* and *Ginzburg* have developed [17–19] a criterion that uses Landau theory to estimate its own demise. More specifically, they argue that for LT to be valid, fluctuations of the order parameter must be small compared to the order parameter itself when both are coarse grained over a volume determined by the correlation length. We shall present a detailed version of their argument once we introduce a specific Landau free energy. Qualitatively, their criterion suggests that LT works well when the coordination number is high, which can be achieved either by large dimensionality or by long-range interactions. Since significant dipolar interactions are present in ferroelectrics, does this mean that Landau theory is always valid in these systems? It is certainly very useful in ferroelectrics but we emphasize that the angular dependence of the dipolar forces leads to non-Landau behavior very close to the transition, though this region is usually practically unobservable (we will be more specific later). Indeed historically the theoretical study of a simplified version of this problem, the uniaxial dipolar model, yielded the first predictions of logarithmic corrections to Landau exponents [20–23]. Detailed measurements confirmed these quantitative results in appropriate experimental systems [24], and this set of findings served as an important benchmark in the development of the renormalization group method.

Many readers may have encountered the phenomenology of Landau theory in the context of magnetism, and thus it is worth contrasting its application

there and in ferroelectrics (and we encourage the interested reader to pursue more on this subject in the chapter by *N. Spaldin* in this volume). First and perhaps foremost, the couplings in a ferromagnet are predominantly short range, since interactions between magnetic dipoles are essentially negligible. More specifically we note that the interaction energy between two magnetic dipoles, each of magnitude one Bohr magneton, at a distance r is

$$F_{\mathrm{M}} = \frac{\mu_o \mu_B}{4\pi r^3} \approx \frac{\alpha^2}{4\pi} \left(\frac{a_B}{r}\right)^3 , \tag{1}$$

where $a_B = 0.05\,\mathrm{nm}$ and $\alpha \approx \frac{1}{137}$, and we are working in atomic units. By contrast, for an electrical dipole of magnitude $p = e\Delta a_B$, the dipolar interaction force is

$$F_{\mathrm{D}} = \frac{p^2}{8\pi\epsilon_o r^3} \approx \frac{\Delta^2}{4\pi} \left(\frac{a_B}{r}\right)^3 , \tag{2}$$

where the parameter $\Delta \approx 1$ is determined by examining atomic displacements and transverse effective charges [25]. The ratio of the ferroelectric to the ferromagnetic dipolar forces is then of order $\frac{\Delta^2}{\alpha^2} \approx (137)^2$, so clearly long-range interactions are more significant in ferroelectrics than in generic magnetic systems. Thus, LT is more reliable for a broader temperature region in these electric dipolar systems than in their magnetic counterparts, though it can provide guiding information in both cases. In conventional ferromagnets magnetic dipolar interactions play a role in the determination of domain structures, whereas in ferroelectrics the analogous dipolar couplings are important at essentially all length scales.

Screening represents a second qualitative distinction between ferroelectric and ferromagnetic systems. This phenomenon is due to the presence of free charges that effectively reduce local fields; it does not have a magnetic analog due to the absence of free magnetic monopoles. Indeed this simple fact about screening has been used to explain why magnetism was known in ancient times but ferroelectricity is a relatively modern discovery [4]. The surface of a ferroelectric crystal attracts free charge from its environment to neutralize the effective surface charge that results from the polarization discontinuity; this partially accounts for the historical name "pyroelectric" to describe transient fields that were observed upon changes in temperature. Screening effects are particularly pronounced in ultrathin ferroelectric films, [26–31] where internal electric fields generated by the ferroelectric dipoles are large enough to produce both electronic and ionic currents. These processes contribute to fatigue, to "imprint" and to the memory of domain patterns stored over time [7]. A detailed understanding of these screening processes, particularly near metal/ferroelectric interfaces in thin-film devices, requires knowledge of metal-induced gap states and charge-compensation processes. Since these are local effects, they can be captured within a Landau–Ginzburg framework and this physics will be discussed later in the chapter.

The third major difference between LT treatments of ferroelectricity and ferromagnetism arises from the strong coupling between the polarization and the lattice, a feature that is usually not very important in the magnetic case. Ferroelectric dipoles are generated by the displacement of atoms, and thus on a local scale there is strong spatial anistropy. Many magnets retain continuous spin symmetry (e.g., xy or Heisenberg), and thus have low barriers associated with the reorientation of the magnetization. By contrast, in ferroelectrics domain walls, discontinuities in the polarization direction, are roughly a few lattice constants in contrast to the mesoscopic length scale associated with their magnetic counterparts. In general, the development of a macroscopic polarization in a ferroelectric will be accompanied by a macroscopic strain, and thus ferroelectricity and ferroelasticity are closely related phenomena. Indeed if this strain is suppressed, the transition temperature and even its order can be modified. Elastic degrees of freedom thus must be represented in a LT for most ferroelectrics.

Let us now turn to a general outline of this chapter. We will begin with a discussion of the homogenous Landau theory for bulk ferroelectrics with spatially uniform polarizations, reviewing first- and second-order transitions and the dielectric response. Next, we allow the polarization to vary with position within a bulk sample, and discuss Landau–Ginzburg theory and correlation functions. Surface boundary conditions, corresponding to the situation for thin films, are then added and the resulting polarization profile is discussed. Here, screening effects, depolarization fields and strain will be important. The enigmatic extrapolation length, borrowed from the literature on surface superconductivity [32], will be described with remarks about its underlying physical meaning. Then we will switch to a treatment of inhomogeneous systems in the bulk, where strain effects and domain formation become very important. We end with a number of open questions for further exploration. For example, is LT appropriate when both long-range strain and Coulomb interactions are present? How can we begin to treat the ever-important question of dynamics of domain motion within this framework? Landau–Ginzburg theory is certainly only useful when its constructing assumptions and its input parameters are appropriate; if so, it is a fairly powerful approach, based almost solely on symmetry, to yield important information about measurable quantities in the vicinity of a phase transition. In this chapter we emphasize the underlying philosophy and methodology of this phenomenology, pointing the interested reader to detailed discussions of successful applications to particular materials including $SrTiO_3$ [33, 34], $BaTiO_3$ [35, 36] and $PbZr_{1-x}Ti_xO_3$ [37]; towards this more pragmatic end, an Appendix of Landau parameter sets for specific common ferroelectric systems is included for easy reference.

2 Landau–Devonshire Theory

2.1 General Phenomenology

To our knowledge, Landau's symmetry-based treatment of phase transitions [1,8–10] was first applied to the case of ferroelectrics by *Devonshire* [14–16], and in this section we will discuss this Landau–Devonshire theory that is appropriate for bulk systems with spatially uniform polarization. In general, the thermodynamic state of any system in equilibrium can be completely specified by the values of specific variables; for bulk ferroelectrics these include the temperature (T), the polarization (P), the electric field (E), the strain (η), and the stress (σ). Usually we apply electric fields E and elastic stresses σ externally, so we can regard the polarization and the strain as "internal" or dependent variables. A fundamental postulate of thermodynamics applied to a ferroelectric is that its free energy $\mathcal{F}$ can be generally expressed as a function of ten variables (three components of polarization, six components of the stress tensor, and finally one of temperature). Our goal here is to write down an ansatz for this free energy, using symmetry arguments whenever possible to pare down the number of terms. The second important thermodynamic principle that we will also employ is that the values of the dependent variables in thermal equilibrium are obtained at the free-energy minimum when the free energy is optimized.

We make the key approximation that in the vicinity of a phase transition we can expand the free energy in powers of the dependent variables with coefficients that can be fitted to experiment or gleaned from microscopic calculations. In the best case, we may be able to truncate this series with only a few terms. In order to be more specific, let us take a simple example where we expand the free energy in terms of a single component of the polarization; for the moment we ignore the strain field, an assumption that might be appropriate for a uniaxial ferroelectric. We shall choose the origin of energy for the free unpolarized, unstrained crystal to be zero, and hence we write

$$\mathcal{F}_{\mathrm{P}} = \frac{1}{2}aP^2 + \frac{1}{4}bP^4 + \frac{1}{6}cP^6 - EP\,, \tag{3}$$

where we have truncated the power series at the sixth term, and a, b and c are coefficients that will be discussed in more detail shortly. Here we will use the notational convention that $\mathcal{F}$ and $F = \int \mathrm{d}V\mathcal{F}$ refer to the free-energy density and the total free energy, respectively. The equilibrium configuration is determined by finding the minima of $\mathcal{F}_{\mathrm{P}}$, where we shall have

$$\frac{\partial \mathcal{F}_{\mathrm{P}}}{\partial P} = 0\,. \tag{4}$$

This equation gives us an expression for the electric field E as a function of the polarization

$$E = aP + bP^3 + cP^4\,. \tag{5}$$

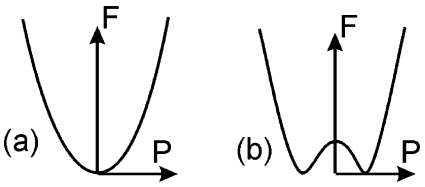

Fig. 2. Free energy as a function of polarization for (**a**) a paraelectric material, and for (**b**) a ferroelectric material

Thus we can determine the linear dielectric susceptibility above the transition by differentiating this equation with respect to P and then setting $P = 0$ to obtain

$$\chi = \frac{P}{E} = \frac{1}{a}\,. \tag{6}$$

In the Landau–Devonshire theory it is assumed that around the Curie point ($T \sim T_0$)

$$a = a_0(T - T_0) \tag{7}$$

and the other coefficients in the free-energy expansion are independent of temperature. Combining the last two equations, we find an expression for the dielectric stiffness

$$\kappa = \frac{1}{\chi} = a_0(T - T_0)\,, \tag{8}$$

which captures the Curie–Weiss behavior (in χ) observed in most ferroelectrics for $T > T_0$; this provides additional support for the linear temperature ansatz for a. For the sake of completeness, we note that the temperature T_0 where a changes sign is close to, but not exactly coincident with, the Curie temperature, as we shall discuss shortly.

If we include the linear temperature dependence of a, we have the general expression for the free energy

$$\mathcal{F}_{\mathrm{P}} = \frac{1}{2}a_0(T - T_0)P^2 + \frac{1}{4}bP^4 + \frac{1}{6}cP^6 - EP\,, \tag{9}$$

where, to our knowledge, a_0 and c are both positive in all known ferroelectrics [3, 4]. Figure 2 shows the free energy as a function of polarization in the paraelectric ($T \gg T_0$) and the ferroelectric ($T \ll T_0$) phases. How this free energy transforms between these two configurations will be determined by the sign of the coefficient b; as we shall see shortly, its sign will determine the nature of the paraelectric–ferroelectric transition, and whether the polarization at $T < T_0$ develops continuously or discontinuously.

2.2 Second-Order (Continuous) Transition

If $b > 0$, then a second-order transition occurs at $T = T_0$, and the free energy will evolve continuously as a function of decreasing temperature from the

first schematic ($P = 0$) in Fig. 2 to the second, that has minima at finite polarizations $P = \pm P_0$. The spontaneous polarization can be estimated by setting $E = 0$ in (5); since all the coefficients are positive, we will only retain the two lowest-order terms. The result is

$$P_0 = \left[\frac{a_0}{b}(T_0 - T)\right]^{\frac{1}{2}} , \tag{10}$$

where we see that the spontataneous polarization P_s will increase with decreasing temperature from the point $T = T_0$. We note that if we determine the dielectric stiffness below the transition ($T < T_0$) then we find

$$\kappa = 2a_0(T_0 - T) , \tag{11}$$

which is to be compared with (8), its value just above T_0; perusal of these two expressions suggests that κ vanishes at $T = T_0$ and that consequently the dielectric suseptibility diverges. In practice, the latter achieves large but finite values in real materials where this expression is appropriate [3, 4]. We can now also solve for the discontinuity in the specific heat at the transition; using $P = 0$ for $T > T_0$ and (10) for $T < T_0$, we determine

$$\Delta C_v = C_v(T = T_0^+) - C_v(T = T_0^-) , \tag{12}$$

where $C_v \equiv -T\frac{\partial^2 \mathcal{F}_P}{\partial T^2}$ to obtain

$$\Delta C_v = \frac{a_0^2 T_0}{2b} \tag{13}$$

for the Landau expression for this quantity. Schematics associated with this second-order phase transition as described by Landau–Devonshire theory are displayed in Fig. 3.

2.3 First-Order (Discontinuous) Transition

Logically (and practically as it turns out), we should also consider the case of $b < 0$ (while c remains positive). This is sketched in Fig. 4.

With the negative quartic coefficient, it should be clear that even if $T > T_0$ (such that the quadratic coefficent is positive) the free energy may have a subsidiary minimum at nonzero P. As a is reduced, which corresponds physically to the reduction of the temperature, this minimum will drop in energy below that of the unpolarized state, and so will be the thermodynamically favored configuration. The temperature at which this happens is, by definition, the Curie temperature T_c, which, however, now exceeds T_0. At any temperature between T_c and T_0 the unpolarized phase exists as a local minimum of the free energy. The most important feature of this phase transition is that the order parameter jumps discontinuously to zero at T_c. This type of phase

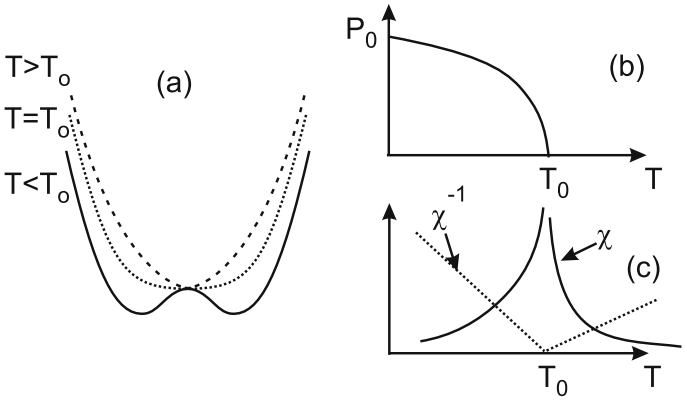

Fig. 3. Second-order phase transition. (**a**) Free energy as a function of the polarization at $T > T_0$, $T = T_0$, and $T < T_0$; (**b**) Spontaneous polarization $P_0(T)$ as a function of temperature; (**c**) The susceptibility χ and its inverse, where $\chi = \partial P/\partial E|_{P_0}$ is evaluated at the equilibrium polarization $P_0(T)$

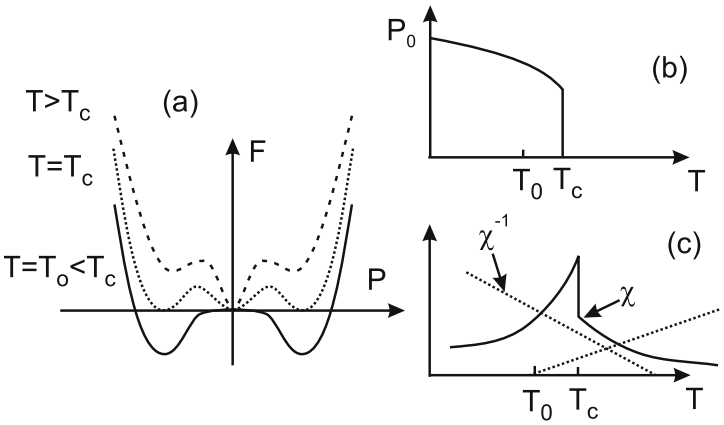

Fig. 4. First-order phase transition. (**a**) Free energy as a function of the polarization at $T > T_c$, $T = T_c$, and $T = T_0 < T_c$; (**b**) Spontaneous polarization $P_o(T)$ as a function of temperature; (**c**) Susceptibility χ

transition is usually called a first-order or discontinuous transition, of which solid–liquid transitions are common examples.

The procedure for finding the spontaneous polarization and the linear dielectric susceptibility is conceptually the same as before, but now one cannot neglect the quartic- and sixth-order terms. Qualitatively we then find a dielectric stiffness (inverse of the linear susceptibility) that does not vanish at T_0, corresponding to the finite jump in both the susceptibility and the spontaneous polarization at the transition. Schematics of the free energy, the

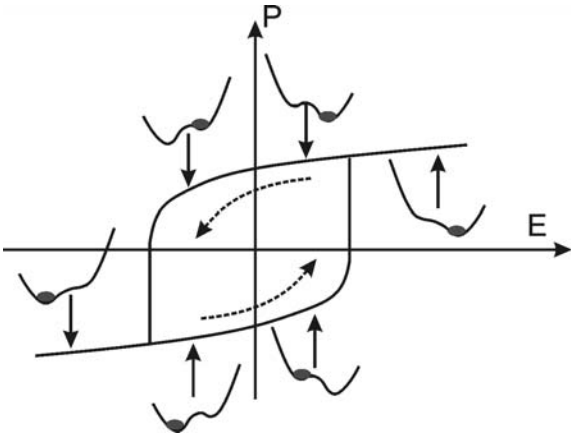

Fig. 5. Schematic picture of hysteresis in an idealized ferroelectric

spontaneous polarization, the dielectric stiffness and the linear susceptibility are shown in Fig. 4. We note that at $T = T_c$ the three minima are energetically degenerate. As a result, the system's behavior at $T = T_c$ will depend on whether it is approaching T_c from lower or higher temperatures. More specifically, the system will be in one of the two finite polarization ($P \neq 0$) minima if it is heated from an initial low temperature $T_i < T_c$, whereas it will be in a paraelectric state ($P = 0$) if the initial temperature is high ($T_i > T_c$). Indeed, the phenomenon of thermal hysteresis, where the transition temperature depends on whether the sample is heated or cooled, is prevalent in a number of first-order ferroelectrics including barum titanate [3]. We emphasize that it is only for $T_0 < T_c$ that the ferroelectric minima are thermodynamically favorable.

In a ferroelectric below T_0 there are (at least) two minima of the free energy, corresponding to spontaneous polarizations of different spatial orientations. The barrier between these minima means that a small electric field will not immediately switch the polarization. We note that the Landau–Devonshire theory described here predicts hysteresis [3, 4], shown schematically in Fig. 5, in the ideal (and fictitious) case where all the dipoles have to be overturned together to switch from one polarization orientation to the other.

We note that for ferroelectrics with either continuous or discontinuous transitions, values of the Landau coefficients can be determined by comparing experimental measurements of κ and P_s to the Landau–Devonshire expressions; such parameter sets for a number of commonly studied materials are included in an appendix at the end of this chapter.

2.4 Coupling to Strain

An important feature of ferroelectric materials is their great sensitivity to elastic stress. In order to understand why this is so, we can again take recourse to Landau theory by adding in strain-dependent terms to (9). The strain in a solid is measured by how the displacement $\boldsymbol{u}$ of a point in the solid varies with position $\boldsymbol{r}$, and since this is the dependence of a vector upon a vector, the answer is a tensor: the strain is usually defined as

$$\eta_{ij} = \frac{1}{2}\left(\frac{\partial u_i}{\partial r_j} + \frac{\partial u_j}{\partial r_i}\right), \tag{14}$$

where here i, j indicate the x, y, z components of the vectors. η is therefore a 3×3 symmetric matrix, with six independent components. In materials that are cubic (or nearly so) there will be three independent components to the strain: the volume strain (uniform in all three directions and two kinds of shear).

In general, the polarization will couple to one or more types of strain, and specifically which ones can generally be seen by inspection. Consider a cubic crystal (e.g., $BaTiO_3$) that undergoes a ferroelectric phase transition to a state where the polarization can point along one of the six orthogonal cubic directions. Now it is clear that there is a special axis (one of the six directions after the symmetry has been broken) and so it would no longer be expected that the crystal as a whole will remain cubic – one expects a distortion into a tetragonal crystal, which can be described by a tetragonal strain η. The fact that the lowest-order coupling allowed in this case is of the form ηP^2 (and not, for example, ηP or $\eta^2 P$) is of course a matter of symmetry.

For a uniaxial ferroelectric, the leading order terms will be of the following form

$$\mathcal{F}_\eta = \frac{1}{2}K\eta^2 + Q\eta P^2 + \cdots - \eta\sigma\,. \tag{15}$$

Here, η is (a component of) the strain field, and the first term represents Hooke's law, namely that the elastic energy stored in a solid is quadratically dependent on the distortion, so K is (one of) the elastic constant(s). The second term is a coupling between the elastic strain and the polarization; the fact that this is linear in the strain and quadratic in the polarization depends on the special symmetry of the transition. While this is the leading term in pseudocubic materials, there are other materials (e.g., KH_2PO_4) where the symmetry is lower, and the coupling can be of the form ηP – linear in both strain and polarization. Materials with a linear relation between stress and polarization are called piezoelectric.

Using the free energy, which now consists of the terms in (9) and (15), $\mathcal{F} = \mathcal{F}_\mathrm{P} + \mathcal{F}_s$. we can now determine the properties in equilibrium by minimizing with respect to both P and η, i. e.,

$$\frac{\partial \mathcal{F}(P,\eta)}{\partial P} = \frac{\partial \mathcal{F}(P,\eta)}{\partial \eta} = 0\,. \tag{16}$$

Let us take the second of these equations first:

$$\frac{\partial \mathcal{F}(P,\eta)}{\partial \eta} = K\eta + QP^2 - \sigma\,. \tag{17}$$

There are a few different limits to consider. First, note that if the polarization is zero, we get Hooke's law $\eta = \sigma/K$. The second – apparently trivial case – is when a stress is applied to force the strain to be exactly zero at all times. This is not as absurd as it seems, because often crystals can be considered to be clamped by their surroundings so that no strain is allowed at all. One common situation is of a thin epitaxial film that is forced to have the lattice constants matched to the substrate, and is free to relax only in the third direction. In the case of perfect "clamping" $\eta = 0$, and the free energy is just as before.

The third case to consider is when no external stresses are applied ($\sigma = 0$), and we then have

$$\eta = -\frac{QP^2}{K}\,, \tag{18}$$

so that a spontaneous (tetragonal strain) occurs proportional to the square of the polarization. Notice now that we can substitute for the strain as a function of polarization, and we have a free energy

$$\mathcal{F}(P,\eta(P)) = \frac{1}{2}aP^2 + \frac{1}{4}(b - 2Q^2/K)P^4 + \frac{1}{6}cP^6 + \cdots - EP\,. \tag{19}$$

In comparison with the clamped system, the only change is to reduce the quartic coefficient (notice that the result is independent of the sign of Q). This means that in the case of an already first-order transition ($b < 0$) the transition is driven even more strongly first order, and T_0 is raised. In many ferroelectrics, the effects of clamping can be large – shifting the transition temperature by tens of Kelvin, and even changing the order of the transition. If $2Q^2/K > b > 0$, a first-order transition becomes second order in a clamped system where the strain is allowed to relax; this is the case [3] in $BaTiO_3$.

Application of an external hydrostatic pressure leads to a shift [38] in T_0 whose sign is determined by that of the volume expansion coefficient; a reduced lattice constant is accompanied by a reduction in T_0, consistent with measurements where similar effects have been achieved by chemical substitution [38]. The effect of biaxial stress, where the crystal contracts along two axes and expands along the third, on T_0 was also studied both theoretically and experimentally [39]; enhancement of T_0 was predicted and observed in barium titanate crystals [39]. We shall see shortly that this effect is even more dramatic in thin films where such elastic effects occur at the interface to the substrate.

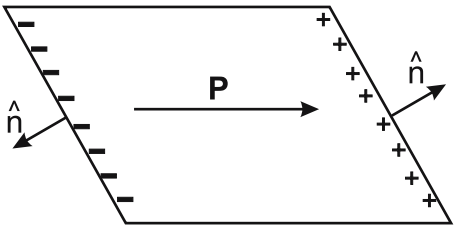

Fig. 6. Surface charge density generated by a bulk polarization at an interface

2.5 Domains

So far we have pretended that the polarization in a ferroelectric can be treated as entirely uniform, and this is far from the case. There are many reasons for the existence of domains, including nonuniform strain, microscopic defects, and the thermal and electrical history of the sample. But even in an ideal crystal, domains are to be expected for energetic reasons associated with electrostatics.

The macroscopic bulk polarization is produced by a displacement of positive charge relative to negative charge; at the surface of the sample there must then be a net charge density of opposite signs on the opposite sides of the crystal (Fig. 6). Any inhomogeneity in the polarization acts like a charge density – and in particular the discontinuity in the polarization at an interface or boundary acts like a surface charge, as can be seen by the following elementary electrostatic argument.

The potential $V(\boldsymbol{r})$ induced by a dipole $\boldsymbol{p}$ at the origin is

$$V(\boldsymbol{r}) = -\frac{1}{4\pi\epsilon_o}\boldsymbol{p}\cdot\boldsymbol{\nabla}\left(\frac{1}{r}\right) , \tag{20}$$

and thus the potential due to a distributed polarization $\boldsymbol{P}(\boldsymbol{r})$ in a volume τ bounded by a surface $\boldsymbol{S}$ is

$$V(\boldsymbol{r}) = \frac{1}{4\pi\epsilon_o}\int_\tau \mathrm{d}\boldsymbol{r'}\, \boldsymbol{P}(\boldsymbol{r'})\cdot\boldsymbol{\nabla}_{\boldsymbol{r'}}\left(\frac{1}{|\boldsymbol{r}-\boldsymbol{r'}|}\right) . \tag{21}$$

Using the product rule: $\boldsymbol{\nabla}\cdot(\boldsymbol{A}f) = f\boldsymbol{\nabla}\cdot\boldsymbol{A} + \boldsymbol{A}\cdot\boldsymbol{\nabla}f$, we have

$$V(\boldsymbol{r}) = \frac{1}{4\pi\epsilon_o}\int_\tau \mathrm{d}\boldsymbol{r'}\left[-\frac{\boldsymbol{\nabla}\cdot\boldsymbol{P}(\boldsymbol{r'})}{|\boldsymbol{r}-\boldsymbol{r'}|} + \boldsymbol{\nabla}\cdot\left(\frac{\boldsymbol{P}(\boldsymbol{r'})}{|\boldsymbol{r}-\boldsymbol{r'}|}\right)\right] , \tag{22}$$

$$= \frac{1}{4\pi\epsilon_o}\left[-\int_\tau \mathrm{d}\boldsymbol{r'}\frac{\boldsymbol{\nabla}\cdot\boldsymbol{P}(\boldsymbol{r'})}{|\boldsymbol{r}-\boldsymbol{r'}|} + \int_{\boldsymbol{S}}\frac{\mathrm{d}\boldsymbol{S}\cdot\boldsymbol{P}(\boldsymbol{r'})}{|\boldsymbol{r}-\boldsymbol{r'}|}\right] , \tag{23}$$

where the last manipulation uses the divergence theorem leading to a surface integral.

The potential appears to be generated by a distributed bulk charge density

$$\rho(\boldsymbol{r}) = -\boldsymbol{\nabla} \cdot \boldsymbol{P}(\boldsymbol{r}) \tag{24}$$

as well as a surface charge density

$$\sigma = \boldsymbol{P} \cdot \hat{\boldsymbol{n}}\,, \tag{25}$$

where $\hat{\boldsymbol{n}}$ is the vector normal to the boundary surface $\boldsymbol{S}$. Occasionally, some books that like to make arbitrary distinctions between "bound" and "free" charge will call the charges generated by an inhomogeneous polarization "fictitious". These charges are fictitious only in the sense that they are conserved – namely if we begin with an electrically neutral system and create a polarization density from it by moving the electrons relative to the ions, the integral of the polarization charge (over the whole system) must vanish. They are in all other respects quite real. The surface charges generate electric fields, both internal and external to the sample, and the fields themselves store energy – just as in a capacitor. In an approximation where the polarization $\boldsymbol{P}$ is assumed to be homogeneous within a domain, and changing abruptly at surfaces or interfaces, only the surface term survives.

The system will minimize its energy by eliminating – as far as is possible – the surface charges, and in a thin film, for example, this makes it clear that the preferred orientation of the polarization will be in the plane of the film, rather than pointing perpendicular to the film. If one has a crystal that is thick in all dimensions, another situation is preferable – to introduce domains where the polarization is oriented to be always parallel to the crystal surface. Such a situation can, of course, only be achieved by introducing domain walls into the bulk, and this will produce polarization charges unless the walls are appropriately oriented.

The interface charge density between two neighboring domains is, by extension of the formula at a free surface,

$$\sigma = (\boldsymbol{P}_1 - \boldsymbol{P}_2) \cdot \hat{\boldsymbol{n}}\,, \tag{26}$$

where $\boldsymbol{P}_1$, $\boldsymbol{P}_2$ are the polarizations of the two domains, and $\hat{\boldsymbol{n}}$ is a unit vector normal to the interface. The two cases when the surface charge will exactly vanish are when the polarizations are antiparallel to each other, and parallel to the domain wall (called a 180° domain wall), or when the domain wall bisects the angle between two domains pointing head-to-tail. Because we are often dealing with nearly cubic crystals where the possible polarizations are at 90° to each other, the latter is often termed a 90° domain wall. Both of these wall types are illustrated in Fig. 7, which is the ideal configuration of the polarization in a "bar" of ferroelectric single crystal – and that bears obvious comparison to the ideal magnetic configuration in a single-crystal bar magnet, that may be familiar to some.

The presence of domain walls involves other energy costs. First, the domain wall is microscopically different from the bulk, and the energy gain of

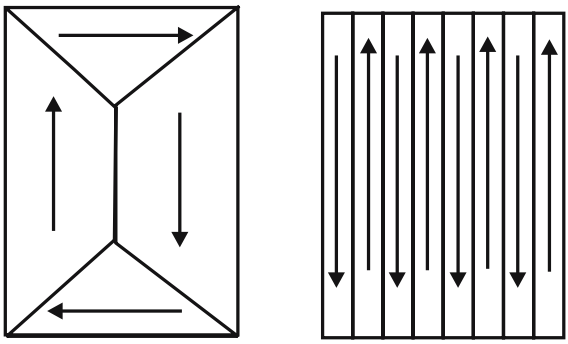

Fig. 7. Ideal domain configuration in a single crystal of cubic ferroelectric material, where the coupling to strain is negligible. On the *right* is the configuration adopted when strain effects are important

forming the polarized ground state has been lost. Secondly, the polarization is coupled to elastic strain – as we saw above – and we must also make sure that the strain fields are compatible. There is no difficulty with a 180° domain wall, but a 90° domain wall produces problems, and the "ideal" configuration of Fig. 7 is by no means ideal in terms of the strain fields. The existence of domains in a sample automatically generates inhomogeneities in the strain that interact in complex ways.

Some contemplation of the two-dimensional pictures above makes it evident that only certain kinds of domain structures are allowed, unless dislocations, cracks, or voids are introduced into the crystal. The moment we have inhomogeneous strain, we must remember to maintain the condition that the displacement field $\boldsymbol{u}(\boldsymbol{r})$ must be *continuous*; however, the free energy depends only on the strains η, which are derivatives of $\boldsymbol{u}$, see (14). Imposing the continuity constraint gives rise to the additional (St. Venant) compatibility conditions on the strain fields [40]

$$\boldsymbol{\nabla} \times (\boldsymbol{\nabla} \times \eta) = 0\,, \tag{27}$$

which formally reduces the number of independent strain components. When dealing with the allowed arrangements of domains of (locally) homogeneous strain (except at the boundary), the application of condition (27) (typically by taking a line integral around the intersection of three domains) determines the legality of various domain arrangements in two and three dimensions.

This condition can also be used to integrate out a single component of the strain, at the expense of introducing long-range forces [41], and this approach can then be used to support calculations and simulations of domain structures in two [42] and three [43] dimensions. This methodology is now quite well advanced in understanding ferroelastic effects on domain structures in martensites [44] though it has not yet been combined with simulations of both the elastic and the ferroelectric order parameter.

There is another feature of ferroelectric domain walls that is not shared by magnetic domains. As far as we are aware, magnetic monopoles do not exist, and therefore the (fictitious in the sense of conserved) magnetic charges that are generated on magnetic boundaries cannot be screened. In ferroelectrics, the surface polarization charges can be, and are, screened by real electrical charges – from impurities, defects, and migrating ions, for example. The motion of charged species (on a fairly slow time scale) to domain walls then provides a mechanism for memory and associated physical phenomena.

This brief introduction to domain structure highlights several issues. The first is that we need to extend the Landau–Devonshire theory of a uniform ferroelectric to incorporate nonuniform polarization. This we do by a parameterization of the free energy now including terms in powers of gradients – this is the Ginzburg–Landau theory, introduced in the next section. Secondly, we noted that the geometry of the sample influences the domain structure, and in particular that there is potentially antagonism between the strain fields and electric fields introduced by the domain structure. The final major point is to note that the effect of inhomogeneities in ferroelectrics is to introduce *long-range* forces, from either charge inhomogeneity or strain fields. It is these two phenomena that complicate a local description of the ferroelectric free energy.

3 Landau–Ginzburg Theory

3.1 General Considerations

The Landau–Devonshire theory that we discussed in the previous section is well suited to the description of a *poled* bulk ferroelectric near its transition (T_0) with a polarization for $T < T_0$ that is spatially uniform. However, we also offered a physical motivation for treating spatially nonuniform polarization in unpoled bulk ferroelectrics, and this will be the subject of our treatment in this section. Generally speaking, Landau–Ginzburg (LG) theory incorporates small spatial variations of the order parameter (here the polarization) within the phenomenological Landau–Devonshire theory with assumptions used originally by Ornstein–Zernike; there, fluctuations of the order parameter at different wavevectors are assumed to be uncorrelated and thus independent.

Let us now discuss specifics of this Landau–Ginzburg approach. Slow variations in the direction of the polarization lead to an additional contribution in the free-energy density ($\Delta\mathcal{F}_{\rm LG}$) that is proportional to $|\nabla P|^2$. Though here, as before, we restrict our discussion to the case of a single-component order parameter, we note that this specific quadratic form of $\Delta\mathcal{F}_{\rm LG}$ is valid for more general vector order parameters based on symmetry considerations [1, 2]. Let us return to the scalar order parameter. Then, if we define a polarization

density $P(r)$ where $\boldsymbol{r}$ is a d-dimensional spatial vector, to lowest order the Landau–Ginzburg free energy is

$$F = a_0(T - T_0) \int \mathrm{d}^d\boldsymbol{r} \left\{P(\boldsymbol{r})\right\}^2 + \gamma \int \mathrm{d}^d\boldsymbol{r} \left\{\nabla P(\boldsymbol{r})\right\}^2 , \tag{28}$$

where the second term is simply the leading contribution in an expansion of polarization–polarization interactions that estimates the additional free-energy cost if the polarizations at different spatial positions are not parallel. Using the fact that the polarization is real (i.e., $P^*(\boldsymbol{q}) = P(-\boldsymbol{q})$), then we can perform a standard Fourier transform to rewrite the Landau–Ginzburg free energy as

$$F = \int \frac{\mathrm{d}^d\boldsymbol{k}}{(2\pi)^d} (a_0(T - T_0) + \gamma k^2)|P(\boldsymbol{k})|^2. \tag{29}$$

We note that here we have two quadratic degrees of freedom; by the equipartition theorem we can then write

$$(a_0(T - T_0) + \gamma k^2)|P(\boldsymbol{k})|^2 = k_\mathrm{B}T\,, \tag{30}$$

where k_B is the Boltzmann constant.

3.2 The Polarization Correlation Function

We are now in a position to determine the static two-site polarization correlation function

$$g(\boldsymbol{r}) = \langle P(\boldsymbol{r})P(\boldsymbol{0})\rangle - \langle P(\boldsymbol{0})\rangle^2\,, \tag{31}$$

which is a measure of the fluctuations of the polarization. We note that in ferroelectrics such quantities can be measured with diffuse X-ray scattering [4, 45]. Taking a Fourier transform of $g(\boldsymbol{r})$ above in the paraelectric phase (where $\langle P(\boldsymbol{0})\rangle = 0$) and assuming that the different wavevector modes are uncorrelated, we obtain

$$g(\boldsymbol{q}) = \langle |P(\boldsymbol{q})|^2\rangle\,, \tag{32}$$

which then, combined with the expression in (30), yields

$$g(\boldsymbol{q}) = \frac{k_\mathrm{B}T}{a_0(T - T_0) + \gamma k^2} \tag{33}$$

as the expression for the Fourier transform of the correlation function. Now we simply take the inverse transform to find

$$g(\boldsymbol{r}) \sim \frac{k_\mathrm{B}T}{\gamma} \frac{e^{-r/\xi}}{r^{d-2}}\,, \qquad T \neq T_0 \tag{34}$$

and

$$g(\boldsymbol{r}) \sim \frac{k_{\mathrm{B}}T}{\gamma}\frac{1}{r^{d-2}}\,, \qquad T = T_0\,, \tag{35}$$

where the correlation length is

$$\xi = \sqrt{\frac{\gamma}{a_0|T-T_0|}} = \sqrt{\frac{\gamma}{a_0 T_0}}\sqrt{\frac{T_0}{|T-T_0|}} \equiv \xi_0|t|^{-1/2}\,, \tag{36}$$

and $t = \frac{T-T_0}{T_0}$ is the reduced temperature. Physically, for $T > T_0$ this correlation length, ξ, corresponds to the length scale over which the polarization exists; it diverges at $T = T_0$, and for $T < T_0$ it is associated with the length scale over which P varies from its equilibrium value. We note that the polarization correlation function is exponentially decreasing above the transition, but has a dimensionally dependent power-law form when $T \sim T_0$. As a final note to this subsection, we remark that the dimensions of γ and $a_0(T-T_0)$ are $\frac{E}{P^2L}$ and $\frac{E}{P^2L^3}$, respectively, so that $[\xi_0] = \sqrt{L^2} = L$ as expected.

3.3 The Levanyuk–Ginzburg criterion

How reliable is this Landau–Ginzburg theory, and when is it no longer valid? The LG approach is a long-wavelength description of a system near a phase transition, where its modes are coarse grained on scales of order of the correlation length ξ. The resulting effective free-energy density is written as an expansion of the order parameter (e.g., P) averaged over a volume Ω_ξ determined by ξ. When are the fluctuations of the order parameter, averaged over the correlation volume Ω_ξ, small in comparison with its coarse-grained average? The answer, relevant for the validity of this long-wavelength approach, is dependent on system dimensionality. We have just seen that the LG approach yields a two-site correlation function, a measure of the order-parameter fluctuations, that increases dramatically at $T \sim T_0$; it is therefore clear that in the immediate vicinity of T_0 the LG expansion is no longer valid. So how close can we get to the transition itself before this approach no longer works?

As it turns out, we can use Landau–Ginzburg theory itself to determine its own fallibility [17–19]. Before we present this argument, let us return to Landau–Devonshire theory and look at its predictions for behavior near the phase transition. We recall the expression for the free energy

$$\mathcal{F}_{\mathrm{P}} = \frac{1}{2}a_0(T-T_0)P^2 + \frac{1}{4}bP^4 - EP\,, \tag{37}$$

which we have truncated at quartic order. The equilibrium value of the polarization corresponds to a free-energy minimum

$$\frac{\partial \mathcal{F}_{\mathrm{P}}}{\partial P} = a_0(T-T_0)P + bP^3 = 0\,, \tag{38}$$

which yields (for $T < T_0$)

$$P = \sqrt{\frac{a_0(T_0 - T)}{b}} \sim (-t)^{1/2}\,, \tag{39}$$

whereas $P = 0$ in the paraelectric phase. The form of the free energy, (37), combined with these results for the polarization imply that the associated specific heat, $C_v = -T\frac{\partial^2 F}{\partial T^2}$, has a discontinuity at the transition so that the mean-field exponent α is zero (i.e., $C_v \sim |t|^0$).

Equipped with this information, we are now ready to determine the condition for when Landau–Ginzburg theory breaks down. Basically this occurs when the fluctuation free energy associated with a typical fluctuation of the order of the correlation length is comparable to the total free energy. The fluctuation free energy per unit volume can be estimated as

$$\mathcal{F}_{\text{fluct}} \sim \frac{kT}{\xi^d} \sim |t|^{\nu d}\,, \tag{40}$$

where we have used $\xi \sim |t|^{-\nu}$. We have defined the specific heat, $C_v \sim |t|^{-\alpha}$ so that two integrations yield $\mathcal{F} \sim |t|^{2-\alpha}$. Thus, for a consistent theory, for $t \to 0$, we must have

$$d^* > \frac{2 - \alpha}{\nu}\,. \tag{41}$$

Inputting the mean-field values ($\alpha = 0$ and $\nu = 1/2$), we get

$$d^* > 4\,, \tag{42}$$

which indicates that above the upper critical dimension, $d^* = 4$, the LG approach is valid. We note that the value of d^* depends on the form of the Landau expansion and can be different for systems with different underlying symmetries [46].

This calculation indicates that for real materials in $d < 4$, the Landau–Ginzburg approach breaks down close to the phase transition ... but how close? Intuitively it seems that the larger the number of neighbors the better it does, which suggests that it works better for systems with long-range forces. Let us use what we have learned to put this speculation on a firmer footing, and here we follow the original Levanyuk–Ginzburg reasoning [17–19]. For $T < T_0$ let us argue that coarse-grained fluctuations in the polarization must be small in comparison with the average polarization itself; this translates into the condition

$$g(\boldsymbol{r}) \ll P^2\,, \tag{43}$$

where $|r| \sim \xi$. Using our previous results in (34) with $d = 3$ and (39), we can rewrite this expression as

$$\frac{k_{\text{B}}T_0}{\gamma\xi(T)} \ll \frac{a_0(T - T_0)}{b}\,, \tag{44}$$

which, when using specific expressions for $\xi(T)$ and C_v in (36) and (13), results in the standard form of the Levanyuk–Ginzburg criterion

$$\mathcal{A}\frac{1}{(\Delta C_v)^2\xi_0^6} \ll |t|\,, \tag{45}$$

where $\mathcal{A}$ is a constant that is unimportant for our present purposes; here the key point is that the range of the interaction, ξ_0, plays an important role in determining the validity of the mean-field theory. More specifically, the Levanyuk–Ginzburg temperature, determined by the expression in (45), is inversely proportional to the *sixth* power of the range of the interaction, and thus Landau–Ginzburg theory should be quite reliable in the vicinity of the paraelectric–ferroelectric transition. We note that if we generalize the condition (43) to d dimensions then, using (35) with $|r| \sim \xi$ and (39), we obtain

$$\mathcal{B}|t|^{\frac{d-2}{2}} \ll |t|^1\,, \tag{46}$$

which is satisfied for $d > d^* = 4$ for arbitrarily small $|t|$ where $\mathcal{B}$ is a constant. We have thus recovered the same result that we obtained earlier in this section, namely that Landau–Ginzburg theory is exact for dimensions $d > 4$ for the ferroelectrics under consideration. Here, we remark that the angular dependence of the dipolar interactions has not been considered here, and it is indeed this feature that leads to logarithmic corrections to mean-field exponents in certain experimentally observable (i.e., $d = 3$) cases [20–23]. We note that here we have referred to this condition as the Levanyuk–Ginzburg criterion (rather than simply that due to Ginzburg) since we have learned[1] that *Levanyuk*, a student of Ginzburg, derived this condition independently of his advisor and indeed published the result in a sole-author publication [17] a year before Ginzburg's paper appeared [18, 19].

3.4 Displacive and Order–Disorder Transitions

The Levanyuk–Ginzburg criterion indicates the validity of the mean-field approach to the transition, but more fundamental in many practical senses is the validity of the continuum approximation underlying the LG theory. A continuum theory is, of course, good close enough to a second-order critical point since the diverging correlation length ξ is much larger than the interatomic spacing – this is the condition that coarse graining works. But *far* from the transition – either well above T_c or well below it – this condition will not necessarily hold.

If one takes the Landau theory literally as a description of the phase transition and its dynamics, the order parameter vanishes uniformly everywhere above the transition temperature. Equivalently, one would say that the lattice displacements corresponding to the electronic polarization are equally

[1] Private communication with D. Khmel'nitskii and J. F. Scott.

uniform – and zero above T_c, finite below. Such a type of transition is termed *displacive*. A contrasting limit for an ordering transition is that of local moment magnetism [47], wherein the magnetic moment on an atom persists above T_c but the long-range order is destroyed. In the case of a ferroelectric (or other structural transition), this limit is described as an *order–disorder* transition, where the local symmetry-breaking distortions are present in every unit cell above T_c, but are randomly oriented at high temperatures, so there is no net polarization. Any real material will of course lie somewhere along the spectrum between these two limits.

We have argued above that one reason for the practical usefulness of the LG approach is that there are intrinsic interactions (elastic and charge) that are long range, and these induce a long correlation length. But there are also conditions related to the underlying microscopic drivers for ferroelectricity that are ineluctably electronic in nature. Although in this chapter we are largely avoiding microscopic theory, here we engage in a short digression on the topic of *electronic ferroelectricity*, which has some relevance to the issue.

Spontaneous development of a ferroelectric moment is always associated with a (broken-symmetry) atomic displacement, and often this is pictured as an essentially rigid displacement of charge. But of course the driving force for ferroelectricity arises from interactions in the electron system, so a completely rigid displacement of ions is not to be expected. One may study this even in linear response theory – how much charge redistribution is produced by a small displacement of the ion – or equivalently how large an electrical dipole is produced by a particular phonon displacement. Phonons in solids can be separated into acoustic and optical branches, where the eigenmodes of the latter describe the relative motion of different ionic species against each other. One may quantify the electronic rigidity for an optical mode by a number known as the transverse electric charge Z^*_T [25], which measures (to linear order) the average electrical dipole moment per unit cell p generated by the corresponding relative ionic displacement u (taken to be the same in every cell), i. e.,

$$p = Z^*_T e u \,, \tag{47}$$

where e is the electron charge. There is a different value of effective charge Z^*_T for each optical mode (and it may be zero if the displacement preserves inversion symmetry); even a nonferroelectric crystal will usually have dipole-active modes. A simple case is just that of the rocksalt structure, where the optical eigenmode is a displacement of the two sublattices relative to each other. The effective charge can be straightforwardly measured by the optical response of an infrared-active phonon. The connection to ferroelectricity is that if such a phonon goes "soft" and acquires a finite frozen amplitude u_0, then $Z^*_T e u_0$ is the approximate magnitude (to linear order) of the ferroelectric moment per unit cell. This is the classic soft-mode theory of ferroelectric instability [48–50].

In the context of the Landau theory, this relates the polarization to the atomic motion. In a rigid-ion picture, one expects $Z^*_{\rm T}$ to reflect the charge on the ion, but it is in fact not uncommon to measure effective charges that are quite large: for example [51] in the rocksalt structure IV-VI compounds ($Z^*_{\rm T}$ values in brackets) PbS (4.8), PbSe (5.8), PbTe (6.5), SnTe(8.1), GeTe(11), where a rigid-ion viewpoint would lead one to expect $Z^*_{\rm T} \leq 2$. Only the last two of these materials (which are the least ionic in the Pauling sense!) become ferroelectric at low temperature. What these large numbers represent physically is of course that as the nuclei are displaced the electron distribution alternates from one side of the ion to another, with the electrons moving much further than the nuclei themselves. This large amplification of motion happens in electronically driven transitions of the Peierls type [52, 53]; it can also happen in cases of electronically driven spontaneous symmetry breaking where the Coulomb interaction favors the breaking of spontaneous orbital symmetry [54–57].

In these cases, the large induced polarization arises because of a broken orbital symmetry. Whatever the underlying model, in what one can see in the not entirely formal limit of a ferroelectric that has $Z^*_{\rm T} \to \infty$, the transition is indeed electronic in nature. Moreover, it corresponds in that case to a metal–insulator transition as well, where the distortion leads to the opening of a small electronic energy gap 2Δ in the spectrum. Such transitions are in fact charge-density wave instabilities in disguise, where the broken symmetry happens also to break inversion symmetry, and the CDW onset is also that of ferroelectricity. The driving force for these transitions is the opening (or increase) of an electronic gap at the Fermi energy (for a review, see [58]).

Suppose for a moment that we can ignore the lattice-dynamical effects on this transition, we can then estimate the transition temperature and correlation length in a weak coupling limit, which is well known to be mathematically just like the Bardeen–Cooper–Schrieffer theory of superconductivity [59–61]:

$$T_{\rm c}^{MF} \propto \Delta \simeq W {\rm e}^{-1/\lambda}\,, \tag{48}$$

$$\frac{\xi_0}{a} \simeq \frac{W}{\Delta}\,, \tag{49}$$

where W is the electronic bandwidth, a the lattice constant, and $\lambda \ll 1$ the effective dimensionless interaction strength (scaled by the electronic bandwidth), which must be small for this kind of theory to be appropriate. In weak coupling, the gap and transition temperature are small (in comparison to the electronic bandwidth) and the correlation length ξ_0 is large.

Now we consider the effect of the coupling to the lattice, and in particular we must take account of dynamical phonons. Provided $k_{\rm B}T_{\rm c}^{MF}$ is much smaller than a characteristic phonon energy $\hbar\omega_{\rm D}$, there will be no appreciable fluctuations of dynamical modes until one is at a temperature very close to the transition, so the mean-field theory is rather good as an estimate of the transition temperature. And, moreover, even above $T_{\rm c}$ the dynamical modes are weakly excited so there are few thermal fluctuations of the lattice. All

that remains is just the (small, in this case) mean-field lattice distortion that smoothly vanishes at T_c. We see that the condition for the displacive limit is that of *ultraweak* coupling, namely that

$$\frac{\hbar\omega_D}{W} \gg e^{-1/\lambda} . \tag{50}$$

However, if this condition is violated, thermal fluctuations of dynamical modes will become important, and the extra entropy associated with the lattice distortions will drive a transition to the paraelectric phase at a temperature well below the mean-field one [62]. Here, we now crossover to the "order–disorder" regime of the transition, and we remark that (as commonly observed in CDW transitions) this crossover happens when λ is still very small, since typically the electronic bandwidth is two to three orders of magnitude larger than a typical phonon energy.

Thus, we see that there are two potentially quite distinct reasons to stabilize the displacive picture. One is the coupling to elastic strain, and the presence of long-range forces, about which we will have more to say later. This is important in all classes of ferroelectrics. A second type is where the transition is predominantly driven by electronic redistribution of states near the Fermi level of a metal or narrow-gap semiconductor, and, furthermore, the displacive limit obtains only when the coupling is very weak, so that electronic gaps are small in comparison to the Debye frequency. These CDW-like systems are rare as classic ferroelectrics, (except maybe for SnTe, which has a transition near 40 K and shows the classic soft-mode behavior [63]), but they are probably quite common in small-moment ferroelectrics where the ferroelectricity is an "accidental" adjunct to a charge-ordering transition. Such is potentially the case in charge-ordered manganites, for example [64].

3.5 Recent Developments in Bulk Ferroelectricity

Landau–Devonshire theory has been successful in reproducing the observed phase behavior in simple ferroelectric compounds (e.g., $BaTiO_3$ and $PbTiO_3$) and these results are described in many textbooks [3–5]. Recently, it was shown [65] that the standard sixth-order free-energy expansion can not account for an observed phase where the polarization is not symmetry-restricted to an axis. More specifically, a monoclinic phase was observed in PZT for a given temperature and compositional range [66], that did not emerge from a standard Landau–Devonshire (sixth-order) treatment [67]. However, this phase did emerge in the observed parameter regime from simulations [68] based on a first-principles effective Hamiltonian approach [69]; this result suggested that no additional physics (or specifically instabilities) were necessary for its description. An eighth-order expansion of the free energy yielded the observed monoclinic phase [65] where it was argued that the higher-order terms might be generated by disorder averaging. This analysis will be relevant for other ferroelectric phases where the polarization is constrained to a symmetry plane.

In the introduction we alluded to a link between first-principles calculations and Landau theory, and here we discuss it more specifically. In the last two decades, there has been great progress in the collective understanding of atomic-scale ferroelectricity through detailed density-functional theory investigations. We refer the interested reader to two recent reviews [70, 71] and other chapters in this book for more information about these developments. First-principles effective Hamiltonians, based on these first-principles approaches with reduced degrees of freedom, have been analyzed by statistical methods to explore the finite-temperature behavior of ferroelectrics. In particular, such an effective Hamiltonian approach was very successful in reproducing the known phase behavior [72, 73] of $BaTiO_3$. More recently, the compatibility of this particular Hamiltonian and the Landau–Devonshire theory of $BaTiO_3$ was demonstrated [74] in a careful Monte Carlo study of the order-parameter configuration space. Thus, first-principles density-functional calculations, via an effective Hamiltonian, can provide the input coefficients for Landau–Ginzburg theory; this bridging of theoretical methods is crucial for studying phenomena on many length scales in ferroelectrics.

In this chapter, we focus primarily on the thermodynamic description of ferroelectrics using Landau–Ginzburg theory. However, the resulting free energy can be incorporated into a treatment of thermally activated dynamical processes, specifically the determination of nucleation rates [75]. We note in passing that the coupling between the polarization and the long-range elastic degrees of freedom in bulk materials implies that nucleation of new ferroelectric regions must be a cooperative effect in that these events cannot occur completely independently. Dynamical studies of field-quenched $BaTiO_3$ crystals provide experimental support for this statement [76, 77]. This observed behavior can be qualitatively described by a modified time-dependent Landau analysis with simple feedback to account for the strain mediation between growing regions [78, 79].

In concluding our discussion on bulk ferroelectricity, we note that there was much work done in this field in the former Soviet Union that was not communicated to the West. This situation was recently summarized by *Ginzburg* [80], and we point the interested reader to these thought-provoking reminiscences.

4 Reduced Size and Other Boundary Effects

4.1 General Discussion

Ferroelectric materials are very sensitive to electromechanical boundary conditions due to the long-range nature of their underlying electrostatic interactions and to the strong coupling between the polarization and the strain [7,70,71]. Thus, the influence of surfaces and other boundary conditions on their collective behavior is very pronounced [81,82]. Furthermore, there are

numerous ways in which the external environment, via applied boundary conditions, can alter ferroelectric behavior; examples include electric fields due to surface charges and homogeneous misfit strains. Finally, there is a significant commercial impetus to use ferroelectrics for portable high-density data storage; for such increasingly miniaturized applications, key size-dependent effects must be understood and modeled in order to optimize design [7, 83]. Typically, the fabricated structures will be of linear dimension 10 nm–1 µm, length scales that are not accessible to purely atomistic methods. However, such approaches can be used towards determining the effects of local variations (e.g., compositions, strains, displacements) in conjunction with specific boundary conditions; the results could then be incorporated into a bridging phenomenological theory that spans physics on longer length scales to enable direct comparison with experimental observation.

In this section we summarize key features of Landau–Ginzburg approaches to ferroelectrics with specific boundary conditions, focusing on the well-studied case of planar geometries. We begin with semi-infinite ferroelectrics with a free surface, a case that can be easily generalized to a freestanding thin film. Because of reduced coordination number at a free surface compared to the bulk, we expect the average polarization to display altered behavior at the boundary that could lead to changes in its overall thermodynamic behavior [84–86]. We observe how this need for a specific boundary condition emerges technically from a Landau–Ginzburg approach of the bulk and the surface free energies. We also discuss the necessary assumptions underlying the emergence of the so-called extrapolation length from such a treatment and suggest a test for this often-used (but rarely justified) approach [87]. If the polarization is normal to the free surface of the ferroelectric film, a geometry that is often used in practice, then depolarization effects must be included and this is the topic of the next subsection. Next, we turn to epitaxial misfit strain, and how it can be turned to dramatically increase the spontaneous polarization of a ferroelectric film beyond that in the bulk. We end with a discussion of inhomogenous strain and polarization configurations, a more recent area of investigation that is of particular relevance to three-dimensional ferroelectric nanostructures [88].

4.2 The Polarization at the Boundary

The presence of the Ginzburg term, $|\boldsymbol{\nabla} P|^2$, in the Landau–Ginzburg free energy implies that a boundary condition is necessary to solve the second-order differential equation that results from the minimization procedure. Let us consider a semi-infinite ferroelectric with a second-order phase transition We begin by considering the bulk free energy, including the new gradient term, of this system

$$\mathcal{F}_{\text{bulk}}^{\text{LG}} = \int \mathrm{d}V \left[\gamma |\boldsymbol{\nabla} P|^2 - \frac{a}{2}|P|^2 + \frac{b}{4}|P|^4 \right] , \tag{51}$$

such that $a > 0$ (implying $T < T_0$). We note that we can use the divergence theorem to split the gradient term in (51) into a surface and a volume integral

$$\int \mathrm{d}V(\boldsymbol{\nabla} P \boldsymbol{\nabla} P) = \int \mathrm{d}V \left[\boldsymbol{\nabla}(P\boldsymbol{\nabla} P) - (P\nabla^2 P)\right] = \int \mathrm{d}S(\hat{n}\cdot\boldsymbol{\nabla} P)P - \int \mathrm{d}V(P\nabla^2 P)\,, \tag{52}$$

where $\hat{\boldsymbol{n}}$ is the normal unit vector to the surface. Borrowing from analogous studies of superconducting [60] and magnetic [89–91] films, we argue that there is a "surface tension" contribution so that the full free energy ($\mathcal{F} = \mathcal{F}^{\mathrm{LG}}_{\mathrm{bulk}} + \mathcal{F}_{\mathrm{stension}}$) is now a sum of interior and surface contributions, $\mathcal{F} = \mathcal{F}_{\mathrm{interior}} + \mathcal{F}_{\mathrm{surface}}$, where

$$\mathcal{F}_{\mathrm{interior}} = \int \mathrm{d}V \left[-\gamma P\nabla^2 P - \frac{a}{2}|P|^2 + \frac{b}{4}|P|^4\right] \tag{53}$$

and

$$\mathcal{F}_{\mathrm{surface}} = \int \mathrm{d}S \left[\gamma(\hat{\boldsymbol{n}}\cdot\boldsymbol{\nabla} P)P + \frac{\alpha(T-T^*)}{2}|P|^2 + \frac{\beta}{4}|P|^4\right]. \tag{54}$$

We note that this form of the "surface tension" free-energy contribution assumes that there exists a temperature T^*, not necessarily equal to the bulk transition temperature T_0, where the surface becomes ferroelectric; here, the coefficients α and β are usually considered to be thickness independent with $\beta \ll \alpha$ [60, 84, 85].

If we vary the free-energy density with respect to δP, we obtain

$$\delta\mathcal{F} = \int \mathrm{d}V \ \left[-\gamma\nabla^2 P - a|P| + b|P|^3\right](\delta P) + \int \mathrm{d}S\left[\gamma(\hat{\boldsymbol{n}}\cdot\boldsymbol{\nabla} P) + \alpha(T-T^*)|P|\right](\delta P)\,. \tag{55}$$

In bulk systems the surface integral in (55) is often neglected, either due to periodic boundary conditions or due to the absence of variation in P on very long length scales. However, this approach cannot be justified for finite-size systems.

For simplicity, let us restrict our attention here to the case where the polarization is only z dependent, the surface defined as $z = 0$, and the sample occupies the space $z > 0$. Then the stationary condition for the total free energy to a small variation $\delta P(z)$ leads to the second-order differential equation

$$-\gamma\frac{\mathrm{d}^2 P}{\mathrm{d}z^2} - aP + bP^3 = 0 \tag{56}$$

together with the boundary condition

$$\gamma\frac{\mathrm{d}P}{\mathrm{d}z} + \alpha(T-T^*)P = 0|_{z\to 0^+} \tag{57}$$

at the surface. We can rewrite the boundary condition as

$$\frac{\mathrm{d}P}{\mathrm{d}z} = -\frac{P}{\delta}\Big|_{z\to 0^+}\,, \tag{58}$$

which results in

$$P = P(0)\mathrm{e}^{-\frac{z}{\delta}}\Big|_{z\to 0^+}\,, \tag{59}$$

with

$$\delta = \frac{\gamma}{\alpha(T-T^*)}\,, \tag{60}$$

where we note that the dimensions of γ and $\alpha(T-T^*)$ are $\frac{E}{P^2L}$ and $\frac{E}{P^2L^2}$, respectively so, that $[\delta] = L$ and δ is the so-called extrapolation length; here $P(0)$, the polarization at the surface, must be determined by an electrical boundary condition. We remark that we must obtain

$$|\delta| > \xi_0 \tag{61}$$

in order for this calculation to be self-consistent, where ξ_0 is the length scale over which the polarization has spatial variation in the bulk. We see that δ is temperature dependent, and its sign is determined by the relative values of T^* and T. For example, if, as we have assumed above, $T < T_0$, and $T_0 < T^*$, then $(T-T^*) < 0$ and $\delta < 0$. In this case, the surface becomes ferroelectric at a temperature higher than that in the bulk, so the polarization at the surface increases as indicated in (59). By contrast, it will decrease at the boundary if $T_0 > T^*$. This approach has been generalized to ferroelectric films [32, 87, 92] with the appropriate boundary conditions at the surfaces/interfaces. The solution of (56) and the film analogs of (59) leads to a thickness-dependent critical temperature that is qualitatively similar to that observed [32, 87, 92]. It can also be extended to the case where the bulk material has a first-order transition [93]; now higher-order terms in the Landau–Ginzburg free energy must be retained. Another generalization is to superlattices with alternating films of two different materials [92, 94].

The scheme that we have just outlined assumes implicitly that the free energy of interest can be clearly separated into two distinct parts, $\mathcal{F}_{\text{interior}}$ and $\mathcal{F}_{\text{surface}}$, that have similar algebraic structures but different transition temperatures. More specifically, there must be a distinct separation of length scales associated with the surface and the interior; this requirement translates into the inequality

$$\xi_0 < |\delta| < L\,, \tag{62}$$

where $L \gg 1$ is the lateral dimension of the sample. To our knowledge, there is no direct experimental confirmation of the extrapolation length, though it

may be indirectly accessible via X-ray diffraction [95] and far-infrared measurements. We note that there is some suggestion [96] that the Landau coefficients for thin films may have some thickness dependence that is not included in this standard treatment. Another complementary approach is to assume a spatially varying transition temperature in the finite-size ferroelectric [97]. This might be a productive way of incorporating known imperfections into the phenomenological theory. Finally, we remind the reader that the Landau–Ginzburg approach assumes that the free energy can be expressed as a polynomial expansion of the average polarization; as finite-size effects become increasingly important such coarse graining may no longer be possible. The possible breakdown of this free-energy ansatz should be checked explicitly with first-principles methods for a variety of sizes and geometries.

4.3 Depolarization Effects

So far we have discussed finite-size planar ferroelectrics where the polarization has been parallel to the surfaces of interest. Now we switch to a geometry where the polarization is normal to the boundary, as displayed in Fig. 8. Physically we expect a buildup of free surface charge that, if uncompensated, results in a depolarizing electric field E_{d}. It is then energetically difficult for the sample to sustain its uniform polarization, and phases with ferroelectric domains often result. Since, as we shall see shortly, the depolarization field increases with decreasing film thickness [26–28], its importance increases with reduced size and it must be incorporated in the phenomenological description of such finite-size ferroelectric systems.

In practice, these depolarization effects can be significantly reduced by the presence of metal electrodes that provide charge compensation at the ferroelectric boundaries. We now develop an expression for the Landau–Ginzburg free energy of a short-circuited ferroelectric capacitor that consists of a ferroelectric film bracketed by two metal electrodes (see Fig. 8). For pedagogical simplicity, we will consider the short-circuited case ($V_{\mathrm{ext}} = 0$) where the length scale of the electrodes is significantly larger than that of the film ($L \gg d$; $L \to \infty$), which is in turn greater than the screening length λ in the electrodes; succinctly, our operating condition is then $L \gg d \gg \lambda$ and a schematic of this situation is displayed in Fig. 8. We will also assume that the polarization gradient is negligible at the ferroelectric/electrode interfaces, namely that $\frac{\mathrm{d}P}{\mathrm{d}z} = 0|_{z=\pm\frac{d}{2}}$, which implies that the inverse extrapolation length in (58) is zero (e.g., $\delta \to \infty$). We note that calculations in this simplified parameter regime yield results that are compatible with experiment [28, 31]. The interested reader is referred to more complex treatments of the depolarization field for other parameter specifications [98].

Let us consider the zero-potential (short-circuited) ferroelectric capacitor shown schematically in Fig. 8a. The spontaneous polarization is displayed. In an idealized system with perfect metal plates, there would be complete

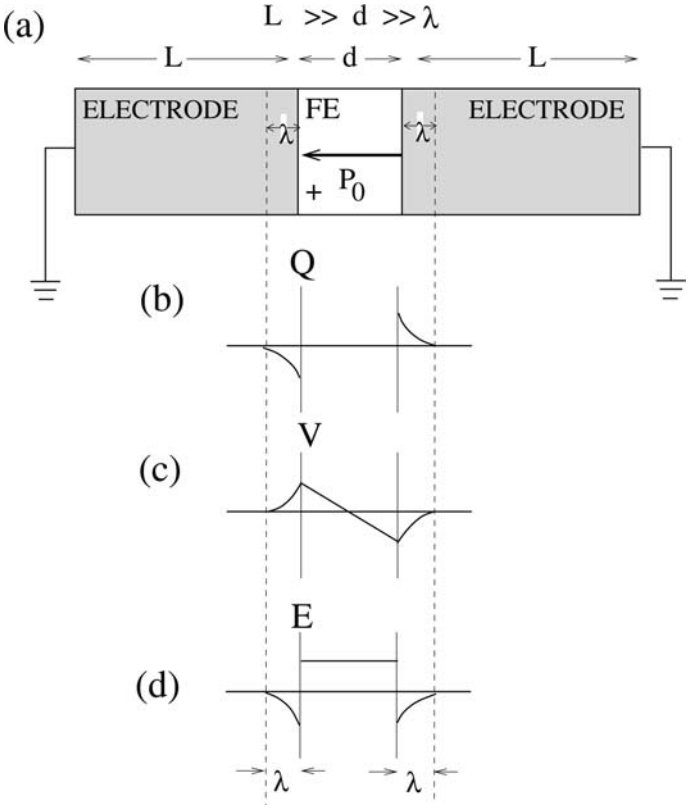

Fig. 8. (**a**) Schematic of short-circuited ferroelectric capacitor with $L \gg d \gg \lambda$ and accompanying plots of the spatial distribution of (**b**) the charge Q, (**c**) the potential V and (**d**) the depolarization field E. Note that the charge distribution in (**b**) would simply be δ functions at the film/electrode interfaces for perfect electrodes; then V and E would simply be constant and zero

charge compensation at the electrode/ferroelectric interface and thus no depolarization field in the film. However, in realistic electrodes, screening charge resides within a small but nonzero distance from the ferroelectric boundary (cf. Fig. 8b). For a short-circuited ferroelectric capacitor, this spatial charge distribution leads to an associated voltage drop in the electrodes and a compensating depolarization potential across the film (cf. Fig. 8c). There is therefore an accompanying depolarization field that, in the case of uniform polarization, will simply scale inversely with film thickness (Fig. 8). Intuitively, we expect the presence of this depolarization field to suppress ferroelectricity since it is antiparallel to the polarization.

More formally, we follow previous treatments [98] in the specific limit $L \gg d \gg \lambda$ to derive the total Landau free energy of the ferroelectric capacitor; this free energy has two contributions

$$F = F_{\rm e} + F_{\rm f}\,, \tag{63}$$

where $F_{\rm e}$ and $F_{\rm f}$ are associated with the electrodes and the film, respectively. We assume that the charge density at each ferroelectric/electrode interface takes the simple Thomas–Fermi form $\rho(z) = \frac{Q}{z}{\rm e}^{-\frac{z}{\lambda}}$, where λ is a screening length [99]. Then, solving for the free energy associated with the field inside each electrode, we find that

$$F_{\rm e} = \frac{\lambda Q^2}{2\epsilon_0\epsilon_{\rm e}}\,, \tag{64}$$

where $\epsilon_{\rm e}$ and ϵ_0 are the permittivities of the electrodes and of free space, respectively. We note that the choice of $\epsilon_{\rm e}$, a quantity usually defined in the long-wavelength limit [100], is tricky since it enters this treatment via a boundary condition at the ferroelectric/electrode interface, and we refer the interested reader to two distinct approaches to this issue [31, 98] where comparisons with experiment are made.

Next we turn to the free energy in the film, which has the form

$$F_{\rm f} = \int_{-d/2}^{d/2} \left[\mathcal{F}_{\rm P} - \frac{1}{2}E_{\rm d}(z)P(z)\right] {\rm d}z\,, \tag{65}$$

where $E_{\rm d}(z)$ is the depolarization field and the second term in (65) above represents its self-energy (and hence the factor of 1/2 [84,85]). Using the fact that there is no free charge in the ferroelectric, we write the depolarization field in the form $E_{\rm d}(z) = E_0 - \frac{P(z)}{\epsilon_0}$ where by continuity at the interface $E_0 = E(\pm\frac{d}{2}) = \frac{Q}{\epsilon_0}$. Now we need to find E_0 in terms of $P(z)$ since we do not know Q. Use of the short-circuit condition leads to the expression

$$E_0 = \frac{1}{\epsilon_0(2\lambda + d)} \int_{-\frac{d}{2}}^{+\frac{d}{2}} P(z)\,{\rm d}z\,, \tag{66}$$

which can then be inputted into the expressions (64) and (65) for $F_{\rm e}$ and $F_{\rm f}$, respectively. We note that for P uniform and $\lambda \ll d$, the depolarization field takes the form

$$E_{\rm d} = E_0 - \frac{P}{\epsilon_0} = \frac{P}{\epsilon_0}\left(\frac{1}{1+\frac{2\lambda}{d}} - 1\right) \sim \frac{2P\lambda}{\epsilon_0 d}\,, \tag{67}$$

which varies inversely with the film thickness d and vanishes in the case of perfect electrodes ($\lambda = 0$); we note that a similar result for $E_{\rm d}$ is found

by introducing an air gap of thickness λ between the film and perfect electrodes [31, 101] thereby displacing the compensating charge from the ferroelectric interface.

The Landau free energy for the ferroelectric capacitor then is

$$F = \left(\int_{-\frac{d}{2}}^{+\frac{d}{2}} \mathcal{F}_{\mathrm{P}} \ \mathrm{d}z \right) + \Delta F \,, \tag{68}$$

where

$$\Delta F = \int_{-\frac{d}{2}}^{+\frac{d}{2}} \frac{P^2(z)}{2\epsilon_0} \, \mathrm{d}z - \frac{1}{2\epsilon_0 d(1+\frac{2\lambda}{d})} \left(1 - \frac{\lambda}{\epsilon_{\mathrm{e}} d(1+\frac{2\lambda}{d})}\right) \left[\int_{-\frac{d}{2}}^{+\frac{d}{2}} P(z) \, \mathrm{d}z \right]^2 , \tag{69}$$

where we reiterate that this free energy is for the limits $L \gg d \gg \lambda$, where $L \to \infty$ and $\delta \to \infty$. We see from (69) that if P is uniform and $\lambda = 0$, then $\Delta F = 0$. However, if $P = P(z)$, ΔF is finite even for perfect electrodes [84, 85]. For uniform P and finite λ, where $\frac{2\lambda}{d} \ll 1$, (69) yields

$$\frac{\Delta F}{d} \sim \frac{P^2}{2\epsilon_0} \left(\frac{\lambda}{\epsilon_{\mathrm{e}} d} \right) , \tag{70}$$

which contributes to the coefficent of the quadratic term in the overall free-energy density. As a result, the expression for the film's transition temperature T^* is

$$\frac{1}{2} a_0 (T^* - T_0) + \frac{\lambda}{2\epsilon_{\mathrm{e}} \epsilon_o d} = 0 \,, \tag{71}$$

which leads to

$$T^* = T_0 - \frac{\lambda}{\epsilon_0 \epsilon_{\mathrm{e}} d a_0} \,, \tag{72}$$

which is shifted from its bulk value (T_0) by a term due to the depolarization field; we note that when $2\lambda \sim d$, a more complicated expression results [102] that suggests that there exists a minimum thickness $d_{\min}$ below which ferroelectricity is unstable [26, 27, 92]. For a given material, characterized by a_0 and T_0, this minimum thickness can be tuned by the choice of electrodes [29–31] whose relevant characteristics enter $d_{\min}$ via λ and ϵ_{e}. However, recent experiments [103–105] indicate the presence of ferroelectricity below this minimum cutoff, which may be consistent with theoretical expectations for a polydomain ferroelectric state [106]. Naturally, the depolarization effects will be significantly reduced if the ferroelectric film is treated as a semiconductor [107] rather than as an insulator. Before closing this section, we note that

recently the dielectric properties of ferroelectric–paraelectric multilayers have also been studied within this type of thermodynamic approach, and it has been found that there exists a critical paraelectric film thickness such that ferroelectricity is completely suppressed due to interlayer electrostatic interactions [108]. We emphasize that the Landau–Ginzburg approach presented to this point has assumed a single-domain (homogeneous) ferroelectric phase, and its generalization to include inhomogeneous effects will be discussed later in this chapter.

4.4 Misfit Epitaxial Strain

The thermodynamic behavior of a ferroelectric film is also sensitive to mechanical boundary conditions due to the strong coupling between the polarization and the strain. Application of pressure, both hydrostatic [38] and biaxial [39], is known to affect the transition temperature of bulk perovskite ferroelectrics. More recently, homogeneous epitaxial strain associated with substrate–film lattice mismatch has been included in a Landau free energy [109]; this approach results in strain-induced shifts in the transition temperature and the spontaneous polarization whose signs depends on details of specific elastic compliances and electrostrictive constants. Furthermore, theoretical studies [109–113] of temperature–misfit strain phase diagrams indicate that there are observable "epitaxial phases" that would not be stable in the bulk. Indeed the effects of homogeneous misfit strain have been characterized and controlled to such a degree that $BaTiO_3$ films have been strain engineered so that their observed spontaneous polarization is more than twice that in the bulk [114]. Furthermore, room-temperature ferrolelectricity has been observed in strained $SrTiO_3$ films [33, 34], where we note that bulk $SrTiO_3$ remains paraelectric down to the lowest observable temperatures [115].

Let us be more specific. In the phenomenological treatment of epitaxially strained ferroelectric films grown on thick substrates [109, 110], the finite-size ferroelectric is approached as a bulk material with homogeneous elastic terms constrained to match the substrate lattice conditions. Here, it is implicit that

$$L \gg d_{\mathrm{c}} > d > \xi_0 \,, \tag{73}$$

where L and d are the substrate and the film thicknesses, respectively, ξ_0 is the correlation length and d_{c} is the critical film thickness above which elastic defects appear; d_{c} varies roughly as the inverse of the lattice mismatch and is usually approximately 10 nm [114]. With this set of modeling assumptions, the inplane strains, η_1, η_2 and η_6 (here we follow the conventional Voigt notation) are constant throughout the film thickness and are completely controlled by the substrate–film lattice mismatch. The associated stresses σ_1, σ_2 and σ_6 are finite but not fixed. By contrast,

$$\sigma_3 = \sigma_4 = \sigma_5 = 0 \,, \tag{74}$$

since there are no tractions acting on the top film surface. For the special case of a (001) ferroelectric film grown on a cubic paraelectric substrate

$$\eta_1 = \eta_2 = \bar{\eta} = \frac{a - a_0}{a}\,, \tag{75}$$

where a and a_0 are the constrained and the free-film lattice constants, respectively. For this simple case of cubic symmetry $\eta_6 = 0$ since the angle between the two lattice vectors remains unchanged ($\theta = \frac{\pi}{2}$). Equations (74) and (75) represent mixed mechanical boundary conditions associated with two-dimensional clamping, and the standard elastic free energy $\mathcal{F}(P, \sigma)$ cannot be used to find the equilibrium properties of these systems [39, 109]. Instead, a Legendre transformation to a modified thermodynamic potential

$$\tilde{\mathcal{F}} = \mathcal{F} + \eta_1\sigma_1 + \eta_2\sigma_2 + \eta_6\sigma_6 \tag{76}$$

must be performed in order to study the equilibrium properties of this constrained film.

For pedagogical simplicity, we consider a uniaxial ferroelectric, where P is the polarization in the z direction. The free energy, with condition (74), of a cubic ferroelectric is [116]

$$\mathcal{F} = \mathcal{F}_{\mathrm{P}} - \frac{1}{2}s_{11}(\sigma_1^2 + \sigma_2^2) - Q_{12}\left[(\sigma_1 + \sigma_2)P^2\right] - s_{12}\sigma_1\sigma_2 - \frac{1}{2}s_{44}\sigma_6^2\,, \tag{77}$$

where Q_{ij} and s_{ij} are the electrostrictive constants and the elastic compliances at constant polarization, respectively. Using $\frac{\partial \mathcal{F}}{\partial \sigma_i} = -\eta_i$, and solving for $\sigma_1 = \sigma_2 = \bar{\sigma}$ (in this special case $\sigma_6 = 0$), we find that

$$\tilde{\mathcal{F}} = \frac{\bar{\eta}^2}{s_{11} + s_{12}} + \frac{1}{2}\tilde{a}P^2 + \frac{1}{4}\tilde{b}P^4 + \frac{1}{6}cP^6\,, \tag{78}$$

where

$$\tilde{a} = a - \frac{4\bar{\eta}Q_{12}}{s_{11} + s_{12}} \tag{79}$$

and

$$\tilde{b} = b + \frac{4Q_{12}^2}{s_{11} + s_{12}}\,, \tag{80}$$

so that the coefficients of both the quadratic and the quartic polarization terms in the Landau free energy are renormalized. This has important implications for the thermodynamic properties of the thin film; more specifically it means that its transition temperature is shifted from the bulk value (T_0)

$$T^* = T_0 + \frac{4\bar{\eta}Q_{12}}{a(s_{11} + s_{12})} \tag{81}$$

as is its spontaneous polarization (please see the discussion preceding (10)) due to the inplane straining of the film by the compressive substrate. The signs of these shifts will be determined by the relative signs and magnitudes of Q_{12}, s_{11} and s_{12}. We note that such misfit epitaxial strain can change the nature of the transition from first to second order ($b < 0$ but $\tilde{b} > 0$). For ferroelectric films with multicomponent polarization and with different orientations, this approach yields a temperature–strain phase diagram with equilibrium phases that are not stable in a mechanically free bulk sample [109–113, 117]. The resulting low-temperature phase diagrams are very sensitive to the Landau coefficients, particularly for increasing misfit strain; here, the phenomenological approach is nicely complemented by first-principles studies that can resolve uncertainties associated with these input parameters [112, 113]. This combined phenomenological–first-principles approach has been very successful in explaining the phase behavior of epitaxially strained films and we refer the interested reader to a sample of recent experimental papers in this field [114, 118–121]. For ultrathin ferroelectric films with biaxial compressive strain at the substrate interface, the competition between elastic and surface effects has also been considered [122]. In particular, we note that if we do include a gradient (Ginzburg) term to the free energy then the epitaxial strain leads to a modified correlation length

$$\tilde{\xi} = \sqrt{\frac{\gamma}{\tilde{a}}}\,, \tag{82}$$

where $\xi = \sqrt{\frac{\gamma}{a}}$ is that associated with the bulk material that is mechanically free [122]. Similar mechanical boundary conditions have also been studied in epitaxially strained superlattices [123–125]. We note that recently a combined numerical–thermodynamic approach resulted in generalized temperature–strain phase diagrams for thin ferroelectric films that include multidomain phases [126] inaccessible by the approaches described here that assume homogeneous polarization.

4.5 Inhomogeneous Effects

In the previous discussion, we assume that the energy cost of uniformly straining the film to lattice match the substrate is significantly less than that associated with other strain-relaxation mechanisms; these include the creation of elastic dislocations, polydomain formation and even multiphase coexistence, which are all inhomogeneous in nature. We expect elastic homogeneity for films thinner than a critical thickess ($d < d_c$), where d_c scales (roughly) inversely with the lattice mismatch [114]. Typically, such coherent epitaxially strained films have thicknesses $d \approx 10\,\text{nm}$, though film-growth parameters can be tuned to achieve $d \approx 50\,\text{nm}$ by kinetically suppressing other elastic relaxation processes [114]. However, the physics of thicker ferroelectric films,

particularly those used in current applications ($d \approx 120\,\mathrm{nm}$) [71], does include inhomogeneous effects and next we review aspects of this topic within a phenomenological framework.

The misfit epitaxial strain decreases roughly exponentially [127–129] with distance ($\eta(z) \sim \eta_0 \mathrm{e}^{-\frac{1}{\lambda}}$) from the film/substrate interface with a "strain depth" of approximately $\lambda \approx 300\,\mathrm{nm}$ and thus is negligible for $d \gg \lambda$. In films of thickness $d_\mathrm{c} < d < \lambda$, elastic defects often form to accomodate film–substrate lattice mismatch. While permitting the film's lattice constants to relax, these defects generate inhomogenous strains that couple to the film's polarization and therefore affect its ferroelectric properties. We note that compositional and thermal gradients can also produce such inhomogeneities [130]. Here, we will focus on such elastic effects. Indeed the epitaxial phenomenological treatment can be generalized to include isotropic inhomogenous strain due to such lattice defects [131]; this results in further contributions to the coefficients of both P^2 and P^4 in the free energy, and thus to a defect-induced change in the transition temperature qualitatively consistent with experiment [131].

The broadening of the dielectric peak in ferroelectric films with decreasing thickness has been observed by several groups [129, 132–134]. In bulk systems, such behavior is often attributed to disorder and/or low-dimensional effects [135] but these explanations are not appropriate for ferroelectric films due to the underlying long-range interactions. Indeed we expect these dipolar systems to be more sensitive to electromechanical boundary conditions than to local fluctuations. This qualitative idea has been confirmed by measurements on ferroelectric free-standing lamellae of sharp dielectric peaks, strongly indicating that it is due to substrate-related effects most probably associated with interfacial lattice mismatch [136].

Recent experiments on the flexoelectric coupling between strain gradients and the polarization indicate that these effects could be important in thin films [137–141]. Theoretically, it has been shown that this flexoelectric effect is enhanced in high-permittivity materials such as ferroelectrics [142, 143] where the coupling is maximized near the dielectric peak. This flexoelectric coupling has been incorporated into a Landau–Ginzburg framework with the goal of studying its effect on the thermodynamic properties of epitaxially strained ferroelectric films [144, 145]. The strain-gradient contribution $\Delta_\mathrm{FC} = \gamma \frac{\mathrm{d}\,\eta(z)}{\mathrm{d}\,z}$, couples to the polarization in the free energy, acting as an effective field, so that the equation for the spontaneous polarization

$$\tilde{a}P + \tilde{b}P^3 = \Delta_\mathrm{FC}|_{P=P_0} \tag{83}$$

can only have finite solutions, even in the absence of an external electric field ($E = 0$); here, $\tilde{a}$ and $\tilde{b}$ are the Landau coefficients that have been renormalized by epitaxial strain. As a result, the inverse dielectric susceptibility

$$\chi^{-1} = 3\tilde{b}P_0^2 + \tilde{a} \tag{84}$$

can never be zero, so the standard singularity in χ is replaced by a broadened peak. Similarly, the temperature scale associated with the onset of reversible polarization is distinct from that of the maximum of χ. This approach also yields a polarization that increases with decreasing film thickness despite the associated reduction and broadening of the dielectric peak; these seemingly contradictory features are consistent with known experiments [144, 145].

We have just seen that the presence of strain gradients via the flexoelectric effect leads to the broadening of the dielectric peak in ferroelectric films. This phenomena can be generalized to consider other effective fields that couple linearly to the polarization [146]; possible origins of this effective field include asymmetric electrodes, compositional and temperature gradients as well as the stress profiles already considered. Qualitatively the effects on the dielectric response will be the same, though naturally quantitative differences will depend on the physical origin of the effective field.

Inhomogeneities, particularly strain and temperature gradients, can also lead to multidomain formation [147,148] as an overall energy-reduction mechanism; this behavior has been observed in relatively thick ($d \approx 500\,\mathrm{nm}$) films [149]. The competition between different strain-relaxation processes including domain formation and misfit dislocations has been studied theoretically [150, 151]. Within the framework of a Landau–Ginzburg theory, the development of domain structure has been addressed [106, 147, 148, 152]; qualitatively this is done by seeking polarization solutions of the form

$$P = P_0 + \delta P_k(z)\mathrm{e}^{\mathrm{i}kx}\,, \tag{85}$$

where $\delta P_k(z) \ll P_0$. Such a treatment in nearly cubic ferroelectrics indicates that a multidomain state may well be stable down to atomic film thicknesses, length scales well below the previous estimates that only described single-domain ferroelectricity [106]. The time evolution of the polarization and therefore the resulting domain structures can also be obtained by numerical studies of the time-dependent Landau–Ginzburg equations [153]; such phase-field studies predict specific domain morphologies [35–37, 154, 155] for epitaxial thin films of a variety of materials including $PbZr_{1-x}Ti_xO_3$, $SrTiO_3$ and $BaTiO_3$. We note that inhomogeneities in multicomponent ferroelectrics may also lead to multiphase coexistence [36, 151, 156, 157], particularly in the region of a first-order phase transition.

5 Summary and (Some) Open Questions

At this point we have discussed the main features associated with ferroelectrics that have been addressed within a phenomenological Landau–Ginzburg theory. Due to their underlying long-range interactions, we have learned that bulk ferroelectrics are well described within this framework; for the same reason, their finite-size counterparts are very sensitive to electromechanical boundary conditions including surface charge and misfit epitaxial

strain. Inhomogeneous effects, particularly strain gradients, have also been discussed. We have now worked our way to the present and naturally there remain a number of challenges that can be addressed within this framework. Let us discuss a few of these:

(i) Strain gradients and finite-size effects in novel nanogeometries
Three-dimensional ferroelectric nanogeometries are being explored as key components in competitive high-density data-storage devices [158]. The complexity of their topologies and their boundary conditions tends to favor inhomogenous polarization and strain configurations (e.g., [159–161]) that remain largely unstudied, particularly from a phenomenological standpoint. For example, the energetics associated with the formation of misfit dislocations in ferroelectrics with curved topologies is known to be different from those in planar structures [162–164], and the associated strain gradients could lead to complex three-dimensional polarization patterns.

(ii) Multiferroics
There exist a number of materials that display both long-range ferroelectricity and incommensurate magnetic order [165] and we refer the interested reader to the chapter by *N. Spaldin* in this volume on this topic. Landau treatments [166–168] for this class of materials have provided symmetry-based arguments for the type of underlying interactions that must be present at the microscopic level; furthermore, the couplings between ferroelectric and magnetic order parameters can be studied in nanostructured electromagnets [169]. The detailed interplay between microscopic and phenomenological models should provide guidance on material parameters necessary to enhance the magnetoelectric couplings, particularly at room temperature for device applications.

(iii) Dynamics
The dynamical dielectric response of ferroelectrics should be accessible via time-dependent Landau–Ginzburg theory, similar to studies performed with this method in ferroelastics [42]. More generally, a detailed phenomenological study of domain nucleation [170], domain motion (and domain interlocking [171]) could be particularly useful for the characterization of switching properties of thin films [172]. Also, glassy behavior has been observed in a number of ferroelectric relaxor materials [173,174], and a phenomenological model of these relaxational dynamics should be feasible.

(iv) Possible breakdown of Landau–Ginzburg theory
Landau–Ginzburg theory may well break down in ultrasmall ferroelectric structures where the necessary averaging of the order parameter (i.e., the polarization) is no longer possible. Also, it remains a challenge to see how this highly local approach can be used to describe nonlocal elastic and Coulomb effects, particularly vis a vis domain formation and energetics.

(v) Quantum critical fluctuations

The paralelectric–ferroelectric transition in the limit $T \to 0$ may well be a textbook candidate [175–178] for quantum critical behavior [179]. Although some theoretical predictions [180] exist, logarithmic corrections to mean-field (Landau) scaling should be both theoretically and experimentally accessible and have yet to be explored. As in the classical case [20–23], ferroelectric materials may well provide the setting for the first detailed study of criticality at a quantum phase transition.

These are only some of the many outstanding challenges that the Landau–Ginzburg theory of ferroelectrics still has to address. Most generally, it can provide a solid bridge between the physics on atomistic scales and macroscopic measurable quantities, particularly in finite-size ferroelectrics where electromechanical boundary conditions are crucial and therefore the physics spans many length scales. In closing, we invite the (hopefully still) curious reader to partake in these and other adventures with this phenomenological approach to ferroelectric materials.

Acknowledgements

We are grateful to M. Dawber, C. Fennie, L. Palova, K. M. Rabe and J. F. Scott for their careful readings of this text, and more generally for numerous discussions about the topics therein. We would also like to thank O. Dieguez and P. Coleman for clarifying aspects of misfit epitaxial strain and surface superconductivity, respectively, for us. Premi Chandra acknowleges support from NSF NIRT DMR-0210575 and the Aspen Center for Physics for hospitality. Peter B. Littlewood acknowledges support from the Engineering and Physical Sciences Research Council, and the hospitality of the National High Magnetic Field Laboratory.

References

[1] L. D. Landau, E. M. Lifshitz: *Statistical Physics* (Pergamon, Oxford 1959) 69, 74, 84
[2] J.-C. Toledano, P. Toledano: *Landau Theory of Phase Transitions* (World Scientific, Singapore 1987) 69, 84
[3] E. Fatuzzo, W. M. Mertz: *Ferroelectricity* (North-Holland, Amsterdam 1967) 69, 75, 76, 78, 80, 91
[4] M. E. Lines, A. M. Glass: *Principles and Applications of Ferroelectrics and Related Materials* (Oxford University Press, Oxford 1977) 69, 72, 75, 76, 78, 85, 91
[5] F. Jona, G. Shirane: *Ferroelectric Crystals* (Dover, New York 1993) 69, 91
[6] B. A. Strukov, A. P. Levanyuk: *Ferroelectric Phenomena in Crystals* (Springer, Berlin 1998) 69
[7] J. F. Scott: *Ferroelectric Memories*, vol. 3, Springer Ser. Adv. Microelectron. (Springer, Berlin 2000) 69, 72, 92, 93

[8] L. D. Landau: Phys. Z. Sowjun. **11**, 545 (1937) 70, 74, 106
[9] L. D. Landau: Zh. Eksp. Teor. Fiz. **7**, 627 (1937) 70, 74, 106
[10] D. ter Haar (Ed.): *Collected Papers of L. D. Landau* (Pergamon, Oxford 1965) contains Engl. transl. of [8] and [9] 70, 74
[11] H. Mueller: Properties of Rochelle salt, Phys. Rev. **57**, 829 (1940) 70
[12] H. Mueller: Properties of Rochelle salt II, Phys. Rev. **58**, 565 (1940) 70
[13] H. Mueller: Properties of Rochelle salt III, Phys. Rev. **58**, 805 (1940) 70
[14] A. F. Devonshire: Philos. Mag. **40**, 1040 (1949) 70, 74
[15] A. F. Devonshire: Philos. Mag. **42**, 1065 (1951) 70, 74
[16] A. F. Devonshire: Adv. Phys. **3**, 85 (1954) 70, 74
[17] A. P. Levanyuk: Sov. Phys. JETP **36**, 571 (1959) 71, 86, 87, 88
[18] V. L. Ginzburg: Fiz. Tverd. Tela **2**, 2031 (1960) 71, 86, 87, 88, 107
[19] V. L. Ginzburg: Sov. Phys. – Solid State **2**, 1824 (1960) engl. transl. of [18] 71, 86, 87, 88
[20] A. I. Larkin, D. E. Khmel'nitskii: Zh. Eksp. Teor. Fiz. **55**, 2345 (1968) 71, 88, 106, 107
[21] A. I. Larkin, D. E. Khmel'nitskii: Zh. Eksp. Teor. Fiz. **56**, 2087 (1969) 71, 88, 106, 107
[22] A. I. Larkin, D. E. Khmel'nitskii: Sov. Phys. JETP **28**, 1245 (1969) english translations of [20] and [21] 71, 88, 106
[23] A. I. Larkin, D. E. Khmel'nitskii: Sov. Phys. JETP **29**, 1123 (1969) english translations of [20] and [21] 71, 88, 106
[24] G. Ahlers, A. Kornbilt, H. J. Guggenheim: Logarithmic corrections to the Landau specific heat near the Curie temperature of the dipolar Ising ferromagnet $LiTbF_4$, Phys. Rev. Lett. **34**, 1227 (1975) 71
[25] M. Born, K. Huang: *Dynamical Theory of Crystal Lattices* (Clarendon Press, Oxford 1954) 72, 89
[26] I. P. Batra, B. D. Silverman: Thermodynamic stability of thin ferroelectric films, Solid State Commun. **11**, 291 (1972) 72, 96, 99
[27] R. Mehta, B. Silverman, J. T. Jacobs: Depolarization fields in thin ferroelectric films, J. Appl. Phys. **44**, 3379 (1973) 72, 96, 99
[28] P. Wurfel, I. P. Batra: Depolarization-field-induced instability in thin ferroelectric films–experiment and theory, Phys. Rev. B **8**, 5126 (1973) 72, 96
[29] P. Ghosez, K. M. Rabe: Microscopic model of ferroelectricity in stress-free $PbTiO_3$ ultrathin films, Appl. Phys. Lett. **76**, 2767 (2000) 72, 99
[30] J. Junquera, P. Ghosez: Critical thickness for ferroelectricity in perovskite ultrathin films, Nature **422**, 506 (2003) 72, 99
[31] M. Dawber, P. Chandra, P. B. Littlewood, J. F. Scott: Depolarization corrections to the coercive field in thin-film ferroelectrics, J. Phys. Condens. Mat. **15**, L393 (2003) 72, 96, 98, 99
[32] D. R. Tilley, B. Zeks: Landau theory of phase transitions in thick films, Solid State Commun. **49**, 823 (1984) 73, 95
[33] J. H. Haeni, P. Irvin, W. Chang, R. Uecker, P. Reiche, Y. L. Li, S. Choudhury, W. Tian, M. E. Hawley, B. Craigo, A. K. Tagantsev, X. Q. Pan, S. K. Streiffer, L. Q. Chen, S. W. Kirchoefer, J. Levy, D. G. Schlom: Room-temperature ferroelectricity in strained $SrTiO_3$, Science **430**, 758 (2004) 73, 100

[34] Y. L. Li, S. Choudhury, J. H. Haeni, M. D. Biegalski, A. Vasudevarao, A. Sharan, H. Z. Ma, J. Levy, V. Gopalan, S. Trolier-McKinstry, D. G. Schlom, Q. X. Jia, L. Q. Chen: Phase transition and domain structures in strained pseudocubic (100) $SrTiO_3$ thin films, Phys. Rev. B **73**, 184112 (2006) 73, 100
[35] Y. L. Li, et al.: A phenomenological thermodynamic potential for $BaTiO_3$ single crystals, J. Appl. Phys. **98**, 064101 (2005) 73, 104
[36] Y. L. Li, L. Q. Chen: Temperature-strain phase diagram for $BaTiO_3$ thin films, Appl. Phys. Lett. **88**, 072905 (2006) 73, 104
[37] Y. Li, S. Y. Hu, L. Q. Chen: Ferroelectric domain morphologies of (001) $PbZr_{1-x}Ti_xO_3$ epitaxial thin films, J. Appl. Phys. **97**, 034112 (2005) 73, 104
[38] W. Merz: The effect of hydrostatic pressure on the Curie point of barium titanate single crystals, Phys. Rev. B **77**, 52 (1950) 80, 100
[39] P. W. Forsbergh: Effect of a two-dimensional pressure on the Curie point of barium titanate, Phys. Rev. B **93**, 686 (1954) 80, 100, 101
[40] E. A. H. Love: *A Treatise on the Mathematical Theory of Elasticity* (Dover, New York 1944) p. 49 83
[41] S. Kartha, J. A. Krumhansl, J. P. Sethna, L. K. Wickham: Disorder-driven pretransitional tweed pattern in martensitic transformations, Phys. Rev. B **52**, 803 (1995) 83
[42] S. R. Shenoy, T. Lookman, A. Saxena, A. R. Bishop: Martensitic textures: Multiscale consequences of elastic compatibility, Phys. Rev. B **60**, R12537 (1999) 83, 105
[43] T. Lookman, A. Saxena, D. A. Dimitrov, A. R. Bishop, R. C. Albers: Signatures of long-range elastic interaction in textured materials, Phys. Rev. B **87**, 55704 (2001) 83
[44] T. Lookman, S. R. Shenoy, K. O. Rasmussen, A. Saxena, A. R. Bishop: Ferroelastic dynamics and strain compatibility, Phys. Rev. B **67**, 24114 (2003) 83
[45] Y. Fujii, Y. Yamada: X-ray critical scattering in ferroelectric tri-glycine sulphate, J. Phys. Soc. Jpn. **30**, 1676 (1971) 85
[46] J. Als-Nielsen, R. Birgeneau: Mean field theory, the Ginzburg criterion and marginal dimensionality of phase transitions, Am. J. Phys. **45**, 554 (1977) 87
[47] R. M. White, T. H. Geballe: *Long-Range Order in Solids* (Academic Press, New York 1979) 89
[48] W. Cochran: Adv. Phys. **9**, 387 (1960) 89
[49] R. A. Cowley: Temperature dependence of a transverse optic mode in strontium titanate, Phys. Rev. Lett. **9**, 159 (1962) 89
[50] A. D. Bruce, R. A. Cowley: *Structural Phase Transitions* (Taylor and Francis, London 1981) 89
[51] E. Burstein, A. Pinczuk, R. F. Wallace: in D. L. Carter, R. T. Bate (Eds.): *Proceedings of the Conference on the Physics of Metals and Narrow Gap Semiconductors* (Pergamon, New York 1970) pp. 251–272 90
[52] P. B. Littlewood, V. Heine: The infrared effective charge in IV-VI compounds. I. A simple one-dimensional model, J. Phys. C: Solid State Phys. **12**, 4431 (1979) 90
[53] P. B. Littlewood: The infrared effective charge in IV-VI compounds. II. A three-dimensional calculation, J. Phys. C: Solid State Phys. **12**, 4441 (1979) 90

[54] T. Portengen, T. Ostreich, L. J. Sham: Linear and nonlinear optical characteristics of the Falicov–Kimball model, Phys. Rev. Lett. **76**, 3384 (1996) 90
[55] T. Portengen, T. Ostreich, L. J. Sham: Theory of electronic ferroelectricity, Phys. Rev. B **54**, 17452 (1996) 90
[56] C. D. Batista, A. A. Aligia: Exact bond ordered ground state for the transition between the band and the mott insulator, Phys. Rev. Lett. **92**, 246405 (2004) 90
[57] C. D. Batista, A. A. Aligia: Dimerized phase of ionic Hubbard models, Phys. Rev. B **71**, 125110 (2005) 90
[58] G. Gruner: *Density Waves in Solids* (Addison-Wesley, Reading 1994) 90
[59] J. Schrieffer: *Theory of Superconductivity* (Benjamin, Reading 1964) 90
[60] P. G. deGennes: *Superconductivity of Metals and Alloys* (Benjamin, New York 1966) 90, 94
[61] M. Tinkham: *Introduction to Superconductivity* (McGraw-Hill, New York 1975) 90
[62] W. L. McMillan: Microscopic model of charge-density waves in $2\,\mathrm{H}{-}\mathrm{TaSe}_2$, Phys. Rev. B **16**, 643 (1977) 91
[63] R. A. Cowley: Self-consistent phonon studies of a model diatomic ferroelectric, Physica A **232**, 585 (1996) 91
[64] D. V. Efremov, J. van den Brink, D. I. Khomskii: Bond- versus site-centred ordering and possible ferroelectricity in manganites, Nature Mater. **3**, 853 (2004) 91
[65] D. Vanderbilt, M. H. Cohen: Monoclinic and triclinicphases in higher-order Devonshire theory, Phys. Rev. B **63**, 094108 (2001) 91
[66] B. Noheda, D. E. Cox, G. Shirane, J. A. Gonzalo, L. E. Cross, S.-E. Park: A monoclinic ferroelectric phase in the $\mathrm{Pb}(\mathrm{Zr}_{1-x}\mathrm{Ti}_x)\mathrm{O}_3$ solid solution, Appl. Phys. Lett. **74**, 2059 (1999) 91
[67] M. J. Haun, E. Furman, S. J. Jang, H. A. McKinstry, L. E. Cross: Thermodynamic theory of PbTiO_3, Ferroelectrics **99**, 13 (1989) 91
[68] L. Bellaiche, A. Garcia, D. Vanderbilt: Finite-temperature properties of $\mathrm{Pb}(\mathrm{Zr}_{1-x}\mathrm{Ti}_x)\mathrm{O}_3$ alloys from first principles, Phys. Rev. B **84**, 5437 (2000) 91
[69] W. Zhong, D. Vanderbilt, K. M. Rabe: First-principles theory of ferroelectric phase transitions for perovskites: The case of BaTiO_3, Phys. Rev. B **52**, 6301 (1995) 91
[70] C. H. Ahn, K. M. Rabe, J.-M. Triscone: Ferroelectricity at the nanoscale: Local polarization in oxide thin films and heterostructures, Science **303**, 488 (2004) 92
[71] M. Dawber, K. M. Rabe, J. F. Scott: Physics of thin-film ferroelectric oxides, Rev. Mod. Phys. **77**, 1083 (2005) 92, 103
[72] W. Zhong, D. Vanderbilt, K. M. Rabe: Phase transitions in BaTiO_3 from first principles, Phys. Rev. Lett. **73**, 1861 (1994) 92
[73] W. Zhong, D. Vanderbilt, K. M. Rabe: First-principles theory of ferroelectric phase transitions for perovskites: The case of BaTiO_3, Phys. Rev. B **52**, 6301 (1995) 92
[74] J. Iniguez, S. Ivantchev, J. M. Perez-Mato, A. Garcia: Landau free energy of BaTiO_3 from first principles, Phys. Rev. B **63**, 144103 (2001) 92

[75] J. S. Langer: Statistical theory of the decay of metastable states, Ann. Phys. (NY) **54**, 258 (1969) 92
[76] D. B. McWhan, et al.: J. Phys. C **18**, L307 (1985) 92
[77] D. A. Neumann, D. B. McWhan, P. Littlewood, G. Aeppli, J. P. Remeika, R. G. Maines: Nucleation near the tricritical point of $BaTiO_3$, Phys. Rev. B **32**, 1866 (1985) 92
[78] P. B. Littlewood, P. Chandra: Delayed nucleation at a weakly first-order transition, Phys. Rev. Lett. **57**, 2415 (1986) 92
[79] P. Chandra: Nucleation in the presence of long-range interactions, Phys. Rev. A **39**, 3672 (1989) 92
[80] V. L. Ginzburg: Phase transitions in ferroelectrics: Some historical remarks, Phys.-Usp. **44**, 1037 (2001) 92
[81] S. Li, J. A. Eastman, Z. Li, C. M. Foster, R. E. Newnham, L. E. Cross: Size effects in nanostructured ferroelectrics, Phys. Lett. **212**, 341 (1996) 92
[82] S. Li, J. A. Eastman, J. M. Vetrone, C. M. Foster, R. E. Newnham, L. E. Cross: Dimension and size effects in ferroelectrics, Jap. J. Appl. Phys. **36**, 5169 (1997) 92
[83] O. Auciello, J. F. Scott, R. Ramesh: The physics of ferrorelectric memories, Physics Today **51**, 22–27 (1998) 93
[84] R. Kretschmer, K. Binder: Surface effects on phase transitions in ferroelectrics and dipolar magnets, Phys. Rev. B **20**, 1065 (1979) 93, 94, 98, 99
[85] K. Binder: Ferroelectrics **35**, 99 (1981) 93, 94, 98, 99
[86] T. C. Lubensky, M. H. Rubin: Critical phenomena in semi-infinite systems. II. Mean-field theory, Phys. Rev. B **12**, 3885 (1975) 93
[87] L.-H. Ong, J. Osman, D. R. Tilley: Landau theory of second-order phase transitions in ferroelectric films, Phys. Rev. B **63**, 144109 (2001) 93, 95
[88] J. F. Scott: Nanoferroelectrics: statics and dynamics, J. Phys. Condens. Mat. **18**, R361 (2006) 93
[89] M. I. Kaganov, A. N. Omelyandchouk: Zh. Eksp. Teor. Fiz. **61**, 1679 (1971) 94
[90] M. I. Kaganov, A. N. Omelyandchouk: Sov. Phys. JETP **34**, 895 (1972) 94
[91] K. Binder, P. C. Hohenberg: Phase transitions and static spin correlations in Ising models with free surfaces, Phys. Rev. B **6**, 3461 (1979) 94
[92] D. R. Tilley: Finite-size effects on phase transitions in ferroelectrics, in C. P. de Araujo, J. F. Scott, G. W. Taylor (Eds.): *Ferroelectric Thin Films: Synthesis and Basic Properties* (Gordon and Breach, Amsterdam 1996) pp. 11–46 95, 99
[93] J. F. Scott, H. M. Duiker, P. D. Beale, B. Pouligny, K. Dimmler, M. Parris, D. Butler, S. Eaton: Properties of ceramic KNO_3 thin-film memories, Physica B **150**, 160 (1988) 95
[94] D. R. Tilley: Landau theory for coupled ferromagnetic and ferroelectric films and superlattices, Solid State Commun. **65**, 657 (1988) 95
[95] K. Ishikawa, T. Uemori: Surface relaxation in ferroelectric perovskites, Phys. Rev B **60**, 11841 (1999) 96
[96] C. Basceri, S. K. Streiffer, A. I. Kingon, R. Waser: The dielectric response as a function of temperature and film thickness of fiber-textured $(Ba_Sr)TiO_3$ thin films grown by chemical vapor deposition, J. Appl. Phys. **82**, 2497 (1997) 96

[97] T. Li, W. Cao: Generalized continuum theory for ferroelectric thin films, Phys. Rev. B **66**, 24102 (2002) 96
[98] D. L. Tilley: Phase transitions in thin films, in N. Setter, E. L. Colla (Eds.): *Ferroelectric Ceramics* (Birkhauser Verlag, Basel 1993) pp. 163–184 96, 98
[99] C. Kittel: *Introduction to Solid State Physics* (J. Wiley and Sons, New York 1976) 98
[100] N. W. Ashcroft, N. D. Mermin: *Solid State Physics* (Holt, Rinehart and Winston, New York 1976) 98
[101] A. M. Bratkovsky, A. P. Levanyuk: Very large dielectric response of thin ferroelectric films with the dead layers, Phys. Rev. B. **63**, 132103 (2001) 99
[102] D. L. Tilley: Phase transitions in ferroelectric films, Ferroelectrics **134**, 313 (1992) 99
[103] D. D. Fong, G. B. Stephenson, S. K. Streiffer, J. A. Eastman, O. Auciello, P. H. Fuoss, C. Thompson: Ferroelectricity in ultrathin perovskite flims, Science **304**, 1650 (2004) 99
[104] D. D. Fong, C. Cionca, Y. Yacoby, G. B. Stephenson, J. A. Eastman, P. H. Fuoss, S. K. Streiffer, C. Thompson, R. Clarke, R. Pindak, E. A. Stern: Direct structural determination in ultrathin ferroelctric films by analysis of synchotron x-ray scattering measurements, Phys. Rev. B **71**, 144112 (2005) 99
[105] Y. S. Kim, D. H. Kim, J. D. Kim, Y. J. Chang, T. W. Noh, J. H. Kong, K. Char, Y. D. Park, S. D. Bu, J.-S. Chung: Critical thickness of ultrathin ferroelectric $BaTiO_3$ films, Appl. Phys. Lett. **86**, 102907 (2005) 99
[106] A. M. Bratkovsky, A. P. Levanyuk: Phase transitions and ferroelectricity in very thin films: Single- versus multidomain states, Integ. Ferroel. **84**, 3 (2006) 99, 104
[107] Y. Watanabe: Theoretical stability of the polarization in a thin semiconducting ferroelectric, Phys. Rev. B **57**, 789 (1998) 99
[108] Z. Ma, F. Zavaliche, L. Chen, J. Ouyang, J. Melnquailis, A. L. Royburd, V. Vaithyananthan, D. G. Schlom, T. Zhao, R. Ramesh: Effect of 90^0 domain movement on the piezoelectric response of patterned $PbZr_{0.2}Ti_{0.8}/SrTiO_3/Si$ heterostructures, Appl. Phys. Lett. **87**, 72907 (2005) 100
[109] N. A. Pertsev, A. G. Zembilgotov, A. K. Tagantsev: Effect of mechanical boundary conditions on phase diagrams of epitaxial ferroelectric thin films, Phys. Rev. Lett. **80**, 1988 (1998) 100, 101, 102
[110] N. A. Pertsev, A. G. Zembilgotov, A. K. Tagantsev: Equilibrium states and phase transitions in epitaxial ferroelectric thin films, Ferroelectrics **223**, 79 (1999) 100, 102
[111] Z.-G. Ban, S. P. Alpay: Phase diagrams and dielectric response of epitaxial barium strontium titanate films: A theoretical analysis, J. Appl. Phys. **91**, 9288 (2002) 100, 102
[112] O. Dieguez, S. Tinte, A. Antons, C. Bungaro, J. B. Neaton, K. M. Rabe, D. Vanderbilt: Ab initio study of the phase diagram of epitaxial $BaTiO_3$, Phys. Rev. B **69**, 212101 (2004) 100, 102
[113] O. Dieguez, K. M. Rabe, D. Vanderbilt: First-principles study of epitaxial strain in perovskites, Phys. Rev. B **72**, 144101 (2005) 100, 102
[114] K. Choi, M. Biegalski, Y. L. Li, A. Sharan, J. Schubert, R. Uecker, P. Reiche, Y. B. Chen, X. Q. Pan, V. Gopalan, L.-Q. Chen, D. G. Schlom, C. B. Eom: Enhancement of ferroelectricity in strained $BaTiO_3$ thin films, Science **306**, 1005 (2004) 100, 102

[115] K. A. Muller, H. Burkard: $SrTiO_3$: An intrinsic quantum paraelectric below 4 K, Phys. Rev. B **19**, 3593 (1979) 100
[116] M. J. Haun, E. Furman, S. J. Jang, H. A. McKinstry, L. E. Cross: Thermodynamic theory of $PbTiO_3$, J. Appl. Phys. **62**, 3331 (1987) 101
[117] A. K. Tagantsev, N. A. Pertsev, P. Muralt, N. Setter: Strain-induced diffiuse dielectric anomaly and critical point in perovskite ferroelectric thin films, Phys. Rev. B **65**, 012104 (2002) 102
[118] X. M. Lu, X. Wu, L. Li, D. Qian, W. Li, Y. Ye, X. Wu, J. Zhu: Switching properties of Nd and La-doped $Bi_4Ti_3O_{12}$ thin films under applied stress, Phys. Rev. B **72**, 212103 (2005) 102
[119] A. K. Soh, Y. C. Song, Y. Ni: Phase field simulations of hysteresis and butterfly loops in ferroelectrics subjected to electro-mechanical coupled loading, J. Am. Ceram. Soc. **89**, 652 (2006) 102
[120] S. Rios, J. F. Scott, A. Lookman, J. McAneney, R. M. Bowman, J. M. Gregg: Phase transitions ni epitaxial $Ba_{0.5}Sr_{0.5}TiO_3$ thin films, J. Appl. Phys. **99**, 24107 (2006) 102
[121] S. K. Choi, S. H. Ahn, W. W. Jung, J. C. Park, S. A. Song, C. B. Lim, Y. Cho: Observation of [110] surface band within 101-a-domain of heteroepitaxial $PbTiO_3$ thin film fabrication by hydrothermal epitaxy, Appl. Phys. Lett. **88**, 52901 (2006) 102
[122] A. G. Zembilgotov, N. A. Pertsev, H. Kohlstedt, R. Waser: Ultrathin epitaxial ferroelectric films grown on compressive substrates: Competation between the surface and the strain effects, J. Appl. Phys. **91**, 2247 (2002) 102
[123] J. B. Neaton, K. M. Rabe: Theory of polarization enhancement in epitaxial $BaTiO_3/SrTiO_3$ superlattices, Appl. Phys. Lett. **82**, 1586 (2003) 102
[124] K. Johnston, et al.: Phys. Rev. B **71**, 100103 (2005) 102
[125] S. M. Nakhmanson, K. M. Rabe, D. Vanderbilt: Polarization enhancement in two- and three-component ferroelectric superlattices, Appl. Phys. Lett. **87**, 102906 (2005) 102
[126] Y. L. Li, S. Choudhury, Z. K. Liu, L. Q. Chen: Effect of external mechanical constraints on the phase diagram of epitaxial $PbZr_{1-x}Ti_xO_3$ thin films–thermodynamic calculations and phase-field simulations, Appl. Phys. Lett. **83**, 1608 (2003) 102
[127] J. W. Matthews, A. E. Blackeslee: Defects in epitaxial multilayers. I. Misfit dislocations, J. Cryst. Growth **27**, 118 (1974) 103
[128] H. J. Kim, S. H. Oh, H. M. Jang: Thermodynamic theory of stree distribution in epitaxial $Pb(Zr,Ti)O_3$ thin films, Appl. Phys. Lett. **75**, 3195 (1999) 103
[129] L. J. Sinnamon, M. M. Saad, R. M. Bowman, J. J. Gregg: Exploring grain size as a cause for "dead-layer" effects in thin film capacitors, Appl. Phys. Lett. **81**, 703 (2002) 103
[130] Z. G. Ban, S. P. Alpay, J. V. Mantese: Fundamentals of graded ferroic materials and devices, Phys. Rev. B **67**, 184104 (2003) 103
[131] D. Balzar, P. A. Ramakrishnan, A. M. Hermann: Defect-related lattice strain and the transition temperature in ferroelectric thin films, Phys. Rev. B **70**, 92103 (2004) 103
[132] T. M. Shaw, Z. Suo, M. Huang, E. Liniger, R. B. Laibowitz, J. D. Baniecki: The effect on the dielectric properties of barium strontium titanatethin films, Appl. Phys. Lett. **75**, 2129 (1999) 103

[133] C. B. Parker, J.-P. Maria, A. I. Kingdon: Temperature and thickness dependent permittivity of (Ba,Sr)TiO_3 thin films, Appl. Phys. Lett. **81**, 340 (2002) 103
[134] A. Lookman, R. M. Bowman, J. M. Gregg, J. Kut, S. Rios, M. Dawber, A. Ruediger, J. F. Scott: Thickness independence of true phase transition temperatures in barium strontium titanate films, J. Appl. Phys. **96**, 555 (2004) 103
[135] J. Cardy: *Scaling and Renormalization in Statistical Physics* (Cambridge University Press, Cambridge 1996) 103
[136] M. M. Saad, P. Baxter, J. Gregg, F. D. Morrison, J. F. Scott: Intrinsic dielectric response in ferroelectric nano-capacitors, J. Phys. C **16**, L451 (2004) 103
[137] W. Ma, L. E. Cross: Appl. Phys. Lett. **79**, 4420 (2001) 103
[138] W. Ma, L. E. Cross: Strain-gradient-induced electric polarization in lead zirconate titanate cermaics, Appl. Phys. Lett. **81**, 3440 (2002) 103
[139] W. Ma, L. E. Cross: Appl. Phys. Lett. **82**, 3293 (2003) 103
[140] W. Ma, L. E. Cross: Appl. Phys. Lett. **86**, 72905 (2005) 103
[141] A. Gruverman, B. J. Rodriguez, A. I. Kingdon, R. J. Nemanich, A. K. Tagantsev, J. S. Cross, M. Tsukada: Mechanical stress effect on imprint behavior of integrated ferroelectric capacitors, Appl. Phys. Lett. **83**, 728 (2003) 103
[142] A. Tagantsev: Pizoelectricity and flexoelectricity in crystalline dielectrics, Phys. Rev. B **34**, 5883 (1986) 103
[143] A. Tagantsev: Phase Transitions **35**, 119 (1991) 103
[144] G. Catalan, L. J. Sinnamon, J. M. Gregg: The effect of flexoelectricity on the dielectric properties of inhomogeneously strained ferroelectric thin films, J. Phys. Condens. Mat. **16**, 2253 (2004) 103, 104
[145] G. Catalan, B. Noheda, J. McAneney, L. J. Sinnamon, J. M. Gregg: Strain gradients in epitaxial ferroelectrics, Phys. Rev. B **72**, 020102 (2005) 103, 104
[146] A. M. Bratkovsky, A. P. Levanyuk: Smearing of phase transition due to a surface effect or a bulk inhomogeneity in ferroelectric nanostructures, Phys. Rev. Lett. **94**, 107601 (2005) 104
[147] A. M. Bratkovsky, A. P. Levanyuk: Abrupt appearance of the domain pattern and fatigue of thin ferroelectric films, Phys. Rev. Lett. **1**, 43177 (2000) 104
[148] A. M. Bratkovsky, A. P. Levanyuk: Formation and rapid evolution of domain structure at phase transitions in slightly inhomogeneous ferroelectrics and ferroelastics, Phys. Rev B **66**, 184109 (2002) 104
[149] A. L. Roytburd, S. P. Alpay, L. A. Bendersky, V. Nagarajan, R. Ramesh: Three-domain architecture of stree-free epitaxial ferroelectric films, J. Appl. Phys. **89**, 553 (2001) 104
[150] J. S. Speck, W. Pompe: Domain configurations due to multiple misfit relaxation mechanisms in epitaxial ferroelectric thin films. I.Theory, J. Appl. Phys. **7**, 466 (1994) 104
[151] J. Slutsker, A. L. Roytburd: Deformation of polydomain crystals, Ferroelectrics **222**, 365 (1999) 104
[152] Y. G. Wang, W. I. Zhong, P. L. Zhang: Surface and size effects in ferroelectric films with domain structures, Phys. Rev. B **51**, 5311 (1995) 104
[153] L. Q. Chen, J. Shen: Applications of semi-implicit fourier-spectral method to phase field equations, Comput. Phys. Commun. **108**, 147 (1998) 104

[154] Y. L. Li, S. Choudhury, J. H. Haeni, M. D. Biegalski, A. Vasudevarao, A. Sharan, H. Z. Ma, J. Levy, V. Gopalan, S. Trolier-McKinstry, D. G. Schlom, Q. X. Jia, L. Q. Chen: Phase transition and domain structures in strained pseudocubic (100) $SrTiO_3$ thin films, Phys. Rev. B **73**, 184112 (2006) 104
[155] Y. Wang, Z.-K. Liu, L.-Q. Chen: Thermodynamic properties of Al, Ni, NiAl and Ni_3Al from first principles calculations, Acta Mater. **52**, 81 (2004) 104
[156] S. Semenovskaya, A. G. Khachaturyan: Coherent structural transformations in random crystalline systems, Acta Mater. **45**, 4367 (1997) 104
[157] A. Roytburd, J. Slutsker: Coherent phase equilibria in a bending film, Acta Mater. **50**, 1809 (2002) 104
[158] Y. Arimoto, H. Ishiwara: Current status of ferroelectric random-access memory, MRS Bull. **29**, 823 (2004) 105
[159] J. F. Scott: Ferroelectrics: Novel geometric ordering of ferroelectricity, Nature **4**, 13 (2005) 105
[160] H. X. Fu, L. Bellaiche: Ferroelectricity in barium titanate quantum dots and wires, Phys. Rev. Lett. **91**, 257601 (2003) 105
[161] I. I. Naumov, L. Bellaiche, H. Fu: Unusual phase transitions in ferroelectric nanodisks and nanorods, Nature **432**, 737 (2004) 105
[162] M. Y. Gutkin, I. A. Ovid'ko, A. G. Sheinerman: Misfit dislocations in wire composite solids, J. Phys. Condens. Mat. **12**, 5391 (2000) 105
[163] A. G. Sherman, M. Y. Gutkin: Misfit disclinations and dislocation walls in a two-phase cylindrical composite, Phys. Stat. Sol. **184**, 485 (2001) 105
[164] M. Y. Gutkin, I. A. Ovid'ko, A. G. Sheinerman: Misfit dislocations in composites with nanowires, J. Phys. Condens. Mat. **15**, 3539 (2003) 105
[165] D. I. Khomskii: Multiferroics: Different ways to combine magnetism and ferroelectricity, J. Mag. Magn. Mat. **306**, 1 (2006) 105
[166] G. Lawes, A. B. Harris, T. Kimura, N. Rogado, R. J. Cava, A. Aharony, O. Entin-Wohlman, T. Yildrim, M. Kenzelmann, C. Broholm, A. P. Ramirez: Magnetically driven ferroelectric order in $Ni_3V_2O_8$, Phys. Rev. Lett. **95**, 87205 (2005) 105
[167] A. B. Harris, G. Lawes: Ferroelectricity in incommensurate magnets, in H. Kronmüller, S. Parkin (Eds.): *Handbook of Magnetism and Advanced Magnetic Materials* (Wiley, New York 2006) 105
[168] M. Mostovoy: Ferroelectricity in spiral magnets, Phys. Rev. Lett. **96**, 67601 (2006) 105
[169] H. Zheng, J. Wang, S. E. Lofland, Z. Ma, L. Mohaddes-Ardabili, T. Zhao, L. Salamanca-Riba, S. R. Shinde, S. B. Ogale, F. Bai, D. Viehland, Y. Jia, D. G. Schlom, M. Wittig, A. Roytburd, R. Ramesh: Multiferroic $BaTiO_3-CoFe_2O_4$ nanostructures, Science **303**, 661 (2004) 105
[170] C. S. Ganpule, V. Nagarajan, S. B. Ogale, A. L. Roytburd, E. D. Williams, R. Ramesh: Domain nucleation and relaxation kinetics in ferroelectric thin films, Appl. Phys. Lett. **77**, 3275 (2000) 105
[171] A. Krishnan, M. M. W. Treacy, M. E. Bisher, P. Chandra, P. B. Littlewood: Efficient switching and domain interlocking observed in polyaxial ferroelectrics, Integr. Ferroelectrics **43**, 31 (2002) 105
[172] J. Fousek, L. E. Cross: Engineering multidomain ferroic samples, Ferroelectrics **252**, 171 (2001) 105

[173] E. V. Colla, L. K. Chao, M. B. Weissman, D. D. Viehland: Aging in a relaxor ferroelectric: Scaling and memory effects, Phys. Rev. Lett. **85**, 3033 (2000) 105
[174] E. V. Colla, L. K. Chao, M. B. Weissmann: Multiple aging mechanisms in relaxor ferroelectrics, Phys. Rev. B **63**, 134107 (2001) 105
[175] D. E. Grupp, A. M. Goldman: Giant piezoelectric effect in strontium titanate at cryogenic temperatures, Science **276**, 382 (1997) 106
[176] P. Coleman: Theory perspective: SCES 05 Vienna, Physica B **378-380**, 1160 (2006) 106
[177] S. E. Rowley, et al.: unpublished 106
[178] J. F. Scott, R. Pirc, A. Levstik, C. Filipic, R. Blinc: Resolving the quantum criticality paradox in O-18 isotopic $SrTiO_3$, J. Phys. Condens. Mat. **18**, L205 (2006) 106
[179] S. Sachdev: *Quantum Phase Transitions* (Cambridge University Press, Cambridge 1999) 106
[180] R. Roussev, A. J. Millis: Theory of the quantum paraelectric–ferroelectric transition, Phys. Rev. B **67**, 014105 (2003) 106
[181] V. L. Ginzburg: Zh. Eksp. Teor. Fiz. **15**, 739 (1945)
[182] V. L. Ginzburg: Zh. Eksp. Teor. Fiz. **19**, 36 (1949)
[183] K.-H. Chew, et al.: Integr. Ferroelectrics **23**, 161 (1999)
[184] D. Khmel'nitskii, J. F. Scott: private communication

Index

First-Principles Studies of Ferroelectric Oxides

Karin M. Rabe[1] and Philippe Ghosez[2]

[1] Department of Physics and Astronomy, Rutgers University,
136 Frelinghuysen Road, Piscataway, NJ 08854-8019, USA
rabe@physics.rutgers.edu
[2] Physique Théorique des Matériaux, Département de Physique,
Université de Liège,
Allée du 6 août, 17 (B5), Liège, B-4000, Belgium
philippe.ghosez@ulg.ac.be

Abstract. The application of first-principles methods to the study of ferroelectric oxides is reviewed. While the main focus is on the perovskites, particularly the most-studied compounds $BaTiO_3$, $PbTiO_3$, and $SrTiO_3$, other oxide families, including $LiNbO_3$, layered perovskites, nitrites and nitrates, and electronic and magnetic ferroelectrics, are included. Results are presented for crystal structure, polarization and dielectric and piezoelectric coefficients. The identification of lattice instabilities through the computation of phonon dispersion relations for a high-symmetry reference phase is presented. Results at nonzero temperature, obtained through effective Hamiltonian and interatomic potential approaches, are given. Calculations for solid solutions, defects, thin films, superlattices and nanostructures are described. Challenges and prospects for future research are identified.

1 Introduction

First-principles calculations of the structure and properties of materials have been shown to yield valuable information about the origin of their behavior at the atomic-scale level for a wide variety of systems. This is particularly true for ferroelectric oxides, whose structural and chemical complexity leads to competing interactions where accurate quantitative information is essential to understanding the behavior. In recent years, the increasing power of first-principles calculations and the increasing experimental control of synthesis and characterization at the atomic scale have led to a convergence of theory and experiment, opening up a meaningful dialogue that allows for the analysis and interpretation of experimental results and the prediction of new materials.

In a single chapter, it is impossible to provide a comprehensive review of all first-principles work on ferroelectric oxides. For fuller descriptions of earlier work and of specific areas, we refer the reader to previous reviews of the subject, including the short reviews of *Vanderbilt* [1], *Bellaiche* [2], *Resta* [3] and *Cohen* [4], and recent topical reviews [5–10]. Longer reviews include one of first-principles investigations of the dielectric properties of oxides [11], one of first-principles studies of relaxor ferroelectics [12] and two on thin-film and nanoscale ferroelectric oxide structures [13, 14]).

K. Rabe, C. H. Ahn, J.-M. Triscone (Eds.): Physics of Ferroelectrics: A Modern Perspective,
Topics Appl. Physics **105**, 117–174 (2007)

In this chapter, we review the literature to show how first-principles calculations have contributed to our understanding of ferroelectrics and advanced research in the field. Our goal is both to highlight important results for researchers in the field of first-principles analysis, and to provide others with a useful guide for understanding and using these results in the study of the physics of ferroelectrics. We begin with an outline of the first-principles methods most commonly applied to ferroelectric oxides; for details of the methods, we refer readers to the original papers. This is followed by a presentation of results for perovskite oxide ferroelectric compounds, for which first-principles analysis has been most fully developed. Next, we review first-principles results for other families of oxide ferroelectrics. The technically challenging study of solid solutions is presented in Sect. 5. Finally, we identify some of the key future directions for first-principles investigations.

2 First-Principles Methods

In this section, we give an overview of the methods for first-principles calculations of the ground-state structural energetics and polarization of ferroelectric crystals at $T = 0$. We include discussion of density-functional theory (DFT), Hartree–Fock (HF), and methods for more accurate treatment of correlation, such as dynamical mean-field theory. For general aspects of the methods, we refer to appropriate review articles and books (for DFT, see [3] and the text by *Martin* [15]; for Hartree–Fock, see [16]; for an application of dynamical mean-field theory see [17]). The following should be consulted for details of the various first-principles implementations: ABINIT [18], VASP [19], PWscf [20], SIESTA [21], WIEN2k [22] and CRYSTAL [23]. Here, we will include only discussion of particular points relevant to ferroelectric oxides and the results reported later in the chapter.

For ground-state crystal-structure prediction, there is a well-established procedure [24] based on the Born–Oppenheimer approximation. A starting structure is chosen, establishing the lattice and space group. The computed atomic forces [25, 26] and stress tensor [27] are used to move the atoms and adjust the lattice parameters until the minimum-energy structure of this type has been identified. Comparison with other choices of lattice and space group then are used to identify the lowest-energy structure of all those considered.

This approach to crystal-structure prediction has been extensively applied to ferroelectric oxides since the early 1990s. Early work by *Cohen* and *Krakauer* [28, 29] on $BaTiO_3$ and $PbTiO_3$ using the linearized augmented-plane-wave (LAPW) method showed that first-principles density-functional methods could predict the ground-state structures of these prototypical compounds with meaningful accuracy. The pseudopotential method was shown to be capable of giving comparable results (see Table 1) as long as the atomic pseudopotential includes high-lying "semicore" states in the valence band [30–33]. A k-point sampling relatively dense for an insulator, with

Table 1. Theoretical lattice constant a_0 (in Å) of the cubic perovskite structure of $BaTiO_3$, and its deviation (in %) from the experimental value of 4.00 Å using different first-principles approaches (DFT, HF or hybrid) with various approximations (LDA, GGA, WDA, and B3LYP) and implementation schemes (full potential (FP) versus pseudopotential (PP), combined with various basis functions such as plane waves (PW), linear augmented plane waves (LAPW), numerical atomic orbitals (NAO), and Gaussian-type functions (GTF))

a_0	Deviation	Theory	Functional	Potential	Basis	Reference
3.942	−1.4	DFT	LDA	FP	LAPW	[28, 35]
3.945	−1.4	DFT	LDA	PP (Vanderbilt)	PW	[32, 36]
3.943	−1.4	DFT	LDA	PP (Teter)	PW	[37]
3.951	−1.2	DFT	LDA	PP (Troullier–Martins)	PW	[38]
3.948	−1.3	DFT	LDA	PP (Troullier–Martins)	NAO	[39]
3.96	−1.0	DFT	LDA	PP (Hay–Wadt)	GTF	[40]
4.027	+0.7	DFT	GGA	FP	LAPW	[35]
4.03	+0.8	DFT	GGA	PP (Troullier–Martins)	NAO	[41]
4.023	+0.6	DFT	GGA	PP (Troullier–Martins)	PW	[38]
4.03	+0.8	DFT	GGA	PP (Hay–Wadt)	GTF	[40]
4.009	+0.2	DFT	WDA	PP (Troullier–Martins)	PW	[38]
4.04	+1.0	hybrid	B3LYP	PP (Hay–Wadt)	GTF	[40]
4.01	+0.2	HF		PP (Hay–Wadt)	GTF	[40]

$6 \times 6 \times 6$ Monkhorst–Pack grids [34] for the primitive perovskite unit cell being now considered standard, is required to capture the mixed ionic–covalent character of the bonding.

For most calculations, the density functional selected is one of the variants of the local density approximation (LDA). As illustrated in Table 1 for $BaTiO_3$, various implementations have been reported (full versus pseudopotential approaches, with different basis functions) providing very similar accuracy. As will be further discussed below, LDA calculations typically underestimate the lattice constants by 1–2 % relative to the experimental values. Generalized gradient approximations (GGA) typically yield larger lattice constants than the LDA, in some cases so much larger as to overestimate the lattice constants [38]. However, a modified GGA introduced in [42] was shown to give consistently accurate values. Another approximate density functional, the weighted density approximation (WDA) [38, 43], offers some improvements over LDA as we shall see below, though its use has not become widespread. LDA is also found to lead to significant underestimates of the bandgap; this is particularly irksome in calculations of perovskite heterostructures. The LSDA+U (local spin-density approximation with Hubbard U) method has proved successful in the study of magnetic ferroelectric oxides [44–46] and a pseudo-self-interaction correction (SIC) scheme was also shown to improve the gap of $BaTiO_3$ [47]. As an alternative to DFT, the Hartree–Fock method has been used in some studies of perovskite oxides [48–

50], and more recently, extended to hybrid functionals that mix Hartree–Fock and a local density functional [40, 51–53]. As expected for Hartree–Fock, the bandgaps are overestimated, and a hybrid approach yields intermediate results with quite reasonable bandgaps. Other methods for an improved treatment of electron correlation include Moller–Plesset expansion (MP2), quantum Monte Carlo (QMC) approaches, and dynamical mean field theory. MP2 is at present practical only in cluster calculations (see, for example, [54]). Results for the latter two methods have begun to appear relatively recently [17], including promising results for highly accurate QMC calculations of perovskite oxide lattice constants.[1]

Because of the strong sensitivity of the polarization and other properties to strain, and the difficulties in remedying this directly through improved functionals, it is a common practice to perform first-principles calculations with the lattice parameters constrained to their experimental values, when known (see discussion in [55], which refers to an earlier discussion in [4]). This generally yields internal structural parameters, phonon frequencies, and dielectric and piezoelectric coefficients in good agreement with experiment. When experimental values for the lattice parameters are not available, using an upward correction of 1% to the computed values can substantially improve the predictive accuracy of such calculations.

A systematic formalism for the definition and first-principles computation of the polarization for periodic crystalline systems [56–58], usually called "the modern theory of polarization," has played a central role in the understanding and computation of polarization and related properties, such as the Born effective charges, the static dielectric tensor and piezoelectric coefficients. A fuller description of this theory and its application to ferroelectrics is given in the chapter by *Resta* and *Vanderbilt* in this volume.

Most density-functional implementations rely on periodic boundary conditions. In bulk crystals, these correspond to electrical boundary conditions in which the macroscopic electric field is zero. Recently, significant progress has been made in methods for computing structure and properties in finite electric fields [59–61]. The key observation was that while in an infinite crystal, the Hamiltonian in a nonzero uniform field is unbounded from below and the true ground state is therefore ill defined, properties measured under an applied field are those of a metastable state in which crystalline periodicity is preserved. This approach has been implemented in ABINIT [18] and PWscf [20], and generalized to include constrained polarization calculations [62] and phonons [63]. The central quantity is the field-dependent polarization P(E). From P(E) and the field-dependent strain, one can extract dielectric and piezoelectric responses at finite field. In cases where the lattice contribution to the polarization dominates, useful results can be more easily obtained using low-order approximations, including the first-principles

[1] L. Wagner and L. Mitas, private communication.

effective Hamiltonian to be discussed below, the constrained polarization approach of [64], and the atomic-force approach of [65, 66].

Given the importance of phonons in the physics of ferroelectrics, particularly the unstable transverse zone-center soft mode of the high-symmetry reference structure, the first-principles computation of phonon frequencies is an extremely valuable tool. For zone-center phonons and very high symmetry points on the zone boundary, phonons can be computed using the frozen-phonon method, which involves computing the forces induced by finite displacement of individual atoms via the Hellmann–Feynman theorem. These calculations can be performed using most standard first-principles total-energy implementations, though it should be noted that the computation of LO modes at the zone center requires the additional implementation of a method for computing polarization in order to obtain Born effective charges, Z^*, by finite differences and the optical dielectric constant, ϵ_∞, using a supercell approach [67]. A different technique, which involves direct computation of the second derivatives of the total energy via density-functional perturbation theory (DFPT) [68–71] allows the computation of the dynamical matrix at any phonon wavevector q with an effort comparable to the frozen-phonon computation at $q = 0$. Both methods give the same result, as the structural energy function is the same in both cases. An interpolation method that uses the Born effective charge tensors Z^*, also computed in density-functional perturbation theory (or by finite difference using polarization differences), to extract the long-range dipolar interaction allows the plotting of the full phonon dispersion throughout the Brillouin zone [72]. Implementations in norm-conserving pseudopotentials (ABINIT [18]), ultrasoft pseudopotentials (PWscf [20]) and LAPW [73] are available, and applications to a wide variety of systems are reviewed in [71].

Other physical properties involving perturbations with respect to atomic displacements, homogeneous electric fields, and homogeneous strains can be computed through analogous methods. The computation of mixed and second derivatives with respect to homogeneous strain, which allows direct computation of the elastic constants and piezoelectric coefficients, can be carried out by finite-difference methods or, alternatively, in the DFPT formalism implemented in ABINIT [74–76]. Derivatives with respect to the homogeneous electric field within DFPT yield additional quantities, such as optical and static dielectric constants, and alternative methods for computing Z^* [69–71,77]. Systematic combinations of six elementary response tensors determine a wide variety of properties, including elastic, piezoelectric and dielectric tensors under various electrical and mechanical boundary conditions [78].

Further application of DFPT and implementations also allow the computation of various additional quantities related to third energy derivatives in a systematic way [71, 79–81]. This includes the computation of properties relevant to the physics of ferroelectric oxides including Raman spectra, nonlinear optical susceptibilities and electro-optic coefficients [82–85].

In the search for the ground state, it is important to keep in mind the limitations of the first-principles method based on optimizing within a selected space group. In particular, the choice of unit cell can obscure the identification of a lower-energy structure with a larger or incompatible unit cell. However, it is possible rigorously to show at least whether the structure of interest is a local minimum in the full space of crystal structures through a stability analysis. This requires computing the full Hessian matrix of second derivatives of the energy with respect to phonons and strain, that is, the phonon dispersion relation of the minimum-energy structure, as well as the elastic constants and the bilinear couplings of the zone-center phonons to strain, to the extent that the latter are allowed to be nonzero by symmetry. This is discussed, for example, in the study of the ground-state structure of $PbTiO_3$ [86].

One of the strengths of first-principles calculations is that, since they do not require any empirical input, they can be carried out for as-yet hypothetical compounds and structures. This is useful in the search for new materials with interesting properties (examples in ferroelectric oxides include Pb_2TiO_4 [87] and $BaTi_2O_5$ [88]), or in determining the unknown structure of phases for which crystallographic data are incomplete or ambiguous. A prototypical example for the perovskite oxides is $PbZrO_3$ [55, 89].

With typically available computer resources, the maximum number of atoms per unit cell is approximately one hundred. This is not a significant limitation for pure bulk compounds and infinite short-period superlattices, for which the periodic boundary conditions typical of first-principles density-functional calculations are also fully appropriate. For other structures, such as solid solutions, and for semifinite or finite systems such as thin films, nanowires and nanoparticles, as well as for molecular dynamics or finite-temperature simulations, the constraints are much more severe. For solid solutions, a periodically repeated supercell (randomly generated or quasirandom [90]) is used. For semi-finite or finite systems, the system is embedded into a supercell surrounded by a vacuum region sufficiently large to minimize artificial interactions with its periodic images. Even with this method, there can be additional difficulties for isolated systems with a total nonzero polarization (for films, if the component of the polarization perpendicular to the surface is nonzero), as the periodic boundary conditions implicitly impose a partial compensation of the depolarization field.

For this reason, interpolative methods have been introduced to handle larger system sizes and to compute the energies of large numbers of configurations. These fall into two main classes: first-principles effective Hamiltonians and interatomic potentials. The first-principles effective Hamiltonian is constructed by projection into a subspace of relevant degrees of freedom, [31, 91–97] in a spirit similar to that of phenomenological Landau–Devonshire (LD) functionals. For ferroelectric perovskites, the effective Hamiltonian is constructed from a Taylor expansion of the energy around the high-symmetry paraelectric phase in terms of the soft-mode degrees of freedom and the ho-

mogeneous strain; the use of symmetry yields a form for the soft-mode and strain dependence identical to that found in Landau–Devonshire functionals, with the local polarization being related to the soft-mode amplitude by a constant factor. All parameters that appear in the expansion are determined from DFT total energy and linear response calculations. Properties at nonzero temperatures and electric fields, including phase diagrams, dielectric, piezoelectric and electro-optic coefficients can be computed by performing Monte Carlo calculations in large supercells containing thousands of primitive perovskite unit cells. In addition, the first-principles effective Hamiltonian has proved useful for the study of solid solutions [12, 98, 99], where large quasirandom supercells are needed to capture the effects of substitutional disorder, and for systems of nontrivial geometry, including thin films and nanoparticles [100–107].

Interatomic potentials with the form of shell models [108, 109] and parameters determined from fitting to first-principles calculations have been developed for several perovskite oxide systems [110–112]. In contrast to the first-principles effective Hamiltonians, such models give a full atomistic description including all phonon branches and can in principle account properly for thermal expansion, which involves anharmonic interactions not just with the soft-mode branch, but with all phonon modes. However, this requires the determination of a far larger number of parameters, and the angular and many-body terms in the potential can be difficult to incorporate accurately. Bond-valence models, with an even simpler form, have been successfully constructed for perovskite oxide systems, including PZT [113, 114]. Properties at nonzero temperatures and electric fields are computed from interatomic potentials or bond-valence models using molecular dynamics, which can be readily performed for systems containing many thousands of atoms.

3 Results for Perovskite Oxide Compounds

The perovskite-structure oxides have been the subject of the majority of first-principles calculations on ferroelectrics, with the focus being on the ground-state structure, lattice dynamics, and dielectric and piezoelectric response functions. In this section we summarize the approach and results of these studies. The most studied ferroelectric perovskites are $BaTiO_3$, $PbTiO_3$ and $KNbO_3$. Results have also been reported for $NaNbO_3$ and $BiFeO_3$, as well as for related perovskite materials, including $SrTiO_3$, $CaTiO_3$, $CdTiO_3$, $BaZrO_3$, $PbZrO_3$, $KTaO_3$, $NaTaO_3$, $SrHfO_3$, $PbVO_3$, $YScO_3$, $BiScO_3$, $BiAlO_3$ and $BiGaO_3$. In this section, we include both nonmagnetic and magnetic systems, focusing on their ferroelectric behavior and related properties. We start this rather lengthy section by discussing results for the ground-state structure and properties, including unstable modes and strain coupling, and highlighting the importance of electrical and mechanical boundary conditions. Then, we review the results of studies at nonzero temperature.

3.1 Ground-State Structure

First, we consider the first-principles calculations for the $Pm\bar{3}m$ cubic perovskite structure. This is the simplest structure to optimize as it has only one free structural parameter: the cubic lattice constant a_0. The computed value is usually compared with an "experimental" value taken as a_0 for the cubic phase just above the transition temperature, or extrapolated to $T = 0$ using the measured thermal expansion coefficient in the high-temperature cubic phase. In Table 2, we present a compilation of the first-principles lattice constants of various cubic perovskite oxides, obtained within different approximations.

The LDA results show systematic underestimates of a_0 of 1–2 %. In most cases, the GGA overcorrects the LDA results; the modified GGA (here called GGA') of [42] being an exception. Although the slight underestimates in LDA calculations might be considered as reasonable for the study of many other classes of materials, in the present case, it can have noticeable, sometimes dramatic, effects on the ferroelectric stability because of the rather strong polarization–strain coupling in perovskite oxides. Therefore, it has become common practice, when calculating properties within the LDA, to adjust the lattice parameters by hand to their experimental values, when they are known.

It should be noted also that the comparison of the computed and "experimental" cubic perovskite lattice constant should be considered as rather a rough guide, as the nature of the ideal $Pm\bar{3}m$ cubic perovskite structure, with all atoms at high symmetry Wyckoff positions, is quite different from that of the observed high-temperature cubic phase, which is characterized by large fluctuating local distortions that give large distributions of the atomic positions around the crystallographic average $Pm\bar{3}m$ structure. This will be discussed further in the section on nonzero temperature.

In virtually all compounds, the cubic perovskite structure is unstable to energy-lowering distortions, the most common being polar zone-center distortions (resulting in ferroelectricity), zone-boundary distortions involving rotations and/or tilting of the oxygen octahedra, or two or more coupled such modes producing additional distortions as allowed by symmetry considerations. A simple rule of thumb for predicting likely distortion is based on ionic radius, specifically the tolerance ratio introduced by Goldschmidt and described more fully in the contribution of *Rabe*, *Dawber*, *Lichtensteiger*, *Ahn* and *Triscone*. It has been noted that while this analysis is widely useful [32], it is not predictive in all cases, for example $BiAlO_3$ and $BiGaO_3$ [123].

In the ferroelectrics $BaTiO_3$ and $PbTiO_3$, we find an instability to a zone-center polar distortion, in which the cations uniformly displace against the oxygen octahedron network. Since this instability is the defining property of the ferroelectric perovskites, we now discuss it at some length. Choosing the two high-symmetry directions [001] or [111] for the polarization yields space groups $P4mm$, with three free internal structural parameters and two lattice

Table 2. Experimental and theoretical lattice constants (in Å) of the cubic perovskite structure of various ABO_3 compounds

Compound	Experiment	Theory	Method	Reference
I–V compounds				
$KNbO_3$	4.016	3.956 (±0.003)	DFT (LDA)	[32, 35, 36, 38]
		4.028 (±0.010)	DFT (GGA)	[35, 38]
		4.011	DFT (WDA)	[38]
$NaNbO_3$	3.937	3.914	DFT (LDA)	[32, 36]
$KTaO_3$	3.983	3.938 (±0.018)	DFT (LDA)	[35, 38, 115]
		4.033 (±0.002)	DFT (GGA)	[35, 38]
		3.972	DFT (WDA)	[38]
II–IV compounds				
$CaTiO_3$	3.836	3.809 (±0.003)	DFT (LDA)	[32, 36]
$SrTiO_3$	3.905	3.862 (±0.012)	DFT (LDA)	[32, 35, 36, 38, 40, 41]
		3.941 (±0.007)	DFT (GGA)	[35, 38, 40]
		3.917	DFT (WDA)	[38]
		3.94	B3LYP	[40]
		3.92	HF	[40]
$BaTiO_3$	4.000	3.947 (±0.013)	DFT (LDA)	[28, 32, 35–38, 40, 41]
		4.028 (±0.005)	DFT (GGA)	[35, 38, 40, 41]
		4.009	DFT (WDA)	[38]
		4.04	B3LYP	[40]
		4.01	HF	[40]
$CdTiO_3$	3.800	3.805	DFT (LDA)	[116]
$PbTiO_3$	3.969	3.888 (±0.005)	DFT (LDA)	[29, 32, 36, 38, 97]
		3.965 (±0.005)	DFT (GGA)	[38, 40]
		3.933	DFT (GGA')	[42]
		3.941	DFT (WDA)	[38]
		3.96	B3LYP	[40]
		3.94	HF	[40]
$PbZrO_3$	4.133	4.115 (±0.008)	DFT (LDA)	[32, 36, 89, 117]
$BaZrO_3$	4.193	4.152 (±0.004)	DFT (LDA)	[32, 36, 118]
		4.207	DFT (GGA)	[119]
$SrZrO_3$	4.101	4.17	DFT (GGA)	[119]
$SrHfO_3$	4.069	4.069	DFT (LDA)	[120]
$PbVO_3$			DFT (LDA)	[121, 122]
III–III compounds				
$BiGaO_3$	–	3.83	DFT (LDA)	[123]
$BiAlO_3$	–	3.75	DFT (LDA)	[123]
$BiScO_3$	–	3.99	DFT (LDA)	[124]
$YScO_3$	–	3.92	DFT (LDA)	[124]

constants, and $R3m$, with two free internal structural parameters and two lattice parameters, respectively. Optimization of the free structural parameters for the tetragonal and rhombohedral symmetries correctly predicts a

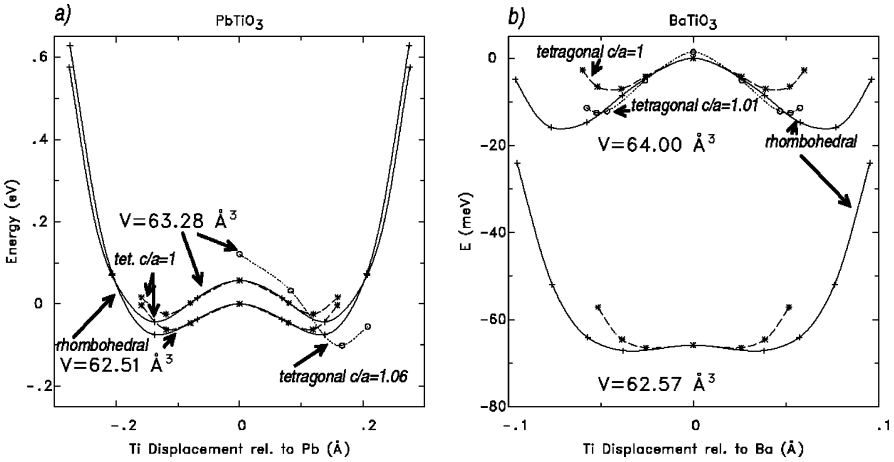

Fig. 1. Total energy as a function of Ti displacement for $PbTiO_3$ and $BaTiO_3$. For both, it is seen that the ground state with a cubic lattice is rhombohedral. For the tetragonal state, the increase in equilibrium polarization with strain relaxation is demonstrated. From [29]

tetragonal ground-state structure of $PbTiO_3$ and a rhombohedral ground-state structure of $BaTiO_3$ [29], as shown in Fig. 1. The symmetry-breaking polar distortion is accompanied by the corresponding strain. As can be seen in the figure, the coupling to strain must be included to reproduce the ground state correctly: if the lattice vectors are fixed as cubic, the ground states of both $BaTiO_3$ and $PbTiO_3$ have the polarization along [111].

The marginal stability of $SrTiO_3$ represents a challenging case for first-principles calculations. Whether a polar instability is obtained depends sensitively on the density functional chosen and on other details of the calculation [32, 125–129]. One source of this sensitivity is variation in the lattice constant in different calculations that, because of the strong polarization-strain coupling, has a strong effect on the ferroelectric instability. The antiferrodistortive oxygen-octahedron rotation in the low-temperature tetragonal phase of $SrTiO_3$ also couples to the polar mode, as will be discussed further in Sect. 3.2. This effect is most noticeable in $SrTiO_3$ because of its marginality, but is present in all perovskites considered. In particular, the systematic underestimate of the lattice constant in LDA calculations tends to reduce the polar instability.

Comparison of the structural parameters of tetragonal $BaTiO_3$ and $PbTiO_3$, obtained in DFT using various functionals, is illustrated in Table 3 (see also the discussion in [38] and Table 5 of [42]). When the lattice parameters are fixed to their experimental values, LDA, GGA and WDA give very similar results for the internal structural parameters, in close agreement with the experiment. However, for both compounds, coupled relax-

ation of atomic positions and unit-cell parameters within the LDA yields a unit-cell volume, a c/a ratio and ferroelectric atomic distortions that are all slightly underestimated. Comparisons of the computed structural parameters for cubic structures at the experimental and theoretical lattice constants, shown in the table, suggest that the underestimate of the ferroelectric distortion mainly arises from the LDA volume underestimate. In $PbTiO_3$, with the GGA constrained to the experimental volume $63.28\,\text{Å}^3$, the computed $c/a = 1.068$ is in much better agreement with the experimental value. However, the fully relaxed GGA calculation yields a supertetragonal high-volume structure ($c/a = 1.24$) [42] quite different from the experimental structure. The WDA leads to only a slight improvement over the GGA result [38]. Only the modified GGA (GGA') of [42] gives accurate structural parameters with full relaxation. For rhombohedral $BaTiO_3$ and rhombohedral $KNbO_3$ at the experimental lattice parameters, it has been shown [38] that the LDA, GGA and WDA give very similar results for the internal structural parameters. Agreement with experiment is quite good except for $KNbO_3$, where the computed displacements are about 30 % smaller than the experimental values.

The supertetragonal structure obtained in GGA calculations might be due to the tendency of GGA to overestimate volume, as a similar structure is observed in LDA calculations for $PbTiO_3$ at negative pressure [132]. In fact, this supertetragonal structure, illustrated in Fig. 2a, can be regarded as a distinct structure type that is competitive with the tetragonal perovskite structure for some compositions. While it is not common as an equilibrium structure, with the exception of $PbVO_3$ [121, 122] or as-yet hypothetical $BiGaO_3$ [123], with $c/a = 1.23$ and 1.3, respectively, it is obtained as the lowest-energy $P4mm$ structure in calculations of $BiFeO_3$ [133], $BiScO_3$ [134] and $BiYO_3$ [134], with $c/a = 1.27$, 1.285 and 1.376 and large polarizations of 1.51, 0.93 and $0.95\,\text{C/m}^2$, respectively, the latter dominated by the displacement of Bi. Note though that for all three compounds, the rhombohedral $R3c$ structure, shown in Fig. 2b, is considerably lower in energy.

3.2 Phonons, Lattice Instabilities and Polarization

One of the most important early advances in the understanding of ferroelectricity was the development of the soft-mode theory of ferroelectrics, which identified an intimate link to the lattice dynamics [135, 136]. Specifically, as a function of temperature the lowest-frequency polar-phonon mode in the paraelectric phase becomes softer, and finally goes to zero frequency, freezing in below T_c to generate the ferroelectric crystal structure. On the other side of the transition, as the phase boundary is approached with increasing temperature in the ferroelectric phase, the lowest-frequency polar phonon becomes softer, decreasing to zero near T_c. The signature of this behavior in a ground-state first-principles calculation is an unstable polar phonon in the high-symmetry reference structure [29, 137]. As the atomic displacement pattern of the unstable mode is frozen in, a double-well structure is obtained in

Table 3. Atomic positions along z in the tetragonal phase of $BaTiO_3$ and $PbTiO_3$. Relaxation of the atomic position has been performed following different theoretical schemes (Th.) and are compared to the experimental value (Exp.): Th.1, atomic relaxation at the experimental tetragonal unit-cell parameters; Th.2, full coupled relaxation of atomic positions and unit-cell parameters; Th.3, atomic relaxation at the experimental cubic unit-cell parameters; Th.4, atomic relaxation at the theoretical cubic unit-cell parameters. Courtesy of Eric Bousquet

Compound	Scheme	a	c/a	V	z(Ti)	z(O_1,O_2)	z(O_3)	Method
$BaTiO_3$	Exp.	3.986	1.010	63.97	0.515	−0.514	−0.023	[130]
	Th.1	3.986	1.010	63.97	0.513	−0.516	−0.025	DFT(LDA)*
	Th.2	3.929	1.010	61.25	0.509	−0.509	−0.013	DFT(LDA)*
	Th.3	4.000	1.000	64.00	0.512	−0.513	−0.021	DFT(LDA)*
					0.514	−0.514	−0.025	DFT(LDA) [30]
	Th.4	3.943	1.000	61.30	0.505	−0.505	−0.007	DFT(LDA)*
$PbTiO_3$	Exp.	3.905	1.063	63.30	0.540	0.612	0.112	[131]
	Th.1	3.905	1.063	63.30	0.548	0.628	0.120	DFT(LDA)*
					0.549	0.630	0.125	DFT(LDA) [86]
					0.539	0.615	0.111	DFT(LDA) [38]
					0.532	0.611	0.105	DFT(GGA) [38]
					0.539	0.614	0.110	DFT(WDA) [38]
	Th.2	3.835	1.063	59.96	0.532	0.606	0.092	DFT(LDA)*
		3.862	1.054	62.22	0.537	0.611	0.100	DFT(LDA) [86]
		3.865	1.046	60.37	0.524	0.589	0.082	DFT(LDA) [42]
		3.847	1.239	70.54	0.553	0.662	0.188	DFT(GGA) [42]
		3.890	1.078	63.47	0.532	0.611	0.108	DFT(GGA') [42]
	Th.3	3.969	1.00	62.52	0.549	0.610	0.097	DFT(LDA)*
	Th.4	3.879	1.00	58.37	0.527	0.573	0.057	DFT(LDA)*

*E. Bousquet and Ph. Ghosez, private communication.

the energy as a function of distortion amplitude. Indeed, there is a strong resemblance between the ground-state distortion and the unstable polar mode of the cubic structure of prototypical cases such as $BaTiO_3$.

Within a quantitative first-principles framework, this correspondence can be made more precise. The main issue that arises is that the displacement pattern corresponding to the unstable eigenvector of the dynamical matrix is, in general, different from the displacement pattern corresponding to the unstable eigenvector of the force-constant matrix, due to the mass factors. For the minimum-energy structure, the latter pattern is the one that is expected to generate the ground-state structure, as it yields the largest negative curvature of the total energy with respect to the overall amplitude of displacements. However, determination of the optimal distortion is very dependent on higher-order terms. The fourth-order term determines the energy gain in the resulting double-well potential; a distortion with large negative curvature may nonetheless yield an optimized distortion energy that is less

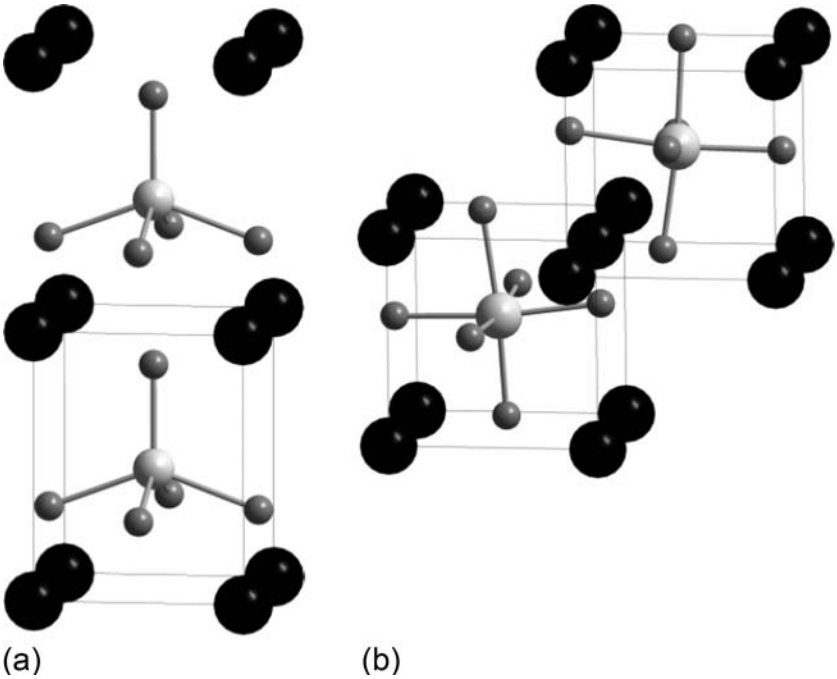

Fig. 2. (**a**) Supertetragonal ABO_3 structure. The A atoms are in *black*, the B atoms in *light gray*, and the oxygen atoms in *dark gray*. (**b**) *R*3*c* structure. From [123]

favorable than a distortion with smaller negative curvature, depending on the relative magnitudes of the respective fourth-order coupling. Moreover, the optimal distortion pattern for a noninfinitesimal distortion amplitude may be modified by higher-order couplings to other modes, and even further modifications may result if the strain is also allowed to change with distortion amplitude. This can be analyzed quantitatively in first-principles studies; for $BaTiO_3$, with the eigenvector dominated by Ti displacement relative to the other atoms, the ground-state distortion is quite accurately given by the unstable mode eigenvector (overlap of 98 %), while for $PbTiO_3$ with its large strain and more highly structured eigenvector, the general agreement is good, though there are quantitative differences [97].

First-principles calculations have provided valuable information for understanding the origin of the instability of the polar mode in cubic perovskite oxide compounds. A pronounced mixed ionic–covalent character for the B−O bonding in these systems [138–141] has been confirmed by first-principles calculations [29, 37, 142, 143]; this is generally agreed to be an important factor in producing the ferroelectric ground-state distortion [144]. Indeed, pure size considerations, as reflected in the tolerance factor, also discussed above, do not distinguish between polar and antipolar offcenterings for the B cation in the oxygen octahedron cage.

In perovskite oxides, with displacement of the B cation relative to the surrounding oxygen octahedron, the empty d orbitals on the B cation (Ti^{4+}, Nb^{5+}, Zr^{4+}, etc.) hybridize with the occupied O $2p$ orbitals, lowering the energy and redistributing the electron density. This mechanism favors uniform displacement of B cations along a B−O−B chain, tending to favor a ferroelectric ground state (though it should be noted that the displacement of parallel chains is nearly independent, as will be evident in the discussion of phonon-dispersion relations, below). Further evidence of the importance of the mixed ionic–covalent character of the bonding is obtained from comparison of $BaTiO_3$ and $PbTiO_3$, exhibiting a difference that extends to a general distinction between alkaline-earth A cations, with a highly ionic character, and Pb or Bi A cations, with a more covalent character due to their lone-pair $6s$ electrons [145]. In $BaTiO_3$, the unstable mode is dominated by the Ti displacement and the Ba $5p$ states do not hydridize significantly with the valence band, while in $PbTiO_3$, the Pb participates in the polar distortion and Pb $6s$ "lone-pair" states hybridize with the oxygen $2p$ states. Similar considerations apply to the behavior of $KNbO_3$: the alkali-metal cation does not participate in the distortion, and the ground-state structure resembles that of $BaTiO_3$.

The covalent interactions tend to be short range, while the ionic electrostatic interactions are long, in fact infinite, range. This has led to a useful picture of ferroelectricity in perovskite oxides as resulting from a delicate balance of short-range and long-range interactions. This picture, first introduced by *Cochran* in the context of a shell model [135], has been confirmed and quantified at the first-principles level [29, 146]. The fact that these interactions are affected differently by pressure, finite-size effects, and other external factors allows for an understanding of the influence of the various factors on the ferroelectric instability (see, for an early example, the discussion in [147]).

The polarization induced by atomic displacements, given by the Born effective charges Z^*, plays a key role in understanding both the polar ground state and the lattice dynamics. The Born effective charges are tensors, defined as the first derivative of polarization with atomic displacement

$$Z^*_{i\alpha\beta} = \frac{\Omega}{e}\frac{\partial P_\alpha}{\partial u_{i\beta}}|_{E_{\mathrm{mac}}=0}\,. \tag{1}$$

As already mentioned in Sect. 2, the Z^* can be readily computed either from finite differences of the polarization, or within DFPT [77]. In a purely ionic model, Z^* is simply the formal charge on the ion: -2 for oxygen, $+2$ for alkaline earths, and $+4$ for titanium. In first-principles calculations (as well as in quantitative optical measurements), it is well established that the Born effective charges characteristic of the ferroelectric perovskite oxides can deviate significantly from these nominal values. The large polarization induced by atomic displacement can be understood in the framework of the modern theory of polarization (Chap. 1) and is part of the evidence for a strong

Table 4. Born effective charges of various ABO_3 compounds in their cubic structure. The Born effective charges of the A and B atoms are compared to the *nominal* ionic charges Z_A and Z_B. (Adapted from [148])

ABO_3	Z^*_A	Z^*_B	$Z^*_{O\parallel}$	$Z^*_{O\perp}$	Z^*_A/Z_A	Z^*_B/Z_B	Method	Reference
nominal	3	3	−2	−2				
$BiAlO_3$	6.22	2.84	−2.34	−3.38	2.07	0.95	DFT (LDA)	[123]
$BiGaO_3$	6.29	3.11	−2.58	−3.40	2.10	1.04	DFT (LDA)	[123]
nominal	2	4	−2	−2				
$CaTiO_3$	2.58	7.08	−5.65	−2.00	1.29	1.77	DFT (LDA)	[142]
$SrTiO_3$	2.56	7.26	−5.73	−2.15	1.28	1.82	DFT (LDA)	[148]
	2.54	7.12	−5.66	−2.00	1.27	1.78	DFT (LDA)	[142]
	2.55	7.56	−5.92	−2.12	1.28	1.89	DFT (LDA)	[126]
	2.4	7.0	−5.8	−1.8	1.2	1.8	experiment	[149]
$BaTiO_3$	2.77	7.25	−5.71	−2.15	1.39	1.81	DFT (LDA)	[148]
	2.75	7.16	−5.69	−2.11	1.38	1.79	DFT (LDA)	[142]
	2.61	5.88	−4.43	−2.03	1.31	1.47	Pseudo-SIC	[47]
	2.9	6.7	−4.8	−2.4	1.45	1.68	experiment	[149]
$BaZrO_3$	2.73	6.03	−4.74	−2.01	1.37	1.51	DFT (LDA)	[142]
$PbTiO_3$	3.90	7.06	−5.83	−2.56	1.95	1.77	DFT (LDA)	[142]
$PbZrO_3$	3.92	5.85	−4.81	−2.48	1.96	1.46	DFT (LDA)	[142]
nominal	1	5	−2	−2				
$NaNbO_3$	1.13	9.11	−7.01	−1.61	1.13	1.82	DFT (LDA)	[142]
$KNbO_3$	0.82	9.13	−6.58	−1.68	0.82	1.83	DFT (LDA)	[150]
	1.14	9.23	−7.01	−1.68	1.14	1.85	DFT (LDA)	[142]
	1.14	9.37	−6.86	−1.65	1.14	1.87	DFT (LDA)	[151]
	1.07	8.12	−5.38	−1.80	1.07	1.62	HF	[48, 49]
nominal	-	6	−2	−2				
WO_3	-	12.51	−9.13	−1.69	-	2.09	DFT (LDA)	[152]

ionic–covalent character for the B−O bonding in these systems as discussed above [37, 138, 142, 150, 153]. For an extensive review of the concept of Born effective charges in ABO_3 compounds, see [148]. First-principles results are presented for some representative systems in Table 4. For the oxygens, the tensor character of the Born effective charge becomes apparent, as the induced polarization for displacement along the B−O chain is typically much larger in magnitude than the induced polarization for displacement in the plane perpendicular to the chain. This, combined with a large Z^* for the B cation, produces a large mode effective charge for the unstable TO polar mode [142], characterized by relative displacement of the cations and oxygens. This is illustrated in Table 5 with the mode effective charge defined as

$$\overline{Z}^*_j = \sum_m M_m^{1/2} Z^*_m \xi_{jm} \,, \tag{2}$$

Table 5. Frequencies (cm^{-1}) and mode effective charges ($|e|$) of IR-active transverse optical (TO) phonon modes of various perovskite oxides as computed by *Zhong* et al. [142]. The mode effective charge was defined there as $\bar{Z}_j^* = \sum_m M_m^{1/2} Z_m^* \xi_{jm}^{TO}$ where ξ is the mode eigenvector. (Adapted from [142])

	TO1		TO2		TO3	
	ω	$\bar{Z}^*$	ω	$\bar{Z}^*$	ω	$\bar{Z}^*$
$BaTiO_3$	$178i$	8.95	177	1.69	468	1.37
$SrTiO_3$	$41i$	7.37	165	3.22	546	3.43
$CaTiO_3$	$153i$	6.25	188	4.94	610	4.50
$KNbO_3$	$143i$	8.58	188	1.70	506	4.15
$NaNbO_3$	$152i$	6.95	115	2.32	556	5.21
$PbTiO_3$	$144i$	7.58	121	4.23	497	3.21
$PbZrO_3$	$131i$	4.83	63	4.86	568	4.30
$BaZrO_3$	95	5.57	193	5.57	514	3.84

where ξ_{jm} is the phonon eigenvector. The large mode effective charge of the unstable mode is the origin of giant LO−TO splitting in these compounds [142].

The spontaneous polarization of the ferroelectric state can be computed directly from the Berry-phase formalism, or estimated using the computed Born effective charges and atomic displacements relative to a nonpolar reference structure using the linearized expression $\Delta P_\alpha = \frac{e}{\Omega} \sum Z^*_{i\alpha\beta} \delta u_{i\beta}$. In the latter context, the large mode effective charge of the unstable TO polar mode can be seen to produce a large polarization for a relatively small distortion. Using either computed or measured structural parameters and computed Z^*, the linearized form has been applied to a range of systems, and its validity examined. For example, application by *Zhong* et al. [142] with experimental structural parameters [154,155] gives 0.30, 0.26 and 0.44 C/m^2 for the tetragonal, orthorhombic and rhombohedral phases of $BaTiO_3$, compared with experimental values of 0.27, 0.30 and 0.33 C/m^2, respectively. For $KNbO_3$, a similar calculation yields 0.40 C/m^2, agreeing exactly with one experimental value [154,155]. The Z^* computed using a different first-principles implementation [150] (see Table 4) yields a slightly lower value of 0.35 C/m^2, which is compared with a different experimental value of 0.37 C/m^2. For $PbTiO_3$ in the tetragonal structure, this analysis [142] yields 1.04 C/m^2 and 0.74 C/m^2 using experimental structural parameters measured at 295 K and 700 K, to be compared with experimental values of 0.75 and 0.50 C/m^2, respectively. This can be compared with a value of 0.88 C/m^2 from a GGA calculation for the computed $PbTiO_3$ tetragonal structure constrained to the experimental volume [156]. It is worth noticing that the linear expression above only provides a rough estimate of the spontaneous polarization since in most cases the Born effective charges are not constant but strongly sensitive to atomic displacements. As a general rule, they are significantly reduced in the ferroelectric

phase compared to the paraelectric one, especially along the polarization direction [37, 46, 157]. Direct application of the Berry-phase formalism to the polar phase should therefore a priori be preferred for accurate calculation of the spontaneous polarization.

The unstable polar-mode characteristic of ferroelectricity is just one of three optical modes of the same symmetry (T_{1u}) in the cubic perovskite structure. In addition, there is a T_{1u} acoustic mode and one T_{2u} mode, and these three-fold degeneracies are indeed found in calculations in periodic boundary conditions, corresponding to zero macroscopic electric field. In systems with symmetry-lowering distortions, there are characteristic changes. For example, in tetragonal $P4mm$ and rhombohedral $R3m$, the degenerate T_{1u} phonons split into A_{1u} and E_u, and the T_{2u} phonon splits and becomes Raman active, which is an experimental fingerprint for the ferroelectric state.

Next, we turn to the full phonon-dispersion relations of these polar insulators. First, it is necessary to treat properly the $q \to 0$ limit for the phonon-dispersion relation, as the long-range electrostatic interactions introduce the possibility of nonzero macroscopic electric fields. This can be done by including a nonanalytic contribution to the dynamical matrix that depends on the Born effective charge tensors Z^* (discussed above) and the electronic dielectric constant ϵ_∞ [158, 159]. While in a simple polar solid such as NaCl with a single optical branch, this results in the well-known splitting of the transverse optical (TO) and longitudinal optical (LO) frequencies according to the Lyddane–Sachs–Teller relation [160], in the perovskites the three polar modes are remixed by the nonanalytic terms, so that there is no longer a one-to-one correspondence between the TO and LO modes [142, 161]. It should be emphasized, though, that it is the unstable TO mode, with $E_{\mathrm{mac}} = 0$, that freezes in to yield the ferroelectric ground state.

The first-principles calculations of the full phonon-dispersion relations for the unstable cubic perovskite structure led to significant new insights into the lattice instabilities and local distortions in ferroelectric oxides.[2] Structural instabilities are manifested as phonons with negative ω^2; these imaginary frequencies are by convention plotted as negative. The phonon dispersions of cubic $BaTiO_3$ [148] and cubic $KNbO_3$ [151] are presented in Fig. 3; as can be seen, they are very similar. LO−TO splitting is apparent in the limit $q \to 0$. It is particularly striking that the instability in the lowest-frequency polar phonon branch is not strongly localized around $q = 0$. There is an extended space of unstable phonons that do not contribute to the ground-state structure; most notably the unstable polar-phonon branch is nearly flat from the zone center out to the zone boundary in the Γ-X and Γ-M directions. By a Fourier transform [151], this can be seen to imply that the cubic structure

[2] It should be noted that these phonon dispersions, being for an unstable hypothetical reference structure, are not directly comparable to experimental results. For the ground-state ferroelectric structure, all phonons would be stable and correspond to measured phonon dispersions in the limit of low temperature.

of these two compounds is unstable against a localized distortion involving atomic displacements in a chain about five lattice constants long, with distortions in adjacent chains being fairly independent (this property proves relevant to the investigation of ferroelectricity in nanowires of $BaTiO_3$ [162]). In addition, this is related to the interpretation of diffuse scattering in the cubic, tetragonal and orthorhombic phases, to be further discussed in Sect. 3.5.

Full phonon dispersions of the unstable cubic perovskite structure have also been reported and analyzed for $SrTiO_3$ [126,127], $PbTiO_3$ [117], $PbZrO_3$ [117], $CaTiO_3$ [163], $BaZrO_3$ [164,165], $BiAlO_3$ [123] and $BiGaO_3$ [123]. Some of them are compared in Fig. 3. $SrTiO_3$, $PbTiO_3$ and $PbZrO_3$ have additional low-lying phonon branches, and in particular have low-frequency oxygen octahedron modes at the zone boundary, as does $BaZrO_3$.

Additional lattice instabilities of the cubic perovskite structure, including rotations and/or tilting of the oxygen octahedra, evident in the phonon-dispersion relations just discussed, can contribute to the ground-state distortion, giving a rich variety of observed perovskite-related structures. In some cases, the distortion is generated by a single mode, as for the ferroelectric structures of $BaTiO_3$ and $PbTiO_3$ and the tetragonal antiferrodistortive structure of $SrTiO_3$. More generally, distortions are produced by two or more modes coupled together, one example being the $R3c$ structure (10 atoms per unit cell), found in several systems, including PZT [167], $BiFeO_3$ [46] and $BiAlO_3$ [123]. Another case in which first-principles methods have proved very successful is the antiferroelectric 40-atom $Pbam$ structure of $PbZrO_3$ [55, 89, 168]. Competition between modes or groups of coupled modes may eliminate instabilities exhibited by the high-symmetry reference structure. For example, in $SrTiO_3$, freezing-in of the R-point antiferrodistortive mode, which produces the nonpolar tetragonal phase below 105 K, suppresses the zone-center polar instability [125, 128]. Conversely, while R-point antiferrodistortive instabilities are found in many perovskite oxides (see Table 1 in [125]), freezing-in of the zone-center polar distortion stabilizes the lattice against these rotational distortions in systems such as $PbTiO_3$ and $BaTiO_3$, where they do not contribute to the ground-state structure. The rotational and ferroelectric instabilities have an opposite dependence on volume: increase in volume tends to destabilize the polar mode, while stiffening the rotational mode [125,169]. Thus, this competition is quite sensitive to changes in the lattice constant by external stress or chemical substitution, which allows some anticipation of the solid-solution phase diagrams on the basis of the endpoint compounds.

Results have been reported for a number of additional compounds. In $CdTiO_3$, the oxygen octahedron rotation around [111] is favored over other distortions considered, including rotation around [001] and tetragonal and rhombohedral ferroelectric distortions [116]. Cubic $CaTiO_3$ has an unstable polar mode [170], but other distortions compete to result in a 20-atom nonpolar $Pbnm$ ground state. $AgNbO_3$ has a 40-atom cell with mixed FE and AFE character and large (14.5°) octahedral rotations [171]. In 5-atom cells, the rhombohedral and tetragonal structures are close in energy, with a sub-

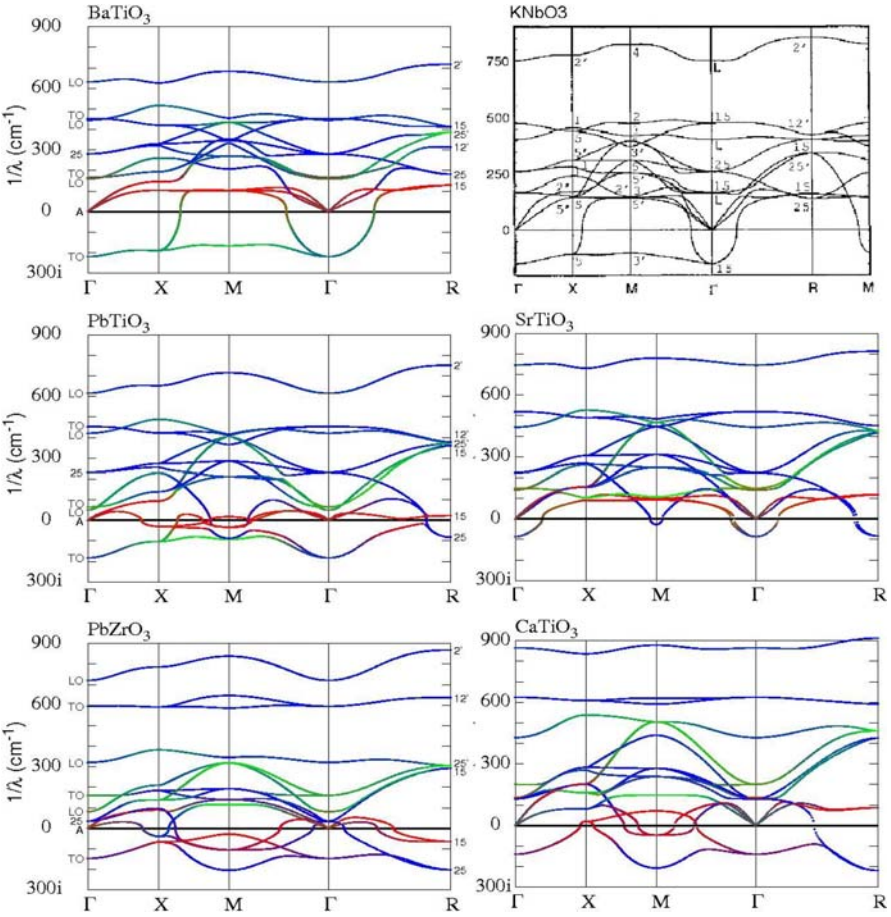

Fig. 3. Phonon dispersions for $BaTiO_3$ [117], $PbTiO_3$ [117], $PbZrO_3$ [117], $KNbO_3$ [151], $SrTiO_3$ [127] and $CaTiO_3$ [163], in the ideal cubic perovskite structure at the experimental lattice constant. Symmetry labels follow the convention of [166], with the A atom at the origin.

stantial polarization close to $70\,\mathrm{C/m^2}$. Similar calculations for 5-atom cells of $BiScO_3$ and $BiYO_3$ showed strong ferroelectric instability, dominated by Bi displacement, with the rhombohedral phase favored over tetragonal [134]. However, rotational distortions are found to be even more energetically favorable [124]. Cubic $BaZrO_3$ does not have a polar instability, and in experimental structural determinations [164] it has been observed to remain cubic down to the lowest temperatures, with the rotational instability mentioned above not expressed either due to a very low T_c or because of quantum fluctuations, analogous to those observed in $SrTiO_3$ and $KTaO_3$ and discussed further below. However, in [165], it was shown that a lower-energy 40-atom

nonpolar $P\bar{1}$ structure with a rotational distortion has a dielectric response in better agreement with experiment than that computed for the cubic phase.

3.3 Polarization–Strain Coupling

The coupling of polarization to strain plays an important role in the physics of perovskite oxide ferroelectrics. The polarization–strain coupling, as defined in the Taylor expansion around the cubic reference state, is responsible for a tetragonal, rather than rhombohedral, ground state for ferroelectric $PbTiO_3$, as discussed above, and for rich phase diagrams for epitaxially-strained thin films, to be discussed below. Moreover, it has been implicated in the first-order character of the ferroelectric–paraelectric transition (Sect. 3.5). Coefficients in the Taylor expansion for the coupled zone-center soft mode and homogeneous strain have been computed from first principles for a set of eight perovskite compounds in [32], and later updated in [36]. This analysis assumes that the soft-mode eigenvector is fixed, independent of strain. These couplings are related to the piezoelectric response of the ferroelectric structures, to be discussed further below.

The strong polarization–strain coupling and the prevalence of competing instabilities can lead to rich structural phase diagrams for the perovskite oxides as some external parameter or constraint is varied. For applied stress σ, in particular hydrostatic pressure, first-principles computation of the zero-temperature phase diagram is straightforward within the Born–Oppenheimer approximation, requiring only the addition of a term $\sigma\eta$ to the total energy being minimized. Within the first-principles framework, it is thus possible to study the effects of ideal hydrostatic pressure over very wide ranges. Recent studies of the pressure-induced phases of $PbTiO_3$ have yielded surprising results. In [172], a rich T−M−R−C phase sequence was found, with the cubic phase favored above a critical pressure of about 22 GPa. In [173, 174], it was found that at higher pressures, the instability of the polar phonon of cubic $PbTiO_3$ turns around and increases with pressure. It is found that the $I4/mcm$ AFD distortion characteristic of $SrTiO_3$ dominates, being increasingly stabilized with increasing pressure, and that there is an additional polar distortion that produces a ferroelectric $I4cm$ ground state. This ferroelectricity at high pressures is consistent with reported Raman observations [173]. The effects of negative pressure on $PbTiO_3$ have also been studied from first principles [175]. As already mentioned in Sect. 3.1, at around −5 GPa, an abrupt transition is found to a supertetragonal structure with $c/a = 1.21$. $BaTiO_3$ undergoes a similar transition, but the critical negative pressure is substantially higher (around −11 GPa).

It is important to note that at least for some materials, including $BaTiO_3$, the neglect of quantum fluctuations in the approach described above gives qualitatively wrong results for the pressure-induced phase sequence and critical pressures. For $BaTiO_3$, using a first-principles effective Hamiltonian approach with a path-integral quantum Monte-Carlo technique, it was shown

in [176] that including quantum fluctuations changes the pressure-induced phase sequence at low temperature from a direct rhombohedral–cubic transition to the same R−O−T−C sequence observed with increasing temperature at zero pressure, consistent with experimental determinations. In fact, it was inferred that the quantum fluctuations have in practice the same effect on relative phase stability as thermal fluctuations, with the pressure-induced changes in the potential energy wells leading to the phase transitions. Quantum fluctuation-induced shifts in the phase boundaries are found to be substantial even at temperatures above 200 K.

In contrast to hydrostatic pressure, coherent epitaxial strain imposes an anisotropic constraint. For perovskites, the most common epitaxial constraint considered is that of the square (001) surface, requiring the inplane lattice vectors to be orthogonal and of equal length, yielding a single epitaxial lattice parameter a. The misfit strain is usually then defined as $(a - a_0)/a_0$, where a_0 is the equilibrium lattice constant for the bulk cubic structure. The effects of epitaxial strain on the structure and properties can be isolated from other effects in thin films (interfaces, free surfaces, defects) by mapping out the phase diagram for the bulk material with the epitaxial constraint imposed. This was first done, in a phenomenological Landau–Devonshire framework, in [177]. The symmetry-lowering effects of the epitaxial contraint lead to a set of lower-symmetry phases, labeled as the c-phase, the r-phase, the a-phase, the aa-phase, and the ac-phase. For the ground state, epitaxial strain phase diagrams have been mapped out from first principles in [178]. In some systems, the effects are quite dramatic. For example, $SrTiO_3$ is driven ferroelectric both by tensile and compressive epitaxial strain [179]. However, in other systems the effects of epitaxial strain on the polarization are less pronounced, for example in PT, PZT and BFO. This has been interpreted as being a result of their large spontaneous polarization in [133] and [180].

3.4 Dielectric and Piezoelectric Responses

Most of the interest in ferroelectric oxides arises from their polarization-related properties, including the dielectric, piezoelectric and electro-optical responses. The distinctive character of these properties can be directly traced to the presence of low-frequency polar phonons, which dominate the properties, producing large lattice responses with high sensitivity to mechanical and electrical boundary conditions. Near phase boundaries, certain response coefficients may in fact diverge as the corresponding mode frequency goes to zero.

The zero-field ground-state static dielectric response at fixed strain can be computed from first principles, as described in detail in [11], by combining the results of calculations for the electronic contribution ϵ_∞, which can be obtained using DFPT techniques, and the lattice contribution obtained

from the Born effective charges and zone-center polar-phonon frequencies, as follows:

$$\epsilon^0_{\alpha\beta} = \epsilon^\infty_{\alpha\beta} + \frac{4\pi}{\Omega_0} \sum_{\mathrm{m}} \frac{p_{m\alpha} \cdot p_{m\beta}}{\omega^2_{\mathrm{m}}} \,, \tag{3}$$

where $p_{m\alpha} = \sum_{\kappa\beta} Z_{\kappa\beta,\alpha} \xi^m_{\kappa\beta} / \sqrt{M}_\kappa$ is the mode polarity for the phonon with frequency ω_m and eigenvector ξ^m. In LDA, the electronic dielectric response ϵ^∞ is well known to be systematically overestimated, a feature that has been related to the lack of polarization dependence of the approximate exchange-correlation functional [181, 182]. However, in ferroelectric oxides, this has a negligible impact on the accuracy of the computed static response as the computed lattice contribution is about an order of magnitude larger than the computed electronic response ϵ^∞. For example, in rhombohedral $BaTiO_3$, the computed value for ϵ_{11} is 69, of which only 6.2 is the electronic response [78, 161]. Most of the lattice contribution comes from the lowest-frequency polar mode, which in many cases also has a large mode effective charge, though the higher-frequency polar modes do make non-negligible contributions. Near a phase boundary, where the soft mode goes to zero frequency, the dielectric response diverges accordingly. First-principles calculations show that low-frequency polar modes also lead to large dielectric responses in nonpolar perovskites [170, 183]. The temperature dependence of the lowest polar-mode frequency will in general lead to a pronounced temperature dependence for ϵ^0; in making comparisons with experiment it should be noted that the first-principles calculation gives the response in the limit $T \to 0$.

For the first-principles study of piezoelectricity, the quantity that is generally computed is $\mathrm{e}_{\alpha,\mu\nu} = \partial P_\alpha / \partial \eta_{\mu\nu}$, the zero-field derivative of polarization with respect to strain. This can be related, using the elastic coefficients, to the direct piezoelectric tensor $\partial P_\alpha / \partial \sigma_{\mu\nu}$, where σ is the stress tensor. Symmetry considerations show that the piezoelectric response of the paraelectric cubic phase is zero. Like the dielectric response, $\mathrm{e}_{\alpha,\mu\nu}$ can be decomposed into two terms: the clamped-ion response, in which the fractional coordinates of the ions remain unchanged and only the homogeneous strain changes, and a contribution produced by the induced relative displacements of ionic sublattices, as follows:

$$\mathrm{e}_{\alpha,\mu\nu} = \mathrm{e}^0_{\alpha,\mu\nu} - \frac{1}{\Omega_0} \sum_{\mathrm{m}} \frac{p_{m\alpha} \cdot g_{m\mu\nu}}{\omega^2_{\mathrm{m}}} \,, \tag{4}$$

where $g_{m\mu\nu} = \sum_{\kappa\beta} \gamma^{\mu\nu}_{\kappa\beta} \xi^{\mathrm{m}}_{\kappa\beta} / \sqrt{M}_\kappa$ depends on the internal strain parameter γ, ξ^{m} and $p_{m\alpha}$ is the mode polarity defined in the previous paragraph. The response is thus largest if the lowest-frequency polar mode in the ferroelectric phase has a frequency close to zero, large mode effective charge, and strong coupling with strain; it is interesting to note that as the phase transition is approached from the ferroelectric side, the response diverges, while it is strictly zero on the paraelectric side. For comparison with experiment, it is

necessary to separate the proper and improper contributions to the piezoelectric response: the proper contribution is what is to be compared with the experimental value, while the improper contribution arises, when the spontaneous polarization is nonzero, from rotation or dilation of the crystal [184]. Computed values for $PbTiO_3$ are reported in Table 4 of [156].

The presence of low-frequency polar modes also leads to large differences between responses for different boundary conditions [78]. Using a systematic DFPT approach described in Sect. 2, calculations of various responses are presented for $BaTiO_3$ in [78]. For example, in a piezoelectric material, the dielectric response at zero stress is larger than the response at fixed strain, because the change in strain allows an increase in the polarization along the applied field direction. This is particularly dramatic in the case of $BaTiO_3$ [78] where ϵ_{11} increases from 69 to 265. Similar considerations can be invoked to explain the large electro-optic response of ferroelectric perovskites, as discussed in [82, 83].

Equations (3) and (4) also can be used to compute the responses in the presence of epitaxial strain constraints. Here, too, the relevant coefficients diverge at phase boundaries as a result of the decreasing frequency of the soft mode [177, 185, 186].

The dielectric and piezoelectric coefficients just discussed describe the response of the system to an infinitesimal electric field. As the field is increased, nonlinearities in P(E) and η(E) become evident. The electric-field dependence of the dielectric response (called the tunability) is of particular technological importance; this has been studied for $SrTiO_3$ in [179]. Nonzero macroscopic fields are also important in very thin films, as discussed in the contribution of *Rabe*, *Dawber*, *Lichtensteiger*, *Ahn* and *Triscone*, due to incomplete compensation of the depolarization field; the structure, phonons and properties of the film are modified accordingly. The electric-field-induced shifts of the phonons have been discussed using both approximate [65] and exact [63] formalisms.

There has been much interest recently in the phenomenon of polarization rotation, where an applied field noncollinear with the spontaneous polarization can induce large responses and even drive the system through additional phase transitions [64, 172, 185, 187, 188]. For small fields, it has been argued that noncollinear responses should generally be larger than collinear ones, as it is easier to rotate the polarization than to change its length. In an important example, a field applied along the [001] direction to a rhombohedral ferroelectric with polarization along [111] will induce a large strain response as the polarization rotates and the system transforms from the rhombohedral to the more highly strained tetragonal phase. This is the accepted mechanism for large piezoelectric response at the rhombohedral–tetragonal morphotropic phase boundary (MPB) in PZT and single-crystal PMN-PT [187, 189]. The path taken by the polarization as it rotates can be quite nontrivial. In [188], it was shown that the polarization for a prototypical tetragonal ferroelectric (PZT $x = 0.5$) in a field along [111] simply rotates in the $(\bar{1}10)$ plane, corresponding to an intermediate A-type monoclinic structure. However, in the

rhombohedral case (PZT $x = 0.47$) with the field along [001], the polarization follows a more complex path, R-M_A-Tri-M_C-T, with the d_{15} piezoelectric coefficients in the triclinic and M_C phases being exceptionally large. At other phase boundaries it has also been possible to identify large responses associated with polarization rotation; for example at the pressure-induced tetragonal–monoclinic transition in $PbTiO_3$ around 10 GPa [172].

The structure and properties of coherent perovskite superlattices can largely be understood by considering the combined effects of epitaxial strain and electric fields on the constituent layers. This proves to be surprisingly useful even when the layers are as thin as a few lattice constants [190, 191]; for example, the symmetry lowering observed in experimental studies of $BaTiO_3/SrTiO_3$ superlattices [192] and in first-principles calculations could be interpreted through this model [193].

3.5 Results at Nonzero Temperature

Part of the fascination of the family of perovskite ferroelectric oxides is related to the fact that they undergo sequences of temperature-driven structural phase transitions. The various functional properties (dielectric, piezoelectric, and optical properties) of direct interest for applications are quite temperature dependent, being especially large or even divergent near the phase-transition temperatures. To be able to explain these important experimental observations, first-principles approaches must thus be able to explicitly account for the effects of temperature.

The most straightforward way would appear to be to perform *ab initio* DFT molecular dynamics simulations [194]. Though there still would be errors due to the density-functional approximation, the Born–Oppenheimer approximation, and neglect of quantum fluctuations, this would treat correctly all the atomic degrees of freedom and their nonlinear interactions. However, this approach is so computationally intensive that currently it is restricted to relatively small systems and time scales [195], while to capture the long-wavelength thermal fluctuations that contribute to the perovskite structural transitions, the simulation cells must contain thousands of atoms. Thus, for finite-temperature investigations it is necessary to use the approximate interpolative methods described in Sect. 2: the first-principles effective Hamiltonian [31, 94, 95, 97] and interatomic potentials [110–112]. This is not necessarily a drawback: because those simplified approaches include the physics in a transparent way, and are also very helpful in clarifying the microscopic mechanisms responsible for ferroelectricity, they aid understanding and assist the experimental–theoretical dialogue.

Here, we present results of first-principles effective Hamiltonian and interatomic potential simulations for three prototypical compounds: $BaTiO_3$, $KNbO_3$ and $PbTiO_3$. In the effective Hamiltonian calculations, only the soft-mode and strain degrees of freedom appear explicitly. The phase diagram is determined by tracking the temperature dependence of these variables. Full

Table 6. Magnitude of the spontaneous polarizations (P_s, in $\mu C/cm^2$) and phase-transition temperatures (T_c, in K) of $BaTiO_3$ as predicted using an effective Hamiltonian ($\mathcal{H}_{eff}$) and a shell-model approach. From [13]

Approach		Experiment [94]	$\mathcal{H}_{eff}$ [13]	$\mathcal{H}_{eff}$ [94]	Shell model [110]
Cubic	P_s	0	0	0	0
↓	T_c	*403*	*335*	*297*	*190*
Tetragonal	P_s	27	30	28	17
↓	T_c	*278*	*240*	*230*	*120*
Orthorhombic	P_s	36	37	35	14
↓	T_c	*183*	*190*	*200*	*90*
Rhombohedral	P_s	33	45	43	12.5

information about the atomic positions is not obtained, as these degrees of freedom have been eliminated. This approximation is also responsible for an incorrect description of thermal expansion, which results from higher-order coupling to the nonsoft-mode degrees of freedom (though corrections within the effective Hamiltonian framework have been suggested [175]). The interatomic-potential simulations in principle include all of this information.

Magnitude of the spontaneous polarizations and phase-transition temperatures of $BaTiO_3$ obtained using an effective Hamiltonian and an interatomic-potential approach are compared in Table 6. For both methods, the phase sequences are correctly reproduced. The transition temperatures have relatively large errors; the possible origins of these have been discussed in [175]. This problem is present even in the interatomic-potential case, so it cannot be attributed exclusively to the treatment of the "irrelevant" degrees of freedom. The effect on T_c of the LDA underestimate of the lattice-constant problem is corrected by introducing an artificial pressure into the simulation so that the lattice constant of the cubic phase matches the experimental value at T_c, though this does not remove the entire discrepancy.

One interesting result emerging from the first-principles analysis relates to the role of strain. In the simulation for $BaTiO_3$, setting the polarization–strain coupling to zero changes the sequence of transitions to a single second-order cubic–rhombohedral transition [95], showing that the stability of the tetragonal and orthorhombic phases depends on strain coupling. This effect can be also easily seen in a simplified eight-site model [196].

In the finite-temperature simulations, it is straightforward to compute response functions to applied electric fields and stresses, either through a finite-difference technique or by direct evaluation of the derivative, which takes the form of a fluctuation average (fluctuations will be discussed further below) [197, 198]. The response functions that have been studied (dielectric, piezoelectric, and electro-optic) are all dominated by the low-frequency polar modes, so that the studies can be carried out either with the first-principles

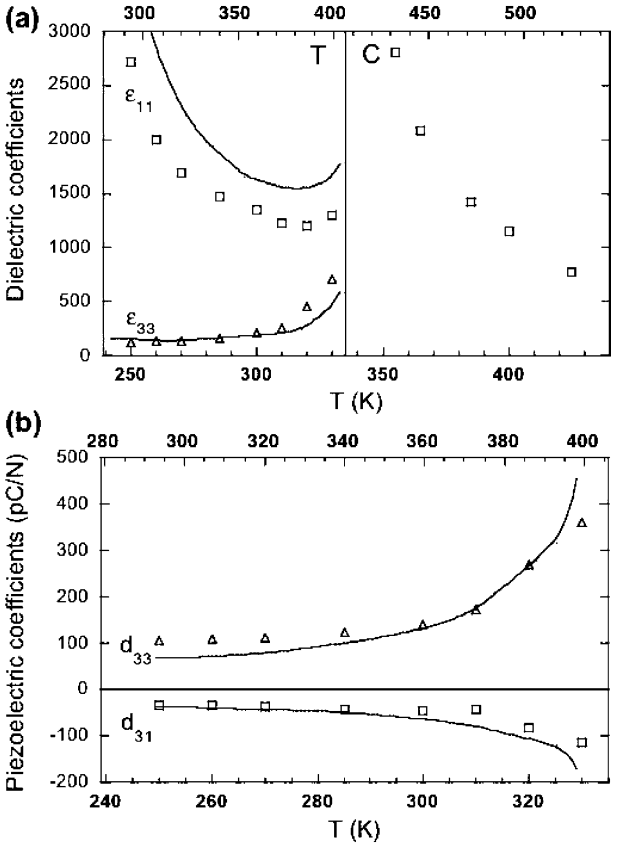

Fig. 4. Temperature dependence of the static dielectric constants (**a**) and piezoelectric constants (**b**) in the cubic (C) and tetragonal (T) phases of $BaTiO_3$. The *bottom* and *top* x-axes correspond to the theoretical and experimental temperatures, respectively. From [13]

effective Hamiltonian or with the interatomic potentials. For comparison with experiment, it is customary to rescale the temperature to match the paraelectric–ferroelectric T_c. This gives excellent agreement, as shown in Fig. 4. Similar curves have been reported for the electro-optic coefficients in the tetragonal phase of $BaTiO_3$ [84].

The connection between effective Hamiltonian and Landau–Devonshire approaches is made stronger by the demonstration that LD parameters can be extracted from first-principles effective Hamiltonian simulations [199]. The analysis for $BaTiO_3$ also showed that the temperature dependence of LD parameters is, in general, not as simple as usually assumed in phenomenological implementations of LD theory.

In addition to information about structure and properties, these simulations can also reveal valuable information about the local fluctuations in the polarization and structure. As mentioned above, the high-temperature cubic phase in particular is characterized by large local fluctuations around the average structure. In $KNbO_3$ and $BaTiO_3$, local fluctuations have also been detected in the diffuse X-ray scattering patterns observed by *Comes* et al. [200] and the first-principles computation of $S(q,\omega)$ reported in [151] shows that these can be interpreted as dynamical local polar distortions with short-range chain correlations. These studies have also shed light on the long-standing issue of whether these transitions should be considered displacive or order–disorder, suggesting that the character in the compounds studied is of an intermediate character.

By applying the epitaxial strain constraint in the Monte Carlo simulations, the first-principles effective Hamiltonian can be used to generate the phase diagram with respect to epitaxial strain and temperature. A study of $BaTiO_3$ is reported in [178]. The topology of the phase diagram near the critical temperature reproduces that found in the phenomenological Landau–Devonshire analysis [177], although the computed transition temperature is too low. No sign of an ac phase was found in the first-principles analysis; the stability of this phase appears to be very sensitive to the choice of Landau–Devonshire parameters [201].

Another application of the first-principles effective Hamiltonian method is to explore the effects of quantum fluctuations at low temperatures. Reported studies include $SrTiO_3$ [125], $KTaO_3$ [202], $BaZrO_3$ [164] and the pressure–temperature phase diagram of $BaTiO_3$ [176]. With the inclusion of quantum fluctuations, the low-temperature structural and dielectric behavior of $SrTiO_3$, $KTaO_3$ and $BaZrO_3$, particularly the saturation in the dielectric constant, are correctly reproduced. Above, we have discussed the effects of pressure on the ground-state structure. In $BaTiO_3$, as discussed above, the quantum fluctuations act in the same way as thermal fluctuations, significantly changing the pressure-induced phase diagram at low temperatures.

4 Results for Other Ferroelectric Oxide Compounds

The same first-principles methods that have been so successfully applied to perovskites can equally well predict the structure and properties of other families of ferroelectric oxides. Though outside the scope of this book, it is worth noting that this is true also for nonoxide ferroelectrics, including halide compounds [203], hydrogen-bonded systems such as KDP (potassium dihydrogen phosphate; KH_2PO_4) [204, 205] or polymeric systems such as PVDF (polyvinylidene fluoride; $[-CH_2-CF_2-]_n$) [206, 207]. While the nonperovskite oxides have been relatively little explored, they are of particular interest as closer examination may reveal novel phenomena. First-principles investigation can bring to light examples with distinct mechanisms for ferroelectric-

ity, including new variations on the soft-mode mechanism, and characteristic physical properties, which may serve as the inspiration for the identification of new ferroelectric materials through a combination of first-principles prediction and experimental synthesis and characterization.

$LiNbO_3$ and $LiTaO_3$ were among the first nonperovskite ferroelectric oxides to be studied from first principles [208, 209]. They have a uniaxial $R3c$ structure related to the perovskite structure by large oxygen octahedron rotations around [111] and displacement of the Li atoms along that axis, as described in more detail in the contribution of *Rabe*, *Dawber*, *Lichtensteiger*, *Ahn* and *Triscone*. The first-principles results show that the Li displacements are strongly coupled to the oxygen displacements, resulting in very deep double-well potentials. In addition, as in the perovskite oxides, there is substantial hybridization between the oxygen and transition-metal orbitals. Studies of the dielectric and dynamical properties including phonon dispersion [210,211] and nonlinear optical properties [82,83,212,213] confirm strong similarities with the perovskite compounds.

The hexagonal $P6_3/mmc$ phase of $BaTiO_3$, found at very high temperatures, has been studied from first principles in [214] and [215]. The physics of the soft modes has been suggested to be closely related to that of the perovskite $BaTiO_3$ phase.

The nitrogen oxide ferroelectrics have low-symmetry phases and rich phase diagrams. The structure, polarization, elastic constants and ground-state piezoelectric response of $NaNO_2$ have been investigated from first principles in [216–219]. The structure and polarization of KNO_3 have been reported in [220]. It was found that in the evolution of the minimum-energy structure, the relative displacement of the charged K and NO_3 groups along the polar axis is accompanied by an inplane rotation of the NO_3 by 60°.

There are several layered structural families based on the stacking of perovskite layers with other oxide arrangements, described in the contribution of *Rabe*, *Dawber*, *Lichtensteiger*, *Ahn* and *Triscone*. The family in which the most ferroelectric compounds have been identified is the Aurivillius series $[Bi_2O_2]$ $[A'_{n-1}B_nO_{3n+1}]$. The case of bismuth titanate $Bi_4Ti_3O_{12}$, potentially interesting in nonvolatile memory applications because of its large polarization, has been explicitly considered [221–223]. The technologically important compound $SrBi_2Ta_2O_9$ (SBT) has also been thoroughly investigated from first principles [223, 224]. In first-principles calculations for the high-symmetry tetragonal phase, an unstable E_u phonon was found that freezes in preferentially in the [110] direction [223]. In [224], additional first-principles calculations (including a full phonon-dispersion relation for the tetragonal phase) and symmetry analysis showed that a second nonpolar mode at the X point couples to this mode, leading to the observed $A21am$ space-group symmetry and naturally accounting for the observation of a nonpolar intermediate phase between the high-temperature tetragonal and low-temperature ferroelectric phases.

The structures of the members of the Ruddlesden–Popper (RP) series $AO[A_nB_nO_{3n}]$ can be viewed as a stacking of AO-terminated ABO_3 perovskite [001] slabs with relative shifts of $(a_0/2)[110]$, the slabs in the nth member of the series having a thickness of n cubic perovskite lattice constants, as discussed in more detail in the contribution of *Rabe*, *Dawber*, *Lichtensteiger*, *Ahn* and *Triscone*. No experimental observation of ferroelectricity in RP compounds has yet been reported, though first-principles calculations show that the as-yet-hypothetical compound Pb_2TiO_4 would be ferroelectric when epitaxially strained [87].

In the Dion–Jacobson series $A[A'_{n-1}B_nO_{3n+1}]$, a polar low-temperature structure has been reported for $CsBiNb_2O_7$ [225]. While ferroelectric switching has not been confirmed experimentally, first-principles analysis of the structure and lattice instabilities suggest that this compound is ferroelectric with a substantial polarization and a high critical temperature [226].

Study of nonperovskite systems has been particularly important in the area of magnetic ferroelectrics, since it has been shown that the perovskite B−O chain instability requires a d^0 state for the B cation, while magnetism would require a partially filled d shell [227] as described more fully in the contribution by *Spaldin* in this volume. Compounds such as $BiMnO_3$ and $BiFeO_3$ rely on the offcentering of the Bi to produce the ferroelectric instability, as described above. In $YCrO_3$, first-principles calculations show a ferroelectric instability associated with Y displacement, competing with a rotational distortion [228]. Ordered mixtures of two different cations can enhance multiferroic behavior by stabilizing a ferrimagnetic ordering that retains a substantial magnetization, for example Bi_2FeCrO_6 [229, 230]. Another mechanism compatible with magnetism is geometrically driven ferroelectricity. One well-studied example is $YMnO_3$, an improper ferroelectric in which a zone-boundary rotation of the oxygen polyhedra induces a zone-center polar distortion [44, 45] (see Fig. 5). $BaMnF_4$ is an example of a geometrically driven proper ferroelectric with the mechanism elucidated in a recent first-principles study [231]. More discussion of these results can be found in the chapter by *Spaldin* in this volume.

As discussed in the contribution by *Rabe*, *Dawber*, *Lichtensteiger*, *Ahn* and *Triscone*, electronic ferroelectrics exhibit a symmetry-breaking instability of the electronic ground state that occurs even if the ions are held fixed. Observation of such behavior has been reported in complex transition-metal oxides with multivalent cations, for example $LuFe_2O_4$ [232], and the importance of electronic correlation in these systems presents challenges for first-principles density-functional approaches. First-principles calculations have been reported for the charge-ordering structural distortion in $BaBiO_3$, where it has been suggested that $Bi^{4+} \rightarrow Bi^{3+} + Bi^{5+}$ (see [233] and references therein). While this ordering does not lower the symmetry enough to support a nonzero polarization, similar ordering in a system with a lower-symmetry cation sublattice could result in ferroelectricity.

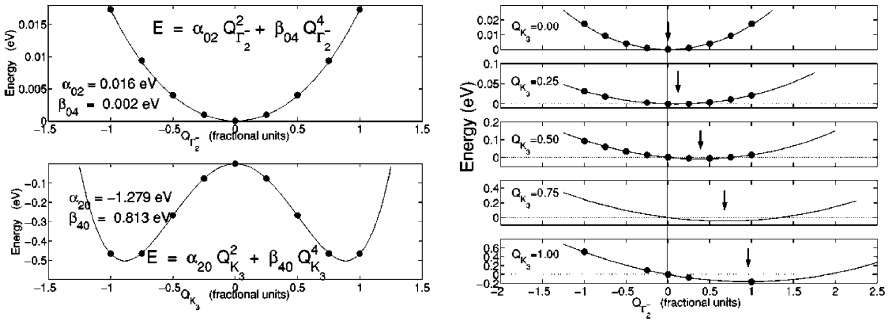

Fig. 5. Energetics of $YMnO_3$. *Left*: Energy as a function of the amplitude of the zone-center polar distortion Γ_2^- (*top*) and the zone-boundary rotational mode K_3 (*bottom*). *Right*: Energy as a function of the amplitude of the zone-center polar distortion Γ_2^- at fixed amplitude of the zone-boundary rotational mode K_3. From [45]

From this brief summary, we see that there are many promising possibilities for designing new ferroelectric materials based on natural and artificially structured reassembly of particular structural motifs. First-principles results have an important role to play in elucidating alternative mechanisms for the occurrence of ferroelectricity, chemical and structural trends in ferroelectric instabilities, and identification of promising compounds for experimental synthesis and characterization. These results can also be productively combined with empirical structural database searches of the type proposed by *Abrahams* (see [234] and earlier works cited therein) as shown in the work of *Kroumova* et al. [235] and *Capialls* et al. [236].

5 Results for Solid Solutions

The ease with which solid solutions can be formed in many ferroelectric perovskites offers tremendous opportunities for broadening the variety of materials and optimizing their properties. For isovalent cation subsitution, for example $Ba_{1-x}Sr_xTiO_3$ or $PbZr_{1-x}Ti_xO_3$ (PZT), the species can in many cases be freely substituted on the same site. For heterovalent cations, for example $PbMg_{1/3}Nb_{2/3}O_3$ (PMN), the ratio is fixed by charge counting, though free alloying is possible with multiple cations that preserve overall change balance, for example PMN:PT. The arrangement of the cations may be random, exhibit short-range order, or even in some cases exhibit long-range order.

The first-principles computation of the structure and properties of these systems, however, presents significant technical challenges. To obtain the periodic boundary conditions required in most implementations, the solid solution is modeled by an ordered supercell that captures the main features of the cation distribution. This "quasirandom" supercell is ideally large enough not only to reproduce the composition, but also the distribution of short-

range environments. For very large supercells, full first-principles calculations are not practical and interpolative methods based on interatomic potentials or first-principles effective Hamiltonians, discussed above in the context of finite-temperature calculations, have been productively applied. An alternative approach that has also been applied to ferroelectrics is the virtual crystal approximation (VCA), where the underlying periodicity of the ideal perovskite is preserved by averaging the potentials on the substitutional site. While proper application of this latter method can lead to useful results for the ground-state structural parameters for comparision with crystallographic data [237], the neglect of the variations in local structure means that phonons, in particular, are not accurately reproduced [238]. For the heterovalent case, the virtual crystal approximation becomes even more problematic.

In the rest of this section, we will review results for a number of systems, studied through some or all of these techniques. One common theme is the relation of the structure and properties of the solid solution to those of the endpoint compounds. There is also considerable interest in identifying composition-driven phase transitions, which appear as vertical or nearly vertical phase boundaries (morphotropic phase boundaries, or MPBs), as these are associated with large responses to applied fields and stresses. The best-known example, to be discussed at greater length below, is the rhombohedral–tetragonal MPB in PZT, to which its excellent piezoelectric behavior is attributed.

$Ba_{1-x}Sr_xTiO_3$ is one of the simplest of the perovskite solid solutions. As x increases, the critical temperatures for the R−O−T−C phase sequence of $BaTiO_3$ decrease smoothly (this is shown in Fig. 7a of the contribution by *Rabe*, *Dawber*, *Lichtensteiger*, *Ahn* and *Triscone*. As seen in the previous discussions of $BaTiO_3$ under pressure and of $SrTiO_3$, it seems that both quantum fluctuations and oxygen octahedron rotations play an important role in the low-temperature $SrTiO_3$-rich portion of the phase diagram; in [239], the classical treatment with no rotations included yields the R−O−T−C phase sequence for all x, while the classical interatomic potential analysis [240], which does include rotation, suggests that the sequence changes to a R−C transition for x below 0.2.

Largely because of its technological importance, PZT is the most studied of the solid solutions. Its rich temperature–composition phase diagram has been recently augmented by the discovery of a new monoclinic phase near the morphotropic phase boundary, as shown in Fig. 7b of the contribution by *Rabe*, *Dawber*, *Lichtensteiger*, *Ahn* and *Triscone*. Zr and Ti being isovalent, virtual crystal approximations can be expected to yield useful results. Calculations of the relative energies of the tetragonal $P4mm$ and rhombohedral $R3m$ and $R3c$ structures as a function of x for one particular implementation of VCA were presented in [237,241], with an accurate determination of the position of the MPB. Numerous investigations of structural energetics at $x = 0.5$ using 10-atom supercells with ordering along [001], [110] and [111] have been reported in [169, 186, 237, 242, 243], the earliest being [244]. The tetragonal

$P4mm$ structure is found to be lowest in energy for all three orderings, though rotational distortions are found to be competitive even at $x = 0.50$ and play an increasingly important role as the proportion of Zr increases [167, 169]. The computed polarization is $0.70\,\mathrm{C/m^2}$ for a tetragonal structure with rocksalt ordering of the cations, and $0.74\,\mathrm{C/m^2}$ for Zr and Ti layers alternating along [001] [242]. Computations of piezoelectric coefficients of the supercells give large responses consistent with experiments [186, 242, 245]. The use of much larger supercells in [246] allows a more realistic analysis of the effect of cation arrangement on the local structure and properties.

The recently discovered monoclinic phase [247] acts as a bridge between the tetragonal and rhombohedral phases at the morphotropic phase boundary at $x = 0.48$, with the polarization rotating in the ac plane. This phase also naturally emerged from the effective Hamiltonian phase diagram study of [98]; low-temperature simulations as a function of x show the monoclinic phase for $0.475 \leq x \leq 0.495$, with lattice parameters in excellent agreement with those experimentally determined in [247]. A monoclinic low-symmetry phase also can be produced by the application of tetragonal stress [172, 185, 244]. It is interesting to note that a phase of such low symmetry would not normally arise in a phenomenological Landau–Devonshire analysis, it being necessary to carry the expansion to eighth order [248]. The difficulty in accurately computing T_c with this approach is again illustrated: the computed value for T_c at $x = 0.50$ is greater than 1000 K, a substantial overestimate of the experimental value of 640 K [98]. However, for comparison of other computed properties with experiment, it appears to be useful simply to rescale the temperature. Then, good agreement is obtained between the room-temperature ceramic averaged $d_{33} = 163\,\mathrm{pC/N}$ obtained from the simulation and the value of 170 pC/N measured experimentally, with a substantial contribution from a large single-crystal d_{15}. With particular choices of atomic short-range order, even larger effects can be obtained [249, 250].

Other alloys based on $PbTiO_3$ have also attracted considerable interest for their possibly favorable piezoelectric properties. The system $CdTiO_3$–$PbTiO_3$ was investigated using ordered supercells in [116]. Alloying with Pb expands the lattice, which tends to suppress the rotational instability relative to the ferroelectric instability. This lowers the relative energy of the FE tetragonal state, though the rotationally distorted structure is still the lowest-energy structure at the 50:50 composition $Pb_{0.5}Cd_{0.5}TiO_3$. The system $AgNbO_3$–$PbTiO_3$ was studied in [171]. While pure $AgNbO_3$ is either weak ferroelectric or antiferroelectric, a 40-atom supercell with rocksalt ordering on both A and B sites (constrained to the interpolated experimental volume) shows a relatively small energy difference between the rhombohedral and tetragonal FE phases, suggesting proximity to an MPB and favorable piezoelectric properties.

The scandate perovskites have also featured in the experimental-theoretical search for new piezoelectric materials. The system $BiScO_3$–$PbTiO_3$ (BS–PT) was investigated in [134], using both the VCA and supercells. For

BS−PT, tetragonality and polarization at the MPB, either by VCA or 10-atom rocksalt supercell, are much larger than those measured experimentally, while the computed piezoelectric response near the MPB is comparable to that of PZT. Further substitutions on the A site, including Th, Bi, Y and Pb, were considered in [124]. As Th enters the A site as Th^{4+}, it is introduced with Pb^{2+} to match the formal 3+ of Sc. LDA calculation for cubic rocksalt ordered $Th_{0.5}Pb_{0.5}ScO_3$ yielded an effective perovskite lattice parameter of $7.55a_B$ ($BiScO_3$ and $YScO_3$ had 7.54 and 7.40, respectively). All had lower energy for rotation around [111] than around [001]. $Th_{0.5}Pb_{0.5}ScO_3$ has the tetragonal structure ($c/a = 1.08$) slightly favored over rhombohedral in the 5-atom ferroelectric states. When both rotational and ferroelectric distortions are frozen in, the resulting $R3$ structure has a substantial polarization arising from Th displacement, though the energy is lowered only an additional 2 mRy/Sc below the structure that includes only the rotational distortion. An even lower energy structure is obtained by combining rotations along $[1\bar{1}0]$ and ferroelectric distortion along [110] to obtain a Cm structure, though it is suggested that the low energy of this structure may be specific to the particular Th–Pb rocksalt ordering. Based on these results, it was suggested that it should be possible to favor ferroelectricity in these system by suppressing rotational distortions through the replacement of some A site ions with larger species.

The physics of relaxor ferroelectrics is quite rich, and appears to depend on chemical disorder and polarization fluctuations at a range of length scales. This presents additional technical challenges for first-principles calculations. Recently, aspects of the structure and polarization relevant to relaxor behavior have been studied for PMN in [251–254], $PbSc_{1/2}Nb_{1/2}O_3$ (PSN) [12, 99, 249, 255–257], $PbFe_{1/2}Nb_{1/2}O_3$ [258] and solutions with $PbTiO_3$ [257], including PMN-PT [259], PZN-PT [259] and PSN-PT [260], as well as other solutions, including $Pb(Sc_{2/3}W_{1/3})O_3$−$Pb(Ti_{/}Zr)O_3$ [261]; these and other studies are reviewed in [12]. In PSN and $PbSc_{1/2}Ta_{1/2}O_3$ (PST), the effect of cation arrangement on properties appears to be particularly strong, exemplified by the ferroelectric vs. relaxor behavior for ordered and disordered forms of PST, respectively [262]. Indeed, these effects are evident in first-principles effective Hamiltonian simulations of PSN [12, 99, 249, 255–257]. With the use of very large ($40 \times 40 \times 40$) supercells in [99, 257], the Burns temperature was identified in PSN and PMN, and its pressure dependence analyzed.

The sensitivity of properties to cation arrangement in perovskite oxides, mentioned above, can be exploited to create new classes of artificially structured materials through control of ordering, compositional grading, compositional modulation, and atomic-scale superlattices. The effects of local electric fields, misfit strains, and atomic and electronic rearrangement at the interfaces combine to yield, in some cases, qualititatively new behavior and lend themselves well to first-principles studies. For more information, the reader is referred to recent reviews, including [6, 13, 14].

The discussion above has been for systems with fixed-ion arrangements. With first-principles calculations, it is possible also to probe questions of the ordering of the cations in substitutional solid solutions. Unlike the isovalent solutions, which show random substitution, the cations in heterovalent solutions arrange themselves with significant degrees of short-range order (for example, to favor local charge neutrality) and, in many cases, long-range order. The effects of these arrangements have been discussed above; however, it is also of interest to understand the factors that result in particular arrangements as the material is prepared.

Ion ordering on a fixed sublattice is naturally described by statistical mechanical models, and such models for metal alloys have been highly developed. In alloy theory models that are based on the cluster expansion (CE) technique, a statistical mechanical model is formulated by fitting a set of effective cluster interactions (a CE Hamiltonian) to a set of first-principles formation energies for various cation configurations. The CE Hamiltonian is then used as input for Monte Carlo simulations to search for new low-energy configurations not included in the fit, or to compute finite-temperature phase diagrams. This approach is suitable for application to perovskite oxide phase diagrams, with first-principles determination of the model parameters. For example, the phase diagrams of PST and PST–PT were studied with this approach in [263–265]. The role of electrostatics was highlighted by a model in which only long-range interactions were included [266, 267]. This reproduces very well the ordering observed in systems where the A cation is Ba, such as BZT or BMN–BZ, while the ordering in Pb-based systems deviates from this model. The need for extra short-range terms has been discussed in [268, 269]. This highlights the important role of covalent bonding in these systems, as well as coupling to local distortions and strain.

6 Results for Defects

While defects can play a quite important role in the physics of ferroelectric oxides, they are quite challenging to study using first-principles methods. In particular, the use of very large supercells is generally required, and the defect–defect interaction must be corrected for. Thus, there are relatively few investigations to date; here we review a representative set of papers on point, line and planar defects, mainly oxygen vacancies and domain walls.

Oxygen vacancies in ferroelectric perovskite oxides have been studied from first principles in [129, 270–276]. The influence of oxygen vacancies on other properties, such as magnetization and magnetoelectric effects, has recently been investigated in $BiFeO_3$ [277].

180° and 90° domain walls in $BaTiO_3$ and $PbTiO_3$ were studied using first-principles effective Hamiltonian and full first-principles calculations in [278, 279]. Both types of walls are found to have a thickness of only one to two lattice constants as illustrated in Fig. 6. This is consistent with the

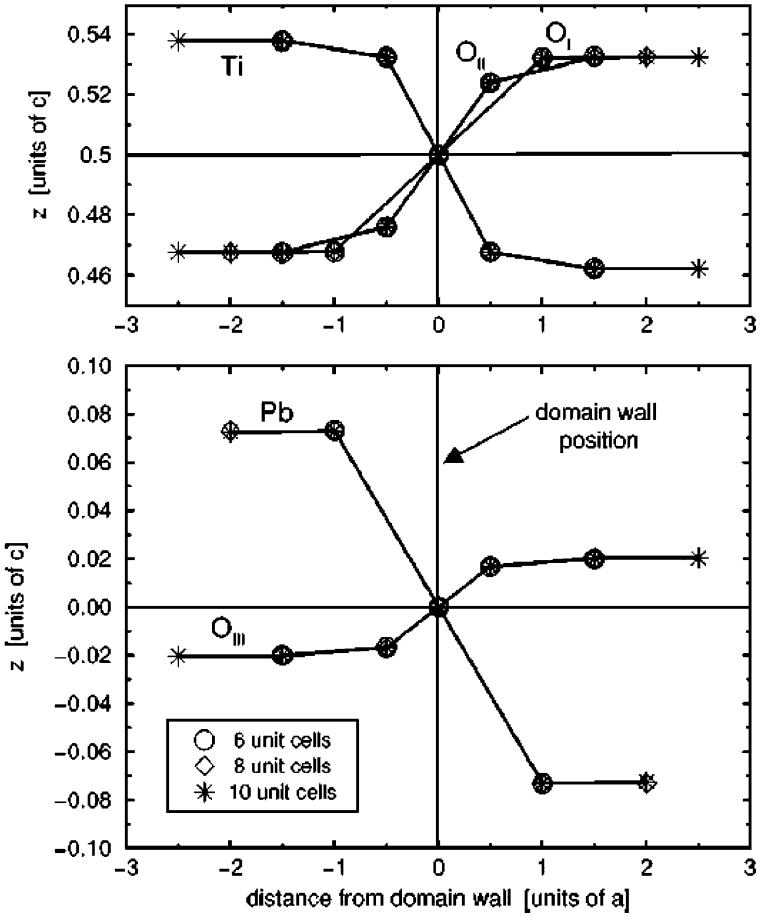

Fig. 6. First-principles description of the evolution of the atomic displacement in the vicinity of a 180° domain wall in $PbTiO_3$. From [279]

calculations presented in [280, 281]. The calculated shift of the atomic planes across the 180° boundary is found to be non-negligible; this may have an impact on the energetics of domain formation in constrained geometries, such as thin films. The interaction of domain walls and oxygen vacancies was studied in [282]. Additional discussion of domain walls, including first-principles results, can be found in the chapters by *P. Chandra* and *P. B. Littlewood* and by *Nicola A. Spaldin* in this volume.

Antiphase boundaries can be considered as a special type of cation ordering, the effects of which have been discussed more generally above, or as a planar defect. The effects on structure and dielectric properties have been studied from first principles in [283, 284].

7 Results for Surfaces, Thin Films, Superlattices, Nanowires and Nanoparticles

One of the most active areas recently in first-principles calculations for ferroelectrics has been in the physics of thin films, superlattices, nanowires and nanoparticles. As this work has been described in detail in several current reviews [6, 8, 10, 13, 14], we will discuss this topic only briefly here.

The physics of free surfaces plays a central role in determining the properties of these systems, due to surface relaxation, reconstruction, and modification of the electrical and mechanical boundary conditions to which the interior is subject. Following procedures established in earlier investigations of semiconductor surfaces, a number of useful surface investigations have been presented, including [50, 285–294]. The polar character of the bulk systems, and of ferroelectric states of the films and particles, requires special attention. For example, as illustrated in Fig. 7, in periodic slab calculations it is necessary to introduce a controlled compensation for the depolarization field in the case that there is a nonzero component of the polarization along the normal to the film [289, 295]; otherwise the large depolarization field will strongly suppress any tendency to a ferroelectric instability.

Recent progress in both experimental and first-principles techniques has led to advances in understanding finite-size effects on ferroelectricity in ultrathin films. Contrary to previous conventional wisdom, perovskite ferroelectric films can sustain a substantial polarization along the normal down to thicknesses of the order of a lattice constant [100, 296], provided that the depolarization field is fully compensated. This has focused attention on the question of the compensation of the depolarization field, its incompleteness for realistic metallic electrodes, and the atomic-scale mechanism for compensation in real systems [297, 298], which continues to stimulate new studies and ideas, for example [102–104, 106, 295, 299, 300]. This involves not only understanding of the effects of free surfaces, but also of the interface and interactions with the substrate, if any. Indeed, there may be interesting physical behavior associated with the substrate, produced by the proximity to the ferroelectric film on it. One example is the ferroelectric field effect [301], and there is evidence also of atomic-scale effects [302] for which first-principles investigation should yield valuable insights. Surface effects are also extremely important in low-dimensional systems such as nanodots and nanowires [162, 303].

The study of ferroelectric multilayers, particularly perovskite superlattices, also has attracted a lot of attention, emphasizing the crucial role of mechanical and electrical boundary conditions. This includes various kinds of "bicolor" superlattices, including $BaTiO_3/SrTiO_3$ [190, 193, 304–306], $PbTiO_3/SrTiO_3$ [191], $KNbO_3/KTaO_3$ [109] and $BaTiO_3/BaO$ [39], as well as tricolor superlattices breaking inversion symmetry ($BaTiO_3/SrTiO_3/CaTiO_3$) [307–310]. Such systems are now also accessible experimentally (see, for example, [311–314] opening the door to the search of artificial materials with tailored properties.

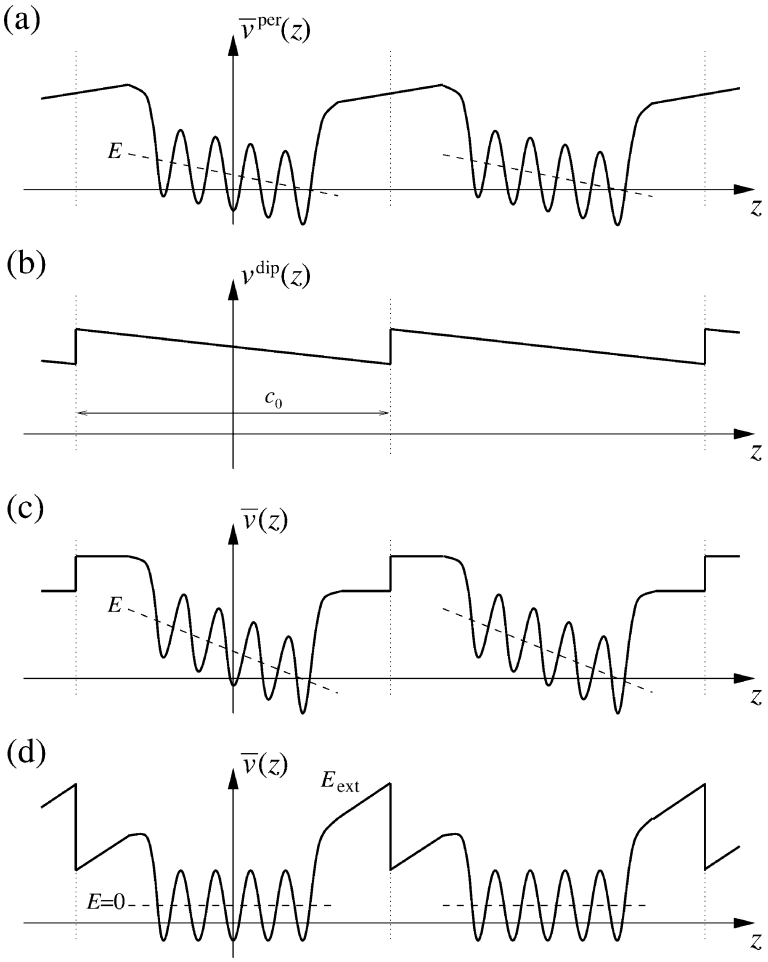

Fig. 7. Schematic representation of the planar averaged electrostatic potential of a slab with a nonvanishing polarization perpendicular to the surface under short-circuit boundary conditions (**a**). A fictitious field to guarantee the continuity of the potential at the boundary of the supercell (*dotted lines*) appears in the supercell. This unphysical field might be compensated by a dipole field (**b**). By tuning the magnitude of the dipole correction properly, adding or subtracting certain amounts to the periodically repeated potential, we can simulate a slab under vanishing displacement field (**c**), or vanishing electric field (**d**) electrical boundary conditions. From [289]

Finite-size effects are expected to be especially important in lower-dimensional ferroelectric nanoscale systems, namely nanowires and nanoparticles, which have been the subject of recent first-principles investigations [103, 104, 162, 303]. Here, as in films, electrostatics plays an essential role in the stability of the ferroelectric state. Electrostatics also has been shown to drive the formation of complex domain and polarization configurations under appropriate boundary conditions, especially in uncompensated small particles [101]. Appropriate treatment of surface relaxation at the atomic scale might also constitute a crucial issue in the study of such ferroelectric nanosystems [162]. First-principles calculations should continue to be extremely valuable to exploring these effects, as well as the effects of the accompanying inhomogeneous strain.

While epitaxial strain has already been discussed above, we should mention again here that because of the large polarization–strain coupling in many perovskite oxide ferroelectrics, this is one of the most important effects in determining the characteristic physics of ferroelectrics in constrained geometries. The interaction of the strain effects with the other factors that contribute to the behavior of thin films should reward further theoretical and experimental study.

8 Challenges and Prospects

The field of first-principles calculations for ferroelectrics has in recent years seen rapid gains in the power of algorithms, of computer resources, and of its conceptual framework. At the same time, experimentalists have made dramatic progress in the synthesis and characterization of complex oxides in general and ferroelectrics in particular, allowing control and measurement on the atomic scale. As already mentioned in the Introduction, these two trends have converged to produce a lively experimental–theoretical dialogue.

The search for new materials is a central focus of this dialogue. As interesting new materials are identified in the laboratory, first-principles methods can be brought to bear to analyze their structure and properties at the atomic scale, and to provide guidance in identifying and exploring related materials. This was the case for PMN−PT and its colossal piezoelectric effects; other new classes of materials that are currently of interest include lead-free piezoelectrics such as $(Na_{1-x}K_x)_{0.5}Bi_{0.5}TiO_3$ [315], novel magnetoelectric multiferroics, and electronic ferroelectrics.

Similarly, first-principles results have come to play an important role in the study of ferroelectricity in constrained geometries at small length scales: thin films, superlattices, nanoparticles and nanowires. The atomic and electronic rearrangements at the surfaces and interfaces, and the strong influence they have on the aggregate properties of the system, can in some cases only directly be probed by such calculations, and more generally are a valuable complement to experimental probes.

Among future challenges for first-principles methods, one of the most relevant to understanding the physical behavior of real ferroelectrics is that of predicting and analyzing dynamical behavior, particularly dielectric loss. This will require development of methods and concepts to deal with the multiscale nature of the defects and microstructure of real ferroelectric materials; such developments are also crucial to the study of other important dynamical phenomena, notably switching. Other properties that arise from electronic excitations, including transport and optical properties, cannot be fully investigated in ground-state density-functional theory, though there may be progress as more powerful methods become developed to the point of being practical for solids as complex as ferroelectrics.

Indeed, new physical ideas and first-principles methods may yet be developed inspired by the needs of studies of ferroelectrics, following the example of the development of the modern theory of polarization. There are still unresolved questions about the application of DFT to polarized systems [181, 316–318], connected to errors in the computed electronic dielectric responses [182] and Born effective charges [316, 319]. Another puzzle is connected to the spurious charge transfer in heterostructures arising from an incorrect conduction-band lineup,[3] apparently inconsistent with the fact that charge density is a ground-state property and thus should be obtainable in a DFT calculation.

From this, we see that there continue to be many new promising research directions, and an increasing integration of first-principles results into the study of the physics of ferroelectrics. Many of the questions raised here in this chapter will be answered in the coming years, and more exciting new systems and puzzles can be expected to emerge and demand lively and vigorous research.

Acknowledgements

Phillipe Ghosez personally acknowledges the support of the VolkswagenStiftung though the project "Nanosized Ferroelectric Hybrids" as well as the European Network of Excellence FAME (Functionalized Advanced Materials Engineering of Hybrids and Ceramics). Karin M. Rabe personally acknowledges the support of ONR grant N00014-00-1-0261. The broader long-term support from ONR for much of the research in the field of first-principles studies of ferroelectrics and piezoelectrics has been one of the most important factors in its development and in many of the papers reviewed here. Much of Karin M. Rabe's work on this review was carried out during a visit to the Materials Department at University of California, Santa Barbara, and at the Aspen Center for Physics. We thank Laurent Bellaiche, Benjamin Burton, Eric Cockayne, Ronald Cohen, Andrew Rappe, David Vanderbilt and Umesh Waghmare for their comments on the manuscript, and Craig Fennie and Eric Bousquet for valuable assistance.

[3] J. Junquera and P. Ghosez, private communication.

References

[1] D. Vanderbilt: First-principles based modeling of ferroelectrics, Curr. Opin. Solid State Mater. Sci. **2**, 701 (1997) 117

[2] L. Bellaiche: Piezoelectricity of ferroelectric perovskites from first principles, Curr. Opin. Solid State Mater. Sci. **6**, 19 (2002) 117

[3] R. Resta: Ab initio simulation of the properties of ferroelectric materials, Modell. Simul. Mater. Sci. Eng. **11**, R69 (2003) 117, 118

[4] R. E. Cohen: Theory of ferroelectrics: A vision for the next decade and beyond, J. Phys. Chem. Solids **61**, 139 (1999) 117, 120

[5] C. H. Ahn, K. M. Rabe, J.-M. Triscone: Ferroelectricity at the nanoscale: Local polarization in oxide thin films and heterostructures, Science **303**, 488 (2004) 117

[6] K. M. Rabe: Theoretical investigations of epitaxial strain effects in ferroelectric oxide thin films and superlattices, Curr. Opin. Solid State Mater. Sci. **9**, 122 (2005) 117, 149, 152

[7] M. Sepliarsky, A. Asthagiri, S. R. Phillpot, M. G. Stachiotti, R. L. Migoni: Atomic-level simulation of ferroelectricity in oxide materials, Curr. Opin. Solid State Mater. Sci. **9**, 107 (2005) 117

[8] I. Ponomareva, I. I. Naumov, I. Kornev, H. Fu, L. Bellaiche: Modelling of nanoscale ferroelectrics from atomistic simulations, Curr. Opin. Solid State Mater. Sci. **9**, 114 (2005) 117, 152

[9] C. Ederer, N. A. Spaldin: Recent progress in first-principles studies of magnetoelectric multiferroics, Curr. Opin. Solid State Mater. Sci. **9**, 128 (2005) 117

[10] I. A. Kornev, H. Fu, L. Bellaiche: Properties of ferroelectric ultrathin films from first principles, J. Mater. Sci. **41**, 137 (2006) 117, 152

[11] U. V. Waghmare, K. M. Rabe: Dielectric properties of simple and complex oxides from first principles, in A. A. Demkov, A. Navrotsky (Eds.): *Materials Fundamentals of Gate Dielectrics* (Springer, New York 2005) 117, 137

[12] B. P. Burton, E. Cockayne, S. Tinte, U. V. Waghmare: First-principles-based simulations of relaxor ferroelectrics, Phase Trans. **79**, 91 (2006) 117, 123, 149

[13] P. Ghosez, J. Junquera: First-principles modeling of ferroelectric oxide nanostructures, in M. Rieth, W. Schommers (Eds.): *Handbook of Theoretical and Computational Nanotechnology*, vol. 7 (ASP, Stevenson Ranch CA 2006) Chap. 13, pp. 623–728 117, 141, 142, 149, 152

[14] M. Dawber, K. M. Rabe, J. F. Scott: Physics of thin-film ferroelectric oxides, Rev. Mod. Phys. **77**, 1083 (2005) 117, 149, 152

[15] R. M. Martin: *Electronic Structure: Basic Theory and Practical Methods* (University Press, Cambridge 2004) 118

[16] R. Dovesi, R. Orlando, C. Roetti, C. Pisani, V. R. Saunders: The periodic Hartree–Fock method and its implementation in the CRYSTAL code, Phys. Stat. Sol. B **217**, 63 (2000) 118

[17] H. Ishida, D. Wortmann, A. Liebsch: Electronic structure of $SrVO_3$(001) surfaces: A local density approximation plus dynamical mean-field theory calculation, Phys. Rev. B **73**, 245421 (2006) 118, 120

[18] X. Gonze, J.-M. Beuken, R. Caracas, F. Detraux, M. Fuchs, G.-M. Rignanese, L. Sindic, M. Verstraete, G. Zerah, F. Jollet, M. Torrent, A. Roy, M. Mikami, P. Ghosez, J.-Y. Raty, D. C. Allan: First-principles computation of material properties: The ABINIT software project, Comput. Mater. Sci. **25**, 478 (2002) URL: `http://www.abinit.org` 118, 120, 121
[19] G. Kresse, J. Furthmüller: Efficient iterative schemes for *ab initio* total-energy calculations using a plane-wave basis set, Phys. Rev. B **54**, 11169 (1996) URL: `http://cms.mpi.univie.ac.at/vasp` 118
[20] S. Baroni, A. Dal Corso, S. de Gironcoli, P. Giannozzi: URL: `http://www.pwscf.org/` 118, 120, 121
[21] J. M. Soler, E. Artacho, J. D. Gale, A. García, J. Junquera, P. Ordejón, D. Sánchez-Portal: The SIESTA method for *ab initio* order-N materials simulation, J. Phys. Condens. Matter **14**, 2745 (2002) URL: `http://www.uam.es/siesta/` 118
[22] P. Blaha, K. Schwarz, G. K. H. Medsen, D. Kvasnicka, J. Luitz: *WIEN2k, An Augmented Plane-Wave + Local-Orbitals Program for Calculating Crystal Properties* (Technische Universität Wien, Austria 2001) URL: `http://www.wien2k.at` 118
[23] V. R. Saunders, R. Dovesi, C. Roetti, M. Causa, N. M. Harrison, R. Orlando, C. M. Zicovich-Wilson: *CRYSTAL'98 User's Manual*, University di Torino, Torino (1998) URL: `http://www.crystal.unito.it/` 118
[24] M. T. Yin, M. L. Cohen: Theory of static structural properties, crystal stability, and phase transformations: Application to Si and Ge, Phys. Rev. B **26**, 5668 (1982) 118
[25] R. P. Feynman: Forces in molecules, Phys. Rev. **56**, 340 (1939) 118
[26] H. Hellmann: *Einführung in die Quantenchemie* (Deuticke, Leipzig 1937) 118
[27] O. H. Nielsen, R. M. Martin: Quantum-mechanical theory of stress and force, Phys. Rev. B **32**, 3780 (1985) 118
[28] R. E. Cohen, H. Krakauer: Lattice dynamics and origin of ferroelectricity in $BaTiO_3$: Linearized-augmented-plane-wave total-energy calculations, Phys. Rev. B **42**, 6416 (1990) 118, 119, 125
[29] R. E. Cohen: Origin of ferroelectricity in perovskite oxides, Nature **358**, 136 (1992) 118, 125, 126, 127, 129, 130
[30] R. D. King-Smith, D. Vanderbilt: A first-principles pseudopotential investigation of ferroelectricity in barium titanate, Ferroelectrics **136**, 85 (1992) 118, 128
[31] K. M. Rabe, U. V. Waghmare: Ferroelectric phase transitions: A first-principles approach, Ferroelectrics **164**, 15 (1994) 118, 122, 140
[32] R. D. King-Smith, D. Vanderbilt: First-principles investigation of ferroelectricity in perovskite compounds, Phys. Rev. B **49**, 5828 (1994) 118, 119, 124, 125, 126, 136
[33] I. Grinberg, N. J. Ramer, A. M. Rappe: Accurate construction of transition metal pseudopotentials for oxides, AIP Conf. Proc. **582**, 211 (2001) 118
[34] H. J. Monkhorst, J. D. Pack: Special points for Brillouin-zone integration, Phys. Rev. B **13**, 5188 (1976) 119
[35] S. Tinte, M. G. Stachiotti, C. O. Rodriguez, D. L. Novikov, N. E. Christensen: Application of the generalized gradient approximation to ferroelectric perovskites, Phys. Rev. B **58**, 11959 (1998) 119, 125

[36] O. Dieguez, K. M. Rabe, D. Vanderbilt: First principles study of epitaxial strain in perovskites, Phys. Rev. B **72**, 144101 (2005) 119, 125, 136
[37] P. Ghosez, X. Gonze, P. Lambin, J. P. Michenaud: Born effective charges of barium titanate: Band-by-band decomposition and sensitivity to structural features, Phys. Rev. B **51**, 6765 (1995) 119, 125, 129, 131, 133
[38] Z. Wu, R. E. Cohen, D. J. Singh: Comparing the weighted density approximation with the LDA and GGA for ground-state properties of ferroelectric perovskites, Phys. Rev. B **70**, 104122 (2004) 119, 125, 126, 127, 128
[39] J. Junquera, M. Zimmer, P. Ordejon, P. Ghosez: First-principles calculation of the band offset at $BaO/BaTiO_3$ and $SrO/SrTiO_3$ interfaces, Phys. Rev. B **67**, 155327 (2003) 119, 152
[40] S. Piskunov, E. Heifets, R. I. Eglitis, G. Borstel: Bulk properties and electronic structure of $SrTiO_3$, $BaTiO_3$, $PbTiO_3$ perovskites: An ab initio HF/DFT study, Comput. Mater. Sci. **29**, 165 (2004) 119, 120, 125
[41] J. Junquera: *Cálculos ab initio de propriedades electrónicas y estructurales de interfases con siluros y titanatos*, PhD thesis, Universidad Autónoma de Madrid, Madrid (2001) 119, 125
[42] Z. Wu, R. E. Cohen: More accurate generalized gradient approximation for solids, Phys. Rev. B **73**, 235116 (2006) 119, 124, 125, 126, 127, 128
[43] N. Marzari, D. J. Singh: Dielectric response of oxides in the weighted density approximation, Phys. Rev. B **62**, 12724 (2000) 119
[44] B. B. van Aken, T. T. M. Palstra, A. Filippetti, N. A. Spaldin: The origin of ferroelectricity in magnetoelectric $YMnO_3$, Nature Mater. **3**, 164 (2004) 119, 145
[45] C. J. Fennie, K. M. Rabe: Ferroelectric transition in $YMnO_3$ from first principles, Phys. Rev. B **72**, 100103 (2005) 119, 145, 146
[46] J. B. Neaton, C. Ederer, U. V. Waghmare, N. A. Spaldin, K. M. Rabe: First-principles study of spontaneous polarization in multiferroic $BiFeO_3$, Phys. Rev. B **71**, 014113 (2005) 119, 133, 134
[47] A. Filippetti, N. A. Spaldin: Strong correlation effects in Born effective charges, Phys. Rev. B **68**, 045111 (2003) 119, 131
[48] S. Dall'Olio, R. Dovesi, R. Resta: Spontaneous polarization as a Berry phase of the Hartree–Fock wave function: The case of $KNbO_3$, Phys. Rev. B **56**, 10105 (1997) 119, 131
[49] L. Fu, E. Yaschenko, L. Resca, R. Resta: Hartree–Fock approach to macroscopic polarization: Dielectric constant and dynamical charges of $KNbO_3$, Phys. Rev. B **57**, 6967 (1998) 119, 131
[50] L. Fu, E. Yaschenko, L. Resca, R. Resta: Hartree–Fock studies of surface properties of $BaTiO_3$, Phys. Rev. B **60**, 2697 (1999) 119, 120, 152
[51] S. Piskunov, E. A. Kotonin, E. Heifets, J. Maier, R. I. Eglitis, G. Borstel: Hybrid DFT calculations of the atomic and electronic structure for ABO_3 perovskite (001) surfaces, Surf. Sci. **575**, 75 (2005) 120
[52] E. Heifets, E. Kotmin, V. A. Trepakov: Calculations for antiferrodistortive phase of $SrTiO_3$ perovskite: Hybrid density-functional study, J. Phys. Condens. Matter **18**, 4845 (2006) 120
[53] F. Cora: The performance of hybrid density-functionals in solid state chemistry: the case of $BaTiO_3$, Mol. Phys. **103**, 2483 (2005) 120

[54] O. E. Kvyatdovskii, F. Karadaq, A. Mamedov, G. A. Zakharov: Cluster ab initio modeling of local lattice instability in relaxor ferroelectrics, Phys. Solid State **46**, 1717 (2004) 120
[55] M. D. Johannes, D. J. Singh: Crystal structure and electric field gradients of $PbZrO_3$ from density-functional calculations, Phys. Rev. B **71**, 21 (2005) 120, 122, 134
[56] R. D. King-Smith, D. Vanderbilt: Theory of polarization of crystalline solids, Phys. Rev. B **47**, 1651 (1993) 120
[57] D. Vanderbilt, R. D. King-Smith: Electric polarization as a bulk quantity and its relation to surface charge, Phys. Rev. B **48**, 4442 (1993) 120
[58] R. Resta: Macroscopic polarization in crystalline dielectrics: The geometric phase approach, Rev. Mod. Phys. **66**, 899 (1994) 120
[59] I. Souza, J. Ìñiguez, D. Vanderbilt: First-principles approach to insulators in finite electric fields, Phys. Rev. Lett. **89**, 117602 (2002) 120
[60] P. Umari, A. Pasquarello: Ab initio molecular dynamics in a finite homogeneous electric field, Phys. Rev. Lett. **89**, 157602 (2002) 120
[61] I. Souza, J. Ìñiguez, D. Vanderbilt: Dynamics of Berry-phase polarization in time-dependent electric fields, Phys. Rev. B **69**, 085106 (2004) 120
[62] O. Dieguez, D. Vanderbilt: First-principles calculations for insulators at constant polarization, Phys. Rev. Lett. **96**, 056401 (2006) 120
[63] X. Wang, D. Vanderbilt: First-principles perturbative computation of phonon properties of insulators in finite electric fields, Phys. Rev. B **74**, 054304 (2006) 120, 139
[64] N. Sai, K. M. Rabe, D. Vanderbilt: Theory of structural response to macroscopic electric fields in ferroelectric systems, Phys. Rev. B **66**, 104108 (2002) 121, 139
[65] I. I. Naumov, H. Fu: Phonon structure in $SrTiO_3$ under finite electric fields: First-principles density-functional approach, Phys. Rev. B **72**, 012304 (2005) 121, 139
[66] H. Fu, L. Bellaiche: First-principles determination of electromechanical responses of solids under finite electric fields, Phys. Rev. Lett. **91**, 057601 (2003) 121
[67] F. Bernardini, V. Fiorentini: Electronic dielectric constants of insulators calculated by the polarization method, Phys. Rev. B **58**, 15292 (1998) 121
[68] S. Baroni, P. Giannozzi, A. Testa: Green's-function approach to linear response in solids, Phys. Rev. Lett. **58**, 1861 (1987) 121
[69] X. Gonze: First-principles responses of solids to atomic displacement and homogeneous electric fields: Implementation of a conjugate-gradient algorithm, Phys. Rev. B **55**, 10337 (1997) 121
[70] X. Gonze, C. Lee: Dynamical matrices, Born effective charges, dielectric permittivity tensors, and interatomic force constants from density-functional perturbation theory, Phys. Rev. B **55**, 10355 (1997) 121
[71] S. Baroni, S. de Gironcoli, A. Dal Corso, P. Giannozzi: Phonons and related crystal properties from density-functional perturbation theory, Rev. Mod. Phys. **73**, 515 (2001) 121
[72] X. Gonze, D. C. Allan, M. P. Teter: Dielectric tensor, effective charges, and phonons in α-quartz by variational density-functional theory, Phys. Rev. Lett. **68**, 3603 (1992) 121

[73] R. Yu, H. Krakauer: Linear-response calculations within the linearized augmented plane-wave method, Phys. Rev. B **49**, 4467 (1994) 121
[74] D. R. Hamann, X. Wu, K. M. Rabe, D. Vanderbilt: Metric tensor formulation of strain in density-functional perturbation theory, Phys. Rev. B **71**, 035117 (2005) 121
[75] D. R. Hamann, X. Wu, K. M. Rabe, D. Vanderbilt: Erratum: Metric tensor formulation of strain in density-functional perturbation theory, Phys. Rev. B **72**, 079901E (2005) 121
[76] D. R. Hamann, K. M. Rabe, D. Vanderbilt: Generalized-gradient-functional treatment of strain in density-functional perturbation theory, Phys. Rev. B **72**, 033102 (2005) 121
[77] P. Ghosez, X. Gonze: Band-by-band decompositions of the Born effective charges, J. Phys. Condens. Matter **12**, 9179–9188 (2000) 121, 130
[78] X. Wu, D. Vanderbilt, D. R. Hamann: Systematic treatment of displacements, strains and electric fields in density-functional perturbation theory, Phys. Rev. B **72**, 035105 (2005) 121, 138, 139
[79] X. Gonze: Perturbation expansion of variational principles at arbitrary order, Phys. Rev. A **52**, 1086 (1995) 121
[80] X. Gonze: Adiabatic density-functional perturbation theory, Phys. Rev. A **52**, 1096 (1995) 121
[81] R. W. Nunes, X. Gonze: Phys. Rev. B **63**, 155107 (2001) 121
[82] M. Veithen, X. Gonze, P. Ghosez: Nonlinear optical susceptibilities, Raman efficiencies, and electro-optic tensors from first-principles density-functional perturbation theory, Phys. Rev. B **71**, 125107 (2005) 121, 139, 144
[83] M. Veithen, X. Gonze, P. Ghosez: First-principles study of the electro-optic effect in ferroelectric oxides, Phys. Rev. Lett. **93**, 187401 (2004) 121, 139, 144
[84] M. Veithen, P. Ghosez: Temperature dependence of the electro-optic tensor and refractive indices of $BaTiO_3$ from first principles, Phys. Rev. B **71**, 132101 (2005) 121, 142
[85] S. A. Prosandeev, U. Waghmare, I. Levin, J. Maslar: First-order Raman spectra of $AB'_{1/2}B_{1/2}O_3$ double perovskites, Phys. Rev. B **71**, 214307 (2005) 121
[86] A. Garcia, D. Vanderbilt: First-principles study of stability and vibrational properties of tetragonal $PbTiO_3$, Phys. Rev. B **54**, 3817 (1996) 122, 128
[87] C. J. Fennie, K. M. Rabe: First-principles investigation of ferroelectricity in epitaxially strained Pb_2TiO_4, Phys. Rev. B **71**, 100102 (2005) 122, 145
[88] U. Waghmare, M. H. F. Sluiter, T. Kimura, T. Goto, Y. Kawazoe: A lead-free high T_c ferroelectric $BaTi_2O_5$: A first-principles study, Appl. Phys. Lett. **84**, 4917 (2004) 122
[89] D. J. Singh: Structure and energetics of antiferroelectric $PbZrO_3$, Phys. Rev. B **52**, 12559 (1995) 122, 125, 134
[90] A. Zunger, S. H. Wei, L. G. Ferreira, J. E. Bernard: Special quasirandom structures, Phys. Rev. Lett. **65**, 353 (1990) 122
[91] K. M. Rabe, J. D. Joannopoulos: Ab initio determination of a structural phase transition temperature, Phys. Rev. Lett. **59**, 570 (1987) 122
[92] K. M. Rabe, J. D. Joannopoulos: Theory of the structural phase transition of GeTe, Phys. Rev. B **36**, 6631 (1987) 122
[93] K. M. Rabe, U. V. Waghmare: First-principles model Hamiltonians for ferroelectric phase transitions, Ferroelectrics **136**, 147 (1992) 122

[94] W. Zhong, D. Vanderbilt, K. M. Rabe: Phase transitions in $BaTiO_3$ from first principles, Phys. Rev. Lett. **73**, 1861 (1994) 122, 140, 141
[95] W. Zhong, D. Vanderbilt, K. M. Rabe: First-principles theory of ferroelectric phase transitions for perovskites: the case of $BaTiO_3$, Phys. Rev. B **52**, 6301 (1995) 122, 140, 141
[96] K. M. Rabe, U. V. Waghmare: Ferroelectric phase transitions from first principles, J. Phys. Chem. Solids **57**, 1397 (1996) 122
[97] U. V. Waghmare, K. M. Rabe: Ab initio statistical mechanics of the ferroelectric phase transition in $PbTiO_3$, Phys. Rev. B **55**, 6161 (1997) 122, 125, 129, 140
[98] L. Bellaiche, A. Garcia, D. Vanderbilt: Finite-temperature properties of $Pb(Zr_{1-x}Ti_x)O_3$ alloys from first principles, Phys. Rev. Lett. **84**, 5427 (2000) 123, 148
[99] B. P. Burton, E. Cockayne, U. V. Waghmare: Correlations between nanoscale chemical and polar order in relaxor ferroelectrics and the lengthscale for polar nanoregions, Phys. Rev. B **72**, 064113 (2005) 123, 149
[100] P. Ghosez, K. M. Rabe: A microscopic model of ferroelectricity in stress-free $PbTiO_3$ ultrathin films, Appl. Phys. Lett. **76**, 2767 (2000) 123, 152
[101] I. I. Naumov, L. Bellaiche, H. Fu: Unusual phase transitions in ferroelectric nanodisks and nanorods, Nature **432**, 737 (2004) 123, 154
[102] I. Kornev, H. Fu, L. Bellaiche: Ultrathin films of ferroelectric solid solutions under residual depolarizing field, Phys. Rev. Lett **93**, 196104 (2004) 123, 152
[103] I. Ponomareva, I. I. Naumov, I. Kornev, H. Fu, L. Bellaiche: Atomistic treatment of depolarizing energy and field in ferroelectric nanostructures, Phys. Rev. B **72**, 140102 (2005) 123, 152, 154
[104] I. Ponomareva, I. I. Naumov, L. Bellaiche: Low-dimensional ferroelectrics under different electrical and mechanical boundary conditions: Atomistic simulations, Phys. Rev. B **72**, 214118 (2005) 123, 152, 154
[105] B.-K. Lai, I. Ponomareva, I. I. Naumov, I. A. Kornev, H. Fu, L. Bellaiche, G. J. Salamo: Electric-field-induced domain evolution in ferroelectric ultrathin films, Phys. Rev. Lett. **96**, 137602 (2006) 123
[106] I. Ponomareva, L. Bellaiche: Influence of the growth direction on properties of ferroelectric ultrathin films, Phys. Rev. B **74**, 064102 (2006) 123, 152
[107] S. Prosandeev, I. Ponomareva, I. Kornev, I. I. Naumov, L. Bellaiche: Controlling toroidal moment by means of an inhomogeneous static field: An ab initio study, Phys. Rev. Lett. **96**, 237601 (2006) 123
[108] H. Bilz, G. Benedek, A. Bussmann-Holder: Theory of ferroelectricity: The polarizability model, Phys. Rev. B **35**, 4840 (1987) 123
[109] M. Sepliarsky, S. R. Phillpot, D. Wolf, M. G. Stachiotti, R. L. Migoni: Long-ranged ferroelectric interactions in perovskite superlattices, Phys. Rev. B **64**, R060101 (2001) 123, 152
[110] S. Tinte, M. G. Stachiotti, M. Sepliarsky, R. L. Migoni, C. O. Rodriguez: Atomistic modeling of $BaTiO_3$ based on first-principles calculations, J. Phys. Condens Matter **11**, 9679 (1999) 123, 140, 141
[111] M. Sepliarsky, Z. Wu, A. Asthagiri, R. E. Cohen: Atomistic model potential for $PbTiO_3$ and PMN by fitting first principles results, Ferroelectrics **501**, 55 (2004) 123, 140

[112] M. Sepliarsky, S. R. Phillpot, D. Wolf, M. G. Stachiotti, R. L. Migoni: Ferroelectric properties of $KNbO_3/KTaO-3$ superlattices by atomic-level simulation, J. Appl. Phys. **90**, 4509 (2001) 123, 140

[113] I. Grinberg, V. R. Cooper, A. M. Rappe: Relationship between local structure and phase transitions of a disordered solid solution, Nature **419**, 909 (2002) 123

[114] Y. H. Shin, V. R. Cooper, I. Grinberg, A. M. Rappe: Development of a bond-valence molecular-dynamics model for complex oxides, Phys. Rev. B **71**, 054104 (2005) 123

[115] A. V. Postnikov, T. Neumann, G. Borstel: Phonon properties of $KNbO_3$ and $KTaO_3$ from first-principles calculations, Phys. Rev. B **50**, 758 (1994) 125

[116] S. V. Halilov, M. Fornari, D. J. Singh: Lattice instabilities in (Pb,Cd)TiO_3 alloys, Appl. Phys. Lett. **81**, 3443 (2002) 125, 134, 148

[117] P. Ghosez, E. Cockayne, U. V. Waghmare, K. M. Rabe: Lattice dynamics of $BaTiO_3$, $PbTiO_3$, and $PbZrO_3$: A comparative first-principles study, Phys. Rev. B **60**, 836 (1999) 125, 134, 135

[118] R. Khenata, M. Sahnoun, H. Baltache, M. Re, A. H. Rashek, N. Illes, B. Bouhafs: First-principles calculations of structural, electronic and optical properties of $BaTiO_3$ and $BaZrO_3$ under hydrostatic pressure, Solid State Commun. **136**, 120 (2005) 125

[119] R. Terki, H. Feraoun, G. Bertrand, H. Aourag: Full potential calculations of structural, elastic and electronic properties of $BaZrO_3$ and $SrZrO_3$, Phys. Stat. Sol. B **242**, 1054 (2005) 125

[120] G. Fabricus, E. L. Peltzer y Blanca, C. O. Rodriguez, A. P. Ayala, P. de la Presa, A. Lopez Garcia: Electronic structure of cubic $SrHfO_3$: Ferroelectric stability and detailed comparison with $SrTiO_3$, Phys. Rev. B **55**, 164 (1997) 125

[121] R. V. Shpanchenko, V. V. Chernaya, A. A. Tsirlin, P. S. Chizhov, D. E. Sklovsky, E. V. Antipov, E. P. Khlybov, V. Pomjakushin, A. M. Balagurov, J. E. Medvedeva, E. E. Kaul, C. Geibel: Synthesis, structure and properties of new perovskite $PbVO_3$, Chem. Mater. **16**, 3267 (2004) 125, 127

[122] A. A. Belik, M. Azuma, T. Saito, Y. Shimakawa, M. Takano: Crystallographic features and tetragonal phase stability of $PbVO_3$, a new member of $PbTiO_3$ family, Chem. Mater **17**, 269 (2005) 125, 127

[123] P. Baettig, C. F. Schelle, R. LeSar, U. V. Waghmare, N. A. Spaldin: Theoretical prediction of new high-performance lead-free piezoelectrics, Chem. Mater. **17**, 1376 (2005) 124, 125, 127, 129, 131, 134

[124] S. V. Halilov, M. Fornari, D. J. Singh: Lattice instabilities and ferroelectricity in $AScO_3$ perovskite alloys, Phys. Rev. B **69**, 174107 (2004) 125, 135, 149

[125] W. Zhong, D. Vanderbilt: Competing structural instabilities in perovskites, Phys. Rev. Lett. **74**, 2587 (1995) 126, 134, 143

[126] C. Lasota, C. Z. Wang, R. C. Yu, H. Krakauer: Ab initio linear response study of $SrTiO_3$, Ferroelectrics **194**, 109 (1997) 126, 131, 134

[127] P. Ghosez, D. Desquesnes, X. Gonze, K. M. Rabe: First-principles study of lattice instabilities in $Ba_xSr_{1-x}TiO_3$, in R. E. Cohen (Ed.): *Fundamental Physics of Ferroelectrics 2000*, AIP Conference Proceedings **535** (American Institute of Physics, Woodbury, New York 2000) pp. 102–110 126, 134, 135

[128] N. Sai, D. Vanderbilt: First-principles study of ferroelectric and antiferrodistortive instabilities in tetragonal $SrTiO_3$, Phys. Rev. B **62**, 13942 (2000) 126, 134
[129] K. Uchida, S. Tsuneyuki, T. Schimizu: First-principles calculations of carrier-doping effects in $SrTiO_3$, Phys. Rev. B **68**, 174107 (2003) 126, 150
[130] G. Shirane, H. Danner, P. Pepinsky: Neutron diffraction study of orthorhombic $BaTiO_3$, Phys. Rev. **105**, 856 (1957) 128
[131] F. Jona, G. Shirane: *Ferroelectric Crystals* (Dover, New York 1993) 128
[132] S. Tinte, K. M. Rabe, D. Vanderbilt: Anomalous enhancement of tetragonality in $PbTiO_3$ induced by negative pressure, Phys. Rev. B **68**, 144105 (2003) 127
[133] C. Ederer, N. A. Spaldin: Effect of epitaxial strain on the spontaneous polarization of thin film ferroelectrics, Phys. Rev. Lett. **95**, 257601 (2005) 127, 137
[134] J. Ìñiguez, D. Vanderbilt, L. Bellaiche: First-principles study of $(BiScO_3)_{1-x}$–$(PbTiO_3)_x$ piezoelectric alloys, Phys. Rev. B **67**, 224107 (2003) 127, 135, 148
[135] W. Cochran: Crystal stability and the theory of ferroelectricity, Adv. Phys. **9**, 387 (1960) 127, 130
[136] P. W. Anderson: in G. Skanavi (Ed.): *Fizika Dielectrikov* (Akad. Nauk, Moscow 1960) 127
[137] K. M. Rabe: *Lattice Instabilities of Complex Perovskite Oxides from First Principles*, Computer Simulation Studies in Condensed Matter Physics XVI, Springer Proceedings in Physics (Springer, New York 2003) 127
[138] W. A. Harrison: *Electronic Structure and the Properties of Solids* (Dover, New York 1980) 129, 131
[139] V. V. Nemoshkalenko, A. N. Timoshevskii: The peculiarities of the electronic structure of $BaTiO_3$ in the $ATiO_3$ (A = Ca, Sr, Ba) series, Phys. Stat. Sol. B **127**, 163 (1985) 129
[140] L. T. Hudson, R. L. Kurtz, S. W. Robey, D. Temple, R. L. Stockbauer: Photoelectron spectroscopic study of the valence and core-level electronic structure of $BaTiO_3$, Phys. Rev. B **47**, 1174 (1994) 129
[141] F. M. Michel-Calendini, H. Chermette, J. Weber: Molecular orbital studies of ABO_3 perovskites by the SCF-MS-Xα method: local densities of states, chemical bonding and optical transitions, J. Phys. C **13**, 1427 (1980) 129
[142] W. Zhong, R. D. King-Smith, D. Vanderbilt: Giant LO–TO splittings in perovskite ferroelectrics, Phys. Rev. Lett. **72**, 3618 (1994) 129, 131, 132, 133
[143] Y. X. Wang, W. L. Zhong, C. L. Wang, P. L. Zhang: First-principles study of the electronic structure of $NaTaO_3$, Solid State Commun. **120**, 137 (2001) 129
[144] M. Posternak, R. Resta, A. Baldereschi: Role of covalent bonding in the polarization of perovskite oxides: The case of $KNbO_3$, Phys. Rev. B **50**, 8911 (1994) 129
[145] R. Seshadri, N. A. Hill: Visualizing the role of Bi 6*s* lone pairs in the off-center distortion in ferromagnetic $BiMnO_3$, Chem. Mater. **13**, 2892 (2001) 130
[146] P. Ghosez, X. Gonze, J.-P. Michenaud: Coulomb interaction and ferroelectric instability of $BaTiO_3$, Europhys. Lett. **33**, 713 (1996) 130
[147] G. A. Samara: Pressure and temperature dependence of the dielectric properties and phase transitions of the ferroelectric perovskites: $PbTiO_3$ and $BaTiO_3$, Ferroelectrics **2**, 277 (1971) 130

[148] P. Ghosez, J.-P. Michenaud, X. Gonze: Dynamical effective charges: The case of ABO_3 compounds, Phys. Rev. B **58**, 6224 (1998) 131, 133
[149] J. D. Axe: Apparent ionic charges and vibrational eigenmodes of $BaTiO_3$ and other perovskites, Phys. Rev. **157**, 429 (1967) 131
[150] R. Resta, M. Posternak, A. Baldereschi: Towards a quantum theory of polarization in ferroelectrics: The case of $KNbO_3$, Phys. Rev. Lett. **70**, 1010 (1993) 131, 132
[151] R. Yu, H. Krakauer: First-principles determination of chain-structure instability in $KNbO_3$, Phys. Rev. Lett. **74**, 4067 (1995) 131, 133, 135, 143
[152] F. Detraux, P. Ghosez, X. Gonze: Anomalously large Born effective charges in cubic WO_3, Phys. Rev. B **56**, 983 (1997) 131
[153] P. Ghosez, X. Gonze, J. P. Michenaud: First-principles calculations of dielectric and effective charge tensors in barium titanate, Ferroelectrics **153**, 91 (1994) 131
[154] T. Mitsui, S. Nomura, M. Adachi, J. Harada, T. Ikeda, E. Nakamura, E. Sawaguchi, T. Shigenari, Y. Shiozagi, J. Tatsuzaki, K. Toyoda, T. Yamada, K. Gesi, Y. Marita, M. Marutake, T. Shiosaki, K. Wakino: *Oxides, Landolt–Börnstein Numerical Data and Functional Relationships in Science and Technology, Group III*, vol. 16, Pt. A (Springer, Berlin 1981) 132
[155] T. Mitsui, M. Adachi, Y. Akishige, K. Deguchi, J. Harada, T. Ikeda, M. Okuyama, E. Sawaguchi, Y. Shiozaki, K. Toyoda, T. Yamada, K. Gesi, T. Hikita, Y. Makita, T. Shigenari, I. Tatsuzaki, T. Yahi: *Oxides, Landolt–Börnstein Numerical Data and Functional Relationships in Science and Technology, Group III*, vol. 28, Pt. A (Springer, Berlin 1990) 132
[156] G. Sághi-Szabó, R. E. Cohen, H. Krakauer: First-principles study of piezoelectricity in $PbTiO_3$, Phys. Rev. Lett. **80**, 4321 (1998) 132, 139
[157] C.-Z. Wang, R. Yu, H. Krakauer: Polarization dependence of Born effective charge and dielectric constant in $KNbO_3$, Phys. Rev. B **54**, 11161 (1996) 133
[158] R. Pick, M. H. Cohen, R. M. Martin: Microscopic theory of force constants in the adiabatic approximation, Phys. Rev. B **1**, 910 (1970) 133
[159] P. Gianozzi, S. de Gironcoli, P. Pavone, S. Baroni: Ab initio calculation of phonon dispersions in semiconductors, Phys. Rev. B **43**, 7231 (1991) 133
[160] C. Kittel: *Introduction to Solid State Physics*, 7th ed. (Wiley, New York 1996) 133
[161] P. Ghosez, J.-P. Michenaud, X. Gonze: Lattice dynamics and ferroelectric instability of barium titanate, Ferroelectrics **194**, 39 (1997) 133, 138
[162] G. Geneste, E. Bousquet, J. Junquera, P. Ghosez: Finite-size effects in $BaTiO_3$ nanowires, Appl. Phys. Lett. **88**, 112906 (2006) 134, 152, 154
[163] E. Cockayne, P. Ghosez, K. M. Rabe: private communication 134, 135
[164] A. R. Akbarzadeh, I. Kornev, C. Malibert, L. Bellaiche, J. M. Kiat: Combined theoretical and experimental study of the low-temperature properties of $BaZrO_3$, Phys. Rev. B **72**, 205104 (2005) 134, 135, 143
[165] J. W. Bennett, I. Grinberg, A. M. Rappe: Effect of symmetry lowering on the dielectric response of $BaZrO_3$, Phys. Rev. B **73**, 180102 (2006) 134, 135
[166] R. A. Cowley: Lattice dynamics and phase transitions of $SrTiO_3$, Phys. Rev. **134**, A981 (1964) 135
[167] K. Leung, E. Cockayne, A. F. Wright: Effective Hamiltonian study of $PbZr_{0.95}Ti_{0.05}O_3$, Phys. Rev. B **65**, 214111 (2002) 134, 148

[168] U. V. Waghmare, K. M. Rabe: Lattice instabilities, anharmonicity and phase transitions in $PbZrO_3$ from first principles, Ferroelectrics **194**, 135 (1997) 134
[169] M. Fornari, D. J. Singh: Possible coexistence of rotational and ferroelectric lattice distortions in rhombohedral $PbZr_xTi_{1-x}O_3$, Phys. Rev. B **63**, 092101 (2001) 134, 147, 148
[170] E. Cockayne, B. P. Burton: Phonons and static dielectric constant in $CaTiO_3$ from first principles, Phys. Rev. B **62**, 3735 (2000) 134, 138
[171] I. Grinberg, A. M. Rappe: Silver solid solution piezoelectrics, Appl. Phys. Lett. **85**, 1760 (2004) 134, 148
[172] Z. Wu, R. E. Cohen: Pressure-induced anomalous phase transitions and colossal enhancement of piezoelectricity in $PbTiO_3$, Phys. Rev. Lett. **95**, 037601 (2005) 136, 139, 140, 148
[173] I. A. Kornev, L. Bellaiche, P. Bouvier, P. E. Janolin, B. Dkhil, J. Kreisel: Ferroelectricity of perovskites under pressure, Phys. Rev. Lett. **95**, 196804 (2005) 136
[174] I. A. Kornev, L. Bellaiche: The nature of ferroelectricity under pressure cond-mat/0608530 136
[175] S. Tinte, J. Ìñiguez, K. M. Rabe, D. Vanderbilt: Quantitative analysis of the first-principles effective Hamiltonian approach to ferroelectric perovskites, Phys. Rev. B **67**, 064106 (2003) 136, 141
[176] J. Ìñiguez, D. Vanderbilt: First-principles study of the temperature-pressure phase diagram of $BaTiO_3$, Phys. Rev. Lett. **89**, 115503 (2002) 137, 143
[177] N. A. Pertsev, A. G. Zembilgotov, A. K. Tagantsev: Effect of mechanical boundary conditions on phase diagrams of epitaxial ferroelectric thin films, Phys. Rev. Lett. **80**, 1988 (1998) 137, 139, 143
[178] O. Dieguez, S. Tinte, A. Antons, C. Bungaro, J. B. Neaton, K. M. Rabe, D. Vanderbilt: Ab initio study of the phase diagram of epitaxial $BaTiO_3$, Phys. Rev. B **69**, 212101 (2004) 137, 143
[179] A. Antons, J. B. Neaton, K. M. Rabe, D. Vanderbilt: Tunability of the dielectric response of epitaxially strained $SrTiO_3$ from first principles, Phys. Rev. B **71**, 024102 (2005) 137, 139
[180] H. N. Lee, S. M. Nakhmanson, M. F. Chisholm, H. M. Christen, K. M. Rabe, D. Vanderbilt, D. H. Lowndes: Suppressed dependence of polarization on epitaxial strain in highly polar ferroelectrics, Phys. Rev. Lett. **98**, 217602 (2007) 137
[181] X. Gonze, P. Ghosez, R. W. Godby: Density-polarization functional theory of the response of a periodic insulating solid to an electric field, Phys. Rev. Lett. **74**, 4035 (1995) 138, 155
[182] P. Ghosez, X. Gonze, R. W. Godby: The long wavelength behavior of the exchange-correlation kernel in the Kohn–Sham theory of periodic systems, Phys. Rev. B **56**, 12811 (1997) 138, 155
[183] E. Cockayne: First-principles calculations of the dielectric properties of perovskite-type materials, J. Eur. Ceram. Soc. **23**, 2375 (2003) 138
[184] D. Vanderbilt: Berry-phase theory of proper piezoelectric response, J. Phys. Chem. Solids **61**, 147 (2000) 139
[185] C. Bungaro, K. M. Rabe: Epitaxially strained $[001](PbTiO_3)_1(PbZrO_3)_1$ superlattice and $PbTiO_3$ from first principles, Phys. Rev. B **69**, 184101 (2004) 139, 148

[186] Z. Wu, H. Krakauer: First-principles calculations of piezoelectricity and polarization rotation in $Pb(Zr_{0.5}Ti_{0.5})O_3$, Phys. Rev. B **68**, 014112 (2003) 139, 147, 148
[187] H. Fu, R. E. Cohen: Polarization rotation mechanism for ultrahigh electromechanical response in single-crystal piezoelectrics, Nature **403**, 281 (2000) 139
[188] L. Bellaiche, A. Garcia, D. Vanderbilt: Electric-field induced polarization paths in $Pb(Zr_{1-x}Ti_x)O_3$ alloys, Phys. Rev. B **64**, 060103 (2001) 139
[189] S. E. Park, T. E. Shrout: Ultrahigh strain and piezoelectric behavior in relaxor based ferroelectric single crystals, J. Appl. Phys. **82**, 1804 (1997) 139
[190] J. B. Neaton, K. M. Rabe: Theory of polarization enhancement in epitaxial $BaTiO_3/SrTiO_3$ superlattices, Appl. Phys. Lett. **82**, 1586 (2003) 140, 152
[191] M. Dawber, C. Lichtensteiger, M. Cantoni, M. Veithen, P. Ghosez, K. Johnston, K. M. Rabe, J.-M. Triscone: Unusual behavior of ferroelectric polarization in $PbTiO_3/SrTiO_3$ superlattices, Phys. Rev. Lett. **95**, 177601 (2005) 140, 152
[192] S. Rios, A. Ruediger, A. Q. Jiang, J. F. Scott, H. Lu, Z. Chen: Orthorhombic strontium titanate in $BaTiO_3$–$SrTiO_3$ superlattices, J. Phys. Condens. Matter **15**, L305 (2003) 140
[193] K. Johnston, X. Y. Huang, J. B. Neaton, K. M. Rabe: First-principles study of symmetry lowering and polarization in $BaTiO_3/SrTiO_3$ superlattices with in-plane expansion, Phys. Rev. B **71**, 100103 (2005) 140, 152
[194] R. Car, M. Parrinello: Unified approach for molecular dynamics and density-functional theory, Phys. Rev. Lett. **55**, 2471 (1985) 140
[195] V. Srinivasan, R. Gebauer, R. Resta, R. Car: $PbTiO_3$ at finite temperature, in P. K. Davies, D. J. Singh (Eds.): *Fundamental Physics of Ferroelectrics 2003* (AIP, Melville, NY 2003) 140
[196] K. M. Rabe, U. V. Waghmare: Strain coupling in the $PbTiO_3$ ferroelectric transition, Philos. Trans. Roy. Soc. Lond. **A354**, 2897 (1996) 141
[197] K. M. Rabe, E. Cockayne: Temperature-dependent dielectric and piezoelectric response of ferroelectrics from first principles, in R. E. Cohen (Ed.): *First-Principles Calculations for Ferroelectrics*, AIP Conference Proceedings 436 (American Institute of Physics, Woodbury, New York 998) p. 61 141
[198] A. Garcia, D. Vanderbilt: Electromechanical behavior of $BaTiO_3$ from first principles, Appl. Phys. Lett. **72**, 2981 (1998) 141
[199] J. Ìñiguez, S. Ivantchev, J. M. Perez-Mato, A. Garcia: Devonshire–Landau free energy of $BaTiO_3$ from first principles, Phys. Rev. B **63**, 144103 (2001) 142
[200] R. Comes, M. Lambert, A. Guinier: The chain structure of $BaTiO_3$ and $KNbO_3$, Solid State Commun. **6**, 715 (1968) 143
[201] N. A. Pertsev, A. G. Zembilgotov, A. K. Tagantsev: Equilibrium states and phase transitions in epitaxial ferroelectric thin films, Ferroelectrics **223**, 79 (1999) 143
[202] A. Akbarzadeh, L. Bellaiche, K. Leung, J. Íñiguez, D. Vanderbilt: Atomistic simulations of the incipient ferroelectric $KTaO_3$, Phys. Rev. B **70**, 054103 (2004) 143
[203] J. W. Flocken, R. A. Guenther, J. R. Hardy, L. L. Boyer: First-principles study of structural instabilities in halide-based perovskites: Competition between ferroelectricity and ferroelasticity, Phys. Rev. B **31**, 7252 (1985) 143

[204] S. Koval, J. Kohanoff, R. L. Migoni, A. Bussman-Holder: Interplay between proton ordering and ferroelectric polarization in H-bonded KDP-type crystals, Comput. Mater. Sci. **22**, 87 (2001) 143
[205] S. Koval, J. Kohanoff, R. L. Migoni, E. Tosatti: Ferroelectricity and isotope effects in hydrogen-bonded KDP crystals, Phys. Rev. Lett. **89**, 187602 (2002) 143
[206] S. M. Nakhmanson, M. Buongiorno Nardelli, J. Bernholc: Ab-initio studies of polarization and piezoelectricity in vinylidene fluoride and BN-based polymers, Phys. Rev. Lett. **92**, 115504 (2004) 143
[207] S. M. Nakhmanson, M. B. Nardelli, J. Bernholc: Collective polarization effects in b-polyvinylidene fluoride and its copolymers with tri- and tetrafluoroethylene, Phys. Rev. B **72**, 115210 (2005) 143
[208] I. Inbar, R. E. Cohen: Comparison of the electronic structure and energetics of ferroelectric $LiNbO_3$ and $LiTaO_3$, Phys. Rev. B **53**, 1193 (1996) 144
[209] I. Inbar, R. E. Cohen: Origin of ferroelectricity in $LiNbO_3$ and $LiTaO_3$, Ferroelectrics **194**, 83 (1997) 144
[210] K. Parlinski, Z. Q. Li, Y. Kawazoe: Ab initio calculations of phonons in $LiNbO_3$, Phys. Rev. B **61**, 272 (2000) 144
[211] V. Caciuc, A. V. Postnikov, G. Borstel: Ab initio structure and zone-center phonons in $LiNbO_3$, Phys. Rev. B **61**, 8806 (2000) 144
[212] M. Veithen, P. Ghosez: Dielectric and dynamical properties of lithium niobate, Phys. Rev. B **65**, 214302 (2002) 144
[213] M. Veithen, X. Gonze, P. Ghosez: Electron localization: Band-by-band decomposition and application to oxides, Phys. Rev. B **66**, 235113 (2002) 144
[214] J. Ìñiguez, A. Garcia, J. M. Perez-Mato: First-principles study of the structural instabilities in hexagonal barium titanate, Ferroelectrics **237**, 329 (2000) 144
[215] J. Ìñiguez, A. Garcia, J. M. Perez-Mato: Analysis of soft optical modes in hexagonal $BaTiO_3$: Transference of perovskite local distortions, J. Phys. Condens. Matter **12**, L387 (2000) 144
[216] K. Kam, J. H. Henkel: Calculated polarization and piezoelectric constants of $NaNO_2$, Phys. Rev. B **17**, 1361 (1978) 144
[217] F. Ishii, T. Oguchi: First-principles calculation of spontaneous polarization and phase stability in $NaNO_2$, J. Phys. Soc. Jpn. **71**, 336 (2002) 144
[218] Y. Noel, M. Catti, R. Dovesi: Ab initio calculation of piezoelectric and ferroelectric properties of $NaNO_2$, Ferroelectrics **300**, 139 (2004) 144
[219] M. Catti, Y. Noel, R. Dovesi: Theoretical study of sodium nitrite piezoelectricity and elasticity, J. Phys. Condens. Matter **17**, 4833 (2005) 144
[220] O. Dieguez, D. Vanderbilt: First-principles calculations at constant polarization, Phys. Rev. Lett. **96**, 056401 (2006) 144
[221] M. Q. Cai, Z. Yin, M.-S. Zhang, Y. Li: Electronic structure of the ferroelectric-layered perovskite bismuth titanate by calculation within density-functional theory, Chem. Phys. Lett. **399**, 89 (2004) 144
[222] M. Q. Cai, Z. Yin, M.-S. Zhang, Y. Li: First-principles study of ferroelectric and non-linear optical properties in bismuth titanate, Chem. Phys. Lett. **401**, 405 (2005) 144
[223] M. G. Stachiotti, C. O. Rodriguez, C. Ambrosch-Draxl, N. E. Christensen: Electronic structure and ferroelectricity in $SrBi_2Ta_2O_9$, Phys. Rev. B **61**, 14434 (2000) 144

[224] J. M. Perez-Mato, M. Aroyo, A. Garcia, P. Blaha, K. Schwarz, J. Schweifer, K. Parlinski: Competing structural instabilities in the ferroelectric Aurivillius compounds, Phys. Rev. B **70**, 214111 (2004) 144
[225] A. Snedden, K. S. Knight, P. Lightfoot: Structural distortions in the layered perovskites $CsANb_2O_7$ (A = Nd, Bi), J. Solid State Chem. **173**, 309 (2003) 145
[226] C. J. Fennie, K. M. Rabe: Ferroelectricity in the Dion–Jacobson $CsBiNb_2O_7$ from first principles, Appl. Phys. Lett. **88**, 262902 (2006) 145
[227] N. A. Hill: Why are there so few magnetic ferroelectrics?, J. Phys. Chem. B **104**, 6694 (2000) 145
[228] A. K. Kundu, S. B. Krupanidhi, U. V. Waghmare, C. N. R. Rao: Biferroic $YCrO_3$, Phys. Rev. B **72**, 220101 (2005) 145
[229] P. Baettig, C. Ederer, N. A. Spaldin: First principles study of the multiferroics $BiFeO_3$, Bi_2FeCrO_6, and $BiCrO_3$: Structure, polarization and ferromagnetic ordering temperature, Phys. Rev. B **72**, 214105 (2005) 145
[230] P. Baettig, N. A. Spaldin: Ab initio prediction of a multiferroic with large polarization and magnetization, Appl. Phys. Lett. **86**, 012505 (2005) 145
[231] C. Ederer, N. A. Spaldin: Origin of ferroelectricity in the multiferroic barium fluorides $BaMF_4$: A first principles study, Phys. Rev. B **74**, 024102 (2006) 145
[232] N. Ikeda, H. Ohsumi, K. Ohwada, K. Ishii, T. Inami, K. Kakurai, Y. Murakami, K. Yoshii, S. Mori, Y. Horibe, H. Kito: Ferroelectricity from iron valence ordering in the charge-frustrated system $LuFe_2O_4$, Nature **436**, 1136 (2005) 145
[233] T. Thonhauser, K. M. Rabe: fcc breathing instability in $BaBiO_3$ from first principles, Phys. Rev. B **73**, 212106 (2006) 145
[234] S. C. Abrahams: Systematic prediction of new ferroeletrics in space group R3, I, Acta Cryst. B **62**, 26 (2006) 146
[235] E. Kroumova, M. I. Aroyo, J. M. Perez-Mato: Prediction of new displacive ferroelectrics through systematic pseudosymmetry search: Results for materials with *Pba*2 and *Pmc*2(1) symmetry, Acta Crystallogr. B **58**, 921 (2002) 146
[236] C. Capialls, M. I. Aroyo, J. M. Perez-Mato: Search for new *Pna*2(1) ferroelectrics, Ferroelectrics **301**, 203 (2004) 146
[237] N. J. Ramer, A. M. Rappe: Virtual-crystal approximation that works: Locating a compositional phase boundary in $Pb(Zr_{1-x}Ti_x)O_3$, Phys Rev. B **62**, 743 (2000) 147
[238] C. Bungaro, K. M. Rabe: unpublished 147
[239] L. Walizer, S. Lisenkov, L. Bellaiche: Finite-temperature properties of (Ba,Sr)TiO_3 systems from atomistic simulations, Phys. Rev. B **73**, 144105 (2006) 147
[240] S. Tinte, M. G. Stachiotti, S. R. Phillpot, M. Sepliarsky, D. Wolf, R. L. Migoni: Ferroelectric properties of $Ba_xSr_{1-x}TiO_3$ solid solutions obtained by molecular dynamics simulation, J. Phys. Condens. Matter **16**, 3495 (2004) 147
[241] N. J. Ramer, A. M. Rappe: Application of a new virtual crystal approach for the study of disordered perovskites, J. Phys. Chem. Solids **61**, 315 (2000) 147

[242] G. Sáhi-Szabó, R. E. Cohen, H. Krakauer: First-principles study of piezoelectricity in tetragonal $PbTiO_3$ and $PbZr_{0.5}Ti_{0.5}O_3$, Phys. Rev. B **59**, 12771 (1999) 147, 148
[243] C. Bungaro, K. M. Rabe: Lattice instabilities of $PbZrO_3/PbTiO_3$[1:1] superlattices from first principles, Phys. Rev. B **65**, 224106 (2002) 147
[244] N. J. Ramer, S. P. Lewis, E. J. Mele, A. M. Rappe: Stress-induced phase transition in $PbZr_{0.5}Ti_{0.5}O_3$, AIP Conf. Proc. **436**, 156 (1998) 147, 148
[245] L. Bellaiche, D. Vanderbilt: Intrinsic piezoelectric response in perovskite alloys: PMN–PT versus PZT, Phys. Rev. Lett. **83**, 1347 (1999) 148
[246] I. Grinberg, V. R. Cooper, A. M. Rappe: Oxide chemistry and local structure of $PbZr_xTi_{1-x}O_3$ studied by density-functional theory supercell calculations, Phys. Rev. B **69**, 144118 (1–17) (2004) 148
[247] B. Noheda, D. E. Cox, G. Shirane, J. A. Gonzalo, L. E. Cross, S. E. Park: A monoclinic ferroelectric phase in the $Pb(Zr_{1-x}Ti_x)O_3$ solid solution, Appl. Phys. Lett. **74**, 2059 (1999) 148
[248] D. Vanderbilt, M. H. Cohen: Monoclinic and triclinic phases in higher-order Devonshire theory, Phys. Rev. B **63**, 094108 (2001) 148
[249] A. M. George, J. Ìñiguez, L. Bellaiche: Anomalous properties in ferroelectrics induced by atomic ordering, Nature **413**, 54 (2001) 148, 149
[250] A. M. George, J. Ìñiguez, L. Bellaiche: Effects of atomic short-range order on the properties of perovskite alloys in their morphotropic phase boundary, Phys. Rev. Lett. **91**, 045504 (2003) 148
[251] S. Tinte, K. M. Rabe, D. Vanderbilt: unpublished 149
[252] S. A. Prosandeev, E. Cockayne, B. P. Burton, S. Kamba, J. Petzelt, Y. Yuzyuk, R. S. Katiyar, S. B. Vakhrushev: Lattice dynamics in $PbMg_{1/3}Nb_{2/3}O_3$, Phys. Rev. B **70**, 134110 (2004) 149
[253] N. Choudhury, Z. G. Wu, E. J. Walter, R. E. Cohen: Ab initio linear response and frozen phonons for the relaxor $PbMg_{1/3}Nb_{2/3}O_3$, Phys. Rev. B **71**, 125134 (2005) 149
[254] N. Choudhury, R. E. Cohen, E. J. Walter: First principles studies of the Born effective charges and electronic dielectric tensors for the relaxor PMN, Comput. Mater. Sci. **37**, 152 (2006) 149
[255] R. Hemphill, L. Bellaiche, A. Garcia, D. Vanderbilt: Finite-temperature properties of disordered and ordered $Pb(Sc_{0.5}Nb_{0.5})O_3$ alloys, Appl. Phys. Lett. **77**, 3642 (2000) 149
[256] U. V. Waghmare, E. J. Cockayne, B. P. Burton: Ferroelectric phase transitions in nano-scale chemically ordered $PbSc_{0.5}Nb_{0.5}O_3$ using a first principles model Hamiltonian, Ferroelectrics **291**, 187 (2003) 149
[257] S. Tinte, B. P. Burton, E. Cockayne, U. V. Waghmare: Origin of the relaxor state in $Pb(B_xB'_{1-x})O_3$ perovskites, Phys. Rev. Lett. **97**, 137601 (2006) 149
[258] W. Bhat, A. M. Umarji, V. B. Shenoy, U. V. Waghmare: Diffuse ferroelectric phase transitions in Pb-substituted $PbFe_{1/2}Nb_{1/2}O_3$, Phys. Rev. B **72**, 014104 (2005) 149
[259] I. Grinberg, A. M. Rappe: Local structure and macroscopic properties in $PbMg_{1/3}Nb_{2/3}O_3$–$PbTiO_3$ and $PbMg_{1/3}Zn_{2/3}O_3$–$PbTiO_3$ solid solutions, Phys. Rev. B **70**, 220101 (2004) 149

[260] R. Haumont, A. Al-Barakaty, B. Dkhil, J. M. Kiat, L. Bellaiche: Morphotropic phase boundary of heterovalent perovskite solid solutions: Experimental and theoretical investigation of $PbSc_{1/2}Nb_{1/2}O_3$−$PbTiO_3$, Phys. Rev. B **71**, 104106 (2005) 149

[261] P. Juhás, I. Grinberg, A. M. Rappe, W. Dmowski, T. Egami, P. K. Davies: Correlations between the structure and dielectric properties of $Pb(Sc_{\frac{2}{3}}W_{\frac{1}{3}})O_3$–$Pb(Ti/Zr)O_3$ relaxors, Phys. Rev. B **69**, 214101 (2004) 149

[262] N. Setter, L. E. Cross: The role of B-site cation disorder in diffuse phase transition behavior of perovskite ferroelectrics, J. Appl. Phys. **51**, 4356 (1980) 149

[263] B. P. Burton, R. E. Cohen: Theoretical study of cation ordering in the system $Pb(Sc_{0.5}Ta_{0.5})O_3$, Ferroelectrics **151**, 331 (1994) 150

[264] B. P. Burton, R. E. Cohen: Nonempirical calculation of the $Pb(Sc_{0.5}Ta_{0.5})O_3$−$PbTiO_3$ quasi-binary phase diagram, Phys. Rev. B **52**, 792 (1995) 150

[265] B. P. Burton: Empirical cluster expansion models of cation order-disorder in $A(B'_{1/3}B_{2/3})O_3$ perovskites, Phys. Rev. B **59**, 6087 (1999) 150

[266] L. Bellaiche, D. Vanderbilt: Electrostatic model of atomic ordering in complex perovskite alloys, Phys. Rev. Lett. **81**, 1318 (1998) 150

[267] L. Bellaiche, J. Padilla, D. Vanderbilt: Heterovalent and A-atom effects in A(B'B)O_3 perovskite alloys, Phys. Rev. B **59**, 1834 (1999) 150

[268] B. P. Burton, E. Cockayne: Why Pb(B,B')O_3 perovskites disorder at lower temperatures than Ba(B,B')O_3 perovskites, Phys. Rev. B **60**, 12542 (1999) 150

[269] Z. Wu, H. Krakauer: Charge transfer electrostatic model of compositional order in perovskite alloys, Phys. Rev. B **63**, 184113 (2001) 150

[270] R. I. Eglitis, N. E. Christensen, E. A. Kotomin, A. V. Postnikov, G. Borstel: First-principles and semiempirical calculations for F centers in $KNbO_3$, Phys. Rev. B **56**, 8599 (2001) 150

[271] E. A. Kotomin, R. I. Eglitis, A. V. Postnikov, G. Borstel, N. E. Christensen: First-principles and semiempirical calculations for bound-hole polarons in $KNbO_3$, Phys. Rev. B **60**, 1 (1999) 150

[272] R. Astala, P. D. Bristowe: Ab initio and classical simulations of defects in $SrTiO_3$, Comput. Mater. Sci. **22**, 81 (2001) 150

[273] H. Crogman, L. Bellaiche: Properties of vacancy-rich ordered (A,[ ])Nb_2O_6 perovskites, Phys. Rev. B **66**, 220103 (2002) 150

[274] E. Cockayne, B. P. Burton: Dipole moment of a Pb−O vacancy pair in $PbTiO_3$, Phys. Rev. B **69**, 144116 (2004) 150

[275] J. P. Buban, H. Iddir, S. Ogut: Structural and electronic properties of oxygen vacancies in cubic and antiferrodistortive phases of $SrTiO_3$, Phys. Rev. B **69**, 180102 (2004) 150

[276] W. D. Luo, W. H. Duan, S. G. Louie, M. L. Cohen: Structural and electronic properties of n-doped and p-doped $SrTiO_3$, Phys. Rev. B **70**, 214109 (2004) 150

[277] C. Ederer, N. A. Spaldin: Influence of strain and oxygen vacancies on the magnetoelectric properties of multiferroic bismuth ferrite, Phys. Rev. B **71**, 224103 (2005) 150

[278] J. Padilla, W. Zhong, D. Vanderbilt: First principles investigation of 180° domain walls in $BaTiO_3$, Phys. Rev. B **53**, 5969 (1996) 150
[279] B. Meyer, D. Vanderbilt: Ab initio study of ferroelectric domain walls in $PbTiO_3$, Phys. Rev. B **65**, 104111 (2002) 150, 151
[280] S. Poykko, D. J. Chadi: Ab initio study of 180° domain wall energy and structure in $PbTiO_3$, Appl. Phys. Lett. **75**, 2830 (1999) 151
[281] S. Poykko, D. J. Chadi: Ab initio study of dipolar defects and 180° domain walls in $PbTiO_3$, J. Phys. Chem. Solids **61**, 291 (2000) 151
[282] L. He, D. Vanderbilt: First-principles study of oxygen-vacancy pinning of domain walls in $PbTiO_3$, Phys. Rev. B **68**, 134103 (2003) 151
[283] H. Li, H. Zheng, L. Salamanca-Riba, R. Ramesh, I. I. Naumov, K. Rabe: Origin of antiphase domain boundaries and their effect on the dielectric constant of $Ba_{0.5}Sr_{0.5}TiO_3$ films grown on MgO substrates, Appl. Phys. Lett. **81**, 4398 (2002) 151
[284] I. A. Kornev, L. Bellaiche: Planar defects and incommensurate phases in highly ordered perovskite solid solutions, Phys. Rev. Lett. **89**, 115502 (2002) 151
[285] R. E. Cohen: Periodic slab LAPW computations for ferroelectric $BaTiO_3$, J. Phys. Chem. Solids **57**, 1393 (1996) 152
[286] J. Padilla, D. Vanderbilt: Ab initio study of $BaTiO_3$ surfaces, Phys. Rev. B **56**, 1625 (1997) 152
[287] F. Cora, C. R. A. Catlow: QM investigations on perovskite-structured transition metal oxides: Bulk, surfaces and interfaces, Faraday Discuss. **114**, 421 (1999) 152
[288] E. Heifets, E. A. Kotomin, J. Maier: Semi-empirical simulations of surface relaxation for perovskite titanates, Surf. Sci. **462**, 19 (2000) 152
[289] B. Meyer, D. Vanderbilt: Ab initio study of $BaTiO_3$ and $PbTiO_3$ surfaces in external electric fields, Phys. Rev. B **63**, 205426 (2001) 152, 153
[290] E. Heifets, R. I. Eglitis, E. A. Kotomin, J. Maier, G. Borstel: Ab initio modeling of surface structure for $SrTiO_3$ perovskite crystals, Phys. Rev. B **64**, 235417 (2001) 152
[291] S. Tinte, M. G. Stachiotti: Surface effects and ferroelectric phase transitions in $BaTiO_3$ ultrathin films, Phys. Rev. B **64**, 235403 (2001) 152
[292] M. Krcmar, C. L. Fu: Structural and electronic properties of $BaTiO_3$ slabs: Mechanism for surface conduction, Phys. Rev. B **68**, 115404 (2003) 152
[293] K. Johnston, M. R. Castell, A. T. Paxton, M. W. Finnis: $SrTiO_3(001)(2)$ reconstructions: First-principles calculations of surface energy and atomic structure compared with scanning tunneling microscopy images, Phys. Rev. B **70**, 085415 (2004) 152
[294] M. Sepliarsky, M. G. Stachiotti, R. L. Migoni: Surface reconstruction and ferroelectricity in $PbTiO_3$ thin films, Phys. Rev. B **72**, 14110 152
[295] A. M. Kolpak, N. Sai, A. M. Rappe: Electrostatic boundary conditions in ferroelectric $PbTiO_3$ thin films, Phys. Rev. B **74**, 054112 (2006) 152
[296] T. Tybell, C. H. Ahn, J.-M. Triscone: Ferroelectricity in thin perovskite films, Appl. Phys. Lett. **75**, 856 (1999) 152
[297] M. Dawber, P. Chandra, P. B. Littlewood, J. F. Scott: Depolarization corrections to the coercive field in thin-film ferroelectrics, J. Phys. Condens. Matter **15**, 393 (2003) 152

[298] J. Junquera, P. Ghosez: Critical thickness for ferroelectricity in perovskite ultrathin films, Nature **422**, 506 (2003) 152
[299] N. Sai, A. M. Kolpak, A. M. Rappe: Ferroelectricity in ultrathin perovskite films, Phys Rev. B **72**, 020101 (2005) 152
[300] D. D. Fong, A. M. Kolpak, J. A. Eastman, S. K. Streiffer, P. H. Fuoss, G. B. Stephenson, C. Thompson, D. M. Kim, K. J. Choi, C. B. Eom, I. Grinberg, A. M. Rappe: Stabilization of monodomain polarization in ultrathin $PbTiO_3$ films, Phys. Rev. Lett. **96**, 127601 (2006) 152
[301] C. H. Ahn, J. M. Triscone, N. Archibald, M. Decroux, R. H. Hammond, T. H. Geballe, O. Fischer, M. R. Beasley: Ferroelectric field-effect in epitaxial thin-film oxide $SrCuO_2/Pb(Zr_{0.5}Ti_{0.48})O_3$ heterostructures, Science **269**, 373 (1995) 152
[302] D. D. Fong, C. Cionca, Y. Yacoby, G. B. Stephenson, J. A. Eastman, P. H. Fuoss, S. K. Streiffer, R. Pindak, E. A. Stern: Direct structural determination in ultrathin ferroelectric films by analysis of synchrotron X-ray scattering measurements, Phys. Rev. B **71**, 144112 (2005) 152
[303] J. E. Spanier, A. M. Kolpak, J. J. Urban, W. S. Yun, L. Ouyang, I. Grinberg, A. M. Rappe, H. Park: Ferroelectric phase transition in individual single-crystalline $BaTiO_3$ nanowires, Nano Lett. **6**, 735 (2006) 152, 154
[304] L. Kim, J. Kim, D. Jung, J. Lee, U. V. Waghmare: Polarization of strained $BaTiO_3/SrTiO_3$ artificial superlattice: First principles study, Appl. Phys. Lett. **87**, 052903 (2005) 152
[305] L. Kim, J. Kim, U. V. Waghmare, D. Jung, J. Lee: Structural transition and dielectric response of an epitaxially strained $BaTiO_3/SrTiO_3$ superlattice: A first principles study, Phys. Rev. B **72**, 214121 (2005) 152
[306] L. Kim, J. Kim, U. V. Waghmare, D. G. Jung, J. Lee: Lattice instabilities of $BaTiO_3/SrTiO_3$ artificial superlattice, Integrated Ferroelectrics **73**, 3 (2005) 152
[307] N. Sai, B. Meyer, D. Vanderbilt: Compositional inversion symmetry breaking in ferroelectric perovskites, Phys. Rev. Lett. **84**, 5636 (2000) 152
[308] M. P. Warusawithana, E. V. Colla, J. N. Eckstein, M. B. Weissman: Artificial dielectric superlattices with broken inversion symmetry, Phys. Rev. Lett. **90**, 036802 (2003) 152
[309] S. M. Nakhmanson, K. M. Rabe, D. Vanderbilt: Predicting polarization enhancement in multicomponent ferroelectric superlattices, Phys. Rev. B **73**, 060101 (2006) 152
[310] S. M. Nakhmanson, K. M. Rabe, D. Vanderbilt: Polarization enhancement in two- and three-component ferroelectric superlattices, Appl. Phys. Lett. **87**, 102906 (2005) 152
[311] M. P. Warusawithana, E. V. Colla, J. N. Eckstein, M. B. Weissman: Artificial dielectric superlattices with broken inversion symmetry, Phys. Rev. Lett. **90**, 036802 (2003) 152
[312] H. N. Lee, H. M. Christen, M. F. Chisholm, C. M. Rouleau, D. H. Lowndes: Strong polarization enhancement in asymmetric three-component ferroelectric superlattices, Nature **433**, 395 (2005) 152
[313] A. Q. Jiang, J. F. Scott, H. Lu, Z. Chen: Phase transitions and polarizations in epitaxial $BaTiO_3/SrTiO_3$ superlattices studied by second-harmonic generation, J. Appl. Phys. **93**, 1180 (2003) 152

[314] W. Tian, J. C. Jiang, X. Q. Pan, J. H. Haeni, Y. L. Li, L. Q. Chen, D. G. Schlom, J. B. Neaton, K. M. Rabe, Q. X. Jia: Structural evidence for enhanced polarization in a commensurate short-period $BaTiO_3/SrTiO_3$ superlattice, Appl. Phys. Lett. **89**, 092905 (2006) 152
[315] J. Kreisel, A. M. Glazer, G. Jones, P. A. Thomas, L. Abello, G. Lucazeau: An X-ray diffraction and Raman spectroscopy investigation of A-site substituted perovskite compounds, J. Phys. Condens. Matter **12**, 3267 (2000) 154
[316] X. Gonze, P. Ghosez, R. Godby: Density-functional theory of polar insulators, Phys. Rev. Lett. **78**, 294 (1997) 155
[317] R. Resta: Density-polarization-functional theory and long-range correlation in dielectrics, Phys. Rev. Lett. **77**, 2265 (1996) 155
[318] R. Ortiz, I. Souza, R. M. Martin: Exchange-correlation hole in polarized insulators: Implications for the microscopic functional theory of dielectrics, Phys. Rev. Lett. **80**, 353 (1998) 155
[319] R. Resta, S. Sorella: Many-body effects on polarization and dynamical charges in a partly covalent polar insulator, Phys. Rev. Lett. **74**, 4738 (1995) 155

Index

Analogies and Differences between Ferroelectrics and Ferromagnets

Nicola A. Spaldin

Materials Department, University of California,
Santa Barbara, CA 93106-5050, USA
nicola@mrl.ucsb.edu

ferro

Fer"ro A prefix, or combining form, indicating ferrous iron as an ingredient; as, ferrocyanide.

[From Latin ferrum, *iron.*]

Source: *Webster's Revised Unabridged Dictionary, (c) 1996, 1998 MICRA, Inc.*

Abstract. We describe the similarities and differences between ferromagnets – materials that have a spontaneous magnetization that is switchable by an applied magnetic field – and ferroelectrics, which have an analogous electric-field switchable electric polarization. After comparing the driving force for ion off-centering that causes the polarization in ferroelectrics with the physics of spin polarization that causes the magnetization of ferromagnets, we analyze the mechanisms of domain formation and resulting domain structures in both material classes. We describe the emerging technologies of ferroelectric and magnetoresistive random access memories, and discuss the behavior of magnetoelecric multiferroics, which combine ferromagnetism and ferroelectricity in the same phase.

The "ferro" part in the name "ferroelectric" is something of a misnomer, since it does not refer to the presence of iron in ferroelectric materials. Rather it arises from the many similarities in behavior between ferroelectrics, with their spontaneous electric polarization, and ferromagnets, with their spontaneous magnetization. Indeed one of the earliest observations of ferroelectricity ([1]) describes the electric hysteresis in Rochelle salt as "analogous to the magnetic hysteresis in the case of iron." A systematic comparison between the behavior of ferromagnets and ferroelectrics, does not, to our knowledge, exist in the literature. The purpose of this chapter is to outline the similarities in behavior between ferromagnets and ferroelectrics, and, perhaps more importantly, to point out the differences in their fundamental physics and consequent applications. We hope that the comparison will be useful both to readers with a background in ferroelectrics, who can benefit from the

K. Rabe, C. H. Ahn, J.-M. Triscone (Eds.): Physics of Ferroelectrics: A Modern Perspective,
Topics Appl. Physics **105**, 175–218 (2007)

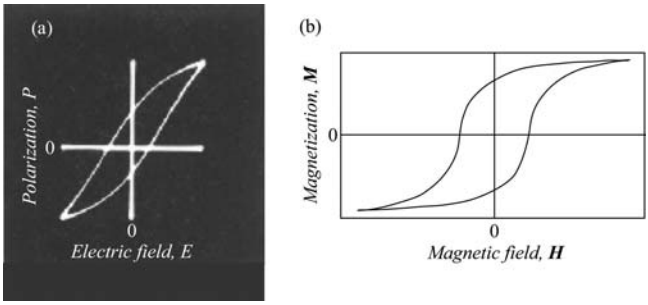

Fig. 1. Comparison of hysteresis loops in (**a**) $BaTiO_3$, a typical ferroelectric [2] (copyright (1950) by the American Physical Society), and (**b**) Fe, a typical ferromagnet [3]. Note that the forms of the hysteresis curves are rather similar in the two cases

techniques, concepts and applications developed in the more mature field of ferromagnetism, as well as ferromagnetism researchers learning about ferroelectrics. We feel that such a discussion is particularly timely in light of the flurry of recent interest in so-called *multiferroic materials*, which are simultaneously ferromagnetic and ferroelectric.

Superficially there are indeed many similarities between ferroelectrics and ferromagnets. Let us start with the basic definition; a ferroelectric is defined to be a material with a spontaneous electric polarization that is switchable by an applied electric field. Likewise, a ferromagnet has a spontaneous magnetization that can be reoriented by an external magnetic field. (Note that in this chapter we will use "polarization" as a generic term to describe both magnetic and electric polarization.) Usually the switching process is associated with a hysteresis, which can be very similar in form in the two cases (Fig. 1). And often a change in the polarization orientation is accompanied by a change in shape. In both cases the macroscopic polarization can be reduced to zero by the presence of *domains*; that is regions of oppositely oriented (and therefore canceling) polarization within the sample. Both ferromagnetic and ferroelectric polarization decrease with increasing temperature, with a phase transition to an unpolarized (paramagnetic or paraelectric) state often occurring at high temperature. Of course, the microscopic features that lead to ferromagnetism and ferroelectricity are quite distinct; ferroelectrics have an asymmetry in *charge* (either ionic or electronic or both), whereas ferromagnets have an asymmetry in electronic *spin*.

On the applications front, the coupling between the polarization order parameter and the lattice strain leads to the properties of piezomagnetism in ferromagnets and piezoelectricity in ferroelectrics. Piezoelectric effects tend to be larger than piezomagnetic, and so ferroelectric piezoelectrics dominate in transducer and actuator technologies. In addition, the hysteresis that causes the spontaneous polarization to persist in the absence of an applied field leads to storage applications in which the direction of either electric or magnetic

polarization represents the "1" or "0" of the data bit. Here, magnetic materials have the largest market share, for example in computer hard disks, and magnetic tape, although ferroelectrics are an upcoming technology for information storage.

This contribution is organized as follows: In Sect. 1 (Fundamentals) we compare the fundamental driving force for ion offcentering that causes the electric polarization in ferroelectrics with the physics of spin-polarization that results in the magnetization of ferromagnets. In addition, we compare the domain structures, and mechanisms of domain formation in ferromagnets and ferroelectrics. In Sect. 2 (Applications) we focus on the use of ferromagnets and ferroelectrics in random access memory (RAM) devices, and compare the emerging technologies of ferroelectric RAM and magnetoresistive RAM. Finally, in Sect. 3 (Multiferroics) we discuss the rather limited class of materials known as magnetoelectric multiferroics that are both ferromagnetic and ferroelectric.

1 Fundamentals

1.1 Understanding the Origin of Spontaneous Polarization

In this section we outline the mechanisms that cause some materials to be either magnetically or electrically polarized, while most are not. We will see that, in spite of the similarities in the macroscopic phenomena described as ferromagnetism or ferroelectricity, the electron-level details that lead to electric or magnetic polarization arise from quite different origins.

1.1.1 What Causes Ferroelectricity?

In order for a material to exhibit a spontaneous electric polarization it must have a noncentrosymmetric arrangement of the constituent ions and their corresponding electrons. To be classified as a ferroelectric, the electric polarization must in addition be switchable, and so a nonreconstructive transition between two stable states of opposite polarization must be accessible at known experimental fields. In this section we review the origins of ionic offcentering in known ferroelectrics, and show that, in most cases, the polar phase is stabilized by energy-lowering chemical-bond formation. Note that a permanent noncentrosymmetric arrangement of the ions is insufficient; some noncentrosymmetric structures, such as the wurtzite structure (Fig. 2), do not permit ferroelectricity since they can not be switched at known experimental electric fields.

Second-Order Jahn–Teller Ferroelectrics

Many ferroelectric structures can be considered to be derivatives of a nonpolar, centrosymmetric prototype phase, of which the most widely studied

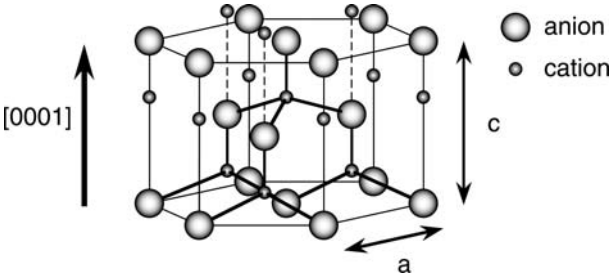

Fig. 2. Materials such as ZnO and GaN, which adopt the noncentrosymmetric wurtzite structure shown here, have spontaneous electric polarization but are not ferroelectric since they do not switch in response to an applied electric field

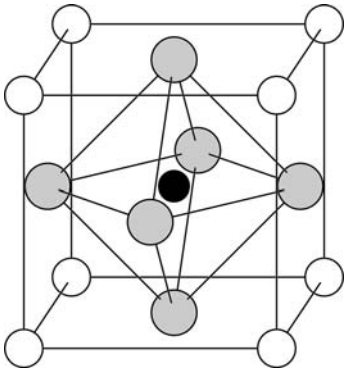

Fig. 3. The centrosymmetric cubic perovskite structure. The small B cation (*in black*) is at the center of an octahedron of oxygen anions (*in gray*). The large A cations (*white*) occupy the unit-cell corners

example is the perovskite structure shown in Fig. 3. The noncentrosymmetric structure is reached by shifting either the A or B cations (or both) offcenter relative to the oxygen anions, and the spontaneous polarization derives largely from the electric dipole moment created by this shift.

If the bonding in an ideal cubic perovskite were entirely ionic, and the ionic radii were of the correct size to ensure ideal packing, then the structure would remain centrosymmetric, and therefore not ferroelectric. This is because, although long-range Coulomb forces favor the ferroelectric state, the short-range repulsions between the electron clouds of adjacent ions are minimized for nonpolar, cubic structures [4, 5]. The existence or absence of ferroelectricity is determined by a *balance* between these short-range repulsions, that favor the nonferroelectric symmetric structure, and additional bonding considerations which act to stabilize the distortions necessary for the ferroelectric phase [6]. The changes in chemical bonding that stabilize distorted structures have long been recognized in the field of coordination chemistry, and are classified as *second-order Jahn–Teller* effects [7–9], or sometimes *pseudo-Jahn–Teller* effects [10], in the chemistry literature.

The origin of the second-order, or pseudo-, Jahn–Teller effect can be seen by writing down a perturbative expansion of the energy of the electronic ground state, $E(Q)$, as a function of the coordinate of the distortion, Q [11]:

$$E(Q) = E(0) + \langle 0|(\delta H/\delta Q)_0|0\rangle Q + \frac{1}{2}\left(\langle 0|(\delta^2 H/\delta Q^2)_0|0\rangle - 2\sum_n' \frac{|\langle 0|(\delta H/\delta Q)_0|n\rangle|^2}{E_n - E(0)}\right) Q^2 + \cdots . \quad (1)$$

Here, $E(0)$ is the energy of the undistorted ground state, and the E_ns are the excited-state energies. The term that is linear in Q is the first-order Jahn–Teller contribution, which is nonzero only for degenerate states. This term is responsible for the characteristic tetragonal distortions in d^1 and d^4 perovskites, for example. Of the second-order terms, the first, $\langle 0|(\delta^2 H/\delta Q^2)_0|0\rangle$, is always positive, whereas the second, $-2\Sigma_n' \frac{|\langle 0|(\delta H/\delta Q)_0|n\rangle|^2}{E_n - E(0)}$ is always negative, provided that it is nonzero. If the second term is larger than the first, then a distortion will cause a second-order reduction in energy. The first term describes the increase in energy on distortion, in the absence of redistribution of the electrons, and is dominated by the Coulomb repulsions between electron clouds. Therefore, it is smallest for closed-shell ions that lack spatially extended valence electrons. Two criteria must be satisfied for the second term to be large. First, the energy denominator, $E_n - E(0)$, must be small, therefore there must be low-lying excited states available. Second, the matrix element $\langle 0|(\delta H/\delta Q)_0|n\rangle$ must be nonzero; this occurs if the product of the symmetry representations for the ground and excited state and the distortion is totally symmetric. Thus, for a noncentrosymmetric distortion, if the ground state is centrosymmetric, then the lowest excited state must be noncentrosymmetric. Note that this term represents the mixing of the ground state with the excited states as a result of the distorting perturbation, and as such is associated with the formation of new chemical bonds in the low-symmetry configuration [12]. A noncentrosymmetric distortion then results if the lowering in energy associated with the mixing of term two is larger than the repulsion opposing the ion shift, described by term one [13].

The effect results in two common and subtly different kinds of ferroelectric distortions. The first is the ligand-field stabilization of the perovskite B-site transition-metal cation by its surrounding anions, as occurs, for example, at the Ti site in $BaTiO_3$. Here, the centrosymmetric, formally d^0 transition metal mixes in oxygen p character as it displaces towards an oxygen ion or group of ions [14] causing an energy-lowering rehybridization. The calculated change in electronic structure associated with the distortion, in particular the strong downshift of the bottom of the valence band, is shown in Fig. 4. At the same time, Ti^{4+} is a closed-shell ion, and so the increase in Coulomb repulsion associated with its offcentering is small, thus a noncentrosymmetric distortion is energetically favorable. The second is driven by stereochemical activity of ns^2 "lone pairs" of electrons, which mix in some cation and anion p character

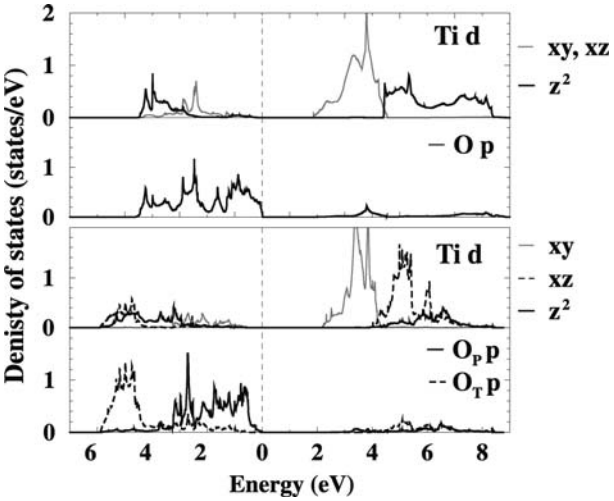

Fig. 4. Calculated orbital resolved densities of states in $BaTiO_3$. The *upper panels* show the Ti d and oxygen p densities of states in cubic paraelectric $BaTiO_3$. The *lower panels* show the densities of states in the same orbitals after the Ti ion is displaced in the z-direction towards the "on-top" oxygen, O_T, in a stylized ferroelectric phase transition. Note the strong increase in hybridization and shift down in energy of the on-top oxygen and the Ti orbitals oriented along the direction of the displacement (d_{xz} and d_z^2). The in-plane oxygens, O_P, and the other Ti d orbitals are largely unaffected. From [14]. Copyright (2002) by the American Physical Society

and thereby lose their center of symmetry. This "stereochemical activity of the lone pair" is the driving force for offcenter distortion in the group IV chalcogenides [15] (for example GeTe). The lone pair can be clearly seen in the right panel of Fig. 5, which shows the calculated electron-localization function [16] of GeTe in the high-symmetry rocksalt structure (left) and the rhombohedral ferroelectric structure (right). Sometimes, both mechanisms occur in the same material, for example in $PbTiO_3$, where the activity of the lead ion [17] causes a strain that stabilizes the tetragonal phase over the rhombohedral phase seen in $BaTiO_3$ [4, 18].

Note that we have so far only considered whether the ions will offcenter at a *local* level; whether or not the local distortions line up (to form a ferroelectric phase) or oppose (to give a structure that is sometimes described as *anti*ferroelectric) depends on other factors, which will be discussed later in the chapter.

Geometrically Driven Ferroelectrics

Note that very few perovskites exist in the ideal cubic structure shown in Fig. 3, and in fact even those that are not ferroelectric have symmetry-lowering distortions from the ideal structure. Of particular relevance here

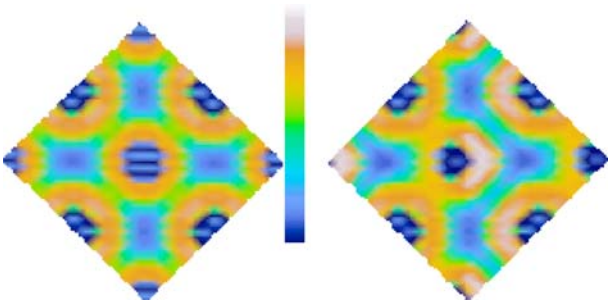

Fig. 5. Calculated valence-electron localization functions (ELFs) in GeTe in the high-symmetry rocksalt structure (*left*) and the rhombohedral ferroelectric structure (*right*). Lighter colors indicate regions of strong electron localization, and darker colors signify poor localization, with the scale bar between the plots running from ELF values = 0.0 to1.0. The Ge atom is at the center of the picture. The lone pair localizes as the Ge atom moves offcenter (to the left) in the ferroelectric structure, and is seen as a lobe-shaped region of high electron localization to the right of the Ge atom. From [15]. Copyright (2003) by the American Physical Society

are rotations, often called "Glazer tilts", of the oxygen octahedra, in which the octahedra are largely undistorted and their corner-sharing connectivity is maintained [19–21]. Such rotations do not result in a ferroelectric state in cubic perovskites, since a rotation of an octahedron in one direction forces its neighbors to rotate in the opposite direction; this retains the center of symmetry (see the sketch in Fig. 6). However, when they occur in materials with different lattice structures and symmetries they can indeed lead to a ferroelectric ground state. Since the driving force for the symmetry-lowering distortion is purely geometric (the ions are not the correct size to exactly maintain the high-symmetry phase) and there is minimal change in chemical bonding between the high-symmetry and ferroelectric phases, we call such materials geometrically driven ferroelectrics. Examples include hexagonal yttrium manganite [22] and tris-sarcosine calcium chloride, $(CH_3NHCH_2COOH)_3CaCl_2$ [23].

Long-Range Ordering

Given the occurrence of local offcentering of the ions, described above, the primary driving force for the long-range cooperative ordering that yields the net ferroelectric polarization is the dipole–dipole interaction. This interaction is analagous to the quantum-mechanical exchange, discussed below, which drives long-range ordering of the magnetic moments in ferromagnets. It has been computed using first-principles density-functional methods for $BaTiO_3$ [24, 25].

In some cases, however, competing effects overcome the dipole–dipole interaction's tendency to promote ferroelectric ordering, and even when the

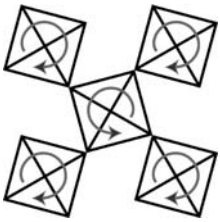

Fig. 6. Tilting of the oxygen octahedra in cubic perovskites (schematic). Notice that when the central octahedron rotates clockwise, its neighbors in the plane are required to rotate anticlockwise in order to maintain the connectivity. As a result the final structure is nonpolar

ions are locally offcentered, they order such that their dipole moments cancel out and there is no net polarization; such behavior is sometimes classified as antiferroelectricity. Note, however, that antiferroelectrics do not form specific antiferroelectric domains (although domains can form from associated ferroelastic coupling in some cases), nor can they be characterized by a prototype/ferroic phase point-group pair [26]. Therefore, although a conceptual analogy to antiferromagnets is appealing, a formal correspondence between antiferroelectrics and antiferromagnets does not exist.

As described in the previous subsection, the so-called "Glazer tiltings" found in many cubic perovskites do not remove the center of symmetry of the structure, and so they do not, on their own, cause a ferroelectric ground state. However many materials *combine* Glazer tiltings with second-order Jahn–Teller ions, and the tiltings can then affect the nature of the SOJT offcentering. Figure 7 shows a schematic of an untilted perovskite (left) in which vertical and horizontal offcentering of the A-site cations are equivalent, compared with a Glazer-tilted perovskite (right), in which the axes for offcentering are inequivalent. Often the tiltings even promote the *antiparallel* alignment of neighboring SOJT ions; the resulting local dipole moments then cancel out to give zero net polarization. Such materials, of which $PbZrO_3$ is the prototype [27], are often described therefore as *antiferroelectric*. In Fig. 8 we show the calculated phonon band structures for cubic $PbTiO_3$ and $PbZrO_3$, from [28]. The imaginary frequency phonons, which indicate instabilities from the cubic phase, are plotted on the negative y-axis. Note that both materials have an unstable Γ point phonon; in $PbTiO_3$ this mode dominates, resulting in the tetragonal ferroelectric ground state. However, in the $PbZrO_3$ case, the nonferroelectric rotational instabilities at M and R are stronger, and combine with the Pb-offcentering $\Sigma(\frac{1}{4}\frac{1}{4}0)$ mode to produce the antiferroelectric ground state.

Finally, we point out that in some materials, multiple distortions can occur that create local dipole moments of different magnitudes but in opposite directions, such that there is an overall polarization that is smaller than that which would be produced by each distortion on its own. Such materials are

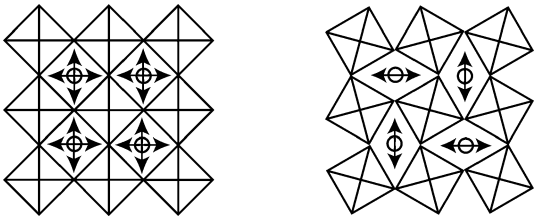

Fig. 7. Comparison of A-site offcentering in non-Glazer-tilted (*left*) and Glazer-tilted (*right*) structures. In high-symmetry structures without tiltings, all of the A-site ions can offcenter in the same geometric direction, favoring a cooperative ferroelectric distortion. In the tilted case, the axes of offcentering on adjacent ions are inequivalent, and antiferroelectric ground states are often favored

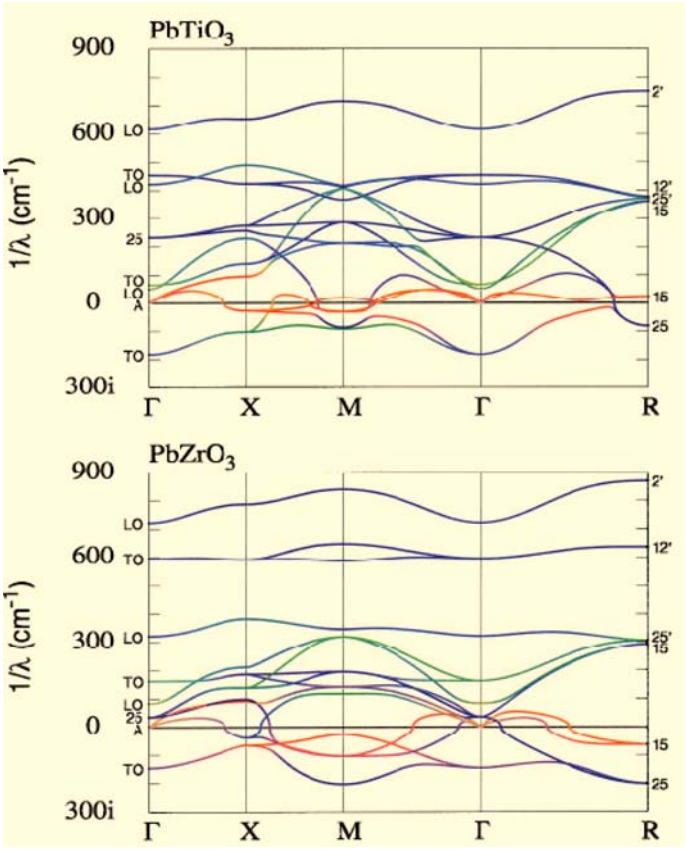

Fig. 8. Calculated phonon-dispersion relations of $PbTiO_3$ and $PbZrO_3$, along high-symmetry lines in the simple cubic Brillouin zone. From [28]. Copyright (1999) by the American Physical Society. Reproduced with permission

described as *ferrielectrics*, by analogy with the ferrimagnets that we discuss below. An example is sodium bismuth titanate, $Na_{0.5}Bi_{0.5}TiO_3$ [29], in which the Ti^{4+} and Bi^{3+} ions move in opposite directions relative to the oxygen framework, giving opposing contributions to the overall polarization.

1.1.2 What Causes Ferromagnetism?

The criterion for the occurrence of magnetism is quite different from that for ferroelectricity. Whereas a ferroelectric requires offcenter displacements of the ions, in a ferromagnet the constituent electrons must have a net angular momentum. This can arise from either the orbital component of the angular momentum, or the spin component (if there are unequal numbers of "up"- and "down"-spin electrons) or both. Indeed there is a strong driving force for electrons to align their spins parallel (creating unequal numbers of up- and down-spin electrons); this is the quantum-mechanical exchange energy. We can develop an intuition for why exchange coupling is such a strong driving force using simple electrostatic arguments: If two electrons in an atom have antiparallel spins, then they are allowed to share the same atomic or molecular orbital. As a result they will overlap spatially, thus increasing the electrostatic Coulomb repulsion. On the other hand, if they have parallel spins, then they must occupy different orbitals and so will have *less* unfavorable Coulomb repulsion. So the orientation of the spins affects the spatial part of the wavefunction, and this in turn determines the electrostatic Coulomb interaction between the electrons. We can make a rough classical estimate of the order of magnitude of the Coulomb repulsion between two electrons by assuming that the average distance between electrons is around 1 Å. Then the Coulomb energy,

$$U = \frac{e^2}{4\pi\epsilon_0 r} \approx \frac{(1.6\times10^{-19})^2}{(1.1\times10^{-10})(1\times10^{-10})}\mathrm{J} \approx 2.1\times10^{-18}\mathrm{J} \approx 13\,\mathrm{eV}\,. \qquad (2)$$

This is a large energy! So, if the electron distribution is changed even by a small amount, the effect on the total energy of the system can be significant. In fact typical exchange energies in solids, defined to be the energy difference per magnetic ion between ferro- and antiferromagnetically ordered arrangements, are of the order of electron volts. (Note that the magnetic dipolar energy between two electrons a few Å apart is $\sim 10^{-6}$ eV!)

There are two phenomenological theories of ferromagnetism that have been successful in explaining many of the properties of ferromagnets – the localized moment theory of Curie and Weiss, which arose from the study of magnetic insulators, and the Stoner band theory of ferromagnetism in metals. In the localized moment picture, local magnetic moments exist on the ions in the solid at all temperatures; below the Curie temperature the moments align to give a ferromagnetic state, and above the Curie temperature they are disordered by thermal energy and there is no net magnetization. Such

behavior is analogous to the order–disorder description of ferroelectrics, in which the constituent ions are always offcentered, but only below the Curie temperature do the directions of offcentering align cooperatively to give a net electric polarization. In the band theory, there are equal numbers of up- and down-spin electrons above the Curie temperature, and hence no magnetic moment. Below T_c the up- and down-spin bands are unequally populated by electrons, leading to a net magnetic moment. Here, the analogy is to the displacive model of ferroelectricity, in which the Curie temperature is coincident with offcentering of the ions. We summarize both models in the next section, and show that, in both cases, tightly bound, localized electrons, such as transition-metal d, or rare-earth f electrons, provide the impetus for magnetism to occur.

Localized Moment Model

In a classic 1907 paper [30], *Weiss* postulated that an internal "molecular field" acts in ferromagnetic materials to align magnetic moments, arising from unequal numbers of up- and down-spin electrons localized on each atom or ion, parallel to each other. This "molecular field" is in fact not the long-range dipolar interaction envisioned originally, but the short-range quantum-mechanical exchange interaction mentioned above. Below the Curie temperature, T_c, the molecular field is so strong that it magnetizes the substance even in the absence of an external applied field. At high enough temperatures, the thermal energy, kT, and associated entropic effects overcome the alignment energy of the molecular field, resulting in random orientation of the magnetic moments and paramagnetic behavior. The Weiss picture leads to the experimentally observed Curie–Weiss law behavior for the susceptibility, χ, of many magnetic materials:

$$\chi = \frac{C}{T - T_c}\,, \tag{3}$$

and also accounts for the observed susceptibility of many antiferromagnets and ferrimagnets.

Stoner Band Model

The Weiss theory breaks down in one important aspect, however: It is unable to account for the measured values of the magnetic moment per atom in some ferromagnetic materials, particularly in ferromagnetic metals. There are two significant discrepancies. First, according to the Weiss theory, the magnetic dipole moment on each atom or ion should be the same in both the ferromagnetic and paramagnetic phases. Experimentally this is not the case. Second, in local moment theory, the magnetic dipole moment on each atom or ion should correspond to an integer number of electrons. Again this result is often not observed. A more successful approach for metals is to use the

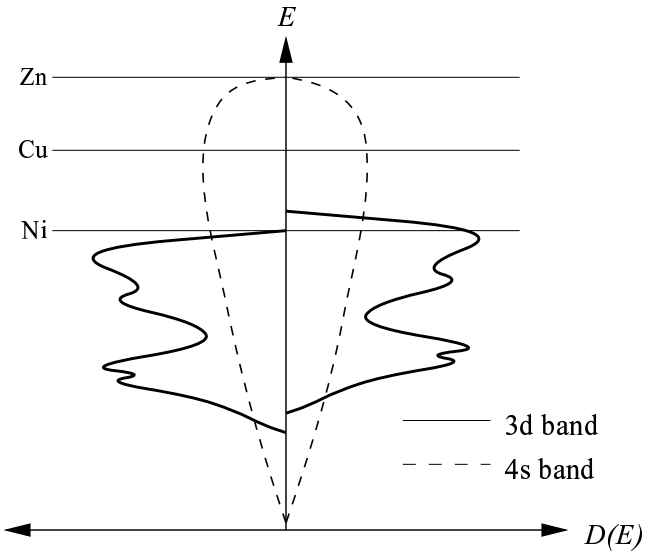

Fig. 9. Schematic 3*d* and 4*s* up- and down-spin densities of states in first-row transition metals, with exchange interaction included

Stoner band theory of ferromagnetism [31], in which the fundamental driving force for ferromagnetism is again the exchange energy, which is minimized if all the electrons have the same spin. Opposing the alignment of spins is the increased band energy involved in transferring electrons from the lowest band states (occupied equally with up- and down-spin electrons) to band states of higher energy. This band energy prevents simple metals from being ferromagnetic.

In the elemental ferromagnetic transition metals, Fe, Ni and Co, the Fermi energy lies in a region of overlapping 3*d* and 4*s* bands. The 4*s* bands are broad, with a low density of states at the Fermi level. Consequently, the energy that would be required to promote a 4*s* electron into a vacant state so that it could reverse its spin is more than that which would be gained by the resulting decrease in exchange energy, and so the 4*s* bands are not spin-polarized. By contrast, the 3*d* band is narrow and has a much higher density of states at the Fermi level. The large number of electrons near the Fermi level reduces the band energy required to reverse a spin, and the exchange effect dominates. The exchange interaction produces an exchange potential that effectively shifts the energy of the 3*d* band for electrons with one spin direction relative to the band for electrons with the opposite spin direction, giving the exchange-split band structure shown in Fig. 9. The magnetic moment does not necessarily correspond to an integer number of electrons, since the electrons are shared between partially filled 4*s*, $3d^{\uparrow}$ and $3d^{\downarrow}$ bands.

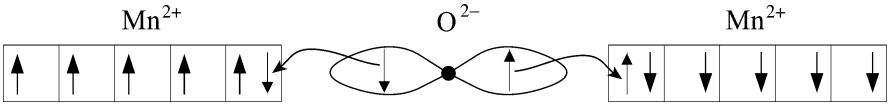

Fig. 10. Schematic of the superexchange mechanism in MnO. The energy is lowered if some covalent bonding occurs between the Mn and O ions. In this case the *left-hand* Mn is up-spin, and so can only bond with the down-spin electron in the appropriately oriented oxygen 2*p* orbital. This leaves the up-spin oxygen electron to bond with the *right-hand* Mn ion, which therefore must be down-spin (and so antiferromagnetic to the left-hand Mn)

Real materials obviously do not behave exactly like either of these simple models, although one or other is usually a fairly reasonable description in most cases. For example, rare-earth magnets contain highly localized *f* electrons that are well described by the Weiss localized moment theory, whereas in metallic ferromagnets the magnetic order, arising from the less strongly localized *d* orbitals, is Stoner-band-like.

Other Kinds of Magnetic Ordering

Although the exchange energy is always minimized when electrons have their spins parallel to each other, in practice there are many other contributions to the electronic energy and the net result, particularly in insulators, is often an antiferromagnetic arrangement. For example, the "superexchange" interaction, in which the magnetic ordering between cations is determined by chemical-bonding considerations with intervening anions, often leads to antiferromagnetism (or ferrimagnetism if the ions are different). Superexchange is illustrated in Fig. 10, for the example of Mn^{2+} ions in which an oxygen atom lies between two filled Mn *d* orbitals, and has some covalent bond formation with both of them. Note that this driving force for antialignment of spins is strikingly different from those described in Sect. 1.1.1 that lead to ferrielectric or antiferroelectric behavior.

Note that, for certain bonding configurations, superexchange interactions can lead to parallel alignment of magnetic moments – for example if an oxygen atom bonds with two Mn *d* orbitals, one of which is empty and the other of which is filled – as illustrated in Fig. 11. Therefore, many magnetic materials contain a combination of ferro- and antiferromagnetically coupled ions. The details of the long-range magnetic ordering are then determined by strain, since ferro- and antiferromagnetically coupled ions have different bond lengths. Minimizing the strain energy usually results in a net antiferromagnetism, for example in $LaMnO_3$, planes of ferromagnetically coupled Mn ions couple antiferromagnetically to each other [32]. But in magnetic ferroelectrics, which we discuss in Sect. 3, the additional strain from the ferroelectric distortion can modify the magnetic ordering.

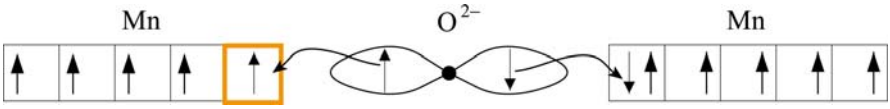

Fig. 11. Superexchange mechanism between one empty (*marked in red*) and one occupied Mn *d* orbital. The oxygen ion makes a ligand-field donation of an electron into the empty Mn *d* orbital (*left*); to optimize the Hund's rule coupling it donates the electron with spin parallel to that of the Mn ion (up-spin). The down-spin oxygen electron forms a partial covalent bond with the electron in the occupied Mn *d* orbital to its right. For this to occur, the right-hand Mn ion must also be up-spin, i.e., parallel to the first

1.2 Domains

The subject of ferroelectric-domain formation was covered in the chapter by *P. Chandra* and *P. B. Littlewood* in this volume. Ferromagnets also form domains, for many of the same reasons. In this section we summarize the domain theory of ferromagnetism, and point out the similarities and differences between ferromagnetic and ferroelectric domains. For a more detailed review of domains in ferromagnets, see the books by *Spaldin* [33] and *Nesbitt* [34], or the review article by *Kittel* and *Galt* [35].

Structure

Domains form so as to minimize the total energy of the material. Although a single ferromagnetic domain, in which all the magnetic moments were aligned, would minimize the *exchange* energy, it also maximizes the magnetostatic energy, which is the main driving force for domain formation. Other contributions, in particular the magnetocrystalline and magnetostrictive energies, determine the size and shape of domains. Figure 12 illustrates the reduction of magnetostatic energy by domain formation. The single-domain sample in Fig. 12a has a large magnetostatic energy, which is reduced somewhat in Fig. 12b by the formation of parallel domains. Of course, at the domain boundaries the magnetic moments are no longer oriented parallel to each other, and so there is an increase in exchange energy. In Fig. 12c the magnetostatic energy is eliminated completely. However, if the material has strong magnetostriction (which causes the sample to change shape in the direction of magnetization) or a strong uniaxial magnetocrystalline anisotropy (which causes the magnetization to align preferentially along a single crystallographic axis), the perpendicular domains shown in Fig. 12c can be unfavorable. In this case a structure with very small perpendicular domains, such as that shown in Fig. 12d, is often the lowest-energy arrangement.

The width of the boundary between magnetic domains (the domain wall) is determined by a balance between the exchange energy (which prefers wide walls, so that adjacent magnetic moments are not too far from being parallel to each other) and the magnetocrystalline energy (which prefers narrow walls,

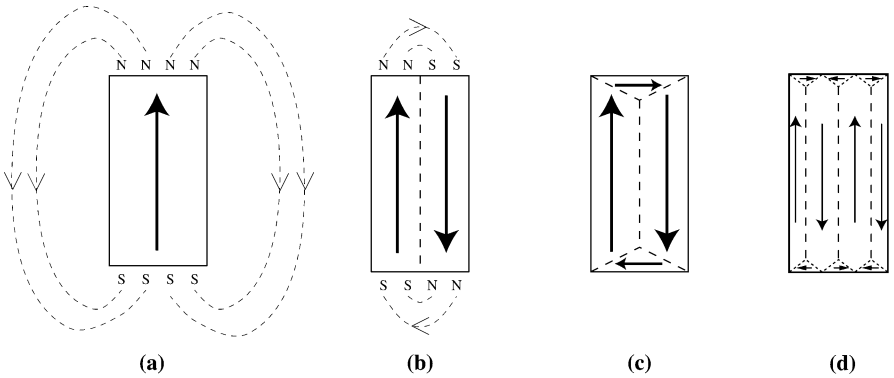

Fig. 12. Reduction of the magnetostatic energy by domain formation in a ferromagnet. The single domain shown in (**a**) optimizes the exchange, magnetocrystalline and magnetostatic energies. Often, the arrangement shown in (**d**) has the lowest total energy

so that the magnetization is aligned most closely to an easy axis). For typical transition metals, domain walls are a few hundred angstroms thick (or consist of a few hundred planes of atoms).

The exchange energy cost per square meter, σ_{ex}, within a domain wall is given by

$$\sigma_{\mathrm{ex}} = \frac{kT_{\mathrm{c}}}{2}\left(\frac{\pi}{N}\right)^2 N\frac{1}{a^2}\,\mathrm{J}\cdot\mathrm{m}^{-2}\,, \tag{4}$$

where $N+1$ is the number of atomic layers in the wall, and a is the spacing between the atoms. The anisotropy energy cost per square meter, σ_{A}, is given by

$$\sigma_{\mathrm{A}} = KNa\,\mathrm{J}\cdot\mathrm{m}^{-2}\,, \tag{5}$$

where K, the magnetocrystalline anisotropy constant, is a measure of the cost of not having all the atoms aligned along easy axes. The exchange energy cost, the anisotropy energy cost and the sum of these two energy costs are plotted in Fig. 13 for iron, for which $K = 0.5\times10^5\,\mathrm{J}\cdot\mathrm{m}^{-3}$, $a = 0.3\,\mathrm{nm}$, and $T_{\mathrm{c}} = 1014\,^{\circ}\mathrm{C}$.

The minimum energy occurs when $\frac{\mathrm{d}(\sigma_{\mathrm{ex}}+\sigma_{\mathrm{A}})}{\mathrm{d}N} = 0$. That is, $\frac{-kT_{\mathrm{c}}}{2}\left(\frac{\pi}{a}\right)^2\frac{1}{N^2} + Ka = 0$. Solving for N gives

$$N = \frac{\pi}{a}\sqrt{\left(\frac{kT_{\mathrm{c}}}{2Ka}\right)}\,. \tag{6}$$

(Note that this also corresponds to the N value for which $\sigma_{\mathrm{ex}} = \sigma_{\mathrm{A}}$.) Substituting the values of K, T_{c} and a for iron into this expression gives $N =$

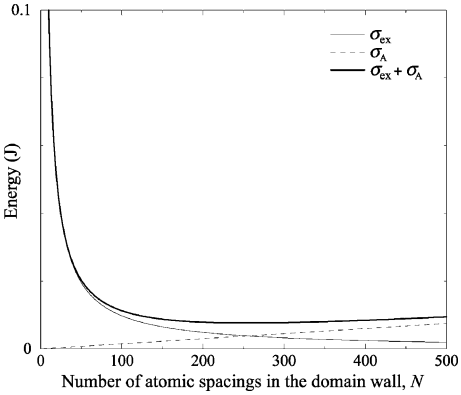

Fig. 13. Variation of exchange energy, anisotropy energy and their sum as a function of domain-wall thickness (obtained using (4) and (5), with parameters for iron)

255. Therefore, the wall thickness, $Na = 76.8\,\mathrm{nm}$, and the wall energy is $7\,\mathrm{mJ}\cdot\mathrm{m}^{-2}$.

Such wide domain walls in ferromagnets are in sharp contrast to those in ferroelectrics, which have been shown both experimentally (using high-resolution transmission electron microscopy) [36] and by ab-initio calculations [37] to have a thickness of only a few lattice constants. In turn, the domain-wall energies in ferroelectrics are considerably larger than those in typical ferromagnets. *Stemmer* et al. [36] compared lattice parameters determined using HRTEM with predictions based on Landau–Ginzburg theory to extract a value of $50\,\mathrm{mJ}\cdot\mathrm{m}^{-2}$ for a 90° domain wall in $PbTiO_3$. For comparison, first-principles calculations [37] give a value of $35\,\mathrm{mJ}\cdot\mathrm{m}^{-2}$ for a 90° domain wall and $\sim 150\,\mathrm{mJ}\cdot\mathrm{m}^{-2}$ for a 180° domain wall (with the exact value depending on the details of the symmetry used in the calculation). The same first-principles study [37] also showed that the change in polarization in ferroelectric domains is accommodated by a reduction in the magnitude of the local atomic displacements at the domain wall. This is in contrast to the situation in magnetic domains, where the local moments are not significantly reduced, but instead rotate their orientation through the width of the wall.

Size Effects

Although the size of an actual domain is influenced by many factors, including the size of the sample, the nature of the surface, and the defect structure, below a certain size (typically a few hundred angstroms), particles contain only one domain. This can be understood qualitatively by arguing that, below this size, the domain wall is just too wide to fit into the particle. We can make a more quantitative estimate of the size of single-domain particles by looking at the balance between the magnetostatic energy and the domain-wall energy (Fig. 14). A single-domain particle (Fig. 14a) has high magnetostatic

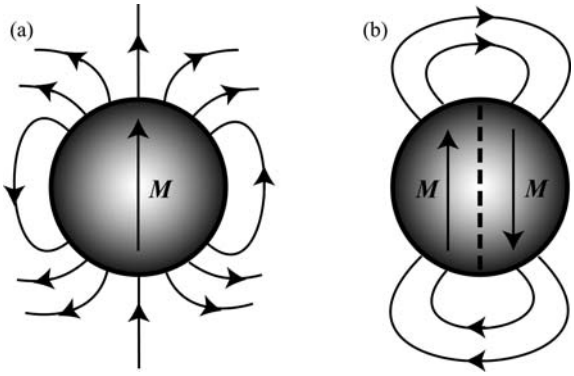

Fig. 14. Balance between magnetostatic and domain-wall energies in single and multidomain particles. (**a**) shows a single-domain particle with high magnetostatic energy. In (**b**), introduction of a domain wall has reduced the magnetization energy but increased the exchange energy

energy but no domain-wall energy, whereas a multidomain particle (Fig. 14b) has lower magnetostatic energy but higher domain-wall energy. In fact, the magnetostatic energy is proportional to the volume of the particle (i.e., r^3, where r is the particle radius), and the domain-wall energy is proportional to the area of the wall, r^2. The dependence of the magnetostatic and exchange energies on particle radius is plotted in Fig. 15. Below some critical radius, r_c, it is energetically unfavorable to form domain walls and a single-domain particle is formed.

So large single-domain particles form if either the domain-wall energy is large (because of, for example, large magnetocrystalline anisotropy) so that wall formation is unfavorable, or if the saturation magnetization is small, so that the magnetostatic energy is small.

Properties of Small Particles

The coercivity of small particles as a function of particle size is shown in Fig. 16. Notice that, as the particle size is reduced into the single-domain region, the coercivity increases. This is because the magnetization-reversal process cannot take place via domain-wall motion, but must rather use the energetically more demanding route of magnetization rotation. Such single-domain particles are useful in, for example, data-storage applications, since their coercive switching fields tend to be large.

Below a certain particle size, known as the superparamagnetic limit, however, we see that the coercive field goes to zero. This occurs when thermal fluctuations are able to exceed the magnetic anisotropy energy that aligns the magnetization in a specific direction. The anisotropy energy is given by the product of the anisotropy constant, K, and the volume of the particle. As the volume is reduced, KV becomes comparable to the thermal energy

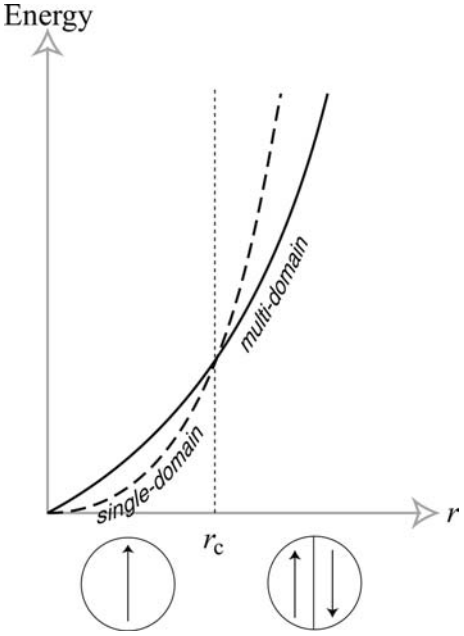

Fig. 15. Relative stability of single- and multidomain particles. The *dashed line* shows the energy associated with the formation of single-domain particles. Below the critical radius, r_c, single-domain particles have a lower energy than multi-domain particles (shown by the *solid line*)

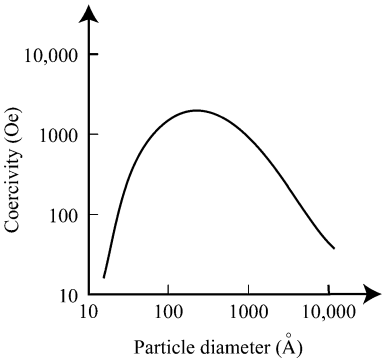

Fig. 16. Coercivity as a function of size for small particles of a ferromagnetic material

kT. As a result, thermal energy can overcome the anisotropy "force" and spontaneously reverse the magnetization of a particle from one easy direction to the other, even in the absence of an applied field. The critical size at which superparamagnetism occurs depends on the anisotropy energy of the particle, but is typically around 100 Å diameter for spherical particles at room temperature. Below this size, a permanent spontaneous magnetization will not be measured.

In contrast, ferroelectricity can be observed down to very small sizes, even on the scale of a few lattice constants, under appropriate electrical and mechanical boundary conditions. More discussion can be found in the chapters by *K. M. Rabe* and *P. Ghosez* (first-principles) and by *C. Lichtensteiger*, *M. Dawber* and *J.-M. Triscone* (finite-size effects) in this volume.

The origin of both the different size dependencies and different domain-wall widths in ferroelectrics and ferromagnets can be understood to result from the different atomic-level mechanisms driving ferromagnetism and ferroelectricity. Ferromagnets prefer wide domain walls, in which adjacent magnetic moments are oriented close to each other, because the exchange coupling between magnetic moments is strong, and the magnetocrystalline anisotropy energy, which couples the spin to the lattice, is driven by spin-orbit coupling, which is comparatively weak.

In ferroelectrics the situation is quite different in that the energies of the "anisotropy" and "exchange" effects are comparable. For example, the calculated energy difference in $BaTiO_3$ between the rhombohedral ground state (in which the atoms displace along the [111] direction) and the higher-energy tetragonal phase (in which they displace along [100]) is around 5 meV [18]. We take this quantity to be the ferroelectric analog of the magnetocrystalline anisotropy energy in ferromagnets. The energy difference between ferroelectric and antiferroelectric configurations (which we call the "ferroelectric exchange energy") for the same set of atomic displacements has been calculated in the context of the study of ferroelectric domain walls; for $BaTiO_3$ it is 15 meV per formula unit [38]. Therefore, the energetic driving force for maintaining wide domain walls (the exchange energy) is comparable in magnitude to that favoring narrow walls (the anisotropy energy) in ferroelectrics. Finally, we point out that the calculated energy difference between the ferroelectric and high-symmetry cubic phase in $BaTiO_3$ at the experimental lattice constant is ∼15 meV [18]. Therefore, it is feasible to include unpolarized layers in the domain walls. In contrast, in typical ferromagnets, the calculated energy differences between ferro- and paramagnetic configurations is of the order of 1 eV. In this case it is easy to see why the full value of the magnetic moment is maintained through the domain wall, and changes from one domain to the other by rotating its orientation.

2 Applications

In principle, ferromagnets and ferroelectrics could find many similar applications. Both have spontaneous and switchable polarizations that can therefore be used for data storage. Both have coupling between the polarization and the strain, which can be exploited in transducer applications such as sensors or actuators. And their large susceptibilities to magnetic or electric fields lead to applications in which they concentrate flux. For example, the high permeability of ferromagnets is exploited in transformer cores, and the large dielectric susceptibility of ferroelectrics is used in capacitor applications. However, their most widespread applications are quite distinct. Piezoelectric ceramics such as PZT have an almost total monopoly on transducer applications such as sonar detectors. The primary reason for this is that typical electrostrictive strains, driven by structural phase transitions, are considerably larger than typical magnetostrictive strains, which are caused by the much weaker spin-orbit interaction. For example, the elongation along the polar axis in tetragonal ferroelectric $PbTiO_3$ is around 1 % of its high-symmetry cubic phase lattice parameter (optimized piezoelectrics such as PZT have even larger responses), whereas length changes caused by magnetization of Fe and Ni are three orders of magnitude smaller. While there has been some recent progress (and considerable current research) on "giant magnetostrictive" materials [39] such as the terbium-dysprosium-iron alloy terfenol-D, shape changes are still not large ($\sim$0.1 %) and other problems such as eddy-current losses and poor durability have limited their adoption in devices. In contrast, magnetic media have a clear lead in tape and disk storage, in large part because of low cost and technology maturity, but also because of the straightforward read process associated with magnetic fringing fields at the surfaces of magnetized samples.

In this section we focus on one specific pair of devices in order to compare and contrast the properties of ferromagnets and ferroelectrics. Instead of choosing the most widely used applications for each, we use random access memories (RAMs) for our case study. Our motivation is twofold: first, the technological objectives of ferroelectric random access memory (FRAM) and magnetoresistive random access memory (MRAM) are similar, allowing for a direct comparison between the two; therefore the distinct architectures that have emerged in the two cases illustrate details of the two phenomena and materials, and the associated differences in system engineering, required to make a working device. And second, both technologies are fairly immature, so exciting new advances emerge regularly.

FRAM and MRAM distinguish themselves from traditional semiconductor random access memory (RAM) by their nonvolatility, that is the fact that they retain data when the power is switched off. In addition to the obvious advantage of not losing the unsaved portion of one's carefully written book chapter during a power outage, this also means lower power consumption (very important for portable technologies) and faster boot-up times for com-

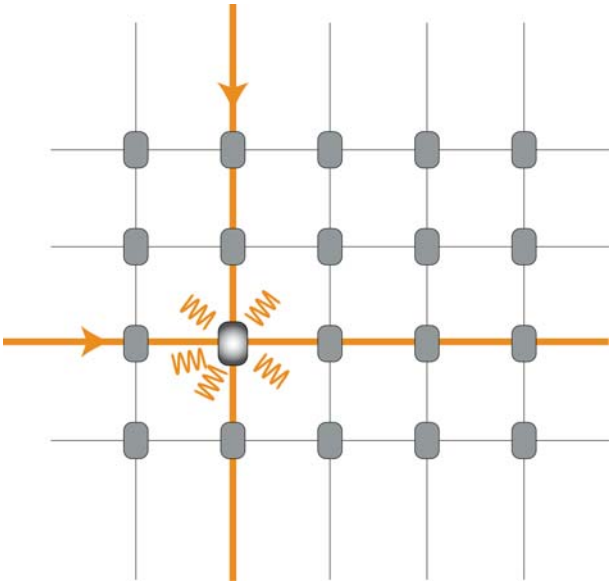

Fig. 17. Crosspoint architecture used for FRAM and MRAM devices

puter applications. Also, both FRAM and MRAM have fast read, write and access times, distinguishing them from existing nonvolatile technologies such as flash and read-only memories (ROMs). Their current limitations are low density and high cost, although current research efforts might well overcome both.

Both MRAM and early (up to around 1980) FRAM devices use what is called a "crosspoint" architecture, in which memory cells are arranged in a square matrix, joined by two perpendicular arrays of wires, as shown in Fig. 17. (The same architecture was also widely used in ferrite-core memories in the 1960s.) To switch a particular magnetic or ferroelectric cell, currents are passed down the horizontal and vertical wires (called "bit lines" and "word lines") that intersect at that cell. The combined action of the magnetic fields associated with the horizontal and vertical currents causes that cell to switch, without (ideally) affecting the other cells in the system. Such crosspoint architectures allow for higher signal-to-noise ratios, and higher densities compared with corresponding serial architectures. However, they have a problem with "crosstalk", in which applying less than the nominal switching voltage along a row (or a column) sometimes also switches an unaddressed bit. This is because the switching is activation-field dependent, so that if $e^{(eE_a/kT)}$ is enough to switch 100% of the time, $e^{(eE_a/2kT)}$ will switch sometimes! In fact, the crosspoint architecture was abandoned for FRAMs and existing commercial devices instead use a passgate architecture with a transistor behind each bit.

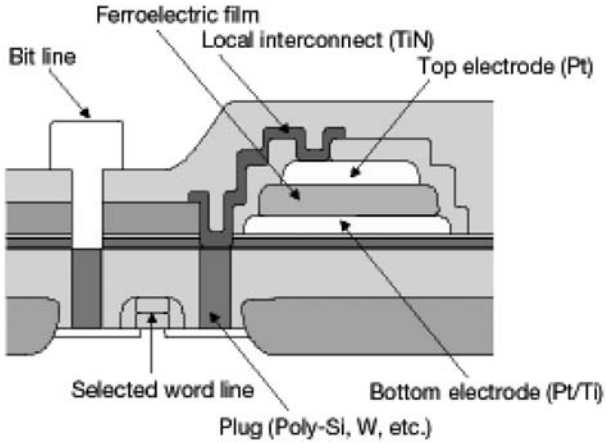

Fig. 18. Schematic cross section of a FRAM unit cell. Courtesy of Fujitsu Limited

2.1 Ferroelectric Random Access Memories

The memory cells in the most well-established FRAM systems consist of two components, the ferroelectric capacitor (whose + or − polarization state gives the "1" or "0" data bit) and a transistor, to isolate the bit from its neighbors. A schematic cross section of a FRAM cell is shown in Fig. 18. Various capacitor structures are in use, including ferroelectric $SrBi_2Ta_2O_9$ between Pt electrodes, and PZT between conducting oxide electrodes. As described above, a bit is written by applying a short voltage pulse of half the strength required for switching along the bit's horizontal connection, and another along its vertical connection.

One disadvantage of most existing schemes is that the read process is destructive. A positive voltage is applied to the memory cell by sending two half-strength positive pulses, as described above for writing. If the cell is already in the + state, then no switching occurs. However, if the cell is in the − state, a large, nonlinear switching response is measured as the polarization reverses. Nondestructive read architectures are more desirable since the state of the bit does not need to be restored after reading, however, they are currently less well developed.

Reference [40] provides a good introductory review on ferroelectric memories. For a more extensive treatment, see the book "Ferroelectric Memories" by *J.F. Scott* [41].

2.2 Magnetoresistive Random Access Memories

Here, we give a summary of current MRAMs; for a more complete review see [42]. The most promising memory cells for MRAM are so-called *magnetic tunnel junctions* (MTJs), which are placed at the intersection of the

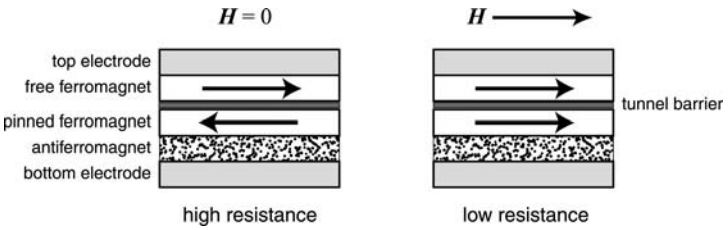

Fig. 19. Schematic of a magnetic tunnel junction in its high-resistance (magnetic layers antiparallel) and low-resistance (magnetic layers parallel) states

bit and word lines. An MTJ consists of two ferromagnetic layers separated by an insulating tunneling barrier. One of the ferromagnetic layers is pinned by an adjacent antiferromagnet to align in a specific direction, while the other is able to reorient in response to an applied field. A schematic of the structure is shown in Fig. 19. The relative orientations of the ferromagnetic layers determine the resistance of the structure (parallel alignment allows current flow, whereas antiparallel has a high resistance). Therefore the parallel and antiparallel arrangements can be used as "1" and "0" data bits, which are easily detectable because of their different conductivities. The discovery of the effect was first reported more than 20 years ago [43], but only at low temperature and at very low bias. The substantial changes in resistance with orientation needed to make a workable device were achieved only recently [44]. Note that large changes in electrical resistivity are not associated with reorientations of ferroelectric polarization, and so an electrical analog of a magnetic tunnel junction does not exist.

The MRAM write process is similar to that of FRAM; A bit is written by passing a sequence of current pulses (not necessarily of equal magnitude) along the appropriate word and bit lines; the combined magnetic fields associated with the current pulses are sufficient to switch the magnetization. In MRAM, however, the read process is more straightforward than in FRAM. The current that passes from the word line, through the bit and into the appropriate bit line is detected. A small current indicates antiparallel alignment of the magnetic layers, whereas a large current passes if the layers are parallel. Schematics of the read and write processes are shown in Fig. 20.

Finally, we point out that is difficult to predict the relative prospects of FRAM and MRAM in the marketplace. A comparison is in fact rather unfair, since they are at quite different levels of maturity, with MRAM showing tremendous promise in the laboratory, but FRAM having already evolved to the production stage. For example, in 2004, every SONY Playstation contained a ferroelectric FRAM, and over a million FRAM chips per month were being sold in sizes of 4 Mbit (Matsushita/Panasonic), 8 Mbit (Infineon/Toshiba product announcement for 2004), up to 32 Mbit (Samsung). Meanwhile, MRAMs were being seriously considered by numerous companies, including for example IBM and Motorola. Suffice to say that both technolo-

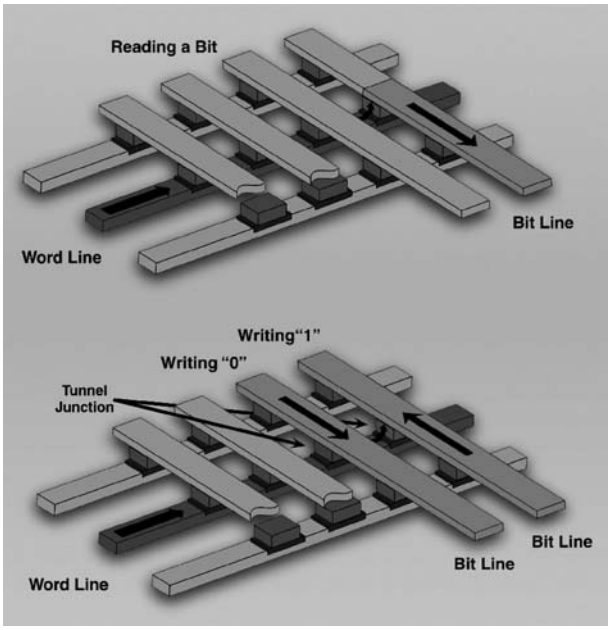

Fig. 20. Schematic of the read and write processes in magnetoresistive random access memories. Courtesy of International Business Machines Corporation. Unauthorized use not permitted

gies have strong supporters and proponents and might find more widespread use within a short to medium time frame.

3 Multiferroics

A multiferroic is a material in which two or all three of ferroelectricity, ferromagnetism and ferroelasticity occur in the same phase [45]. In this section we briefly summarize the current state of research in the field of ferromagnetic ferroelectric multiferroics. (For reviews see [46–48].) We emphasize that such materials are still uncommon, and many aspects of their behavior are not yet well understoond. As such they are a ripe and rapidly emerging area for future research.

Part of the motivation for the study of multiferroics lies in their potential applications. (We emphasize that at this stage these are rather speculative.) Possibilities include multiple-state memory elements [49], in which data is stored both in the electric and the magnetic polarizations, or novel memory media that might allow writing of a ferroelectric data bit, and reading of the magnetic field generated by association. This would remove the disadvantage of the destructive read process currently associated with ferroelectric memories. One can envisage magnetic-field-tunable electrical and optical properties

(such as dielectric or nonlinear optical response) or electric-field-tunable magnetic behavior. Finally, unusual actuators or transducers, in which the ability to couple either to the electric or the magnetic polarization is exploited, could be developed.

The remainder of this section is organized as follows: First, we discuss the chemical and physical origins behind the scarcity of the coexistence of ferromagnetism and ferroelectricity. Then we review the phenomenon of magnetoelectric coupling. A survey of some known magnetic ferroelectrics follows, with a discussion of open problems, and future work concludes the section.

3.1 The Scarcity of Ferromagnetic Ferroelectrics

The fundamental physics behind the scarcity of ferromagnetic ferroelectrics has been reviewed by *Hill* in [50] and [51]. To summarize, the most common mechanism for stabilizing offcentering in perovskite oxide ferroelectrics, the ligand-field stabilization of the small cation by the surrounding oxygens described in Sect. 1.1.1, does not occur if the small cation is magnetic. In simple chemical terms, the second-order Jahn–Teller effect occurs for transition-metal ions with formally empty d-states (that exhibit "d^0-ness") whereas, as explained in Sect. 1.1.2, the existence of magnetism requires localized, in this case d, electrons. This is the reason why none of the common (ferro- or antiferro-) magnetic perovskite structure oxides (for example $LaMnO_3$, $SrRuO_3$, $GdFeO_3$) shows ferroelectric behavior.

In order for ferroelectricity and magnetism to coexist, the atoms that offcenter to give the electric dipole moment therefore tend to be different from those that carry the magnetic moment. In the perovskite structure oxides, this can be achieved by exploiting the stereochemical activity of the lone pair on the large (A-site) cation to provide the ferroelectricity, while keeping the small (B-site) cation magnetic. This is the mechanism for ferroelectricity in the Bi-based magnetic ferroelectrics, the most widely studied of which is bismuth ferrite, $BiFeO_3$ [52]. Another option is to make a double perovskite in which one of the sublattices is magnetic, and the other consists of ferroelectric d^0 cations. This has been successful in a number of cases, however, the magnetic and electric ordering temperatures tend to be low because of dilution of the sublattices. Reference [53] contains a review of double perovskites that had been tried before 1970; some modern examples include B-site ordered Pb_2CoWO_6 [54] (ferromagnetic and ferroelectric), B-site disordered Pb_2FeTaO_6 [54, 55] (ferroelectric and antiferromagnetic) and Pb_2FeNbO_6 [56], which is ferroelectric and antiferromagnetic, with weak ferromagnetism below around 10 K. Also, note that there is no incompatibility between the coexistence of magnetic ions and the geometrically driven ferroelectrics described in Sect. 1.1.1, and the antiferromagnetic ferroelectric $YMnO_3$ falls into this class. Finally, we mention an intriguing recent report of a small ferroelectric polarization in magnetic $TbMnO_3$ [57]. At low temperature, and in a certain magnetic-field range, the stable magnetic ground state

is an incommensurate sinusoidal spin spiral that lacks inversion symmetry. Within this magnetic state, the structure is described by a polar space group, and ferroelectricity is symmetry-allowed. The resulting polarization is small since there is no "driving force" for offcentering, however, since it is caused directly by the magnetic ordering, strong, and possibly novel magnetoelectric interactions should be expected.

We also point out that, in order to be ferroelectric, a material must be insulating (otherwise the mobile charges would screen out the electric polarization). This adds an additional constraint, because many ferromagnets tend to be metallic, with most magnetic insulators having antiferromagnetic ordering. Recent predictions of large polarization and magnetization in ferrimagnetic materials [58] might circumvent this problem. The insulating requirement can also cause problems if samples are leaky since this can suppress ferroelectric behavior even if the structure is noncentrosymmetric. This is a common problem in the case of magnetic ferroelectrics, since magnetic transition-metal ions are often able to accommodate a wider range of valence states than their diamagnetic counterparts. This in turn can lead to oxygen nonstoichiometry and hopping conductivity.

3.2 Magnetoelectric Coupling

The independent existence of two or more ferroic order parameters in one material results in fascinating physics in its own right [51], but the *coupling* between magnetic and electric degrees of freedom gives rise to additional phenomena. The linear and quadratic magnetoelectric (ME) effects, in which a magnetization linear or quadratic in the applied field strength is induced by an electric field (or an electric polarization is induced by a magnetic field), are already well established [59]. The free energy, G, can be expanded in terms of the electric field, E, and the magnetic field, M as:

$$G(E,H) = G_0 + P_i E_i + M_i H_i + \frac{1}{2}\epsilon_{ij} E_i E_j + \frac{1}{2}\mu_{ij} H_i H_j + \alpha_{ij} E_i H_j + \frac{1}{2}\beta_{ijk} E_i H_j H_k + \frac{1}{2}\gamma_{ijk} H_i E_j E_k + \cdots . \quad (7)$$

Here, P_i and M_i are the spontaneous polarization and magnetization, respectively, in direction i, ϵ and μ are the dielectric permittivity and magnetic permeability, α is the linear magnetoelectric susceptibility tensor, and β and γ are the bilinear magnetoelectric susceptibility tensors describing the "EHH" and "HEE" responses, respectively. The symmetry groups that permit the occurence of the linear and bilinear magnetoelectric effects, and the form of the corresponding tensors have been tabulated [60, 61]; importantly the linear magnetoelectric effect can only occur in crystals with ferromagnetic or antiferromagnetic point groups, although bilinear effects can occur in diamagnetic and paramagnetic materials. A table of magnetoelectric coefficients in materials that show the linear magnetoelectric effect is given in [62]; values

include (in rationalized Gaussian units) 1.75×10^{-2} for $TbPO_4$ (the largest value resported for a single-phase material) and 1×10^{-4} for Cr_2O_3. Note that the SI value (in s/m) is $\frac{4\pi}{3\times 10^8}$ times the rationalized Gaussian value.

Recently, more complex coupling scenarios have been investigated. Examples are the coupling of the antiferromagnetic and ferroelectric domains in hexagonal $YMnO_3$ [63] or the large magnetocapacitance near the ferromagnetic Curie temperature in ferroelectric $BiMnO_3$ [64]. Especially interesting are scenarios where the direction of the magnetization or electric polarization can be modified by an electric or magnetic field, respectively. Early work on nickel-iodine boracite [65] showed that, below $\sim 60\,K$, reversal of the spontaneous electric polarization rotates the magnetization by 90°, indicating that the axis of the magnetization, but not its sense, can be controlled by an electric field. Conversely, the small ($0.08\,\mu C/cm^2$) electric polarization in perovskite $TbMnO_3$ was recently rotated by 90° using a magnetic field at low temperatures ($\sim$ 10–20 K) [57]. And recent computational studies [66] have suggested that electric-field-induced 180° switching of the magnetization should be possible in materials in which the origin of the magnetization is the spin-orbit coupling.

3.3 Some Materials Examples

3.3.1 $BiFeO_3$

$BiFeO_3$ is probably the most well-studied multiferroic, and certainly the most well-studied Bi-based perovskite ferroelectric. It is of tremendous interest, not just for its multiferroic properties, but also because it does not contain lead, and therefore is a candidate replacement for traditional PZT in Pb-free piezoceramics. It has a rhombohedrally distorted perovskite structure with space group $R3c$ [67,68] (Fig. 21), and has long been known to be ferroelectric, with a Curie temperature of $\sim 1100\,K$ [69]. It is a G-type antiferromagnet, in which the Fe magnetic moments are coupled ferromagnetically within the pseudocubic (111) planes and antiferromagnetically between adjacent planes, and the Néel temperature is $\sim 640\,K$ [70]. Superimposed on the antiferromagnetic ordering, there is a spiral spin structure [71] in which the antiferromagnetic axis rotates through the crystal with an incommensurate long-wavelength period of $\sim 620\,Å$. This spiral spin structure leads to a cancellation of any macroscopic magnetization that might occur through a canting of the antiferromagnetic sublattices (so-called weak ferromagnetism [72, 73]) and also inhibits the observation of the linear [74], although not the quadratic [75], magnetoelectric effect. The spiral spin structure can be suppressed, and the linear magnetoelectric effect observed, by doping [76] or by application of a high magnetic field [74].

The ferroelectricity in $BiFeO_3$ is driven by the stereochemically active lone pairs on the Bi ions, which cause large relative displacements of the Bi and O ions along the [111] direction [77]. These displacements are noticeably

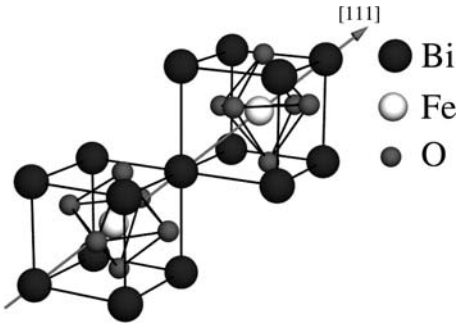

Fig. 21. Schematic view of the *R*3*c* structure built up from two cubic perovskite unit cells. The cations are displaced along the [111] direction relative to the anions and the oxygen octahedra rotate with alternating sense around the [111] axis. From [66]. Copyright (2005) by the American Physical Society

extreme when compared with those in nonlone-pair-active perovskite ferroelectrics such as $BaTiO_3$ or $KNbO_3$, but are consistent with those observed in other Bi-based perovskites [78]. These large displacements combine with anomalously large Born effective charges to produce one of the highest theoretical polarizations known, $\sim 90\,\mu C/cm^2$, plus or minus the polarization quantum [77]. The majority of recent measurements [52, 79] are consistent with this value, although there have been reports of giant ($> 150\,\mu C/cm^2$) polarization (see for example [80]), of thickness-dependent polarization in thin films [52] and a number of reports of rather small polarizations [69, 81, 82], likely as a result of incomplete switching and unsaturated hysteresis loops. Table 1 (taken from [77]) summarizes the experimental data. The wide spread is perhaps a consequence of an intrinsic difficulty in multiferroics; transition-metal ions can readily adopt different valence states, and so defects such as oxygen vacancies are easily accommodated. These in turn cause hopping conductivity, poor insulation, leaky hysteresis loops and unreliable ferroelectric response.

Two recent reports of spontaneous magnetization in thin-film samples [52, 84] are particularly intriguing. A likely origin of the magnetization is a canting of the antiferromagnetic sublattices, combined with a suppression of the spiral in the thin film, resulting in a macroscopic magnetization. Such weak ferromagnetism is intimately connected with the symmetry of the system [72]; in $BiFeO_3$ it can occur if the sublattice magnetizations are oriented in the (111) plane so that the symmetry is reduced to the magnetic space group Bb or Bb'. A recent first-principles study concluded [66] that the preferred orientation of the magnetic moments is indeed within the (111) plane, compatible with the existence of weak ferromagnetism, and that the magnetic moments cant away from the collinear direction (while remaining in the (111) plane) by an angle of about 1° (Fig. 22). This leads to a small but measurable magnetization of approximately $0.05\,\mu_B$ per iron ion provided that the long-

Table 1. Various measured values for the polarization in $BiFeO_3$, in chronological order with the oldest at the top

Ref.	P ($\mu C/cm^2$)	Sample type
[69]	6.1	bulk single crystals
[81]	2.5	$(Bi_{0.7}Ba_{0.3})(Fe_{0.7}Ti_{0.3})O_3$ films (300 nm) on Nb-doped $SrTiO_3$
[82]	2.2	polycrystalline films (200 nm)
[52]	50–90	thin films (400–100 nm) on $SrRuO_3/SrTiO_3$
[83]	35.7	polycrystalline films (350 nm)
[79]	8.9	bulk ceramics
[80]	158	polycrystalline films (300 nm)

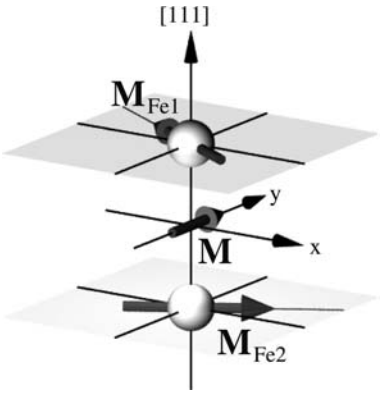

Fig. 22. Calculated magnetic structure including the spin-orbit interaction: The two iron magnetic moments rotate in the (111) plane so that there is a resulting spontaneous magnetization, **M**. From [66]. Copyright (2005) by the American Physical Society

wavelength spiral is suppressed. This value is consistent with values reported in [84] and for the thicker samples in [52], however, [52] also reports an increase in magnetization as film thickness is decreased, which remains to be explained.

The details of the thickness dependence of the polarization and magnetization are still not well understood and provide strong motivation for further work both on $BiFeO_3$ and on other multiferroic thin films.

3.3.2 $BiMnO_3$

$BiMnO_3$ is unusual because (as established in early work [85–87]) it is a ferromagnetic insulator, with a Curie temperature of around 100 K. Motivated by the observation of ferroelectricity in $BiFeO_3$, *Hill* and *Rabe* [88] used density-functional theory to search for ferroelectricity in $BiMnO_3$, and indeed found a strong ferroelectric instability consisting in large part of relative Bi−O displacements. A subsequent structure determination using both electron and neutron diffraction [89] indicated monoclinic symmetry with a $C2$ space group, both compatible with the existence of ferroelectricity. And a calculation of the electron localization function for the experimentally determined structure [90] showed that the lone pairs on the Bi play a crucial role in stabilizing the ferroelectric ground state. Motivated by these results, ferroelectric hysteresis loops were measured in polycrystalline samples, as reproduced in Fig. 23. The electric hysteresis persisted into the ferromagnetic regime, suggesting a coexistence of ferromagnetism and ferroelectricity, although the very small values for saturation polarization, and the loss of switching response near room temperature, are indicative of incomplete polarization switching and leakage in the material.

Although there had been a number of reproducible reports of ferromagnetism in $BiMnO_3$ in the 1960s, when the material was revisited in the 1990s a number of researchers suggested that the magnetic ordering was probably driven by defects such as oxygen vacancies, rather than being intrinsic to the system. This assessment was based on the robust antiferromagnetic behavior of the closely related perovskite, $LaMnO_3$, which is well explained by Goodenough's valence-bond-theory considerations [32]. However, it is important to remember that, even in $LaMnO_3$, each Mn ion has four neighbors that are ferromagnetically coupled to it, and two that are antiferromagnetically coupled; i.e., the majority of Mn−Mn interactions are in fact ferromagnetic. Since ferro- and antiferromagnetic coupling lead to different Mn−Mn distances, the stress in the $LaMnO_3$ lattice is reduced if the orbitals order to align all the ferromagnetic interactions in one plane, with adjacent planes coupled antiferromagnetically to each other, as shown in Fig. 24a. However, analysis of Mn−O bond lengths in $BiMnO_3$ indicates the presence of an unusual orbital ordering, shown in Fig. 24, which is driven by strain introduced by the stereochemically active Bi lone pairs. This arrangement does not lead to cancellation of the feromagnetic interactions, and results in a net ferromagnetism in $BiMnO_3$ [92]. Thus, the lone pairs are responsible for *both* the ferroelectricity *and* the ferromagnetism.

The most recent experiments observed a centrosymmetric-to-noncentrosymmetric structural phase transition at $T_E = 750$–770 K [64], and found a magnetocapacitance effect in which changes in dielectric constant were induced by applied magnetic fields near the magnetic ordering temperature [64].

This small literature of work on $BiMnO_3$ and $BiFeO_3$ is encouraging because it establishes the viability of inducing ferroelectric distortions using the

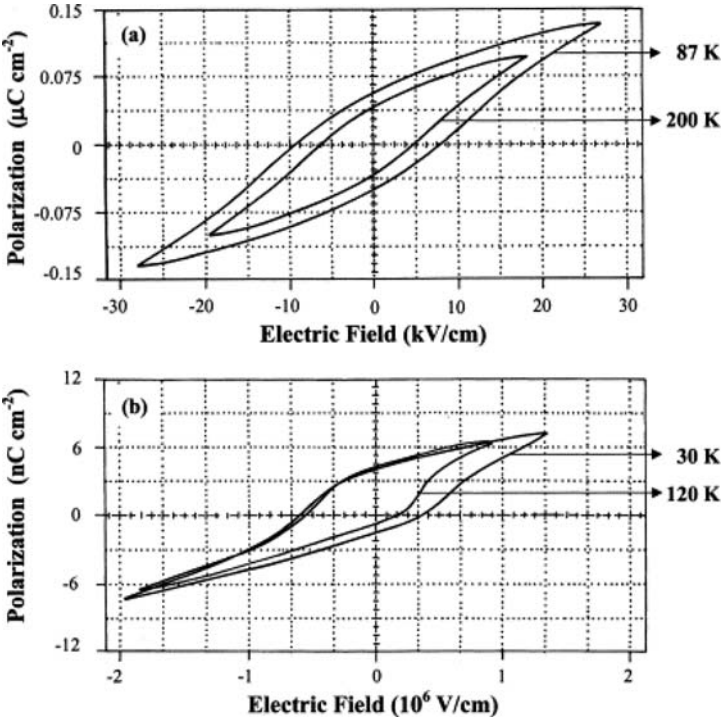

Fig. 23. *P–E* hysteresis loops of: (**a**) polycrystalline $BiMnO_3$ and (**b**) thin film of $BiMnO_3$ on Si(100) through the ferromagnetic Curie temperature. From [91]

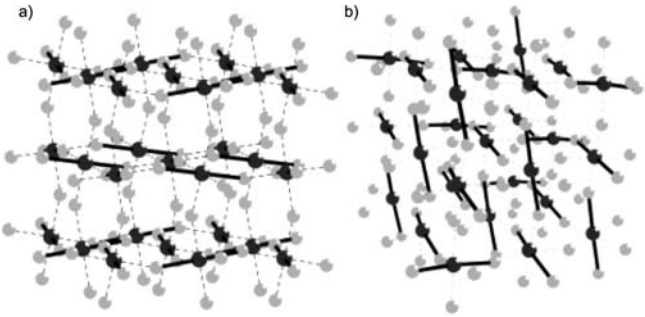

Fig. 24. The two-dimensional orbital ordering in $LaMnO_3$ (**a**) is compared with the three-dimensional orbital ordering in $BiMnO_3$ (**b**). The *bold lines* represent the orientation of the d_{z^2} orbitals, as revealed by elongations of the MnO_6 octahedra. The *black circles* show the positions of the Mn ions, and the *gray circles* represent the oxygens. From [92]. Copyright (2002) by the American Physical Society

A-site cation, even in materials in which the B-site cation is not ferroelectrically active. In addition, it shows that such materials can have ferromagnetic ground states. However, it also highlights some problems that might be generic to all multiferroics. First, the samples tend to be leaky, and the ferroelectric hysteresis is lost at temperatures far below the 750 K phase transition to the centrosymmetric phase, as a result of the conductivity. This might be expected to occur in many multiferroics, since the transition-metal ions that must be incorporated in order to provide magnetism are notoriously flexible in their choice of oxidation state. Perhaps choosing more robust ions such as Fe^{3+} (d^5) and Cr^{3+} (d^3) might alleviate this problem. Next, insulating ferromagnetism is notoriously difficult to obtain, and even in materials such as $BiMnO_3$, it is not very robust. Therefore a *room-temperature* ferromagnetic ferroelectric, with large magnetization and electric polarization, might continue to be elusive.

3.3.3 $YMnO_3$

$YMnO_3$ is an antiferromagnetic ferroelectric, in which the mechanism for ferroelectricity has only recently been identified [93, 94]. Although the antiferromagnetic arrangement of the magnetic moments yields no net magnetization, we discuss $YMnO_3$ here because the mechanism for the ferroelectricity is compatible with the existence of magnetic ions, and so is promising for the design of new ferromagnetic ferroelectrics. $YMnO_3$ forms in a hexagonal structure consisting of layers of MnO_5 trigonal bipyramids, with Y^{3+} ions occupying sevenfold coordinated interstices. The MnO_5 trigonal bipyramids are in-plane corner linked to form nonconnected layers and the apical oxygen ions (O_T) form two close-packed layers, separated by a layer of Y^{3+} ions. A schematic view of the crystal structure is given in Fig. 25. Early (1960s) work [95, 96] established $YMnO_3$ to be ferroelectric, with space group $P6_3cm$, and revealed an A-type antiferromagnetic ordering with noncollinear Mn spins oriented in a triangular arrangement [97, 98]. However, these early structure determinations incorrectly concluded that the ferroelectric polarization arises from an offcenter distortion of the Mn ion towards one of the apical oxygen ions. (*Yakel* et al. [95] reported the two Mn-O_T distances to be 1.84 Å and 1.93 Å.)

Recent single-crystal X-ray diffraction measurements by *van Aken* et al. [22, 99–101] show that the reported offcentering of the Mn ions is incorrect [95, 102], and in fact the Mn ions remain at the center of the oxygen bipyramids. (The modern results are more accurate because the *hkl* reflections with both $l < 0$ and $l > 0$ are measured. This is necessary for such twinned and noncentrosymmetric crystals due to anomalous corrections on the scattering factors). Instead, the main difference between the high- and low-temperature structures is that in the high-temperature phase all ions are constrained to planes, parallel to the *ab* plane. Below the transition temperature the structure loses the mirror planes perpendicular to the hexagonal *c*-axis. First-principles density-functional calculations by *van Aken* et al. [93]

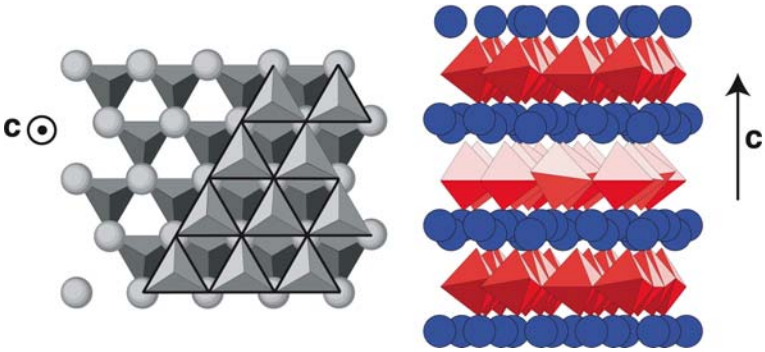

Fig. 25. The crystal structure of $YMnO_3$ in the paraelectric (*left*) and ferroelectric (*right*) phases. The trigonal bipyramids depict the MnO_5 polyhedra and the spheres represent Y ions. The *left panel* shows the stacking of two consecutive MnO_5 layers and the sandwiched Y layer looking down the *c*-axis in the paraelectric phase. The *right panel* shows the layered nature of $YMnO_3$ and the out-of-plane displacements that cause the ferroelectric dipole moment.

confirm the experimental ground-state structure, and reproduce the experimentally reported ferroelectric polarization [103] ($\sim 6\,\mu C/cm^2$). The structures of the high- and low-symmetry phases are shown in Fig. 26, with the experimental bond lengths indicated.

Density-functional calculations also indicate that no significant changes in chemical bonding occur between the high- and low-symmetry phases, and that the Born effective charges remain close to the formal ionic charges; this is consistent with the small values of ferroelectric polarization compared to those in conventional perovskite ferroelectrics such as $BaTiO_3$ or $PbTiO_3$. Indeed, in this case, the ferroelectric phase transition is driven entirely by electrostatic forces and size effects. The Y^{3+} ion is too small to fill the A-site of the high-symmetry structure, and below the Curie temperature the structure collapses to reduce the volume at the Y^{3+} site. The details of the temperature phase diagram have, however, proved difficult to establish unambiguously. Observation of features at two separate temperatures in high-temperature diffraction [104] led to the suggestion that the transition from the paralectric $P63/mmc$ to the ferroelectric $P63\,cm$ phase takes place in two steps. As temperature is reduced, the unit-cell-tripling K_3 mode would first lower the symmetry but not lead to a ferroelectric polarization.

At a significantly lower temperature a ferroelectric transition would take place without further reduction in symmetry. This would be consistent with earlier reports of no symmetry-lowering structural phase transition at the ferroelectric T_c [105, 106]. However, first-principles calculations show that the polarization is nonzero once the K_3 mode sets in, so that there is a single improper ferroelectric transition; the lower-temperature feature could

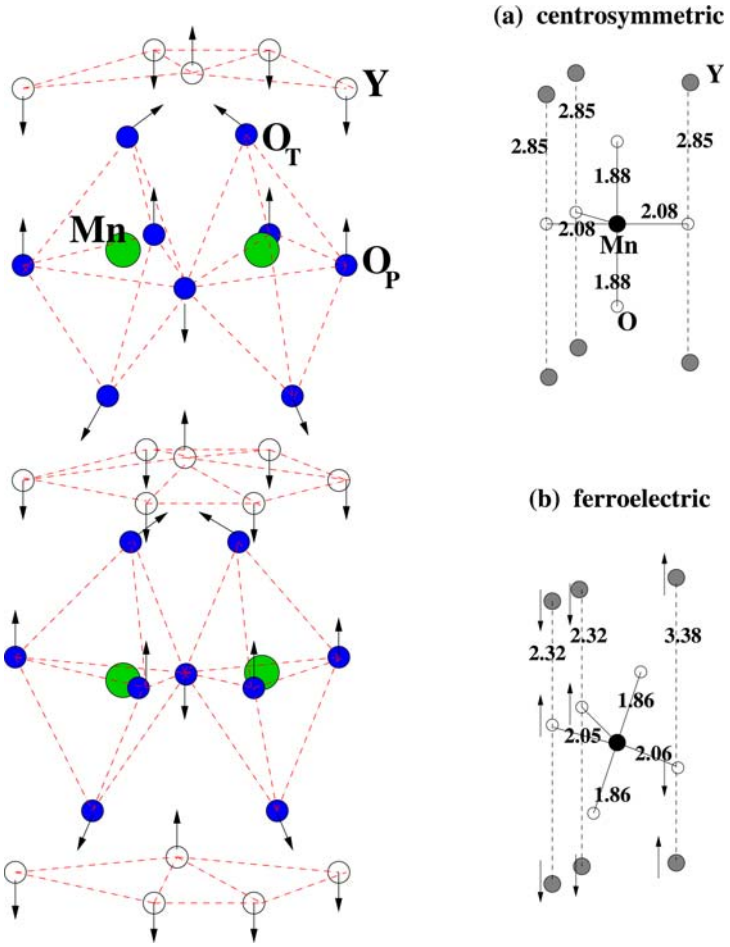

Fig. 26. *Left:* 3-dimensional schematic view of $YMnO_3$ in one of the two ferroelectric polarized states. *Right:* MnO_5 polyhedra surrounded by Y layers. (**a**) and (**b**) panels show the measured atomic positions in the centrosymmetric and ferroelectric structure, respectively [107, 108]. In all cases the *arrows* indicate the directions of the atomic displacements moving from the centrosymmetric to the ferroelectric structure

be attributed to nonlinearity in the dependence of the polarization on the K_3 amplitude [94].

The possibility of designing new magnetic ferroelectrics using this "geometrically driven" mechanism to provide the ferroelectricity has not yet been extensively explored. In principle, however, it holds tremendous promise, since no chemical rehybridization is required to drive the offcentering, and so there is no incompatibility with the presence of magnetic ions.

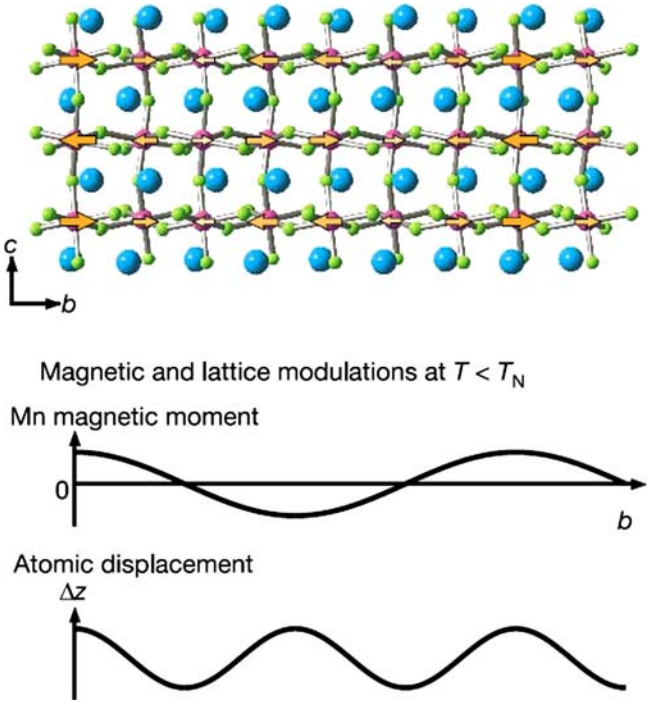

Fig. 27. Sketch of the crystal structure of $TbMnO_3$. The *arrows* indicate the magnitudes of the local magnetic moments at the Mn ions. The *lower plots* show how the atomic displacements from the ideal centrosymmetric positions correlate with the magnitude of the Mn magnetic moments. Adapted by permission from [57]

3.3.4 $TbMnO_3$

Finally we mention an entirely new mechanism for combining magnetism and ferroelectricity that has recently been demonstrated in $TbMnO_3$ [57]. Although the effect occurs only at very low temperatures, and leads to small ($\sim 10^{-2}\,\mu C/cm^2$) polarizations, it is intriguing because the ferroelectricity occurs *as a result of* the magnetic ordering, and hence is intimately coupled. Below $\sim 30\,K$, the magnetic ordering in $TbMnO_3$ is a spin spiral that is incommensurate with the crystal structure, and lacks inversion symmetry. As a result, when the spin spiral occurs, ferroelectricity becomes symmetry allowed, and a small polarization develops (Fig. 27).

3.4 Composites

Composite materials containing both ferromagnets and ferroelectrics offer an alternative to single-phase multiferroics. A number of architectures have

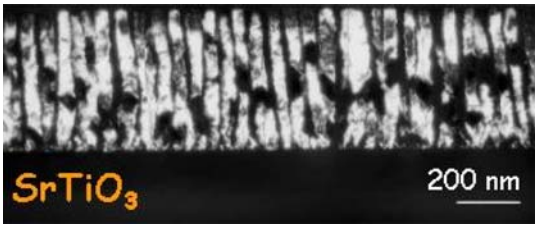

Fig. 28. Pillars of cobalt ferrite grown within a barium titanate matrix. From [112]

been tried, largely focused on bulk ceramics. In particular, thick-film bi- and multilayers of nickel ferrite and lead titanate [109], and of lanthanum manganites and lead zirconium titanate [110] as well as particulate composites of PZT/Ni-ferrite [111] show robust magnetoelectric properties. Most recently, "nanopillars" of cobalt ferrite, $CoFe_2O_4$, have been grown within a barium titanate matrix using pulsed vapor deposition (see Fig. 28) [112]. This approach is particularly promising for obtaining thin films with large magnetoelectric coefficients, because epitaxial matching between the ferroelectric and the ferrimagnet is obtained in three dimensions (rather than just two as in multilayers). Preliminary results are encouraging, and the field is ripe for further experimental and theoretical exploration.

4 Outlook

It is clear that ferromagnets and ferroelectrics share more in common than the roots of their names, in spite of having some important differences. In particular, many growth methods, characterization techniques and theoretical implementations, are applicable to both areas. However their respective research fields have, in large part, developed independently, with little overlap between their researchers. We hope that this chapter will ease the transition for workers wishing to move between the two fields, and even provide some motivation for crossfertilization and collaboration.

Acknowledgements

The author's work in this field has benefited from discussions and collaborations with a large number of colleagues, in particular Bas van Aken, Pio Baettig, Claude Ederer, Manfred Fiebig, Alessio Filippetti, Daniil Khomskii, Tsuyoshi Kimura, Richard LeSar, Thomas Palstra, Stuart Parkin, Warren Pickett, Karin Rabe, R. Ramesh, Darrell Schlom, Hans Schmid, Jim Scott, Chuck Schelle, Ram Seshadri and Umesh Waghmare. Funding during the time spent writing this chapter was provided by the NSF's *Chemical Bonding Centers* program, Grant No. CHE-0434567.

References

[1] J. Valasek: Piezoelectric and allied phenomena in rochelle salt, Phys. Rev. **17**, 475 (1921) 175

[2] A. von Hippel: Ferroelectricity, domain structure, and phase transitions of barium titanate, Rev. Mod. Phys. **22**, 221–237 (1950) 176

[3] R. S. Tebble, I. C. Skidmore, W. D. Corner: The Barkhausen effect, Proc. Phys. Soc. A **63**, 739–761 (1950) 176

[4] R. E. Cohen: Origin of ferroelectricity in perovskite oxides, Nature **358**, 136–138 (1992) 178, 180

[5] R. E. Cohen: Theory of ferroelectrics: A vision for the next decade and beyond, J. Phys. Chem. Solids **61**, 139–146 (2000) 178

[6] H. D. Megaw: Origin of ferroelectricity in barium titanate and other perovskite-type crystals, Acta Crystallogr. **5**, 739–749 (1952) 178

[7] P. S. Halasyamani, K. R. Poeppelmeier: Non-centrosymmetric oxides, Chem. Mater. **10**, 2753–2769 (1998) 178

[8] U. Opik, M. L. H. Pryce: Studies of the Jahn–Teller effect I: A survey of the static problem, Proc. Roy. Soc. A **238**, 425–447 (1957) 178

[9] R. F. W. Bader: An interpretation of potential interaction constants in terms of low-lying excited states, Mol. Phys. **3**, 137–151 (1960) 178

[10] I. B. Bersuker: Modern aspects of the Jahn–Teller theory and applications to molecular problems, Chem. Rev. **101**, 1067–1114 (2001) 178

[11] J. K. Burdett: Use of the Jahn–Teller theorem in inorganic chemistry, Inorg. Chem. **20**, 1959–1962 (1981) 179

[12] I. B. Bersuker: *The Jahn–Teller Effect and Vibronic Interactions in Modern Chemistry* (Plenum 1984) 179

[13] M. Atanasov, D. Reinen: Density functional studies on the lone pair effect of the trivalent group V elements: I. Electronic structure, vibronic coupling, and chemical criteria for the occurrence of lone pair distortions in AX_3 molecules (A=N to Bi; X=H, and F to I), J. Phys. Chem. A **105**, 450–5467 (2001) 179

[14] A. Filippetti, N. A. Hill: Coexistence of magnetism and ferroelectricity in perovskites, Phys. Rev. B **65**, 195120 (2002) 179, 180

[15] U. V. Waghmare, N. A. Spaldin, H. C. Kandpal, R. Seshadri: First principles indicators of metallicity and cation off-centricity in the IV-VI rock-salt chalcogenides of divalent Ge, Sn and Pb, Phys. Rev. B **67**, 125111 (2003) 180, 181

[16] B. Silvi, A. Savin: Classification of chemical bonds based on topological analysis of electron localization functions, Nature **371**, 683–685 (1994) 180

[17] Y. Kuroiwa, S. Aoyagi, A. Sawada, J. Harada, E. Nishibori, M. Takata, M. Sakata: Evidence for Pb−O covalency in tetragonal $PbTiO_3$, Phys. Rev. Lett. **87**, 217601 (2001) 180

[18] R. E. Cohen, H. Krakauer: Electronic-structure studies of the differences in ferroelectric behavior of $BaTiO_3$ and $PbTiO_3$, Ferroelectrics **136**, 65–83 (1992) 180, 193

[19] A. M. Glazer: The classification of tilted octahedra in perovskites, Acta Crystallogr. B **28**, 3384–3392 (1972) 181

[20] P. M. Woodward: Octahedral tilting in perovskite. I. Geometrical considerations, Acta Crystallogr. B **53**, 32–43 (1997) 181

[21] P. M. Woodward: Octahedral tilting in perovskite. II. Structure stabilizing forces, Acta Crystallogr. B **53**, 44–66 (1997) 181
[22] B. B. van Aken, A. Meetsma, T. T. M. Palstra: Hexagonal $YMnO_3$, Acta Crystallogr. C **57**, 230–232 (2001) 181, 206
[23] G. V. Kozlov, A. A. Volkov, J. F. Scott, G. Feldkamp, J. Petzelt: Millimeter-wavelength spectroscopy of the ferroelectric phase transition in tris-sarcosine calcium chloride $[(CH_3NHCH_2COOH)_3CaCl_2]$, Phys. Rev. B **28**, 255–261 (1983) 181
[24] W. Zhong, R. D. King-Smith, D. Vanderbilt: Giant LO-TO splittings in perovskite ferroelectrics, Phys. Rev. Lett. **72**, 3618–3621 (1994) 181
[25] W. Zhong, D. Vanderbilt, K. Rabe: Phase-transitions in $BaTiO_3$ from first-principles, Phys. Rev. Lett. **73**, 1861–1864 (1994) 181
[26] H. Schmid: *Some Supplementing Comments on the Proceedings of MEIPIC-5* (Kluwer, Dordrecht 2004) 182
[27] D. J. Singh: Structure and energetics of antiferroelectric $PbZrO_3$, Phys. Rev. B **52**, 12559–12563 (1995) 182
[28] P. Ghosez, E. Cockayne, U. V. Waghmare, K. M. Rabe: Lattice dynamics of $BaTiO_3$, $PbTiO_3$, and $PbZrO_3$: A comparative first-principles study, Phys. Rev. B **60**, 836–843 (1999) 182, 183
[29] G. O. Jones, P. A. Thomas: Investigation of the structure and phase transitions in the novel A-site substituted distorted perovskite compound $Na_{0.5}Bi_{0.5}TiO_3$, Acta Crystallogr. B **58**, 168–78 (2002) 184
[30] P. Weiss: L'hypothèse du champ moléculaire et la propriété ferromagnétique, J. Phys. **6**, 661 (1907) 185
[31] E. C. Stoner: Atomic moments in ferromagnetic metals and alloys with non-ferromagnetic elements, Philos. Mag. **15**, 1018–34 (1933) 186
[32] J. B. Goodenough: Theory of the role of covalence in the perovskite-type manganites [LaM(II)]MnO_3, Phys. Rev. **100**, 564–573 (1955) 187, 204
[33] N. A. Spaldin: *Magnetic Materials; Fundamentals and Device Applications* (Cambridge Univ. Press, Cambridge 2003) 188
[34] E. A. Nesbitt: *Ferromagnetic Domains*, Technical report, Bell Telephone Laboratories (1962) 188
[35] C. Kittel, J. K. Galt: Ferromagnetic domain theory, Solid State Phys. **3**, 437–564 (1956) 188
[36] S. Stemmer, S. K. Streiffer, F. Ernst, M. Rühle: Atomistic structure of 90° domain walls in ferroelectric $PbTiO_3$ thin films, Philos. Mag. A **71**, 713–724 (1995) 190
[37] B. Meyer, D. Vanderbilt: *Ab initio* study of ferroelectric domain walls in $PbTiO_3$, Phys. Rev. B **65**, 104111–1–11 (2002) 190
[38] J. Padilla, W. Zhong, D. Vanderbilt: First-principles investigation of 180° domain walls in $BaTiO_3$, Phys. Rev. B **53**, R5969–5973 (1996) 193
[39] G. Engdahl: *Handbook of Giant Magnetostrictive Materials* (Academic Press, New York 2000) 194
[40] O. Auciello, J. F. Scott, R. Ramesh: The physics of ferroelectric memories, Physics Today **51**, 22–27 (1998) 196
[41] J. F. Scott: *Ferroelectric Memories* (Springer 2000) 196
[42] S. Parkin, X. Jiang, C. Kaiser, A. Panchula, K. Roche, M. Samant: Magnetically engineered spintronic sensors and memory, Proc. IEEE **91**, 661–680 (2003) 196

[43] M. Julliére: Tunneling between ferromagnetic films, Phys. Lett. A **54**, 225–226 (1975) 197
[44] J. S. Moodera, L. R. Kinder, T. M. Wong, R. Meservey: Large magnetoresistance at room temperature in ferromagnetic thin film tunnel junctions, Phys. Rev. Lett. **74**, 3273–3276 (1995) 197
[45] H. Schmid: Multiferroic magnetoelectrics, Ferroelectrics **162**, 317–338 (1994) 198
[46] M. Fiebig: Revival of the magnetoelectric effect, J. Phys. D: Appl. Phys. **38**, R1–R30 (2005) 198
[47] N. A. Spaldin, M. Fiebig: The renaissance of magnetoelectric multiferroics, Science **309**, 391–392 (2005) 198
[48] C. Ederer, N. A. Spaldin: Recent progress in first-principles studies of magnetoelectric multiferroics, Curr. Opin. Solid St. M. **9**, 128–139 (2006) cond-mat/0512330 198
[49] V. E. Wood, A. E. Austin: in *Magnetoelectric Interaction Phenomena in Crystals* (Gordon and Breach 1975) 198
[50] N. A. Hill: Why are there so few magnetic ferroelectrics?, J. Phys. Chem. B **104**, 6694–6709 (2000) 199
[51] N. A. Hill: Density functional studies of multiferroic magnetoelectrics, Annu. Rev. Mater. Res. **32**, 1–37 (2002) 199, 200
[52] J. Wang, J. B. Neaton, H. Zheng, V. Nagarajan, S. B. Ogale, B. Liu, D. Viehland, V. Vaithyanathan, D. G. Schlom, U. V. Waghmare, N. A. Spaldin, K. M. Rabe, M. Wuttig, R. Ramesh: Epitaxial $BiFeO_3$ multiferroic thin film heterostructures, Science **299**, 1719 (2003) 199, 202, 203
[53] S. M. Skinner: Magnetically ordered ferroelectric materials, IEEE Trans. Parts, Mater. Packag. **PMP-6**, 68–90 (1970) 199
[54] W. Brixel, J.-P. Rivera, A. Steiner, H. Schmid: Magnetic field induced magnetoelectric effects, $(ME)_H$, in the perovskites Pb_2CoWO_6 and Pb_2FeTaO_6, Ferroelectrics **79**, 201–4 (1988) 199
[55] N. Lampis, P. Sciau, A. Geddo-Lehmann: Rietveld refinements of the paraelectric and ferroelectric structure of $PbFe_{0.5}Ta_{0.5}O_3$, J. Phys. Condens. Matter **12**, 2367–2378 (2000) 199
[56] N. Lampis, P. Sciau, A. Geddo-Lehmann: Rietveld refinements of the paraelectric and ferroelectric structure of $PbFe_{0.5}Nb_{0.5}O_3$, J. Phys. Condens. Matter **11**, 3489–3500 (1999) 199
[57] T. Kimura, T. Goto, H. Shintani, K. Ishizaka, T. Arima, Y. Tokura: Magnetic control of ferroelectric polarization, Nature **426**, 55–58 (2003) 199, 201, 209
[58] P. Baettig, N. A. Spaldin: Ab initio prediction of a multiferroic with large polarization and magnetization, Appl. Phys. Lett. **86**, 012505 (2005) 200
[59] M. Fiebig, V. Eremenko, I. E. Chupis (Eds.): *Proceedings of the 5th International Workshop on Magnetoelectric Interaction Phenomena in Crystals* (Kluwer, Dordrecht 2004) 200
[60] E. Ascher: Higher-order magnetoelectric effects, Philos. Mag. **17**, 149–157 (1968) 200
[61] H. Grimmer: The forms of tensors describing magnetic and toroidal properties, Ferroelectrics **161**, 181–189 (1994) 200
[62] H. Schmid: Magnetoelectric effects in insulating magnetic materials, in W. S. Weiglhoger, A. Lakhtakia (Eds.): *Introduction to Complex Mediums for Optics and Electromagnetics* (SPIE 2003) pp. 167–195 200

[63] M. Fiebig, T. Lottermoser, D. Fröhlich, A. V. Goltsev, R. V. Pisarev: Observation of coupled magnetic and electric domains, Nature **419**, 818–820 (2002) 201
[64] T. Kimura, S. Kawamoto, I. Yamada, M. Azuma, M. Takano, Y. Tokura: Magnetocapacitance effect in multiferroic $BiMnO_3$, Phys. Rev. B **67**, 180401(R) (2003) 201, 204
[65] E. Ascher, H. Rieder, H. Schmid, H. Stössel: Some properties of ferromagnetoelectric nickel-iodine boracite, $Ni_3B_7O_{13}I$, J. Appl. Phys. **37**, 1404–1405 (1966) 201
[66] C. Ederer, N. A. Spaldin: Weak ferromagnetism and magnetoelectric coupling in bismuth ferrite, Phys. Rev. B **71**, 060401(R) (2005) 201, 202, 203
[67] C. Michel, J.-M. Moreau, G. D. Achenbach, R. Gerson, W. J. James: The atomic structure of $BiFeO_3$, Solid State Commun. **7**, 701–703 (1969) 201
[68] F. Kubel, H. Schmid: Structure of a ferroelectric and ferroelastic monodomain crystal of the perovskite $BiFeO_3$, Acta Crystallogr. B **46**, 698–702 (1990) 201
[69] J. R. Teague, R. Gerson, W. J. James: Dielectric hysteresis in single crystal $BiFeO_3$, Solid State Commun. **8**, 1073–1074 (1970) 201, 202, 203
[70] S. V. Kiselev, R. P. Ozerov, G. S. Zhdanov: Detection of magnetic order in ferroelectric $BiFeO_3$ by neutron diffraction, Sov. Phys. Dokl. **7**, 742–744 (1963) 201
[71] I. Sosnowska, T. Peterlin-Neumaier, E. Streichele: Spiral magnetic ordering in bismuth ferrite, J. Phys. C **15**, 4835–4846 (1982) 201
[72] I. E. Dzyaloshinskii: Thermodynamic theory of "weak" ferromagnetism in antiferromagnetic substances, Sov. Phys. JETP **5**, 1259–1272 (1957) 201, 202
[73] T. Moriya: Anisotropic superexchange interaction and weak ferromagnetism, Phys. Rev. **120**, 91–98 (1960) 201
[74] Y. F. Popov, A. K. Zvezdin, G. P. Vorob'ev, A. M. Kadomtseva, V. A. Murashev, D. N. Rakov: Linear magnetoelectric effect and phase transitions in bismuth ferrite, $BiFeO_3$, JETP Lett. **57**, 69–73 (1993) 201
[75] C. Tabarez-Muñoz, J.-P. Rivera, A. Bezinges, A. Monnier, H. Schmid: Measurement of the quadratic magnetoelectric effect on single crystalline $BiFeO_3$, Jpn. J. Appl. Phys. **24**, 1051–1053 (1985) 201
[76] I. Sosnowska, W. Schäfer, W. Kockelmann, K. H. Andersen, I. O. Troyanchuk: Crystal structure and spiral magnetic ordering in $BiFeO_3$ doped with manganese, Appl. Phys. A **74**, S1040–S1042 (2002) 201
[77] J. B. Neaton, C. Ederer, U. V. Waghmare, N. A. Spaldin, K. M. Rabe: First-principles study of spontaneous polarization in multiferroic $BiFeO_3$, Phys. Rev. B **71**, 014113 (2005) 201, 202
[78] J. Íñiguez, L. Bellaiche, D. Vanderbilt: First-principles study of $(BiScO_3)_{1-x}$–$(PbTiO_3)_x$ alloys, Phys. Rev. B **67**, 224107 (2003) 202
[79] Y. P. Wang, L. Zhou, M. F. Zhang, X. Y. Cheng, J.-M. Liu, Z. G. Liu: Room-temperature saturated ferroelectric polarization in $BiFeO_3$ ceramics synthesized by rapid liquid phase sintering, Appl. Phys. Lett. **84**, 1731 (2004) 202, 203
[80] K. Y. Yun, D. Ricinschi, T. Kanashima, M. Noda, M. Okuyama: Jpn. J. Appl. Phys. **43**, L647 (2004) 202, 203

[81] K. Ueda, H. Tabata, T. Kawai: Coexistence of ferroelectricity and ferromagnetism in $BiFeO_3-BaTiO_3$ thin films at room temperature, Appl. Phys. Lett. **75**, 555–557 (1999) 202, 203
[82] V. R. Palkar, J. John, R. Pinto: Observation of saturated polarization and dielectric anomaly in magnetoelectric $BiFeO_3$ thin films, Appl. Phys. Lett. **80**, 1628 (2002) 202, 203
[83] K. Y. Yun, M. Noda, M. Okuyama: Prominent ferroelectricity of $BiFeO_3$ thin films prepared by pulsed-laser deposition, Appl. Phys. Lett. **83**, 3981 (2003) 203
[84] W. Eerenstein, F. D. Morrison, J. Dho, M. G. Blamire, J. F. Scott, N. Mathur: Comment on 'epitaxial $BiFeO_3$ multiferroic thin film heterostructures', Science **307**, 1203a (2005) 202, 203
[85] F. Sugawara, S. Iida: New magnetic perovskites $BiMnO_3$ and $BiCrO_3$, J. Phys. Soc. Jpn. **20**, 1529 (1965) 204
[86] F. Sugawara, S. Iida, Y. Syono, S. Akimoto: Magnetic properties and crystal distortions of $BiMnO_3$ and $BiCrO_3$, J. Phys. Soc. Jpn. **26**, 1553–1558 (1968) 204
[87] V. A. Bokov, I. E. Myl'nikova, S. A. Kizhaev, M. F. Bryzhina, N. A. Grigorian: Structure and magnetic properties of $BiMnO_3$, Sov. Phys. Solid State **7**, 2993–2994 (1966) 204
[88] N. A. Hill, K. M. Rabe: First principles investigation of ferromagnetism and ferroelectricity in $BiMnO_3$, Phys. Rev. B **59**, 8759–69 (1999) 204
[89] T. Atou, H. Chiba, K. Ohoyama, Y. Yamaguichi, Y. Syono: Structure determination of ferromagnetic perovskite $BiMnO_3$, J. Solid State Chem. **145**, 639–642 (1999) 204
[90] R. Seshadri, N. A. Hill: Visualizing the role of Bi 6*s* "lone pairs" in the off-center distortion in ferromagnetic $BiMnO_3$, Chem. Mater. **13**, 2892–2899 (2001) 204
[91] A. Moreira dos Santos, S. Parashar, A. R. Raju, Y. S. Zhao, A. K. Cheetham, C. N. R. Rao: Evidence for the likely occurence of magnetoferroelectricity in the simple perovskite $BiMnO_3$, Solid State Commun. **122**, 49–52 (2002) 205
[92] A. Moreira dos Santos, A. K. Cheetham, T. Atou, Y. Syono, Y. Yamaguchi, K. Ohoyama, H. Chiba, C. N. R. Rao: Orbital ordering as the determinant for ferromagnetism in biferroic $BiMnO_3$, Phys. Rev. B **66**, 064425 (2002) 204, 205
[93] B. B. van Aken, T. T. M. Palstra, A. Filippetti, N. A. Spaldin: The origin of ferroelectricity in magnetoelectric $YMnO_3$, Nature Mater. **3**, 164–170 (2004) 206
[94] C. J. Fennie, K. M. Rabe: Ferroelectric transition in $YMnO_3$ from first principles, Phys. Rev. B **72**, 100103(R) (2005) 206, 208
[95] H. L. Yakel, W. C. Koehler, E. F. Bertaut, E. F. Forrat: On the crystal structure of the manganese (III) trioxides of the heavy lanthanide and yttrium, Acta Crystallogr. **16**, 957–962 (1963) 206
[96] G. A. Smolenskii, V. A. Bokov: Coexistence of magnetic and electric ordering in crystals, J. Appl. Phys. **35**, 915–918 (1964) 206
[97] E. F. Bertaut, R. Pauthenet, M. Mercier: Proprietes magnetiques et structures du manganite d'yttrium, Phys. Lett. **7**, 110–111 (1963) 206
[98] E. F. Bertaut, R. Pauthenet, M. Mercier: Sur des proprietes magnetiques du manganite d'yttrium, Phys. Lett. **18**, 13 (1965) 206

[99] B. B. van Aken, A. Meetsma, T. T. M. Palstra: Hexagonal $LuMnO_3$ revisited, Acta Crystallogr. E **57**, i38 (2001) 206
[100] B. B. van Aken, A. Meetsma, T. T. M. Palstra: Hexagonal $LuMnO_3$ revisited, Acta Crystallogr. E **57**, i87 (2001) 206
[101] B. B. van Aken, A. Meetsma, T. T. M. Palstra: Hexagonal $LuMnO_3$ revisited, Acta Crystallogr. E **57**, i101 (2001) 206
[102] M. Isobe, N. Kimizuka, M. Nakamura, T. Mohri: Structure of $YbMnO_3$, Acta Crystallogr. C **47**, 423–425 (1991) 206
[103] N. Fujimura, T. Ishida, T. Yoshimura, T. Ito: Epitaxially grown $YMnO_3$ film: New candidate for nonvolatile memory devices, Appl. Phys. Lett. **69**, 1011–1013 (1996) 207
[104] T. Lonkai, D. G. Tomuta, U. Amann, J. Ihringer, R. W. A. Hendrikx, D. M. Tobbens, J. A. Mydosh: Development of the high temperature phase of hexagonal manganites, Phys. Rev. B **69**, 134108 (2004) 207
[105] K. Łukaszewicz, J. Karut-Kalicinska: X-ray investigations of the crystal structure and phase transitions of $YMnO_3$, Ferroelectrics **7**, 81–82 (1974) 207
[106] T. Katsufuji, S. Mori, M. Masaki, Y. Moritomo, N. Yamamoto, H. Takagi: Dielectric and magnetic anomalies and spin frustration in hexagonal $RMnO_3$ (R=Y, Yb and Lu), Phys. Rev. B p. 104419 (2001) 207
[107] B. B. van Aken, A. Meetsma, Y. Tomioka, Y. Tokura, T. T. M. Palstra: Structural response to O*-O' and magnetic transitions in orthorhombic perovskites, Phys. Rev. B **66**, 224414 (2002) 208
[108] B. B. van Aken: Ph.D. thesis, University of Groningen URL: `www.ub.rug.nl/eldoc/dis/science/b.b.van.aken` 208
[109] G. Srinivasan, E. T. Rasmussen, J. Gallegos, R. Srinivasan, Y. I. Bokhan, V. M. Laletin: Magnetoelectric bilayer and multilayer structures of magnetostrictive and piezoelectric oxides, Phys. Rev. B **64**, 214408 (2001) 210
[110] G. Srinivasan, E. T. Rasmussen, B. J. Levin, R. Hayes: Magnetoelectric effects in bilayers and multilayers of magnetostrictive and piezoelectric perovskite oxides, Phys. Rev. B **65**, 134402 (2002) 210
[111] J. Ryu, A. Vázquez Carazo, K. Uchino, H.-E. Kim: Piezoelectric and magnetoelectric properties of lead zirconate titanate / Ni-ferrite particulate composites, J. Electroceram. **7**, 17–24 (2001) 210
[112] H. Zheng, J. Wang, S. E. Lofland, Z. Ma, L. Mohaddes-Ardabili, T. Zhao, L. Salamanca-Riba, S. R. Shinde, S. B. Ogale, F. Bai, D. Viehland, Y. Jia, D. G. Schlom, M. Wuttig, A. Roytburd, R. Ramesh: Multiferroic $BaTiO_3$–$CoFe_2O_4$ nanostructures, Science **303**, 661–663 (2004) 210

Index

Growth and Novel Applications of Epitaxial Oxide Thin Films

Agham-Bayan Posadas[1], Mikk Lippmaa[2], Fred J. Walker[1], Matthew Dawber[3], Charles H. Ahn[1,4], and Jean-Marc Triscone[3]

[1] Department of Applied Physics, Yale University, New Haven CT 06520-8284, USA
agham-bayan.posadas@yale.edu
charles.ahn@yale.edu
fred.walker@yale.edu
[2] Institute for Solid State Physics, University of Tokyo, 5-1-5 Kashiwanoha, Kashiwa, 277-8581 Chiba, Japan
mlippmaa@issp.u-tokyo.ac.jp
[3] Condensed Matter Physics Department, University of Geneva, 24 Quai Ernest Ansermet, CH-1211 Geneva 4, Switzerland
matthew.dawber@physics.unige.ch
jean-marc.triscone@physics.unige.ch
[4] Department of Physics, Yale University, New Haven CT 06520-8120, USA
charles.ahn@yale.edu

Abstract. This chapter addresses key developments in the ability to grow epitaxial oxide films and provides examples of possible applications of these structures.

1 Introduction

Over the past two decades, a tremendous amount of progress has been achieved in the epitaxial growth[1] of thin films of various complex oxides, including ferroelectrics. Many groups are now capable of routinely growing single-crystalline films of ferroelectrics, high-T_c superconductors, colossal magnetoresistive (CMR) materials, magnetic, dielectric, conducting, and other types of oxides over a wide range of thicknesses and with a high degree of control over the properties and structures. Such progress has been driven and made possible by several key aspects. First, the availability of various single-crystalline oxide substrates has been crucial in the ability to grow high-quality single-layer epitaxial complex oxide films with properties equaling, and sometimes surpassing, the bulk single-crystal forms of the materials. In the late 1980s and early 1990s, substrate development was driven

[1] Epitaxy literally means "from the surface" and was first used in the mineralogical literature to describe the formation of crystalline materials that always had crystallographic relationships as determined by faceting. In modern thin-film growth, epitaxy refers to the deposition of a crystalline layer that is in registry to an underlying crystalline substrate.

K. Rabe, C. H. Ahn, J.-M. Triscone (Eds.): Physics of Ferroelectrics: A Modern Perspective, Topics Appl. Physics **105**, 219–304 (2007)

by the efforts of researchers to grow complex materials such as the high-T_c superconductors $YBa_2Cu_3O_x$ and $Bi_2Sr_2Ca_nCu_{n+1}O_x$. The newly developed substrates were not only structurally matched to the high-T_c superconductors, but some also possessed dielectric properties tailored to fit some specific microwave applications of the materials. Much study has also been devoted to substrate preparation in order to obtain an atomically flat surface, which is crucial in certain applications such as field-effect devices, as well as in the ability to grow high-quality multilayers and superlattices. Because of the importance of having a good substrate, new substrates are continually being developed even today, as exemplified by the development of rare-earth scandate single crystals. These recent developments are being driven by the desire to tune the strain of the film to be grown to obtain greatly improved properties as well as to induce new phenomena. High-quality substrates that span the entire range of lattice constants of the perovskite structure and that can be made atomically flat are becoming available.

A second key to progress in epitaxial growth has been the continuous improvement in the various growth techniques. In the 1990s, most oxide film growth was done using sputtering and pulsed laser deposition (also known as laser ablation). The principle behind these two techniques is to eject the source material by either a plasma or a laser, with the ejected material eventually finding its way onto the substrate. Many improvements in these techniques were driven by the goal of obtaining high-quality complex oxide films with atomically smooth surfaces. More recently, the use of molecular beam epitaxy (MBE) in growing complex oxides has become feasible. The development of MBE techniques for oxide growth has opened up the ability to have submonolayer control over film deposition. Oxide MBE has enabled the growth of complex oxide superlattices that are similar to semiconductor superlattices in terms of quality, which has resulted in the ability to test idealized theoretical models, particularly in the field of studying the effect of strain on ferroelectricity. The ability to grow virtually any complicated structure has made real-time feedback between theory and experiment a reality. Oxide MBE has also been crucial in the ability to integrate complex oxides directly onto semiconductors, in particular onto silicon, where SiO_2 formation is intolerable for certain applications.

A third key in the development of epitaxial film growth techniques has been the adaptation of concepts used in the semiconductor field to fabricate multiple materials systems that can be used as a new experimental platform for the study of complex oxides. One such device concept that has recently gained attention is the growth of complex oxide superlattices. These superlattices allow one to potentially customize the properties of the entire system for a specific experiment or application. For example, one can use strained-layer superlattices to achieve a large increase in the polarization of a ferroelectric film while drastically reducing leakage currents. There are also technological driving factors that are involved in the development of epitaxial complex oxides. One example is the need to replace SiO_2 with high-k dielectrics for

continued scaling of silicon-based metal-oxide-semiconductor field effect transistors to the sub-65-nm regime. There is also a continuing search for a suitable gate dielectric for wide-bandgap semiconductors such as GaN and SiC. Furthermore, the possibility for various integrated sensor-transistors where the transistor is directly coupled to the environment for greater sensitivity, lower power operation, and higher operating speed is a strong motivation for further work in this area. This type of application requires direct interfacing between a functional complex oxide and a traditional semiconductor, and achieving an abrupt interface turns out not to be straightforward.

2 Thin-Film Growth of Complex Oxides

In order to grow high-quality thin films of complex oxides that typically contain three or more elements, one must use film-deposition techniques that allow one to either a) stoichiometrically transfer the composition of the source material to the substrate or b) allow one to precisely control (with monolayer or better degree of precision) the fluxes of the elements involved. This is primarily because of the multicomponent nature of the typical complex oxide, and also because many of these materials do not have line compositions. This means that, unlike in the growth of compound semiconductors, one cannot have an excess of one element over another (with the exception of oxygen) without also resulting in an excess of that element in the film. Three film-deposition techniques are now routinely used to grow epitaxial films of complex oxides: pulsed laser deposition or PLD, sputter deposition, and molecular beam epitaxy. These three techniques fall under the broad category of film deposition methods known as physical vapor deposition (PVD), where chemical reactions are not involved in the growth of the film. This section looks more closely at each of the three techniques. Aspects applicable to all three methods are discussed first (vacuum chamber and substrate heating), followed by specific aspects of each growth method.

2.1 Vacuum Chamber

A large number of variations of the basic physical vapor deposition system exists, but many features are common to most setups. The essential components of a modern PVD system are shown in Fig. 1. A thin film is grown on a substrate that is held on a sample manipulator. In the simplest cases the sample may be attached to a fixed heater element, but it is more common to have a manipulator that also allows the sample to be rotated, shifted, and possibly tilted in the chamber. Mechanical manipulation is necessary in ultrahigh vacuum systems for loading and unloading samples, but also for positioning the sample for in-situ diagnostics, for example, by electron diffraction.

Depending on the specific deposition technique and source material, thin-film growth is done at background gas pressures ranging from ultrahigh vacuum (UHV) up to pressures on the order of a few Torr. Although thin films,

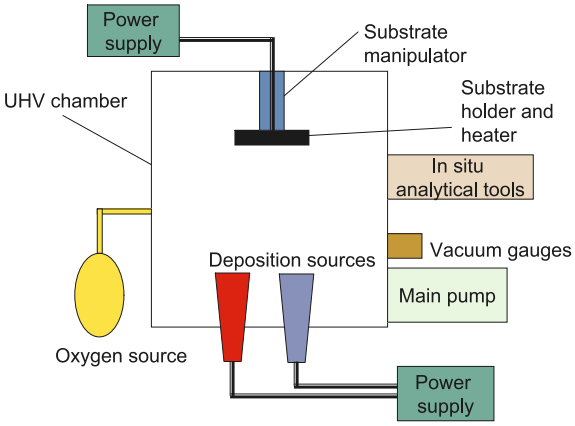

Fig. 1. Schematic diagram of a basic PVD system

especially oxides, are usually not grown in UHV conditions because of the presence of relatively large amounts of oxygen, particularly for sputter and pulsed laser deposition, it is still often necessary to have a UHV-capable deposition chamber in order to reduce the level of contaminants in the deposition system during growth and to perform vacuum annealing of samples. Well-designed deposition chambers can reach base pressures of $\approx 10^{-10}$ Torr, and a load-lock chamber is used for changing samples and targets to keep the main chamber clean. The vacuum pump can be attached directly to the chamber with a gate valve. For sputtering and PLD, in order to work at gas pressures above 1 mTorr, it is possible to close or throttle the gate valve and use a separate bypass valve to reduce the gas flow through the main pump. An angle valve in parallel with the gate valve performs well as a bypass line and can be adjusted so that the backpressure of the main pump does not exceed safe limits, even when the pressure in the chamber approaches 1 Torr.

The process gas is usually fed into the chamber with a molecular leak valve. A nozzle can be used to direct the fresh gas directly at the sample surface. Pressure measurements can be done with multiple gauges, combining convectron-type, ion, and absolute-pressure capacitive gauges. Since each gauge measures pressure at a different point in the chamber, care needs to be taken when trying to estimate the true partial pressure of oxygen at the sample surface, especially when a nozzle is used on the gas-feed line.

2.2 Temperature Control and Monitoring

Many oxide materials need to be grown at elevated temperatures to obtain a suitable crystal structure, phase, domain structure, lattice orientation, or simply to improve crystallinity. The easiest way to heat a sample to moderate temperatures is to use a resistive block heater or a ceramic heater. A substrate can be attached to the heater by silver paste or clamped directly to

the heater surface. The sample temperature can be monitored by attaching a thermocouple to the heater block or heater surface. Resistive-heater designs are common in simple deposition systems that do not require very high temperatures [1]. The cost of the heater element is low, and due to their compact size, heater blocks can be integrated into complex sample manipulators and goniometers [2].

It is common to use oxygen as a background gas during oxide thin-film growth. Due to oxidation, the use of resistive block heaters can become problematic at temperatures above about 500 °C. Metals and alloys that are commonly used at high temperatures under UHV conditions cannot generally be used in the presence of oxygen. (Metals like molybdenum and tungsten form oxides that are volatile at low temperatures [3].) These problems limit the choice of materials that can be used as heaters. Many alloys are normally protected by the formation of oxides on the metal surface. Common protective layers consist of Cr_2O_3 or Al_2O_3. At reduced pressures chromium oxides are volatile above 1000 °C [4]. Even alloys normally protected by a layer of SiO_2 may not survive at low pressures if the oxide layer is reduced to SiO, which is also volatile [5]. Oxidized nickel appears to be sufficiently stable up to the melting point of nickel at 1455 °C. Due to oxidation, the highest temperature where resistive heaters have been used for PLD of oxide films is around 1000 °C [6].

A more practical solution is to use radiative heaters based on halogen or quartz lamps [7]. Such heaters can work in the presence of oxygen and heat samples to about 1000 °C. The temperature limit is set by the type of sample mounting and the maximum power that can be handled by lamps in vacuum. Multiple lamps can be used to heat large-area samples homogeneously, as shown in Fig. 2a. It is possible to build lamp-based blackbody sample stages, where a substrate is held by its edges and kept in thermal equilibrium with the heater. The advantage of this technique is reduced contamination of the sample because it is only supported by the edges. True thermal equilibrium is, however, impossible to achieve because the substrate must be at least partly exposed to a vapor source for deposition to occur. Large lamp heaters also bring a large amount of heat into a vacuum system. Thermal management usually involves carefully placed heat reflectors and shields, combined with water-cooled shrouds. Without water cooling, multiple kilowatt-level heaters would quickly heat up the chamber walls and other vacuum components, causing excessive outgassing and sample contamination.

For small samples of up to about 20 mm in diameter, it is more practical to use a single lamp and to focus the light onto the sample with a water-cooled gold-plated mirror. This design is illustrated in Fig. 2b. Water cooling is still essential because the heating power of the lamp is in the range of 1 kW. This power level is sufficient to evaporate the gold plating from the mirror if it is not water cooled. Since the lamp is not a point light source, the heater can provide a reasonably homogeneous heating spot for direct sample heating or for use with a metal sample holder, as shown in Fig. 2b.

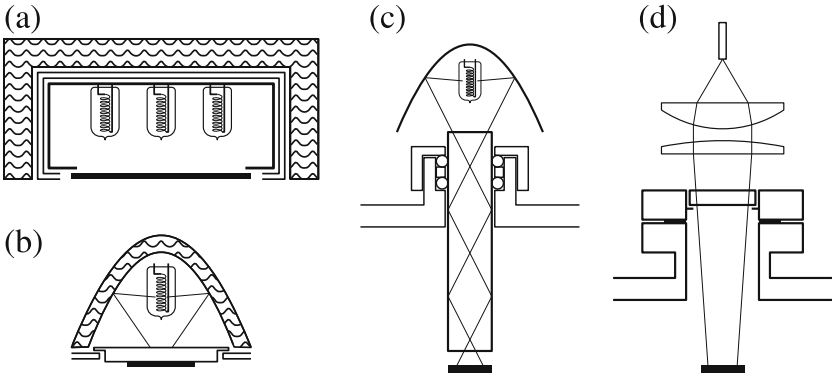

Fig. 2. Radiative substrate heaters. (**a**) A blackbody thermal equilibrium heater for large substrates, (**b**) a focused light lamp heater for small substrates, (**c**) delivery of optical power into a chamber with a light guide, (**d**) using a fiber-coupled laser for sample heating

Placing heating lamps in a vacuum chamber presents two problems: the need to use in-vacuum water cooling and the difficulty of working in a higher-temperature range. The power rating for lamps is usually given with the assumption that the lamps are cooled by ambient air. In vacuum it is usually possible to use only about half the rated power to avoid melting of the quartz body. To obtain kW-level heating power thus dictates the use of physically large lamps, which increase the size of the whole heater assembly.

Despite these limitations, lamp heaters can offer high reliability and good temperature stability in either UHV or ambient pressure environments. Lamp heaters have low cost and can be easily controlled with commercial power controllers using thermocouple feedback.

One way to improve on conventional in-vacuum lamp heaters is to move the light source outside of the vacuum system. This is particularly useful if the deposition system also contains in-situ characterization tools that require better access to the sample. Light can be brought to the sample with a quartz light guide [8], as shown in Fig. 2c. The quartz rod is mounted on a differentially pumped o-ring feedthrough and can deliver kW-level light power to the sample stage. The cooling of the lamp can now be done in air, reducing price and simplifying the vacuum-system design. Temperatures of up to 1500 °C have been obtained with this technique [9].

It is possible to improve heating efficiency by using a laser as a light source [10]. In this case, light can be brought to the chamber with an optical fiber and focused on a sample with simple collimation optics, as shown in Fig. 2d [11]. Rigid uncoated fibers can also be used inside vacuum chambers, bringing the heating laser light close to a sample. This can be useful for more complex sample-stage designs [12].

A laser heater heats only the minimum necessary area of the sample or sample holder, reducing outgassing. For thin-film growth optimization, it is even possible to use a focused heating laser spot to generate controlled temperature gradients in a sample [13]. The temperature range of a laser heater is limited by the heating area and the maximum laser power. The main heat-loss path from a sample is through the sample holder and sample stage. Additional heat loss starts to occur at high background pressures, increasing the necessary heating power to maintain a constant temperature. At least for small samples, it is easy to achieve essentially any temperature up to the melting points of many oxides, even in the presence of oxygen. In practical designs, the limiting factor for sample temperature is the sample-holder material.

The method of mounting a sample is critical for all radiative heating schemes. Many substrate materials can be heated directly by the infrared light from incandescent lamps. The largest benefit of direct optical heating is the ability to work with large substrates. If a sample holder is used, it is problematic to attach a large substrate to a holder while ensuring good heat contact over the whole substrate area. This is possible, at least in principle, with metal alloys and silver or platinum paste, but removal of large samples can be difficult without breaking the substrate. Another important benefit is reduced contamination of the sample. This is particularly important for samples that are characterized by magnetization measurements, since small traces of metal from the sample holder can attach to the backside of a substrate. Due to the small volume of a thin-film sample, even small amounts of metal contamination can distort the measured magnetization curves.

Direct optical heating is not an option for some of the most common substrate materials, such as nondoped $SrTiO_3$ and $LaAlO_3$. In these cases it is necessary to mount a substrate on a holder that is heated by the light source. A sample can be clamped to a sample holder directly, but this usually leads to poor thermal contact and uneven substrate heating, and thus direct clamping is usually only an option for low-temperature work. A common technique is to use silver paste between the substrate and sample holder. If the paste is applied evenly so that no bubbles are trapped under the substrate, good thermal contact can be achieved. Samples mounted with silver paste need to be degassed before heating to high temperature, however, adding delay to the film-fabrication process. If the sample needs to be processed close to the melting point of silver, it may be necessary to use additional clamping to prevent the sample from detaching from the holder. Silver paste can be problematic for mounting large samples, as it can be difficult to remove a substrate without cracking, as mentioned above. If the deposition temperature is above 900 °C, it is possible to use platinum paste instead of silver [13].

The substrate temperature is a critical process parameter for thin-film growth. Unfortunately, it is also one of the most difficult parameters to measure and control accurately. For resistive heaters and radiative heating systems, where a large sample holder block is used, it may be feasible to use

embedded thermocouples. The temperature reading from the heater block, however, is not the true temperature of the substrate surface. Thermocouples are also deliberately placed away from the hottest central part of the heater; otherwise oxidation at very high temperatures can reduce the lifetime of a thermocouple or disturb the homogeneity of the sample temperature.

The surface temperature of a substrate or a film can, in principle, be measured directly by optical pyrometry. A pyrometer measures the intensity of the light radiated from the sample surface and calculates the temperature assuming that the sample is a gray body, i.e., emits blackbody radiation, but with an emissivity factor of less than unity. The temperature range and requirements for optics depend on the working wavelength range and the type of sensor used in the pyrometer. The wavelength of maximum emission intensity from a blackbody is described by Wien's law. At room temperature the emission maximum is at about 10 µm, gradually shifting to shorter wavelengths at higher temperatures, reaching 2 µm at 1200 °C. For working temperatures above 1000 °C, it is common to use Si detectors that operate at 0.96 µm. Due to the shift of the thermal emission spectrum towards the infrared at lower temperatures, these sensors are not accurate below about 600 °C. In this range, better sensitivity can be obtained with InGaAs sensors that detect near-infrared radiation at 1.5 to 2.5 µm. Such pyrometers cover nearly the whole thin-film growth temperature range from 200 to 1500 °C. For accurate measurement of temperatures below 200 °C, it is necessary to use even longer wavelength detectors, like PbSe at 4 µm or thermopiles that sense a wide spectral range from 8 to 14 µm. Detection at longer wavelengths has the added advantage that many oxide substrates, such as $SrTiO_3$ have absorption bands above 12 µm, which means that the pyrometers can actually see thermal emission from the substrate, not from the sample holder. Most undoped oxides are transparent at 2 µm, which means that a pyrometer with an InGaAs or PbSe sensor looking at undoped $SrTiO_3$ will mostly measure thermal emission from the sample holder behind the substrate rather than the substrate itself. The intensity of infrared emission from the sample is given by Stefan's law, $I = \epsilon\sigma AT^4$, where ϵ is the emissivity, σ is Stefan's constant, A is the detection area, and T is the absolute temperature. Due to the T^4 dependence of emission intensity, even a small error in the estimate of the sample emissivity will result in a large error in the calculated temperature. This is a particularly serious problem at very high temperatures or for samples with very low emissivities. If a substrate is mounted on a shiny metal sheet, like nickel, the effective emissivity of a $SrTiO_3$ substrate at 2 µm can be easily reduced to about 0.3.

The problem of transparent substrates can, to some extent, be solved by using a very long wavelength pyrometer, since oxides like $SrTiO_3$ and $LaAlO_3$ have absorption bands above 12 µm and thus significantly higher effective emissivities [14]. Thermopile detectors work well in the 8 µm to 14 µm spectral range, but require special viewports on the vacuum chamber. Sensitivity is

also lower at higher temperatures, where the thermal emission maximum shifts closer to the visible range of the spectrum.

Another difficulty in estimating the surface temperature of a sample arises at the start of a deposition run. If the emissivity of the film material differs significantly from the substrate, for example when depositing a black film on a transparent substrate, the pyrometer will detect a change in the emitted infrared intensity and will show a gradual increase of temperature. In reality, if the sample is attached to a large metal holder, the true surface temperature probably changes very little, and what the pyrometer is detecting is a change in emissivity. If the pyrometer is the only feedback channel for temperature control, the only choice is to determine the substrate temperature before starting film growth and to use constant heating power during the actual deposition. The problem of determining the accurate absolute temperature of a sample means that published temperature values can have large systematic errors. It is therefore common that film-growth conditions, especially the temperature, need to be optimized for each individual deposition system.

2.3 Pulsed Laser Deposition

Pulsed laser deposition (PLD) is a thin-film growth technique where material is evaporated from a solid target with a laser pulse and transferred, through a gas phase, to the growth front of a film. The evaporated material is transferred from the evaporation target to the film surface without gas-phase reactions. The main advantage of PLD is the use of a solid target that generally has the desired film stoichiometry. An intense laser pulse can heat a small volume at the surface of the target to very high temperatures, where a plasma is formed and essentially all elements in the target material evaporate simultaneously. The stoichiometry of the target is thus directly transferred to the film and the problem of controlling the ratios of several elements in the film can be solved by preparing a target pellet with the desired composition. Oxide targets are commonly made by standard powder ceramic techniques, where the desired composition can be obtained by simply mixing precursors in suitable weight ratios. This is technically much easier than, for example, measuring and adjusting the flux ratios of individual atomic sources in the MBE process.

Since PLD is not element specific, it is easy to switch from one composition to another by simply changing targets. Many common PLD systems contain a carousel that can hold several different targets. The same film-growth system can thus be used to grow many different compounds with only minor adjustments to the process parameters. This multitarget capability is also useful for fabricating heterostructures, superlattices, and devices.

Another advantage of PLD is the ability to use a suitable background gas in the deposition chamber. This is particularly important when working with oxides, because it is possible to introduce oxygen into the growth chamber at pressures of up to about 1 Torr. For comparison, MBE can only work under

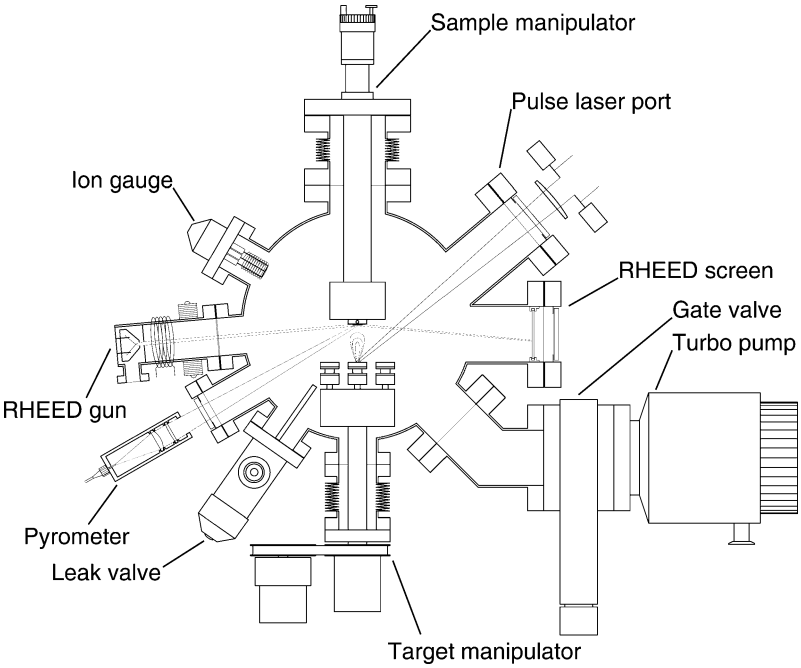

Fig. 3. Components of a pulsed laser deposition system, including manipulators, sample heating, vacuum pumps and gauges, and analysis tools, such as RHEED

high-vacuum conditions, and sputtering requires the presence of other gases, such as argon.

2.3.1 Laser

Pulsed laser deposition is a very flexible film-growth technique in terms of ablation target material selection and geometry. The layout shown in Fig. 3 is vertical, with the sample manipulator at the top of the chamber and the targets at the bottom, but many other orientations are also possible. The layout of the sample and the position of the targets are often dictated by external factors, such as the position of the deposition laser and other process-monitoring equipment. An important process parameter for PLD is the distance between the target and the sample. Multiple targets can be easily integrated into PLD systems, and a target manipulator usually allows targets to be changed, scanned, and moved to the desired distance from the sample. Light from a pulsed ablation laser enters the chamber through an optical viewport and is focused on the target surface at an angle.

The ablation plume generated by an intense laser pulse is perpendicular to the target surface. The plume size and shape depend on the energy of the laser pulse and the shape and size of the laser spot that is projected onto

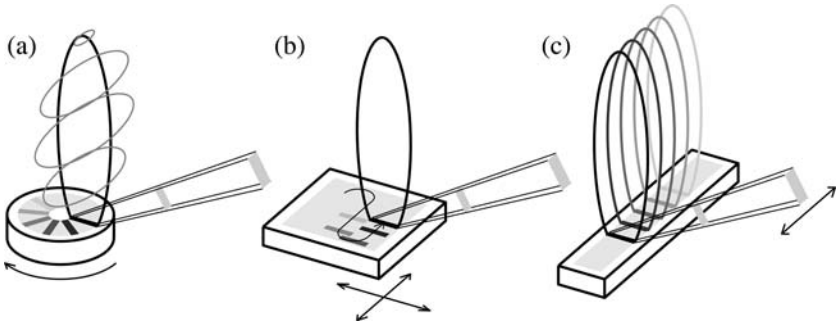

Fig. 4. Target and laser scanning. Targets can be rotated (**a**) or scanned (**b**) in order to erode the surface evenly. In special cases, such as large-area film growth, it is also possible to scan the laser beam across the target surface (**c**). The scan path and the plume shape are also illustrated. The asymmetry of the plume shape is shown in (**a**)

the target surface. The distance from the target to the substrate is usually a few centimeters. For shorter distances, it is difficult to hit the target surface with a laser beam, and for much longer distances the deposition rate would become unacceptably low.

The ablation laser usually illuminates an area of about a square millimeter on the target surface. The target would erode quickly if laser pulses were continuously fired at the same spot. To avoid such erosion, targets can be continuously rotated, as shown in Fig. 4a, consuming the target material uniformly. Target rotation is mechanically the most simple solution, but it can be difficult to orient the laser spot in a radial direction on the target, as shown in Fig. 4a. Over time, erosion still occurs, and a groove develops on the target surface. If the ablation laser hits the edge of the groove, the emitted plume will tilt, causing inhomogeneous deposition profiles. Groove formation can be further reduced by scanning a target in x–y directions, as shown in Fig. 4b. If the motion is controlled by a computer, any desired area of the target can be uniformly eroded. This is particularly useful when small or irregular single crystals are used as PLD targets. Large-area film depositions have also used laser-beam scanning (Fig. 4c), but this is not optimal due to film composition variations at the edges of the plume.

A variety of different lasers can be used for PLD work. The most common types are excimer gas lasers and frequency-multiplied Nd:YAG solid-state lasers. Among the excimer lasers, KrF (248 nm), ArF (193 nm), and XeCl (308 nm) are the most common. Compact high-power YAG lasers also exist, delivering up to about 100 mJ at the fourth harmonic (266 nm). The two types of lasers differ considerably in terms of spatial and temporal beam characteristics. Glass lasers generally output a well-defined circular beam at the fundamental wavelength (1064 nm for Nd:YAG). Even after multiplication to the third or fourth harmonic, the laser output can still be handled as

an approximately parallel beam with a semi-Gaussian intensity cross section. The typical pulse length of a high-power YAG laser is around 4 or 5 ns.

Excimer lasers output longer pulses, with most of the pulse energy delivered in ≈ 20 ns. Laser light is generated in a large gas volume, and excimer lasers therefore have very low beam quality. Commonly used high-power excimer lasers output a rectangular beam, with 10 mm × 20 mm being a fairly typical beam area. In addition to a large beam cross section, the divergence can be very high, up to ≈ 5 mrad. Both the beam size and divergence are also functions of the laser discharge voltage. When excimer lasers are used, it is therefore necessary to take special precautions in conditioning the beam before entry into an ablation chamber. In the simplest layout, an aperture is placed in front of the laser, removing low-energy edges of the beam and extracting a beam with a nearly top-hat intensity profile. This beam is then focused on the target surface with a single lens. More elaborate setups are necessary if the energy density needs to be controlled accurately. In that case, zoom lenses with true imaging optics and beam-energy homogenizers may be used.

2.3.2 Targets

For oxide thin-film growth, the targets are usually pressed ceramic pellets that contain the desired material composition. Synthesis of the target material is done by conventional powder ceramic techniques, and conventional bulk analysis techniques can be used to ensure that the target has the desired composition. In many cases, instead of composition analysis, it is sufficient to verify by X-ray diffraction that the pellet consists of the desired target phase and contains no extra phases. It is generally advisable to use targets with the highest possible density. For ceramic powders, this can be achieved in a laboratory environment by simple cold isostatic pressing.

For some materials, large single crystals are available. The use of single-crystal targets is preferable because it reduces the number of particles that are ejected from the target by laser pulses. In the case of pressed powder targets, it is common to see particles on the surface of a film grown by PLD. The particles are a serious problem when very flat film surfaces are required, for example for device fabrication. A number of schemes have been developed to avoid particles from a target reaching the film surface. The earliest attempts to eliminate this problem made use of the fact that evaporated atoms travel at much higher speeds than large clusters or macroscopic particles. It is possible to use fast-spinning shutters to catch the slower particles before they reach the substrate [15, 16]. *Tselev* et al. [17] have developed methods for deflecting the evaporated atoms in an ablation plume and also review many of the other techniques that have been developed. Some of these techniques, such as off-axis or shadowed depositon, are problematic in terms of composition control; others, such as fast shutters or crossed plumes, significantly complicate the vacuum-system design. It is generally easier to reduce the problem by

improving the morphology of the target, i.e., using single crystals. The use of x–y rastering of targets instead of simple rotation also appears to reduce the ejection of particles, mostly because the chances for eroding columnar spikes into the target surface are reduced [18, 19].

The assumption made in PLD experiments is that the stoichiometry of the target is directly transferred to the film. Whether this assumption holds true or not depends on the composition of the target and the intended use of the film. PLD originally gained in popularity due to successful growth of high-temperature superconductor films, such as $YBa_2Cu_3O_{7-\delta}$. This particular materials system is not sensitive to slight compositional variations on the order of a few per cent because the material segregates into the stoichiometric phase and islands of $BaCuO_2$ or CuO, depending on which way the stoichiometry is skewed [20, 21]. The segregated phases have no influence on the transport measurements, and a film as a whole still shows a very sharp superconducting transition at a temperature that coincides with the bulk value.

Problems appear when some of the elements in the film are much more volatile than others. For example, sodium can be easily lost when depositing $La_{1/2}Na_{1/2}TiO_3$ films by PLD due to re-evaporation from the film surface [22]. Evaporation loss of sodium increases with sample temperature, and it is therefore necessary to optimize simultaneously the growth temperature and the Na:La enrichment factor in the target to obtain stoichiometric films. In this particular material, it is possible to use an intentionally non-stoichiometric, Na-rich target to compensate for evaporation losses during high-temperature growth if only structural and dielectric properties are of interest.

More significant difficulties appear when samples are used for leakage current, breakdown field, carrier concentration, or mobility measurements. These parameters are sensitive to very small composition deviations, because unless the nonstoichiometry of the film can be corrected by bulk segregation of a secondary phase, any cation ratio deviations from the ideal values will induce lattice defects in the film. The defects function as dopants and thus affect the number of carriers, carrier trapping, carrier mobility, etc. A good example in this sense is the prototypical perovskite, $SrTiO_3$, which can transform from an insulator into a metal at carrier concentrations that are in the range of $10^{19}\,\mathrm{cm}^{-3}$. A composition deviation of 0.1% would be much larger than the characteristic impurity concentration that is known to alter the electronic phase of the material. Composition variations of a fraction of a per cent are, unfortunately, not reliably measurable by standard composition analysis methods, such as inductively coupled plasma emission spectroscopy or electron probe microanalysis, and often go undetected for this reason.

2.3.3 Ablation Process

The main process parameters that can be used to control the stoichiometry of a film grown by PLD are the laser energy, power density, and the laser spot size on a target surface. These parameters control the evaporation process. Other important parameters are the background gas pressure and the target–sample distance. In some cases, the film composition is also a function of sample temperature. As mentioned before, this happens when volatile elements are present in the film.

The ablation process has been studied in great detail by various authors [23,24]. The ablation process itself is strongly dependent on the risetime, length, and wavelength of the laser pulse. The ablation conditions that are found in publications should therefore be qualified with the type of laser and wavelength that was used. The most popular lasers for PLD are gas excimer lasers, which produce a pulse that has a half-width of about 20 ns. Solid-state lasers, such as Nd:YAG, ususally have shorter pulses, in the range of 4 to 5 ns. A recent trend is to use ps or even fs lasers for ablation experiments, although due to cost and low pulse energies these lasers are not widely used. The ablation mechanism is very different in all three cases.

The laser pulse initially causes a strong electronic excitation in the target material. Electronic excitation is possible even when the bandgap of the target material is higher than the photon energy of the laser, i.e., it is possible to use a KrF excimer laser with a photon energy of 5 eV to ablate sapphire, which has a bandgap energy of about 9.5 eV [25, 26]. The possible mechanisms are multiphoton absorption and initial absorption at defect sites. It is easier to ablate a polycrystalline Al_2O_3 target than a single-crystal target with small excimer lasers (20 ns, 200 mJ pulse), which appears to support the idea that absorption at least initially occurs at defects.

The absorbed laser energy is transferred to ions in the surface layer on a picosecond timescale, also forming an ablation plasma plume above the surface. In the case of a femto- or picosecond laser pulse, the excitation ends at this point, and the plasma can expand, finally reaching the substrate. A more complicated process occurs for longer laser pulses because the heating time is long enough for a macroscopic region of the target to melt. The depth of melting depends on the laser wavelength and pulse length. This effect is generally detrimental to the PLD process because melting can cause stoichiometry gradients in the sample, especially if the material melts incongruently. Even in simple targets, such as silicon, the ablating laser may erode the surface unevenly. Due to shadowing, any surface instabilities that do appear get amplified to the point where sharp needle-like cones form on the target surface, pointing towards the incident laser [19, 27]. The process is illustrated in Fig. 5. Target surface roughening of this nature can cause the plume to tilt, altering the plume stoichiometry and resulting in the ejection of macroscopic particles from the target. As shown in Fig. 5c, macroscopic particle ejection may be caused by the erosion of the asperities or by the

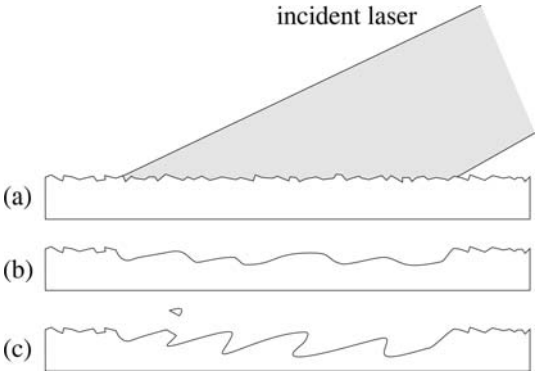

Fig. 5. Target-surface degradation. An originally flat target surface (**a**) is melted by the ablation laser. Uneven etching and redeposition of ablated material amplifies any surface inhomogeneities, resulting in sharp asperities on the target surface (**b**), which can act as sources of macroscopic particles, ejected from the target surface during ablation (**c**)

ejection of liquid droplets from the parts of the surface that are exposed to the highest laser light intensity [28]. This problem is particularly serious for low melting point materials, such as Si, but also for many metals, where the thickness of the molten layer is increased due to better thermal conduction. For such materials PLD is not an optimal deposition technique.

The particular mechanism that is responsible for particle ejection from PLD targets can, to some extent, be inferred from the morphology of the target [29] and the shape of the particles observed on the film surface by scanning probes, such as atomic force microscopy (AFM). Microprobe composition analysis can also be used. Nonstoichiometric segregating particles tend to grow in the film [21], while macroscopic particles ejected from a target tend to have diameters that are much larger than the film thickness. Liquid droplets impacting the film surface can also be identified by their characteristic shape, as shown in Fig. 6. Analysis of particle shapes by AFM is often sufficient to determine if the particles present on the film surface are caused by liquid droplets originating at the target, solid particles ejected from a target, or secondary phases segregating in the film during growth [21, 30].

Target surface erosion can be avoided or at least reduced by decreasing the thickness of the molten layer that forms during a laser pulse. The practical solution is to use the shortest available laser wavelength, which has a smaller absorption length in the target material. This is one of the reasons why KrF excimer lasers are popular, and in the case of YAG lasers, the third or fourth harmonic is used. The formation of needle-like asperities on a target surface can also be reduced by suitable combination of target scanning and rotation, which ensures that, over time, all points on the target surface are hit by the ablation laser from different directions.

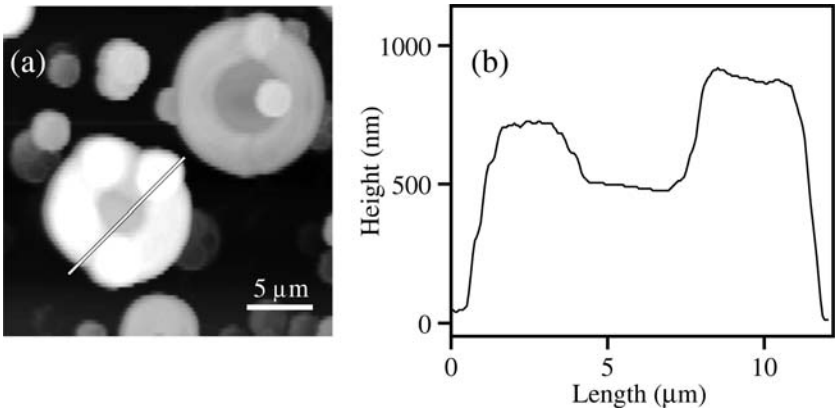

Fig. 6. (**a**) An AFM image of ring-like structures formed by an impact of liquid droplets on a film surface during ablation of a Si−Al−Ba alloy. (**b**) Height profile taken along the path indicated in the AFM image

Due to the formation of a plasma plume close to the target surface, it is not possible to define the maximum target temperature that is reached during an ablation pulse, but estimates based on the velocity of ions in the ejected plume suggest temperatures in the range of 6000 K to 12 000 K [31]. Estimating the true target surface temperature is complicated by the fact that the plasma plume forms on a picosecond timescale, while the laser pulse may last for 5 ns to 20 ns. As a result, there is also significant gas-phase plasma heating by the laser pulse, and the velocity of atoms in the plume therefore depends strongly on the laser fluence, with values of about 10 km/s being quite common. For a target–sample distance of 50 mm, the plume thus reaches the film surface in 5 µs. The kinetic energy of a Sr atom travelling at 10^4 m/s would be nearly 50 eV. The types of ionic and atomic species present in the plume can be inferred from the optical emission spectra of the plume. For complex oxides, the plume consists of a mixture of single ions, neutral atoms, and some oxide species. Plume emission spectra of high-temperature superconductors have been carefully studied, and BaO, YO, CuO, etc., have been observed during the ablation of Y−Ba−Cu−O targets [31].

The ablation plume is strongly peaked along the surface normal of the target. Measurement of film-thickness profiles on large samples shows that the plume consists of an ablative component, where the deposition rate is proportional to $\cos^n \theta$, and a Knudsen component, proportional to $\cos \theta$ [32]. The spread of the plume depends on the size of the laser spot on the target surface, laser power density, and background gas pressure. The plume contains atoms that can be neutral or ionized. The level of ionization also depends on the ablation conditions. The expansion of various plume components is not uniform, and although the angular dependence of ablated material can often

be described with a $\cos^n \theta$ dependence (Fig. 7a), there are small differences in the expansion for the higher- and lower-energy particles.

The ablation plume functions as a mass filter, with lighter elements having a slightly higher density in the center of the plume, effectively having a higher n in the $\cos^n \theta$ angular dependence. The effect is presumably more pronounced in compositions that consist of cations with large mass ratios, but stoichiometry variations of around 0.5% can be seen even in fairly simple cases, such as $SrTiO_3$, where the Sr/Ti mass ratio is 1.8. The center of $SrTiO_3$ films tend to be slightly Ti-rich when analyzed by microspot X-ray fluorescence.

The mass-separation effect in laser-ablation plumes is a function of laser power density. For excimer lasers, with a 20 ns and 100 mJ pulse focused to a 1 mm^2 spot on the target, the power density is 500 MW/cm^2. The same spot size for a YAG laser with a 50-mJ and 4-ns pulse would increase the power density to over 1 GW/cm^2. This power density can be easily increased by focusing the laser to a smaller spot area, and it is thus realistically possible to operate a PLD chamber in the range of 10^{10} W/cm^2, where even isotopic enrichment [33] has been observed, although this usually happens with picosecond lasers that can approach 10^{14} W/cm^2 [34, 35].

These power-density estimates assume that the laser pulse has a square temporal shape. In reality, the time profile of an excimer pulse consists of an initial fast edge and a fairly long decay [36]. Even in the case of high-power YAG lasers, the pulse shape is not Gaussian because in order to reach high output power from a physically small laser, multimode operation is used. A nonseeded laser therefore outputs a pulse that can have very fast high-amplitude components. While such time-profile details can usually be ignored when discussing target surface heating, they do affect the way a laser pulse interacts with the plasma that forms at the target surface within a few hundred picoseconds. In practice, it is the risetime of the laser pulse that matters the most for laser ablation. Lasers with faster pulse risetimes can achieve equivalent evaporation characteristics at a lower integrated pulse energy [36].

2.3.4 Film Growth Using PLD

The strongly forward-peaked expansion of the ablation plume results in a narrow region on a substrate where the film-deposition rate can be considered homogeneous. A number of process parameters affect the plume shape and size. The most important factors are the ambient background gas pressure, the laser energy density, and the laser spot size on the target surface. In most cases, the $\cos^n \theta$ approximation works well in describing practical plume profiles, as shown in Fig. 7b.

Due to geometric constraints, as shown in Fig. 3, the ablation laser beam hits the target surface at an angle of about 30° to 45°. As a result, the laser spot shape on the target surface is asymmetric, elongated along the beam

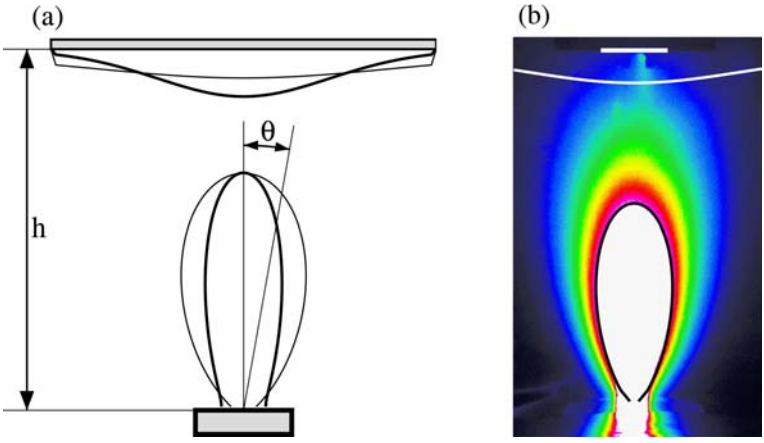

Fig. 7. (**a**) The ablation-plume shapes and the corresponding film-thickness profiles for a strongly peaked plume with $n = 20$ (*thick line*) and a wide plume with $n = 5$ (*thin line*). (**b**) A false-color photograph of a $SrTiO_3$ target ablation plume. The superimposed black curve is given by $\cos^{10}\theta$. The size and position of a 10-mm wide substrate and the estimated film thickness profile are shown in *white*

direction. The forward peaking of the plume depends on the interaction area at the target surface, with a smaller ablation spot resulting in a wider plume with a lower n. An asymmetric laser spot thus also distorts the shape of the plume and plume cross sections along the laser-beam direction, and directions perpendicular to the laser beam can have quite different film-thickness profiles, as illustrated for two different laser spot sizes in Fig. 7a and in Fig. 4a. As a result, the thickness profiles observed on PLD samples tend to be shaped like ovals, and the thickness inhomogeneity between the edge of a sample and the center can easily reach 30% [37].

The thickness inhomogeneity of PLD films is accompanied by small stoichiometric variations as well. In general, lighter elements tend to be concentrated at the center of the film, while the concentration of heavier elements increases towards the edges. A number of schemes have been developed to alleviate this problem. The simplest technique is to increase the distance (h in Fig. 7a) between the target and the substrate. Typical distances that are used in PLD chambers vary from about 30 mm to 80 mm. Increasing the distance further would reduce the deposition rate to impractically low levels. In the case of epitaxial oxide films, the substrate material cost is also significant and it is therefore common to use small film samples. Characteristic sample sizes are 5 mm to 10 mm. While this approach is adequate for characterizing materials, it is not suitable when films are grown for device applications because larger samples need to be processed. Larger films can still be grown by PLD, but sample- or target-scanning techniques have to be used. Rotating

the substrate above an offcenter plume is technically the easiest solution and can provide reasonable thickness homogeneity across several tens of mm [37].

It is more difficult to correct for the compositional variations across the film surface. Attempts to do so have shown promising results for materials like $BaZrO_3$ and $PbZr_xTi_{1-x}O_3$, although variations on the order of a few per cent still remain [37]. Whether such composition variations are critical or not depends on the materials system and the intended use of the film. In the case of high-temperature superconductors, for example, excellent results have been obtained in repairing compositional errors by scanning the laser beam across a target surface and thus periodically shifting the position of the plume relative to the center of the substrate [38]. In ferroelectric films destined for device applications, it is necessary to control the density of structural defects at a much lower level than is measurable by X-ray diffraction. It is common to observe variations of electronic properties of films grown by PLD across the surface of a substrate. Parameters such as dielectric constants, leakage currents, photoconductivity, and carrier mobility are particularly sensitive even to very low concentrations of defects, below $10^{20}\,cm^{-3}$, in the films. Even in seemingly simple materials, such as $SrTiO_3$, it is therefore difficult to fabricate films that have similar dielectric behavior as high-quality bulk crystals [39,40]. While the concentration of defects in thin films is expected to be higher due to the kinetic nature of the film-growth process, the variation of composition on the order of a per cent across the film surface will dominate the defect density. Variation of material properties across the substrate must be considered when evaluating oxide-based electronic devices [41].

It is also important to note that the kinetic energy of individual ions in a plume can exceed 100 eV. This energy is high enough to cause sputtering at the film surface. Due to the variation of deposition rate across the film surface, the sputtering rate is also position dependent. Resputtering of material from the film surface is a particularly serious issue in compounds such as $PbZr_xTi_{1-x}O_3$ (PZT) that contain volatile heavy elements. It has been shown [42] that PZT films grown by PLD suffer from a considerable loss of Pb at the center of the film, where resputtering by the plume is the strongest. There is no simple way to correct this problem, except by increasing the target–substrate distance and possibly using a lower energy sensity for the deposition laser. If the energy is reduced close to the ablation threshold, compositional deviations may start to occur in the target as well [30, 43].

Resputtering can also affect materials that do not contain volatile elements, such as $SrTiO_3$. This is a particular problem for the growth of superlattices and heterostructures because sputtering by the plume is inevitable, and it can seriously affect the structure of the interface layers. This can be observed by measuring the inplane transport properties of $SrTiO_3$ heterostructures during and immediately after deposition. A sharp increase of conductivity can be observed, even when insulating oxides are grown on normally insulating $SrTiO_3$ substrates [44]. In this case, the plume removes oxy-

gen from the interface, inducing conductivity in a thin layer of $SrTiO_3$ close to the interface.

As long as the film-thickness profiles on the sample surface are reasonably homogeneous, it is possible to use intentionally off-stoichiometric targets to correct for nonstoichiometries occurring either due to evaporation, resputtering, or the high volatility of particular elements. This technique can be used to grow films of $La_{1/2}Na_{1/2}TiO_3$ at elevated temperatures that would normally result in a large loss of Na from the film [22]. High-quality films that show no dielectric phase transitions at low temperatures can be grown by using an offstoichiometric target with a Na/La ratio of 1.75. In this case the growth temperature could be increased to 600 °C, yielding superior crystallinity. The technique, however, is time consuming to set up because the target composition has to be retuned for each deposition system.

2.4 Sputter Deposition

Sputtering is the process of removing atoms from the surface of a target by kinetic-energy transfer from an incoming flux of highly energetic particles. This technique, in particular geometries or with specific deposition parameters, shares with PLD the main feature of being able to stoichiometrically transfer the composition of the target to the growing film [45, 46], and this characteristic makes it highly suited to the growth of multielement compounds, such as complex oxides, with relative ease compared to thermal processes, such as evaporation and MBE. This short overview describes the operational principles and general aspects of sputter deposition as applied to the growth of complex oxides. Many details and historical developments are left out, and readers are referred to the many excellent texts that have been written on the topic [45, 47–49]. In addition, aspects of thin-film growth by PLD described above also apply to sputtering. In particular, aspects regarding the vacuum chamber and temperature monitoring and control of the substrate are essentially the same for all of the deposition techniques described in this chapter. The form of the source material, known as the target, is also the same as in PLD, where a ceramic disk of the material to be grown is typically used. Readers are referred to Sect. 2.3.2 for more information on targets.

2.4.1 Sputtering Process

Sputtering involves the ejection of atoms from the surface of a target, which serves as the source material for film deposition. There are several types of sputter deposition techniques, depending on how the flux of energetic particles that bombards the target surface is created, the kinetic-energy range of the bombarding particles, and the geometry of the system [50–52]. The interaction between a solid and an incident flux of energetic particles depends on the binding energy of the solid and on the specific kinetic energy of

the incident particle. There is typically a threshold kinetic energy before any significant quantity of atoms of the target is dislodged. In technical terms, the sputtering yield (defined as the number of ejected target atoms per incident particle) is said to be negligible below this threshold, which is typically in the range of $\approx 10\,\text{eV}$. As the kinetic energy of the incident particles is increased to the range of 50 eV to 1000 eV, one enters the so-called "knock-on" regime [53–55], where the incident particle dislodges a few surface atoms that transfer their energies to surrounding atoms in a series of collisions. This series of somewhat random collisions can cause a near-surface atom to be occasionally hit from below causing that atom to be ejected from the target surface. This knock-on regime is where sputter-deposition systems are operated. At higher incident energies (2–20 keV), each incident particle essentially vaporizes a small region of the target in a cascade collision involving a very large number of atoms of the target. At even higher energies, on the order of 50 keV to 100 keV, the scattering cross section becomes small and the incident ions are essentially implanted into the target [53–55].

The basic method of generating the incident flux of particles in sputter deposition is through the creation of a plasma or glow discharge in an inert-gas environment. The inert-gas ions produced are accelerated towards the target by an electric field. A schematic of the electrode configuration for the basic sputtering process is shown in Fig. 8. The source material or target is attached to the cathode. An electric field of sufficient strength is applied between the anode and cathode, causing the ionization of the gas between the electrodes. The gas is typically Ar, which is ionized to Ar^+. The Ar^+ ions are accelerated by the electric field towards the target, while electrons are attracted to the anode. The heavy Ar^+ ions bombard the target, transferring their kinetic energy to the target, causing the atoms at or near the surface of the target to be ejected. The ejected target atoms are then collected onto a heated substrate.

2.4.2 The Sputtering of Insulators

Because many functional complex oxides, such as ferroelectric oxides, are insulators, the basic dc-sputtering setup described above and shown in Fig. 8 does not work. Charge will build up at the surface of the insulating target and will eventually cancel out the external electric field, causing the plasma to be extinguished. This limitation can be overcome by applying an alternating electric field instead of a dc electric field. At low frequencies, both electrons and ions can respond to the oscillating field. In this regime, during one half of the cycle, sputtering of the target (attached to the cathode) occurs, and during the other half of the cycle, sputtering of the anode occurs. This anode sputtering is known as resputtering [56] and is detrimental to film growth, since the film is being sputtered away during one half of the electric-field cycle. One solution to this problem is to use high frequencies in the RF regime. By exploiting the fact that the heavy Ar^+ ions cannot respond to

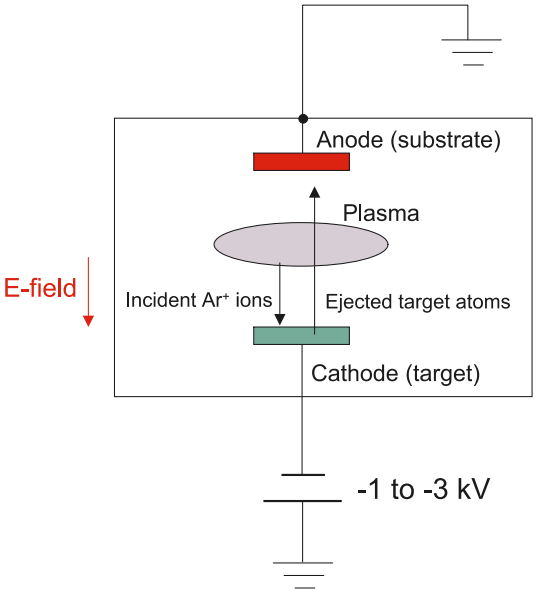

Fig. 8. Schematic diagram of a basic sputtering system. The target is attached to the cathode, which is negatively biased compared to the rest of the system

an RF electric field while the electrons still can, sputtering of insulators is achievable without also resputtering the deposited film [57].

Most sputtering systems used for growing oxides utilize electromagnetic fields with a frequency of 13.56 MHz to generate the plasma. The target is attached to the powered electrode while the rest of the vacuum chamber, including the substrate, is normally grounded. The RF electric field generates a plasma, but only the electrons are light enough to respond to the alternating field at this frequency. The heavy Ar^+ ions see only the average electric field. The target, which is located at the "cathode", is normally much smaller than the "anode" (typically the chamber itself). The smaller area of the cathode results in a higher electron concentration during each half-cycle compared to the electron concentration at the anode. After a few cycles, this results in a net negative dc bias at the target compared to ground. It is this self-generated negative dc bias at the target that the Ar^+ ions see. The target self-bias accelerates the Ar^+ ions towards the target, causing sputtering of the target surface atoms. A schematic of a typical RF sputtering setup is shown in Fig. 9.

2.4.3 Process Gas

As with PLD, a background gas at relatively high pressure can be utilized during the deposition, and in fact, sputtering requires a sufficient gas pressure before a plasma can be generated. In most oxide deposition processes,

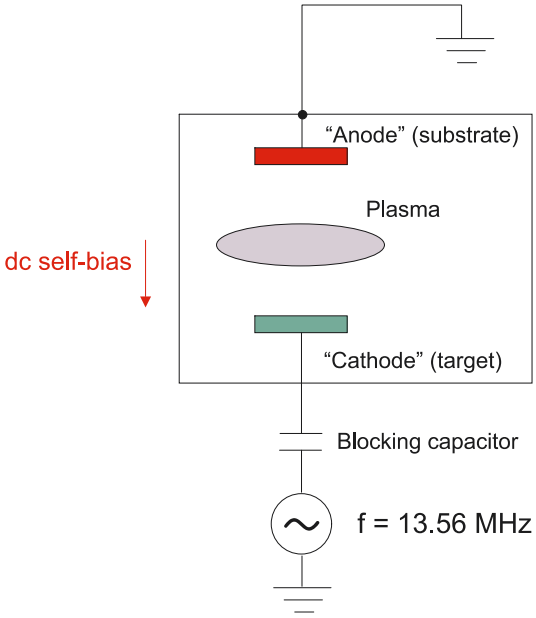

Fig. 9. Schematic diagram of a typical RF sputtering system. The Ar^+ ions cannot follow the RF field and respond only to the dc self-bias

an amount of oxygen is also introduced in addition to the argon gas, usually on the order of 10%–50%. The oxygen is primarily to ensure that the oxide is oxidized as grown [58]. Also, the total gas pressure used during the sputter-deposition process itself is another control parameter that can be adjusted, in addition to the usual substrate temperature and source flux. A higher background gas pressure results in increased thermalization of the ejected target atoms, resulting in more uniform growth [58]. However, this increased pressure also affects the efficiency of the sputtering process, causing a reduction in the growth rate [59].

Another potential issue with the use of oxygen in the sputtering atmosphere is the creation of O^- ions (in addition to O_2^+ ions). These negative oxygen ions tend to be accelerated towards the substrate, causing resputtering of the growing film. This process produces a preferential resputtering, often leading to off-stoichiometric films [56]. This can be partially suppressed by sputtering at high pressure and/or by using a geometry known as off-axis sputtering [60]. The main feature of off-axis sputtering (shown in Fig. 10) is that the target and substrate are positioned such that they are at some large angle with respect to each other, typically 90°. The off-axis geometry greatly reduces resputtering and has been known to produce atomically smooth films at the expense of a reduced deposition rate (since most of the flux is ejected with momenta perpendicular to the target surface).

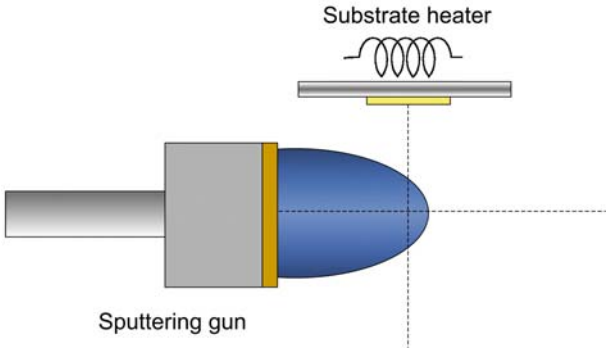

Fig. 10. Off-axis sputtering geometry showing relative position of sputtering gun and substrate

2.4.4 Preferential Sputtering

The sputtering yield is defined as the number of ejected target atoms per incident bombarding ion. The yield depends on the chemical-bonding environment and the atomic mass of the ejected species [61]. For multielement sources typically used for complex oxide growth, each element has its own sputtering yield. Some elements sputter more easily than others, which can cause problems with the film composition. Fortunately, this problem with preferential sputtering is relatively easy to overcome. The phenomenon of preferential sputtering will result in one element being ejected more often than another element. However, this also results in the target surface being depleted of the element that sputters more easily, leaving the target surface with a composition that is low in the element that sputters easily and high in the element that does not sputter easily. At some point, equilibrium will be attained such that the actual flux of ejected atoms from both species will be the same as the bulk composition of the target. It is therefore important for sputtering deposition processes to perform a "presputtering" or "conditioning" of the target for a sufficiently long time (several hours is typical) at the plasma conditions to be used for the actual growth. This target presputtering ensures that the flux is stoichiometric. This, however, is not always sufficient to ensure stoichiometric films since, as mentioned above, preferential resputtering caused by oxygen ions can occur. Presputtering also cleans the target surface of any extrinsic impurities resulting from the handling of the target prior to mounting in the growth chamber.

2.4.5 Technical Considerations in Sputter Deposition

One important innovation that was made in sputtering technology was the implementation of the magnetron configuration [62], which involves the use of a cylindrical magnet whose magnetic field lines are directed along the

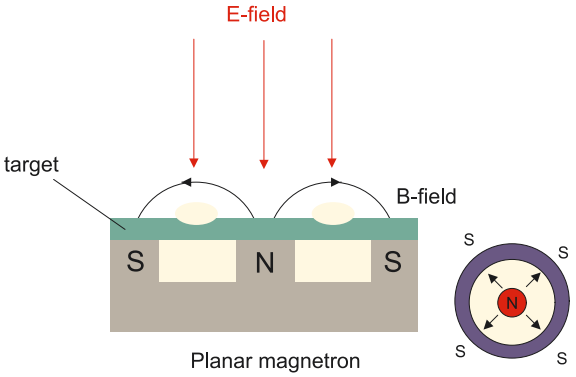

Fig. 11. Electric and magnetic field configuration in a planar magnetron. The electrons are primarily confined in a torus-shaped area in front of the target

radial direction. This magnet is typically situated behind the target. The radial magnetic field in combination with the perpendicular electric field at the target surface serves to confine the electrons in a torus-shaped region in front of the target surface, thus increasing the ionization probablity near the target, leading to higher deposition rates [47, 63]. Figure 11 shows the standard magnetron setup. Further optimizations of the basic magnetron, such as the unbalanced magnetron, have been developed and are described in [63] and [64].

For RF sputtering systems, another important aspect is the RF power supply. Most RF power supplies are designed for specific impedances (typically 50 Ω pure resistive) and thus entails an additional requirement for proper operation. The impedance of the plasma, which depends on the growth chamber and sputtering-gun geometry, has both resistive and reactive components, and must be matched to the power-supply impedance in order for the supplied power to be transferred as efficiently as possible to the plasma [57]. This impedance matching is commonly done by using an automatic impedance-matching network, which consists of two variable capacitors (one in series and one in parallel) along with a large inductor. The variable capacitors are automatically adjusted by feedback from measurements of the reflected RF power, which is minimized. During the growth, the plasma impedance can drift because of the growing film and the conditions of the target, especially if the film and substrate have very different conductances, necessitating the continuous adjustment of the matching network. For this reason, it is preferable to have automatic (rather than manual) tuner networks for sputter-deposition systems.

Sputtering systems also require water cooling of the sputtering guns. The Ar-ion bombardment of the target causes the target and the magnet behind the target to heat up. Without water cooling, the temperature can rise, melting the target and destroying the magnet. Also, similar to PLD, most oxide

targets are ceramics that are bonded by some kind of solder to a copper backing plate, which is attached to the end of the sputtering gun. The solder can melt at around 300 °C, resulting in target bonding failure if there is insufficient water cooling. In some sputter-deposition systems, especially older systems, because the water goes through the powered electrode, the water must have a specific resistivity range so that there is minimal ion transfer to/from the cooling water.

2.4.6 Reactive Sputtering

A less commonly used method to grow complex oxides is reactive sputtering [65, 66]. Reactive sputtering involves sputtering from elemental (metal) sources in the presence of oxygen. The chemical reaction between the metal atoms and oxygen at the substrate surface produces the oxide film. One advantage of reactive sputtering is that one can employ dc sputtering systems, which are less expensive than RF systems, since metal targets do not have the problem of charging. Also, there is more flexibility in composition control of the film, but this composition flexibility can also be a disadvantage. The lack of line compositions in complex oxides requires one to have a very high degree of control over the source fluxes and oxygen partial pressure in order to obtain high-quality epitaxial films. For this reason, reactive sputtering is more typically used to grow simple oxides and not complex oxides. In order to achieve composition flexibility and control at the same time, one often uses molecular beam epitaxy, which is described in the next section.

2.5 Oxide Molecular Beam Epitaxy

Molecular beam epitaxy [67] is a crystal-growth technique that builds the crystal structure of a growing thin film with atomic-layer precision through flux control of thermally evaporated beams of the film's constituent elements in a vacuum. These beams are directed at a crystalline substrate to form the film of interest through reaction and crystallization (see Fig. 12).

Conceptually, the process of MBE as described above is simple in that changing the sequence of materials deposited can result in a predetermined crystal structure. Many of the creative crystal structures are, in fact, devices that have been designed and grown using MBE and owe their technological success to the simplicity of the MBE growth process. The challenge of MBE comes when the structure and chemistry of the surface do not follow from the sequence of materials deposited. In this case, the film grower relies on electron-spectroscopic techniques that are inherently surface sensitive and that work well in the vacuum environment of MBE to provide feedback to the growth process. These two strengths of MBE, conceptual simplicity and powerful characterization techniques, have combined to make MBE both scientifically and technologically successful.

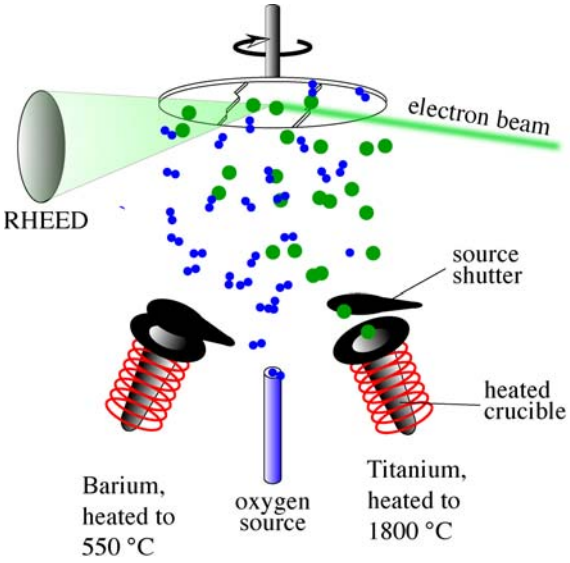

Fig. 12. Oxide MBE hardware. This schematic view of components contained in a vacuum chamber illustrates the geometry for a typical MBE system. The components are designed to directly access the fundamental parameters of crystal growth on a surface. The substrate is heated using techniques similar to those described in Sect. 2.2. For uniform deposition of the metal component (*green spheres*), the substrate can be rotated during growth, which also allows complete characterization of reciprocal space using RHEED (see Sect. 2.5.2). Metals are evaporated from precisely heated crucibles and shuttered to control the deposition of individual, atomic-scale layers. The rate and level of metal deposition is controlled during growth using feedback from RHEED, which gives a different pattern characteristic of the growing surface, as observed on a fluorescent screen opposite the focused source of high-energy electrons. Not shown for clarity is a quartz crystal monitor that is moved to the position of the substrate for calibration of the deposition rate and removed during growth. Oxygen is supplied by directing a beam of molecular or atomic oxygen, or ozone through a nozzle (*blue spheres*). Other components include a residual-gas analyzer for measuring the chemical make-up of the gases in the vacuum chamber in addition to a hot-filament, ionization gauge for measuring the overall level of vacuum

For MBE, technological success has meant implementation in the commercial production of devices. This was true first for laser diodes used in compact disc players and continues today for high-speed transistors used in cell phones. While MBE is not generally considered to be a commercial production tool, the power of MBE combined with the imperative of an application has motivated a number of companies to practice commercial MBE.

Scientifically, we are interested here in its inherent precision in structural control at interfaces and surfaces, which is essential for controlling ferroelectric properties. Electrical and structural boundary conditions have been

shown to strongly couple to the polarization of a ferroelectric thin film. Precise structural control at interfaces and surfaces also means that first-principles theoretical techniques such as density-functional theory can be used to understand the structure–property relationships we are interested in for ferroelectric devices [68].

2.5.1 Hardware

Atomic-layer control is achieved by careful arrangement of the components of the MBE system (Fig. 12). Shuttered, thermal-evaporation sources are aimed at a heated substrate where the evaporant condenses and reacts. The manipulator that holds the substrate can also be raised and lowered parallel to the substrate surface normal, as well as rotated around the surface normal. Ideally, provision is made for optional shielding of the substrate (not shown in Fig. 12) from deposition when the sources are operating and their shutters are open. Epitaxy of the growing film is measured using a focused, high-energy electron beam (10–35 kV) that is directed from the side of the chamber onto the sample at a low (0.5 to 5°) incident angle, a technique called reflection high energy electron diffraction (RHEED). The diffracted electron beam is imaged using a fluorescent screen mounted on the side of the growth chamber opposite to the electron gun. The low incident angle guarantees a small penetration depth, on the order of a few angstroms, into a flat surface so that the observed diffraction is mostly from the growing film surface. The deposition rate from individual sources is calibrated using a thickness rate monitor, such as a quartz microbalance that can be moved into the substrate position. The deposition rate is typically calibrated before film growth with the substrate shielded from the sources.

Thermal evaporation sources consist of a heater that surrounds a crucible that holds either liquid or solid metal. Flux control is accomplished by controlling the crucible temperature, as measured using a thermocouple. In addition, a cold shutter gates the evaporant to the substrate. Efficient sources use heat shields to surround the heater and hot crucible, along with a cooling shroud to absorb excess heat. Heating from a hot source leads to degassing of the vacuum chamber walls; these unintended gases impinge on the substrate and can be incorporated as impurities and possibly affect the thermodynamics and kinetics of film growth. The flux profile from a point-source crucible varies as the cosine of the incident angle relative to the substrate normal. If the source is tilted, as it must be in order to aim multiple sources at a single substrate, then the flux will fall off from the near edge to the far edge, leading to flux and thickness nonuniformities. A uniform, time-averaged flux across the substrate is achieved by continuously rotating the sample during growth. Rotation has the added advantage of allowing a complete characterization of the surface structure via RHEED during growth.

The range of metals that are incorporated in the perovskite structure that one might be interested in growing is large, and thus one is interested

in evaporating a diverse set of metals. The practical difficulty of holding a hot metal in a crucible can be a difficult issue. To see how this issue is resolved in practice, the example of evaporating titanium for $BaTiO_3$ growth is discussed below. For reasonable growth rates of 10 Å/s, the vapor pressure of the titanium should be about 10^{-2} Torr for a source that is 40 cm from the substrate. The temperature of Ti required to reach this vapor pressure is 1750 °C, at which temperature titanium is molten.

The common refractory materials used for crucibles react with or dissolve into titanium and fail at these temperatures. Pure titanium in graphite reacts at a eutectic of 1648 °C, and titanium is continuously soluble in tantalum [69]. To solve this problem, one observes that there exists a carbide of titanium that will contain a carbon–titanium solution up to 2776 °C. In practice, one can use an alloy of titanium and carbon that has the composition of the C:Ti liquidus at 1800 °C, or 1.4 wt%. When this charge melts at the eutectic temperature of 1648 °C, a carbide forms at the crucible wall in contact with the melt that contains the molten alloy. Using this technique, high fluxes can be obtained. Pure titanium may also be sublimed near its melting temperature of 1670 °C. Increasing the surface area of the evaporant and placing it closer to the substrate also achieves higher fluxes. In practice, this has been done using a titanium sphere that is heated radiatively without a crucible [70].

Barium, strontium and calcium can be contained in a tantalum crucible. These alkaline-earth metals can be purified to 99.995%, with the major impurities being the other alkaline-earth metals. The metals are packed in argon, and air exposure must be avoided while the metal is being transferred into the crucible. Once loaded into crucibles, the alkaline-earth metals should first be heated near the operating temperature for a few days to remove adsorbed hydrogen and water from unintentional air exposure. The hydrogen evolved decreases during this process from a chamber pressure of 10^{-5} Torr to 5×10^{-9} Torr. The hydrogen background remains at a level of 5×10^{-9} Torr during growth. While the presence of hydrogen during growth does not appear to affect the growth of the oxides, the consequences on properties and growth are still being investigated.

2.5.2 RHEED

In this subsection we describe RHEED as a flexible tool for characterizing atomic surface structure and morphology during growth; many of the results summarized in this chapter rely on this technique. Before the advent of differentially pumped RHEED guns that were designed to operate in the low-vacuum environments of PLD and chemical vapor deposition (CVD) [71], RHEED was the exclusive domain of MBE [72]. RHEED is relatively inexpensive, and because of its side-view geometry (Fig. 12), it is straightforwardly integrated into most MBE growth-chamber designs. Because of these advantages, RHEED has been one of the most important tools for study-

ing thin-film nucleation and growth, and has been an indispensable tool for developing processes for the growth of thin-film oxides.

A fundamental characteristic of RHEED is the strength of the scattering process; as a result, the diffraction pattern in grazing incidence is sensitive to the structure of a flat surface. The surface sensitivity can be understood as arising from the grazing incident angle. For 10-keV electrons, the penetration depth at normal incidence is on the order of 30 Å. For an incident angle of 1°, penetration is trigonometrically reduced by a factor of 57 to give a penetration depth on a smooth surface of only 0.5 Å. Consequently, only the surface diffraction is observed.

The surface diffraction observed using RHEED is an image of the reciprocal lattice of the surface structure. The reciprocal lattice is the discrete set of wavevectors for plane waves with the periodicity of the real lattice. Because the surface breaks the periodicity of the lattice in the z-direction (perpendicular to the surface), a discrete set of wavevectors of the reciprocal lattice exists only in the two dimensions parallel to the surface. Perpendicular to the surface, all values of wavevector are allowed so that the reciprocal lattice is a collection of rods perpendicular to the surface.

In RHEED, the diffraction is from electrons with a relatively short wavelength of 0.12 Å for 10-keV electrons. The resulting diffraction pattern from planes of reciprocal space is imaged on a fluorescent screen opposite the RHEED gun. The sample is rotated about its surface normal for a complete characterization of the scattering in reciprocal space.

For a perfect surface, the rods are narrow, and spots are observed along an arc on the RHEED screen where the inplane momentum transfer of the scattered electrons has the value of the reciprocal lattice. If broad rods or streaks are observed, this is due to poor crystallinity where the rows of atoms are partially disordered and are arranged with a range of angles relative to the incident beam. The surface diffraction collected in this way sensitively characterizes the rich variety of surface structures and phases that arise from the deposition of submonolayer to monolayer amounts of material.

RHEED is also effective at determining surface roughness, a consequence of the low incident angle. Any surface asperity due to roughness or the nucleation of islands results in three-dimensional scattering that is characterized by the observation of Bragg spots. These spots are observed because the incident electron beam is incident on the island at a high angle and can diffract from a three-dimensional set of planes in a volume that is on the order of the penetration depth, ≈ 30 Å. This property of RHEED is useful for identifying the nucleation of unwanted phases by indexing the diffraction pattern and measuring the lattice parameters.

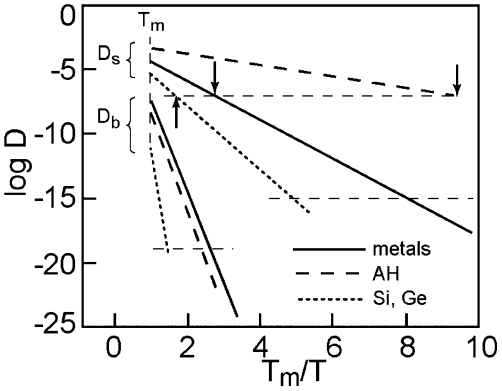

Fig. 13. Global growth characteristics. The temperature dependences of surface diffusivities, D_s, and bulk diffusivities, D_b, are plotted as a function of growth temperature normalized to the absolute melting temperature, T_m. This diagram summarizes three material classes: metals, alkali halides (AH), and the covalently bonded semiconductors, silicon and germanium. The arrows indicate growth temperatures for atomically smooth homoepitaxy. Above surface diffusivities of 10^{-8} to $10^{-7}\,cm^2/s$, films are expected to grow smoothly. Above $D_s > 10^{-15}\,cm^2/s$, RHEED oscillations are expected. Bulk diffusion will significantly impact superlattice growth for $D_b > 10^{-19}\,cm^2/s$. (Figure taken with permission from [73])

2.5.3 Fundamentals of Growth

The success of MBE in producing complex devices and intricately layered crystal structures can be attributed to the fundamentals of atomic diffusion and nucleation on a surface and in the bulk (Fig. 13) [73]. Due to the reduced coordination of surfaces relative to the bulk and the availability of empty lattice sites, surface diffusion is fast and bulk diffusion is slow, so that the nucleation of layers is easy, while diffusion into the bulk is difficult. The process for forming a layered crystal structure starts with a substrate that is stepped (Fig. 20), which, as will be discussed in Sect. 3, is required for growing high-quality layers. The features of this surface that are important for epitaxy are atomic-height steps and large-area terraces that are atomically flat facets between steps. If an atom can diffuse to a step, it will stick because of the increased coordination at lattice sites of the step. This mode of growth has been aptly described as step-flow growth, in that the steps simply move without changing the surface [73]. Because the surface does not change, no change is observed in the RHEED pattern.

Sufficient energy for this diffusion is normally supplied by thermal excitations from a hot substrate. If the growth rate is high enough and the substrate temperature is low enough, then before the deposited atoms can reach a step, multiple atoms nucleate to form an island on the terrace, which contributes to the roughness of the surface. As deposition proceeds, the density of these islands increases until a full atomic layer has been deposited and the surface

is again smooth. Diffraction from the surface now oscillates as the surface roughness changes in a periodic way. It has been observed that this process cannot proceed indefinitely because islands will nucleate on islands, etc., so at low temperatures or high deposition rates the surface eventually becomes rougher and the oscillations in surface diffraction are damped. The smoothest layers are deposited at high temperatures where the surface diffusion coefficient exceeds 10^{-8} to $10^{-7}\,\mathrm{cm}^2/\mathrm{s}$ [73] (see arrows in Fig. 13).

In order for the atomically smooth layer to remain unchanged so that it performs its function in a working device, the constituents of the layer must not diffuse into the bulk for the duration of device synthesis [73]. While bulk diffusion is inherently much slower than surface diffusion, the distance over which diffusion destroys the layer is on the order of an atomic layer, and the bulk diffusion coefficient needs to be less than $10^{-19}\,\mathrm{cm}^2/\mathrm{s}$ (lower dashed line of Fig. 13).

The two criteria of sufficient surface diffusion and insufficient bulk diffusion define a kinetic window of crystal growth. For metals, this window is narrow, at a substrate temperature of $\approx 1/3$ the melting temperature in absolute temperature units (T_m). For alkali halides this window is very large and ranges from 1/9 to 1/3 of T_m. For covalently bonded materials, such as Si and Ge, the window ranges from 1/2 the melting temperature to the melting temperature itself [73].

To apply these rules of thumb to the oxides we used as examples in this subsection, we note that the alkali halides are ionically bonded, just like the alkaline-earth oxides, and the perovskite oxides have both ionic and covalent bonding character and so should have surface diffusion coefficients similar to the covalently bonded materials. The melting temperatures of the alkaline-earth oxides range from 2191 K for BaO to 3125 K for MgO; for $CaTiO_3$ the melting temperature is 2521 K. We can use these melting temperatures as a starting point for determining the substrate temperature for atomically smooth growth.

A second consideration of particular importance in the growth of oxides involves the thermodynamics and kinetics of the metal–oxygen pair. In what follows, we will find that kinetics dominate the formation of the alkaline-earth oxides and perovskites. In the case of titanium oxide, the thermodynamics are characterized by the heats of reaction across the phase diagram for the Ti−O system [74]. While other phases are possible, we consider here four phases in the order of oxygen content, close-packed hexagonal titanium metal, rock-salt TiO, hexagonal Ti_2O_3 and tetragonal anatase TiO_2. Using the compiled heats of reaction, one finds that TiO_2 is thermodynamically stable at 800 K down to 10^{-14} Torr. While the stoichiometry does not depend on equilibrium considerations for these oxides, one can control the nucleation of different phases by changing the relative arrival rate of titanium and oxygen.

By way of illustration, an epitaxial multilayer of the titanium oxides was grown on the basal plane of an Al_2O_3 substrate [75]. The growth of this multilayer was accomplished by codepositing titanium and oxygen onto Al_2O_3.

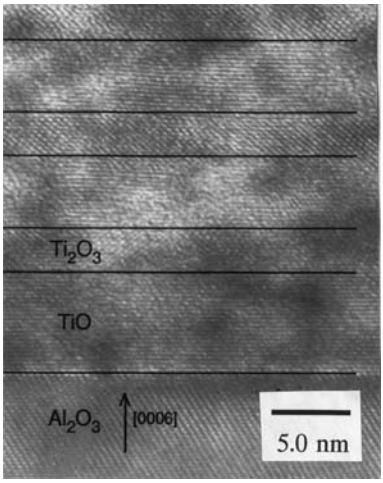

Fig. 14. Oxide multilayer. The micrograph is a high-resolution transmission electron micrograph of a TiO/Ti_2O_3 multilayer viewed in cross-section. The images are taken down the azimuth of Ti_2O_3 and the Al_2O_3 crystal. Note that the polar truncation of the TiO (111) surface is stabilized in this multilayer oxide heterostructure (see [75])

For a growth rate of 0.06 Å/s, the arrival rate of oxygen is high enough at 5×10^{-6} Torr to completely react with the titanium on the surface to form TiO_2. As the pressure is reduced to 5×10^{-7} Torr, TiO will nucleate, while Ti_2O_3 will nucleate at an intermediate pressure. One can grow a multilayer of two oxides by valving the oxygen source to vary the arrival rate of oxygen between 5×10^{-7} Torr and 1×10^{-6} Torr. One chooses a substrate temperature of 900 °C based on the melting point of covalently bonded TiO_2. The basal plane of Ti_2O_3 grows on the basal plane of sapphire, and the (111) plane of rocksalt TiO grows on the basal plane of Ti_2O_3. This sequence is repeated to form the oxide multilayer (Fig. 14). This illustration is a simple example of controlling crystal structure using the easily manipulated variables of MBE. More complex examples exist in the literature, for example, where oxygen stoichiometry can be varied by changing the arrival rate in a PLD deposition of $LaTiO_{3+b/2}$ [76]. Here, the properties were observed to change for this perovskite oxide from a metal to a ferroelectric by simple manipulation of the oxygen content.

Because kinetics is such an important aspect of MBE, the form of oxygen that is supplied to the substrate for reaction is an important consideration. While molecular oxygen is the easiest form to deliver to the growing film, diatomic oxygen is relatively unreactive due to the large binding energy of the molecule (5.2 eV) [77]. Therefore, atomic sources of oxygen [78] produced by both RF plasma and ozone sources [79] have been used in the MBE growth of perovskite oxides.

The above considerations apply to homoepitaxial growth, where the crystal being grown is the same as the substrate, as well as to heteroepitaxy, where the crystal being grown is different from the substrate. For the latter case, the task of matching materials is more than just matching symmetries and lattice parameters, but also making a transition in bonding across a heteroepitaxial interface with atomic-layer precision. In the following, we describe the physics of forming a heteroepitaxial interface.

For oxides, a simple example is the growth of $SrTiO_3$ (001) on MgO (001). Both crystals have stable (001) faces, and both are cubic with a mismatch of 7.5% when oriented with their respective a-axes aligned, the so-called "cube-on-cube" orientation. When the structures are examined, the SrO plane of the perovskite $SrTiO_3$ is that of a simple rocksalt structure, just like the plane of MgO of the (001) face. However, to achieve lattice matching, these two planes must be rotated 45° to one another. If this is done, then there is no way to match the electrostatics of these ionic planes. If the anions of the SrO plane are aligned with the cations of the MgO plane, then there will be some anions with anions as nearest neighbors. This situation is energetically unstable due to Coulomb repulsion. On the other hand, if the TiO_2 plane of the $SrTiO_3$ is matched to the (001) face of MgO, then the cations of the top plane can be matched with the anions of the MgO substrate to achieve a low-energy interface. The solution is to take advantage of the layer-sequencing ability of MBE to start with the TiO_2 plane of $SrTiO_3$ to start the heteroepitaxy.

Similar electrostatic arguments were invoked to explain the epitaxy of silicon on $LaAlO_3$ [80]. In this example, the interface was formed by heating silicon deposited on a $LaAlO_3$ substrate, which was subsequently annealed. Electron micrographs of the interface after this process revealed that the interface developed a 3×1 reconstruction between the silicon lattice and the $LaAlO_3$ lattice, which has a lattice misfit of only 1.3%. To understand why the interface rearranges itself from the bulk truncations of matched crystals, the electrical structure of the interface needs to be examined. Although $LaAlO_3$ is a perovskite with a structure analogous to the structure of $SrTiO_3$, the cation sublattices have different valences. Simply viewed, the Sr valence is 2+ and the Ti valence is 4+ in $SrTiO_3$ with oxygen at 2−. This arrangement means that each atomic plane of $SrTiO_3$ is neutral, making the (001) face stable. For $LaAlO_3$, however, the valences of both La and Al are 3+, which means that the AlO_2 plane has a net negative charge, while the LaO plane has a net positive charge. These two planes combine to form a (001) truncation of $LaAlO_3$ that is polar. The sharp truncation of (001) $LaAlO_3$ is stabilized by a 3×1 reconstruction of the interface. This example not only demonstrates other ways to fit an oxide on silicon, but is an example of the rich variety of electrical structures possible at oxide interfaces [81].

In Sect. 4.2, another oxide/silicon interface will be described in detail. In contrast to the $Si/LaAlO_3$ interface, this interface can be built up systematically using the layer-sequencing capability of MBE. Each of the layers of the interface is stable, and the components consist of the rocksalt alkaline

Table 1. Lattice parameters and chemical stability

Material	Lattice parameter (Å)	Gibbs energy of formation (kJ/mol) [77]
MgO	4.2112 [87]	−569.3
CaO	4.8112 [88]	−603.3
SrO	5.16 [87]	−561.9
BaO	5.539 [89]	−525.1

earth oxides and the cubic perovksite $SrTiO_3$. In the following two subsections we describe the details and characteristics of the MBE growth of each component in a way that illustrates the fundamentals discussed above.

2.5.4 Alkaline-Earth Oxide Growth

The alkaline-earth oxides of magnesium, calcium, strontium and barium have all been grown and studied using MBE. They possess the rock-salt structure and are ionic crystals, just like the alkali halides that have been extensively studied since 1928, when *Royer* first developed the rules for epitaxy [67]. The alkaline-earth oxides, however, are difficult to study due to their hygroscopic nature, and there are a limited number of ways to study intrinsic properties, one of which is to grow them in vacuum [82].

The attractive properties for epitaxial growth of the alkaline-earth oxides are their simple chemistry and crystal structure, their range of lattice parameters, and their limited reactivity (see Table 1). By alloying the various alkaline-earth oxides by codepositing the alkaline-earth metals, the lattice parameter of an oxide surface can be varied from 4.21 Å to 5.54 Å. A lattice-matched oxide surface can be grown and used as a substrate for the growth of other cubic oxides [83–86].

Growing these oxides is straightforwardly accomplished by evaporating the alkaline-earth metals in the presence of molecular oxygen. The compound itself, MO, can also be evaporated using a high-energy (6 keV) electron beam to sublime the molecule. When a reactive method is chosen, oxygen and the alkaline-earth metal readily react via:

$$\mathrm{Ba} + \mathrm{O}_2 \Leftrightarrow \mathrm{BaO} + \mathrm{O}. \tag{1}$$

While this reaction seems elementary, it shows that during growth four different molecules are on the surface: barium metal, molecular oxygen, molecular barium oxide and atomic oxygen.

The metal–oxygen reaction has been studied in the MBE environment at room temperature, and the metal on the surface has been found to oxidize at oxygen arrival rates equivalent to 1×10^{-7} Torr for a metal flux of 0.1 ML/s (1 ML of oxide is based on the bulk lattice parameter of the oxide) [90]. This corresponds to an approximately 10:1 ratio of arrival rate for molecular oxygen to alkaline-earth metal at the growth pressure. At these pressures,

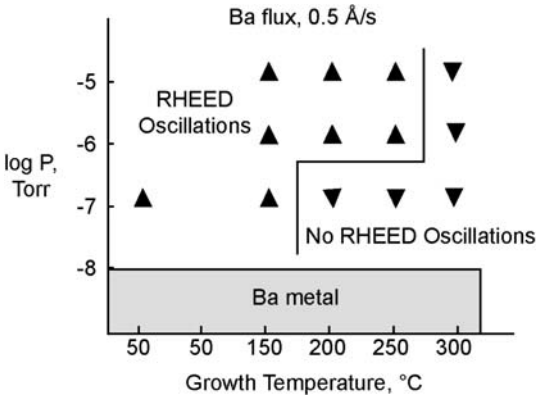

Fig. 15. Temperature and pressure diagram describing conditions for ledge growth of BaO. Flat, homoepitaxial growth is realized for conditions to the right of the solid boundary in the graph and defines the conditions for synthesizing devices with atomically sharp interfaces (taken from [92])

the mean free path of metal atoms is much larger than the distance to the shutter, and molecular beams are easily achieved.

Substrate temperatures for ledge growth have also been measured using RHEED oscillations for MgO [91] and BaO [92] (Fig. 15). The substrate temperatures required for smooth growth are typically very low because of the high mobilities of all of the species present on a growing surface. The high mobility is a direct consequence of the strong ionic bonding of the oxides that has been studied in the alkali halides [93].

We have empirically determined the growth conditions for flat growth of BaO and graphically represent them in Fig. 15. The growth rate was 1 ML of BaO every 5 s, resulting in a surface with ledges spaced ≈ 300 Å apart. Above a temperature of 275 °C, BaO grows with a flat morphology regardless of oxygen pressure. For oxygen pressures below 3×10^{-7} Torr, the substrate temperature can be reduced to 175 °C. The low growth temperature required for smooth growth of the alkaline-earth oxides means that they are easily incorporated into multilayer heterostructures without phase separation [94] or interdiffusion [93].

2.5.5 Perovskite Growth

Since the discovery of high-temperature superconducting oxides, there has been an explosion of interest in perovskite oxides for use in heterostructure devices [95]. The properties of these oxides can range from superconducting to ferroelectric to ferromagnetic. The variety of properties is achieved by changing the composition on the cation sublattice of the perovskite structure, ABO_3, or closely related structures. Functionality has been realized when

ferroelectric perovskites are integrated with semiconductors [96–99] or other oxides.

The growth of perovskite thin films by MBE is associated with a number of challenges when compared to other techniques, such as sputtering, metal-organic-chemical-vapor deposition (MOCVD), or PLD. The most notable is stoichiometry control of the line-compound ABO_3. While the oxygen content is controlled by absorption, the arrival rates of the A cation and the B cation must be matched for perovskites such as $SrTiO_3$ and $BaTiO_3$. Some ferroelectric perovskites, such as $PbTiO_3$ have one volatile cation component, and the stoichiometry can be serendipitously controlled within a thermodynamic growth window of substrate temperature and PbO overpressure [100]. While maintaining the correct stoichiometry is a challenge, a key advantage of MBE is the ability to control the formation of heterostructural interfaces with atomic-layer precision. The following discussion focuses on this strength.

The perovskites that we consider here are $SrTiO_3$ and $BaTiO_3$, both of which have a structure based on the cubic perovskite structure. As mentioned earlier, this structure consists of neutral cation–oxide layers, BaO or SrO in one layer and TiO_2 in the next, which allows the perovskite structure to be built up in a layer-by-layer fashion. Conversely, codepositing the cations builds the structure up in a unit cell-by-unit cell fashion.

For layer-by-layer deposition, the reaction described by (1) takes place during BaO deposition as the atoms diffuse on the TiO_2-truncated surface, while the following reaction takes place on the BaO-truncated $BaTiO_3$ surface:

$$\mathrm{Ti} + \mathrm{O_2} \Leftrightarrow \mathrm{TiO_2}. \tag{2}$$

The most straightforward approach to ensuring correct stoichiometry is to measure the flux from each cell before deposition by closing the shutter covering the substrate. After calibration, film growth can begin by sequentially opening each shutter for an amount of time that corresponds to 1 ML of growth. While the deposition rate can be calibrated sufficiently accurately with a quartz crystal monitor by averaging over many monolayers of deposition, real-time monitoring of a single monolayer is not accurate enough because of thermal drift of the quartz oscillator frequency. The thermal drift is a consequence of the changing heat load on the quartz crystal that is exposed to the hot evaporation source. When the shutter is opened, the temperature of the crystal changes enough to change the frequency of the crystal that is equivalent to tens of angstroms of elemental deposition. A second problem with this method is that, even with calibration, the flux from the source can also drift.

The perovskite structure can accommodate an excess of alkaline-earth metal as extra planes that have the rocksalt structure and are commensurate with the perovskites lattice. Ordered lattices with extra planes make up a series of Ruddleson–Popper phases that can be viewed as superlattices of

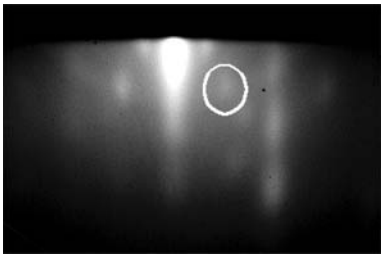

Fig. 16. Nucleation of incommensurate rough islands on a $BaTiO_3$ surface with excess TiO_2. If the stoichiometry is not controlled using the methods outlined in the text, then rough islands of other phases containing barium and titanium will nucleate. These islands show up in RHEED as Bragg spots (circled in figure) due to the large volume of material that diffracts

alkaline-earth oxide and the perovskite [101]. Excess TiO_2 forms phases that are not commensurate with the growing perovskite surface and nucleate as rough islands on an otherwise flat perovskite surface (see Fig. 16). These islands destroy the layered structure, and flat growth cannot be continued.

A class of methods for controlling the stoichiometry takes advantage of the fact that the surface diffraction is different for each deposited layer, BaO or TiO_2 [101–103]. If RHEED is observed during growth and the intensity is monitored in different regions of reciprocal space, then the intensity is observed to change, depending on whether the surface is being covered with BaO or TiO_2. When the intensity reaches a predetermined value for a complete monolayer, deposition of that layer is stopped, and deposition of the next layer is started.

An example of this approach is to monitor the RHEED pattern that is characteristic of surface reconstructions that form at 1/2 ML over coverage of either BaO or TiO_2 [102, 103]. If one starts with a flat, TiO_2-truncated surface and adds 1/2 ML more of TiO_2, a doubling of the surface periodicity is observed along the $\langle 210 \rangle$ direction of (001) $BaTiO_3$ (see Fig. 17). If one assumes that the intensity of this diffraction feature is directly proportional to the amount of excess TiO_2 on the surface, then one can control growth by opening the shutter over the Ti source to expose the BaO-truncated surface until this feature is just barely observed, at which time the shutter is closed. From a fit of the TiO_2 peak, one estimates that the coverage can be controlled to within about 0.03 ML, with the error arising from the high background around the peak. Ideally, this should be a null technique because a stoichiometric surface should have no peaked intensity at this position in reciprocal space.

Next, we consider oxygen stoichiometry. The reactions in (1) and (2) take place sequentially if one grows layer-by-layer, as discussed above. An alternative is to match both metal deposition rates and deposit both met-

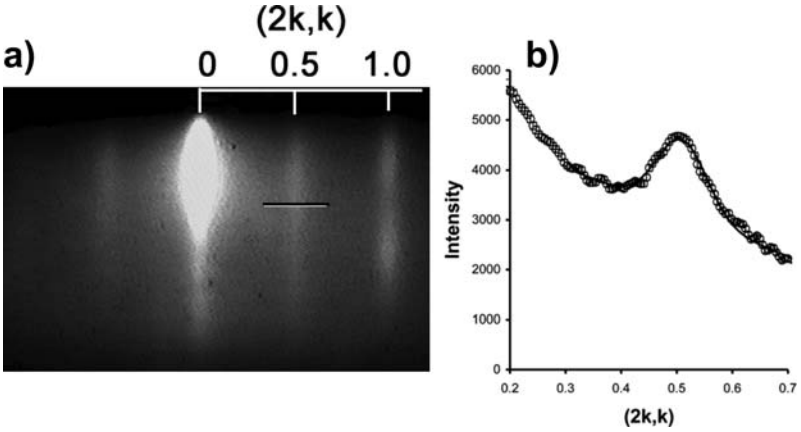

Fig. 17. RHEED stoichiometry control. If the RHEED is monitored near the ⟨210⟩ direction of (001)$BaTiO_3$, then excess titanium can be detected at submonolayer levels. This excess can then be corrected before nucleation of other phases as islands. The RHEED image shows that the $BaTiO_3$ surface with excess TiO_2 is atomically flat by the rod-like diffraction evident in panel (**a**). Panel (**b**) is a line scan through the (1,0.5) rod and can be used to quantify the amount of excess TiO_2 to within ≈ 0.03 monolayer

als simultaneously. For this case, the following reaction takes place on the growing surface:

$$\mathrm{Ba} + \mathrm{Ti} + \frac{3}{2}\mathrm{O}_2 \Leftrightarrow \mathrm{BaO} + \mathrm{TiO}_2. \tag{3}$$

These techniques have been compared by measuring the crystalline perfection of the resulting films [103] as characterized by X-ray rocking curves. This investigation showed that the codeposition route was superior because it promotes a more complete oxidation of the titanium, as measured by X-ray photoelectron spectroscopy (XPS). One possible explanation for this result may be the presence of atomic oxygen during codeposition in (3), which reacts more rapidly than molecular oxygen, with oxygen vacancies trapped in the growing surface. Substoichiometric oxides can be avoided by using more reactive sources of oxygen such as ozone [104] or RF-generated atomic oxygen [78].

3 Substrates

Even with access to advanced physical vapor deposition techniques that are able to transfer the composition of the desired material to the substrate, it is difficult to obtain a single-crystalline epitaxial film, much less a multilayered structure, without the availability of atomically flat substrates. When thin

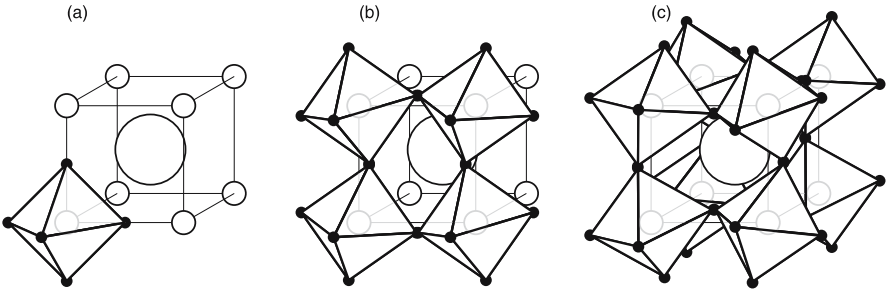

Fig. 18. Typical oxide crystal structures and lattice distortions: (**a**) perfect cubic perovskite, (**b**) tetragonal distortion, (**c**) $GdFeO_3$-type orthorhombic distortion

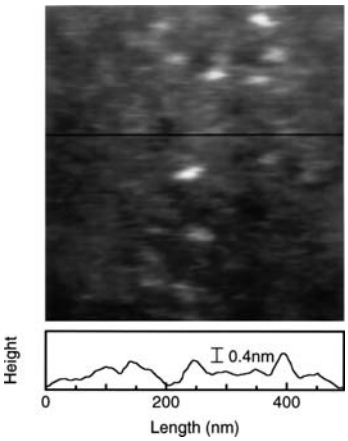

Fig. 19. Polished $SrTiO_3$ substrate surface (Shinkosha). Image size is 0.5 µm × 0.5 µm

films of complex oxides are grown by atomic-layer techniques, especially when the film thickness is in the nanometer range, it is necessary to start from an atomically flat substrate surface because it would otherwise be difficult to guarantee correct atomic-scale layer ordering during film growth. Rough starting surfaces can cause a variety of structural defects and thus alter the dielectric, ferroelectric and other properties of a film. Surface flatness over longer distances, on the order of µm, is also necessary when films are grown for device applications, such as tunnel junctions or field-effect devices. Surface flatness over multiple layers is also critical when growing superlattices. Any roughness on the substrate surface can lead to unintentional electrical shorts in thin barrier layers.

When compared to well-established substrates, such as silicon, oxide crystal surfaces are generally harder to prepare with a similar degree of perfection, which is partly due to the complexity of the lattice and the large number of constituent elements.

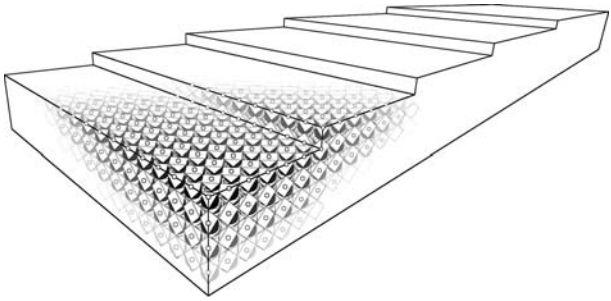

Fig. 20. Model of a step-and-terrace perovskite surface. All terraces have the same terminating atomic layer if all steps have the same height, equal to a single perovskite unit cell. The miscut angle determines the average terrace width

Among oxide substrate materials, $SrTiO_3$ has probably been characterized in the greatest detail. The techniques and problems that arise in the preparation of a well-ordered crystal surface for thin-film growth are discussed here by using $SrTiO_3$ as an example.

$SrTiO_3$ is a cubic perovskite at room temperature with a lattice constant of 0.3905 nm. The basic perovskite unit cell of $SrTiO_3$ at room temperature is shown in Fig. 18a, where the B-site cations are drawn at the corners of the unit cell, surrounded by oxygen octahedra. The A-site cation is at the center of the cell. $SrTiO_3$ single crystals show a structural transition to a tetragonal phase when cooled below 105 K. The presence of even lower symmetry phases below about 50 K has been suggested, based on X-ray analysis [105]. The tetragonal low-temperature phase is illustrated in Fig. 18b. The oxygen octahedra surrounding the Ti atoms are tilted in the a–b plane, resulting in a doubling of the lattice constant along the a- and b-axes [106]. The tetragonal distortion is quite small, with $c/a = 1.00056$ [105].

$SrTiO_3$ substrates usually have the (001) orientation, ideally exposing a surface terminated by the TiO_2 layer. Other cut directions can also be used to obtain a tetragonal (110) or a hexagonal (111) surface. Typical oxide substrates delivered by commercial crystal vendors have a polished surface with very low average roughness. An atomic force microscope (AFM) image of a mechanochemically polished $SrTiO_3$ substrate is shown in Fig. 19. The cross section of the image shows that the peaks and valleys rarely exceed the height of a single perovskite unit cell, which is approximately 0.4 nm. On an atomic scale, however, this surface is not well ordered, exposing all possible atomic layers at the surface. The polishing process can also contaminate the surface with elements that are not normally present in the crystal, such as Si, if silica-based polishing agents are used. The polishing is done at room temperature and can induce significant strain in the surface layer of the crystal [107]. There is therefore no guarantee that such a surface would be thermally stable above room temperature.

Preparation of an atomically flat and well-ordered oxide surface is a challenging task. An atomically flat surface should show a regular step-and-terrace structure, determined by the miscut angle of the crystal (Fig. 20). If all steps on such a surface have the height of a single unit cell, one can assume that all terraces are terminated by a chemically identical atomic layer.

A variety of surface-preparation techniques have been developed for obtaining clean crystal surfaces. Some techniques, such as sublimation of Bi films [108], are mainly useful for removing carbon contamination from a surface without affecting the structure of the surface layer. This is mostly useful for surface-sensitive analysis of samples prepared by ex-situ techniques. Other methods, such as ion bombardment [109] have also been used, but due to mass-dependent sputtering rates of atoms on the surface, this technique can result in stoichiometry changes in the surface layer. Generally, the preferred method for converting an atomically rough polished surface into a well-ordered step-and-terrace surface is to use wet etching and high-temperature annealing. Various combinations of these steps have been used to obtain very high quality $SrTiO_3$ substrates [110–112].

Substrate annealing, without wet etching, can be used to improve the flatness of various substrate materials. Unfortunately, simple annealing of a polished $SrTiO_3$ surface does not yield the desired result [113]. Although high-temperature annealing promotes recrystallization of the surface layer of the substrate and thus helps to planarize a roughly polished surface, there are also a number of problems that can appear in annealed perovskite crystals. The biggest problems relate to the thermodynamic stability of the crystal, imperfect control of the terminating layer, and step-edge dynamics.

Various studies have shown that the stoichiometry of $SrTiO_3$ single crystals tends to change during high-temperature annealing [114,115]. The dominant mechanism is the formation of oxygen vacancies, especially when annealing is done at low oxygen pressure in a film-deposition chamber. Increasing the background oxygen pressure during annealing can prevent such vacancy formation, but it still leaves the possibility of cation-vacancy formation. In ternary ABO_3 oxides, the probability of cation-vacancy formation does not drop at high temperature, even when the oxygen pressure is increased [116]. In the case of $SrTiO_3$, the most likely point defects are thus oxygen and Sr vacancies. This in turn can lead to macroscopic segregation of Sr on the surface of the crystal [114, 117].

The segregation effects have an obvious influence on the crystal termination. Although an annealed $SrTiO_3$ crystal typically assumes a predominantly TiO_2-terminated surface, there is still a significant amount of Sr present as well. The composition of the terminating layer of a substrate can be studied by AFM and ion-scattering spectroscopy. AFM can be used to analyze the surface composition if macroscopic surface segregation takes place. Topographic images can be used to detect the presence of step-edge heights that are not multiples of the unit-cell height. If, for example, SrO forms islands on the substrate surface, one would expect to see 0.2-nm or 0.6-nm high

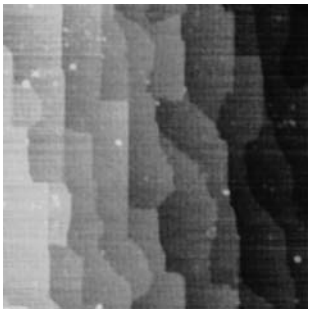

Fig. 21. Step bunching observed by AFM on a 0.5 wt% Nb-doped $SrTiO_3$ (001) surface. The image size is 2 µm × 2 µm. One and two unit-cell high steps can be seen on the surface after annealing in air for 1 h

step edges in addition to single unit-cell 0.4-nm edges [111]. A more useful technique, however, is to use friction-force microscopy (FFM), where the lateral friction force of the AFM tip is measured as the tip is dragged over the sample surface. The interaction force between a tip and the surface depends on the chemical composition of the surface layer and thus affects the lateral force exerted on the AFM tip. The likely mechanism for different interaction forces is the reaction of the crystal surface with atmospheric moisture, resulting in higher friction over a SrO-covered surface than a TiO_2-covered surface [118]. Friction-force microscopy can be used to detect nanometer-scale regions where the predominant termination character changes [119].

Another problem caused by high-temperature annealing is related to step-edge dynamics of vicinal $SrTiO_3$ surfaces. An annealed substrate surface should ideally show nearly straight and equidistant single unit-cell steps. Annealing $SrTiO_3$ substrates at 1000 °C or higher, particularly at high oxygen pressures, can easily induce step-edge faceting and step bunching. An example of a 0.5 wt% Nb-doped $SrTiO_3$(001) substrate annealed for 1 h in air in a furnace is shown in Fig. 21. Bunched steps of two unit cells are present on this surface; bunched step edges can be several unit cells high and disrupt the growth of thin epitaxial layers.

One way to improve the surface flatness while avoiding compositional changes is to use wet etching [110,120]. Various etching procedures have been developed for $SrTiO_3$. Planarization of polished $SrTiO_3$ can, for example, be achieved by etching in a buffered hydrofluoric acid (BHF), $NH_4F{-}HF$. The pH of the acid has to be adjusted carefully; values above 5 tend to leave etch residue on the surface, while a pH below 4 results in a high density of square etch pits. This behavior is not unique to etching with BHF; similar behavior applies to other etchants as well, such as HCl [121].

The planarization process can be followed in real time by performing AFM measurements of the substrate surface inside an acid bath [122]. The acid dissolves the SrO layer preferentially and thus quickly removes any segregated

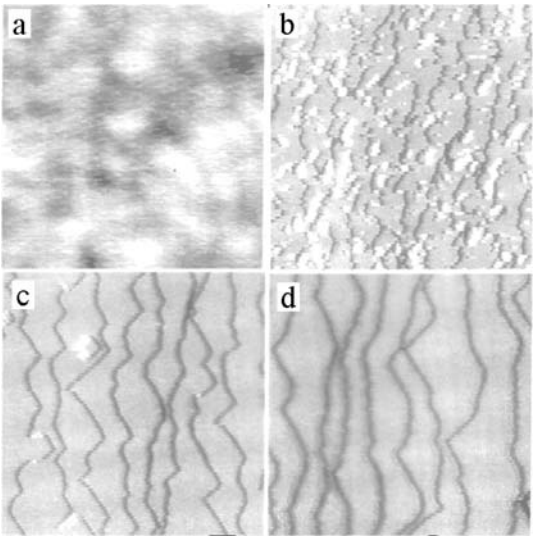

Fig. 22. Surface-morphology evolution of a $SrTiO_3$ (001) substrate during BHF etching. Images were taken at etching times of (**a**) 0 min, (**b**) 5 min, (**c**) 8 min, and (**d**) 12 min [122]. Image sizes are $1 \times 1\,\mu m^2$

Sr from the surface. After that, etching proceeds in step-flow mode if the pH of the acid is chosen suitably. In such a process, Sr is removed from the step edges, also lifting off the covering TiO_2 layer. The step-flow etching process is very efficient at planarizing a polished crystal surface within a few minutes. The choice of the pH is important because there is a possibility that the acid will form an etch pit in the middle of a terrace. The step flow thus has to proceed at a rate that is fast enough for the newly formed etch pit to be removed by the constantly shifting step edges before the pit depth increases. The process is illustrated in Fig. 22., where one can see the progression of an etched substrate surface to an atomically flat step-and-terrace surface.

The etching rate depends on the pH and also on the morphology of the step edges. The fact that etch pits are rectangular, rather than circular in shape, shows that the etching rate of kink sites on the step edges is faster than for ridge sites. This is also shown by the fact that the step edges move approximately $\sqrt{2}$ times more quickly when the miscut direction is at a 45° angle to the high-symmetry [100] and [010] directions. The drawback of the etching-rate variation is that the etching rate needs to be adjusted for each substrate, depending on the miscut direction.

Other etching techniques can be used if the substrates are well polished and planarization can be achieved by an annealing step. For example, *Koster* et al. [111] have studied the effectiveness of soaking a $SrTiO_3$ crystal in water to promote the formation of Sr hydroxide groups wherever Sr is present on the crystal surface. This method is more gentle on the crystal than pro-

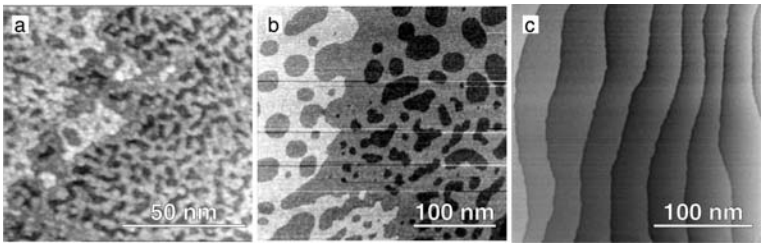

Fig. 23. Recrystallization of the $SrTiO_3$ surface during annealing. (**a**) Formation of nm-scale islands starts at temperatures below 500 °C. (**b**) Nearly uniform terraces reform above 700 °C. (**c**) A regular step-and-terrace structure can be regained above 900 °C [124]. The images are taken from different samples, which is why the average terrace width varies

longed BHF etching, because the TiO_2-terminated surface is stable in water. The Sr hydroxides can be efficiently removed by a brief BHF etching step, which reduces the chance of creating etch pits at the surface. A drawback of this method is the need for a final annealing at around 950 °C in order to obtain a well-defined step-and-terrace surface. As discussed earlier, this can cause Sr segregation, and thus the termination of the final crystal surface by the TiO_2 layer is still not perfect when characterized by ion scattering or photoemission spectroscopy.

The nature of the nonstoichiometric surface layer that forms in $SrTiO_3$ at high temperature has been studied by various structural and composition analysis techniques [113, 114, 117, 123]. Instead of the bulk changes that affect a layer several tens of nm in depth, for thin-film growth, the behavior of the few topmost unit cells is what is crucial.

It is known that at intermediate annealing temperatures the step edges on vicinal $SrTiO_3$ form meandering patterns due to recrystallization of the crystal surface [120]. The recrystallization process can be monitored directly by in-situ high-temperature scanning tunneling microscopy (STM). The degradation of a polished and etched $SrTiO_3$ surface starts at a very low temperature. Ion-scattering spectroscopy shows the appearance of Sr on the surface when a crystal is heated to 300 °C [112]. STM measurements of surfaces heated to 550 °C show that the crystal surface breaks up to a depth of at least three unit cells, and an atomically smooth surface is regained only after annealing at temperatures well above 700 °C [124]. In order to regain a regular step surface in one or two hours, the temperature needs to be even higher, ususally in the 900 °C to 1000 °C range.

The surface appears to go through two transformation stages. The first change occurs in the 300 °C to 500 °C range, where a surface that has been prepared at room temperature by polishing and possibly etching breaks up, forming many nm-scale islands with a height of 1 or 2 unit cells on the surface (Fig. 23a). This change can be easily detected by scanning probe microscopy

and coincides with the appearance of Sr scattering peaks in ion-scattering spectra [112]. The final recrystallization starts to occur above 700 °C, as seen by in-situ STM (Fig. 23b) [125]. It is interesting to note that the temperature where long-range step-edge changes start to occur coincides with the temperature where bulk diffusion starts to bring Sr to the crystal surface, possibly hinting at a link between the presence of defects and diffusion at the crystal surface. Straight step edges can only be obtained after long annealing, typically on the order of 1 h (Fig. 23c). The time required to obtain straight step edges and hole-free terraces depends on the miscut angle of the substrate, with the annealing time being proportional to the average terrace width. It is generally advisable to perform the recrystallization anneal at the lowest temperature where the required annealing time is still experimentally acceptable. Although the surface-diffusion processes can be sped up considerably by increasing the annealing temperature above 1000 °C, the risk of generating macroscopic SrO_x segregation and step-edge faceting or bunching also increases. In general, atomically well-ordered surfaces of cubic perovskites are difficult to produce. Cleaving is possible for various layered compounds, but in the case of cubic crystals such as $SrTiO_3$, this would again produce a surface with a mixed termination. The best way to obtain atomically well-ordered surfaces appears to be long-term annealing at moderate temperatures [114, 126].

While the surface structure and treatment procedures for obtaining high-quality oxide substrates have been studied in great detail for $SrTiO_3$, much less work has been done on other substrate materials. Epitaxial thin films usually have a significant lattice mismatch with the substrate, and the residual strain in the film can have a strong effect on the ferroelectric, dielectric, magnetic, and transport properties of the film. An obvious way of controlling strain effects in thin films is to use a substrate with a suitable in-plane lattice parameter. Some of the more common substrate materials that can be used for oxide thin-film growth are compared in Table 2.

A popular substrate material with a smaller lattice parameter than $SrTiO_3$ is $LaAlO_3$. The crystal structure of $LaAlO_3$ is rhombohedral at room temperature, but a transition to a cubic phase occurs above 800 K [128, 135]. As a result of this phase transition, crystal surfaces heated above the transition temperature develop an irreversible twin structure [113, 136]. Atomically flat step-and-terrace (001) surfaces can still be prepared by etching polished substrates in concentrated HCl under ultrasonic agitation at room temperature for 5 min and annealing the substrates in air at 1000 °C for a few hours. All steps on the surface have a height of a single pseudocubic perovskite unit cell, but due to the twin formation, the direction of surface steps varies from place to place, depending on which twin grain is observed. Coaxial impact collision ion-scattering spectroscopy (CAICISS) analysis [137] has shown that the terminating layer consists of AlO_2, with less than 10% of LaO on the surface. The presence of residual La on the surface is likely due to similar mechanisms as were discussed in the case of $SrTiO_3$. All step edges on atom-

Table 2. Lattice parameters and crystal structures of selected substrate materials

Material	Structure	Lattice constants	
$SrTiO_3$	cubic $> 105\,K$	$a = 3.905\,Å$	[105, 106]
	tetragonal $< 105\,K$	$c/a = 1.00056$	
$BaTiO_3$	cubic $> 390\,K$	$a = 4.01\,Å$	[127]
	tetragonal $> 270\,K$	$a = 3.99\,Å$	
		$c = 4.04\,Å$	
	orthorhombic $> 180\,K$	$c = 3.98\,Å$	
		$a = 4.01\,Å$	
	rhombohedral $< 180\,K$	$a = 4.00\,Å$	
$LaAlO_3$	cubic $> 800\,K$	$a = 3.81\,Å$	[128]
	rhombohedral $< 800\,K$	$a = 5.36\,Å$	
		(3.79 Å)	
LSAT	cubic $> 150\,K$	$a = 3.87\,Å$	[129]
	tetragonal $< 150\,K$	$a = 5.46\,Å$	
		$c = 7.73\,Å$	
		(3.86 Å)	
$NdGaO_3$	orthorhombic	$a = 5.43\,Å$	[130]
		$b = 5.50\,Å$	
		$c = 7.71\,Å$	
		(3.86 Å)	
$LaGaO_3$	orthorhombic $< 420\,K$	$a = 5.49\,Å$	[131]
		$b = 5.53\,Å$	
		$c = 7.78\,Å$	
		(3.89 Å)	
	rhombohedral $> 420\,K$	$a = 3.93\,Å$	
$KTaO_3$	cubic	$a = 3.99\,Å$	[132]
MgO	cubic	$a = 4.21\,Å$	[133]
$DyScO_3$	orthorhombic	$a = 5.44\,Å$	[134]
		$b = 5.71\,Å$	
		$c = 7.89\,Å$	
		(3.94 Å)	
$GdScO_3$	orthorhombic	$a = 5.49\,Å$	[134]
		$b = 5.75\,Å$	
		$c = 7.93\,Å$	
		(3.97 Å)	

ically flat surfaces have a single unit-cell height, which means that there is no macroscopic segregation of La atoms on the surface.

The dielectric constant of $LaAlO_3$ is 24, which is much lower than $SrTiO_3$, even at room temperature. This makes $LaAlO_3$ a suitable substrate for mi-

crowave applications. The dielectric loss figure of $LaAlO_3$ is 10^{-3} at room temperature, but drops sharply when cooled below 100 K [138]. One problem for applications, however, is that the twinning that occurs at 800 K means that the structure of a film that is grown at a high temperature may change when cooled to the usual characterization temperatures at or below 300 K. These problems can be mostly avoided by using a solid-solution crystal $(LaAlO_3)_{0.3}-(Sr_2AlTaO_6)_{0.7}$ (LSAT) [139,140]. This crystal remains cubic at room temperature, although a lower-symmetry phase appears below 150 K [129].

Atomically flat LSAT surfaces can be obtained by annealing in air for 2 h at 1300 °C. The annealed surfaces usually show slightly meandering step edges with a height of approximately 0.4 nm, which equals half of the LSAT unit-cell height. The dominant terminating layer is the B-site of the crystal, which in this case is the $AlO_{2-\delta}/TaO_{2-\delta}$ layer. The contribution from the A-site layer is less than 10% in CAICISS time-of-flight spectra [141].

A very different surface appears on annealed $NdGaO_3$ crystals. Atomically flat terraces can be obtained by annealing polished crystals in air without the need for chemical etching. Ion-scattering measurements have shown that unlike most other substrates, $NdGaO_3$ (001) surfaces are terminated by the A-site NdO layer. This property makes $NdGaO_3$ useful for the growth of high-quality $YBa_2Cu_3O_{7-\delta}$ high-temperature superconductor films with reduced twinning [142, 143]. The lattice parameters of gallates can also be tuned by selecting a suitable A-site cation. The most common cases for substrates are $NdGaO_3$ and $LaGaO_3$. Rare-earth gallates generally have the $GdFeO_3$ structure, with each orthorhombic unit containing four basic perovskite units, as illustrated in Fig. 18c [144,145]. For the purpose of oxide film growth, the crystal surface can be viewed as a distorted perovskite with displaced oxygen ions.

Thermal expansion in gallates is anisotropic, with values ranging from $\alpha_b = 2.3 \times 10^{-6}\,K^{-1}$ to $\alpha_a = 11.3 \times 10^{-6}\,K^{-1}$ in $NdGaO_3$ [130,131,146]. The thermal stability of gallates is lower than for other commonly used substrates, and decomposition of the crystal and segregation of Ga to the surface has been observed after annealing $NdGaO_3$ wafers above 1000 °C [147].

The Nd and La gallate substrates have a pseudocubic unit cell that is slightly smaller than $SrTiO_3$. For $NdGaO_3$, for example, using the orthorhombic (110) surface would give an average pseudocubic surface with a lattice parameter of 3.86 Å. One advantage of using nontitanate substrates is the lower dielectric constant of gallates (compared to $SrTiO_3$) at room temperature [138, 145]. These two materials are not sensitive to oxygen loss and do not suffer from charge-transfer effects that are commonly seen in $SrTiO_3$. $NdGaO_3$ is therefore a convenient substrate for measuring transport properties of very thin oxide films [148].

For substrate materials that have larger lattice parameters than $SrTiO_3$, $KTaO_3$, MgO, and rare-earth scandates, such as $DyScO_3$, are used. $KTaO_3$ is a cubic perovskite with a lattice constant of 0.3989 nm and a thermal expan-

sion coefficient of $6.7 \times 10^{-6}\,^{\circ}\mathrm{C}^{-1}$ [132, 149]. Unlike $SrTiO_3$, which becomes tetragonal below 105 K, $KTaO_3$ remains cubic at all temperatures from the melting point down to the mK range [150]. It is possible to dope $KTaO_3$ with Ca, resulting in an n-type semiconductor with a gap of 3.5 eV [151, 152]. The room-temperature mobility of carriers in $KTaO_3$ is $30\,\mathrm{cm}^2/\mathrm{V}\cdot\mathrm{s}$, which is 5 times higher than in $SrTiO_3$, making $KTaO_3$ an attractive candidate for use in oxide electronics [152, 153].

Pure $KTaO_3$ is also an incipient ferroelectric that does not have an obvious ferroelectric transition, although ferroelectric-like behavior has been reported below 1 K [154]. $KTaO_3$ can be driven into a ferroelectric state when Ta is partially replaced with Nb. $KTa_{1-x}Nb_xO_3$ is ferroelectric in the $x > 0.05$ doping range, with some of the highest known dielectric constant values at room temperature, approaching 10^4 [152]. The ferroelectric transition temperature can be tuned from about 70 K for $x = 0.05$ to 700 K for $x \approx 1$ [155].

The use of $KTaO_3$ as a thin-film substrate became popular due to thermal stability and lattice match with high-T_c superconductors, such as $YBaCu_3O_7$ and $Sr_{1-x}La_xCuO_2$ [132, 149, 156]. In addition to superconductors, the growth of various ferroelectrics, such as $KNbO_3$ and $Pb_{1-x}La_xTiO_3$, on $KTaO_3$ has also been reported [157–159].

Reliable surface treatment for obtaining an atomically flat surface for high-quality film growth is less well established than for $SrTiO_3$. Various etching procedures have been explored, but these do not always result in atomically flat step-and-terrace surfaces [149]. A combination of etching polished crystals in buffered KOH, followed by annealing at 750 °C, has been shown to produce a step-and-terrace surface [160].

Cubic MgO is another material that is widely used as a thin-film substrate. The lattice parameter of MgO is 0.4212 nm, making it one of the largest unit cells available among oxide substrates. The thermal expansion coefficient is $8 \times 10^{-6}\,\mathrm{K}^{-1}$. The dielectric constant is 9.8 with a loss tangent of about 10^{-5} at 10 GHz [133]. The dielectric constant is relatively low among other oxide substrates and does not depend strongly on temperature or frequency, which is why MgO is often used as a substrate for the fabrication of microwave devices and thin films that are characterized at microwave frequencies. Optical transparency is good, ranging from the infrared to the ultraviolet. MgO is also one of the most inexpensive oxide substrate materials.

The highest-quality crystal surface can be obtained by cleaving MgO crystals in vacuum. Steps with a single unit-cell height, 0.4 nm, and single atomic-layer height (0.2 nm) can be seen on such surfaces [161]. Significant relaxation of atomic positions occurs at the step edges, which can affect nucleation and initial growth on MgO [162].

Vacuum cleaving, however, is not a practical choice for thin-film work. Instead, it is common to use mechanically polished surfaces that can be further processed by chemical etching, for example in phosphoric acid, followed by annealing in air or oxygen at temperatures around 1100 °C. The exact choice of annealing time and temperature can have a strong influence on the films

grown on MgO substrates. In particular, domain formation and orientation in thin films are strongly affected [163]. The surface morphology of MgO (001) substrates appears to depend on the impurity concentration and crystal quality of a particular batch of substrates. For that reason, optimal processing conditions vary, but in general, annealing for a few hours at about 1100 °C appears to give good surface flatness. Higher temperatures can result in excessive surface roughening, and longer annealing times increase the amount of residual Ca in the crystal that segregates to the surface [164]. A combination of etching, annealing in air, followed by a brief anneal in the deposition chamber under UHV conditions, produces the best surface in terms of atomic ordering and reproducibility [165].

Typical MgO crystals also have significant impurity concentrations, in the tens to hundreds of parts per million (ppm). The dominant impurity is Ca. Large MgO crystals are also not true single crystals. Instead, crystals consist of many millimeter-scale grains that are delineated by low-angle grain boundaries. The size, shape, and angular distribution of MgO grains can be analyzed with a high-resolution 4-axis X-ray diffractometer [166]. The grain boundaries can affect the step formation on the surface and the segregation of impurities [167]. When substrates are annealed for several hours at 1200 °C and higher, large three-dimensional islands form on the crystal surface. The segregated islands mostly consist of Ca, as shown by Auger, photoemission, and ion-scattering spectroscopy [168–170].

Although MgO is not particularly hygroscopic, damage by atmospheric moisture has been noted. The dominant damage mechanism appears to be localized erosion of the MgO surface by the formation of small etch-pit-like features [171]. Prolonged exposure of a cleaved crystal to ambient atmosphere can result in micrometer-scale particles appearing on the surface [113]. The most common substrate orientation for MgO is [001]. Other orientations are also possible, such as [110] or [111], but in the case of MgO, these surfaces are not charge neutral and usually facet during etching and annealing [172, 173].

The range of lattice constants between $SrTiO_3$ and $KTaO_3$ can be covered by various rare-earth scandates. The most common compositions used for substrates are $DyScO_3$ and $GdScO_3$, with pseudocubic lattice parameters of 0.3943 nm and 0.3967 nm, respectively. $DyScO_3$ has the smallest lattice parameter in the scandate family. The largest lattice parameter is 0.405 nm for $LaScO_3$. All of these crystals have the $GdFeO_3$-type orthorhombic structure, but the distortion from simple cubic perovskite structure is small [134]. The surfaces of scandate crystals have not been characterized as well as other more popular materials, but annealing substrates at 1100 °C in oxygen for 12 h, followed chemical etching, has been found to improve the quality of films grown on $DyScO_3$ [174].

Scandate substrates are particularly useful for studying strain effects in ferroelectric films. The lattice constants of $DyScO_3$ and $GdScO_3$, for example, can be used to grow $SrTiO_3$ films with a large tensile in-plane strain [175,

176], $BaTiO_3$ films with compressive strain [177], and strain-free infinite-layer compounds [174].

Another substrate material that can be useful for strain-effect studies is the prototypical ferroelectric, $BaTiO_3$. With a cubic lattice parameter of 4.01 Å, it is one of the largest cubic perovskite unit cells and is useful for looking at tensile strain effects in thin oxide films. The main difficulty with $BaTiO_3$ as a substrate material is the cubic-to-tetragonal phase transition that occurs at around 120 °C. The room-temperature tetragonal phase is ferroelectric but usually has a multidomain structure, with the tetragonal *c*-axis pointing randomly in any of the three high-symmetry directions of a crystal. Although single-domain $BaTiO_3$ substrates are commercially available, once the crystal is heated to a typical film-growth temperature and then cooled back to room temperature, the multidomain structure reappears. For this reason, the main use of $BaTiO_3$ as a substrate has been limited to the observation of stepwise strain-related transition in films as the sample is cooled across the tetragonal, monoclinic, or rhombohedral phase transitions of $BaTiO_3$. Jumps in resistivity have been observed in superconducting films [178], and both transport and magnetization have been modulated by strain in $SrRuO_3$ films [179] and in colossal magnetoresistance manganite films [180].

4 Applications of Epitaxial Oxide Thin Films

With the availability of both atomically flat substrates and film-deposition methods specialized for the growth of complex oxide materials, one can now deposit extremely high quality single-layer complex oxide materials and measure their properties. In addition, one can use advanced film-deposition techniques to combine various materials, each with their distinct functionality, to fabricate novel, artificially layered materials systems that are tailored for a specific application or study. For example, one can fabricate superlattices to optimize a set of properties for a specific application or to have an ideal system to study interface charge transfer. In addition, functional oxides can be integrated directly onto various semiconductors for studying the chemical physics of highly dissimilar interfaces, as well as to fabricate functional transistors that respond to control parameters other than electric fields, such as pressure, temperature, and magnetic fields. This section gives a flavor of the various developments and prospects for possible applications of artificially structured epitaxial complex oxide heterostructures and superlattices. We focus on two examples, strain engineering and ferroelectric superlattices, and complex oxide growth on elemental semiconductors. Other exciting developments, such as oxide ferroelectric field-effect devices and the idea of realizing electronic nanofeatures using an atomic force microscopy controlled local ferroelectric field effect proposed in 1997 [181] and explored in superconductors, [182, 183] are not discussed here. A review of these developments can be found in [184].

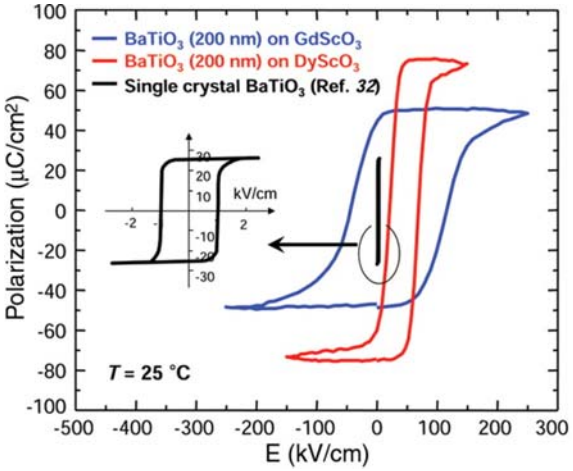

Fig. 24. Enhancement of the polarization values in $BaTiO_3$ achieved by epitaxial growth on scandate substrates [177]

4.1 Strain Engineering and Superlattices

4.1.1 Strain Engineering in Epitaxial Thin Films

The manipulation of material properties through strain engineering or the construction of artificially layered ferroelectric superlattices is an exciting and active area of research. The power of strain engineering for ferroelectric materials has been dramatically demonstrated by the achievement of enormous enhancements of the polarization and transition temperature in $BaTiO_3$ [177], as shown in Fig. 24, and the ability to force $SrTiO_3$ to be a room-temperature ferroelectric [176]. These experiments used the advanced deposition techniques described above, along with high-quality scandate substrates to grow epitaxial films under a high degree of epitaxial strain.

Strain engineering has a strong theoretical basis in Landau–Ginzburg theory [185], which showed the capacity to produce new phases and modified transition temperatures (as for example in $PbTiO_3$ (Fig. 25)) when films are epitaxially constrained by a substrate. More recently, first-principles calculations have reinforced these ideas and provide a powerful approach for the accurate prediction of strain–temperature phase diagrams of ferroelectric materials (a detailed discussion can be found in [186]). Though there are some differences in the specific predictions for certain materials according to the theoretical approach used, in general both theory and experiment point to strain engineering as a powerful means to deliver materials with exceptional properties, or to grow films in different phases from those in which they are normally found as bulk materials. In Fig. 26, the degree to which the transition temperature can be expected to be modified (based on Landau theory) in both $BaTiO_3$ and $SrTiO_3$ is demonstrated, along with the experimentally

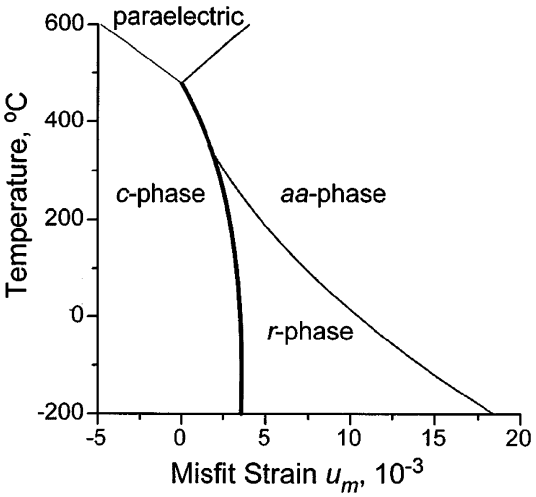

Fig. 25. Phase diagram of (001) single-domain $PbTiO_3$ thin films epitaxially grown on different cubic substrates providing various misfit strains in the heterostructures. The second- and first-order phase transitions are shown by *thin* and *thick* lines, respectively [185]. The aa-phase is orthorhombic, the r-phase monolinic, and the c-phase tetragonal

realized transition temperatures in these materials grown on scandate substrates [176, 177].

4.1.2 Strain in Superlattices

Superlattices have the potential to take strain engineering one step further. One limitation on the capacity for strain engineering to deliver useful devices is the limitation on the thickness that can be achieved while maintaining the coherent growth required to maintain the epitaxial strain condition imposed by the substrate. Superlattices can often be grown to greater thicknesses coherently than films of a single material, with the superlattice structure impeding the formation of misfit dislocations. For example, in the case of a $BaTiO_3/SrTiO_3$ superlattice on a $SrTiO_3$ substrate, by alternating $BaTiO_3$ and $SrTiO_3$ layers the epitaxial strain from the substrate can be kept throughout the sample to much greater thicknesses than in $BaTiO_3$ alone. Two points should be borne in mind: one is simply that the overall lattice misfit of the $BaTiO_3/SrTiO_3$ superlattice relative to the substrate is less than that of $BaTiO_3$ alone; second, the layered structure itself may inhibit the formation of misfit dislocations by reducing the thickness of the individual layers that are under strain. One also sees in the case of $PbTiO_3/SrTiO_3$ superlattices (shown in Fig. 27) that very thin, high-quality layers of $SrTiO_3$ can be grown within the $PbTiO_3$ layers at much lower temperatures (here at 460 °C) than would be required for the growth of thick $SrTiO_3$ films [187]. It turns out that

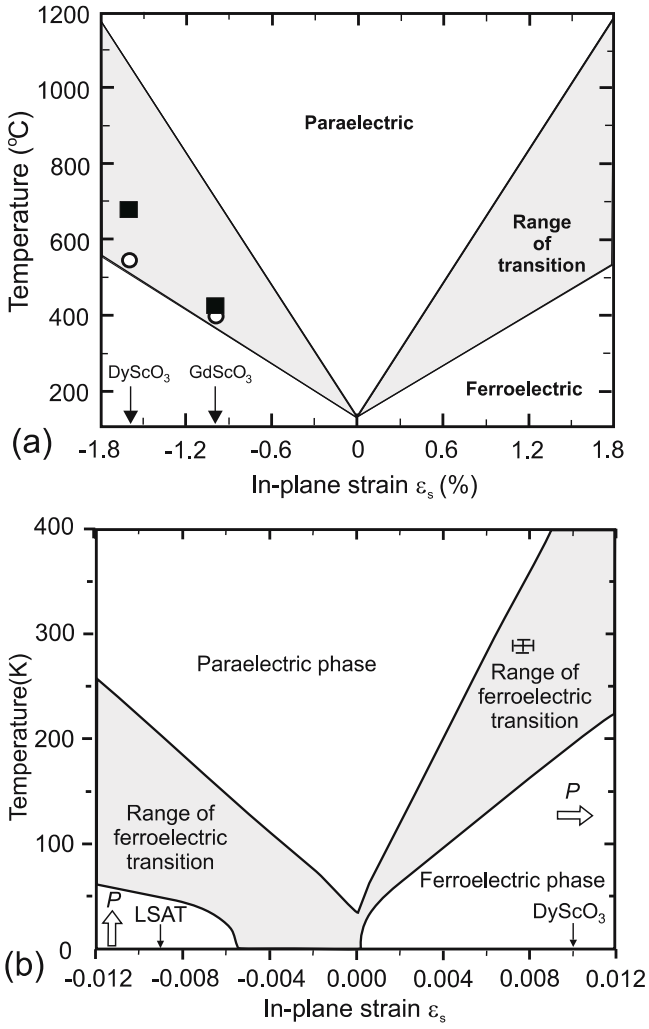

Fig. 26. Expected T_c of (**a**) (001) $BaTiO_3$ (from [177]) and (**b**) (001) $SrTiO_3$ (from [176]) based on a thermodynamic analysis. The range of transitions represents the uncertainty in the predicted T_c resulting from the spread in reported property coefficients. Note that the vertical scales are in K (*bottom*) and °C (*top*), and strains are in % for the top figure as in the original work

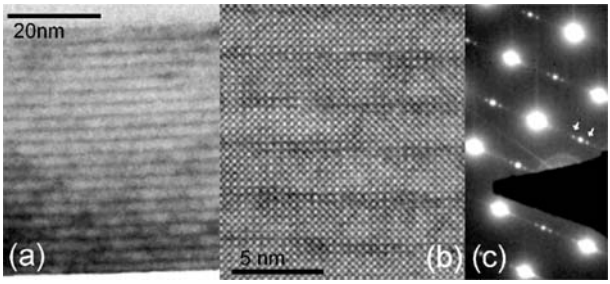

Fig. 27. Cross-sectional TEM images of a 20-bilayer $(PbTiO_3)_3/(SrTiO_3)_3$ sample. (**a**) Bright-field image shows the intended layering of the structure. (**b**) High-resolution TEM shows the perfect crystalline structure of the material. (**c**) Diffraction image demonstrating superlattice periodicity [187]

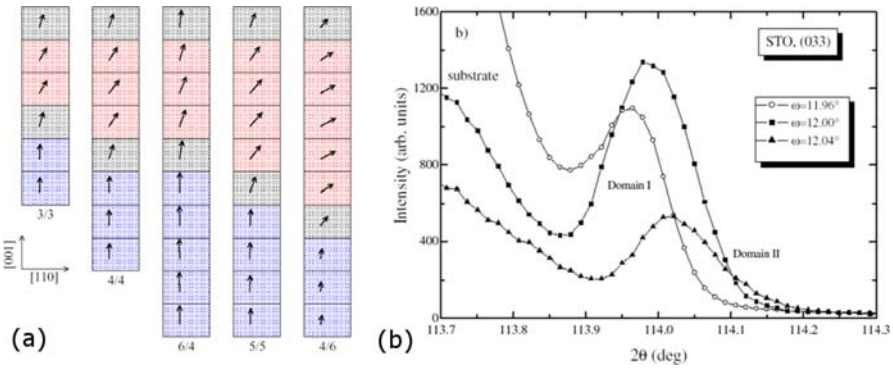

Fig. 28. (**a**) First-principles calculations of a number of $BaTiO_3/SrTiO_3$ superlattices, showing the tilting of the polarization in the $SrTiO_3$ layers. $BaTiO_3$ is *colored blue*, $SrTiO_3$ is *red*, and interfacial layers are *gray* [190] (**b**) X-ray diffraction ω scans around the (033) reflection for the STO layer in a relaxed $(BaTiO_3)_{10}/(SrTiO_3)_{10}$ superlattice. The splitting of the peak is an indication of orthogonal symmetry, indicating an in-plane distortion in the $SrTiO_3$ layers [189]

the requirements for growth of thin layers of material within a superlattice are somewhat relaxed, which is attractive from a practical point of view.

Superlattices can also be grown with layers sufficiently thick that the substrate constraint is either partially or fully relaxed, allowing more complicated strain interactions between the component layers. An example of the striking behavior that can occur in relaxed superlattices is that in $BaTiO_3/SrTiO_3$ superlattices, where it has been shown both experimentally [188,189] and theoretically [190] that the $SrTiO_3$ layers (and not the $BaTiO_3$ layers) acquire an in-plane polarization.

4.1.3 Electrostatic Coupling Between Layers

From the ability to impose strains from the substrate to the ability to utilize strain interactions between layers, there is a large scope for using strain interactions to tune the properties of ferroelectric materials. However, strain is not the only interaction of importance. Electrostatics emerges as perhaps a dominant determining factor of superlattice properties. As demonstrated theoretically in $BaTiO_3/SrTiO_3$ [191], and from both experiment and theory in $PbTiO_3/SrTiO_3$ [187], the polarization of superlattices of these materials as a function of the ratio of the thicknesses of the constituent layers is largely determined by the requirement that the system maintain a constant electrical displacement throughout the system (in the absence of free charge). In readily polarizable materials, this translates to the polarization being close to constant from one layer to the next due to the large electrostatic energy penalty that arises for a discontinuity of the polarization at the interface between two materials. Nevertheless, the unusual recovery of the polarization observed recently for low ratios of $PbTiO_3/SrTiO_3$ [187] points to the fact that electrostatics may not give the whole picture. In addition, $SrTiO_3$ is a highly polarizable material, and it may be that if a less-polarizable material is used, then the electrostatic energy penalty for polarizations may not be as dominant in determining the overall properties of the superlattice. Recently, *Nakhmanson* et al. [192] have proposed a model derived from first-principles simulations of the $BaTiO_3/SrTiO_3/CaTiO_3$ system, in which, in addition to electrostatic terms, they propose an additional interaction term that takes into account the thickness of the constituent layers.

There have been a number of papers that look at superlattices within the framework of Landau theory, and a variety of terms have been proposed to account for the coupling between layers [193–195]. The coupling of domains between layers has recently been looked at by *Stephanovich* et al. [196], and recently a series of papers that used Landau theory with primarily electrostatic coupling have pointed to large enhancements of dielectric properties (both in size and tunability of the dielectric constant) [197, 198].

4.1.4 Selected Examples of Material Combinations

$BaTiO_3/SrTiO_3$ Superlattices

Perhaps the most-studied superlattice system, both experimentally and theoretically, is the $BaTiO_3/SrTiO_3$ superlattice. Much of this work was motivated by the findings of *Tabata* et al. [199], which suggested extremely high dielectric constants could be produced in these materials. It has been demonstrated by *O'Neill* et al. [200] that this high dielectric constant was due to Maxwell–Wagner relaxation. However, superlattices remain an attractive candidate for engineering high dielectric constant materials, and theoretical and experimental work in this direction is proceeding.

$KNbO_3/KTaO_3$ Superlattices

Another combination that has been studied in detail is the $KNbO_3/KTaO_3$ system [157, 201]. One of the interesting aspects of the theoretical modeling (shell-model molecular dynamics) [202, 203] on this system is that in contrast to the results obtained from first-principles calculations on $BaTiO_3/SrTiO_3$ or $PbTiO_3/SrTiO_3$, there is considerable variation of the polarization within the layers of the superlattice. Also, it has been shown experimentally in this system that antiferroelectricity can be induced by the superlattice ordering of a ferroelectric and a paraelectric material [201].

$PbTiO_3/SrTiO_3$ Superlattices

After some initial work by *Jiang* et al. [204], who used MBE to produce high-quality $PbTiO_3/SrTiO_3$ superlattices, this particular combination did not receive much attention until recently. In contrast to $BaTiO_3/SrTiO_3$, the lattice mismatch between these two materials is extremely small. While this means that strain interactions between the constituent layers are potentially less interesting, it also means that this superlattice is more straightforward to grow, and excellent-quality superlattice samples can be grown to large thicknesses using off-axis RF sputtering [187]. This system can be viewed as a model for studying electrostatic and other interactions while removing the lattice-mismatch effect that might otherwise control the behavior. Despite the lack of complicated strain interactions, this system does exhibit some rather surprising behavior, with an unexpected recovery of the ferroelectric polarization in samples with very thin $PbTiO_3$ layers [187].

$PbTiO_3/PbZrO_3$ Superlattices

In contrast to the examples discussed so far, this system combines a ferroelectric and an antiferroelectric material, as opposed to a ferroelectric and a paraelectric. Furthermore, it resembles one of the most commercially important ferroelectric solid solutions, lead zirconate titanate (PZT). One of the key applications for PZT is in piezoelectric devices, due to its high piezoelectric coefficient when its composition lies close to the morphotropic phase boundary at a Zr:Ti ratio of 52:48. Theoretical results suggest that artificially induced compositional ordering could increase the already high values achieved in this compound as a solid solution [205]. Another detailed first-principles study of the $PbTiO_3/PbZrO_3$ 1/1 superlattice has been carried out by *Bungaro* and *Rabe* [206]. Although a few experimental examples of this system [207, 208] do exist, it does not appear that the possibilities of this system have yet been explored thoroughly experimentally.

Tricolor Superlattices

Tricolor superlattices, where the superlattice period contains 3 materials rather than 2, are of special interest, as the first principles study of *Sai*

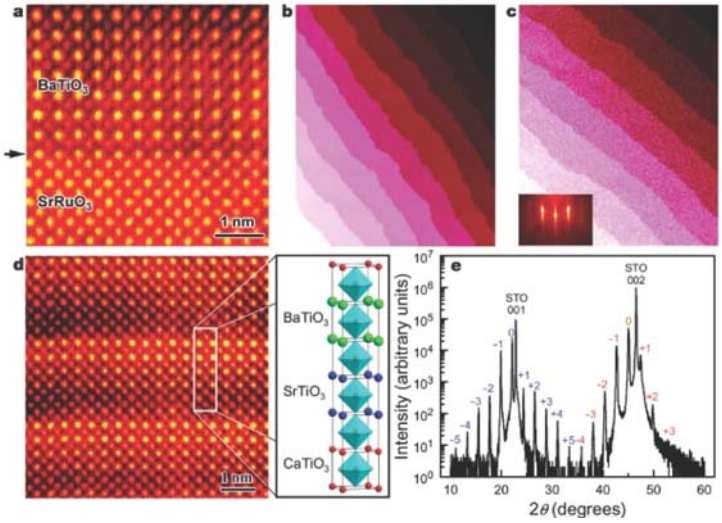

Fig. 29. (**a**) Cross-sectional Z-contrast image of the interfaces between $BaTiO_3$ and $SrRuO_3$ films, indicated by the *black arrow*. (**b**,**c**) AFM topographic images (image size: $4 \times 5\,\mu m^2$) with single terrace steps (approx 0.4 nm) (**b**) of $SrRuO_3$ and (**c**) of a 200 nm-thick $(SrTiO_3)_2(BaTiO_3)_2(CaTiO_3)_2$ superlattice. *Inset* in (**c**) shows a RHEED pattern confirming the smooth surface. (**d**) Cross-sectional Z-contrast image of compositionally abrupt interfaces in $(SrTiO_3)_2(BaTiO_3)_2(CaTiO_3)_2$; the diagram shows its atomic structure. (The *light blue octahedra* and the *red*, *green* and *blue spheres* represent TiO_6, and Ca, Ba and Sr, respectively.) (**e**) XRD θ–2θ scan of a $(SrTiO_3)_2(BaTiO_3)_6(CaTiO_3)_2$ superlattice, confirming the long-range periodicity and high crystallinity. The STO (001) and (002) peaks are from the $SrTiO_3$ substrate, and the first and second sets of superlattice peaks are marked with *blue* and *red numbers*, respectively [211]

et al. [209] showed the possibility of producing ferroelectric systems with broken inversion symmetry based on these systems. Pioneering work has been realized by *Waruswithana* et al. [210] and *Lee* et al. [211] who grew tricolor ferroelectric superlattices of $BaTiO_3/SrTiO_3/CaTiO_3$ (see Fig. 29). It remains challenging, however, to experimentally demonstrate breaking of inversion symmetry, since most ferroelectric samples display asymmetry in their electrical properties due to extrinsic considerations, such as the nature of the electrode/ferroelectric interfaces or gradients in defect densities in the samples that arise during the growth process.

Multiferroic Superlattices

Multiferroic materials are currently of significant interest. One of the key possibilities is to use ferroelectric/magnetic bilayers or superlattice structures to look for coupling between ferroelectric and magnetic ordering. In the case of $BaTiO_3$ and $CoFe_2O_4$, the superlattice geometry was found to

provide less-effective coupling than a columnar nanostructure [212]. There are also interesting possibilities in using materials that are already multiferroic by themselves, for example $BiFeO_3$ [213], in multilayer structures [214]. Another approach in this direction is to use the ferroelectric field effect to charge dope materials, as has already been done to modify superconducting properties [183, 184].

Ferroelectric/Ferroelectric Superlattices

Work combining two ferroelectric materials together in a superlattice structure, for example $PbTiO_3$ and $BaTiO_3$ [215], is less common than studies that combine a ferroelectric and a nonferroelectric. Using this approach, one can consider more subtle aspects than simply engineering giant figures of merit by combining two materials with similar polarizations but different switching properties. This possibility may give insights into switching processes and domain dynamics.

Interfacial Charge States

In another oxide superlattice, non-ferroelectric $LaAlO_3/SrTiO_3$, discontinuity of the charge states of the layers at a LaO/TiO_2 interface leads to a conductive interface between two band insulators (see Fig. 30) [216, 217]. If it is possible to generate similar conducting interfaces between a ferroelectric insulator and another insulator, one can conceive of tuning the extent of the ferroelectric coupling between layers, adding another degree of control in material design. Reference [216] demonstrates the physics of this approach and also highlights the use of RHEED monitoring of PLD growth in order to obtain interfaces of the desired nature. The ability to control accurately the termination of the interfaces gives yet another parameter that could conceivably be modified to manufacture a tailored material.

4.1.5 X-Ray Characterization of Superlattices

Due to their additional periodicity, superlattices can produce impressive X-ray diffraction patterns, and these contain a large amount of information about the structure of the material. One can assess the quality of the sample and also use it as a tool for probing the underlying physics.

In the development of oxide materials, useful parallels can be found with earlier work on semiconductors (see, for example, the comparison of MBE-grown $BaTiO_3/SrTiO_3$ and GaAs/AlAs superlattices in [218]). For example, in analyzing X-ray diffraction patterns, it is useful to refer to the techniques used to analyze $GaAs/Al_xGa_{1-x}As$ superlattices. Here, the nth peak of a superlattice diffraction pattern in the (001) direction from a sample with a superlattice wavelength of n unit cells gives the average c-axis lattice parameter. In the case of $GaAs/Al_xGa_{1-x}As$, this information can be used to

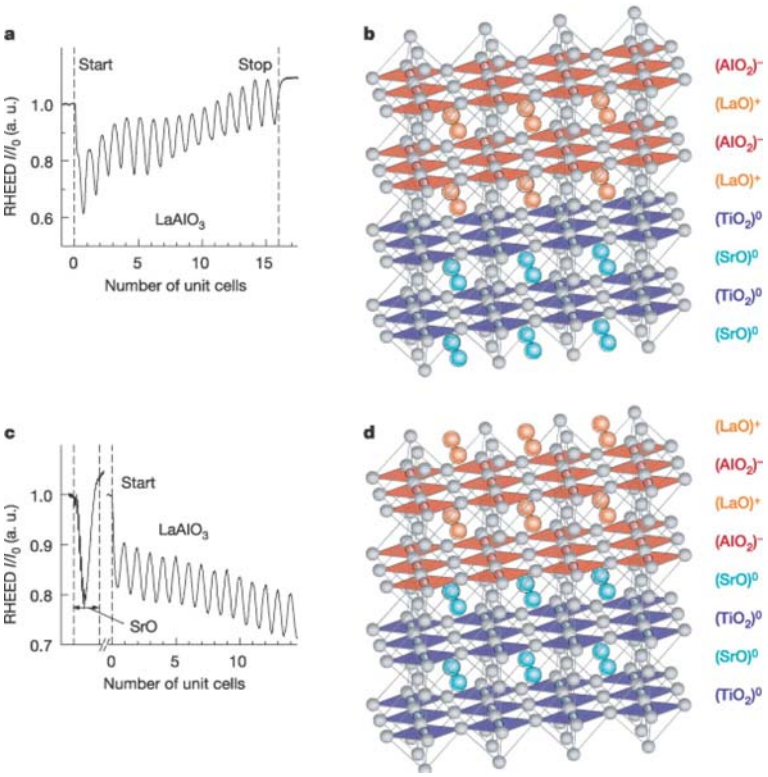

Fig. 30. (**a**) RHEED intensity oscillations of the specular reflected beam for the growth of $LaAlO_3$ directly on the TiO_2-terminated $SrTiO_3$ (001) surface. (**b**) Schematic of the resulting $(LaO)^+/(TiO_2)^0$ interface, showing the composition of each layer and the ionic charge state of each layer. (**c**) RHEED oscillations for the growth of $LaAlO_3$, after a monolayer of SrO was deposited on the TiO_2 surface. (**d**) Schematic of the resulting $(AlO_2)^-/(SrO)^0$ interface [216]

determine the composition of the superlattice. The lattice-parameter difference between GaAs and AlAs is only 0.008 Å (0.15%), and yet, a reliable extraction of the composition can be achieved. In ferroelectric oxides, where one wishes to use a similar measurement to quantify the lattice distortions related to the ferroelectric polarization, one is aided greatly by the strong strain–polarization coupling typical of ferroelectric perovskites. For example, in the case of $PbTiO_3$, the difference in the *c*-axis lattice parameter between the ferroelectric (4.152 Å) and paraelectric (4.022 Å) lattice parameter is 0.13 Å (3.2%). One can thus use X-ray diffraction as a powerful tool to study the ferroelectric properties of a superlattice (Figs. 31 and 32) [187]. When combined with other measurements, the relationship between electrical and structural properties can be explored in depth.

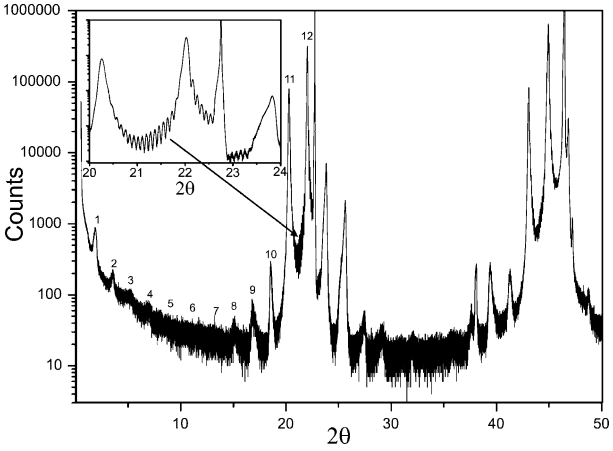

Fig. 31. θ–2θ X-ray diffractogram for a 20-bilayer $(PbTiO_3)_9/(SrTiO_3)_3$ superlattice [187]

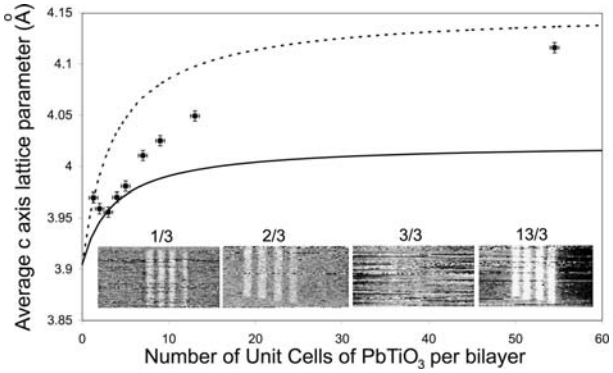

Fig. 32. Average c-axis lattice parameter plotted against the number of unit cells of lead titanate per bilayer showing the suppression and recovery of ferroelectricity. Complementary piezoelectric microscopy images are shown as *insets* [187]

4.2 Crystalline Oxides on Semiconductors (COS)

Incorporating a ferroelectric as a functional element into a device was accomplished early in the history of the transistor. In a series of patents, *Looney* et al. [96] were the first to describe the invention of a ferroelectric transistor where the state of the conducting channel was determined by the sign of the out-of-plane polarization. However, a nonferroelectric layer of glue that screened the field effect of the ferroelectric oxide prevented practical implementation of this device. The development of crystalline oxides on semiconductors eliminated the glue at the ferroelectric oxide/semiconductor

interface and replaced it with an atomically sharp, heteroepitaxial transistion [219].

A parallel and currently more urgent technology driver is an atomically sharp transition from oxide to semiconductor in metal-oxide-semiconductor field-effect transistor (MOSFET) devices, which is required to continue the advance in transistor speed as described by Moore's law, an historical observation of the exponential increase in transistor speed and integration [220]. This requirement of scaling is described by the International Technology Roadmap for Semiconductors (ITRS) [221]. In the 2005 version of the ITRS, the scaling of the MOSFET is followed to the year 2016, at which time the channel length should be 9 nm. All dimensions of the transistor scale more or less proportionally so that for 9 nm channel lengths, the thickness of the gate oxide, silicon dioxide, at this point must be less than 5 Å. This dimension is on the order of an atomic layer and is the length scale of the desired heteroepitaxial transition.

It is also at this scale that the concept of an interface phase is useful for designing and understanding heteroepitaxial interfaces. A type of interface phase was originally proposed in 1929 to explain the rectifying behavior of point metal contacts with semiconductors. Here, the phase was envisioned as a chemical inhomogeneity of high resistivity. Seminal work by *Schottky* [222] in 1938 describes a layer of space charge that is expected to be at the interface of a semiconductor–metal contact and results in the observed rectifying behavior, without invoking a chemical inhomogeneity. *Walker* et al. have revisited the role of an interface phase and found that it is inherent for any semiconductor–metal or semiconductor–oxide junction, and thus adding a missing piece of Schottky's formalism [223].

The concept of the interface phase was outlined by *Cahn* and *Hilliard* in 1958 [224] for inhomogeneous systems: the order parameter of the interface rearranges itself to minimize its depth gradient. In Cahn and Hilliard's example, the order parameter was density or composition and was used to describe wetting. For thin films, the following are examples of this interface phase: sub-oxides at the amorphous silicon dioxide/silicon interface, the electronic changes observed at polar oxide heterojunctions [225], and submonolayer silicide formation for crystalline oxides on silicon. For amorphous silicon dioxide on silicon, the dominant energetic consideration is steric hindrance at the interface, and as a consequence, the interface is composed of a graded layer of suboxides of SiO_2 [226]. Similar bonding considerations for a crystalline interface between the oxide and silicon are paramount, and one finds that a submonolayer of silicide is required to promote epitaxy of oxides on semiconductors [227].

The principles of growth of crystalline oxides on silicon are described below. Many of the details are structural and are derived from RHEED observations under different growth conditions. This approach was first outlined in 1991 by *McKee* et al. for the growth of $BaTiO_3$ on silicon [227]. The key to the growth of crystalline oxides on semiconductors (COS) is the deposition

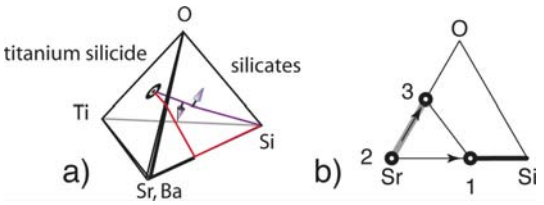

Fig. 33. Phase-diagram representation of heteroepitaxy. A successful route of many possible layer sequences is outlined *in red* in panel (**a**). This route avoids silicates and titanium silicides that do not form surface structures compatible with both silicon and the alkaline-earth oxide (schematically indicated in panel (**a**) by *arrows*). The specific route to the alkaline-earth oxide is shown in panel (**b**) as three steps that establishes the tie line between a monolayer silicide and alkaline-earth oxide (*solid line*). The deposition of extra alkaline-earth metal (3/8 ML) ensures that, during the oxidation step (schematically indicated by the two *arrows* in panel (**b**)), the surface composition remains in the lower left-hand corner of the three-component phase diagram, avoiding the formation of silicates

of a silicide prior to oxide growth. In this way the reaction between BaO and silicon is controlled and confined to a thickness of less than 1 monolayer (ML).

4.2.1 Layer-Sequenced COS Growth

The beginning of crystalline oxide growth involved clean silicon or germanium, and the endpoint is a perovskite oxide. These endpoints are plotted on a set of three component phase diagrams in order to consider possible approaches to making the heteroepitaxial transition (Fig. 33). The direct route from silicon to $SrTiO_3$ has been shown not to work thermodynamically because titanium reacts with silicon and oxygen to form an amorphous silicate and polycrystalline silicide. While thermodynamic considerations alone do not mean that this route will be unsuccessful, the property that disqualifies this approach is the lack of a commensurate and crystalline structure for the silicate or silicide, even at submonolayer coverages. This fact is observed by RHEED when $SrTiO_3$ is directly deposited on silicon by a disappearance of diffraction from an ordered surface after less than 1 ML coverage. As can be seen in the set of three component phase diagrams, there is more than one way to get from silicon to $SrTiO_3$. In the following discussion, we describe a successful path.

One starts with clean silicon that is prepared using standard wet chemical cleaning followed by a UV-ozone produced oxide. This oxide is easily sublimed at 850 °C in UHV to produce a clean 2×1 Si(001) surface. It is important in the cleaning process that SiC is not observed in the RHEED. Subsequent growth is disrupted if even small amounts are present.

One begins with deposition of Sr metal and proceeds along the Si−Sr phase line in Fig. 33 to produce an intermediate silicide. The growth conditions required in order to synthesize a crystalline ordered layer that does not

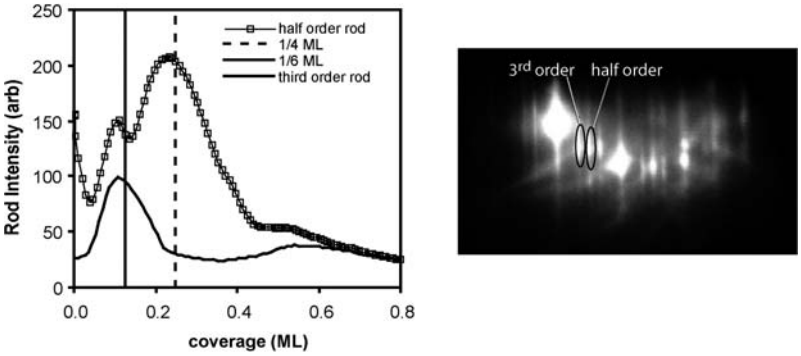

Fig. 34. RHEED control of silicide deposition. The diffracted intensity at the 3rd-order and half-order rod locations along the ⟨110⟩ Si(001) surface indicates where surface phases are complete

react uncontrollably is to deposit 1/4 ML at temperatures between 550 °C and 700 °C onto a clean 2 × 1 Si(001) surface. This step can be controlled by RHEED by stopping the Sr deposition when the 1/4 ML 2 × 1 phase is completed (see Fig. 34). One stops the Sr deposition when diffraction from the 3 × 2 phase is observed to disappear [228]. For this process to work, we assume that the fractional coverage of the 1/6 ML phase is proportional to the intensity of the 3rd-order rod, while the coverage of the 1/4 ML structure is proportional to the intensity of the half-order rod [74]. This progression is shown in Fig. 34 and shows the 3rd-order rod peaking at 1/6 ML and the half-order rod peaking at 1/4 ML. This diffraction is consistent with chains of alkaline-earth metal atoms ordering along ⟨110⟩ directions with triple the ⟨110⟩ Si lattice spacing, which is then fully replaced at 1/4 ML by alkaline-earth metal atoms at double the ⟨110⟩ lattice spacing. At 1/4 ML, the first step in the growth of COS is complete, and one arrives at Step 1 in Fig. 33b. The importance of this step has been tested by attempts to grow lattice-matched oxides on clean silicon, as well as on 1/6 ML Sr covered Si(001) (see Fig. 36). At least 1/4 ML is required to promote epitaxy.

The next step involves forming an ordered metal surface that can be subsequently oxidized. This step allows a clean transition from the silicide to the oxide, where one finds that an ordered 3 × 1 metal surface forms at 3/8 additional alkaline-earth metal coverage, which is flat and commensurate with the silicon. Because the surface mobility of the metal is high, one performs this deposition at substrate temperatures between 100 and 200 °C. The RHEED pattern indicates that it is highly ordered and flat. At this point one is at Step 2 in Fig. 33b.

To get to Step 3 in Fig. 33b, one oxidizes the 3/8 ML alkaline-earth metal layer by leaking molecular oxygen into the chamber with the substrate at 100 °C. If the arrival rate of oxygen is kept below 1 Langmuir/s, this oxidation can be controlled by limiting the oxygen exposure at about 10 s. The RHEED

pattern that results is, like the 1/4 ML silicide, a 2×1 pattern, highly ordered and flat. The RHEED is consistent with an ordered alkaline-earth oxide layer on top of the silicide.

Some of the silicide remains after the oxidation step has been concluded, as determined using Z-contrast microscopy, as well as by looking at the phase of the RHEED oscillations during growth of the growing oxide on the silicide. In such an experiment, *Norga* et al. [229] found that 0.41 ML of the Sr deposited in the first step does not oxidize and remains at the interface. Z-contrast microscopy shows a Sr layer with double the periodicity of the silicon in the [110] direction, consistent with the 2×1 diffraction observed at 1/4 ML [219]. At the end of the oxide growth step, one achieves a transition from silicon to alkaline-earth oxide with a transition layer of silicide in between, where local equilibrium between adjacent layers maintains the stability of the heterostructures.

Continued deposition of alkaline-earth metal in the presence of oxygen results in highly ordered and flat $Ba_{0.7}Sr_{0.3}O$. At this point the difficult steps of heteroepitaxy have been completed and a transition to homoepitaxial growth is required. Because one wants atomically abrupt surfaces and interfaces, one needs to establish conditions (including oxygen pressure and substrate temperature) for flat growth, using surface and bulk diffusion to establish a growth window, as described in the molecular beam epitaxy section.

With the completion of the alkaline-earth oxide, one follows the layer sequencing indicated in bold in Fig. 33a. This route avoids the formation of silicates, as shown by the photoelectron spectra for silicon coming from a silicon-oxide interface that is buried. (Photoelectrons can be measured through oxide films up to 50 Å thick.) Figure 35 compares the Si-2*p* peak spectrum taken from the 1/4-ML silicide structure with that from a 6-ML thick (BaSr)O oxide on silicon. There is no evidence of silicon in a silicate or silicon dioxide. Silicon in silicates or SiO_2 would have peaks at 102.5 eV and 104 eV, respectively [230, 231]. The shoulder seen in the spectrum from the oxide interface has been attributed to an electron energy-loss process from the barium 4*d* peaks [232] (not shown in the graph).

For the growth of the perovskite, the transition from homoepitaxy to heteroepitaxy must be made in a different growth regime. The Ti−O bond in perovskites such as $SrTiO_3$ has a covalent part. Growth temperatures for flat, crystalline $SrTiO_3$ are greater than 550 °C [233, 234]. However, one observes that the diffraction from the surface of alkaline-earth oxide films thinner than 10 ML deteriorates above 400 °C. This is not attributable to a thermodynamically driven reaction with the oxide because, as shown in Fig. 36, the alkaline-earth oxide is still observed even after a 700 °C anneal, as was done for the structure shown in the micrograph. Moreover, films thicker than approximately 50 Å are stable at temperatures of greater than 700 °C.

The growth of crystalline perovskite thin films requires growth temperatures above 550 °C. Since one cannot use such high growth temperatures, one deposits the perovskite in a layer-by-layer fashion at low temperatures,

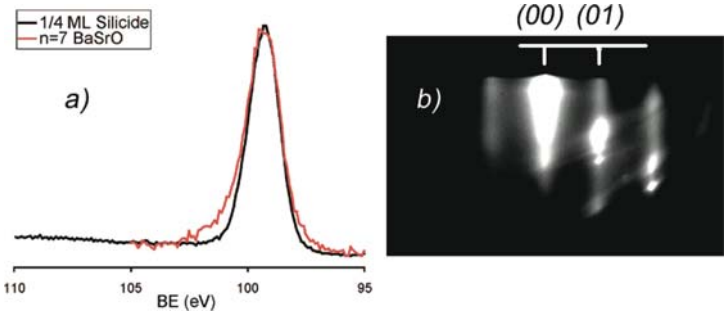

Fig. 35. XPS and RHEED of a 6-ML alkaline-earth oxide on silicon. After the heteroepitaxial transition is finished, the crystalline quality of the lattice-matched $Ba_{0.7}Sr_{0.3}O$ is seen in panel (**b**)). The silicates of Fig. 33 have been avoided as shown by X-ray photoelectron spectroscopy in panel (**a**). The core-level spectrum for silicates would show up as a peak at a binding energy of 104 eV

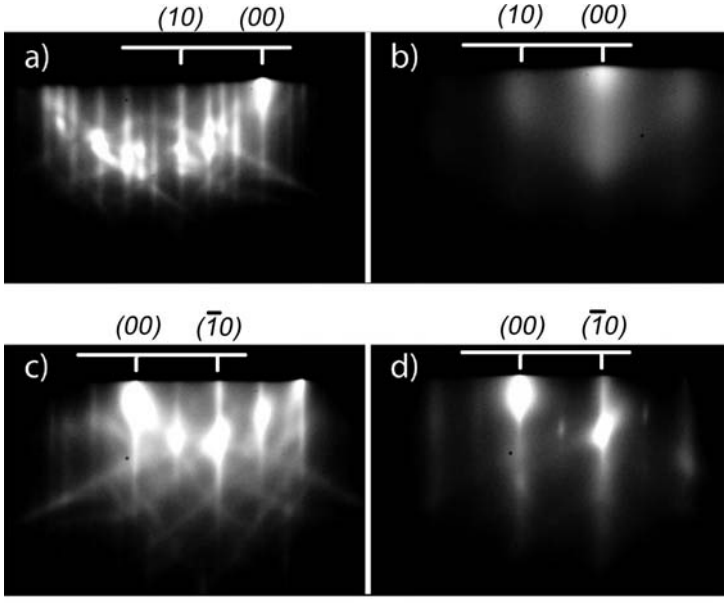

Fig. 36. Oxide growth from two different starting surface phases. (**a**,**b**) Epitaxy of the lattice-matched $Ba_{0.7}Sr_{0.3}O$ from the 3×2 Sr:Si(001) surface phase (panel (**a**)). The resulting diffraction pattern after 1 ML is shown in panel (**b**), showing poor epitaxy. (**c**,**d**) Epitaxy from the 2×1 Sr:Si(001) phase (panel (**c**)). The resulting diffraction pattern after 1 ML is shown in panel (**d**), showing that the 2×1 Sr:Si(001) phase facilitates the epitaxy of lattice-matched $Ba_{0.7}Sr_{0.3}O$ on silicon. Note that for all RHEED images shown in this chapter, the out-of-plane scattering vector for the diffraction is vertical and increasing going down the page. The scale in the panels locates the Si(001) surface mesh rods

$T_g = 200\,°C$, and subsequently anneals in vacuum to recrystallize the amorphous film to obtain an epitaxial, single-crystal film of perovskite grown on an AO template.

The deposition of the elemental metals is done in 10^{-6} Torr oxygen to form the oxide. The total thickness of the deposition can be anywhere from 3 to 10 unit cells thick. The result is an amorphous RHEED pattern. Recrystallization of the amorphous film takes place at 550 °C after about 60 s [235]. The resulting $SrTiO_3$ shows a sharp diffraction pattern that, for films less than 50 Å thick, is commensurate with the silicon with a +1.5% strain [68, 219]. This is determined by comparing the in-plane lattice parameter of the diffraction with that for clean silicon. Large critical thicknesses on the order of 80 Å thick have been observed for $BaTiO_3$ growth on $SrTiO_3$, a +2.3% misfit [236].

The completion of $SrTiO_3$ defines what is meant by COS. The general formula one introduces for COS is $(AO)_n(A'BO_3)_m$, where $(AO)_n$ is n monolayers of alkaline-earth oxide and 2 monolayers make up one unit cell of the rocksalt structure. $(A'BO_3)_m$ is m unit cells of the perovskite structure, where A′ is Sr, Ba, or Ca, and B is titanium. As discussed earlier, a number of transition metals, Zr as an example, can also replace titanium for increased flexibility in materials choice. An example of $n = 3$ and $m = 3$ is shown in Fig. 36.

Variations in the COS approach have been described by *A. Herrera-Gomez* et al. [237] and *Mari* and *Ishiwara* [238]. These processes result in an oxide on silicon by chemically reducing an approximately 20-Å thick silicon dioxide film with Sr metal to SiO at temperatures high enough to drive off SiO. These temperatures are lower than those required to drive off SiO_2 and so may be more amenable to production. If excess Sr is supplied to the initial SiO_2 film, then heating in vacuum will desorb the silicon dioxide and some of the excess Sr [237, 238]. This process will leave a coverage of Sr on the surface that depends critically on the thermal history of the substrate [229, 237]. The resulting mixture of surface structures is dictated by the thermodynamics of the individual surface phases. After this deoxidation process is complete [237], the oxide growth continues within the framework described here at some point between 1 and 2 on the diagram of Fig. 33b.

4.2.2 How the Silicide Facilitates Epitaxy

In this section we explore ways to understand how the transition between covalent bonding of the semiconductor and the ionic bonding of the oxide is buffered by the silicide, including how the bonds change symmetry across the interface from tetrahedral in the silicon to spherical in the oxide. Experimentally, the key to this transition was found to be the preparation of ordered surface phases prior to oxide growth. To understand why the 1/4 ML surface phase facilitates epitaxy one examines first the physical structure of the Sr−Si surface phases at 1/4 and 1/6 ML. Next, systematic changes that

can be made to interface structure via experiment and density-functional theory (DFT) are studied to learn about the role of the Sr that remains at the interface.

One piece of evidence for the structure of the surface phase is the temperature at which an ordered surface phase forms, which occurs above a substrate temperature of 550 °C [223]. On the other hand, RHEED from the 2×1 surface phase at 1/4 ML coverage remains unchanged down to room temperature, implying that the formation of the 2×1 surface phase is kinetically suppressed at room temperature.

This kinetic limitation is consistent with the $SrSi_2$ stoichiometry observed in Z-contrast microscopy [219]. The development of this stoichiometry requires diffusion of silicon from terraces to steps, which takes place at temperatures above 550 °C (see Fig. 12). Surface diffusion of silicon is also required to explain STM images of the 3×2 surface phase formed at high temperatures [239]. Here, the Sr atoms appear to be sitting below the surrounding terrace of dimerized silicon atoms. These features require the removal of at least some of the silicon dimers.

One then starts with the interface structure derived from the Z-contrast images and explores the role of each component of the interface in buffering the transition in bonding. The structure of the interface considered here is based on a c 4×2 surface mesh with two alkaline-earth metal atoms (from Be to Ba) per unit cell located at hollow sites of the undimerized silicon surface (see Fig. 37). The four silicon atoms in the silicide are also located on hollow sites, displaced half of a surface mesh spacing away from the bridge site of bulk, tetrahedral-coordinated silicon. Various components of the interface phase can be identified: the bulk silicon substrate, the Sr in the silicide, the silicon in the silicide, and the bulk-terminated alkaline-earth oxide film.

The following discussion relies on the structure as deduced by Z-contrast microscopy (Fig. 38). Additional experimental methods are desirable to locate all of the atoms in the structure (oxygen and silicon) such as X-ray crystal truncation rod measurements. Other structures have been proposed that rely on total-energy calculations to determine the structure with the lowest energy [240, 241]. DFT calculations conclude that there are lower-energy structures than the one treated here, the main difference being that the other structures do not involve a silicide between the oxide and silicon. The lowest-energy surface structures are simple adsorbed alkaline-earth metal structures that order in every other ⟨110⟩ row of the silicon surface. A series of phases such as those observed in RHEED is realized for these models by increasing the density of metal atoms in the ⟨110⟩ chains.

To explore the role of each component layer, one systematically changes the interface both experimentally and theoretically and observes how the properties respond. To do this experimentally, one changes the alkaline-earth metal at the interface from Be to Ba, while keeping the composition of the oxide fixed and measuring the band offset between oxide and silicon. The band offset between the silicon and alkaline-earth oxide is sensitive to the

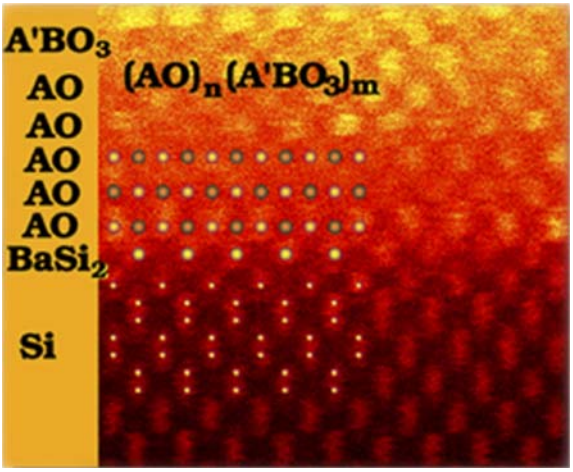

Fig. 37. Z-contrast microscopy of an $n = 3$, $m = 3$ COS heterostructure. The key to a heteroepitaxial transition to $SrTiO_3$ is a lattice-matched alkaline-earth oxide. The image is taken down the $\langle 110 \rangle$ direction of the Si(001) substrate and the $\langle 100 \rangle$ direction of the alkaline-earth oxide and perovskite. 3 ML of alkaline-earth oxide forms the substrate for subsequent perovskite epitaxy

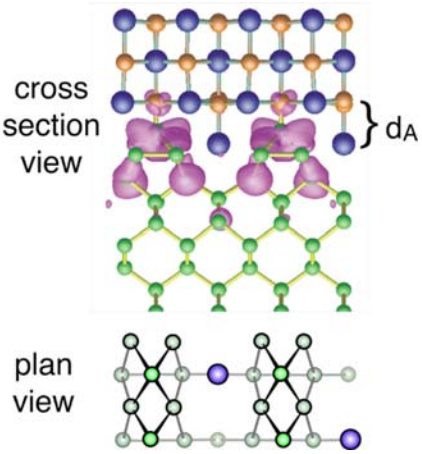

Fig. 38. COS interface structure. The interface structure shown here was determined experimentally using Z-contrast microscopy (cross section and plan view). The *green spheres* are silicon atoms, the *blue spheres* are alkaline-earth metal atoms, and the *yellow spheres* are oxygen atoms. The oxide layers of the cross-sectional view are removed in the plan view to clearly show the positions of the atoms in a single $c4 \times 2$ surface mesh of the interface phase [223]

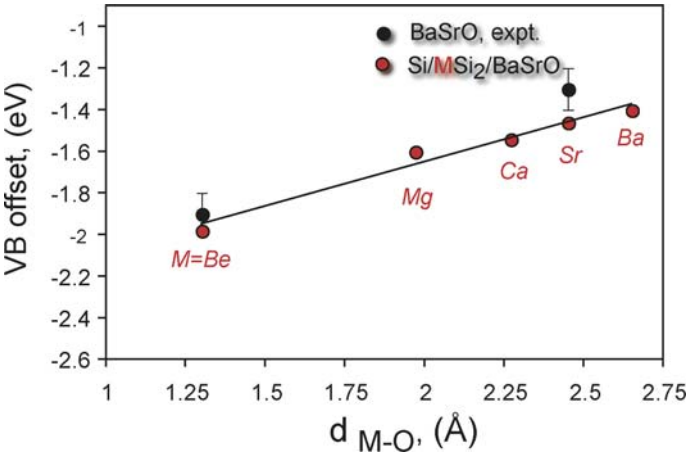

Fig. 39. Variation of alkaline-earth oxide–silicon band offset. As the alkaline-metal atoms are moved, either by DFT calculation (*solid line*) or experimentally by changing the ionic size of the alkaline-earth metal ion (*points*), the band offset varies linearly with distance. This variation shows that the plane of alkaline-earth metal atoms are positively charged with 2+ valence. Figure taken from [223]

magnitude of the polarization at the interface, which is modulated by changing the composition of the interface phase. The dipole contribution to the band offset is determined by how charge rearranges itself at the interface phase and is given by:

$$\Delta V = \frac{\mathrm{e}^2}{4\pi} \int (\bar{n}(z) - n_0) z \, \mathrm{d}z \,, \tag{4}$$

where n_0 is the average electronic density of the oxide and the silicon substrate, and $\bar{n}(z)$ is the macroscopic average of the electronic density across the interface where both electron densities are planar averages. If the alkaline-earth metal in the silicide becomes ionic by donating its two electrons to the interface (it is less electronegative than silicon), then changing the position of this plane of atoms normal to the interface (the distance d_{A} in Fig. 38) should change the magnitude of one of the interface dipoles. Indeed, DFT calculations of charge density of the occupied states for this interface structure show that the negative charge is located around the silicon atom in the silicide and leaks a few atomic planes into the silicon substrate (purple plot of electron density in Fig. 38). The alkaline-earth metal now plays the role of a test charge on the interface, allowing one to determine the character of the interface bonding.

Calculations show that the distance between oxide and alkaline-earth metal in the silicide influences the band offset in a way that is consistent with simply moving the positive, ionic component of the interface dipole (Fig. 39). In addition to the theoretical observation of charge localized on the silicon

atoms of the silicide, one also finds from DFT calculations that the Si−O bond length remains constant as the interface dipole changes strength. This implies that the strong covalent silicon–oxygen bond involving the silicon in the silicide and the first alkaline-earth oxide plane controls the epitaxial interface. Furthermore, the electrons involved in this bonding are donated by the alkaline-earth metal in the silicide and thus keep the interface charge neutral. These structural and chemical properties of the interface phase facilitate the epitaxy of crystalline oxides on silicon.

Much of the recent work in the growth of crystalline oxides on semiconductors is aimed at replacing SiO_2 in metal oxide semiconductor transistors [242], where variations on $SrTiO_3$ are possible in order to manipulate the electronic structure [243] or ferroelectric functionality [68, 236]. This layer-sequencing approach has also motivated fresh attempts at crystalline oxide growth on semiconductors other than silicon, such as Ge [104] and GaAs [244, 245]. Similar efforts for growing epitaxial oxides on wide-bandgap semiconductors are also being pursued [246, 247]. Further applications can be imagined if the $SrTiO_3$ on silicon is used as a substrate itself for the deposition of other functional components of a device such as ferroelectrics [248] and other semiconductors [115, 249].

4.3 Conclusions

The continuing advances in epitaxial growth techniques and surface characterization, combined with the availability of high-quality single-crystalline substrates, has spurred these new applications of complex oxide thin-films, which allows one to examine new phenomena as well as to develop new kinds of devices. The combination of advances in thin-film fabrication technology and new materials opens up broad avenues for both new device applications and a deeper understanding of the materials themselves.

Acknowledgements

Matthew Dawber and Jean-Marc Triscone acknowledge support by the Swiss National Science Foundation through the National Center of Competence in Research “Materials with Novel Electronic Properties – MaNEP” and Division II, and ESF (Thiox). Charles Ahn acknowledges primary support from the National Science Foundation under Contract No. MRSEC DMR 0520495 and DMR 0705799 and ONR, along with support from the Packard and Sloan Foundations. Mikk Lippmaa acknowledges useful discussions and technical support by T. Ohnishi. Fred J. Walker acknowledges discussions and support by R. A. McKee and sponsorship from the Division of Materials Sciences and Engineering, Office of Basic Energy Sciences, U.S. Department of Energy at Oak Ridge National Laboratory under contract DE-AC05-00OR22725 with UT-Batelle, LLC and at the University of Tennessee under contract DE-FG02-01ER45937.

References

[1] T. E. Jones, W. C. McGinnis, J. S. Briggs: Compact substrate heater for use in an oxidizing environment, Rev. Sci. Instrum. **65**, 977 (1994) 223

[2] A. Schmehl, R. R. Schulz, J. Mannhart: Eucentric four-axis ultrahigh vacuum goniometer for reflection high-energy electron diffraction applications, Rev. Sci. Instrum. **76**, 123901 (2005) 223

[3] D. B. Lee, G. Simkovich: Oxidation of molybdenum chromium palladium alloys, Oxid. Met. **31**, 265 (1989) 223

[4] I. Zaplatynsky: Volatization of oxides during oxidation of some superalloys at 1200 degrees C, Oxid. Met. **11**, 289 (1977) 223

[5] G. R. Wallwork, A. Z. Hed: Some limiting factors in use of alloys at high temperatures, Oxid. Met. **3**, 171 (1971) 223

[6] J. C. Clark, J. P. Maria, K. J. Hubbard, D. G. Schlom: An oxygen-compatible radiant substrate heater for thin film growth at substrate temperatures up to 1050 degrees C, Rev. Sci. Instrum. **68**, 2538 (1997) 223

[7] R. C. Estler, N. S. Nogar, R. E. Muenchausen, X. D. Wu, S. Foltyn, A. R. Garcia: A versatile substrate heater for use in highly oxidizing atmospheres, Rev. Sci. Instrum. **62**, 437 (1991) 223

[8] P. Vase, Y. Q. Shen, T. Holst, M. Hagensen, T. Freltoft: Substrate heater for large-area $YBa_2Cu_3O_x$ films growth without electrical feedthroughs, Physica C **235–240**, 641 (1994) 224

[9] M. Orita, H. Ohta, H.Hiramatsu, M. Hirano, S. Den, M. Sasaki, T. Katagiri, H. Mimura, H. Hosono: Pulsed laser deposition system for producing oxide thin films at high temperature, Rev. Sci. Instrum. **72**, 3340 (2001) 224

[10] K. H. Wu, C. L. Lee, J. Y. Juang, T. M. Uen, Y. S. Gou: In-situ growth of $Y_1Ba_2Cu_3O_{7-x}$ superconducting thin-films using a pulsed neodymium yttrium-aluminium-garnet laser with CO_2-laser heated substrates, Appl. Phys. Lett. **58**, 1089 (1991) 224

[11] S. Ohashi, M. Lippmaa, N. Nakagawa, H. Nagasawa, H. Koinuma, M. Kawasaki: Compact laser molecular beam epitaxy system using laser heating of substrate for oxide film growth, Rev. Sci. Instrum. **70**, 178 (1999) 224

[12] M. Lippmaa, T. Furumochi, S. Ohashi, M. Kawasaki, H. Koinuma, T. Satoh, T. Ishida, H. Nagasawa: High-temperature goniometer for thin film growth and ion scattering studies, Rev. Sci. Instrum. **72**, 1755 (2001) 224

[13] T. Koida, D. Komiyama, H. Koinuma, M. Ohtani, M. Lippmaa, M. Kawasaki: Temperature-gradient epitaxy under in situ growth mode diagnostics by scanning reflection high-energy electron diffraction, Appl. Phys. Lett. **80**, 565 (2002) 225

[14] A. C. Westerheim, B. I. Choi, M. I. Flik, M. J. Cima, R. L. Slattery, A. C. Anderson: Radiative substrate heating for high-T(C) superconducting thin-film deposition-film-growth-induced temperature variation, J. Vac. Sci. Technol. **10**, 3407 (1992) 226

[15] A. R. Beavitt: A wide-band particle eliminator, Thin Solid Films **1**, 69 (1967) 230

[16] H. Dupendant, J. P. Gavigan, D. Givord, A. Lienard, J. P. Rebouillat, Y. Souche: Velocity distribution of micronsized particles in thin-film laser ablation deposition (LAD) of metals and oxide superconductors, Appl. Surf. Sci. **43**, 369 (1989) 230

[17] A. Tselev, A. Gorbunov, W. Pompe: Cross-beam pulsed laser deposition: General characteristic, Rev. Sci. Instrum. **72**, 2665 (2001) 230
[18] C. Doughty, A. T. Findikoglu, T. Venkatesan: Steady-state pulsed-laser deposition target scanning for improved plume stability and reduced particle density, Appl. Phys. Lett. **66**, 1276 (1995) 231
[19] L. Cultrera, D. Guido, A. Perrone, M. I. Zeifman: Plume separation effect in pulsed laser ablation deposition, Appl. Phys. A **79**, 1181 (2004) 231, 232
[20] J. P. Gong, M. Kawasaki, K. Fujito, R. Tsuchiya, M. Yoshimoto, H. Koinuma: Investigation of precipitate formation on laser ablated $YBa_2Cu_30_7$-delta thin-films, Phys. Rev. B **50**, 3280 (1994) 231
[21] N. Kanda, M. Kawasaki, T. Kitajima, H. Koinuma: Diagnosis of precipitate formation in pulsed-laser deposition of $YBa_2Cu_3O_7$-delta by means of in situ laser-light scattering and ex situ atomic force microscopy, Phys. Rev. B **56**, 8419 (1997) 231, 233
[22] R. M. V. Rao, H. Munekata, K. Shimada: Quantum paraelectric $La_{1/2}Na_{1/2}TiO_3$ films as capacitor dielectrics for temperature- and electric-field-insensitive applications, J. Appl. Phys. **88**, 3756 (2000) 231, 238
[23] P. R. Willmott, J. R. Huber: Pulsed laser vaporization and deposition, Rev. Mod. Phys. **72**, 315 (2000) 232
[24] D. B. Chrisey, G. K. Huber (Eds.): *Pulsed Laser Deposition of Thin Films* (Wiley, New York 1994) 232
[25] F. G. Will, H. G. deLorenzi, K. H. Janora: Conduction mechanism of single-crystal alumina, J. Am. Ceram. Soc. **75**, 295 (1992) 232
[26] R. H. French, D. J. Jones, S. Loughin: Interband electronic-structure of alpha-alumina up to 2167 K, J. Am. Ceram. Soc **77**, 412 (1994) 232
[27] A. J. Pedraza, J. D. Fowlkes, D. H. Lowndes: Silicon microcolumn arrays grown by nanosecond pulsed-excimer laser irradiation, Appl. Phys. Lett. **74**, 2322 (1999) 232
[28] A. Jacquot, B. Lenoir, M. O. Boffoué, A. Dauscher: Influence of target morphology on droplet emission and thickness profiles with pulsed laser deposited bismuth films, Appl. Phys. A **69**, S195 (1999) 233
[29] J. C. Miller, J. R. F. Haglund (Eds.): *Laser Ablation and Desorption*, vol. 30, Experimental Methods in the Physical Sciences (Academic Press, San Diego 1998) p. 84 233
[30] J. M. Huijbregtse, B. Dam, J. H. Hector, R. Griessen: High-quality off-stoichiometric $YBa_2Cu_3O_7$-delta films produced by diffusion-assisted preferential laser ablation, J. Appl. Phys. **86**, 6528 (1999) 233, 237
[31] P. E. Dyer, R. D. Greenough, A. Issa, P. H. Key: Spectroscopic and ion probe measurements of KRF laser ablated y−ba−cu−o bulk samples, Appl. Phys. Lett. **53**, 534 (1988) 234
[32] M. A. Herman, H. Sitter: *Molecular Beam Epitaxy, Fundamentals and Current Status*, vol. 7, 2nd ed., Springer Series in Materials Science (Springer, Berlin 1996) p. 38 234
[33] P. D. Gupta, R. Bhatanagar, D. D. Bhawalkar: Isotopic enhancement in laser-produced plasmas, J. Appl. Phys. **51**, 3422 (1980) 235
[34] P. A. VanRompay, Z. Zhang, J. A. Nees, P. P. Pronko: Isotope separation and enrichment by ultrafast laser ablation, Proc. SPIE **3934**, 43 (2000) 235

[35] P. P. Pronko, P. A. VanRompay, Z. Zhang, J. A. Nees: Isotope enrichment in laser-ablation plumes and commensurately deposited thin films, Phys. Rev. Lett. **83**, 2596 (1999) 235
[36] L. D. Laude, C. Dicara, K. Kolev, H. Schillinger: Excimer laser ablation: Energy or power density? A different approach, Proc. SPIE **5448**, 144 (2004) 235
[37] J. F. M. Cillessen, M. J. M. de Jong, X. Croize: Improved uniformity of multielement thin films prepared by off-axis pulsed laser deposition using a new heater design, Rev. Sci. Instrum. **67**, 3229 (1996) 236, 237
[38] A. Wong, R. Liang, M. Gardner, W. N. Hardy: Reproducible growth of highly crystalline $YBa_2Cu_3O_7$ thin films on $SrTiO_3$ by scanning pulsed laser deposition, J. Appl. Phys. **82**, 3019 (1997) 237
[39] H.-C. Li, W. Si, A. D. West, X. X. Xi: Near single crystal-level dielectric loss and nonlinearity in pulsed laser deposited $SrTiO_3$ thin films, Appl. Phys. Lett. **73**, 190 (1998) 237
[40] M. Lippmaa, N. Nakagawa, M. Kawasaki, S. Ohashi, Y. Inaguma, M. Itoh, H. Koinuma: Step-flow growth of $SrTiO_3$ thin films with a dielectric constant exceeding 10(4), Appl. Phys. Lett. **74**, 3543 (1999) 237
[41] T. Ohnishi, M. Lippmaa, T. Yamamoto, S. Meguro, H. Koinuma: Improved stoichiometry and misfit control in perovskite thin film formation at a critical fluence by pulsed laser deposition, Appl. Phys. Lett. **87**, 241919 (2005) 237
[42] S. K. Hau, K. H. Wong, P. W. Chan, C. L. Choy: Intrinsic resputtering in pulsed-laser deposition of leadzirconate-titanate thin-films, Appl. Phys. Lett. **66**, 245 (1995) 237
[43] B. Dam, J. Rector, M. F. Chang, S. Kars, D. G. Degroot, R. Griessen: Laser-ablation threshold of $YBa_2Cu_3O_{6+x}$, Appl. Phys. Lett. **65**, 1581 (1994) 237
[44] K. Shibuya, T. Ohnishi, T. Uozumi, M. Lippmaa, H. Koinuma: The effect of annealing on $SrTiO_3$ field-effect transistor devices, Thin Solid Films **486**, 195 (2005) 237
[45] P. R. Willmott: Deposition of complex multielemental thin films, Prog. Surf. Sci. **76**, 163 (2004) 238
[46] G. Betz, G. K. Wehner: Sputtering of multicomponent materials, Top. Appl. Phys. **52**, 11 (1983) 238
[47] S. M. Rossnagel: Thin film deposition with physical vapor deposition and related technologies, J. Vac. Sci. Technol. A **21**, S74 (2003) 238, 243
[48] A. Matthews: Plasma-based physical vapor deposition surface engineering processes, J. Vac. Sci. Technol. A **21**, S224 (2003) 238
[49] R. A. Baragiola: Sputtering: Survey of observations and derived principles, Philos. Trans. R. Soc. Lond. A **362**, 29 (2004) 238
[50] P. J. Martin: Ion-based methods for optical thin-film deposition, J. Mater. Sci. **21**, 1 (1986) 238
[51] S. M. Rossnagel: Sputter deposition for semiconductor manufacturing, IBM J. Res. Devel. **43**, 163 (1999) 238
[52] U. Helmersson, M. Lattemann, J. Bohlmark, A. P. Ehiasarian, J. T. Gudmundsson: Ionized physical vapor deposition (IPVD): A review of technology and applications, Thin Solid Films **513**, 1 (2006) 238
[53] M. V. Ramana Murty: Sputtering: The material erosion tool, Surf. Sci. **500**, 523 (2002) 239
[54] V. S. Smentkowski: Trends in sputtering, Prog. Surf. Sci. **64**, 1 (2000) 239

[55] P. Sigmund: Sputtering by ion bombardment theoretical concepts, Top. Appl. Phys. **47**, 9 (1979) 239
[56] H.-U. Habermeier, G. Beddies, B. Leibold, G. H. Lu, G. Wagner: Y−Ba−Cu−O high-temperature superconductor thin-film preparation by pulsed laser deposition and RF-sputtering – A comparative study, Physica C **180**, 17 (1991) 239, 241
[57] E. Kawamura, V. Vahedi, M. A. Lieberman, C. K. Birdsall: Ion energy distributions in RF sheaths; review, analysis and simulation, Plasma Sources Sci. Technol. **8**, R45 (1999) 240, 243
[58] L. Fabrega, E. Koller, J. M. Triscone, O. Fischer: Epitaxial growth of "infinite layer" thin films and multilayers by RF magnetron sputtering, J. Mater. Res. **13**, 2195 (1998) 241
[59] J. M. E. Harper: Particle bombardment effects in thin film deposition, in O. Auciello, A. Gras-Marti, J. A. Valles-Abarca, D. L. Flamm (Eds.): *Plasma Surface Interactions and Processing of Materials* (Kluwer Academic, Amsterdam 1990) p. 251 241
[60] C. B. Eom, J. Z. Sun, B. M. Lairson, S. K. Streiffer, A. F. Marshall, K. Yamamoto, S. M. Anlage, J. C. Bravman, T. H. Geballe: Synthesis and properties of $YBa_2Cu_3O_7$ thin-films grown insitu by 90-degrees off-axis single magnetron sputtering, Physica C **171**, 354 (1990) 241
[61] M. Stepanova, S. K. Dew: Estimates of differential sputtering yields for deposition applications, J. Vac. Sci. Technol. A **19**, 2805 (2001) 242
[62] J. A. Thornton: Magnetron sputtering – Basic physics and application to cylindrical magnetrons, J. Vac. Sci. Technol. **15**, 171 (1978) 242
[63] P. J. Kelly, R. D. Arnell: Magnetron sputtering: A review of recent developments and applications, Vacuum **56**, 159 (1999) 243
[64] I. Petrov, F. Adibi, J. E. Greene, W. D. Sproul, W. D. Munz: Use of an externally applied magnetic-field to control ion neutral flux ratios incident at the substrate during magnetron sputter deposition, J. Vac. Sci. Technol. A **10**, 3283 (1992) 243
[65] C. R. Aita: Tailored ceramic film growth at low temperature by reactive sputter deposition, Rev. Solid State Mater. Sci. **23**, 205 (1998) 244
[66] J. Musil, P. Baroch, J. Vlcek, K. H. Nam, J. G. Han: Reactive magnetron sputtering of thin films: Present status and trends, Thin Solid Films **475**, 208 (2005) 244
[67] D. W. Pashley: The study of epitaxy on thin surface films, Adv. Phys. **5**, 173 (1956) 244, 253
[68] J. C. Woicik, H. Li, P. Zschack, E. Karapetrova, P. Ryan, C. R. Ashman, C. S. Hellberg: Anomalous lattice expansion of coherently strained $SrTiO_3$ thin films grown on Si(001) by kinetically controlled sequential deposition, Phys. Rev. B **73**, 024112 (2006) 246, 285, 289
[69] T. B. Massalski: *Binary Alloy Phase Diagrams* (American Society for Metals, Ohio 1986) 247
[70] C. D. Theis, D. G. Schlom: Cheap and stable titanium source for use in oxide molecular beam epitaxy systems, J. Vac. Sci. Technol. A **14**, 2677 (1996) 247
[71] S. Nayak, D. E. Savage, H. N. Chu, M. G. Lagally, T. F. Kuech: In situ RHEED and AFM investigation of growth front morphology evolution of Si(001) grown by UHV-CVD, J. Cryst. Growth **157**, 168 (1995) 247

[72] A. Y. Cho: Growth of periodic structures by molecular-beam method, Appl. Phys. Lett. **19**, 467 (1971) 247
[73] M. H. Yang, C. P. Flynn: Growth of alkali-halides from molecular-beams – global growth-characteristics, Phys. Rev. Lett. **62**, 2476 (1989) 249, 250
[74] M. W. Chase, Jr.: *NIST-JANAF Thermochemical Tables*, 4th ed. (NIST,AIP, 1998) 250, 282
[75] F. J. Walker, R. A. McKee: High temperature stability of molecular-beam epitaxy-grown multilayer ceramic composites – TiO/Ti_2O_3, J. Cryst. Growth **116**, 235 (1992) 250, 251
[76] F. B. Wang, J. Li, P. Wang, X. H. Zhu, M. J. Zhang, Z. H. Peng, S. L. Li, L. P. Yong, Y. F. Chen, X. S. Sun, D. N. Zheng: Effect of oxygen content on the transport properties of $LaTiO_{3+\beta/2}$ thin films, J. Phys. Condens. Mattter **18**, 5835 (2006) 251
[77] D. R. Lide: *CRC Handbook of Chemistry and Physics* (CRC, Boca Raton 1995) 251, 253
[78] S. A. Chambers: Epitaxial growth and properties of thin film oxides, Surf. Sci. Rep. **39**, 105 (2000) 251, 257
[79] D. D. Berkley, B. R. Johnson, N. Anand, K. M. Beuchamp, L. E. Conroy, A. M. Goldman, J. Maps, K. Mauersberger, M. L. Mecartney, J. Morton, M. Tuominen, Y. J. Zhang: Insitu formation of superconducting $YBa_2Cu_3O_{7-x}$ thin-films using pure ozone vapor oxidation, Appl. Phys. Lett. **53**, 1973 (1988) 251
[80] D. O. Klenov, D. G. Schlom, H. Li, S. Stemmer: The interface between single crystalline (001) $LaAlO_3$ and (001) silicon, Jpn. J. Appl. Phys **44**, L617 (2005) 252
[81] C. J. Forst, K. Schwarz, P. E. Blochl: Structural and electronic properties of the interface between the high-k oxide $LaAlO_3$ and Si(001), Phys. Rev. Lett. **95**, 137602 (2005) 252
[82] Y. Kado, Y. Arita: Heteroepitxaial growth of SRO films on Si substrates, J. Appl. Phys. **61**, 2398 (1987) 253
[83] R. A. McKee, F. J. Walker, J. R. Conner, E. D. Specht, D. E. Zelmon: Molecular-beam epitaxy of epitaxial barium silicide, barium oxide, and barium-titanate on silicon, Appl. Phys. Lett. **59**, 782 (1991) 253
[84] O. Nakagawara, M. Kobayashi, Y. Yoshino, Y. Katayama, H. Tabata, T. Kawai: Effects of buffer layers in epitaxial growth of $SrTiO_3$ thin film on Si(100), J. Appl. Phys. **78**, 7226 (1995) 253
[85] F. J. Walker, R. A. McKee, H. W. Yen, D. E. Zelmon: Optical clarity and wave-guide performance of thin-film perovskites on MGO, Appl. Phys. Lett. **65**, 1495 (1994) 253
[86] R. A. McKee, F. J. Walker: Patent No. 5,693,140 (September 18, 1995) 253
[87] D. Taylor: Thermal expansion data. 1. Binary oxides with the sodium chloride and wurtzite structures, Trans. Brit. Ceram. Soc. **83**, 5 (1984) 253
[88] H. R. L. D. K. Smith: Low-temperature thermal expansion of LiH MGO and CaO, J. Appl. Crystallogr. **1**, 246 (1968) 253
[89] L. Liu, W. A. Bassett: Effect of pressure on crystal-structure and lattice parameters of BaO, J. Geophys. Res. **77**, 4934 (1972) 253
[90] J. Lettieri, J. H. Haeni, D. G. Schlom: Critical issues in the heteroepitaxial growth of alkaline-earth oxides on silicon, J. Vac. Sci. Technol. A **20**, 1332 (2002) 253

[91] S. Yadavalli, M. H. Yang, C. P. Flynn: Low-temperature growth of MGO by molecular-beam epitaxy, Phys. Rev. B **41**, 7961 (1990) 254
[92] F. J. Walker, R. A. McKee: High-k crystalline gate dielectrics: A research perspective, in H. R. Huff, D. C. Gilmer (Eds.): *High Dielectric Constant Materials – VLSI MOSFET Applications* (Springer, Berlin 2005) p. 607 254
[93] M. H. Yang, C. P. Flynn: Growth of alkakli-halides by molecular-beam epitaxy, Phys. Rev. B **41**, 8500 (1990) 254
[94] E. S. Hellman, E. H. Hartford: Epitaxial solid-solution films of immiscible MGO and CaO, Appl. Phys. Lett. **64**, 1341 (1994) 254
[95] R. Ramesh, V. G. Keramidas: Metal-oxide heterostructures, Annu. Rev. Mater. Sci. **25**, 647 (1995) 254
[96] D. H. Looney: (1957), Patent No. 2,791,758 255, 279
[97] J. A. Morton: (1957), US Patent No. 2,791,761 255
[98] I. M. Ross: (1957), US Patent No. 2,791,760 255
[99] W. L. Brown: (1957), US Patent No. 2,791,759 255
[100] D. G. Schlom, J. H. Haeni, J. Lettieri, C. D. Theis, W. Tian, J. C. Jiang, X. Q. Pan: Oxide nano-engineering using MBE, Mater. Sci. Eng. B **87**, 282 (2001) 255
[101] J. H. Haeni, C. D. Theis, D. G. Schlom: RHEED intensity oscillations for the stoichiometric growth of $SrTiO_3$ thin films by reactive molecular beam epitaxy, J. Electroceramics **4**, 385 (2000) 256
[102] R. A. McKee, F. J. Walker: US Patent No. 6,306,668 (September 23, 1999) 256
[103] Z. Yu, Y. Liang, C. Overgaard, X. Hu, J. Curless, H. Li, Y. Wei, B. Craigo, D. Jordan, R. Droopad, J. Finder, K. Eisenbeiser, D. Marshall, K. Moore, J. Kulik, P. Fejes: Advances in heteroepitaxy of oxides on silicon, Thin Solid Films **462–463**, 51 (2004) 256, 257
[104] R. A. McKee, F. J. Walker, M. F. Chisholm: Physical structure and inversion charge at a semiconductor interface with a crystalline oxide, Science **293**, 468 (2001) 257, 289
[105] F. W. Lytle: X-ray diffractometry of low-temperature phase transformations in strontium titanate, J. Appl. Phys. **35**, 2212 (1964) 259, 265
[106] H. Unoki, T. Sakudo: Electron spin resonance of fe^{3+} in $SrTiO_3$ with special reference to 110 degrees K phase transition, J. Phys. Soc. Jpn. **23**, 546 (1967) 259, 265
[107] K. Aso: Residual-stress in damaged $SrTiO_3$ single crystals, Jpn. J. Appl. Phys. **15**, 1243 (1976) 259
[108] S. Watanabe, T. Hikita, M. Kawai: Cleaning the surface of $SrTiO_3$(100) and $LaAlO_3$(100) under moderate temperature condition by Bi adsorption, J. Vac. Sci. Technol. A **9**, 2394 (1991) 260
[109] T. Terashima, K. Iijima, K. Yamamoto, K. Hirata, Y. Bando, T. Takada: Insitu reflection high-energy electron diffraction observation during growth of $YBa_2Cu_3O_{7-x}$, Jpn. J. Appl. Phys. **28**, L987 (1989) 260
[110] M. Kawasaki, K. Takahashi, T. Maeda, R. Tsuchiya, M. Shinohara, O. Ishiyama, T. Yonezawa, M. Yoshimoto, H. Koinuma: Atomic control of the $SrTiO_3$ crystal-surface, Science **266**, 1540 (1994) 260, 261
[111] G. Koster, B. L. Kropman, G. J. H. M. Rjinders, D. H. A. Blank, H. Rogalla: Quasi-ideal strontium titanate crystal surfaces through formation of strontium hydroxide, Appl. Phys. Lett. **73**, 2920 (1998) 260, 261, 262

[112] T. Ohnishi, K. Shibuya, M. Lippmaa, D. Kobayashi, H. Kumigashira, M. Oshimam, H. Koinuma: Preparation of thermally stable TiO_2-terminated $SrTiO_3$(100) substrate surfaces, Appl. Phys. Lett. **85**, 272 (2004) 260, 263, 264

[113] R. Sum, H. P. Lang, H.-J. Güntherodt: Scanning force microscopy study of single-crystal substrates used for thin-film growth of high-temperature superconductors, Physica C **242**, 174 (1995) 260, 263, 264, 268

[114] K. Szot, W. Speier: Surfaces of reduced and oxidized $SrTiO_3$ from atomic force microscopy, Phys. Rev. B **60**, 5909 (1999) 260, 263, 264

[115] Y. Liang, D. A. Bonnell: Atomic structures of reduced $SrTiO_3$ (001) surfaces, Surf. Sci. Lett. **285**, L510 (1993) 260, 289

[116] U. Balachandran, N. G. Eror: Electrical-conductivity in lanthanum-doped strontium titanate, J. Electrochem. Soc. **129**, 1021 (1982) 260

[117] R. Meyer, R. Waser, J. Helmbold, G. Borchardt: Cationic surface segregation in donor-doped $SrTiO_3$ under oxidizing conditions, J. Electroceram. **9**, 101 (2002) 260, 263

[118] K. Iwahori, S. Watanabe, M. Kawai, K. Kobayashi, H. Yamada, K. Matsushige: Effect of water adsorption on microscopic friction force on $SrTiO_3$ (001), Appl. Phys. Lett. **93**, 3223 (2003) 261

[119] J. Fompeyrine, R. Berger, H. P. Lang, J. Perret, E. Machler, G. Cerber, J. P. Locquet: Local determination of the stacking sequence of layered materials, Appl. Phys. Lett. **72**, 1697 (1998) 261

[120] M. Kawasaki, A. Ohtomo, T. Arakane, K. Takahashi, M. Yoshimoto, H. Koinuma: Atomic control of $SrTiO_3$ surface for perfect epitaxy of perovskite oxides, Appl. Surf. Sci. **107**, 102 (1996) 261, 263

[121] K. Szot, W. Speier, R. Carius, U. Zastrow, W. Beyer: Localized metallic conductivity and self-healing during thermal reduction of $SrTiO_3$, Phys. Rev. Lett. **88**, 75508 (2002) 261

[122] M. Lippmaa, K. Takahashi, A. Ohtomo, S. Ohashi, T. Ohnishi, N. Nakagawa, T. Sato, M. Iwatsuki, H. Koinuma, M. Kawasaki: Atom technology for Josephson tunnel junctions: $SrTiO_3$ substrate surface, Mater. Sci. Eng. B **56**, 111 (1998) 261, 262

[123] K. Szot, W. Speier, J. Herion, C. Freiburg: Restructuring of the surface region in $SrTiO_3$, Appl. Phys. A **64**, 55 (1997) 263

[124] M. Lippmaa, K. Takahashi, S. Ohashi, N. Nakagawa, T. Sato, M. Iwatsuki, H. Koinuma, M. Kawasaki: Dynamics of $SrTiO_3$ surface during wet etching and high-temperature annealing, Ferroelectrics **224**, 373 (1999) 263

[125] M. Lippmaa, M. Kawasaki, A. Ohtomo, T. Sato, M. Iwatsuki, H. Koinuma: Observation of $SrTiO_3$ step edge dynamics by real-time high-temperature STM, Appl. Surf. Sci. **130**, 582 (1998) 264

[126] M. Lippmaa, N. Nakagawa, T. Kinoshita, T. Furumochi, M. Kawasaki, H. Koinuma: Growth dyanmics of oxide thin films at temperatures above 1000 degrees C, Physica C **335**, 196 (2000) 264

[127] H. F. Kay, P. Vousden: Symmetry changes in barium titanate at low temperatures and their relation to its ferroelectric properties, Philos. Mag. **40**, 1019 (1949) 265

[128] S. Geller, P. M. Raccah: Phase transitions in perovskite-like compounds of rare earths, Phys. Rev. B **2**, 1167 (1970) 264, 265

[129] B. C. Chakoumakos, D. G. Schlom, M. Urbanik, J. Luine: Thermal expansion of $LaAlO_3$ and (La,Sr)(Al,Ta)O_3, substrate materials for superconducting thin-film device applications, J. Appl. Phys. **83**, 1979 (1998) 265, 266

[130] O. Chaix-Pluchery, B. Chenevier, J. J. Robles: Anisotropy of thermal expansion in $YAlO_3$ and $NdGaO_3$, Appl. Phys. Lett. **86**, 251911 (2005) 265, 266

[131] I. Utke, C. Klemenz, H. J. Scheel, P. Nüesch: High-temperature X-ray measurements of gallates and cuprates, J. Cryst. Growth **174**, 813 (1997) 265, 266

[132] R. Feenstra, L. A. Boatner, J. D. Budai, D. K. Christen, M. D. Galloway, D. B. Poker: Epitaxial superconducting thin-films of $YBa_2Cu_3O_{7-x}$ on $KTaO_3$ single crystals, Appl. Phys. Lett. **54**, 1063 (1989) 265, 267

[133] T. Konaka, M. Sato, H. Asano, S. Kubo: Relative permittivity and dielectric loss tangent of substrate materials for high-Tc superconducting film, J. Supercond. **4**, 283 (1991) 265, 267

[134] J. Schubert, O. Trithaveesak, A. Petraru, C. L. Jia, R. Uecker, P. Reiche, D. G. Schlom: Structural and optical properties of epitaxial $BaTiO_3$ thin films grown on $GdScO_3$(110), Appl. Phys. Lett. **82**, 3460 (2003) 265, 268

[135] G. W. Berkstresser, A. J. Valentino, C. D. Brandle: Growth of single-crystals of lanthanum aluminate, J. Cryst. Growth **109**, 467 (1991) 264

[136] D. Reagor, F. Garzon: Dielectric and optical-properties of substrates for high-temperature superconductor films, Appl. Phys. Lett. **56**, 2741 (1991) 264

[137] M. Katayama, E. Nomura, N. Kanekama, H. Soejima, M. Aono: Coaxial impact-collision ion-scattering spectroscopy (CAICISS) – A novel method for surface-structure analysis, Nucl. Instrum. Methods B **33**, 857 (1988) 264

[138] J. Konopka, I. Wolff: Dielectric-properties of substrates for deposition of high-Tc thin-films up to 40 GHz, IEEE Trans. Microwave Theory Technol. **40**, 2418 (1992) 266

[139] D. J. Tao, H. Wu, X. D. Xu, R. S. Yan, F. Y. Liu, A. P. B. Sinha, X. P. Jiang, H. L. Hu: Czochralski growth of (La,Sr)(Al,Ta)O_3 single crystal, Opt. Mater. **23**, 425 (2003) 266

[140] M. Berkowski, J. Fink-Finowicki, R. Diduszko, P. Byszewski, R. Aleksiyko, R. Kikalejshvili-Domukhovska: Growth and structure of $SrAl_{0.5}Ta_{0.5}O_3$:$LaAlO_3$ solid solutions single crystals, J. Cryst. Growth **257**, 146 (2003) 266

[141] T. Ohnishi, K. Takahashi, M. Nakamura, M. Kawasaki, M. Yoshimoto, H. Koinuma: A-site layer terminated perovskite substrate: $NdGaO_3$, Appl. Phys. Lett. **74**, 2531 (1999) 266

[142] D. Schweitzer, T. Bollmeier, B. Stritzker, B. Rauschenbach: Twinning of $YBa_2Cu_3O_7$ thin films on different substrates, Thin Solid Films **280**, 147 (1996) 266

[143] M. L. Lucia, J. Santamaria, F. SanchezQuesada, W. Lopera, M. E. Gomez, P. Prieto: Influence of epitaxial properties on the mutual inductance response of high-quality YBCO thin films, Physica C **260**, 149 (1996) 266

[144] S. Geller: Crystallographic studies of perovskite-like compounds. 4. Rare earth scandates, vanadites, galliates, orthochromites, Acta Crystallogr. **10**, 243 (1957) 266

[145] R. L. Sandstrom, E. A. Giess, W. J. Gallagher, A. Segmuller, E. I. Cooper, M. F. Chisholm, A. Gupta, S. Shinde, R. B. Laibowitz: Lanthanum gallate substrates for epitaxial high-temperature superconducting thin films, Appl. Phys. Lett. **53**, 1874 (1988) 266

[146] H. J. Scheel, M. Berkowski, B. Chabot: Substrates for high-temperature superconductors, Physica C **185–189**, 2095 (1991) 266

[147] E. Talik, A. Kruczek, H. Sakowska, Z. Ujma, M. Gala, M. Neumann: XPS characterisation of neodymium gallate wafers, J. Alloys Compd. **377**, 259 (2004) 266

[148] T. Mihara, K. Shibuya, T. Ohnishi, H. Koinuma, M. Lippmaa: Transport properties of ultrathin oxide films and nanostructures, Thin Solid Films **486**, 63 (2005) 266

[149] W. Prusseit, L. A. Boatner, D. Rytz: Epitaxial $YBa_2Cu_3O_7$ growth on $KTaO_3$ (001) single-crystals, Appl. Phys. Lett. **63**, 3376 (1993) 267

[150] J. R. Thompson, L. A. Boatner, J. O. Thomson: Very low temperature search for superconductivity in semiconducting $KTaO_3$, J. Low Temp. Phys. **47**, 467 (1982) 267

[151] L. S. Senhouse, Jr., M. V. DePaolis, Jr., T. C. Loomis: Calcium concentration vs net ionized donor concentration in single-crystal $KTaO_3$, Appl. Phys. Lett. **8**, 173 (1966) 267

[152] S. H. Wemple, A. Jayaraman, M. DiDomenico, Jr.: Evidence from pressure experiments for electron scattering by ferroelectric lattice mode in ABO_3 semiconductors, Phys. Rev. Lett. **17**, 142 (1966) 267

[153] K. Ueno, I. H. Inoue, T. Yamada, H. Akoh, Y. Tokura, H. Takagi: Field-effect transistor based on $KTaO_3$ perovskite, Appl. Phys. Lett. **84**, 3726 (2004) 267

[154] J. E. Geusic, S. K. Kurtz, T. J. Nelson, S. H. Wemple: Nonlinear dielectric properties of $KTaO_3$ near its curie point, Appl. Phys. Lett. **2**, 185 (1963) 267

[155] P. Buffat, J. D. Ganière, M. Rappaz, D. Rytz: Natural and etched surfaces in para-electric and ferroelectric $KTa_{1-x}Nb_xO_3$ – A study by scanning electron-microscopy and X-ray topography, J. Cryst. Growth **74**, 353 (1986) 267

[156] S. Karimoto, K. Ueda, M. Naito, T. Imai: Single-crystalline superconducting thin films of electron-doped infinite-layer compounds grown by molecular-beam epitaxy, Appl. Phys. Lett. **79**, 2767 (2001) 267

[157] H. M. Christen, L. A. Boatner, J. D. Budai, M. F. Chisholm, L. A. Gea, P. J. Marrero, D. P. Norton: The growth and properties of epitaxial $KNbO_3$ thin films and $KNbO_3/KTaO_3$ superlattices, Appl. Phys. Lett. **68**, 1488 (1996) 267, 275

[158] A. F. Chow, D. J. Lichtenwalner, R. R. Woolcott, T. M. Graettinger, O. Auciello, A. I. Kingon, L. A. Boatner, N. R. Parikh: Epitaxial $KNbO_3$ thin-films on $KTaO_3$, $MgAl_2O_4$, and MGO substrates, Appl. Phys. Lett. **65**, 1073 (1994) 267

[159] Y. Kim, A. Erbil, L. A. Boatner: Substrate dependence in the growth of epitaxial $Pb_{1-x}La_xTiO_3$ thin films, Appl. Phys. Lett. **69**, 2187 (1996) 267

[160] H. M. Christen, L. A. Boatner, J. D. Budai, M. F. Chisholm, C. Gerber, M. Urbanik: Semiconducting epitaxial films of metastable $SrRu_{0.5}Sn_{0.5}$ O_3, Appl. Phys. Lett. **70**, 2147 (1997) 267

[161] N. Ikemiya, A. Kitamura, S. Hara: Surface structures of MgO(100) and $SrTiO_3$(100) as revealed by atomic force microscopy, J. Cryst. Growth **160**, 104 (1996) 267

[162] P. W. Tasker, D. M. Duffy: The structure and properties of the stepped surface of MgO and NiO, Surf. Sci. **137**, 91 (1984) 267
[163] B. H. Moeckly, S. E. Russek, D. K. Lathrop, R. A. Buhrman, J. Li, J. W. Mayer: Interface stability and the growth of optical quality perovskites on MgO, Appl. Phys. Lett. **57**, 1687 (1990) 268
[164] M. Murugesan, H. Obara, Y. Nakagawa, S. Kosaka, H. Yamasaki: Influence of MgO substrate annealing on the microwave properties of laser ablated yba2cu3oz thin films, Supercond. Sci. Technol. **17**, 113 (2004) 268
[165] S. S. Perry, P. B. Merrill: Preparation and characterization of MgO(100) surfaces, Surf. Sci. **383**, 268 (1997) 268
[166] L. D. Madsen, R. Charavel, J. Birch, B. Svedberg: Assessment of MgO(100) and (111) substrate quality by X-ray diffraction, J. Cryst. Growth **209**, 91 (2000) 268
[167] Y. Yan, M. F. Chisholm, G. Duscher, A. Maiti, S. J. Pennycook, S. T. Pantelides: Impurity-induced structural transformation of a MgO grain boundary, Phys. Rev. Lett. **81**, 3675 (1998) 268
[168] R. V. Smilgys, S. W. Robey, C. K. Chiang, T. J. Hsieh: J. Vac. Sci. Technol. A **11**, 1361 (1993) 268
[169] T. Minamikawa, T. Suzuki, Y. Yonezawa, K. Segawa: Jpn. J. Appl. Phys. **34**, 4038 (1995) 268
[170] R. Souda, Y. Hwang, T. Aizawa, W. Hayami, K. Oyoshi, S. Hishita: Ca segregation at the MgO(001) surface studied by ion scattering spectroscopy, Surf. Sci. **387**, 136 (1997) 268
[171] C. Duriez, C. Chapon, C. R. Henry, J. M. Rickard: Structrual characterization of MgO(100) surfaces, Surf. Sci. **230**, 123 (1990) 268
[172] R. Plass, J. Feller, M. Gajdardziska-Josifovska: Morphology of MgO(111) surfaces: Artifacts associated with the faceting of polar oxide surfaces into neutral surfaces, Surf. Sci. **414**, 26 (1998) 268
[173] V. E. Henrich: Thermal faceting on (110) and (111) surfaces of MgO, Surf. Sci. **57**, 385 (1976) 268
[174] S. Karimoto, M. Naito: Electron-doped infinite-layer thin films with T_c over 40 K grown on $DyScO_3$ substrates, Appl. Phys. Lett. **84**, 2136 (2004) 268, 269
[175] W. Chang, J. A. Bellotti, S. W. Kirchoefer, J. M. Pond: Strain tensor effects on $SrTiO_3$ incipient ferroelectric phase transition, Integr. Ferroelectr. **77**, 173 (2005) 268
[176] J. H. Haeni, P. Irvin, W. Chang, R. Uecker, P. Reiche, Y. L. Li, S. Choudhury, W. Tian, M. E. Hawley, B. Craigo, A. K. Tagantsev, X. Q. Pan, S. K. Streiffer, L. Q. Chen, S. W. Kirchoefer, J. Levy, D. G. Schlom: Room-temperature ferroelectricity in strained $SrTiO_3$, Nature **430**, 758 (2004) 268, 269, 270, 271, 272
[177] K. J. Choi, M. Biegalski, Y. L. Li, A. Sharan, J. Schubert, R. Uecker, P. Reiche, Y. B. Chen, X. Q. Pan, V. Gopalan, L. Q. Chen, D. Schlom, C. B. Eom: Enhancement of ferroelectricity in strained $BaTiO_3$ thin films, Science **306**, 1005 (2004) 269, 270, 271, 272
[178] Z. Z. Li, A. Perrin, J. Padiou, M. Sergent, J. Godard: Physical film substrate interactions in $YBa_2Cu_3O_{7-x}$ thin films grown on (001)$BaTiO_3$ single-crystals, Mater. Lett. **7**, 178 (1988) 269

[179] M. K. Lee, T. K. Nath, C. B. Eom, M. C. Smoak, F. Tsui: Strain modification of epitaxial perovskite oxide thin films using structural transitions of ferroelectric $BaTiO_3$ substrate, Appl. Phys. Lett. **77**, 3547 (2000) 269

[180] D. Dale, A. Fleet, J. D. Brock, Y. Suzuki: Dynamically tuning properties of epitaxial colossal magnetoresistance thin films, Appl. Phys. Lett. **82**, 3725 (2003) 269

[181] C. H. Ahn, T. Tybell, L. Antognazza, K. Char, R. H. Hammond, M. R. Beasley, O. Fischer, J. M. Triscone: Local, nonvolatile electronic writing of epitaxial $Pb(Zr_{0.52}Ti_{0.48})O_3/SrRuO_3$ heterostructures, Science **276**, 1100 (1997) 269

[182] C. H. Ahn, S. Gariglio, P. Paruch, T. Tybell, L. Antognazza, J.-M. Triscone: Electrostatic modulation of superconductivity in ultrathin $GdBa_2Cu_3O_{7-x}$ films, Science **284**, 1152 (1999) 269

[183] K. S. Takahashi, M. Gabay, D. Jaccard, K. Shibuya, T. Ohnishi, M. Lippmaa, J.-M. Triscone: Local switching of two-dimensional superconductivity using the ferroelectric field effect, Nature **441**, 195 (2006) 269, 277

[184] C. H. Ahn, J.-M. Triscone, J. Mannhart: Electric field effect in correlated oxide systems, Nature **424**, 1015 (2003) 269, 277

[185] N. A. Pertsev, A. G. Zembilgotov, A. K. Tagantsev: Effect of mechanical boundary conditions on phase diagrams of epitaxial ferroelectric thin films, Phys. Rev. Lett. **80**, 1988 (1998) 270, 271

[186] M. Dawber, K. M. Rabe, J. F. Scott: Physics of thin-film ferroelectric oxides, Rev. Mod. Phys. **77**, 1083 (2005) 270

[187] M. Dawber, C. Lichtensteiger, M. Cantoni, M. Veithen, P. Ghosez, K. Johnston, K. M. Rabe, J.-M. Triscone: Unusual behavior of the ferroelectric polarization in $PbTiO_3/SrTiO_3$ superlattices, Phys. Rev. Lett **95**, 177601 (2005) 271, 273, 274, 275, 278, 279

[188] A. Q. Jiang, J. F. Scott, H. Lu, Z. Chen: Phase transitions and polarizations in epitaxial $BaTiO_3/SrTiO_3$ superlattices studied by second-harmonic generation, J. Appl. Phys. **93**, 1180 (2003) 273

[189] S. Rios, A. Ruediger, A. Q. Jiang, J. F. Scott, H. Lu, Z. Chen: Orthorhombic strontium titanate in $BaTiO_3$–$SrTiO_3$ superlattices, J. Phys. Condens. Matter **15**, 305 (2003) 273

[190] K. Johnston, X. Huang, J. B. Neaton, K. M. Rabe: First-principles study of symmetry lowering and polarization in $BaTiO_3/SrTiO_3$ superlattices with in-plane expansion, Phys. Rev. B **71**, 100103(R) (2005) 273

[191] J. B. Neaton, K. M. Rabe: Theory of polarization enhancement in epitaxial $BaTiO_3/SrTiO_3$ superlattices, Appl. Phys. Lett. **82**, 1586 (2003) 274

[192] S. M. Nakhmanson, K. M. Rabe, D. Vanderbilt: Predicting polarization enhancement in multicomponent ferroelectric superlattices, Phys. Rev. Lett. **73**, 060101(R) (2006) 274

[193] B. D. Qu, W. L. Zhong, R. H. Prince: Interfacial coupling in ferroelectric superlattices, Phys. Rev. B **55**, 11218 (1997) 274

[194] Y. Q. Ma, J. Shen, X. H. Xu: Coupling effects in ferroelectric superlattice, Solid State Commun. **114**, 461 (2000) 274

[195] K.-H. Chew, Y. Ishibashi, F. G. Shin, H. L. W. Chan: Theory of interface structures in double-layer ferroelectrics, J. Phys. Soc. Jpn. **72**, 2364 (2003) 274

[196] V. A. Stephanovich, I. A. Luk'yanchuk, M. G. Karkut: Domain-enhanced interlayer coupling in ferroelectric/paraelectric superlattices, Phys. Rev. Lett. **94**, 047601 (2005) 274
[197] A. L. Roytburd, S. Zhong, S. P. Alpay: Dielectric anomaly due to electrostatic coupling in ferroelectric-paraelectric bilayers and multilayers, Appl. Phys. Lett. **87**, 092902 (2005) 274
[198] S. Zhong, S. P. Alpay, J. V. Mantese: High dielectric tunability in ferroelectric-paraelectric bilayers and multilayer superlattices, Appl. Phys. Lett. **88**, 132904 (2006) 274
[199] H. Tabata, H. Tanaka, T. Kawai: Formation of artificial $BaTiO_3/SrTiO_3$ superlattices using pulsed-laser deposition and their dielectric properties, Appl. Phys. Lett. **65**, 1970 (1994) 274
[200] D. O'Neill, R. M. Bowman, J. M. Gregg: Dielectric enhancement and Maxwell–Wagner effects in ferroelectric superlattice structures, Appl. Phys. Lett. **77**, 1520 (2000) 274
[201] J. Sigman, D. P. Norton, H. M. Christen, P. H. Fleming, L. A. Boatner: Antiferroelectric behavior in symmetric $KNbO_3/KTaO_3$ superlattices, Phys. Rev. Lett. **88**, 097601 (2002) 275
[202] M. Sepliarsky, S. R. Phillpot, D. Wolf, M. G. Stachiotti, R. L. Migoni:: Ferroelectric properties of $KNbO_3/KTaO_3$ superlattices by atomic-level simulation, J. Appl. Phys. **90**, 4509 (2001) 275
[203] M. Sepliarsky, S. R. Phillpot, M. G. Stachiotti, R. L. Migoni: Ferroelectric phase transitions and dynamical behavior in $KNbO_3/KTaO_3$ superlattices by molecular-dynamics simulation, J. Appl. Phys. **91**, 3165 (2002) 275
[204] J. C. Jiang, X. Q. Pan, W. Tian, C. D. Theis, D. G. Schlom: Abrupt $PbTiO_3/SrTiO_3$ superlattices grown by reactive molecular beam epitaxy, Appl. Phys. Lett. **74**, 2851 (1999) 275
[205] N. Huang, Z. R. Liu, Z. Q. Wu, J. Wu, W. H. Duan, B. L. Gu, X. W. Zhang: Huge enhancement of electromechanical responses in compositionally modulated $Pb(Zr_{1-x}Ti_x)O_3$, Phys. Rev. Lett. **91**, 067602 (2003) 275
[206] C. Bungaro, K. M. Rabe: Epitaxially strained [001]-$(PbTiO_3)(1)(PbZrO_3)(1)$ superlattice and $PbTiO_3$ from first principles, Phys. Rev. B **69**, 184101 (2004) 275
[207] I. Kanno, S. Hayashi, R. Takayama, T. Hirao: Superlattices of $PbZrO_3$ and $PbTiO_3$ prepared by multi-ion-beam sputtering, Appl. Phys. Lett. **68**, 328 (1996) 275
[208] T. Choi, J. Lee: Structural and dielectric properties of artificial $PbZrO_3/PbTiO_3$ superlattices grown by pulsed laser deposition, Thin Solid Films **475**, 283 (2005) 275
[209] N. Sai, B. Meyer, D. Vanderbilt: Compositional inversion symmetry breaking in ferroelectric perovskites, Phys. Rev. Lett. **84**, 5636 (2000) 276
[210] M. P. Warusawithana, E. V. Colla, J. N. Eckstein, M. B. Weissman: Artificial dielectric superlattices with broken inversion symmetry, Phys. Rev. Lett. **90**, 036802 (2003) 276
[211] H. N. Lee, H. M. Christen, M. F. Chisholm, C. M. Rouleau, D. H. Lowndes: Strong polarization enhancement in asymmetric three-component ferroelectric superlattices, Nature **433**, 395 (2005) 276

[212] H. Zheng, J. Wang, S. E. Lofland, Z. Ma, L. Mohaddes-Ardabili, T. Zhao, L. Salamanca-Riba, S. R. Shinde, S. B. Ogale, F. Bai, D. Viehland, Y. Jia, D. G. Schlom, M. Wuttig, A. Roytburd, R. Ramesh: Multiferroic $BaTiO_3$–$CoFe_2O_4$ nanostructures, Science **303**, 661 (2004) 277

[213] J. Wang, J. B. Neaton, H. Zheng, V. Nagarajan, S. B. Ogale, B. Liu, D. Viehland, V. Vaithyanthan, D. G. Schlom, U. V. Waghmare, N. A. Spaldin, K. M. Rabe, M. Wuttig, R. Ramesh: Epitaxial $BiFeO_3$ multiferroic thin film heterostructures, Science **299**, 1719 (2003) 277

[214] H. Bea, M. Bibes, M. Sirena, G. Herranz, K. Bouzehouane, E. Jacquet, S. Fusil, P. Paruch, M. Dawber, J. P. Contour, A. Barthelemey: Combining half-metals and multiferroics into epitaxial heterostructures for spintronics, Appl. Phys. Lett. **88**, 062502 (2006) 277

[215] F. Le Marrec, R. Farhi, M. El Marssi, J. L. Dellis, M. G. Karkut, D. Ariosa: Ferroelectric $PbTiO_3/BaTiO_3$ superlattices: Growth anomalies and confined modes, Phys. Rev. B **61**, R6447 (2000) 277

[216] A. Ohtomo, H. Y. Hwang: A high-mobility electron gas at the $LaAlO_3/SrTiO_3$ heterointerface, Nature **427**, 423 (2004) 277, 278

[217] M. Huijben, G. Rjinders, D. H. A. Blank, S. Bals, S. VanAert, J. Verbeeck, G. VanTendeloo, A. Brinkman, H. Hilgenkamp: Electronically coupled complementary interfaces between perovskite band insulators, Nature Mater. **5**, 556 (2006) 277

[218] C. H. Ahn, K. M. Rabe, J.-M. Triscone: Local polarization in oxide thin films and heterostructures, Science **303**, 408 (2004) 277

[219] R. A. McKee, F. J. Walker, M. F. Chisholm: Crystalline oxides on silicon: The first five monolayers, Phys. Rev. Lett. **81**, 3014 (1998) 280, 283, 285, 286

[220] D. A. Muller: A sound barrier for silicon?, Nature Mater. **4**, 645 (2005) 280

[221] International Technology Roadmap for Semiconductors (2005) URL: `http://www.itrs.net/Links/2005ITRS/Home2005.htm` 280

[222] W. Schottky: Semi-conductor theory in barrier layers, Naturwissenschaften **26**, 843 (1938) 280

[223] R. A. McKee: The interface phase and the Schottky barrier for a crystalline dielectric on silicon, Science **300**, 1726 (2003) 280, 286, 287, 288

[224] J. W. Cahn, J. E. Hilliard: Free energy of a nonuniform system. 1. Interfacial free energy, J. Chem. Phys. **28**, 258 (1958) 280

[225] N. Nakagawa, H. Y. Hwang, D. A. Muller: Why some interfaces cannot be sharp, Nature Mater. **5**, 204 (2006) 280

[226] G. Lucovsky, Y. Wu, H. Nimi, V. Misra, J. C. Philips: Bonding constraints and defect formation at interfaces between crystalline silicon and advanced single layer and composite gate dielectrics, Appl. Phys. Lett. **74**, 2005 (1999) 280

[227] R. A. McKee, F. J. Walker, J. R. Conner, E. D. Specht, D. E. Zelmon: Molecular-beam epitaxy of epitaxial barium silicide, barium oxide and barium-titanate on silicon, Appl. Phys. Lett. **59**, 782 (1991) 280

[228] R. A. McKee, F. J. Walker, J. R. Conner, R. Raj: $BaSi_2$ and thin-film alkaline-earth silicides on silicon, Appl. Phys. Lett. **63**, 2818 (1993) 282

[229] G. J. Norga, C. Marchiori, A. Guiler, J. P. Locquet, C. Rossel, H. Siegwart, D. Caimi, J. Fompeyrine, T. Conard: Phase of reflection high-energy electron diffraction oscillations during (Ba,Sr)O epitaxy on Si(100): A marker of Sr barrier integrity, Appl. Phys. Lett. **87**, 262905 (2005) 283, 285

[230] C. D. Wagner, et al.: *Handbook of X-Ray Photoelectron Spectroscopy* (Perkin-Elmer Corporation, Eden Prarie 1979) 283
[231] S. A. Chambers, Y. Liang, Z. Yu, R. Droopad, J. Ramdani: Band offset and structure of $SrTiO_3$/Si(001) heterojunctions, J. Vac. Sci. Technol. A **19**, 934 (2001) 283
[232] J. Zachariae, H. Pfnur: Growth conditions, stoichiometry, and electronic structure of lattice-matched SrO/BaO mixtures on Si(100), Phys. Rev. B **72**, 075410 (2005) 283
[233] G. H. Lee, B. C. Shin, I. S. Kim: Critical thickness of $BaTiO_3$ film on $SrTiO_3$ (001) evaluated by reflection high-energy electron diffraction, Mater. Lett. **50**, 134 (2001) 283
[234] H. Tabata, H. Tanaka, T. Kawai: Formation of artificial $BaTiO_3$/$SrTiO_3$ superlattices using pulsed-laser deposition and their dielectric properties, Appl. Phys. Lett. **65**, 1970 (1994) 283
[235] S. Jeon, F. J. Walker, C. A. Billman, R. A. McKee, H. Hwang: Electrical characteristics of epitaxially grown $SrTiO_3$ on silicon for metal-insulator-semiconductor gate dielectric applications, IEEE Electron Device Lett. **24**, 218 (2003) 285
[236] V. Vaithyanathan, J. Lettieri, W. Tian, A. Sharan, A. Vasudevarao, Y. L. Li, A. Kochhar, H. Ma, J. Levy, P. Zschack, J. C. Woicik, L. Q. Shen, V. Gopalan, D. G. Schlom: *c*-axis oriented epitaxial $BaTiO_3$ films on (001)Si, J. Appl. Phys. **100**, 024108 (2006) 285, 289
[237] A. Herrera-Gomez, F. S. Aquirre-Tostado, Y. Sun, P. Pianetta, Z. Yu, D. Marshall, R. Droopad, W. E. Spicer: Photoemission from the Sr/Si(001) interface, J. Appl. Phys. **90**, 6070 (2001) 285
[238] H. Mori, H. Ishiwara: Epitaxial-growth of $SrTiO_3$ films on Si(100) substrates using a focused electron beam evaporation method, Jpn. J. Appl. Phys. **30**, L1415 (1991) 285
[239] X. Hu, X. Yao, C. A. Peterson, D. Sarid, Z. Yu, J. Wang, D. S. Marshall, R. Droopad, J. A. Hallmark, W. J. Ooms: The (3×2) phase of Ba adsorption on Si(001)-2×1, Surf. Sci. **445**, 256 (2000) 286
[240] C. J. Forst, C. R. Ashman, K. Schwarz, P. E. Blochl: The interface between silicon and a high-k oxide, Nature **427**, 53 (2004) 286
[241] C. R. Ashman, C. J. Forst, K. Schwarz, P. E. Blochl: First-principles calculations of strontium on Si(001), Phys. Rev. B **69**, 075309 (2004) 286
[242] Z. Yu, Y. Liang, C. Overgaard, X. Hu, J. Curless, H. Li, Y. Wei, B. Craigo, D. Jordan, R. Droopad, J. Finder, K. Esienbeiser, D. Marshall, K. Moore, J. Kulik, P. Fejes: Advances in heteroepitaxy of oxides on silicon, Thin Solid Films **462–63**, 51 (2004) 289
[243] C. Rossel, B. Mereu, C. Marchiori, D. Caimi, M. Sousa, A. Guiller, H. Siegwart, R. Germann, J. P. Locquet, J. Fompeyrine, D. J. Webb, C. Dieker, J. W. Seo: Field-effect transistors with $SrHfO_3$ as gate oxide, Appl. Phys. Lett. **89**, 053506 (2006) 289
[244] Y. Liang, J. Kulik, T. C. Eschrich, R. Droopad, Z. Yu, P. Maniar: Heteroepitaxy of perovskite oxides on GaAs(001) by molecular beam epitaxy, Appl. Phys. Lett. **85**, 1217 (2004) 289
[245] R. F. Klie, Y. Zhu, E. I. Altman, Y. Liang: Atomic structure of epitaxial $SrTiO_3$–GaAs(001) heterojunctions, Appl. Phys. Lett. **87**, 143106 (2005) 289

[246] A. Posadas, J. B. Yau, C. H. Ahn, J. Han, S. Gariglio, K. Johnston, K. M. Rabe, J. B. Neaton: Epitaxial growth of multiferroic $YMnO_3$ on GaN, Appl. Phys. Lett. **87**, 171915 (2005) 289
[247] W. A. Doolittle, A. G. Carver, W. Henderson: Molecular beam epitaxy of complex metal-oxides: Where have we come, where are we going, and how are we going to get there?, J. Vac. Sci. Technol. B **23**, 1272 (2005) 289
[248] A. Lin, X. Hong, V. Wood, A. A. Vervkin, C. H. Ahn, R. A. McKee, F. J. Walker, E. D. Specht: Epitaxial growth of $Pb(Zr_{0.2}Ti_{0.8})O_3$ on Si and its nanoscale piezoelectric properties, Appl. Phys. Lett. **78**, 2034 (2001) 289
[249] K. Eisenbeiser, R. Emrick, R. Droopad, Z. Yu, J. Finder, S. Rockwell, J. Holmes, C. Overgaard, W. Ooms: GaAs MESFETs fabricated on Si substrates using a $SrTiO_3$ buffer layer, IEEE Electron Device Lett. **23**, 300 (2002) 289

Index

Ferroelectric Size Effects

Céline Lichtensteiger, Matthew Dawber, and Jean-Marc Triscone

DPMC – University of Geneva,
24 Quai Ernest Ansermet, 1211 Geneva 4, Switzerland
celine.lichtensteiger@physics.unige.ch
matthew.dawber@physics.unige.ch
jean-marc.triscone@physics.unige.ch

Abstract. In this chapter, we have reviewed, with a focus on our own efforts, the history, current and future perspectives on the problem of ferroelectric size effects. This past decade has seen an explosion of activity in the field of nanoscale ferroelectrics, with a broad spectrum of novel and artificial materials explored, and a huge potential for new discoveries and novel applications and devices. It is safe to say that although we are at present building a solid understanding of the fundamental driving force for ferroelectric size effects, we can expect some new and fascinating physics to manifest itself as we continue to push the envelope in this exciting and rapidly developing area.

1 Size Effects in Ferroelectrics

Ferroic materials, ferromagnets, ferroelectrics and ferroelastics are similarly named for the reason that they all exhibit hysteretic responses to driving forces. For both ferroelectrics and ferromagnets, size effects are of keen interest for very practical reasons: their ferroic behavior makes them useful for storing information and the smaller they can be made the more information can be stored.

In ferromagnets, the nature of the problem is quite well defined: when the size of ferromagnetic nanoparticles decreases, the magnetic anisotropy energy decreases at the same time. When this energy becomes smaller than the thermal energy $k_{\mathrm{B}}T$ of the grains, thermal fluctuations will flip the magnetic moment of the nanoparticles randomly and cause the loss of a macroscopic magnetic moment. This effect is referred to as the superparamagnetic limit [1]. This limit is typically 50 nm, which corresponds to a storage density of $\sim 40\,\mathrm{Gb/m^2}$.

In ferroelectrics, size effects turn out to be a more loosely defined problem. In the context of ferroelectric nanoparticles, the term "superparaelectric" limit has become popular [2], a notion that may be somewhat confusing. An analogy to the superparamagnetic limit would give the following: the depth of the $PbTiO_3$ double well is typically of -0.1 to $-0.2\,\mathrm{eV}$/unit cells, around 4 to 8 times $k_{\mathrm{B}}T$ at room temperature, leading one to consider that in principle even one unit cell of a ferroelectric material might be resistant to thermal fluctuations. In reality this is not the case: ferroelectricity is instead limited

K. Rabe, C. H. Ahn, J.-M. Triscone (Eds.): Physics of Ferroelectrics: A Modern Perspective,
Topics Appl. Physics **105**, 305–338 (2007)

by the relevant electrical and mechanical boundary conditions [3], and in fact more frequently by the practical issues involved in producing high-quality samples on the extreme nanoscale.

2 Size Effects in the Ginzburg–Landau–Devonshire Theory

Historically, there have been many attempts to study the size dependence of ferroelectric properties, leading to a rich literature of both experimental and theoretical studies.

Within the Ginzburg–Landau–Devonshire-type phenomenological theory, *Kretschmer* and *Binder* [4] introduced a framework for considering size effects through two lengths, the *correlation length* and the *extrapolation length*. This framework was then expanded and applied to a number of situations by *Tilley* and *Zeks* [5].

The idea of an intrinsic size effect is largely driven by the concept of a correlation volume, this being related to the required number of aligned dipoles for ferroelectricity to occur. In fact, the strong long–range interactions along the polar axis and the weaker interactions perpendicular to this axis lead to an anisotropic correlation volume. Reducing the sample size below the critical length parallel to the polar axis modifies the balance between the short-range forces, which favor a centrosymmetric paraelectric phase, and the long–range interactions. Thus, an instability of the ferroelectric phase might be expected for films below a certain thickness. Extremely pertinent to this discussion, however, is the question of what the size of this correlation length should be. In fact this depends greatly on how close to the phase transition the system is, as it is given by

$$\xi = \sqrt{\frac{\kappa}{|\alpha|}}\,, \tag{1}$$

where $\alpha = \gamma(T - T_0)$ and κ is a material constant. While it is only a few lattice parameters far from the transition temperature, it should diverge close to the phase transition.

The intrinsic surface effect on the polarization in ferroelectrics was first studied by *Kretschmer* and *Binder* in 1979 [4]. They used a phenomenological approach to describe polarization variations at the film surface. To do so, a surface term was added to the Ginzburg–Landau–Devonshire expansion of the total free energy, leading to the introduction of the so-called extrapolation length δ, such that

$$\mathrm{d}P/\,\mathrm{d}z = -P_0/\delta\,. \tag{2}$$

A positive extrapolation length δ indicates a decrease of the polarization near the surface, while a negative extrapolation length indicates an increase, in

comparison with the bulk of the film. By introducing this term, a polarization gradient is introduced into the film. This concept has then been used in many papers to calculate polarization profiles.

While useful, the weakness of the phenomenological approach resides in the fact that an extrapolation length has to be introduced. Theoretical works based on Ginzburg–Landau–Devonshire theory predicted that ferroelectricity is suppressed in small particles and thin films [6, 7] at relatively large sizes compared to what has been recently observed experimentally.

3 Extrinsic Size Effects

In many cases, and especially in the past, samples below a certain size did not display ferroelectricity, not because intrinsic size effects had suppressed it but rather due to difficulties in fabrication.

As an example, we can consider the case of $BaTiO_3$ thin films. *Feuersanger* et al. [8, 9] reported in 1963–1964 that in stoichiometric $BaTiO_3$ films prepared by electron-beam evaporation the ferroelectric phase becomes unstable for film thicknesses below about 0.1 µm. Later, similar measurements by *Slack* and *Burfoot* [10] in 1971 on flash-evaporated $BaTiO_3$ films showed that even the thinnest films they fabricated (~ 0.04 µm) showed ferroelectric switching behavior. Measurements by *Tomashpolski* et al. [11–14] in 1974 on vacuum-deposited $BaTiO_3$ films showed sharp, well-defined, dielectric anomalies near 120 °C down to film thicknesses of 0.023 µm. For a film thickness of 0.01 µm, this anomaly disappeared but an anomaly near 0 °C was still evident.

More recent results, on a range of materials, point to a much lower critical thickness, with ferroelectricity detected in polymer films down to 10 Å (*Bune* et al. in 1998 [15]) and in perovskite $Pb(Zr_{0.2}Ti_{0.8})O_3$ films down to 40 Å – 10 unit cells (*Tybell* et al. in 1999 [16]). Very recently, X-ray synchrotron studies have revealed periodic 180° stripe domains in 12 to 420 Å thick epitaxial films of $PbTiO_3$ grown on insulating $SrTiO_3$ substrates [17, 18].

The fact that the experimentally obtained minimum thickness for a ferroelectric thin film has decreased by orders of magnitude over the years is a clear sign that for the most part the suppression was due to limitations on sample quality. For example, dead layers, grain boundaries and defects such as oxygen vacancies are all known to have strong influences on ferroelectric properties.

Frequently, a surface layer with significantly different properties from those in the interior of the film can exist. The idea of a space-charge layer near the surface of a ferroelectric dates back to *Känzig* in 1955 [19]. Typically, this space charge is considered to be mainly due to oxygen vacancies. The presence of oxygen vacancies at the surface layers and their redistribution with electrical cycling has been suggested as the cause of polarization

fatigue [20–22] and in general oxygen vacancies are widely implicated in most of the failure mechanisms of ferroelectric capacitors.

A nonswitching dielectric "dead layer" [23–25] could be considered to arise from many causes, for example pinning of domain walls [26] or screening of the internal field by a depletion layer [27]. Damage can also be created at the surface layer by bombardment of the sputtering ions during the deposition of a top electrode [23], or by changes in stoichiometry due to the loss of volatile elements such as lead or oxygen.

Dead layers can suppress ferroelectricity directly and also give rise to measurement issues. For example, in bulk, the maximum in the dielectric constant is fairly well correlated with the transition temperature, but this is not always the case in thin films if there is a dead layer. As pointed out in [28], a series capacitor model is required to extract the true transition temperature, which in the case of $Ba_xSr_{1-x}TiO_3$ has been shown to be independent of thickness [29], in contrast to the temperature at which the permittivity maximum occurs, which can depend quite strongly on thickness.

4 Effect of Screening

In recent years, a degree of maturity in materials-processing techniques was reached, allowing fundamental size effects to be experimentally probed rather than those simply imposed by processing limitations. Thankfully, along with the experimental advances, one of the most significant developments in the study of ferroelectricity has been the development of powerful first-principles calculations [30]. Not only have these shed enormous light on the fundamental origin of ferroelectricity, but they are also an ideal way of probing the nature of ferroelectric size effects.

The predominant role of electrostatic boundary conditions in controlling ferroelectricity in very thin films has now been demonstrated from first principles [31–33], but in fact the idea of imperfect screening has considerable history; in the 1970s [34, 35], researchers at IBM studied the effect that a finite screening length for the electrodes would have on the critical thickness of films within the framework of the Ginzburg–Landau–Devonshire theory.

Simple Electrostatic Model

In an idealized ferroelectric capacitor where the plates are perfect conductors, as shown schematically in Fig. 1a,b, the screening charges are located precisely at the electrode/ferroelectric interface, exactly compensating the surface charges of the polarization P in the ferroelectric film. However, in realistic electrodes the screening charges are distributed over a small but finite region in the metal, as shown in Fig. 1c. The crucial physics associated with realistic electrodes is incomplete compensation: screening charges in the

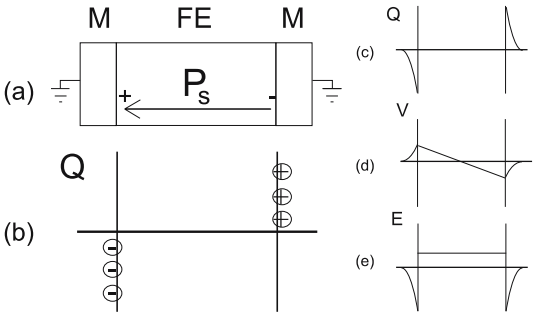

Fig. 1. (**a**) Schematic representation of a short-circuited electrode/ferroelectric/electrode structure with the ferroelectric film homogeneously polarized with spontaneous polarization P_s. (**b**) Schematic representation of the associated charge distribution in the presence of perfect electrodes. (**c**) Charge distribution, (**d**) voltage and (**e**) field profiles in the presence of realistic electrodes. Here, the film is taken to be a perfect insulator. From *Dawber* et al. [37]

metal plates are displaced from the interfaces. For a short-circuited ferroelectric capacitor, this spatial charge distribution creates finite dipoles at the interfaces and leads to an associated voltage drop

$$\Delta V = \frac{\lambda_{\text{eff}}}{\epsilon_0} P \tag{3}$$

at each interface (Fig. 1d), and a compensating depolarization potential across the film is necessary to ensure that the whole structure is an equipotential [34]. There is therefore an associated finite depolarization field $\mathcal{E}_{\text{d}}$ in the film, as shown in Fig. 1e. Assuming two similar interfaces with the top and bottom electrodes, then

$$\mathcal{E}_{\text{d}} = -2\frac{\Delta V}{d} = -2\frac{\lambda_{\text{eff}}}{d\epsilon_0} P\,, \tag{4}$$

where d is the thickness of the film. The parameter λ_{eff} has the dimension of a length and will be referred to as the *effective screening length* of the system [36]. A small screening length would mean a better screening of these surface charges, and therefore a smaller depolarization field and a more stable ferroelectric phase.

The depolarization field in the sample increases as the sample thickness is decreased and eventually suppresses ferroelectricity. There are other ways that a system can try to avoid a depolarization field, the most obvious being the formation of a ferroelectric domain structure [17, 18], but it is also becoming apparent that surface molecules and the nature of the bonding at the interface are key controlling factors in how well a ferroelectric can retain its properties as its size is reduced [38].

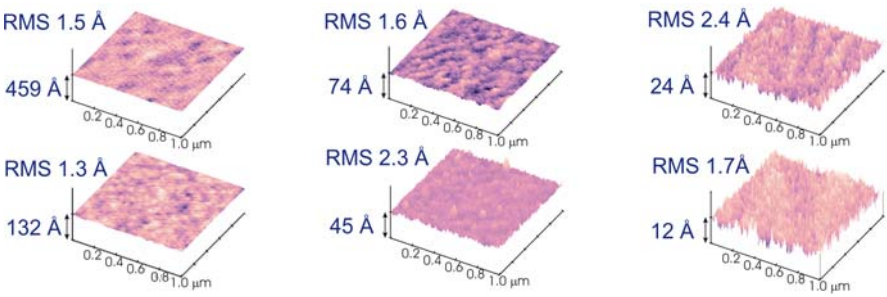

Fig. 2. Topography images in three dimensions obtained for scan areas of 1 μm^2 on $PbTiO_3$ thin films of $\sim$ 459, 132, 74, 45, 24 and 12 Å thickness, giving root-mean-square values of 1.5, 1.3, 1.6, 2.3, 2.4 and 1.7 Å respectively. The vertical scales used in these 3D representations are equal to the thickness of the samples, allowing a comparison of the roughness of the surface with the total film thickness. As can be seen from the data, the average thickness remains well defined, even for ultrathin films down to three unit cells

4.1 Recent Experimental Work: Ultrathin Films on Metallic Electrodes

The experimental approach used by our group to address the problem was to measure tetragonality versus film thickness in thin $PbTiO_3$ films using X-ray diffraction [39] and X-ray photoelectron diffraction [40, 41]. The X-ray photoelectron diffraction technique was also used to study the noncentrosymmetry of the unit cells in the same samples.

Using offaxis radio-frequency magnetron sputtering [42] onto metallic Nb-$SrTiO_3$ substrates, a series of epitaxial *c*-axis oriented $PbTiO_3$ perovskite films was grown, with thicknesses ranging from 500 Å down to one unit cell (a detailed description of the deposition parameters can be found in [43]).

To probe finite-size effects in thin films, a key requirement is to have materials with smooth surfaces, and therefore a well-defined thickness. In order to get information about the surface quality of the films, atomic force microscope topographic measurements were performed on all the samples, showing that the films are essentially atomically smooth with a root-mean-square roughness between 2 and 6 Å over $10 \times 10\,\mu m^2$ areas. The vertical scales used in the 3D representations in Fig. 2 are equal to the thickness of the samples, allowing a comparison of the roughness of the surface with the total film thickness. As can be seen from the data, the average thickness remains well defined, even for ultrathin films down to 3 unit cells.

The piezoresponse mode of the atomic force microscope was used to probe the domain structure of different films [44, 45]. Ten stripes were drawn using alternate +12 V and −12 V voltages applied to the tip over a $1.6 \times 1.6\,\mu m^2$ area. In Fig. 3, the $3.2 \times 1.6\,\mu m^2$ background piezoresponse signal containing the written stripes was then compared to the signal from the stripes,

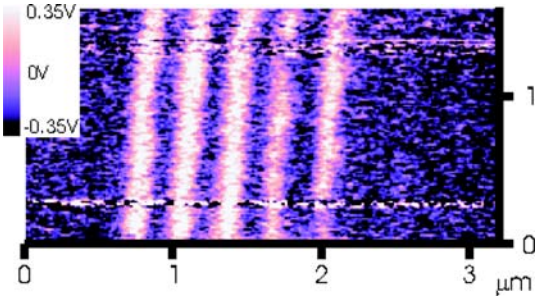

Fig. 3. Piezoresponse signal obtained after writing ten stripes using alternate +12 V and −12 V voltages applied to the tip

and found to be equal to the signal obtained for the +12 V written stripes suggesting a single polarization in the as-grown sample. All the investigated films were found to be "monodomain-like" over the studied areas, typically a few μm^2.

X-Ray Diffraction

X-ray measurements allowed us to precisely determine the thickness of the films and the c-axis lattice-parameter value, and to confirm epitaxial growth. Bulk $PbTiO_3$ is tetragonal and ferroelectric at room temperature, with $T_C = 763\,K$, $a = 3.902$–$3.904\,Å$ and $c = 4.135$–$4.156\,Å$ [46, 47]. θ–2θ scans give information on the c-axis value (c). Examples are shown in Fig. 4 for films of 396, 132 and 73 Å, revealing the thin high-intensity substrate diffraction peak as well as the broader film diffraction peak. The θ–2θ diffractograms, revealing only $(00l)$ reflections, demonstrate that the films are purely c-axis with the polarization normal to the film surface.

Laue oscillations in θ–2θ scans and low-angle reflectometry (see inset of Fig. 4 (top)) allow, through simulation, the precise determination of the number of planes involved in the diffraction, and thus the film thickness, as well as the deposition rate, even for films down to 24 Å.

Since at room temperature the a-axis lattice parameter of ferroelectric bulk $PbTiO_3$ is 3.902–3.904 Å [46, 47], very close to the 3.905 Å of the $SrTiO_3$, the films are expected to be coherent with their a-axis equal to the $SrTiO_3$ lattice parameter. Grazing incidence diffraction on a ~ 86 Å thin film confirmed this picture displaying a unique (200) reflection. Measurements of the $PbTiO_3$ (101) reflection for the thickest films (~ 504 Å and ~ 396 Å) gave an estimation of $a = 3.90 \pm 0.01$ Å. The a-axis value used below in the theoretical modeling is thus taken as constant and equal to 3.905 Å.

Being able to systematically measure the c-axis lattice parameter down to 24 Å is of interest since its value can be correlated to the macroscopic polarization, as demonstrated below. Indeed, our experiments can be described

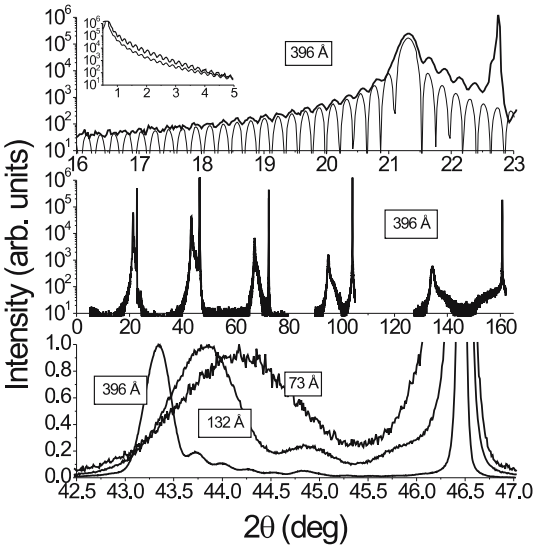

Fig. 4. *Top*: Low-angle and (001) X-ray diffraction measurements (*thick lines*) and simulations (*thin lines*) for a 396 Å thick film. *Middle*: θ–2θ diffractogram revealing (00l) reflections from $l = 1$ to 5 for the same 396 Å thick film. *Bottom*: θ–2θ diffractograms around (002) for three films of different thicknesses: 396, 132 and 73 Å, respectively, allowing the decrease of the c-axis with thickness to be clearly seen. From [39]

using the model Hamiltonian approach (see [39, 48] and the chapter by *K. M. Rabe* and *P. Ghosez* in this book for more details):

$$H_{\mathrm{mod}}^{\mathrm{film}} = H_{\mathrm{mod}}^{\mathrm{bulk}}[\xi, e_{\alpha\beta}] - \mathcal{E}_{\mathrm{d}} P \,, \tag{5}$$

where $H_{\mathrm{mod}}^{\mathrm{bulk}}[\xi, e_{\alpha\beta}]$ is the bulk model Hamiltonian expressed as a function of the ferroelectric distortion ξ and taking into account the strain e, $\mathcal{E}_{\mathrm{d}}$ is the depolarization field and P the polarization. Perfect pseudomorphic thin films on top of a cubic substrate are considered and the inplane strains ($e_{xx} = e_{yy}$) are fixed throughout the structure independently of the film thickness, in order to constrain the a-axis lattice constant imposed by the $SrTiO_3$ substrate (3.905 Å). In the model Hamiltonian approach, the strains are defined with reference to the bulk *cubic* structure of $PbTiO_3$ so that the epitaxial growth imposes $e_{xx} = e_{yy} = (a_{\mathrm{STO}} - a_{\mathrm{PTO}})/a_{\mathrm{PTO}}$ with $a_{\mathrm{STO}} = 3.905$ Å and $a_{\mathrm{PTO}} = 3.969$ Å. The energy is then minimized for different thicknesses in terms of ξ (supposed uniform and perpendicular to the film, $\xi = \xi_z$) and e_{zz}.

From the values of ξ_z we deduce P_z, using

$$P_z = \frac{1}{\Omega_0} \xi_z Z^* \,, \tag{6}$$

where Z^* is the Born effective charge. In this calculation, the polarization is enforced to be uniform throughout the whole film. Indeed, a relaxation of this constraint shows that the histogram of the possible values of P_z is extremely sharp around a given value of the polarization, confirming the validity of the uniform approach. However, surface effects, i.e., surface relaxation/rumpling, are not taken into account.

From the values of e_{zz} we deduce c/a, using the definition of strain within the model Hamiltonian approach with respect to the cubic phase:

$$e_{zz} \equiv \frac{c - a_{\mathrm{PbTiO_3}}}{a_{\mathrm{PbTiO_3}}}\,, \tag{7}$$

$$\rightarrow c = a_{\mathrm{PbTiO_3}}(1 + e_{zz})\,, \tag{8}$$

$$\rightarrow \frac{c}{a_{\mathrm{SrTiO_3}}} = \frac{a_{\mathrm{PbTiO_3}}}{a_{\mathrm{SrTiO_3}}}(1 + e_{zz})\,. \tag{9}$$

A direct relation between ξ and c/a can be obtained from a second-order development:

$$\left(\frac{c}{a}\right) = \left(\frac{c}{a}\right)_0 + \left.\frac{\partial\left(\frac{c}{a}\right)}{\partial\xi}\right|_{\xi=0} \cdot \xi + \frac{1}{2}\left.\frac{\partial^2\left(\frac{c}{a}\right)}{\partial\xi^2}\right|_{\xi=0} \cdot \xi^2\,. \tag{10}$$

By symmetry, the second term on the right has to be equal to zero, giving

$$\left(\frac{c}{a}\right) = \left(\frac{c}{a}\right)_0 + \alpha\xi^2\,. \tag{11}$$

Using again (6), we get that

$$\left(\frac{c}{a}\right) = \left(\frac{c}{a}\right)_0 + \alpha' P^2\,. \tag{12}$$

We thus see that *measuring the evolution of c/a with thickness allows us to probe the evolution of polarization as a function of film thickness.*

It was found that c decreases with decreasing thickness, suggesting a reduction of the polarization for the thinnest films.

Figure 5 shows this result: the film tetragonality, i.e., the c/a ratio, is plotted as a function of film thickness for different series of samples (top). As can be seen, the data for both series collapse and the c/a ratio decreases very substantially for films thinner than 200 Å.

We also note that a very similar reduction of tetragonality has recently been observed by *Tybell*[1]. It has also been checked experimentally that the c-axis values did not change after the deposition of a gold electrode and shorting of the gold electrode and the metallic substrate (insuring short-circuit conditions).

These results will be analyzed later.

[1] private communication with Thomas Tybell

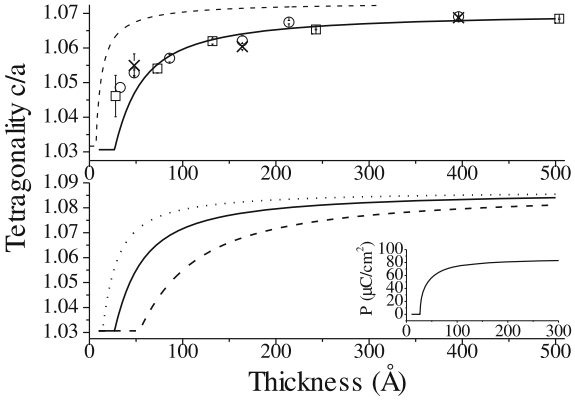

Fig. 5. Evolution of the c/a ratio with the film thickness. *Top*: experimental results for different series (*circles* and *squares*), and with a gold top electrode added (*crosses*); the *dashed line* is the phenomenological theory prediction (see main text) assuming a ratio between the extrapolation and the correlation length $\delta/\xi = 1.41$ [49]; the *solid line* is the model Hamiltonian prediction for $\lambda_{\text{eff}} = 0.12$ Å, rescaled to give a maximum tetragonality in agreement with the experimental data. *Bottom*: results from the model Hamiltonian calculations for $\lambda_{\text{eff}} = 0.23$ Å (*dashed line*), $\lambda_{\text{eff}} = 0.12$ Å (*solid line*) and $\lambda_{\text{eff}} = 0.06$ Å (*dotted line*). *Inset*: thickness dependence of the spontaneous polarization P from the model Hamiltonian for $\lambda_{\text{eff}} = 0.12$ Å. From [39]

X-Ray Photoelectron Diffraction

Another interesting approach to probing ferroelectricity in ultrathin films is to use X-ray photoelectron diffraction [50, 51], an element-specific and surface-sensitive (20–30 Å, depending on the electron mean free path) technique. X-ray photoelectron diffraction has been widely used in surface crystallography and studies of the orientation of adsorbed molecules, surface segregation, and interdiffusion at interfaces. Because of the chemical sensitivity of photoemission, a given atom type is chosen by selecting one of its core levels. The local geometry around the selected atom can be probed by performing intensity versus emission-angle scans of a chosen photoemission line. The resolution of this technique is sufficient to directly probe the intracell atomic displacements associated with ferroelectricity, and to measure the material tetragonality.

The outgoing photoemitted electrons exhibit a strongly anisotropic angular intensity distribution. This angular distribution is due to the interference of the directly emitted photoelectron wave with the scattered electron waves. The analysis of the interference (or diffraction) patterns is facilitated by the so-called forward-focusing effect taking place for photoelectron kinetic energies greater than ≈ 0.5 keV. When considering a row of atoms, scattering at the first few atoms along this row focuses the electron flux in the emitter-

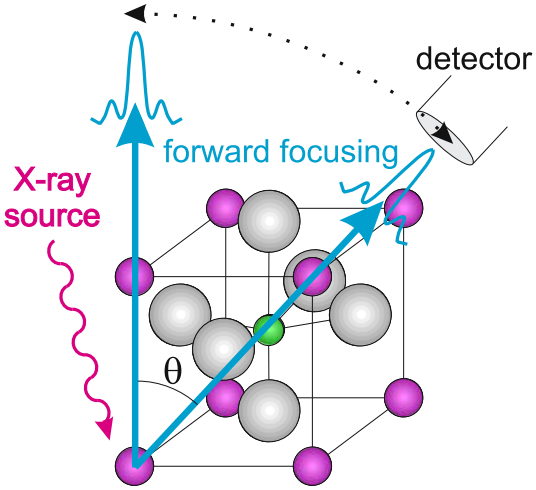

Fig. 6. Schematic representation of the forward-focusing effect with Pb atoms as the emitter in a $PbTiO_3$ unit cell. Core electrons have well-defined binding energies, and their photoemission spectra exhibit characteristic emission lines. By selecting a particular emission line, photoelectrons from a given emitter can be chosen, thus probing the local real-space environment of the emitter. The interpretation is facilitated by forward focusing of the electron flux along the emitter-scatterer direction

scatterer direction. This enhancement of the intensity in the emitter-scatterer direction is schematically illustrated in Fig. 6. The forward-focusing effect is further amplified for electron scattering by heavy atoms. In a semiclassical picture this can be understood as the focusing of the electron wave by the high number of protons in high atomic number atoms. Note that, despite the forward-focusing effect, the experimentally measured angles are sensitive to multiple interferences, refraction and possible anisotropic atom vibrations at the surface. In the present case of $PbTiO_3$, Pb scattering is highly dominant compared to the scattering by other elements.

In order to probe the tetragonality of the films, i.e., the c/a ratio of the Pb lattice, Pb was chosen as the emitter atom (Pb $4f_{7/2}$ core level, $E_{kin} = 1115.5\,eV$), and Pb−Pb forward-focusing directions were used. Since Pb atoms are absent from the substrate, this study can be done down to a monolayer of ferroelectric material.

As a second step, in order to probe the noncentrosymmetry, O was chosen as the emitter atom (O 1s core level, $E_{kin} = 724.1\,eV$), since it has the largest displacement [46] and has Pb scatterers as nearest neighbors (Fig. 7). However, the O contribution from the Nb−$SrTiO_3$ substrate becomes non-negligible for films thinner than the photoelectron inelastic mean free path, making the study of films thinner than 20 Å more difficult.

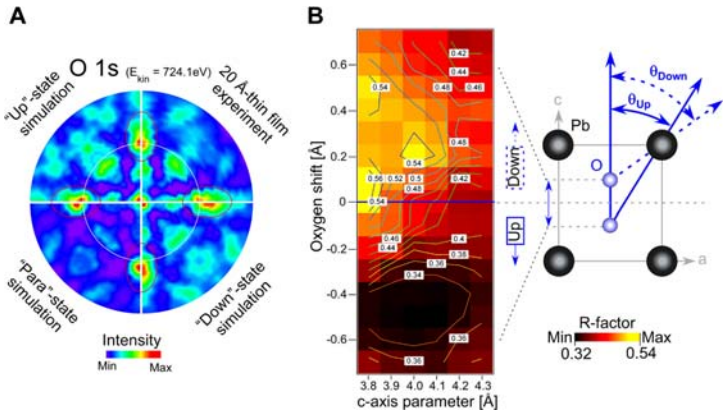

Fig. 7. (**A**) Stereographic projection of experimental and theoretical O 1 s emission line intensities on quarter hemispheres for four different cases: experimental data for a 20 Å thin film and theoretical simulations taking into account "up"-, "para"- and "down"-state structures. Normal emission corresponds to the center of the plot and grazing emission ($\theta = 70°$) to the outer border. (**B**) R-factor calculation to quantify the agreement between experiment and simulations for different structures, where a low R-factor corresponds to good agreement. A cut in the (100)-plane containing Pb and O atoms is shown to facilitate the discussion. A downward shift of Pb and O atoms optimizes the fit. From [40]

4.1.1 Results of Combined Experimental and Theoretical Investigations

The model Hamiltonian used following (5) predicts a critical thickness below which the spontaneous polarization vanishes and the c/a ratio of the resulting paraelectric phase saturates at 1.03, as a result of the mechanical constraint imposed by the substrate. This can be seen in Fig. 5 (bottom). Above the critical thickness, the spontaneous polarization gradually increases up to the bulk value, as does the c-axis lattice parameter, due to the polarization–strain coupling, known to be particularly large in $PbTiO_3$ [52]. The evolution of c/a is thus a signature of the progressive change of P and suppression of ferroelectricity in ultrathin films.

The model Hamiltonian, although appropriately describing $PbTiO_3$, is known to overestimate the polarization–strain coupling. At the bulk level, the model predicts $c/a = 1.09$ while the experimental value is equal to ~ 1.06 [48]. In order to remove this bulk overestimation, and for a direct comparison of the theoretical and experimental *evolution* of c/a, the theoretical curves in Fig. 5 (top) have been renormalized to give a tetragonality of 1.068 at 500 Å, in agreement with the experimental data. Only the strength of the polarization–strain coupling is rescaled, while the c/a value of the paraelectric phase, a priori properly predicted through the macroscopic elastic constants, can be kept unchanged, at a value of 1.03.

First-principles results for the $SrRuO_3/BaTiO_3$ interface [36] yield $\lambda_{\text{eff}} = 0.23$ Å. Because the screening might be slightly different for the present system composed of distinct interfaces, the theoretical results are reported in Fig. 5 (bottom) for slightly different values of λ_{eff}; λ_{eff} is not strictly identical to the Thomas–Fermi screening length: it does not scale with the metal carrier density only, but depends on both the metal and the metal/ferroelectric interface. Consequently, it is not trivial to estimate how it will evolve from one interface to another. The value deduced from the $SrRuO_3/BaTiO_3$ interface provides a relevant order of magnitude but it might be slightly different from that of the $PbTiO_3/Nb{-}SrTiO_3$ interface. To take this effect into account, the theoretical Fig. 5 (bottom) displays three different theoretical curves, corresponding to three slightly different screening parameters λ_{eff}; $\lambda_{\text{eff}} = 0.23$ Å, $\lambda_{\text{eff}} = 0.12$ Å, and $\lambda_{\text{eff}} = 0.06$ Å. Whatever the value of λ_{eff}, the general predictions of the model remain unchanged: there is a substantial reduction of the spontaneous polarization in ultrathin films, together with a concomitant reduction of the tetragonality. Only small quantitative differences are observed. The best agreement with the experimental data is obtained for $\lambda_{\text{eff}} = 0.12$ Å. This short screening length might suggest a better screening for the present system but might also be partly attributed to an overestimate of the theoretical critical thickness due to the simplicity of the model Hamiltonian and to the fact that the simulations were performed at $T = 0$. A similar model for $BaTiO_3$ predicts a critical thickness of 35 Å, larger than the first-principles value of 24 Å reported in [33].

Looking at the experimental points on Fig. 5 (top), both the *range* of thicknesses at which the c/a ratio starts to decrease and the *shape* of the evolution agree with the prediction of the model Hamiltonian calculations for $\lambda_{\text{eff}} = 0.12$ Å. This supports an incomplete screening of the depolarization field as the driving force for a global reduction of the polarization in perovskite ultrathin films. In contrast, the phenomenological theory including only an intrinsic suppression of ferroelectricity at the surface through the so-called extrapolation length parameter δ [49] predicts a much sharper decay with no substantial decrease of polarization predicted above 50 Å, which is not borne out by the experimental observations.

Importantly, the thinnest films have a much higher tetragonality than the value of 1.03 expected for the paraelectric phase from the macroscopic theory of elasticity. The 1.03 tetragonality corresponds to the paraelectric phase (zero polarization) strained by the $SrTiO_3$ substrate. Since $PbTiO_3$ is subject to a compressive strain, it will tend to minimize the elastic energy by elongating along the normal direction. This is completely independent of the polarization state, and can be predicted by the macroscopic theory of elasticity. So, below the critical thickness, the depolarization field has suppressed the polarization with the result of a centrosymmetric unit cell for $PbTiO_3$, but the system is tetragonal due to the lattice mismatch between the paraelectric $PbTiO_3$ and $SrTiO_3$. This tetragonality remains constant as the film thickness increases as long as the material stays paraelectric. As soon

as a spontaneous polarization appears, the related offcenter displacement between the center of effective negative charges and positive charges along the c-axis produces an additional elongation of the c-axis value, and thus a larger tetragonality.

No saturation of c/a, the signature of a complete suppression of ferroelectricity, was experimentally identified, clearly implying that films much thinner than 50 Å are still ferroelectric. Moreover, if we additionally take into account surface relaxation/rumpling [40], we find for a paraelectric film of just one unit cell a tetragonality of 1.01. This even lower paraelectric limit confirms that even the thinnest film measured by X-ray diffraction is still ferroelectric.

To follow the behavior below 24 Å we need to consider the X-ray photoelectron diffraction measurements. Considering first oxygen as the emitter atom, a fully automated computer code for calculating electron diffraction in atomic clusters via multiple scattering [53], based on the muffin-tin potential approximation [54], was used to calculate the X-ray photoelectron diffraction pattern. Comparison between the experimental measurement and the simulations (Fig. 7), both by visual examination and mathematical analysis, confirms that the measured interference pattern is best simulated with the "up"-state. This demonstrates unambiguously that, for a film as thin as 20 Å, the O atoms have a noncentrosymmetric position in the Pb cage corresponding to a nonvanishing spontaneous polarization.

In the surface region (five top unit cells) that is probed by the X-ray photoelectron diffraction technique, the evidence of polar atomic distortion may also arise from the natural atomic relaxation at the film surface and interface already present in the paraelectric phase. A proper interpretation of the data therefore requires independent quantification of both the polarization and the surface effects. From the ab-initio calculations, we know that the surface effect alone would give a picture resembling a "down"-state, the corresponding O−Pb atoms being shifted in the opposite direction from what is observed (see [40]), confirming that the shift is due to the polarization effect. The possibility of a surface antiferrodistortive reconstruction, as reported by *Streiffer* et al. [17, 18, 55], was explored but no evidence for it was found in our room-temperature experiments.

An interesting phenomenon happened here. The X-ray photoelectron diffraction measurements show that the samples are monodomains with an "up"-polarization. But the opposite polarization was determined using atomic force microscopy on the as-grown samples. After X-ray photoelectron diffraction, it was checked on the thickest films ($\sim$ 500 Å) using the same atomic force microscope procedure that the polarization was still up, meaning that X-ray photoelectron diffraction uniformly switches the polarization of the films by exposure to a conventional X-ray source, attesting to the switchable character of the polarization. The details behind the switching are presently not known, but we believe that it occurs at the initial stage of the experiment while the measurement itself is essentially done in zero field. Indeed, our re-

sults do not depend on the X-ray intensity, suggesting that the films are in an equilibrium state during the measurements. The influence of the X-ray intensity on the tetragonality was measured. A modification of the tetragonality would have indicated, via the polarization–strain coupling, a variation of the spontaneous polarization. But no dependence on the X-ray power was found.

In a second step, considering Pb as the emitter atom, X-ray photoelectron diffraction was used to determine the tetragonality. As demonstrated by the X-ray diffraction measurements, below 200 Å the tetragonality decreases as the film thickness decreases. With X-ray photoelectron diffraction, using Pb as emitter, the tetragonality was measured down to the unit-cell level as shown in Fig. 8. The absolute values of c/a, deduced from the forward-focusing angles, are particularly large. This might reflect a strong enhancement of the polarization in the probed surface region (of the order of 80%), even larger than in the theoretical prediction of *Ghosez* et al. [31]. The large increase of c/a suggested by the X-ray photoelectron diffraction measurements could also be explained by a strong increase of the strain–polarization coupling at the surface. It is difficult to discriminate between the two possible effects discussed above and a combination of both might be happening. Moreover, as previously stated, X-ray photoelectron diffraction does not necessarily measure the precise atom–atom directions, and the anomalously large forward-focusing c/a might also be partly related to other effects (anisotropic atom vibrations at the surface, refraction and multiple-scattering interferences). Therefore, a comparison with X-ray diffraction [39] may be done at the relative level, explaining why we superimposed the different results in one graph in Fig. 8, but used two distinct scales.

To study the evolution of the tetragonality as a function of the film thickness, the measured X-ray photoelectron diffraction values are compared to the c/a values obtained by X-ray diffraction. The X-ray photoelectron diffraction measurement in Fig. 8 confirms the evolution of c/a obtained from the X-ray diffraction measurements and agrees with the theoretical prediction (solid line) relying on the suppression of polarization due to imperfect screening of the depolarization field. The similar thickness dependence for the X-ray photoelectron diffraction (very surface sensitive) and the X-ray measurements (average of the whole film) implies that the polarization evolves at the surface in the same way as at the interior of the film and that there is no thick paraelectric dead layer at the surface. In addition, the X-ray photoelectron diffraction tetragonality measurement shows a continuous decrease of tetragonality down to the thickness of one unit cell. Note that a film with a thickness of one unit cell corresponds to two Pb−O and one Ti−O layers. Two ribbons are drawn in Fig. 8, labeled 1 and 2. They indicate the regions within which c/a values of 1.03 and 1.01 are crossed with respect to both c/a scales. For film thicknesses above two unit cells, the c/a values are larger than 1.03, the value expected at the bulk level for the paraelectric phase (resulting from the mechanical constraint imposed by the substrate). This observation directly

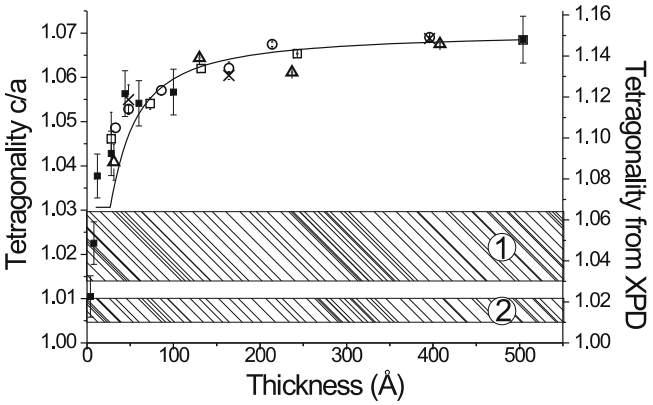

Fig. 8. Tetragonality (c/a ratio) as a function of film thickness: X-ray diffraction results for different series (*open circles*, *open squares* and *open triangles*), and with a gold top electrode added (*crosses*); X-ray photoelectron diffraction results (*full squares*); result from model Hamiltonian calculations with $\lambda_{\text{eff}} = 0.12$ Å (*solid line*). Ribbons, labeled 1 and 2, are discussed in the text. The *right scale* indicates the c/a values extracted from the X-ray photoelectron diffraction experiment

implies, via the polarization–strain coupling, that the films still have a finite – although reduced – spontaneous polarization. At thicknesses of one or two unit cells, as can be seen in Fig. 8, c/a drops even more, reaching a value close to 1.01 for the one unit-cell thick film. This further decrease highlights that macroscopic elasticity no longer applies at such thicknesses where the interlayer atomic distances are affected by surface relaxation and rumpling, as discussed in [40]. The measured tetragonality agrees with the computed value of 1.01 for the one-unit-cell thick relaxed paraelectric film, suggesting the absence of any additional ferroelectric distortion at this thickness.

This study thus directly demonstrates noncentrosymmetry, unambiguously a result of ferroelectricity in $PbTiO_3$ thin films down to 20 Å. The measurements of the tetragonality, with a continuous decrease down to the bare substrate, show that even extremely thin films (3 unit cells) have a c/a value larger than 1.03, attesting to the presence of a nonvanishing spontaneous polarization at this thickness scale. As the film thickness is reduced to a single unit cell, the experiments, together with calculations, strongly suggest that both noncentrosymmetry and tetragonality are governed by surface effects, giving rise, for our geometry, to a polar relaxed structure but probably without a switchable ferroelectric distortion.

4.1.2 Other Similar Studies

The effect of thickness scaling for ultrathin perovskite films in the presence of real electrodes was studied by the group of *Ramesh* in thin c-axis oriented $Pb(Zr_{0.2}Ti_{0.8})O_3/SrRuO_3$ heterostructures grown epitaxially and coherently

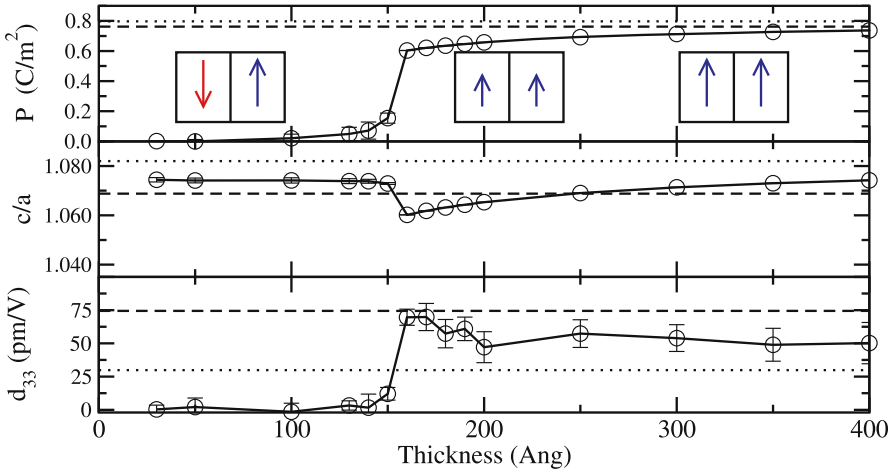

Fig. 9. Theoretical thickness dependence of the normal average polarization P, the tetragonality c/a, and the out-of-plane piezoelectric constant d_{33} at room temperature. The evolution of the domain structure from monodomain to polydomain is represented in the *inset*. From [57]

on $SrTiO_3$ insulating substrates by pulsed laser deposition [56]. This work also suggests that the nature of the electrostatics at the ferroelectric electrode interface plays a significant role in the scaling of ferroelectric thin films. However, in contrast to our own work, they did not find a concomittant decrease in the tetragonality, while a drastic reduction in the switched polarization was observed, as shown in Fig. 9. This apparent contradiction was explained theoretically on the basis of a polydomain-formation model.

The group of *Noh* also studied the thickness-dependent ferroelectric properties in fully strained $SrRuO_3/BaTiO_3/SrRuO_3$ ultrathin capacitors, with ultrathin $BaTiO_3$ layers from 30 to 5 nm [58] and measured the decrease in polarization from electrical measurements. X-ray diffraction measurements showed a decrease of the c-axis lattice constant as the film thickness decreases, although remaining larger than the bulk value for all the samples. They also have claimed to measure the depolarization field from the relaxation-time characteristic of the polarization [59], as shown in Fig. 10.

4.2 Scaling of the Coercive Field

Beyond the changes in polarization, one of the most relevant parameters that changes significantly as the sample thickness is reduced is the coercive field. For the last forty years the semiempirical scaling law [60, 61], $E_c(d) \propto d^{-2/3}$, has been used successfully to describe the thickness dependence of the coercive field in ferroelectric films ranging from 100 µm to 200 nm [62]. A new derivation of this scaling law based on inhomogeneous, as opposed to homo-

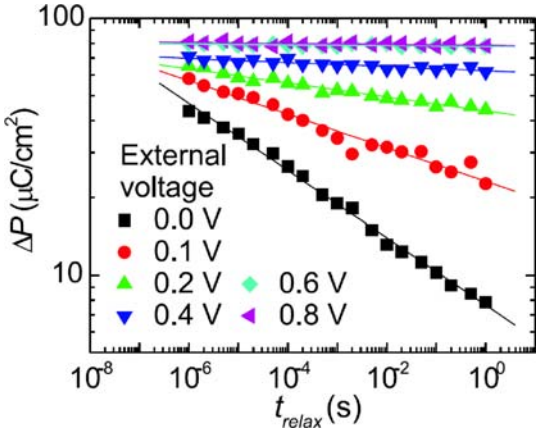

Fig. 10. Dependence of the polarization relaxation time under external voltages in a 15-nm thick $BaTiO_3$ capacitor. From [59]

geneous, nucleation has recently been developed by *Chandra* et al. [63]. In the ultrathin polyvinyliden fluoride films of *Bune* et al. [15], a deviation from this relationship was seen for the thinnest films [64]. Although they attribute this to a new kind of switching taking place (simultaneous reversal of polarization, as opposed to nucleation and growth of domains), *Dawber* et al. [37] have shown, on the contrary, that if the effects of a finite depolarization field due to incomplete screening in the electrode are taken into account, then the scaling law holds over six decades of thickness and the coercive field does not deviate from the value predicted by the scaling law as shown in Fig. 11. Recently, *Pertsev* et al. [65] measured coercive fields in very thin $PbZr_{0.52}Ti_{0.48}O_3$ films. Although they have used a different model to explain their data, it can be seen that in fact the $d^{-2/3}$ scaling law describes the data very well.

It is an interesting point that if the depolarization field exceeds the coercive field then the material is expected to form a polydomain ground state. In practical terms this may sometimes be the meaningful definition of the "critical thickness for ferroelectricity", rather than defining it as the thickness at which the system goes from ferroelectric to paraelectric.

4.3 Thin Films on Insulating Substrates

In the work of *Streiffer* et al. [17, 18], thin *c*-axis oriented $PbTiO_3$ perovskite films were grown epitaxially and coherently on $SrTiO_3$ insulating substrates by metalorganic chemical vapor deposition. In-situ X-ray synchrotron diffraction studies revealed 180° stripe domains with periods 1.2–10 nm (going as $\sim d^{1/2}$), and PbO-terminated surface c(2 × 2) reconstruction, in films from 420 down to 12 Å thickness. Because here the films are grown on an insu-

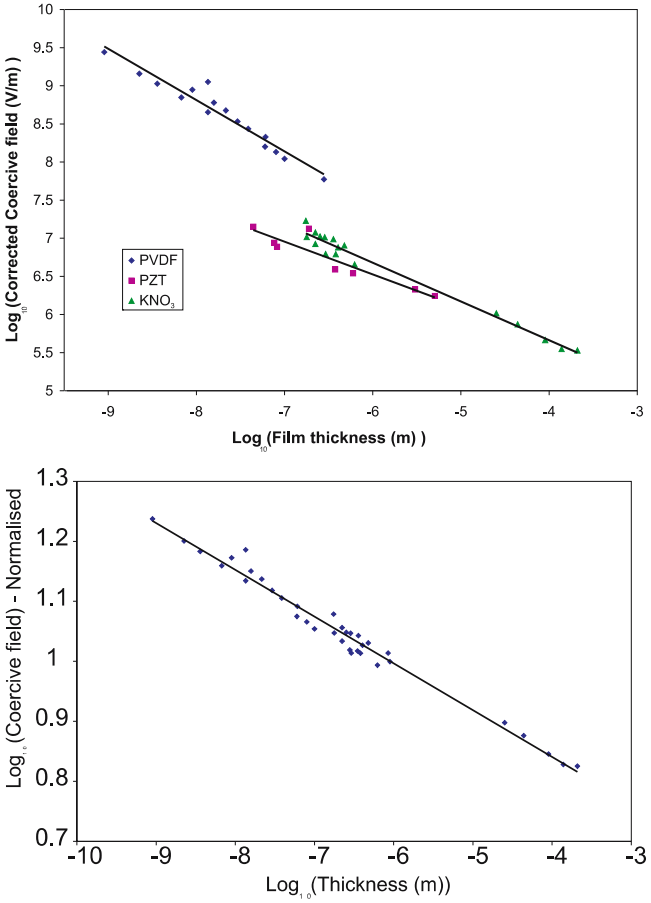

Fig. 11. The scaling of coercive field with thickness in ferroelectrics, from mm to nm scale. The *bottom* figure is the three sets of data from the *upper* figure all normalized to the same value at $10^{-6.5}$ m. From [37]

lating substrate, domains of opposite polarization are formed to reduce the depolarization field.

In their work on epitaxial $PbTiO_3$ thin films grown on insulating $SrTiO_3$ and conducting Nb-doped $SrTiO_3$ substrates, *van Helvoort* et al. [66] showed that all their samples, with thicknesses ranging from 50 to 200 Å, displayed a compressively strained layer at the $PbTiO_3/SrTiO_3$ interface, with the strain vector parallel to the polarization direction. They also showed that the width of this strained layer, $\sim$ 15–30 Å, was dependent on the electrode environment. These findings rely on low-angle annular dark-field scanning transmission electron microscopy. The X-ray diffraction analysis revealed a gradual decrease in their measured *c*-axis lattice parameter from the bulk value of 4.16 Å, for films thinner than $\sim$ 200 Å. The size of the strained

interfacial layer was measured to be 27–30 Å (∼ 7 unit cells) for $PbTiO_3$ grown on insulating $SrTiO_3$, and 18–20 Å (∼ 5 unit cells) for $PbTiO_3$ grown on conducting Nb-doped $SrTiO_3$ (similar to the value found for $PbTiO_3$ grown on insulating $SrTiO_3$, but covered by a Pt/Au electrode), independent of thickness. If we attribute this decrease of the *c*-axis to a decrease of the polarization, the data suggest that the polarization is reduced for films grown on insulating $SrTiO_3$.

All these data show that when films are grown on insulating materials, some alternative mechanism is used to compensate the depolarization field, and there appears to be a number of possibilities, i.e., the formation of a domain structure, screening via surface adsorbates, or formation of a strained interfacial layer. In general, all these screening mechanisms would be expected to be less effective than a conducting electrode.

5 Superlattices

Growing superlattices is an interesting way of making artificial materials by combining epitaxially perovskites with different electronic properties and lattice parameters. Historically, much of this effort has been focused on $BaTiO_3/SrTiO_3$ [67–74]. Other combinations that have been studied include $KNbO_3/KTaO_3$ [75–78], $PbTiO_3/SrTiO_3$ [79], $PbTiO_3/BaTiO_3$ [80], $PbTiO_3/PbZrO_3$ [81, 82], and tricolor superlattices of $SrTiO_3/BaTiO_3/CaTiO_3$ [83, 84].

Other studies have shown that superlattices can be designed with unusual properties. For example, a superlattice consisting of thin layers of $BaCuO_2$ and $SrCuO_2$ exhibits superconductivity, whereas neither of these two oxides is superconducting by itself [85], or a superlattice consisting of thin layers of $SrZrO_3$ and $SrTiO_3$ exhibits ferroelectricity, whereas neither of these two oxides is ferroelectric [86]. *Warusawithana* et al. [83] first and more recently *Lee* et al. [84] (see also [87]) assembled their superlattice with three different building blocks: $BaTiO_3$, $SrTiO_3$ and $CaTiO_3$. The use of three different compounds breaks the inversion symmetry normally associated with ferroelectricity, resulting in asymmetric polarization and an extra degree of freedom for optimizing the ferroelectric properties [88]. Experimental efforts in superlattices with compositional breaking of inversion symmetry are starting also on magnetic systems (*Ogawa* et al. [89]).

All these studies show that such structures can be built with atomic precision and they can possess properties that surpass those of the individual building blocks, and underline the potential of designing artificial superlattices with unique properties.

The construction of ferroelectric superlattices also allows one to study the behavior of the polarization as the thickness of a ferroelectric layer in a dielectric environment is reduced. In $BaTiO_3/SrTiO_3$, first-principles studies [71] suggest that both the $SrTiO_3$ and $BaTiO_3$ layers are polarized such

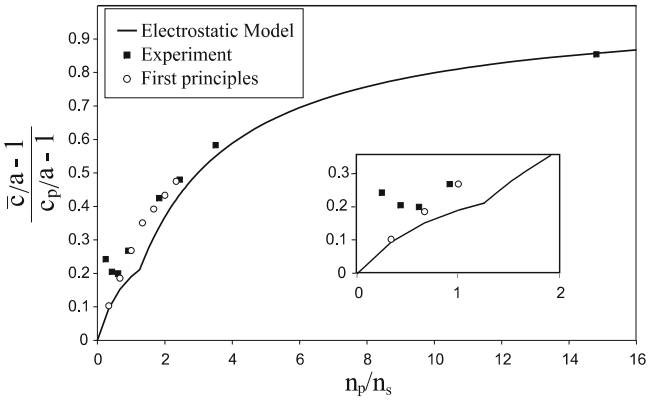

Fig. 12. Comparison of results from the first-principles calculations (*open circles*), the electrostatic model (*solid line*) and experiment (*solid squares*), obtained by plotting the fractional change in the superlattice tetragonality $\frac{\bar{c}}{a} - 1$ relative to the estimated tetragonality of bulk $PbTiO_3$ with the inplane lattice parameter constrained to the $SrTiO_3$ substrate. *Inset*: close-up of the region with the anomalous recovery. From [90]

that the polarization is approximately uniform throughout the superlattice. The driving force behind this is the large electrostatic energy penalty for a buildup of charge at the interface caused by discontinuous polarization in the normal direction. This suggests that superlattices present an opportunity to create a model system for studying ferroelectric size effects with electrostatics as the driving force.

In a very similar way to the studies on thin films, we can use X-ray diffraction to follow the evolution of the polarization in $PbTiO_3/SrTiO_3$ superlattices by following the evolution of the average c-axis lattice parameter, $\bar{c}$, as the $PbTiO_3$ layer thickness is varied while the $SrTiO_3$ layer thickness is kept constant at 3 unit cells. If the wavelength of the superlattice is $n\bar{c}$ then the nth peak in a θ–2θ scan will always correspond to $\bar{c}$ irrespective of the value of n, allowing the average c-axis lattice parameter of the superlattice to be easily determined. In practice, this peak is easily identifiable due to its high intensity and proximity to the substrate peak. Intuitively, one expects a decrease of the ferroelectric polarization as the thickness of the $PbTiO_3$ layers relative to the $SrTiO_3$ layers is reduced, which should result in a concomitant decrease of the average lattice parameter. For samples with a ratio of $PbTiO_3/SrTiO_3$ greater than one, this is in fact what we observed, as shown in Fig. 12.

We were able to understand the behavior using an electrostatic model in which the energy of the superlattice was considered as the weighted sum of the material energy, the energy cost of a particular polarization for $PbTiO_3$ and $SrTiO_3$ (computed from first principles), and an electrostatic energy cost

for a difference in polarization in the two materials, an expression derived by considering the electrostatic boundary conditions in the problem. This model is indeed very similar in conception to that used for understanding the decrease in polarization as the thickness of a $PbTiO_3$ film is decreased. The full details of this model can be found elsewhere [90], the key point being that the electrostatic energy of a given layer in a superlattice with layer thicknesses l_p and l_s is obtained from short-circuit boundary conditions for each bilayer as a function of the polarizations P_p^0 and P_s^0, assuming continuity of the electric displacement, and is given by

$$E_{elec}(P_p^0, P_s^0) = \frac{l_p l_s}{\varepsilon_0(l_p + l_s)}(P_s^0 - P_p^0)^2 . \tag{13}$$

The most important point to draw from this is that there is a large energy cost if the polarizations differ in the two materials. Therefore, the values of the polarization in the two materials always remain very similar for any geometry. In addition, the size of this polarization is predicted to decrease as the fraction of $PbTiO_3$ relative to $SrTiO_3$ is reduced. In Fig. 12 we show the evolution of the tetragonality with $PbTiO_3$ thickness for the experimental results, the electrostatic model, and full first-principles calculations, in each case normalized by the estimated tetragonality of fully ferroelectric $PbTiO_3$.

It can be seen that for samples that have more $PbTiO_3$ than $SrTiO_3$ the experimental data and theoretical predictions are in fairly good agreement. However, neither theoretical approach can account for the observed experimental behavior when the ratio of $PbTiO_3$ to $SrTiO_3$ is further decreased. Here, we see an increase of the lattice parameter, which corresponds to a recovery of the ferroelectricity, confirmed by using piezoelectric atomic force microscope measurements. At this point the recovery is not understood, but it suggests the possibility that at reduced dimensions the unusual and potentially useful behavior that might be obtained is beyond even that which is theoretically anticipated.

From a different perspective, putting its limitations aside, the possession of a simple model to describe the system is a tremendous tool for accelerating the progress towards the research goal of tailored materials for advanced applications, moving us from simple trial and error towards targeted fabrication of the most interesting geometries and combinations of materials.

6 Other Geometries

To this point we have focused on size effects due to the reduction of the thicknes of a thin film, as this is the most experimentally accessible size effect that can be studied by the growth of epitaxial thin films. Naturally, however, reducing the size of a ferroelectric sample in more than one dimension will also have significant effects, and in a technological context where devices are

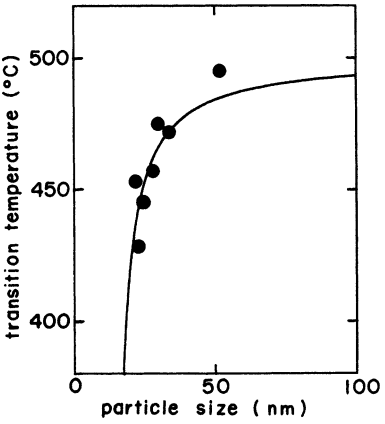

Fig. 13. Transition temperature versus particle size measured in $PbTiO_3$ ultrathin particles by *Ishikawa* et al. [91]

rarely infinite planes, these effects are at least as, if not more, relevant than those related to reduction of film thickness.

6.1 Nanoparticles

Many results have suggested that T_C decreases for particles below a characteristic size. Transition temperature versus particle size was measured in 1988 in $PbTiO_3$ ultrafine particles by *Ishikawa* et al. [91]. $PbTiO_3$ fine particles were prepared by an alkoxide method and Raman studies of the samples were performed for different average particle size as a function of temperature. The ferroelectric T_C was indirectly measured as the temperature at which the frequency of the soft–mode E(1TO) vanished. T_C was found to decrease with decreasing particle size with $d_{crit} = 12.6\,nm$, as shown in Fig. 13. Size effects on ferroelectricity of ultrafine particles of $PbTiO_3$ were also studied by *Jiang* and *Zhong* et al. [92, 93]. Particles ranging from 20 to 2000 nm in diameter were produced by a sol-gel process followed by calcining at different temperatures. High-resolution transmission electron microscopy was used to image the nanostructure of these ultrafine ferroelectric lead titanate particles. High-resolution images and selected-area diffraction patterns showed that all the particles had tetragonal structure; the c/a ratio and domain size both decreased with decreasing particle size and the particles became monodomain when their diameter was less than 20 nm. A domain-wall width of 14 Å was deduced from strain contrast shown by 90° domain walls.

In 1989, *Uchino* et al. [94] performed a detailed study of the variation of the tetragonal distortion c/a with particle size in $BaTiO_3$ and, having identified the T_C as that temperature at which c/a tends to 1, estimated the critical size for the existence of ferroelectricity $d_{crit} = 120\,nm$. *Tsunekawa* et al. [95] studied the critical size and anomalous lattice expansion in nanocrystalline $BaTiO_3$ particles prepared by the alkoxide method, with sizes ranging from 250 to 15 nm in diameter. The lattice constants were obtained from the elec-

tron-diffraction patterns of various orientations of single particles in the size range of 15–250 nm in diameter and indicated a change from a tetragonal (ferroelectric) phase to a cubic (paraelectric) one occurring around 80 nm in diameter.

The ability to produce still smaller nanoparticles continues to evolve. Sol-gel synthesis of freestanding ferroelectric $PbZr_{0.5}Ti_{0.5}O_3$ nanoparticles of 10–30 nm was demonstrated by *Liu* et al. [96]. *O'Brien* et al. [97] demonstrated the synthesis of monodisperse nanoparticles of barium titanate with diameters ranging from 6 to 12 nm using sol-gel techniques combined with nanoparticle-synthesis methods.

6.2 Areal Size Effects

Size effects related to reduction of the areal size of ferroelectrics are perhaps of more practical significance than those related to thickness, because the critical area limits the maximum density of any ferroelectric memory device.

A number of approaches have been used to fabricate ferroelectric capacitors with small areas [2]. These include focused-ion-beam milling, electron-beam direct writing, and a number of techniques for producing arrays of nanoscale capacitors by self-patterning. In the focused-ion-beam milling procedure, the minimum size can be limited by the implantation of Ga ions that occurs in the processing, though some steps can be taken to "repair" this damage after deposition. The electron-beam direct writing technique has been successful in producing some extremely small structures, but is a time-consuming technique. Both focused-ion-beam [98,99] and electron-beam direct writing [100] have been used to fabricate structures with lateral size below 100 nm. It does not appear that reduction of areal capacitor size to this point significantly affects the ferroelectric properties, provided damage is not caused to the material in fabrication.

6.3 Self-Patterning

For practical applications, the idea of producing ferroelectric nanostructures by self-patterning methods is extremely appealing. One way to produce self-patterned arrays of nanocrystals is to induce ordering by making use of interactions between islands through the substrate. This approach could be used to produce arrays of metallic nanoelectrodes on top of a ferroelectric film [101, 102] or alternatively arrays of crystals from the ferroelectric materials themselves [103, 104]. The description of self-patterned ferroelectric nanocrystals by the models of Schukin and Williams has been undertaken by *Dawber* et al. [105]. Two groups have grown $PbTiO_3$ nanocrystals on Pt/Si(111) substrates to measure size effects in ferroelectricity [106, 107]. These studies both show a lack of piezoresponse in structures below ~ 20 nm in lateral size. There remain questions over whether this is a limitation of the

measuring technique, or whether mechanical constraints hinder the piezoresponse of the nanocrystal, and it seems unlikely that this represents a fundamental size limit for ferroelectricity. *Chu* et al. [108] have highlighted the role that misfit dislocations can play in hampering ferroelectricity in small structures.

6.4 Novel Ferroelectric Geometries

Recently, some interesting novel geometries for ferroelectric materials, briefly discussed below, have been explored.

6.4.1 Nanotubes

Ferroelectric nanotubes can now be grown within a silicon matrix. $BaTiO_3$ and $PbZr_{0.52}Ti_{0.48}O_3$ tubes with diameters from 500 nm up to several µm, wall thickness of 90–100 nm, and lengths of more than 100 µm were realized by a fabrication method based on wetting of the pore wall of porous templates. Piezoresponse scanning probe microscopy showed ferroelectric switching in submicrometer tubes (lead zirconate titanate tube with an outer diameter of 700 nm and wall thickness of 90 nm) [109]. High aspect ratio transparent strontium-bismuth-tantalate nanotubes, with wall thickness of $\sim$ 40 nm, diameters ranging from a few hundred nanometers to 4 µm and lengths about 100 µm, were realized using liquid-source misted chemical deposition [109–111]. A variety of applications for these structures could be envisaged including pyroelectric detectors, piezoelectric ink-jet printers, and 3D trenched capacitors for high-density memories. Little is known about what effect this geometry has on the ferroelectric properties.

6.4.2 Nanowires – Nanorods

Ferroelectric materials can also be grown as "nanowires" or "nanorods" [112–114]. These structures can be realized using solution-phase decomposition of bimetallic alkoxide precursors in the presence of coordinating ligands. Single-crystal $BaTiO_3$ and $SrTiO_3$ nanowires of diameters 5–70 nm and length reaching up to 10 µm have been achieved. Scanning probe microscopy investigations showed that local nonvolatile electric polarization can be reproducibly induced and manipulated on nanowires as small as 10 nm in diameter. First-principles simulations clearly have enormous potential in helping to understand the ferroelectric behavior of nanosize ferroelectric objects and the effect that unusual geometries will have. There have been some studies of this kind on nanodisks and nanowires [115–117].

References

[1] V. Skumryev, S. Stoyanov, Y. Zhang, G. Hadjipanayis, D. Givord, J. Nogues: Beating the superparamagnetic limit with exchange bias, Nature **423**, 850–853 (2003) 305

[2] A. Ruediger, T. Schneller, A. Roelofs, S. Tiedke, T. Schmitz, R. Waser: Nanosize ferroelectric oxides – tracking down the superparaelectric limit, Appl. Phys. A **80**, 1247–1255 (2005) 305, 328

[3] P. Ghosez, J. Junquera: First-principles modeling of ferroelectric oxide nanostructures, in M. Rieth, W. Schommers (Eds.): *Nanocomposites, Nano-Assemblies, and Nanosurfaces*, vol. 9, Handbook of Theoretical and Computational Nanotechnology (American Scientific Publishers, Stevenson Ranch 2006) 306

[4] R. Kretschmer, K. Binder: Surface effects on phase transitions in ferroelectrics and dipolar magnets, Phys. Rev. B **20**, 1065–1076 (1979) 306

[5] D. R. Tilley, B. Zeks: Landau theory of phase transitions in thick films, Solid State Commun. **49**, 823 (1984) 306

[6] S. Li, J. A. Eastman, Z. Li, C. M. Foster, R. E. Newnham, L. E. Cross: Size effects in nanostructures ferroelectrics, Phys. Lett. A **212**, 341–346 (1996) 307

[7] S. Li, J. A. Eastman, J. M. Vetrone, C. M. Foster, R. E. Newnham, L. E. Cross: Dimension and size effects in ferroelectrics, Jpn. J. Appl. Phys. **36**, 5169–5174 (1997) 307

[8] A. E. Feuersanger, P. Lublin: Electrical properties and structure of barium titanate films, J. Electrochem. Soc. **110**, C192 (1963) 307

[9] A. E. Feuersanger, A. K. Hagenlocher, A. L. Solomon: Preparation and properties of thin barium titanate films, J. Electrochem. Soc. **111**, 1387–1391 (1964) 307

[10] J. R. Slack, J. C. Burfoot: Electrical properties of flash evaporated ferroelectric $BaTiO_3$ thin films, J. Phys. C **4**, 898–909 (1971) 307

[11] Y. Y. Tomashpolski: Structure studies of ferroelectric vacuum deposits, Ferroelectrics **7**, 253–255 (1974) 307

[12] Y. Y. Tomashpolski, M. A. Sevostia, M. V. Pentegov: Ferroelectric vacuum deposits of complex oxide type structure, Ferroelectrics **7**, 257–258 (1974) 307

[13] Y. Y. Tomashpolski, M. A. Sevostia: Structure of barium-titanate films produced by vacuum evaporation, Kristallografija **19**, 1040 (1974) 307

[14] Y. Y. Tomashpolski, M. A. Sevostia: Ferroelectric nucleus in barium-titanate, Fiz. Tverd. Tela **16**, 2689–2692 (1974) 307

[15] A. V. Bune, V. M. Fridkin, S. Ducharme, L. M. Blinov, S. P. Palto, A. V. Sorokin, S. G. Yudin, A. Zlatkin: Two-dimensional ferroelectric films, Nature (London) **391**, 874–877 (1998) 307, 322

[16] T. Tybell, C. H. Ahn, J.-M. Triscone: Ferroelectricity in thin perovskite films, Appl. Phys. Lett. **75**, 856–858 (1999) 307

[17] S. K. Streiffer, J. A. Eastman, D. D. Fong, C. Thompson, A. Munkholm, M. V. Ramana Murty, O. Auciello, G. R. Bai, G. B. Stephenson: Observation of nanoscale 180 stripe domains in ferroelectric $PbTiO_3$ thin films, Phys. Rev. Lett. **89**, 067601 (2002) 307, 309, 318, 322

[18] D. D. Fong, G. B. Stephenson, S. K. Streiffer, J. A. Eastman, O. Auciello, P. H. Fuoss, C. Thompson: Ferroelectricity in ultrathin perovskite films, Science **304**, 1650–1653 (2004) 307, 309, 318, 322
[19] W. Känzig: Space charge layer near the surface of a ferroelectric, Phys. Rev. **98**, 549 (1955) 307
[20] I. K. Yoo, S. B. Desu: Mechanism of fatigue in ferroelectric thin films, Phys. Sat. Sol. A **133**, 565 (1992) 308
[21] M. Dawber, J. F. Scott: A model for fatigue in ferroelectric perovskite thin films, Appl. Phys. Lett. **76**, 1060–1062 (2000) 308
[22] V. C. Lo: Modeling the role of oxygen vacancy on ferroelectric properties in thin films, J. Appl. Phys. **92**, 6778–6786 (2002) 308
[23] P. K. Larsen, G. J. M. Dormans, D. J. Taylor, P. J. van Veldhoven: Ferroelectric properties and fatigue of $PbZr_{0.51}Ti_{0.49}O_3$ thin films of varying thickness: Blocking layer model, J. Appl. Phys. **76**, 2405–2413 (1994) 308
[24] S. L. Miller, R. D. Nasby, J. R. Schwank, M. S. Rodgers, P. V. Dressendorfer: Device modeling of ferroelectric capacitors, J. Appl. Phys. **68**, 6463–6471 (1990) 308
[25] A. K. Tagantsev, M. Landivar, E. Colla, N. Setter: Identification of passive layer in ferroelectric thin films from their switching parameters, J. Appl. Phys. **78**, 2623–2630 (1995) 308
[26] N. I. Lebedev, A. S. Sigov: Surface inhomogeneties and coercive field of thin ferroelectric film, Integr. Ferroelectr. **4**, 21 (1994) 308
[27] A. K. Tagantsev: Size effects in polarization switching in ferroelectric thin films, Integr. Ferroelectr. **16**, 237 (1997) 308
[28] O. G. Vendik, S. P. Zubko: Ferroelectric phase transition and maximum dielectric permittivity of displacement type ferroelectrics ($Ba_xSr_{1-x}TiO_3$), J. Appl. Phys. **88**, 5343–5350 (2000) 308
[29] A. Lookman, R. M. Bowman, J. M. Gregg, J. Kut, S. Rios, M. Dawber, A. Ruediger, J. F. Scott: Thickness independence of true phase transition temperatures in barium strontium titanate films, J. Appl. Phys. **96**, 555–562 (2004) 308
[30] M. Dawber, K. M. Rabe, J. F. Scott: Physics of thin ferroelectric oxides, Rev. Mod. Phys. **77**, 1083–1130 (2005) 308
[31] P. Ghosez, K. M. Rabe: Microscopic model of ferroelectricity in stress-free $PbTiO_3$ ultrathin films, Appl. Phys. Lett. **76**, 2767–2769 (2000) 308, 319
[32] B. Meyer, D. Vanderbilt: Ab-initio study of $BaTiO_3$ and $PbTiO_3$ surfaces in external electric fields, Phys. Rev. B **63**, 205426 (2001) 308
[33] J. Junquera, P. Ghosez: Critical thickness for ferroelectricity in perovskite ultrathin films, Nature (London) **422**, 506–509 (2003) 308, 317
[34] R. R. Mehta, B. D. Silverman, J. T. Jacobs: Depolarization fields in thin ferroelectric films, J. Appl. Phys. **44**, 3379–3385 (1973) 308, 309
[35] I. P. Batra, P. Wurfel, B. D. Silverman: Depolarization field and stability considerations in thin ferroelectric films, J. Vac. Sci. Technol. **10**, 687–692 (1973) 308
[36] J. Junquera, K. M. Rabe, P. Ghosez: Effects of the depolarizing fields in perovskite ultrathin films (2003), unpublished 309, 317
[37] M. Dawber, P. Chandra, P. B. Littlewood, J. F. Scott: Depolarization corrections to the coercive field in thin-film ferroelectrics, J. Phys. Condens. Matter **15**, L393–L398 (2003) 309, 322, 323

[38] D. D. Fong, A. M. Kolpak, J. A. Eastman, S. K. Streiffer, P. H. Fuoss, G. B. Stephenson, C. Thompson, D. M. Kim, K. J. Choi, C. B. Eom, I. Grinberg, A. M. Rappe: Stabilization of monodomain polarization in ultrathin $PbTiO_3$ films, Phys. Rev. Lett. **96**, 1–4 (2006) 309

[39] C. Lichtensteiger, J.-M. Triscone, J. Junquera, P. Ghosez: Ferroelectricity and tetragonality in ultrathin $PbTiO_3$ films, Phys. Rev. Lett. **94**, 047603 (2005) 310, 312, 314, 319

[40] L. Despont, C. Lichtensteiger, C. Koitzsch, F. Clerc, M. G. Garnier, F. J. Garcia de Abajo, E. Bousquet, P. Ghosez, J.-M. Triscone, P. Aebi: Direct evidence for ferroelectric polar distortion in ultrathin lead titanate perovskite films, Phys. Rev. B **73**, 094110 (2006) 310, 316, 318, 320

[41] L. Despont, C. Lichtensteiger, F. Clerc, M. G. Garnier, F. J. Garcia de Abajo, M. A. Van Hove, J.-M. Triscone, P. Aebi: X-ray photoelectron diffraction study of ultrathin $PbTiO_3$ films, Eur. Phys. J. B **49**, 141–146 (2006) 310

[42] C. B. Eom, J. Z. Sun, B. M. Lairson, S. K. Streiffer, A. F. Marshall, K. Yamamoto, S. M. Anlage, J. C. Bravman, T. H. Geballe, S. S. Laderman, R. C. Taber, R. D. Jacowitz: Synthesis and properties of $YBa_2Cu_3O_7$ thin films grown in situ by 90° off-axis single magnetron sputtering, Physica C **171**, 354–383 (1990) 310

[43] C. Lichtensteiger, J.-M. Triscone: Investigation of ferroelectricity in ultrathin $PbTiO_3$ films, Integr. Ferroelectr. **61**, 143–148 (2004) 310

[44] T. Tybell, C. H. Ahn, J.-M. Triscone: Control and imaging of ferroelectric domains over large areas with nanometer resolution in atomically smooth epitaxial $Pb(Zr_{0.2}Ti_{0.8})O_3$ thin films, Appl. Phys. Lett. **72**, 1454–1456 (1998) 310

[45] A. K. Sarin Kumar, P. Paruch, D. Marré, L. Pellegrino, T. Tybell, S. Ballandras, J.-M. Triscone: A novel high frequency surface acoustic wave device based on piezoelectric interdigital transducers, Ferroelectrics **63**, 55–62 (2004) 310

[46] R. J. Nelmes, W. F. Kuhs: The crystal structure of tetragonal $PbTiO_3$ at room temperature and at 700 K, Solid State Commun. **54**, 721–723 (1985) 311, 315

[47] J. Joseph, T. M. Vimala, V. Sivasubramanian, V. R. K. Murthy: Structural investigations on $Pb(Zr_xTi_{1-x})O_3$ solid solutions using the X-ray Rietveld method, J. Mater. Sci. **35**, 1571–1575 (2000) 311

[48] U. V. Waghmare, K. M. Rabe: Ab initio statistical mechanics of the ferroelectric phase transition in $PbTiO_3$, Phys. Rev. B **55**, 6161–6173 (1997) 312, 316

[49] A. G. Zembilgotov, N. A. Pertsev, H. Kohlstedt, R. Waser: Ultrathin epitaxial ferroelectric films grown on compressive substrates: Competition between the surface and strain effects, J. Appl. Phys. **91**, 2247–2254 (2002) 314, 317

[50] W. F. Egelhoff, Jr: X-ray photoelectron and Auger electron forward scattering. a new tool for surface crystallography, Crit. Rev. Solid State Mater. Sci. **16**, 213–235 (1990) 314

[51] C. S. Fadley: *Synchrotron Radiation Research: Advances in Surface Science*, R. Z. Bachrach edn (Plenum, New York 1990) 314

[52] R. E. Cohen: Origin of ferroelectricity in perovskite oxides, Nature (London) **358**, 136–138 (1992) 316

[53] F. J. Garcia de Abajo, M. A. Van Hove, C. S. Fadley: Multiple scattering of electrons in solids and molecules: A cluster-model approach, Phys. Rev. B **63**, 075404 (2001) 318
[54] J. B. Pendry: *Low Energy Electron Diffraction* (Academic Press, London 1974) 318
[55] A. Munkholm, S. K. Streiffer, M. V. Ramana Murty, J. A. Eastman, C. Thompson, O. Auciello, L. Thompson, J. F. Moore, G. B. Stephenson: Antiferrodistortive reconstruction of the $PbTiO_3$ (001) surface, Phys. Rev. Lett. **88**, 016101 (2002) 318
[56] V. Nagarajan, S. Prasertchoung, T. Zhao, H. Zheng, J. Ouyang, R. Ramesh, W. Tian, X. Q. Pan, D. M. Kim, C. B. Eom, H. Kohlstedt, R. Waser: Size effects in ultrathin epitaxial ferroelectric heterostructures, Appl. Phys. Lett. **84**, 5225–5227 (2004) 321
[57] V. Nagarajan, J. Junquera, J. Q. He, C. L. Jia, R. Waser, K. Lee, Y. K. Kim, S. Baik, T. Zhao, R. Ramesh, P. Ghosez, K. M. Rabe: Scaling of structure and electrical properties in ultrathin epitaxial ferroelectric heterostructures, J. Appl. Phys. **100**, 051609 (2006) 321
[58] J. Y. Jo, Y. S. Kim, D. H. Kim, J. D. Kim, Y. J. Chang, J. H. Kong, Y. D. Park, T. K. Song, J.-G. Yoon, J. S. Jung, T. W. Noh: Thickness-dependent ferroelectric properties in fully-strained $SrRuO_3/BaTiO_3/SrRuO_3$ ultra-thin capacitors, Thin Solid Films **486**, 149–152 (2005) 321
[59] D. J. Kim, J. Y. Jo, Y. S. Kim, Y. J. Chang, J. S. Lee, J.-G. Yoon, T. K. Song, T. W. Noh: Polarization relaxation induced by a depolarization field in ultrathin ferroelectric $BaTiO_3$ capacitors, Phys. Rev. Lett. **95**, 237602 (2005) 321, 322
[60] V. Janovec: On the theory of the coercive field of single-domain crystals of $BaTiO_3$, Czech. J. Phys. **8**, 3 (1958) 321
[61] H. F. Kay, J. W. Dunn: Thickess dependence of nucleation field of triglycine sulphate, Philos. Mag. **7**, 2027 (1962) 321
[62] J. F. Scott: *Ferroelectric Memories* (Springer, Berlin 2000) 321
[63] H. K. Chan, C. H. Lam, F. G. Shin: Time-dependent space-charge-limited conduction as a possible origin of the polarization offsets observed in compositionally graded ferroelectric films, J. Appl. Phys. **95**, 2665–2671 (2004) 322
[64] S. Ducharme, V. M. Fridkin, A. V. Bune, S. P. Palto, L. M. Blinov, N. N. Petukhova, S. G. Yudin: Intrinsic ferroelectric coercive field, Phys. Rev. Lett. **84**, 175–178 (2000) 322
[65] N. A. Pertsev, J. Rodriguez Contreras, V. G. Kukhar, B. Hermanns, H. Kohlstedt, R. Waser: Coercive field of ultrathin $Pb(Zr_{0.52}Ti_{0.48}O_3)$ epitaxial films, Appl. Phys. Lett. **83**, 3356–3358 (2003) 322
[66] A. T. J. van Helvoort, O. Dahl, B. G. Soleim, R. Holmestad, T. Tybell: Imaging of out-of-plane interfacial strain in epitaxial $PbTiO_3/SrTiO_3$ thin films, Appl. Phys. Lett. **86**, 092907 (2005) 323
[67] H. Tabata, H. Tanaka, T. Kawai: Formation of artificial $BaTiO_3/SrTiO_3$ superlattices using pulsed laser deposition and their dielectric properties, Appl. Phys. Lett. **65**, 1970–1972 (1994) 324
[68] Y. Ishibashi, N. Ohashi, T. Tsurimi: Structural refinement of X-ray diffraction profile for artificial superlattices, Jpn. J. Appl. Phys. **39**, 186–191 (2000) 324

[69] O. Nakagawara, T. Shimata, T. Makino, S. Arai, H. Tabata, T. Kawai: Epitaxial growth and dielectric properties of (111) oriented $BaTiO_3/SrTiO_3$ superlattices by pulsed-laser deposition, Appl. Phys. Lett. **77**, 3257–3259 (2000) 324

[70] T. Shimuta, O. Nakagawara, T. Makino, S. Arai, H. Tabata, T. Kawai: Enhancement of remanent polarization in epitaxial $BaTiO_3/SrTiO_3$ superlattices with "asymmetric" structure, J. Appl. Phys. **91**, 2290–2294 (2002) 324

[71] J. B. Neaton, K. M. Rabe: Theory of polarization enhancement in epitaxial $BaTiO_3/SrTiO_3$ superlattices, Appl. Phys. Lett. **82**, 1586–1588 (2003) 324

[72] K. Johnston, X. Huang, J. B. Neaton, K. M. Rabe: First-principles study of symmetry lowering and polarization in $BaTiO_3/SrTiO_3$ superlattices with inplane expansion, Phys. Rev. B **71**, 100103 (2005) 324

[73] A. Q. Jiang, J. F. Scott, H. Lu, Z. Chen: Phase transitions and polarizations in epitaxial $BaTiO_3/SrTiO_3$ superlattices studied by second-harmonic generation, J. Appl. Phys. **93**, 1180–1185 (2003) 324

[74] S. Rios, A. Ruediger, A. Q. Jiang, J. F. Scott, H. Lu, Z. Chen: Orthorhombic strontium titanate in $BaTiO_3{-}SrTiO_3$ superlattices, J. Phys. Condens. Matter **15**, L305 (2003) 324

[75] H.-M. Christen, L. A. Boatner, J. D. Budai, M. F. Chisholm, L. A. Gea, P. J. Marrero, D. P. Norton: The growth and properties of epitaxial $KNbO_3$ thin films and $KNbO_3/KTaO_3$ superlattices, Appl. Phys. Lett. **68**, 1488–1490 (1996) 324

[76] J. Sigman, D. P. Norton, H. M. Christen, P. H. Fleming, L. A. Boatner: Antiferroelectric behavior in symmetric $KNbO_3/KTaO_3$ superlattices, Phys. Rev. Lett. **88**, 097601 (2002) 324

[77] M. Sepliarsky, S. R. Phillpot, D. Wolf, M. G. Stachiotti, R. L. Migoni: Ferroelectric properties of $KNbO_3/KTaO_3$ superlattices by atomic-level simulation, J. Appl. Phys. **90**, 4509–4519 (2001) 324

[78] M. Sepliarsky, S. R. Phillpot, M. G. Stachiotty, R. L. Migoni: Ferroelectric phase transitions and dynamical behavior in $KNbO_3/KTaO_3$ superlattices by molecular-dynamics simulation, J. Appl. Phys. **91**, 3165–3171 (2002) 324

[79] J. C. Jiang, X. Q. Pan, W. Tian, C. D. Theis, D. G. Schlom: Abrupt $PbTiO_3/SrTiO_3$ superlattices grown by reactive molecular beam epitaxy, Appl. Phys. Lett. **74**, 2851–2853 (1999) 324

[80] F. Le Marrec, R. Farhi, M. El Marssi, J. L. Dellis, M. G. Karkut: Ferroelectric $PbTiO_3/BaTiO_3$ superlattices: Growth anomalies and confined modes, Phys. Rev. B **61**, R6447–R6450 (2000) 324

[81] C. Bungaro, K. M. Rabe: Lattice instabilities of $PbZrO_3/PbTiO_3$ [1:1] superlattices from first principles, Phys. Rev. B **65**, 224106 (2002) 324

[82] C. Bungaro, K. M. Rabe: Epitaxially strained [001]-$(PbTiO_3)_1(PbZrO_3)_1$ superlattice and $PbTiO_3$ from first principles, Phys. Rev. B **69**, 184101 (2004) 324

[83] M. P. Warusawithana, E. V. Colla, J. N. Eckstein, M. B. Weissman: Artificial dielectric superlattices with broken inversion symmetry, Phys. Rev. Lett. **90**, 036802 (2003) 324

[84] H. N. Lee, H. M. Christen, M. F. Chisholm, C. M. Rouleau, D. H. Lowndes: Strong polarization enhancement in asymmetric three-component ferroelectric superlattices, Nature (London) **433**, 395–399 (2005) 324

[85] D. P. Norton, B. C. Chakoumakos, J. D. Budai, D. H. Lowndes, B. C. Sales, J. R. Thompson, D. K. Christen: Superconductivity in $SrCuO_2$–$BaCuO_2$ superlattices: Formation of artificially-layered superconducting materials, Science **265**, 2074–2077 (1994) 324
[86] T. Tsurumi, T. Harigai, D. Tanaka, S.-M. Nam, H. Kakemoto, S. Wada, K. Saito: Artificial ferroelectricity in perovskite superlattices, Appl. Phys. Lett. **85**, 5016–5018 (2004) 324
[87] G. Rijnders, D. H. A. Blank: Build your own superlattice, Nature (London) **433**, 369–370 (2005) 324
[88] N. Sai, B. Meyer, D. Vanderbilt: Compositional inversion symmetry breaking in ferroelectric perovskites, Phys. Rev. Lett. **84**, 5636–5639 (2000) 324
[89] Y. Ogawa, H. Yamada, T. Ogasawara, T. Arima, H. Okamoto, M. Kawasaki, Y. Tokura: Nonlinear magneto-optical Kerr rotation of an oxide superlattice with artificially broken symmetry, Phys. Rev. Lett. **90**, 217403 (2003) 324
[90] M. Dawber, C. Lichtensteiger, M. Cantoni, M. Veithen, P. Ghosez, K. Johnston, K. M. Rabe, J.-M. Triscone: Unusual behavior of the ferroelectric polarization in $PbTiO_3/SrTiO_3$ superlattices, Phys. Rev. Lett. **95**, 177601 (2005) 325, 326
[91] K. Ishikawa, K. Yoshikawa, N. Okada: Size effect on the ferroelectric phase transition in $PbTiO_3$ ultrafine particles, Phys. Rev. B **37**, 5852–5855 (1988) 327
[92] B. Jiang, J. L. Peng, L. A. Bursill, W. L. Zhong: Size effects on ferroelectricity of ultrafine particles of $PbTiO_3$, J. Appl. Phys. **87**, 3462–3467 (2000) 327
[93] W. L. Zhong, B. Jiang, P. L. Zhang, J. M. Ma, H. M. Cheng, Z. H. Yang, L. X. Li: Phase transition in $PbTiO_3$ ultrafine particles of different sizes, J. Phys. Condens. Matter **5**, 2619–2624 (1993) 327
[94] K. Uchino, E. Sadanaga, T. Hirose: Dependence of the crystal structure on particle size in barium titanate, J. Am. Ceram. Soc. **72**, 1555 (1989) 327
[95] S. Tsunekawa, S. Ito, T. Mori, K. Ishikawa, Z.-Q. Li, Y. Kawazoe: Critical size and anomalous lattice expansion in nanocrystalline $BaTiO_3$ particles, Phys. Rev. B **62**, 3065–3070 (2000) 327
[96] C. Liu, B. Zou, A. J. Rondinone, Z. J. Zhang: Sol-gel synthesis of free-standing ferroelectric lead zirconate titanate nanoparticles, J. Am. Ceram. Soc. **123**, 4344–4345 (2001) 328
[97] S. O'Brien, L. Brus, C. B. Murray: Synthesis of monodisperse nanoparticles of barium titanate: towards a generalized strategy of oxide nanoparticles synthesis, J. Am. Ceram. Soc. **123**, 12085–12086 (2001) 328
[98] C. S. Ganpule, A. Stanishevsky, Q. Su, S. Aggarwal, J. Melnagilis, E. Williams, R. Ramesh: Scaling of ferroelectric properties in thin films, Appl. Phys. Lett. **75**, 409 (1999) 328
[99] C. S. Ganpule, A. Stanishevsky, S. Aggarwal, J. Melngailis, E. Williams, R. Ramesh, V. Joshi, C. Paz de Araujo: Scaling of ferroelectric and piezoelectric properties in $Pt/SrBi_2Ta_2O_9/Pt$ thin films, Appl. Phys. Lett. **75**, 3874–3876 (1999) 328
[100] M. Alexe, C. Harnagea, W. Erfurth, D. Hesse, U. Gösele: 100-nm lateral size ferroelectric memory cells fabricated by electron-beam direct writing, Appl. Phys. A **70**, 247 (2000) 328

[101] M. Alexe, J. F. Scott, C. Curran, N. D. Zakharov, D. Hesse, A. Pignolet: Self-patterning nano-electrodes on ferroelectric thin films for gigabit memory applications, Appl. Phys. Lett. **73**, 1592–1594 (1998) 328
[102] M. Alexe, A. Gruverman, C. Harnagea, N. D. Zakharov, A. Pignolet, D. Hesse, J. F. Scott: Switching properties of self-assembled ferroelectric memory cells, Appl. Phys. Lett. **75**, 1158–1160 (1999) 328
[103] A. Seifert, A. Vojta, J. S. Speck, F. F. Lange: Microstructural instability in single-crystal thin films, J. Mater. Res. **11**, 1470–1482 (1996) 328
[104] I. Szafraniak, C. Harnagea, R. Scholz, S. Bhattacharyya, D. Hesse, M. Alexe: Ferroelectric epitaxial nanocrystals obtained by a self-patterning method, Appl. Phys. Lett. **83**, 2211–2213 (2003) 328
[105] M. Dawber, I. Szafraniak, M. Alexe, J. F. Scott: Self-patterning of arrays of ferroelectric capacitors: Description by theory of substrate mediated strain interactions, J. Phys. Condens. Matter **15**, L667–L671 (2003) 328
[106] A. Roelofs, T. Schneller, K. Szot, R. Waser: Piezoresponse force microscopy of lead titanate nanograins possibly reaching the limit of ferroelectricity, Appl. Phys. Lett. **81**, 5231–5233 (2002) 328
[107] H. Nonomura, H. Fujisawa, M. Shimizu, H. Niu, K. Honda: Self-assembled $PbTiO_3$ nano-islands prepared on $SrTiO_3$ by metalorganic chemical vapor deposition, Jpn. J. Appl. Phys. **42**, 5918–5921 (2003) 328
[108] M.-W. Chu, I. Szafraniak, R. Scholtz, C. Harnagea, D. Hesse, M. Alexe, U. Gösele: Impact of misfit dislocations on the polarization instability of epitaxial nanostructured ferroelectric perovskites, Nature Mater. **3**, 87–90 (2004) 329
[109] Y. Luo, I. Szafraniak, N. D. Zakharov, V. Nagarajan, M. Steinhart, R. B. Wehrspohn, J. H. Wendorff, R. Ramesh, M. Alexe: Nanoshell tubes of ferroelectric lead zirconate titanate and barium titanate, Appl. Phys. Lett. **83**, 440–442 (2003) 329
[110] F. D. Morrison, L. Ramsay, J. F. Scott: High aspect ratio piezoelectric strontium-bismuth-tantalate nanotubes, J. Phys. Condens. Matter **15**, L527–L532 (2003) 329
[111] D. D. Morrison, Y. Luo, I. Szafraniak, V. Nagarajan, R. B. Wehrspohn, M. Steinhart, J. H. Wendorff, N. D. Zakharov, E. D. Mishina, K. A. Vorotilov, A. S. Sigov, S. Nakabayashi, M. Alexe, R. Ramesh, J. F. Scott: Ferroelectric nanotubes, Rev. Adv. Mater. Sci. **4**, 114–122 (2003) 329
[112] W. S. Yun, J. J. Urban, Q. Gu, H. Park: Ferroelectric properties of individual barium titanate nanowires investigated by scanned probe microscopy, Nano Lett. **2**, 447–450 (2002) 329
[113] J. J. Urban, W. S. Yun, Q. Gu, H. Park: Synthesis of single-crystalline perovskite nanorods composed of barium titanate and strontium titanate, J. Am. Ceram. Soc. **124**, 1186–1187 (2002) 329
[114] J. J. Urban, J. E. Spanier, L. Ouyang, W. S. Yun, H. Park: Single-crystalline barium titanate nanowires, Adv. Mater. **15**, 423–426 (2003) 329
[115] H. Fu, L. Bellaiche: Ferroelectricity in barium titanate quantum dots and wires, Phys. Rev. Lett. **91**, 257601 (2003) 329
[116] I. Naumov, L. Bellaiche, H. Fu: Unusual phase transitions in ferroelectric nanodisks and nanorods, Nature (London) **432**, 737–740 (2004) 329
[117] G. Geneste, E. Bousquet, J. Junquera, P. Ghosez: Finite-size effects in $BaTiO_3$ nanowires, Appl. Phys. Lett. **88**, 112906 (2006) 329

Index

Nanoscale Studies of Domain Walls in Epitaxial Ferroelectric Thin Films

Patrycja Paruch[1,2], Thierry Giamarchi[1], and Jean-Marc Triscone[1]

[1] DPMC, University of Geneva,
24 Quai E. Ansermet, 1211 Geneva 4, Switzerland
[2] Laboratory of Atomic and Solid State Physics, Cornell University,
Ithaca, NY 14853, USA
patrycja.paruch@cornell.edu

Abstract. Nanoscale ferroelectric domains in epitaxial $Pb(Zr_{0.2}Ti_{0.8})O_3$ thin films were investigated using atomic force microscopy to allow the static roughness configuration and dynamic response of ferroelectric domain walls in these materials to be accessed. The observed dependence of domain size on writing time revealed a two-step switching process in which nucleation under the atomic force microscope tip is followed by radial domain growth. We obtained a non-linear dependence of domain wall velocity on the electric field, $v \propto \exp -(1/E)^{\mu}$, characteristic of a creep process. The domain wall motion was analyzed both in the context of stochastic nucleation in a periodic potential as well as that of an elastic manifold in a disorder potential, in better agreement with the dimensionality of the system and the values of the dynamic exponent $\mu \sim 0.6$. Independent measurements of domain wall roughness in the same films revealed a power law growth of the correlation function of relative displacements $B(L) \propto L^{2\zeta}$ with $\zeta \sim 0.26$ at short length scales L, followed by an apparent saturation at large L. These results give rise to a clear physical picture of domain walls in ferroelectrics as elastic sheets in the presence of "random-bond" disorder, and where dipolar interactions play an important role, effectively increasing the dimensionality of the system to 2.5, in agreement with theoretical predictions.

1 Introduction

The diverse electronic properties of ferroelectric perovskites make them particularly interesting for miniaturized multifunctional devices such as memories [1, 2], actuators, filters [3] and sensors [4] in which their piezoelectric and pyroelectric properties as well as their switchable ferroelectric polarization can be exploited. Since the proposed applications generally rely on multidomain configurations with coexisting regions of opposite polarization separated by thin elastic interfaces, or ferroelectric domain walls, understanding the mechanisms that control domain evolution in the presence of electric fields or temperature variations is of crucial importance. In particular, it is the static and dynamic behavior of domain walls that determines domain stability and growth at the microscopic level of individual domains, and therefore their usefulness for potential applications, and that will be examined in this chapter.

K. Rabe, C. H. Ahn, J.-M. Triscone (Eds.): Physics of Ferroelectrics: A Modern Perspective,
Topics Appl. Physics **105**, 339–362 (2007)

After a brief introduction to the static and dynamic physics of elastic interfaces in disordered elastic systems (for a detailed presentation, the reader is directed to [5, 6]), we present a review of the noninvasive, local atomic force microscopy studies of ferroelectric domains in epitaxial $Pb(Zr_{0.2}Ti_{0.8})O_3$ (PZT) thin films, demonstrating domain-wall motion in these films to be a disorder-controlled creep process [7, 8], with short length scale measurements of static roughness [9] consistent with so-called "random bond" disorder in the presence of dipolar interactions. Finally, we discuss these results in the context of recent studies of domain-wall kinetics.

The films described in these studies were all grown on single-crystal (001) oriented Nb-doped (0.5%) $SrTiO_3$ substrates by inverted off-axis radio-frequency magnetron sputtering, in a mixture of argon and oxygen ($Ar{:}O_2$ = 58:42) at 180 mTorr and at a substrate temperature of $\sim$ 500 °C. After growth, the films were cooled to ambient temperature under a continuous flow of process gas. Subsequent film characterization by X-ray diffraction and atomic force microscopy revealed "cube-on-cube" growth of *c*-axis oriented PZT. Multiple orders of finite-size-effect peaks indicated high-quality crystallization and allowed precise measurement of film thickness. AFM measurements of the sample topography revealed extremely flat and uniform surfaces over large areas, with a measured root-mean-square roughness of ~ 3 Å over a 5 µm × 5 µm for typical films.

2 Ferroelectric Domain Walls as Elastic Disordered Systems

To understand the microscopic static and dynamic behavior of ferroelectric domain walls, it is useful to consider these objects within the broader framework of disordered elastic systems. Ferroelectric materials are characterized by energetically equivalent, degenerate ground states with oppositely directed, switchable remanent polarization, and separated by an energy barrier, as shown schematically in Fig. 1. Unlike ferromagnetic materials, in which the direction of magnetization essentially rotates freely through 180° between oppositely polarized domains, giving rise to relatively wide domain walls, ferroelectrics present a polarization axis determined by the crystalline structure of the material. As a result, the orientation of the polarization changes very abruptly between oppositely polarized domains, with zero magnitude locally at the center of the extremely thin domain walls. In $PbTiO_3$, for example, a domain wall thickness of $\sim$ two lattice constants was determined by first-principles calculations [10].

These domain walls can be considered as elastic objects, whose surface tends to be minimized in order to decrease the total energy of the system. However, the walls may meander from an elastically optimal flat configuration to take advantage of particularly favorable regions of the potential

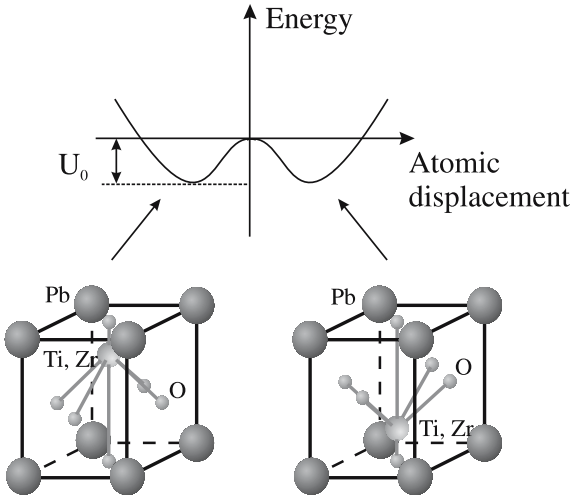

Fig. 1. Schematic diagram of a $Pb(Zr_{0.2}Ti_{0.8})O_3$ unit cell, with energy vs. atomic displacement (the ionic motion at the phase transition is exaggerated for the purpose of the illustration) showing two degenerate ground states separated by an energy barrier U_0. The Pb and Ti/Zr ions are positively charged and the O ions are negatively charged, giving opposite polarization directions P_{DOWN} and P_{UP} as a function of their displacement from their positions in the cubic paraelectric unit cell (figure after [7])

landscape. The dynamic response of the system can be accessed by the application of an electric field that asymmetrizes the ferroelectric double-well potential, favoring one polarization state by reducing the energy necessary to create a nucleus with polarization parallel to the field, and thereby promotes domain-wall motion. From the point of view of elastic disordered phenomena, epitaxially grown monocrystalline perovskite thin films are particularly useful as a model system for experimental study, allowing precise control of crystalline quality and film thickness over three orders of magnitude, from $\sim$ 0.1 nm to hundreds of nm using modern oxide growth techniques (see Chap. 6) and where nanometer resolution of ferroelectric domain structure is possible with atomic force microscopy.

3 Static and Dynamic Behavior of Elastic Disordered Systems

From a fundamental physics perspective, understanding the behavior of elastic objects pinned by periodic or disorder potentials is of crucial importance for a large number of physical systems ranging from vortex lattices in type II superconductors [6, 11, 12], charge-density waves [13, 14] and Wigner crystals [15, 16] to interfaces during growth [17] and fluid-invasion [18] processes,

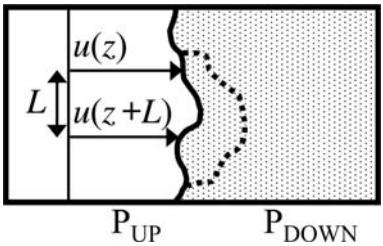

Fig. 2. Domain wall as elastic manifold trapped in a random disorder potential. In equilibrium, the domain wall exhibits a characteristic roughness, measured by the correlation function $B(L) = \overline{\langle [u(z+L) - u(z)]^2 \rangle}$ of the displacements $u(z)$ from an elastically ideal flat configuration with respect to the length L of the domain wall. In the presence of a small driving force $f < f_c$ due to the applied electric field E, the domain wall can move to another favorable configuration in the disorder potential, as shown by the dotted line, via a nonlinear response, known as creep (figure after [8]).

and magnetic domain walls [19,20]. The common feature of the different elastic disordered systems is the presence of a d-dimensional deformable object whose energy can be described by elasticity theory and whose optimal $T = 0$ configuration would be flat or spatially homogeneous. However, these elastic objects interact with the potential of the disordered (crystalline) medium in which they are embedded. The presence of a commensurate potential due to the underlying crystal lattice favors the positioning of the manifold in potential minima, but maintains its flat configuration. However, random variations of the potential due to the presence of disorder allow the manifold to meander from the elastically ideal flat configuration to take advantage of particularly favorable regions of the potential landscape. Thermal fluctuations also tend to roughen the manifold since this increases the entropy.

The resulting distortion of the elastic object from its flat configuration is given by the displacement vector $u(z)$, where z are the d internal coordinates, such that the total spatial dimension is $D = d + 1$, as shown in Fig. 2 for a one-dimensional manifold of thickness ξ.

In general, many types of disorder are possible: macroscopic defects like twin planes or columnar irradiation tracks have a significant spatial extent, and probably act as strong pinning centers. For this discussion, we consider only high-quality films in which the dominant disorder can be reduced to a random, spatially varying density of point defects (vacancies, impurities, etc.), and weak collective pinning. Theoretically, two classes of disorder have been intensively studied. For "random-bond" disorder, equivalent to defects that locally modify the ferroelectric double-well potential depth, but maintain

its symmetry, one can model the disorder by a random potential acting at the position of the interface and

$$U_{\text{disorder}} = \int \mathrm{d}^d z V(u(z), z)\,. \tag{1}$$

Another form of disorder, so-called "random field", occurs when defects locally asymmetrize the ferroelectric double-well potential, leading to a different form for U_{disorder}. If the disorder is weak, the central-limit theorem allows its approximation by a Gaussian random potential. The disorder is then only characterized by its correlation length r_{f} and the strength of the random potential. In the absence of an external driving force, the configuration of the manifold results from the competition between the elastic forces and the random potential. This configuration can be characterized by measuring the correlation function of relative displacements, which shows a power law governed by different exponents

$$B(L) = \overline{\langle [u(z+L) - u(z)]^2 \rangle} = \xi^2 \left(\frac{L}{L_{\text{c}}} \right)^{2\zeta}\,, \tag{2}$$

where $\langle \cdots \rangle$ denotes thermal averaging (thermodynamic equilibrium) and $\overline{\cdots}$ denotes an ensemble average over the realization of the disorder. In a realistic experimental situation the ensemble average is performed by averaging over all pairs of points separated by a distance L, assuming that the system is self-averaging.

The roughness exponent ζ is a function of the type of disorder present in the film, and the dimensionality of the manifold. For a line ($d = 1$) and purely thermal fluctuations in the absence of disorder, $\zeta = 0.5$. In a random-bond scenario, an exact value of $\zeta = 2/3$ has been calculated for a line [21–23] and $\zeta \sim 3/5$ [24, 25] is expected for two-dimensional interfaces. In a random-field scenario the roughness exponent has been calculated as $\zeta = \frac{4-d}{3}$.

The competition between elasticity and disorder present in the static description also governs the dynamical behavior of the interface in the presence of an external force. For ferroelectric domain walls, this driving force is due to either externally applied or internal electric fields, or to line tension of domain walls with nonzero curvature, all promoting domain-wall motion and thus the growth or decay of domains. Although at $T = 0$ the domain wall is pinned by the disorder until a critical force f_{c} is reached, at finite temperatures it can be driven by forces below f_{c}, since barriers to motion, however high, can always be passed via thermal activation. This response to a small external force is of special theoretical and practical interest. Initially thermal activation above the pinning barriers was believed to lead to a linear response at finite temperature [26]. However, it was subsequently realized that a pinning potential, either commensurate [6] or disordered, [5, 6, 27–29], can lead to diverging barriers and thus to a nonlinear response, known as creep, where the velocity is of the form $v \propto \exp(-\beta U_{\text{c}}(f_{\text{c}}/f)^{\mu})$. β is the inverse temperature,

U_c a characteristic energy and f_c a critical force. The dynamical exponent μ again reflects the nature of the disorder and the dimensionality of the system. From the values of ζ calculated for the one- and two-dimensional random-bond-disorder systems, one can obtain values of $\mu = 0.25$ and $\mu \sim 0.5$–0.6, for the dynamical exponent in these scenarios. For random-field disorder, the calculated value of ζ gives $\mu = 1$ for any interface with dimensionality between 1 and 4.

Despite extensive studies of the creep process in periodic vortex systems [6, 11, 12], precise determination of the exponents has proven difficult, given the many scales present in this problem although results in agreement with the theoretical predictions of $\zeta = 0$ have been observed [30]. For interfaces, creep and disorder-controlled domain-wall roughening have been quantitatively confirmed in ultrathin magnetic films [19], where exponents $\mu = 0.25$ and $\zeta = 2/3$ have been measured, in good agreement with the value predicted for one-dimensional (line) domain walls in a random-bond disorder. In ferroelectric materials, a phenomenological model derived from measurements of domain growth in bulk samples [31–33] initially suggested that the domain walls were pinned by the periodic potential of the crystal lattice itself. However, thermally activated decay of naturally occurring domains in cleaved triglycine sulfate single crystals studied at room temperature and under heating suggested random-bond disorder-governed behavior [34, 35]. In addition, recent measurements of the piezoelectric effect [36], dielectric permittivity [37], and dielectric dispersion [38] in ferroelectric ceramics and sol-gel films have shown features that cannot be described by the existing phenomenological theories. Quantitative nanoscale studies of individual ferroelectric domain walls offered a promising means of resolving these open questions.

4 Experimental Observation of Domain-Wall Creep

Using a metallic AFM tip to create nanoscale circular domains by the application of voltage pulses with different magnitude (writing voltage) and duration (writing time), the dependence of domain size on these parameters can be measured. As reported in [39] for epitaxial $PbZr_{0.2}Ti_{0.8}O_3$ thin films, a linear dependence of domain size on the writing voltage was observed, subsequently confirmed in other ferroelectric materials [40], above a threshold related to the minimum field required for switching, as shown in Fig. 3 for 4 different samples 37.0–95.4 nm thick and a voltage range of 4–20 V.

Domain radius was also observed to logarithmically depend on the writing time for times longer than $\sim 10\,\mu s$, as shown in Fig. 4, with a 500% change in domain radius observed in the time range from $\sim 10\,\mu s$ to $\sim 10\,s$. For shorter times, the domain radii appeared to saturate at $\sim 20\,nm$, a size we relate to the 25–50 nm nominal radius of curvature of the AFM tip used

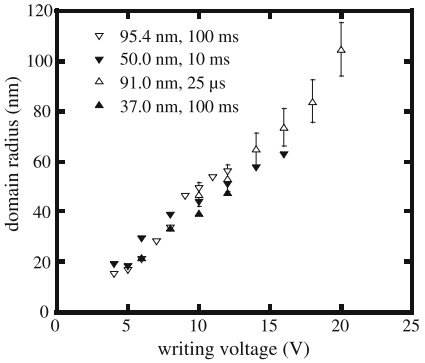

Fig. 3. Domain radius as a function of the writing voltage for 37.0-, 50.0-, 91.0- and 95.4-nm thick $PbZr_{0.2}Ti_{0.8}O_3$ films, where writing times of 100 ms, 10 ms, 25 µs and 100 ms, respectively, were used. The domain radius appears to depend linearly on the writing voltage applied to create the domain. The error bars shown for the 91.0 nm sample are representative of those in the other samples, and are due to the spread of domain radii for a given writing voltage and writing time

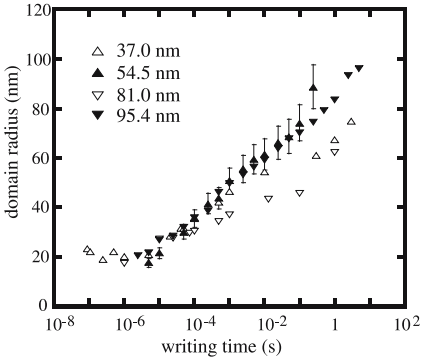

Fig. 4. Domain radius as a function of the writing time for 37.0-, 54.5-, 81.0- and 95.4-nm thick $PbZr_{0.2}Ti_{0.8}O_3$ films. For writing times shorter than $\sim$ 10 µs, the domain radius appears to saturate at $\sim$ 20 nm, a limit related to the size of the AFM tips used in the experiment. For longer writing times, domain size appears to grow logarithmically. All domains, including those written with the shortest ($\sim$ 100 ns) pulses, remained completely stable through the one-week duration of the measurements

for these experiments. For each writing time, multidomain arrays were written, and the domain radius was calculated by averaging over the measured domain radii along their vertical and horizontal axes, with a rms error of $\sim 10\%$. All imaged domains appeared homogeneous and well defined and no randomly nucleated domains were observed. These data suggest a two-step switching process where initial rapid nucleation and forward growth across the thickness of the sample occur under the AFM tip, and are followed by slower radial motion of the domain wall outwards, perpendicular to the polarization direction, increasing the lateral size of the domain. We analyzed this radial domain-wall motion in the framework of a pinned elastic system by comparing the velocity and the driving force exerted on the wall, in our case due to the electric field E applied by the tip. Considering arrays written with consecutive pulse durations, we extracted the domain-wall velocity as $v = \frac{r(t_2)-r(t_1)}{t_2-t_1}$, the difference in domain radii at the two subsequent writing times divided by the difference in the writing times themselves. The electric-field distribution was obtained by modeling the tip as a charged sphere, with radius α taken as equal to the domain saturation size of 20 nm. Applying a voltage V to the tip at the surface of the ferroelectric film with dielectric constant ϵ produces a charge $q = 4\pi\epsilon\epsilon_0\alpha V$ on the model tip. Taking into account both the effect of the film and the conductive substrate, we are able to find the field $E_\perp(r, z)$ at any point (r, z) within the film. r is the horizontal distance (in the plane of the film) away from the center of the spherical tip, and z is the depth within the film (up to thickness λ) from the center of the tip. In our experiments, the domain radii remain comparable to the size of the tip, so further simplification can be obtained by considering only the first order of image-charge reflections in the film and the substrate. Since the voltage drop V across the film is simply the integral of this field over the film thickness $V = \int_0^{\alpha+\lambda} E_\perp(r, z)\,\mathrm{d}z$ we can define the average field across the film $E(r) = \overline{E_\perp}(r)$, which shows a $1/r$ dependence in this first-order approximation.[1] As one moves further away from the tip, a crossover to higher orders of r dependence in the denominator is expected for the field. This simplified model shows reasonable agreement with a more accurate numerical simulation of a hyperbolic tip in contact with a ferroelectric film grown on a metallic substrate.[2] Here, a $1/r$ dependence of the electric field is observed

[1] We also note that the linear dependence of domain size on the writing voltage strongly supports the $E(r) \propto 1/r$ dependence obtained in our simple electric-field model. This can be rapidly seen when a more general form for the electric field $E(r) \propto 1/r^\nu$ is considered. Integrating (4) with this electric-field dependence, we obtain $r^{\nu\mu} = V^\mu \ln t$. Thus, for a given writing time, domain size would be expected to show a power-law dependence on the writing voltage $r^\nu \propto V$. Instead, we observed a clear linear dependence, suggesting that indeed $\nu = 1$.

[2] private communication with Ø. Dahl and T. Tybell, Norwegian University of Science and Technology, Trondheim (2003).

out to $r \sim 300\,\mathrm{nm}$, for a tip $1\,\mu\mathrm{m}$ high with $\alpha = 20\,\mathrm{nm}$ radius of curvature. Beyond this, a crossover to $1/r^2$ and even steeper field decay occurs.

Although the field $E(r)$ is highly inhomogeneous at large length scales, it can be taken as constant over the very small thickness of the ferroelectric domain wall. One can thus relate the velocity $v(r)$ of the domain wall at a distance r from the tip to a field $E(r) = \frac{V\alpha}{r\lambda}$, where $r = \frac{r(t_1)+r(t_2)}{2}$. An Arrhenius plot of the velocity against the inverse field, shown in Fig. 5, reveals that our data are in good agreement with a creep behavior

$$v \sim \exp -\frac{U_\mathrm{c}}{k_\mathrm{B}T}\left(\frac{E_0}{E}\right)^{\mu} \tag{3}$$

over multiple decades of velocity, from 10^{-3} to 10^{-9} m/s, and for fields varying from 10^7 to 5×10^8 V/m.[3] The values of the dynamical exponent μ were found to be ~ 0.6 in most samples, although with some samples showing values closer to 1. These data were the first indication that domain-wall motion in ferroelectric thin films was a creep process, and led us to investigate its microscopic origins.

5 Domain-Wall Creep in a Commensurate Potential

Early studies [31, 32] of domain growth carried out by optical and etching techniques on bulk samples reported a nonlinear electric-field dependence of the velocity $v \propto \exp -1/E$ known as Merz's law (with implicit values of $\mu = 1$, if these results are to be considered in the general framework of creep). At the time, a phenomenological theory based on the stochastic nucleation of new domains at existing domain boundaries was put forward by Miller and Weinreich to explain the observed behavior [33]. The wall moves forward due to the formation of a nucleus as shown in Fig. 6. The energy change due to the formation of a nucleus is

$$\Delta F = -2P_\mathrm{s}EV + \sigma_\mathrm{w}A + U_\mathrm{depolarization}\,. \tag{4}$$

Nucleation and subsequent domain-wall motion would occur if the energy gain due to switching a volume V of ferroelectric with spontaneous polarization P_s to the polarization state energetically favorable with respect to the

[3] We note that during AFM writing, the exact magnitude of the effective field is difficult to quantify, because of both the effects of a possible dielectric gap [41] and variations in tip shape. Local piezoelectric hysteresis measurements on 120–800-Å thick films show that the minimum switching field is $\sim$ 6–16 times larger than the bulk coercive field, an effect that is not observed with macroscopic electrodes on the similar films. The effective field E in the experiments is therefore presumably $\sim$ one order of magnitude smaller than that calculated as $E(r)$ in this study. This has no effect on the exponent μ governing the exponential velocity dependence. Unless otherwise noted, the values reported are the directly calculated ones, with no further corrections.

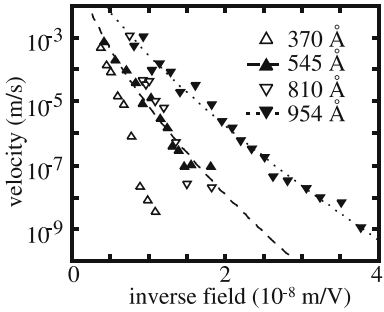

Fig. 5. Domain wall speed as a function of the inverse applied electric field for 37.0-, 54.5-, 81.0- and 95.4-nm thick $PbZr_{0.2}Ti_{0.8}O_3$ films. The data agree with the creep equation $v \sim \exp[-\frac{R}{k_B T}\left(\frac{E_0}{E}\right)^{\mu}]$ with $\mu = 0.93$, 0.62, 1.09, and 0.69, respectively. Fits of the data to $\log v = A(1/E)^{\mu}$ are shown for the 54.5 and 95.4 nm films. The 10% root-mean-square error in the local electric field is given by the precision of the domain-size measurements

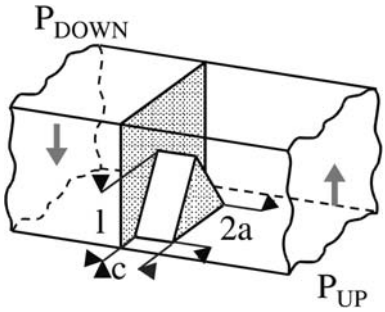

Fig. 6. Schematic drawing of a triangular step nucleated at the surface of the film on a 180° domain wall, as described by Miller and Weinreich [33]. The applied electric field E is parallel to P_{DOWN}, favoring domain-wall motion to the right (figure after [33]).

direction of the applied field E would balance the energy cost of extending the surface A of the domain wall (with a surface energy density of σ_w) as well as the incurred depolarization energy cost $U_{depolarization}$. In fact, this mechanism is identical[4] to that of an elastic manifold weakly driven in a periodic pinning potential (tilted washboard potential, as described for example in [6]). The nucleus thickness (c in Fig. 6) is the distance between two mimima of the periodic potential given by the ferroelectric crystal lattice spacing.

[4] In the absence of a depolarization field the nucleus is isotropic. Taking into account the depolarization changes the shape of the nucleus, but does not affect in an essential way the physics leading to the creep process.

Since the energy gain due to the displacement of a nucleus into the neighboring pinning valley grows with the volume of the nucleus, while the energy cost essentially scales with its surface, for small electric fields ($E \to 0$) a large nucleus can be expected. Depending on the wall dimensionality d, balancing the two energy terms $V \sim L^d$ and $A \sim L^{d-1}$, where L is the spatial extension of the nucleus, leads to different behavior. For a one-dimensional domain wall (string, $d = 1$), the nucleus consists of two point-like kinks, whose activation energy therefore always remains finite, and the system exhibits a *linear* response to small driving forces. For a two-dimensional domain wall on the other hand, minimizing (4) gives $L^* \sim 1/E$, showing that the size of the nucleus grows as the electric field decreases. In this scenario the energy barriers to domain-wall motion, and thus nucleus growth, grow as $\Delta(E) \sim 1/E$, using (4), giving a nonlinear response with $v \propto \exp -1/E$. The stochastic nucleation proposed by Miller and Weinreich can thus explain the observed nonlinear response *only if* the domain wall itself is a two-dimensional surface embedded in a three-dimensional crystal. This means that the dimensions of the nucleus, at a given field E, have to be smaller than the thickness of the system. Otherwise, the energy of the nucleus saturates, resulting in the linear response of the one-dimensional scenario. It is also important to note that if the creep consists of motion in a commensurate potential the dynamical exponent is constrained to be $\mu = 1$. As already mentioned, this particular scenario is microscopically related to the intrinsic periodic pinning of the domain wall by the ferroelectric crystal lattice potential. The strength of this potential was calculated in ab-initio studies of 180° domain walls in $PbTiO_3$, showing that the wall energy varies from $132\,mJ/m^2$ to $169\,mJ/m^2$ depending on whether the domain wall is centered on a Pb−O or Ti−O_2 plane in the crystal [10].

To test whether the observed creep behavior is indeed due to the stochastic nucleation process, we calculated the size of the critical nucleus, following the formulation derived by Miller and Weinreich for the energetically most favorable dagger-shaped nucleus of horizontal extension a, height l and thickness c forming at an existing 180° domain wall, as shown in Fig. 6 [33], where P_s is the polarization, b the inplane lattice constant, ϵ the dielectric constant of PZT at ambient conditions, and E the applied electric field. The depolarization energy can be written as $U_{\text{depolarization}} = \frac{2\sigma_p b a^2}{l}$, with $\sigma_p = [4P_s^2 b \ln(0.7358a/b)]/\epsilon$ [33]. By minimizing the free-energy change due to nucleation with respect to the dimensions of the nucleus a and l, with c taken as equivalent to the lattice constant b (the distance between two min-

ima in the commensurate potential), the size of the critical nucleus $a^\star$ and $l^\star$, as well as the activation energy $\Delta F^\star$, can be calculated as [33]:

$$
\begin{aligned}
a^\star &= \frac{\sigma_\mathrm{w}(\sigma_\mathrm{w}+2\sigma_\mathrm{p})}{P_\mathrm{s}E(\sigma_\mathrm{w}+3\sigma_\mathrm{p})}\,,\\
l^\star &= \frac{\sigma_\mathrm{w}^{1/2}(\sigma_\mathrm{w}+2\sigma_\mathrm{p})}{P_\mathrm{s}E(\sigma_\mathrm{w}+3\sigma_\mathrm{p})^{1/2}}\,,\\
\Delta F^\star &= \frac{4b}{P_\mathrm{s}E}\sigma_\mathrm{p}(\sigma_\mathrm{w}+2\sigma_\mathrm{p})\left(\frac{\sigma_\mathrm{w}}{\sigma_\mathrm{w}+3\sigma_\mathrm{p}}\right)^{3/2}\,.
\end{aligned}
\tag{5}
$$

To compute the actual values, standard parameters for PZT ($P_\mathrm{s} = 0.40\,\mathrm{C/m^2}$, $\epsilon = 100$, $b = 3.96\,\text{Å}$), and the ab-initio value for the domain-wall energy density[5] $\sigma_\mathrm{w} = 0.132\,\mathrm{mJ/m^2}$ can be used. In our case, the applied electric field varied from ~ 2 to $20\,\mathrm{MV/m}$ (with the factor 10 correction), depending on the thickness of the sample used and the distance from the AFM tip, with the most intense fields for thin films and small domains. Corresponding values of σ_p were between 1.6 and $0.9\,\mathrm{J/m^2}$. Since σ_p is therefore greater than σ_w, following Miller and Weinreich, the expressions for the critical values can be simplified to:

$$
\begin{aligned}
a^\star &= \frac{2}{3}\frac{\sigma_\mathrm{w}}{P_\mathrm{s}E}\,,\\
l^\star &= \frac{2\sigma_\mathrm{w}^{1/2}\sigma_\mathrm{p}^{1/2}}{\sqrt{3}P_\mathrm{s}E}\,,\\
\Delta F^\star &= \frac{8b}{3\sqrt{3}P_\mathrm{s}E}\sigma_\mathrm{p}^{1/2}\sigma_\mathrm{w}^{3/2}\,.
\end{aligned}
\tag{6}
$$

For the field range used, these equations would give critical values of $a^\star \sim$ 12.5–125 nm and $l^\star \sim$ 53–710 nm. These results imply that for the given electric field range, the vertical size of the critical nucleus would exceed the thickness of the film itself. This suggests that the films are in a 2-dimensional limit, with the domain walls acting as a quasi-one-dimensional manifold, for which the Miller and Weinreich stochastic nucleation model, or alternatively, weakly driven motion through a commensurate potential, could not explain the nonlinear response observed. In addition, the values for the activation energy of $\sim 0.6\times10^{-21}$–0.5×10^{-20} would suggest extensive domain-wall motion as a result of thermal activation already at room temperature, a phenomenon not observed in PZT. Finally, the values of the dynamical exponent we observe, generally not equal to one, are also a strong indication that an alternative microscopic mechanism for the observed creep process should be considered.

[5] This value is computed for $PbTiO_3$. The presence of Zr in PZT would lead to local variations of this energy density.

6 Domain-Wall Creep in a Random Potential

In the alternative scenario of a canonical "glassy" system, an elastic manifold is weakly collectively pinned by the quenched disorder potential present in the medium, with important consequences for both its static and dynamic behavior. Disorder is present in any realistic system: in $PbZr_{0.2}Ti_{0.8}O_3$, vacancies and other defects in the lattice structure are likely sources of disorder. Another possibility is the presence of Zr atoms (the material is essentially a solid solution of 20% $PbZrO_3$ in 80% $PbTiO_3$), although preliminary studies of domain-wall dynamics in pure $PbTiO_3$ show similar static and dynamic exponents. In ferroelectric films the presence of disorder would dominate domain-wall behavior for both 1- and 2-dimensional walls at large scales. However, given the thinness of the domain wall, we note that the commensurate potential of the crystal is also present in the problem, although possibly at length scales below those experimentally accessible with our current system.

In order to analyze the effects of disorder on domain-wall motion we again consider the energy of a segment of ferroelectric domain wall of length L displaced by $u(z)$ from the elastically ideal flat configuration as shown on Fig. 2. The energy scales as[6]

$$U(u,L) = \sigma_{\mathrm{w}} u^2 L^{d-2} - U_{\mathrm{disorder}}[u] - 2P_{\mathrm{s}} E L^d u\,, \tag{7}$$

where the first term describes the elastic-energy contribution, and is expressed for a local elasticity.[7] A more accurate description of long-range forces, such as dipolar forces, modifies the elasticity and amounts to replacing d by $(3d-1)/2$ in the following formulas (see [42] and References therein). The second term is due to pinning by the disorder potential, and the third is the energy due to the application of an external electric field. U_{disorder} depends on the precise nature of the disorder.

As detailed in Sect. 3, in the absence of an external electric field E, an equilibrium roughness configuration of the domain wall would be expected, characterized by a power-law growth of $B(L)$ with different exponents. For r smaller than a characteristic length, the Larkin length L_{c} [43,44], $B(L)$ grows as $B(L) \sim L^{4-d}$. Below this length there is no metastability and no pinning of the elastic interface. Above the Larkin length, the growth still follows a power law, but with an exponent 2ζ ($B(L) \sim L^{2\zeta}$) dependent on the nature of the disorder. The Larkin length corresponds to the length for which the displacements are of the order of the size of the interface or the correlation

[6] There are constants of order one, dependent on the dimension d, which have been omitted from each term in the energy. These constants will not affect the creep exponent μ.

[7] Note that in order to take into account the depolarization effects lengths along the vertical axis have to be scaled by a factor $(\sigma_{\mathrm{p}}/\sigma_{\mathrm{w}})^{1/2}$, as in (6). Here, L denotes lengths perpendicular to the polarization direction.

length of the random potential[8] $B(L_c) = \max(\xi, r_f)$. The Larkin length is thus the smallest length at which the wall can be weakly pinned, and above which it can adjust elastically to optimize its local configuration.[9] Above R_c one can thus write

$$B(L > L_c) = \max(\xi, r_f)^2 \left(\frac{L}{L_c}\right)^{2\zeta} . \tag{8}$$

L_c is also the length scale at which pinning appears in the system in the presence of a driving force. Using[10] (7) for $u \sim \xi$ and $L = L_c$ one can directly obtain[11] the critical field E_c

$$E_c \simeq \frac{\sigma_w \xi}{P_s} \left(\frac{1}{L_c}\right)^2 . \tag{9}$$

In our case, a rough estimate of the values of E_c may thus be obtained by extrapolating the linear behavior of the velocity, which occurs at high field values. Although we were unable to extend our measurement significantly into this region, we can nonetheless at least place a lower bound on the value of E_c of 180 MV/m, as indicated on Fig. 7 for one of our thinner films, where higher values of the field could be implemented. Taking ξ to be of the order of a unit cell, we can use the field data to extract an approximate value of $L_c \sim 0.2$ nm, below the limit of resolution of our measurement.

In the creep regime, we can rewrite (7). For simplicity we write formulas for the isotropic case. Using the scaling $u \sim \xi(L/L_c)^\zeta$ one obtains

$$E(u, L) = U_c \left(\frac{L}{L_c}\right)^{d-2+2\zeta} - 2P_s E L_c^d \xi \left(\frac{L}{L_c}\right)^{d+\zeta} , \tag{10}$$

where $U_c = \sigma_w \xi^2 L_c^{d-2}$. Minimizing the energy with respect to the external field E, we obtain the size of the minimal nucleus as

$$L_{creep}/L_c = (f_c/f)^{1/(2-\zeta)} , \tag{11}$$

with $f = 2P_s E$. The minimal barrier height to be passed by thermal activation thus corresponds to the length L^*, leading to a velocity of the form

$$v \propto \exp\left(-\beta U_c (f_c/f)^{\frac{d-2+2\zeta}{2-\zeta}}\right) , \tag{12}$$

[8] In this simplified description we assume that the temperature is low enough to neglect thermal effects.

[9] Above L_c, the domain wall can also remain locally pinned on individual strong pinning sites, but in the present discussion, only weak collective pinning is considered.

[10] We now denote simply by ξ the $\max(\xi, r_f)$.

[11] As before, the length here is the length perpendicular to the polarization direction.

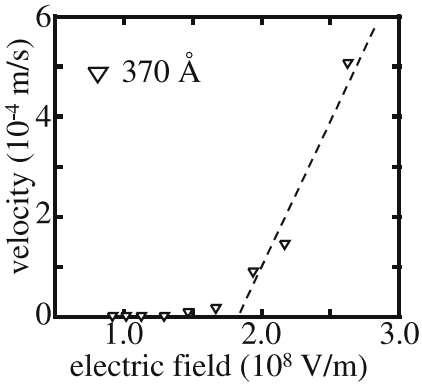

Fig. 7. Domain-wall velocity as a function of the applied electric field in a 37-nm $PbZr_{0.2}Ti_{0.8}O_3$ film. Extrapolating the linear behavior at high fields allows the critical field E_c to be estimated as 180 MV/m (figure after [8]).

if one assumes an Arrhenius law in passing the barriers. The very slow (creep) response is due to the fact that for a small force the system would have to rearrange large portions of the interface to be able to find a new metastable state of low enough energy. The barriers a domain wall must pass to make such a rearrangement therefore diverge as the force goes to zero.

The expression (11) gives the critical nucleus size L_{creep} as a function of the applied field E and L_c. We note that this expression is independent of the dimensionality of the film, and that the applied and critical fields are present as a ratio, thus removing the uncertainty associated with the correction of the field in the AFM tip–ferroelectric thin-film configuration. As for the case of the periodic potential, these expressions are valid if the size of the nucleus is smaller than the thickness of the sample. Otherwise, one of the dimensions of the nucleus should be replaced by the thickness, transforming a two-dimensional interface into a one-dimensional line. A crucial difference between the periodic and the disordered cases is that creep due to disorder can still exist in the one-dimensional situation, contrary to the periodic case. Note that the question of whether the films should be considered as one- or two-dimensional depends on which mechanism controls the nucleus. A film could thus be in the one-dimensional limit for the periodic potential, thereby invalidating the periodic potential as a possible origin for the creep process, and still be in the two-dimensional limit for the disorder provided that the size of the nucleus due to disorder remains smaller than the thickness of the film. Although creep is still present in the one-dimensional disordered case, the value of the exponent μ depends on the dimension. Using the values for E_c and L_c we obtained, we can estimate the size of the critical nucleus for the creep process and compare it with that found for the Miller–Weinreich formulation. In our system, the applied field is a function of the distance r away from the tip center. Using the largest possible (random-field) value of ζ

we find L_{creep} to vary between 0.2 and 1 nm in the thinnest films (29.0–51.0 nm), and 0.2 and 2.5 nm in the thickest films (95.0–130.0 nm). We note that the formalism used in the section on incommensurate pinning of the domain wall was developed in particular to describe linear domain walls, with an applied force, and therefore domain-wall creep, perpendicular to the wall. However, in the case of the circular domains we investigated, $L_{\mathrm{creep}} \sim 0.01r$, where r is the radius of the domain, so the approximation of a linear domain wall seems reasonable.

7 Experimental Observation of Domain-Wall Roughness

Although the studies of domain-wall dynamics allowed us to determine that indeed disorder, rather than a commensurate pinning potential, was the mechanism governing the observed radial creep of domain walls in epitaxial thin films, questions about the exact nature of this disorder remained open. In order to ascertain the precise physics of the pinned domain walls and also the possible role of the long-range dipolar interactions that exist in ferroelectric materials, a direct analysis of the static domain-wall configuration was performed, allowing the roughness exponent ζ and the effective domain-wall dimensionality d_{eff} to be extracted. To measure domain-wall roughness, we wrote linear domain structures with alternating polarization by applying alternating $\pm$ writing voltages while scanning the AFM tip in contact with the film, then imaged the resulting domain walls with the maximum resolution of our experimental setup ($\sim$ 2–5 nm), allowing us to extract the correlation function of relative displacements $B(L)$. As shown in Fig. 8 for the three different films used, we observe the expected power-law growth of $B(L)$ at short length scales,[12] comparable to the $\sim$ 50–100 nm film thickness, followed by saturation of $B(L)$ in the 100–1000 nm^2 range, indicating the absence of large-scale relaxation of the domain walls at ambient conditions from their initial straight configuration determined by the AFM tip position during writing.

[12] We note that that the observed power-law growth nonetheless extends out to length scales above the resolution limit determined by the tip size ($\sim$ 5 nm) and its interaction with the ferroelectric film, where inherent noise in the AFM measurement could give rise to artefacts such as spurious correlations at short lenght scales ($\sim$ 10–20 nm). We specifically chose a minimal pixel size of 5–10 nm (depending on the two image sizes used) to try and minimize the contribution of such artefacts, with most of our data points for the correlation thus being taken over greater scales. For the correlation function of relative displacements at ambient conditions, we observe the power-law growth behavior from which we derive the 2.5 effective dimensionality out to length scales of the order of 100 nm (6–16 pixel scales), well into the limit where the effects of small length scale noise can be safely disregarded. Moreover, we clearly demonstrate the reproducibility of the imaging of particular nanoscale features in multiple sequential length scans of the same domain wall.

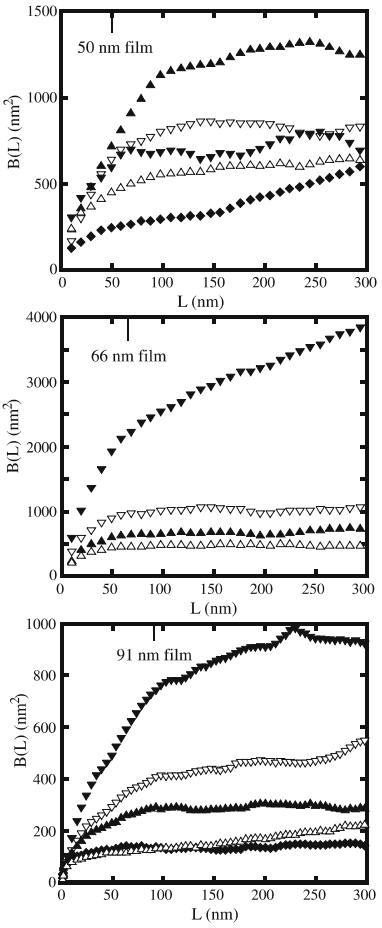

Fig. 8. Average displacement correlation function $B(L)$ for different sets of ferroelectric domain walls in 50-, 66- and 91-nm thick $PbZr_{0.2}Ti_{0.8}O_3$ films, shown out to $L = 300\,\text{nm}$. Power-law growth of $B(L)$ is observed at short length scales, followed by saturation, suggesting a nonequilibrium configuration at large L ((**a**) and (**c**) after [9])

At ambient conditions, no relaxation from this flat as-written configuration at large L was apparent over an observation period of one month [9], indicating that room-temperature thermal activation alone is not sufficient to equilibrate the domain walls over their entire length. These results are in agreement with our previous studies [3,8] in which both linear and nanoscopic circular domains remained completely stable over 1–5 month observation periods. Such high stability is inherent to the physics of an elastic disordered system, where energy barriers between different metastable states diverge as the electric field driving domain-wall motion goes to zero, which makes relax-

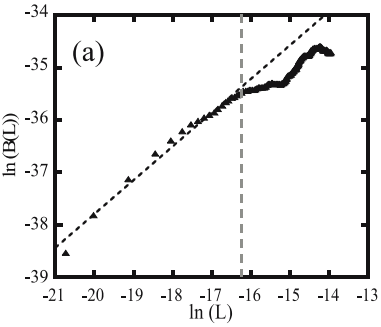

Fig. 9. Typical ln–ln plot of $B(L)$. Fitting the linear part of the curve (left of the vertical line) gives 2ζ. Average values of the characteristic roughness exponent ζ extracted from the equilibrium portion of the $B(L)$ data are 0.26, 0.29 and 0.22 in the 50-, 66- and 91-nm thick $PbZr_{0.2}Ti_{0.8}O_3$ samples, respectively (figure after [9]).

ation exceedingly slow. In fact, we believe that even the relaxation leading to the observed power-law growth of $B(L)$ at smaller length scales is not purely thermal, but occurs due to subcritical stray fields during the writing process itself. When the direction of the applied electric field is reversed to form the alternating domain structure, the neighboring region already written with the opposite polarity nonetheless experiences the resulting electric field, allowing the domain wall to locally reach an equilibrium configuration. To ensure that domain-wall relaxation was not hindered by the pinning planes of the lattice potential in the ferroelectric films [10, 45], we also wrote sets of domain walls at different orientations with respect to the crystalline axes. We found no correlation between the roughness of domain walls and their orientation in the crystal. This result is in agreement with the analysis of the previous section, pointing out the negligible role of the commensurate potential compared to the effects of disorder.

From the short length scale power-law growth of $B(L)$, we extract a value for the roughness exponent ζ, characterizing the roughness of the domain wall in the random-manifold regime where an interface individually optimizes its energy with respect to the disorder potential landscape. As shown in Fig. 9, a linear fit of the lower part of the $\ln(B(L))$ vs. $\ln(L)$ curve allows 2ζ to be determined. Average values of $\zeta \sim 0.26$, 0.29 and 0.22 were obtained for the 50, 66 and 91 nm thick films, respectively.

In addition to the investigations of static domain-wall roughness described above, we independently measured domain-wall dynamics in each film, obtaining values of 0.59, 0.58 and 0.51 for the dynamical exponent μ in the 50-, 66- and 91-nm thick films, respectively.[13]

[13] These μ values are lower than the three values measured in [7], but consistent with all the subsequent measurements performed on nine other films, all grown under similar conditions.

8 Domain Walls in the Presence of Random-Bond Disorder and Dipolar Interactions

In this section we show how these data, analyzed in the theoretical framework of a disordered elastic system, provide information on the microscopic mechanism governing domain-wall behavior. The direct measurement of domain-wall roughness clearly rules out the lattice potential as a dominant source of pinning. In that case, the walls would have been flat with $B(L) \sim a^2$, where the lattice spacing $a \sim 4\,\text{Å}$ is the period of the pinning potential [10]. Given the stability and reproducibility of the wall position over time, the effect of thermal relaxation on the observed increase of $B(L)$ can also be ruled out. The measured roughness must thus be attributed to disorder. As discussed in Sect. 3, for random-bond disorder, the roughness exponent $\zeta_{\text{RB}} = 2/3$ in $d_{\text{eff}} = 1$ and $\zeta_{\text{RB}} \sim 0.2084(4 - d_{\text{eff}})$ for other dimensions, while for random-field disorder $\zeta_{\text{RF}} = (4 - d_{\text{eff}})/3$. Should the wall be described by standard (short-range) elasticity, d_{eff} in the above formulas is simply the dimension d of the domain wall ($d = 1$ for a line, $d = 2$ for a sheet). However, in ferroelectrics the stiffness of the domain walls and thus their elasticity under deformations in the direction of polarization is different from that for deformations perpendicular to the direction of polarization because of long-range dipolar interactions. The elastic energy (expressed in reciprocal space) thus contains not only a short-range term $H = \frac{1}{2}\sum_q C_{\text{el}}(q)u^*(q)u(q)$ with $C_{\text{el}} = \sigma_{\text{w}}q^2$ but also a correction term due to the dipolar interaction $C_{\text{dp}} = \frac{2P_{\text{s}}^2}{\epsilon_0\epsilon}\frac{q_y^2}{q} + \frac{P_{\text{s}}^2\xi}{\epsilon_0\epsilon}\left(\frac{-3}{4}q_x^2 + \frac{1}{8}q^2\right)$ where y is the direction of the polarization, P is the ferroelectric polarization and ϵ and ϵ_0 are the relative and vacuum dielectric constants. Because q_y now scales as $q_y \sim q_x^{3/2}$, the effective dimension d_{eff} to use in the above formulas is $d_{\text{eff}} = (3d - 1)/2$ [42, 46]. Using the above expressions for the roughness exponent we see that the measured $\zeta \sim 0.26$ value would give $d_{\text{eff}} \geq 3$ for random-field disorder, ruling out this scenario. On the other hand, random-bond disorder would give $d_{\text{eff}} \sim 2.5$–2.9, a much more satisfactory value, which is compatible with a scenario of two-dimensional walls (sheets) in random-bond disorder with long-range dipolar interactions.

This conclusion can be independently verified by the dynamic measurements, since the creep exponent μ is related to the static roughness exponent ζ via $\mu = \frac{d_{\text{eff}} - 2 + 2\zeta}{2 - \zeta}$. The values of these two exponents from the independent static and dynamic measurements can therefore be used to calculate d_{eff}. For the 50-, 66- and 91-nm thick films we find $d_{\text{eff}} = 2.4$, 2.5 and 2.5, respectively, in good agreement with the expected theoretical value for a two-dimensional elastic interface in the presence of disorder and dipolar interactions. Taken together, these two independent analyses provide strong evidence that the pinning in thin ferroelectric films is indeed due to disorder in the random-bond universality class. Note that for the short-range domain-wall relaxation observed, the walls are in the two-dimensional limit. However, if equilibrium

domain-wall roughness could be measured for larger L, a crossover to one-dimensional behavior would be expected, with a roughness exponent $\zeta = 2/3$.

9 Recent Studies of Ferroelectric Domain-Wall Dynamics

Until recently, detailed nanoscopic experimental studies of ferroelectric domain walls have been relatively rare. However, the available, and continually expanding technological tools permitting direct access to individual ferroelectric domains at the necessary scales have resulted in significant interest in the subject. In bulk single crystals of lithium niobate, recent work has focused on the ultrahigh-voltage regime leading to "domain breakdown", the formation of filamentous equilibrium length scale domains by rapid forward growth [47]. In the framework of an elastic disordered system, as mentioned in Sect. 3 subcritical domain-wall motion was probed in single-crystal films of triglycine sulfate [34], where thermally activated domain growth and dynamic scaling in agreement with predictions for random-bond disorder were independently observed, concurrently with our studies of the same phenomena in $PbZr_{0.2}Ti_{0.8}O_3$. In triglycine sulfate films, where the disorder potential appears to be relatively weak, the effects of line tension due to domain curvature and thermal evolution even at ambient temperature can be readily accessed [35], in contrast to the epitaxial $PbZr_{0.2}Ti_{0.8}O_3$ films, which show much higher domain stability [48]. Subsequent nanoscopic AFM studies of ferroelectric domains in lithium niobate [40, 49] also showed a similar linear dependence of domain size on the magnitude of the applied voltage, and an exponential dependence of domain-wall velocity on the applied electric field, using the charged-sphere model for the tip, as described in [7]. Domain-wall creep was also accessed by susceptibility measurements in single crystals of periodically poled potassium titanate phosphate [50] and potassium hydride phosphate [51], eliminating many of the possible effects of grain boundaries and other macroscopic defects present in sol-gel films. In these studies, the authors indirectly probe domain-wall behavior in both subcritical and sliding regimes, and find critical exponents, in agreement with quenched random-field models for an elastic interface. More experimental observations in both single crystals and epitaxial thin films, focusing especially on the microscopic nature of the disorder and its interaction with domain walls, would obviously be very useful. In this respect, promising new techniques, such as time-resolved X-ray microdiffraction, allowing ferroelectric domain-wall motion to be accessed in real time,[14] could yield interesting results.

[14] private communication with A. Grigoriev (2005)

10 Conclusions

Using the unprecedented control and precision provided by AFM, we were able to study the growth of individual nanoscale ferroelectric domains in epitaxial thin films, investigating the static and dynamic behavior of domain walls. Our studies demonstrate that domain-wall motion in ferroelectric thin films is a creep process in which $v \propto \exp(-\beta U_c(E_c/E)^{\mu})$, with a dynamical exponent $\mu \sim 0.6$. This process controls the lateral growth of domains in low electric fields applied by an AFM tip. A detailed analysis of the possible microscopic origins of the observed domain-wall creep suggests that it is the result of competition between elastic behavior and pinning in a disorder potential. The reduced dimensionality of our thin films compared to the size of the critical nucleus precludes pinning in the commensurate potential of the crystal itself as the mechanism for the nonlinear field dependence of the velocity. All the domains show high stability (up to 4 months for the longest-duration experiments), inherently explained by the physics of a system in which elasticity and pinning by a disorder potential compete, leading to glassy behavior in the presence of low electric fields. In addition, we were able to extract the power-law growth of the correlation function of relative displacement $B(L) \propto \left(\frac{L}{L_c}\right)^{2\zeta}$ from the short length scale roughness configuration of domain walls, with a static roughness exponent $\zeta \sim 0.2$. Combining these two independent results, a value of 2.5 was obtained for the effective dimensionality d_{eff}, in very good agreement with theoretical predictions for 2-dimensional elastic interfaces in the presence of random-bond disorder and dipolar interactions. However, many intriguing questions about these low-dimensionality systems remain open: the possibility of 1-dimensional behavior at higher length scales, a greater role of the commensurate lattice potential in films where the disorder potential is weaker, and the thermal response of the system are all potential research avenues. The precise control of the crystalline quality and thickness possible with current oxide growth techniques, as well as the nanoscale resolution provided by atomic force microscopy, make epitaxial ferroelectric perovskite thin films a useful and readily accessible model system for the study of elastic interfaces in disordered media, and we hope will be the focus of many future studies.

Acknowledgements

The authors would like to thank X. Hong and C. H. Ahn for many useful discussions. This work was supported by the Swiss National Science Foundation through the National Center of Competence in Research "Materials with Novel Electronic Properties-MaNEP" and Division II. Further support was provided by the New Energy and Industrial Technology Development Organization (NEDO) and the European Science Foundation (THIOX).

References

[1] J. F. Scott, C. A. P. de Araujo: Ferroelectric memories, Science **246**, 1400 (1989) 339

[2] R. Waser, A. Rüdiger: Ferroelectrics: Pushing towards the digital storage limit, Nature Mater. **3**, 81 (2004) 339

[3] A. K. S. Kumar, P. Paruch, J. M. Triscone, W. Daniau, S. Ballandras, L. Pellegrino, D. Marré, T. Tybell: High-frequency surface acoustic wave device based on thin-film piezoelectric interdigital transducers, Appl. Phys. Lett. **85**, 1757 (2004) 339, 355

[4] C. Caliendo, I. Fratoddi, M. V. Russo: Sensitivity of a platinum-polyyne-based sensor to low relative humidity and chemical vapors, Appl. Phys. Lett. **80**, 4849 (2002) 339

[5] T. Giamarchi, A. B. Kolton, A. Rosso: Dynamics of disordered elastic systems, in M. C. Miguel, J. M. Rubi (Eds.): *Jamming, Yielding and Irreversible Deformation in Condensed Matter* (Springer, Berlin 2006) p. 91, cond-mat/0503437 340, 343

[6] G. Blatter, M. V. Feigel'man, V. B. Geshkenbein, A. I. Larkin, V. M. Vinokur: Vortices in high-temperature superconductors, Rev. Mod. Phys. **66**, 1125 (1994) 340, 341, 343, 344, 348

[7] T. Tybell, P. Paruch, T. Giamarchi, J.-M. Triscone: Domain wall creep in epitaxial ferroelectric $Pb(Zr_{0.2}Ti_{0.8})O_3$ thin films, Phys. Rev. Lett. **89**, 097601 (2002) 340, 341, 356, 358

[8] P. Paruch, T. Giamarchi, T. Tybell, J.-M. Triscone: Nanoscale studies of domain wall motion in ferroelectric thin films, J. Appl. Phys. 100, 051608 (2006) 340, 342, 353, 355

[9] P. Paruch, T. Giamarchi, J.-M. Triscone: Domain wall roughness in epitaxial ferroelectric $Pb(Zr_{0.2}Ti_{0.8})O_3$ thin films, Phys. Rev. Lett. **94**, 197601 (2005) 340, 355, 356

[10] B. Meyer, D. Vanderbilt: Ab initio study of ferroelectronic domain walls in $PbTiO_3$, Phys. Rev. B **65**, 104111 (2002) 340, 349, 356, 357

[11] T. Nattermann, S. Scheidl: Vortex glass phases in type-II superconductors, Adv. Phys. **49**, 607 (2000) 341, 344

[12] T. Giamarchi, S. Bhattacharya: Vortex phases, in C. Berthier, et al. (Eds.): *High Magnetic Fields: Applications in Condensed Matter Physics and Spectroscopy* (Springer, Berlin 2002) p. 314, cond-mat/0111052 341, 344

[13] G. Grüner: The dynamics of charge density waves, Rev. Mod. Phys. **60**, 1129 (1988) 341

[14] T. Nattermann, S. Brazovskii: Pinning and sliding of driven elastic systems: From domain walls to charge density waves, Adv. Phys. **53**, 177 (2004) 341

[15] E. Y. Andrei, G. Deville, D. C. Glattli, F. I. B. Williams, E. Paris, B. Etienne: Observation of a magnetically induced wigner solid, Phys. Rev. Lett. **60**, 2765 (1988) 341

[16] T. Giamarchi: Electronic glasses, in S. I. di Fisica (Ed.): *Quantum Phenomena in Mesoscopic System* (IOS, Amsterdam 2003) cond-mat/0403531 341

[17] M. Kardar: Dynamic scaling phenomena in growth processes, Physica B **221**, 60 (1996) 341

[18] D. Wilkinson, J. F. Willemsen: Invasion percolation: A new form of percolation theory, J. Phys. A **16**, 3365 (1983) 341

[19] S. Lemerle, J. Ferré, C. Chappert, V. Mathet, T. Giamarchi, P. Le Doussal: Domain wall creep in an ising ultrathin magnetic film, Phys. Rev. Lett. **80**, 849 (1998) 342, 344
[20] V. Repain, M. Bauer, J. P. Jamet, J. Ferré, A. Mougin, C. Chappert, H. Bernas: Creep motion of a magnetic wall: Avalanche size divergence, Europhys. Lett. **68**, 460 (2004) 342
[21] D. A. Huse, C. L. Henley: Pinning and roughening of domain walls in ising systems due to random impurities, Phys. Rev. Lett. **54**, 2708 (1985) 343
[22] M. Kardar, D. R. Nelson: Commensurate-incommensurate transitions with quenched random impurities, Phys. Rev. Lett. **55**, 1157 (1985) 343
[23] D. A. Huse, C. L. Henley, D. S. Fisher: Huse, Henley and Fisher respond., Phys. Rev. Lett. **55**, 2924 (1985) 343
[24] D. E. Wolf, J. Kertész: Surface width exponents for three- and four-dimensional eden growth, Europhys. Lett. **4**, 651 (1987) 343
[25] B. M. Forrest, L. H. Tang: Surface roughening in a hypercube-stacking model, Phys. Rev. Lett. **64**, 1405 (1990) 343
[26] P. W. Anderson, Y. B. Kim: Hard superconductivity: Theory of the motion of Abrikosov flux lines, Rev. Mod. Phys. **36**, 39 (1964) 343
[27] L. B. Ioffe, V. M. Vinokur: Dynamics of interfaces and dislocations in disordered media, J. Phys. C **20**, 6149 (1987) 343
[28] T. Nattermann: Interface roughening in systems with quenched random impurities, Europhys. Lett. **4**, 1241 (1987) 343
[29] P. Chauve, T. Giamarchi, P. Le Doussal: Creep and depinning in disordered media, Phys. Rev. B **62**, 6241 (2000) 343
[30] D. T. Fuchs, E. Zeldov, T. Tamegai, S. Ooi, M. Rappaport, H. Shtrikman: Possible new vortex matter phases in $Bi_2Sr_2CaCu_2O_8$, Phys. Rev. Lett. **80**, 4971 (1998) 344
[31] W. J. Merz: Domain formation and domain wall motions in ferroelectric $BaTiO_3$ single crystals, Phys. Rev. **95**, 690 (1954) 344, 347
[32] F. Fatuzzo, W. J. Merz: Switching mechanism in triglycine sulfate and other ferroelectrics, Phys. Rev. **116**, 61 (1959) 344, 347
[33] R. C. Miller, G. Weinreich: Mechanism for the sidewise motion of 180° domain walls in barium titanate, Phys. Rev. **117**, 1460 (1960) 344, 347, 348, 349, 350
[34] V. Likodimos, M. Labardi, M. Allegrini: Kinetics of ferroelectric domains investigated by scanning force microscopy, Phys. Rev. B **61**, 14440 (2000) 344, 358
[35] V. Likodimos, M. Labardi, M. Allegrini: Domain pattern formation and kinetics on ferroelectric surfaces under thermal cycling using scanning force microscopy, Phys. Rev. B **66**, 024104 (2002) 344, 358
[36] D. Damjanovic: Logarithmic frequency dependence of the piezoelectric effect due to pinning of ferroelectric-ferroelastic domain walls, Phys. Rev. B **55**, R649 (1997) 344
[37] D. V. Taylor, D. Damjanovic: Domain wall pinning contribution to the nonlinear dielectric permittivity in $Pb(Zr,Ti)O_3$ thin films, Appl. Phys. Lett. **73**, 2045 (1998) 344
[38] V. Mueller, Y. Shchur, H. Beige, S. Mattauch, J. Glinnemann, G. Heger: Dielectric dispersion due to weak domain wall pinning in RbH_2PO_4, Phys. Rev. B **65**, 134102 (2002) 344

[39] P. Paruch, T. Tybell, J.-M. Triscone: Nanoscale control of ferroelectric polarization and domain size in epitaxial $PbZr_{0.2}Ti_{0.8}O_3$ thin films, Appl. Phys. Lett. **79**, 530 (2001) 344
[40] K. Terabe, M. Nakamura, S. Takekawa, K. Kitamura, S. Higuchi, Y. Gotoh, Y. Cho: Microscale to nanoscale ferroelectric domain and surface engineering of a near-stoichiometric $LiNbO_3$ crystal, Appl. Phys. Lett. **82**, 433 (2003) 344, 358
[41] S. V. Kalinin, D. A. Bonnell: Local potential and polarization screening on ferroelectric surfaces, Phys. Rev. B **63**, 125411 (2001) 347
[42] T. Emig, T. Nattermann: Disorder driven roughening transitions of elastic manifolds and periodic elastic media, Eur. Phys. J. B **8**, 525 (1999) 351, 357
[43] A. I. Larkin: Effect of inhomogeneities on structure of mixed state of superconductors, Sov. Phys. JETP **31**, 784 (1970) 351
[44] A. I. Larkin, Y. N. Ovchinnikov: Pinning in type-II superconductors, J. Low Temp. Phys **34**, 409 (1979) 351
[45] S. Pöykkö, D. J. Chadi: Ab initio study of 180° domain wall energy and structure in $PbTiO_3$, Appl. Phys. Lett. **75**, 2830 (1999) 356
[46] T. Nattermann: The incommensurate-commensurate transition in random-field model, J. Phys. C **16**, 4125 (1983) 357
[47] M. Molotskii, A. Agronin, P. Urenski, M. Shvebelman, G. Rosenman, Y. Rosenwaks: Ferroelectric domain breakdown, Phys. Rev. Lett. **90**, 107601 (2003) 358
[48] P. Paruch, J.-M. Triscone: High-temperature ferroelectric domain stability in epitaxial $PbZr_{0.2}Ti) \cdot 8\,O_3$ thin films, Appl. Phys. Lett. **88**, 162907 (2006) 358
[49] R. J. Rodriguez, A. J. Nemanich, A. Kingon, A. Gruverman, S. V. Kalinin, K. Terabe, X. Y. Liu, K. Kitamura: Domain growth kinetics in lithium niobate single crystals studied by piezoresponse force microscopy, Appl. Phys. Lett. **012906** (2005) 358
[50] T. Braun, W. Kleeman, J. Dec, P. A. Thomas: Creep and relaxation dynamics of domain walls in periodically poled $KTiOPO_4$, Phys. Rev. Lett. **94**, 117601 (2005) 358
[51] D. R. Taylor, J. T. Love, G. J. Topping, J. G. A. Dane: Crossover from pure to random-field critical susceptibility in $KH_2As_xP_{1-x}O_4$, Phys. Rev. B **72**, 052109 (2005) 358

Index

APPENDIX A – Landau Free-Energy Coefficients

Long-Qing Chen

Department of Materials Science and Engineering,
The Pennsylvania State University, University Park, Pennsylvania 16802 USA

The thermodynamics of ferroelectrics is usually described by the phenomenological Landau–Devonshire theory. Using the free energy for the unpolarized and unstrained crystal as the reference, the free energy of a ferroelectric crystal as a function of strain and polarization can be written as (see, e.g., [1])

$$\begin{aligned} F(\varepsilon, P) = & \frac{1}{2}\alpha_{ij}P_iP_j + \frac{1}{3}\beta_{ijk}P_iP_jP_k + \frac{1}{4}\gamma_{ijkl}P_iP_jP_kP_l \\ & + \frac{1}{5}\delta_{ijklm}P_iP_jP_kP_lP_m + \frac{1}{6}\omega_{ijklmn}P_iP_jP_kP_lP_mP_n \\ & + \frac{1}{2}c_{ijkl}\varepsilon_{ij}\varepsilon_{kl} - a_{ijk}\varepsilon_{ij}P_k - \frac{1}{2}q_{ijkl}\varepsilon_{ij}P_kP_l + \cdots , \end{aligned} \tag{1}$$

where α_{ij}, β_{ijk}, γ_{ijkl}, δ_{ijklm}, and ω_{ijklmn} are the phenomenological Landau–Devonshire coefficients, and c_{ijkl}, a_{ijk}, and q_{ijkl} are the elastic, piezoelectric, and electrostrictive constant tensors, respectively. If the parent phase is centrosymmetrical, all odd terms are absent:

$$\begin{aligned} F(\varepsilon, P) = & \frac{1}{2}\alpha_{ij}P_iP_j + \frac{1}{4}\gamma_{ijkl}P_iP_jP_kP_l + \frac{1}{6}\omega_{ijklmn}P_iP_jP_kP_lP_mP_n \\ & + \frac{1}{2}c_{ijkl}\varepsilon_{ij}\epsilon_{kl} - \frac{1}{2}q_{ijkl}\varepsilon_{ij}P_kP_l + \cdots . \end{aligned} \tag{2}$$

In (2), the set of coefficients, α, γ and ω, in the Helmholtz free energy correspond to those measured under a clamped boundary condition.

Under the stress-free boundary condition, the macroscopic shape change of a crystal due to the ferroelectric phase transition is described by the spontaneous strain that can be obtained through the derivative of the Helmholtz free energy (2) with respect to strain, i.e.,

$$\sigma_{ij} = c_{ijkl}\varepsilon^0_{kl} - \frac{1}{2}q_{ijkl}P_kP_l = 0 . \tag{3}$$

Solving (3) for strain, we have

$$\varepsilon^0_{kl} = \frac{1}{2}s_{ijkl}q_{klmn}P_mP_n = Q_{ijmn}P_mP_n , \tag{4}$$

where s_{sijkl} is the elastic compliance tensor and

$$Q_{ijmn} = \frac{1}{2}s_{ijkl}q_{klmn} . \tag{5}$$

K. Rabe, C. H. Ahn, J.-M. Triscone (Eds.): Physics of Ferroelectrics: A Modern Perspective,
Topics Appl. Physics **105**, 363–372 (2007)

Substituting the spontaneous strain (4) back into the free-energy expression (2), we have

$$G(P) = \frac{1}{2}\alpha_{ij}P_iP_j + \frac{1}{4}\left(\gamma_{ijkl} - \frac{1}{2}s_{mnor}q_{mnij}q_{orkl}\right)P_iP_jP_kP_l + \frac{1}{6}\omega_{ijklmn}P_iP_jP_kP_lP_mP_n + \cdots, \tag{6}$$

or

$$G(P) = \frac{1}{2}\alpha_{ij}P_iP_j + \frac{1}{4}\left(\gamma_{ijkl} - 2c_{mnor}Q_{mnij}Q_{orkl}\right)P_iP_jP_kP_l + \frac{1}{6}\omega_{ijklmn}P_iP_jP_kP_lP_mP_n + \cdots. \tag{7}$$

The fourth-order coefficients are different for the clamped (2) and stress-free (7) boundary conditions, and they are related by

$$\gamma'_{ijkl} = \gamma_{ijkl} - \frac{1}{2}s_{mnor}q_{mnij}q_{orkl} = \gamma_{ijkl} - 2c_{mnor}Q_{mnij}Q_{orkl}, \tag{8}$$

where γ'_{ijkl} is the fourth-order coefficient for the stress-free boundary condition. In general, experimentally determined coefficients correspond to γ' since it is usually easier to do measurements under stress-free boundary conditions.

In the following, the Landau–Devonshire coefficients are presented for a number of oxides, including the well-studied systems $BaTiO_3$, $SrTiO_3$ and PZT, collected from the open literature. All the data were provided for the stress-free boundary conditions unless noted otherwise. They are all in SI units with the temperature in K.

1 $BaTiO_3$

For $BaTiO_3$, a Landau–Devonshire potential up to eighth order has been employed,

$$\begin{aligned} G(P_x,P_y,P_z) = {} & \alpha_1\left(P_x^2+P_y^2+P_z^2\right)+\alpha_{11}\left(P_x^4+P_y^4+P_z^4\right) \\ & +\alpha_{12}\left(P_x^2P_y^2+P_y^2P_z^2+P_x^2P_z^2\right)+\alpha_{111}\left(P_x^6+P_y^6+P_z^6\right) \\ & +\alpha_{112}\left[P_x^2\left(P_y^4+P_z^4\right)+P_y^2\left(P_x^4+P_z^4\right)+P_z^2\left(P_x^4+P_y^4\right)\right] \\ & +\alpha_{123}P_x^2P_y^2P_z^2+\alpha_{1111}\left(P_x^8+P_y^8+P_z^8\right) \\ & +\alpha_{1112}\left[P_x^6\left(P_y^2+P_z^2\right)+P_y^6\left(P_x^2+P_z^2\right)+P_z^6\left(P_x^2+P_y^2\right)\right] \\ & +\alpha_{1122}\left(P_x^4P_y^4+P_y^4P_z^4+P_x^4P_z^4\right) \\ & +\alpha_{1123}\left(P_x^4P_y^2P_z^2+P_y^4P_z^2P_x^2+P_z^4P_x^2P_y^2\right). \end{aligned} \tag{9}$$

Two sets of coefficients for (9) are given in Table 1. The elastic and electrostrictive coefficients are listed separately in Table 2. The free energy under

Table 1. Landau–Devonshire potential coefficients for $BaTiO_3$ (SI units and T in K)

Coefficients	Sixth order [2, 3]	Eight-order [4]
$\alpha_1(10^5\,\mathrm{C}^{-2}\cdot\mathrm{m}^2\cdot\mathrm{N})$	$3.34(T-381)$	$4.124(T-388)$
$\alpha_{11}(10^6\,\mathrm{C}^{-4}\cdot\mathrm{m}^6\cdot\mathrm{N})$	$4.69(T-393)-202$	-209.7
$\alpha_{12}(10^8\,\mathrm{C}^{-4}\cdot\mathrm{m}^6\cdot\mathrm{N})$	3.23	7.974
$\alpha_{111}(10^7\,\mathrm{C}^{-6}\cdot\mathrm{m}^{10}\cdot\mathrm{N})$	$-5.52(T-120)+276$	129.4
$\alpha_{112}(10^9\,\mathrm{C}^{-6}\cdot\mathrm{m}^{10}\cdot\mathrm{N})$	4.47	-1.950
$\alpha_{123}(10^9\,\mathrm{C}^{-6}\cdot\mathrm{m}^{10}\cdot\mathrm{N})$	4.919	-2.5009
$\alpha_{1111}(10^{10}\mathrm{C}^{-8}\cdot\mathrm{m}^{14}\cdot\mathrm{N})$	0.0	3.863
$\alpha_{1112}(10^{10}\mathrm{C}^{-8}\cdot\mathrm{m}^{14}\cdot\mathrm{N})$	0.0	2.529
$\alpha_{1122}(10^{10}\mathrm{C}^{-8}\cdot\mathrm{m}^{14}\cdot\mathrm{N})$	0.0	1.637
$\alpha_{1123}(10^{10}\mathrm{C}^{-8}\cdot\mathrm{m}^{14}\cdot\mathrm{N})$	0.0	1.367

Table 2. Elastic and electrostrictive coefficients of $BaTiO_3$ [1, 3, 5–9]. (Note that additional data on the elastic constants of $BaTiO_3$ can be found in [1] and [8])

$c_{11}(10^{11}\,\mathrm{N}\cdot\mathrm{m}^{-2})$	1.78
$c_{12}(10^{11}\,\mathrm{N}\cdot\mathrm{m}^{-2})$	0.964
$c_{44}(10^{11}\,\mathrm{N}\cdot\mathrm{m}^{-2})$	1.22
$Q_{11}(\mathrm{C}^{-2}\cdot\mathrm{m}^4)$	0.10, 0.11
$Q_{12}(\mathrm{C}^{-2}\cdot\mathrm{m}^4)$	-0.034, -0.045
$Q_{44}(\mathrm{C}^{-2}\cdot\mathrm{m}^4)$	0.029, 0.059

a constant strain, ε, can be easily obtained from the above stress-free free energy through

$$F(P,\varepsilon) = G(P,\sigma=0) + \frac{1}{2}c_{ijkl}\left(\varepsilon_{ij}-\varepsilon^0_{ij}\right)\left(\varepsilon_{kl}-\varepsilon^0_{kl}\right)\,, \tag{10}$$

where ε^0_{ij} is given by (4).

2 $SrTiO_3$

To describe both the proper ferroelectric and the antiferroelastic distortion (AFD) structural transition in $SrTiO_3$ requires both the spontaneous polarization $P=(P_x,P_y,P_z)$ and the structural order parameter $\mathbf{q}=(q_1,q_2,q_3)$ as the order parameters.

The structural order parameter represents the linear oxygen displacement that corresponds to simultaneous out-of-phase rotations of oxygen octahedra around one of their four-fold symmetry axes. A fourth-order Landau polyno-

mial as a function of the polarization and structural order parameter is given by

$$G(P_i, q_i) = A_{ij}P_iP_j + A_{ijkl}P_iP_jP_kP_l + B_{ij}q_iq_j + B_{ijkl}q_iq_jq_kq_l + C_{ijkl}P_iP_jq_kq_l\,, \tag{11}$$

where $i, j = x, y, z$, A_{ijkl}, B_{ijkl} and C_{ijkl} are constants and A_{ij} and B_{ij} are functions of temperature. Keeping only the terms allowed by the cubic symmetry of the $SrTiO_3$ crystal, one has

$$\begin{aligned} G = {} & \alpha_1\left(P_x^2 + P_y^2 + P_z^2\right) + \alpha_{11}\left(P_x^4 + P_y^4 + P_z^4\right) \\ & + \alpha_{12}\left(P_x^2P_y^2 + P_y^2P_z^2 + P_x^2P_z^2\right) + \beta_1\left(q_x^2 + q_y^2 + q_z^2\right) \\ & + \beta_{11}\left(q_x^4 + q_y^4 + q_z^4\right) + \beta_{12}\left(q_x^2q_y^2 + q_y^2q_z^2 + q_x^2q_z^2\right) \\ & - t_{11}\left(P_x^2q_x^2 + P_y^2q_y^4 + P_z^2q_z^2\right) \\ & - t_{12}\Big[P_x^2\left(q_y^2 + q_z^2\right) + P_y^2\left(q_x^2 + q_z^2\right) + P_z^2\left(q_x^2 + q_y^2\right)\Big] \\ & - t_{44}\left(P_xP_yq_xq_y + P_yP_zq_yq_z + P_zP_xq_zq_x\right), \end{aligned} \tag{12}$$

where α_{ij}, β_{ij}, and t_{ij} are assumed to be constants and α_1 and β_1 depend on temperature.

ε_{ij}^0 is the stress-free strain or the transformation strain as a result of the structural and/or ferroelectric transitions,

$$\varepsilon_{ij}^0 = Q_{ijkl}p_kp_l + \Lambda_{ijkl}q_kq_l\,, \tag{13}$$

in which Q_{ijkl} and Λ_{ijkl} represent, respectively, the electrostrictive coefficient and the linear–quadratic coupling coefficient between the strain and structural order parameter.

3 $PbZr_{1-x}Ti_xO_3$ (PZT)

Existing experimental measurements in PZT have been fitted to a sixth-order polynomial:

$$\begin{aligned} G(P_x, P_y, P_z) = {} & \alpha_1\left(P_x^2 + P_y^2 + P_z^2\right) + \alpha_{11}\left(P_x^4 + P_y^4 + P_z^4\right) \\ & + \alpha_{12}\left(P_x^2P_y^2 + P_y^2P_z^2 + P_x^2P_z^2\right) + \alpha_{111}\left(P_x^6 + P_y^6 + P_z^6\right) \\ & + \alpha_{112}\Big[P_x^2\left(P_y^4 + P_z^4\right) + P_y^2\left(P_x^4 + P_z^4\right) + P_z^2\left(P_x^4 + P_y^4\right)\Big] \\ & + \alpha_{123}P_x^2P_y^2P_z^2\,. \end{aligned} \tag{14}$$

Table 3. Landau–Devonshire coefficients for $SrTiO_3$ (SI units and T in K) [10–15]

$\alpha_1(10^5\,\mathrm{C}^{-2}\cdot\mathrm{m}^2\cdot\mathrm{N})$	$405\,[\coth(54/T)-\coth(54/30)]$
	$263.5\,[\coth(42/T)-0.90476]\,, T<50\,\mathrm{K}$
	$7.37(T-28), T>70\,\mathrm{K}$
	$7.06(T-35.5), T>100\,\mathrm{K}$
$\alpha_{11}(10^9\,\mathrm{C}^{-4}\cdot\mathrm{m}^6\cdot\mathrm{N})$	1.70
$\alpha_{12}(10^9\,\mathrm{C}^{-4}\cdot\mathrm{m}^6\cdot\mathrm{N})$	1.37
$Q_{11}\ (\mathrm{C}^{-2}\cdot\mathrm{m}^4)$	$0.0457, 0.08, 0.066$
$Q_{12}\ (\mathrm{C}^{-2}\cdot\mathrm{m}^4)$	$-0.0135, -0.015, -0.013$
$Q_{44}\ (\mathrm{C}^{-2}\cdot\mathrm{m}^4)$	0.00957
$c_{11}\ (10^{11}\,\mathrm{N}\cdot\mathrm{m}^{-2})$	$3.156, 3.181, 3.36, 3.48$
$c_{12}\ (10^{11}\,\mathrm{N}\cdot\mathrm{m}^{-2})$	$1.01, 1.025, 1.027, 1.07$
$c_{44}\ (10^{11}\,\mathrm{N}\cdot\mathrm{m}^{-2})$	$1.19, 1.215, 1.236, 1.27$
$\beta_1\ (10^{29}\,\mathrm{N}\cdot\mathrm{m}^{-4})$	$1.32\,[\coth(145/T)-\coth(145/105)]$
$\beta_{11}\ (10^{50}\,\mathrm{N}\cdot\mathrm{m}^{-4})$	$1.69, 1.58, 1.20, 0.996$
$\beta_{12}\ (10^{50}\,\mathrm{N}\cdot\mathrm{m}^{-6})$	$3.88, 3.78, 2.88, 2.73$
$\Lambda_{11}10^{18}\,\mathrm{m}^{-2}$	$8.7, 14.7, 9.32, 8.35$
$\Lambda_{12}10^{18}\,\mathrm{m}^{-2}$	$-7.8, -7.34, -6.4, -5.54$
$\Lambda_{44}10^{18}\,\mathrm{m}^{-2}$	$-9.2, -9.88, -6.93, -7.56$
$t_{11}\ (10^{29}\,\mathrm{C}^{-2}\cdot\mathrm{N})$	$-1.74, -2.10$
$t_{12}\ (10^{29}\,\mathrm{C}^{-2}\cdot\mathrm{N})$	$-0.755, -0.845$
$t_{44}\ (10^{29}\,\mathrm{C}^{-2}\cdot\mathrm{N})$	5.85

The corresponding Landau–Devonshire and electrostrictive coefficients are given by [16–20]

$$\alpha_1 = (T-T_0)/2\varepsilon_0 C_0, \varepsilon = 8.85\times10^{-12},$$
$$\alpha_{11} = (10.612-22.655x+10.955x^2)\times10^{13}/C_0,$$
$$\alpha_{111} = (12.026-17.296x+9.179x^2)\times10^{13}/C_0,$$
$$\alpha_{112} = (4.2904-3.3754x+58.804e^{-29.397x})\times10^{14}/C_0,$$
$$\alpha_{12} = \eta_1/3-\alpha_{11}, \alpha_{123} = \eta_2-3\alpha_{111}-6\alpha_{112},$$
$$\eta_1 = \left[2.6213+0.42743x-(9.6+0.012501x)\,e^{-12.6x}\right]\times10^{14}/C_0,$$
$$\eta_2 = \left[0.887-0.76973x+(16.225-0.088651x)\,e^{-21.255x}\right]\times10^{15}/C_0,$$
$$T_0 = 462.63+843.4x-2105.5x^2+4041.8x^3-3828.3x^4+1337.8x^5,$$
$$C_0 = \left(\frac{2.1716}{1+500.05(x-0.5)^2}+0.131x+2.01\right)\times10^5\,,\ \text{when } 0.0\le x\le0.5,$$
$$C_0 = \left(\frac{2.8339}{1+126.56(x-0.5)^2}+1.4132\right)\times10^5\,,\ \text{when } 0.5\le x\le1.0,$$
$$Q_{11} = \frac{0.029578}{1+200(x-0.5)^2}+0.042796x+0.045624,$$
$$Q_{12} = \frac{0.026568}{1+200(x-0.5)^2}+0.012093x-0.013386,$$
$$Q_{44} = \frac{1}{2}\left(\frac{0.025325}{1+200(x-0.5)^2}+0.020857x+0.046147\right),$$

Table 4. The compliance tensor was estimated for a number of compositions [21]

Ti content x	0.4	0.5	0.6	0.7	0.8	0.9
s_{11} ($10^{-12}\,\mathrm{m^2/N}$)	8.8	10.5	8.6	8.4	8.2	8.1
s_{12} ($10^{-12}\,\mathrm{m^2/N}$)	−2.9	−3.7	−2.8	−2.7	−2.6	−2.5
s_{44} ($10^{-12}\,\mathrm{m^2/N}$)	24.6	28.7	21.2	17.5	14.4	12

Table 5. Landau–Devonshire potential coefficients for $PbTiO_3$ (SI units and T in K) [16, 22]

$\alpha_1(10^5\,\mathrm{C^{-2}\cdot m^2N})$	$3.8(T-752)$	Q_{11} ($\mathrm{C^{-2}\cdot m^4}$)	0.089
$\alpha_{11}(10^8\,\mathrm{C^{-4}\cdot m^6N})$	−0.73	Q_{12} ($\mathrm{C^{-2}\cdot m^4}$)	−0.026
$\alpha_{12}(10^8\,\mathrm{C^{-4}\cdot m^6N})$	7.5	Q_{44} ($\mathrm{C^{-2}\cdot m^4}$)	0.0675
$\alpha_{111}(10^8\,\mathrm{C^{-6}\cdot m^{10}N})$	2.6	s_{11} ($\mathrm{C^{-12}\cdot m^2/N}$)	8.0
$\alpha_{112}(10^8\,\mathrm{C^{-6}\cdot m^{10}N})$	6.1	s_{12} ($\mathrm{C^{-12}\cdot m^2/N}$)	−2.5
$\alpha_{123}(10^8\,\mathrm{C^{-6}\cdot m^{10}N})$	−37	s_{44} ($\mathrm{C^{-12}\cdot m^2/N}$)	9.0

where x is the mole fraction of $PbTiO_3$ in PZT. The units are SI with the temperature in K. The elastic compliance values for a number of selected compositions were provided in [21] (Table 4).

4 $PbTiO_3$

For pure $PbTiO_3$, the free-energy coefficients are given in Table 5.

5 $LiTaO_3$ and $LiNbO_3$

$LiNbO_3$ and $LiTaO_3$ belong to the $\bar{3}m$ point group. Denoting the crystallographic uniaxial directions as the z-axis, the free-energy expansion is given by [23]

$$\begin{aligned} F = & -\frac{\alpha_1}{2}P_z^2 + \frac{\alpha_2}{4}P_z^4 + \frac{\alpha_3}{2}\left(P_x^2 + P_y^2\right) + \beta_1\varepsilon_3^2 + \beta_2\left(\varepsilon_1+\varepsilon_2\right)^2 \\ & +\beta_3\left[\left(\varepsilon_1-\varepsilon_2\right)^2 + \varepsilon_6^2\right] + \beta_4\varepsilon_3\left(\varepsilon_1+\varepsilon_2\right) + \beta_5\left(\varepsilon_4^2+\varepsilon_5^2\right) \\ & +\beta_6\left[\left(\varepsilon_1-\varepsilon_2\right)\varepsilon_4 + \varepsilon_5\varepsilon_6\right] + \gamma_1\left(\varepsilon_1+\varepsilon_2\right)P_z^2 + \gamma_2\varepsilon_3 P_z^2 \\ & +\gamma_3\left[\left(\varepsilon_1-\varepsilon_2\right)P_yP_z + \varepsilon_6P_xP_z\right] + \gamma_4\left(\varepsilon_5P_xP_z + \varepsilon_4P_yP_z\right), \end{aligned} \tag{15}$$

where electrostriction terms that do not involve the primary z component of polarization have been ignored. The corresponding coefficients are given in Table 6 (noted that in this example, α_i are determined at constant zero strain rather than constant zero stress).

Table 6. Landau-Devonshire potential coefficients for $LiTaO_3$ and $LiNbO_3$ [23]

Coefficients	$LiTaO_3$	$LiNbO_3$
$\alpha_1(10^9\,\mathrm{C}^{-2}\cdot\mathrm{N}\cdot\mathrm{m}^2)$	1.256	2.012
$\alpha_2(10^9\,\mathrm{C}^{-2}\cdot\mathrm{N}\cdot\mathrm{m}^2)$	5.043	3.608
$\alpha_3(10^9\,\mathrm{C}^{-2}\cdot\mathrm{N}\cdot\mathrm{m}^2)$	2.22	1.345
$\beta_1(10^{10}\,\mathrm{N}\cdot\mathrm{m}^{-2})$	13.55	12.25
$\beta_2(10^{10}\,\mathrm{N}\cdot\mathrm{m}^{-2})$	6.475	6.4
$\beta_3(10^{10}\,\mathrm{N}\cdot\mathrm{m}^{-2})$	4.925	3.75
$\beta_4(10^{10}\,\mathrm{N}\cdot\mathrm{m}^{-2})$	7.4	7.5
$\beta_5(10^{10}\,\mathrm{N}\cdot\mathrm{m}^{-2})$	4.8	3
$\beta_6(10^{10}\,\mathrm{N}\cdot\mathrm{m}^{-2})$	−1.2	0.9
$\gamma_1(10^9\,\mathrm{C}^{-2}\cdot\mathrm{N}\cdot\mathrm{m}^2)$	−0.202	0.216
$\gamma_2(10^9\,\mathrm{C}^{-2}\cdot\mathrm{N}\cdot\mathrm{m}^2)$	1.317	1.848
$\gamma_3(10^9\,\mathrm{C}^{-2}\cdot\mathrm{N}\cdot\mathrm{m}^2)$	−2.824	−0.33
$\gamma_4(10^9\,\mathrm{C}^{-2}\cdot\mathrm{N}\cdot\mathrm{m}^2)$	4.992	3.9

Table 7. Landau-Devonshire potential coefficients for $SrBi_2Nb_2O_9$ (E is Young's modulus and ν is Poisson's ratio) [24]

$\alpha_1(10^6\,\mathrm{C}^{-2}\cdot\mathrm{m}^2\cdot\mathrm{N})$	$1.03(T-663)$	$Q_{11}(10^{-3}\,\mathrm{C}^{-2}\cdot\mathrm{m}^4)$	0.385
$\alpha_{11}(10^8\,\mathrm{C}^{-4}\cdot\mathrm{m}^6\cdot\mathrm{N})$	−0.94	$Q_{12}(10^{-3}\,\mathrm{C}^{-2}\cdot\mathrm{m}^4)$	−0.04
$\alpha_{12}(10^8\,\mathrm{C}^{-4}\cdot\mathrm{m}^6\cdot\mathrm{N})$	9.38	$Q_{44}(10^{-3}\,\mathrm{C}^{-2}\cdot\mathrm{m}^4)$	0.05
$\alpha_{111}(10^8\,\mathrm{C}^{-6}\cdot\mathrm{m}^{10}\cdot\mathrm{N})$	11.8	$E(10^{-12}\,\mathrm{m}^2/\mathrm{N})$	0.29
$\alpha_{112}(10^8\,\mathrm{C}^{-6}\cdot\mathrm{m}^{10}\cdot\mathrm{N})$	23.6	$\nu(10^{-12}\,\mathrm{m}^2/\mathrm{N})$	0.31

6 $Sr_{0.8}Bi_{2.2}Ta_2O_9$

For $Sr_{0.8}Bi_{2.2}Ta_2O_9$, the only existing Landau free-energy description is a single double-well potential [25],

$$F = -2.03\times10^5(T-620)P^2 + 3.75\times10^9P^4\,, \tag{16}$$

where T is in K and F and P are in SI units.

7 $SrBi_2Nb_2O_9$

The thermodynamics of $SrBi_2Nb_2O_9$ ferroelectrics was modeled using the following free-energy function,

$$\begin{aligned} G(P_x,P_y) = {} & \alpha_1\left(P_x^2+P_y^2\right)+\alpha_{11}\left(P_x^4+P_y^4\right)+\alpha_{12}P_x^2P_y^2 \\ & +\alpha_{111}\left(P_x^6+P_y^6\right)+\alpha_{112}\left(P_x^2P_y^4+P_y^2P_x^4\right)\,. \end{aligned} \tag{17}$$

Due to the lack of experimental data in this system, many of the coefficients were estimated (Table 7).

References

[1] F. Jona, G. Shirane: *Ferroelectric Crystals* (Macmillan, New York 1962) 363, 365

[2] W. R. Buessem, L. E. Cross, A. K. Goswami: Phenomenological theory of high permittivity in fine-grained barium titanate, J. Am. Ceram. Soc. **49**, 33 (1966) 365

[3] J. Bell, L. E. Cross: A phenomenological Gibbs function for $BaTiO_3$ giving correct E-field dependence of all ferroelectric phase-changes, Ferroelectrics **59**, 197–203 (1984) 365

[4] Y. L. Li, L. E. Cross, L. Q. Chen: A phenomenological thermodynamic potential for $BaTiO_3$ single crystals, J. Appl. Phys. **98**, 064101 (2005) 365

[5] A. F. Devonshire: Theory of barium titanate, Philos. Mag. **42**, 1065–1079 (1951) 365

[6] D. Berlincourt, H. Jaffe: Elastic and piezoelectric coefficients of single-crystal barium titanate, Phys. Rev. **111**, 143–148 (1958) 365

[7] T. Yamada: Electromechanical properties of oxygen-octahedra ferroelectric crystals, J. Appl. Phys. **43**, 328 (1972) 365

[8] Landolt-Börnstein: *Numerical Data and Functional Relationships in Science and Technology, Group III*, vol. 36a, New Series (Springer, Heidelberg 2002) pp. 23–26 365

[9] A. Yamanaka, M. Kataoka, Y. Inaba, K. Inoue, B. Hehlen, E. Courtens: Evidence for competing orderings in strontium titanate from hyper-Raman scattering spectroscopy, Europhys. Lett. **50**, 688–694 (2000) 365

[10] N. A. Pertsev, A. K. Tagantsev, N. Setter: Phase transitions and strain-induced ferroelectricity in $SrTiO_3$ epitaxial thin films, Phys. Rev. B **61**, R825–829 (2000) 367

[11] N. A. Pertsev, A. K. Tagantsev, N. Setter: Erratum: Phase transitions and strain-induced ferroelectricity in $SrTiO_3$ epitaxial thin films, Phys. Rev. B **65**, 219901 (2002) 367

[12] H. Uwe, T. Sakudo: Stress-induced ferroelectricity and soft phonon modes in $SrTiO_3$, Phys. Rev. B **13**, 271 (1976) 367

[13] A. K. Tagantsev, E. Courtens, L. Arzel: Prediction of a low-temperature ferroelectric instability in antiphase domain boundaries of strontium titanate, Phys. Rev. B **64**, 224107 (2001) 367

[14] J. C. Slonczewski, H. Thomas: Interaction of elastic strain with the structural transition of strontium titanate, Phys. Rev. B **1**, 3599 (1970) 367

[15] R. O. Bell, G. Rupprecht: Elastic constants of strontium titanate, Phys. Rev. **129**, 90 (1963) 367

[16] M. J. Haun, E. Furman, S. J. Jang, H. A. McKinstry, L. E. Cross: Thermodynamic theory of $PbTiO_3$, J. Appl. Phys. **62**, 3331–3338 (1987) 367, 368

[17] M. J. Haun: Ph.D. thesis, The Pennsylvania State University (1988) 367

[18] M. J. Haun, E. Furman, S. J. Jang, L. E. Cross: Thermodynamic theory of the lead zirconate-titanate solid-solution system: 1. Phenomenology, Ferroelectrics **99**, 13–25 (1989) 367

[19] M. J. Haun, E. Furman, H. A. McKinstry, L. E. Cross: Thermodynamic theory of the lead zirconate-titanate solid-solution system: 2. Tricritical behavior, Ferroelectrics **99**, 27–44 (1989) 367

[20] M. J. Haun, Z. Q. Zhuang, E. Furman, S. J. Jang, L. E. Cross: Thermodynamic theory of the lead zirconate-titanate solid-solution system: 3. Curie constant and 6th-order polarization interaction dielectric stiffness coefficients, Ferroelectrics **99**, 45–54 (1989) 367
[21] N. A. Pertsev, V. G. Kukhar, H. Kohlstedt, R. Waser: Phase diagrams and physical properties of single-domain epitaxial $Pb(Zr_{1-x}Ti_x)O_3$ thin films, Phys. Rev. B **67**, 054107 (2003) 368
[22] N. A. Pertsev, A. G. Zembilgotov, A. K. Tagantsev: Effect of mechanical boundary conditions on phase diagrams of epitaxial ferroelectric thin films, Phys. Rev. Lett. **80**, 1988–1991 (1998) 368
[23] D. A. Scrymgeour, V. Gopalan, A. Itagi, A. Saxena, P. J. Swart: Phenomenological theory of a single domain wall in uniaxial trigonal ferroelectrics: Lithium niobate and lithium tantalate, Phys. Rev. B **71**, 184110 (2005) 368, 369
[24] Y. L. Li, L. Q. Chen, G. Asayama, D. G. Schlom, M. A. Zurbuchen, S. K. Streiffer: Ferroelectric domain structures in $SrBi_2Nb_2O_9$ epitaxial thin films: Electron microscopy and phase-field simulations, J. Appl. Phys. **95**, 6332–6340 (2004) 369
[25] M. Tanaka, K. Hironaka, A. Onodera: Thermal behavior of ferroelectric switching properties of SBT thin films, Ferroelectrics **266**, 103–110 (2002) 369

Index

Appendix B – Material–Substrate Combinations Tables

Céline Lichtensteiger and Matthew Dawber

DPMC – University of Geneva
24 Quai Ernest Ansermet, 1211 Geneva 4, Switzerland
celine.lichtensteiger@physics.unige.ch
matthew.dawber@physics.unige.ch

A key appeal of epitaxial ferroelectric thin films is that they possess a variety of functional properties. It is found that these properties can be varied according to the choice of substrate used for the growth. The choice is not unlimited, however, some materials being much easier to grow on one substrate than another (usually because of a more similar crystal lattice). The technique used for the deposition can also be important in determining the properties of the resulting film. Motivated by this we present here some tables in which we have collected a limited number of references that detail the properties of particular material/substrate combinations when a particular growth method has been used. We hope this will be useful to researchers as an aid in assessing the best approach to take when they are contemplating embarking on a research project that calls for a ferroelectric thin film with specific properties. Neither the materials, nor the references, are intended to be in any way a complete list. In terms of materials we have listed mainly the materials that have been studied quite extensively as epitaxial thin films, and are therefore reasonably well characterized ($BaTiO_3$,$BiFeO_3$, $Pb(Mg_{1/3}Nb_{2/3})O_3$–$PbTiO_3$ (PMN–PT), $Pb(Zr,Ti)O_3$ (PZT), and some layered perovksite ferroelectrics). Furthermore, we have reproduced for convenience the table that first appears in the chapter by *Agham-Bayan Posadas* in this volume that gives the lattice parameters of a number of the most popular substrate materials.

K. Rabe, C. H. Ahn, J.-M. Triscone (Eds.): Physics of Ferroelectrics: A Modern Perspective,
Topics Appl. Physics **105**, 373–384 (2007)

Table 1. $BaTiO_3$.

Substrate	**Lattice mismatch**	**Growth method**	**Structure**	**Lattice parameters (Å)**	**Thickness (nm)**	**Electrode**	**TC (K)**	P (mC/cm^2)	**Ref.**
$KTaO_3$	−0.28 %	PLD	tetragonal	a=3.995 c=4.041	40		∼ 500		[1]
$SrTiO_3$	−2.18 %	PLD	tetragonal	a=3.905 c=4.27	30	$SrRuO_3$		∼ 35	[2]
(110)$GdScO_3$	−1.0 %	MBE	tetragonal	a=3.964 c=4.0693	200		∼ 900		[3]
(110)$DyScO_3$	−1.7 %	MBE	tetragonal	a=3.940 c=4.0953			∼ 810		[3]
$GdScO_3$	−1.0 %	PLD	tetragonal	a=3.965 c=4.0692	200	$SrRuO_3$	∼ 690	∼ 50	[3]
$DyScO_3$	−1.7 %	PLD	tetragonal	a=3.939 c=4.0989	50	$SrRuO_3$	∼ 950		[3]
$SrTiO_3$	−2.18 %	PLD	tetragonal	a=3.905 c=4.27	30	$SrRuO_3$		∼ 43	[4]

Table 2. $Pb(Mg_{1/3}Nb_{2/3})O_3$-$PbTiO_3$ (PMN-PT).

Materials	Substrate	Growth method	Thickness (nm)	Bottom electrode	Top electrode	ϵ_r	T_C	P (mC/cm^2)	E_c (kv/cm)	Ref.
PMN-PT	(100)$SrTiO_3$	MOCVD	> 2000	(100)$SrRuO_3$						[5]
0.67PMN–0.33PT	(001)$SrTiO_3$	90° offaxis magnetron sputtering	520	epitaxial $SrRuO_3$		1000	145 °C (single crystals: 150 °C)	20	25	[6]
0.9PMN–0.1PT	(001)$LaAlO_3$, (La,Sr)(Al,Ta)O_3, $SrTiO_3$ and MgO	PLD	100	40 nm $La_{0.5}Sr_{0.5}CoO_3$	40 nm $La_{0.5}Sr_{0.5}CoO_3$					[7]
PMN	(100)$SrTiO_3$	MOCVD		(100)$SrRuO_3$		1100		16		[8]
0.7PMN–0.3PT	$LaAlO_3$	PLD		$SrRuO_3$		1500		13–20		[9]

Table 3. $BiFeO_3$.

Materials	Substrate	Growth method	Structure	Lattice parameters (Å)	Thickness (nm)
$BiFeO_3$	(001)$SrTiO_3$	PLD		$a = 3.905$ $c = 4.104$	35 and 20
$BiFeO_3$	(001)$SrTiO_3$	PLD		$a = 3.905$ $c = 4.073$	5
$BiFeO_3$	(001)$SrTiO_3$	PLD	slightly modified MA type monoclinic structure	$c = 3.997$ $\beta = 89.2°$ $a_{MA}/\sqrt{2} = 3.907$ $b_{MA}/\sqrt{2} = 3.973$	200
$BiFeO_3$	$(111)_c$, $(001)_c$ and $(110)_c SrTiO_3$	PLD	rhombohedral	$d\langle 001\rangle = 3.959$	200
$BiFeO_3$	Si substrate with $SrTiO_3$ as a template layer	PLD	monoclinic	out-of-plane lattice constant 3.95 Å (pseudocubic unit)	200
$BiFeO_3$	$(001)_c$ single crystal $SrTiO_3$	PLD	significant epitaxial constraint, monoclinically distorted from the rhombohedral structure	$d\langle 001\rangle = 4.001$ $d\langle 101\rangle = 2.792$ $d\langle 111\rangle = 2.278$	200
$BiFeO_3$	$(110)_c$ single crystal $SrTiO_3$	PLD	significant epitaxial constraint, monoclinically distorted from the rhombohedral structure	$d\langle 001\rangle = 3.984$ $d\langle 101\rangle = 2.828$ $d\langle 111\rangle = 2.307$	200
$BiFeO_3$	$(111)_c$ single crystal $SrTiO_3$	PLD	unconstrained single domaine with rhombohedral crystal structure as bulk	$d\langle 001\rangle = 3.959$ $d\langle 101\rangle = 2.810$ $d\langle 111\rangle = 2.306$	200
$BiFeO_3$	(001)$SrTiO_3$	PLD	tetragonal-like with the c-axis normal to the substrate surface, with a small monoclinic distortion of about 0.5°	$a = 3.935$ and $c = 4.0$ in a 200 nm sample	50–500
$(Bi_{0.7}Ba_{0.3})(Fe_{0.7}Ti_{0.3})O_3$	Nb-doped $SrTiO_3$(100)	PLD			

Table 3. continued

Bottom electrode	Top electrode	ϵ_r	d_{33} (pm/V)	P ($\mu C/cm^2$)	Saturation magn.	ME coef. (dE/dH)	Ref.
$La_{2/3}Sr_{1/3}MnO_3$ buffer layer 11 nm							[10]
$La_{2/3}Sr_{1/3}MnO_3$ buffer layer 11 nm							[10]
$SrRuO_3$ 500 Å							[11]
$SrRuO_3$ 500 Å				100	0.6 emu/g		[12]
$SrRuO_3$ 200 Å	Pt	≈ 170	≈ 60 (≈ 30 for 100 nm and ≈ 120 for 400 nm)	45			[13]
$SrRuO_3$ 500 Å				55			[14]
$SrRuO_3$ 500 Å				80			[14]
$SrRuO_3$ 500 Å				100			[14]
$SrRuO_3$			70	50–60	5–150 emu/cm^{-3}	3 V/cm. Oe at zero field	[15]
				2.5	0.2 emu/g		[16]

Table 4. $Pb(Zr,Ti)O_3$ (PZT)

Materials	Substrate	Lattice mismatch	Growth method	Structure	Lattice parameters (Å)
$Pb(Zr,Ti)O_3$ 45/55					
$Pb(Zr,Ti)O_3$ 52/48	Si + 100 Å epitaxial (001) $SrTiO_3$ by MBE		off-axis RF magnetron sputtering (600 °C – oxygen pressure of 400 m Torr)		
$Pb(Zr,Ti)O_3$ 52/48	$SrTiO_3$(100)	3.35 %	off-axis RF magnetron sputtering (600 °C – oxygen pressure of 400 m Torr)		
$PbTiO_3$	$SrTiO_3$(100)		hydrothermal method at 150 °C	*c* domain and small amount of *a* domain	4.13 for *c*-domains and 3.92 for *a* domains
$Pb(Zr,Ti)O_3$	(100)$SrTiO_3$		MOCVD		
$PbTiO_3$	$SrTiO_3$(110) etched 0.5 mm thick		hydrothermal method at 150 °C	*c*-axis	4.158
$PbTiO_3$	$SrTiO_3$(110) etched 0.5 mm thick		hydrothermal method at 150 °C	*c*-axis	4.153
$Pb(Zr,Ti)O_3$	$SrTiO_3$(100)		hydrothermal method at 150 °C		4.134
$Pb(Zr,Ti)O_3$ 40/60	Si[100] with $SrTiO_3$ template layer (15 nm)		sol-gel and spin-coating	polycrys-talline	
$Pb(Zr,Ti)O_3$ 40/60	Si[100] with $SrTiO_3$ template layer (15 nm)		sol-gel and spin-coating	(001)-texture	
$Pb(Zr,Ti)O_3$ 40/60	Si[100] with $SrTiO_3$ template layer (15 nm)		sol-gel and spin-coating	epitaxial	Si(011) = 3.82 $SrTiO_3$(001) = 3.09 LSCO = 3.85 PZT = 4.04
$Pb(Zr,Ti)O_3$	platinum-buffered silicon		screen printing		
$Pb(Zr,Ti)O_3$ 52/48	(100) $SrTiO_3$ and (100) Si with an yttria stabilized zirconia buffer layer		90° off-axis sputtering		

Table 4. continued

Thickness (nm)	Bottom electrode	Top electrode	d_{33}	P (mC/cm^2)	Ec (kv/cm)	Ref.
400	$SrRuO_3$	200 mm diameter polycrystalline $SrRuO_3$	53 pm/V	52		[17]
400–4000	epitaxial $SrRuO_3$ by 90° off-axis RF magnetron sputtering		330 pm/V			[18]
	epitaxial $SrRuO_3$ by 90° off-axis RF magnetron sputtering		200 pm/V			[18]
430	50 nm $SrRuO_3$ RF sputtered	platinum 0.083 mm^2 evaporated	97 pC/N	60		[19]
> 2000	(100)$SrRuO_3$					[5]
100	50 nm $SrRuO_3$ RF sputtered	platinum 0.083 mm^2 evaporated		96.5	290	[6]
50	50 nm $SrRuO_3$ RF sputtered	platinum 0.083 mm^2 evaporated				[6]
500	$SrRuO_3$ RF sputtered epitaxial 200 nm			19.2	21.8	[7]
120	$(La_{0.5}Sr_{0.5})CoO_3$ 70 nm RF sputtering	$(La_{0.5}Sr_{0.5})CoO_3$ 70 nm RF sputtering - Pt	25 pm/V			[20]
	$(La_{0.5}Sr_{0.5})CoO_3$ 70 nm RF sputtering	$(La_{0.5}Sr_{0.5})CoO_3$ 70 nm RF sputtering - Pt	75 pm/V			[20]
	$(La_{0.5}Sr_{0.5})CoO_3$ 70 nm RF sputtering	$(La_{0.5}Sr_{0.5})CoO_3$ 70 nm RF sputtering - Pt	125 pm/V			[20]
up to 12 000			50 pC/N	2.5	40	[21]
						[22]

Table 5. Bismuth-layered ferroelectric perovskites

Materials	Substrate	Growth method	Structure
$SrBi_4Ti_4O_{15}$	(111)Pt/TiO_2/SiO_2/(100)Si	MOCVD	single-axis, *c*-oriented
$SrBi_2Ta_2O_9$	$SrZrO_3$/$(Y_2O_3)_x(ZrO_2)_{1-x}$/Si	PLD	*a*-axis oriented
$SrBi_2Ta_2O_9$	Pt/Ti/SiO_2/Si(100)	PLD	polycrystalline
$Bi_{4-x}Nd_xTi_3O_{12}$	(100)$SrTiO_3$	PLD	epitaxial (001)-oriented
$Bi_{4-x}Nd_xTi_3O_{12}$	(110)$SrTiO_3$	PLD	epitaxial (118)-oriented
$Bi_{4-x}Nd_xTi_3O_{12}$	(111)$SrTiO_3$	PLD	epitaxial (104)-oriented
$Bi_{3.25}La_{0.75}Ti_3O_{12}$	yttria-stabilized zirconia-bufferedSi(100)	PLD	epitaxially twinned a axis oriented
$Bi_{3.25}La_{0.75}Ti_3O_{12}$	(001)$SrTiO_3$	PLD	epitaxially twinned (001)-oriented
$Bi_{3.25}La_{0.75}Ti_3O_{12}$	(011)$SrTiO_3$	PLD	epitaxially twinned (118)-oriented
$Bi_{3.25}La_{0.75}Ti_3O_{12}$	(111)$SrTiO_3$	PLD	epitaxially twinned (104)-oriented
$SrBi_2Ta_2O_9$	MgO(100)	PLD	*c*-oriented
$SrBi_2Ta_2O_9$	(110)-oriented $SrLaGaO_4$ (lattice parameters: tetragonal, $a = 0.3843$ nm, $c = 1.268$ nm)	PLD	epitaxial with a mix of (100) and (116) orientations
$SrBi_2Ta_2O_9$	(100)- $SrPrGaO_4$ (tetragonal, $a = 0.3813$ nm, $c = 1.253$ nm)	PLD	(001)-oriented
$SrBi_2Ta_2O_9$	MgO(111)/YSZ(100)/Si(100)	PLD	non-*c*-axis-oriented, (103) orientation
$Sr_{0.8}Bi_{2.2}Ta_2O_9$	(001)$LaAlO_3$	PLD	epitaxial growth along (001)
$SrBi_2Nb_2O_9$	(110)$SrTiO_3$	PLD	nearly phase pure epitaxial films with the *c*-axis of the films at 45° with respect to the substrate normal
$SrBi_2Nb_2O_9$	(111)-oriented $SrTiO_3$	PLD	(103)-oriented, nearly phase pure epitaxial film
$SrBi_2Ta_2O_9$	(001) $LaAlO_3$ (cubic $a = 3.81$ Å), (001)$SrTiO_3$ (cubic $a = 3.905$ Å) and (001)$LaAlO_3$–Sr_2AlTaO_6 (cubic $a = 7.737$ Å)	PLD	(001)-oriented
$SrBi_2Ta_2O_9$	(001)-oriented Nb-doped $SrTiO_3$	PLD	(001)-oriented
$SrBi_2Ta_2O_9$	(011)-oriented Nb-doped $SrTiO_3$	PLD	(116)-oriented
$SrBi_2Ta_2O_9$	(111)-oriented Nb-doped $SrTiO_3$	PLD	(103)-oriented
$SrBi_2Ta_2O_9$	(110) MgO	RF magnetron sputtering	orthorhombic, *a*-/*b*-axis oriented
$SrBi_2Ta_2O_9$	(100) MgO	RF magnetron sputtering	orthorhombic, *c*-axis oriented
$SrBi_2Ta_2O_9$	(100) $SrTiO_3$	MOCVD	(001)-oriented
$SrBi_2Ta_2O_9$	(110) $SrTiO_3$	MOCVD	(116)-oriented
$SrBi_2Ta_2O_9$	(001)$LaAlO_3$–Sr_2AlTaO_6 and (100)$LaSrAlO_4$	PLD	(001) and (110)

Table 5. continued

Thickness (nm)	Bottom electrode	Top electrode	ϵ_r	P (mC/cm^2)	E_c (kv/cm)	Ref.
	(100)*c*-oriented $LaNiO_3$		140			[23]
						[24]
350	Pt	gold				[25]
	$SrRuO_3$			not ferroelectric	not ferroelectric	[26]
	$SrRuO_3$			6	120	[26]
	$SrRuO_3$			20	50	[26]
	$SrRuO_3$			32		[27]
	$SrRuO_3$			0.6		[28]
	$SrRuO_3$			10.4		[28]
	$SrRuO_3$			16		[28]
100			270			[29]
						[30]
						[30]
	(111)$SrRuO_3$			5.2	76	[31]
	$LaNiO_3$		270	not ferroelectric	not ferroelectric	[32]
300	epitaxial $SrRuO_3$		235	11.4		[33]
500	epitaxial (111)$SrRuO_3$		185	15.7		[34]
100-500						[35]
			133	not ferroelectric	not ferroelectric	[36]
			155	4.8	84	[36]
			189	5.2	52	[36]
						[37]
						[37]
200	(100) $SrRuO_3$		70 at 1 kHz	not ferroelectric	not ferroelectric	[38]
200	(110) $SrRuO_3$		140 at 1 kHz	11.4	80	[38]
						[39]

Table 6. Lattice parameters and crystal structures of selected substrate materials (details and references in chapter by *Posadas*)

Material	Structure		Lattice constants
$SrTiO_3$	cubic	$> 105\,K$	$a = 3.905\,Å$
	tetragonal	$< 105\,K$	$c/a = 1.00056$
$BaTiO_3$	cubic	$> 390\,K$	$a = 4.01\,Å$
	tetragonal	$> 270\,K$	$a = 3.99\,Å$
			$c = 4.04\,Å$
	orthorhombic	$> 180\,K$	$c = 3.98\,Å$
			$a = 4.01\,Å$
	rhombohedral	$< 180\,K$	$a = 4.00\,Å$
$LaAlO_3$	cubic	$> 800\,K$	$a = 3.81\,Å$
	rhombohedral	$< 800\,K$	$a = 5.36\,Å$
			$(3.79\,Å)$
LSAT	cubic	$> 150\,K$	$a = 3.87\,Å$
	tetragonal	$< 150\,K$	$a = 5.46\,Å$
			$c = 7.73\,Å$
			$(3.86\,Å)$
$NdGaO_3$	orthorhombic		$a = 5.43\,Å$
			$b = 5.50\,Å$
			$c = 7.71\,Å$
			$(3.86\,Å)$
$LaGaO_3$	orthorhombic	$< 420\,K$	$a = 5.49\,Å$
			$b = 5.53\,Å$
			$c = 7.78\,Å$
			$(3.89\,Å)$
	rhombohedral	$> 420\,K$	$a = 3.93\,Å$
$KTaO_3$	cubic		$a = 3.99\,Å$
MgO	cubic		$a = 4.21\,Å$
$DyScO_3$	orthorhombic		$a = 5.44\,Å$
			$b = 5.71\,Å$
			$c = 7.89\,Å$
			$(3.94\,Å)$
$GdScO_3$	orthorhombic		$a = 5.49\,Å$
			$b = 5.75\,Å$
			$c = 7.93\,Å$
			$(3.97\,Å)$

References

[1] F. He, B. O. Wells: Appl. Phys. Lett. **88**, 152908 (2006) 374
[2] Y. S. Kim, et al.: Appl. Phys. Lett. **86**, 102907 (2005) 374
[3] Choi, et al.: Science **306**, 1005 (2004) 374
[4] O. S. Kim, et al.: Phys. Rev. Lett. **95**, 237602 (2000) 374
[5] S. Yokoyama: MRS Symp. Proc. **902E**, 0902–T03–29.1 (2006) 375, 379
[6] S. D. Bu, et al.: Appl. Phys. Lett. **79**, 3482 (2001) 375, 379
[7] V. Nagarajan: Appl. Phys. Lett. **77**, 438 (2000) 375, 379
[8] G. Bai, et al.: Appl. Phys. Lett. **76**, 3106 (2000) 375
[9] J.-P. Maria: J. Appl. Phys. **84**, 5147 (1998) 375
[10] H. Béa, et al.: Jpn. J. Appl. Phys. **45**, L187 (2006) 377
[11] G. Xu, et al.: Appl. Phys. Lett. **86**, 182905 (2005) 377
[12] F. Bai, et al.: Appl. Phys. Lett. **86**, 032511 (2005) 377
[13] J. Wang, et al.: Appl. Phys. Lett. **85**, 2574 (2004) 377
[14] J. Li, et al.: Appl. Phys. Lett. **84**, 5261 (2004) 377
[15] J. Wang, et al.: Science **299**, 1719 (2003) 377
[16] K. Ueda, et al.: Appl. Phys. Lett. **75**, 555 (1999) 377
[17] A. Grigoriev, et al.: PRL p. 96 (2006) 379
[18] D. M. Kim, et al.: APL p. 88 (2006) 379
[19] T. Morita, Y. Cho: APL p. 88 (2006) 379
[20] Y. Wang, et al.: Appl. Phys. Lett. **80**, 97 (2002) 379
[21] Chen: J. Appl. Phys. **77**, 3349 (1995) 379
[22] C. B. Eom, et al.: Appl. Phys. Lett. **63**, 2570 (1993) 379
[23] K. Takahashi: Chem. Vap. Deposition **12**, 136 (2006) 381
[24] D. Miu, et al.: Materials Letters **59**, 1243 (2005) 381
[25] S. Zhang, et al.: J. Cryst. Growth **262**, 348 (2004) 381
[26] A. Garg: Appl. Phys. Lett. **83** (2414) 381
[27] H. N. Lee: Science **296**, 2006 (2002) 381
[28] H. N. Lee: Appl. Phys. Lett. **80** (1040) 381
[29] K. Kotani: Jpn. J. Appl. Phys. **41**, 6790 (2002) 381
[30] H. N. Lee: Appl. Phys. Lett. **79** (2961) 381
[31] H. N. Lee: Appl. Phys. Lett. **78** (2922) 381
[32] S. Chattopadhyay: Appl. Phys. Lett. **78** (3514) 381
[33] J. Lettieri: Appl. Phys. Lett. **77** (3090) 381
[34] J. Lettieri: Appl. Phys. Lett. **76** (2937) 381
[35] J. Lettieri, et al.: Thin Solid Films **379**, 64 (2000) 381
[36] H. N. Lee: J. Appl. Phys. **88** (6658) 381
[37] S. E. Moon: Appl. Phys. Lett. **75** (2827) 381
[38] K. Ishikawa: Appl. Phys. Lett. **75** (1970) 381
[39] J. Lettieri: Appl. Phys. Lett. **73** (2923) 381

Index

Topics in Applied Physics

88 **Optical Nanotechnologies**
The Manipulation of Surface and Local Plasmons
By J. Tominaga and D. P. Tsai (Eds.) 2003, 168 Figs. XII, 212 pages

89 **Solid-State Mid-Infrared Laser Sources**
By I. T. Sorokina and K. L. Vodopyanov (Eds.) 2003, 263 Figs. XVI, 557 pages

90 **Single Quantum Dots**
Fundamentals, Applications, and New Concepts
By P. Michler (Ed.) 2003, 181 Figs. XII, 352 pages

91 **Vortex Electronis and SQUIDs**
By T. Kobayashi, H. Hayakawa, M. Tonouchi (Eds.) 2003, 259 Figs. XII, 302 pages

92 **Ultrafast Dynamical Processes in Semiconductors**
By K.-T. Tsen (Ed.) 2004, 190 Figs. XI, 400 pages

93 **Ferroelectric Random Access Memories**
Fundamentals and Applications
By H. Ishiwara, M. Okuyama, Y. Arimoto (Eds.) 2004, Approx. 200 Figs. XIV, 288 pages

94 **Silicon Photonics**
By L. Pavesi, D.J. Lockwood (Eds.) 2004, 262 Figs. XVI, 397 pages

95 **Few-Cycle Laser Pulse Generation and Its Applications**
By Franz X. Kärtner (Ed.) 2004, 209 Figs. XIV, 448 pages

96 **Femtsosecond Technology for Technical and Medical Applications**
By F. Dausinger, F. Lichtner, H. Lubatschowski (Eds.) 2004, 224 Figs. XIII 326 pages

97 **Terahertz Optoelectronics**
By K. Sakai (Ed.) 2005, 270 Figs. XIII, 387 pages

98 **Ferroelectric Thin Films**
Basic Properies and Device Physics for Memory Applications
By M. Okuyama, Y. Ishibashi (Eds.) 2005, 172 Figs. XIII, 244 pages

99 **Cryogenic Particle Detection**
By Ch. Enss (Ed.) 2005, 238 Figs. XVI, 509 pages

100 **Carbon**
The Future Material for Advanced Technology Applications
By G. Messina, S. Santangelo (Eds.) 2006, 245 Figs. XXII, 529 pages

101 **Spin Dynamics in Confined Magnetic Structures III**
By B. Hillebrands, A. Thiaville (Eds.) 2006, 164 Figs. XIV, 345 pages

102 **Quantum Computation and Information**
From Theory to Experiment
By H. Imai, M. Hayashi (Eds.) 2006, 49 Figs. XV, 281 pages

103 **Surface-Enhanced Raman Scattering**
Physics and Applications
By K. Kneipp, M. Moskovits, H. Kneipp (Eds.) 2006, 221 Figs. XVIII, 464 pages

104 **Theory of Defects in Semiconductors**
By D. A. Drabold, S. K. Estreicher (Eds.) 2007, 60 Figs. XIII, 297 pages

105 **Physics of Ferroelectrics**
A Modern Perspective
By K. Rabe, Ch. H. Ahn, J.-M. Triscone (Eds.) 2007, 129 Figs. XII, 390 pages